PREDICTION OF FLOW IN DIESEL ENGINE CYLINDERS

by

Richard James Robert Johns, B.Sc.

Thesis submitted for the degree of
Doctor of Philosophy
of the University of London and for the
Diploma of Imperial College

Mechanical Engineering Department,
Imperial College of Science and
Technology,
London. SW7 2BX

April 1980

ABSTRACT

This study describes the development and application of a theoretical method for calculating the flow and heat transfer in the cylinder of a reciprocating diesel engine.

The procedure operates by solving the partial differential equations that govern the conservation of mass, momentum and thermal energy, whilst the effects of turbulence are included by solving two additional differential equations for the turbulent kinetic energy and its dissipation rate. The complex shape of the piston bowl and time-varying dimensions of the solution domain are accommodated by formulating the equations in an axisymmetric, general curvilinear-orthogonal co-ordinate system and applying a co-ordinate transformation, such that the computational grid that is superimposed upon the flow field and used for the solution of finite-difference approximations to the differential equations, is always bounded by the cylinder head, cylinder wall and piston surfaces. The curvilinear-orthogonal grid for the piston bowl is obtained á priori by solving numerically a pair of Laplace equations for the physical co-ordinates.

The accuracy and stability of alternative methods of differencing the differential equations are investigated and recommendations are made for a scheme that is stable and reasonably accurate for the conditions found in engine cylinders.

The method is subsequently applied to 6 test cases for which experimental data are available. The results of this study indicate that good qualitative and reasonable quantitative agreement can usually be obtained, although under certain conditions, the predictions are

substantially in error. Various reasons are suggested to account for the discrepancies observed.

Finally, the flow structure in a number of diesel engine piston bowls typical of current design are analysed in depth. Here, a number of common features and differences between the flow structures in the various bowls are identified and reasons are put forward to explain these.

ACKNOWLEDGEMENTS

First and foremost, I would like to express gratitude to my supervisor, Dr. A.D. Gosman, for encouragement, guidance, suggestions and criticisms throughout this research project.

I would also like to thank other members of the Fluids Section at Imperial College, namely, Mr. A.P. Morse, Dr. A.P. Salooja, Mr. R. Watford, Dr. A.P. Watkins and Mr. M. Yianneskis for many interesting discussions and for providing experimental data.

I am indebted to past and present colleagues at Perkins Engines, including Dr. C. Goodwin, Mr. M. Hawkins, Mr. I.D. Middlemiss, Mr. A. Rogers, Mr. W. Tipler, Mr. K.L. Walker and Dr. E.A. Warman, without whose support this project would not have been possible.

Finally, I would like to thank my parents and Trudy for their support and encouragement.

CONTENTS

List of Tables

List of Figures

CHAPTER 1

INTRODUCTION

Preliminary Remarks

For many years, the engine industry has persued an approach of cut-and-try development aided by various thermo-chemical cycle simulation methods to both improve existing engines and develop new designs. These methods proved adequate when allowed to dictate their own slow evolutionary pace, but the current pressures of, on the one hand, government legislation against the emission of numerious pollutants, and on the other, from the rise in the cost of crude oil, have provided an impetus to produce cleaner and more energy-efficient engines. In the small-engine (1.5 to 6 litres) market, the direct-injection (DI) diesel engine is generally more efficient than its two main rivals, namely the indirect-injection (IDI) prechamber diesel and petrol engines using either conventional or stratified-charge combustion systems. Although the capital and maintainence costs of a diesel engine are higher than those of an equivalent conventional petrol unit, because of the heavier structure and fuel-injection equipment required for the former, in the eyes of the consumer, this is apparently outweighed by the generally lower cost of diesel fuel (with the exception of the UK), better fuel consumption and the increased reliability and time between servicing, as evidenced by the recent dramatic growth of the diesel-powered passenger car market.

During the last decade, the author's company has persued a policy of developing a more efficient, cleaner and quieter DI

combustion system. This work has been largely experimental in nature, that is, reliance has been placed on test-bed analysis of different combustion bowl shapes, swirl levels, fuel injection characteristics etc. as reported, for example, by Middlemiss (1978). It become apparent during the early stages of this program that information about the flow structure inside the cylinder would provide a greater understanding of the fuel-air mixing and combustion processes. This is particularly true for the DI combustion system as described below.

The production of nitrogen oxide (NO) during combustion is determined to a large extent by the gas temperature, as the dissociation of the oxygen molecules into atomic oxygen, required to initiate the NO formation chain reaction (Zeldovich et al, 1947), occurs only at elevated temperatures. High temperatures occur within the combustion chamber whenever the heat-release rate is large, and this in turn depends upon a number of factors which include fuel quality and quantity, the gas temperature and the fuel-air mixing process. The fuel quality and gas temperature (and to a lesser extent the pressure) determine the duration of the ignition delay period (Henein and Bolt, 1969), which is defined as the time interval between the start of injection and the start of combustion, during which the fuel mixes with the air and undergoes chemical reactions that are progressively more exothermic until at the end of this period, the mixture formed commences burning as a premixed flame (Lyn, 1963). The duration of the ignition delay is a major factor in determining the amount of fuel-air mixture in a "ready-to-burn" state and consequently the intensity of the initial

heat-release. Low cetane number fuels and/or advanced injection timings both increase the duration of the ignition delay. After this essentially premixed-burning stage, the combustion rate is governed largely by the rate of mixing of the remaining fuel and surrounding air and it is during this period that the NO is formed in fuel-lean regions (Henein, 1976). When the temperature falls during expansion, the NO concentration does not decrease to its equilibrium value but remains nearly constant (Starkman and Newall, 1967).

Reduction of the ignition delay is desirable in that it is accompanied by lower gas temperatures and reduced nitrogen oxide emissions. This can be accomplished relatively easily by retarding the start of injection; however, the advantage gained is offset by both increased smoke formation from the now longer mixing-controlled phase of the combustion process that occurs after the initial premixed burning stage, and the cycle efficiency is reduced as a result of the late burning. At retarded injection timings, it is found that an increase in the fuel-air mixing rate improves cycle efficiency as a consequence of the increased combustion rate and reduces smoke formation because of the reduction in locally fuel-rich zones within the combustion chamber (Kahn and Wang, 1973).

The re-entrant bowl piston, of which a number of designs are shown in cross-section in fig. 1.1 (taken from Middlemiss, 1978), provides a means of increasing the mixing rate due to the high velocities and turbulence levels induced in the bowl near TDC. Thus, retarded injection timings may be used to reduce the formation of nitrogen oxides without incurring the penalties of lower cycle efficiency and increased smoke.

In addition to the parameters already mentioned, a number of other factors, such as intake port design,are known to influence the combustion process by altering the air motion within the

cylinder. In the past, simple theoretical models have been constructed to analyse individual aspects of the air motion (see e.g. Fitzgeorge and Allison, 1963). However, the strong inter-relationship between different features of the flow, for example, squish-swirl interactions near TDC, prevents these models from yielding anything but the crudest of qualitative information to the development engineer, indeed, such models may on occasions provide misleading information. As an illustration of this latter point, calculations of in-cylinder swirl using the Fitzgeorge and Allison (1963) method for two different inlet ports of helical and directed designs were found to give identical swirl momentums at inlet valve closing (Brandl et al, 1979). In practice however, the performance of otherwise identical engines was found to vary dramatically when fitted with these two alternative inlet systems. The performance differences were attributed to variations in the spatial distributions of momentum within the cylinder, an aspect not addressed by the simple model. Similar changes in engine performance have been noted for other design changes (Middlemiss, 1978) and have pointed to the need to understand the underlying physics. This in turn has given rise to, on the one hand, multi-dimensional prediction methods that are capable, at least in principle, of calculating the important properties of the flow throughout the combustion chamber, and on the other, advanced measurement methods such as Laser Doppler Anemometry.

This thesis focusses attention on the theoretical aspects of in-cylinder air motion. The specific objective of this work is to develop a numerical calculation procedure for predicting the flow in engine cylinders equipped with piston bowls such as those shown in fig. 1.1, although the method developed is not necessarily

restricted to diesel engines and is equally applicable to any axisymmetric geometry.

The Present Contribution

The work presented in this thesis is concerned with developing a computer-based numerical method for solving the partial differential equations governing the conservation of mass, momentum and energy for the turbulent flow and heat transfer processes in a co-ordinate frame that allows the important features of a moving piston and complex piston bowl shapes to be included in a realistic fashion, whilst the effects of turbulence are incorporated using a contemporary two-equation turbulence model. Specifically, this work makes contributions in the following areas:

1. The formulation of the governing equations in a general curvilinear-orthogonal axisymmetric co-ordinate system that allows expansion and contraction of the solution domain in the swept volume and the accurate representation of complex piston-bowl or head geometries.
2. Discretisation of the above equations in various forms and examination of their relative accuracy and stability. Recommendations are made for a scheme offering reasonably accurate and numerically stable solutions for the conditions found in reciprocating engines.
3. Validation of the theoretical model by comparison with data from six different experiments performed by other workers and identification of the capabilities and limitations of the model.

4. Flow analyses using the new prediction method for a variety of re-entrant bowl pistons where a number of features of commonality and differences between the designs are identified.

Contents of Thesis

Chapter 2 describes both experimental and theoretical work by previous researchers. The intake-generated flow and the effects of the subsequent compression process on both the mean flow and the turbulence structure are examined. Squish and swirl are especially important aspects of the flow and these are dealt with separately. Measurements of the flow in axisymmetric engines are valuable for the purpose of validating the theoretical model developed in later chapters and a number of experiments in both axisymmetric and nearly-axisymmetric engine configurations are described. Finally, the efforts of other research groups in the sphere of multi-dimensional in-cylinder flow modelling are reviewed and the advantages and shortcomings of the physical modelling and numerical solution methods they devised are identified and compared with the method developed here.

In chapter 3, the differential equations governing the turbulent in-cylinder flow are assembled. They are first developed in a general curvilinear-orthogonal axisymmetric co-ordinate system, a contemporary two-equation model being used to represent the effects of turbulence. A co-ordinate transformation is subsequently applied which allows the solution domain to be always bounded by the cylinder head, cylinder wall and piston surfaces.

Finite difference approximations to the differential equations are derived in chapter 4 by integrating the latter over finite volumes formed by the intersection of iso-co-ordinate lines of an orthogonal grid. The orthogonal grid is obtained á priori for each geometry by solving numerically a pair of Laplace-like equations for the physical co-ordinates; this is described in Appendix 1. The difference equations are presented in a general fashion such that the fully-implicit and time-centred formulations may be easily extracted. A stability analysis of the latter is undertaken and the effects of grid spacing and time-step on the solution are quantified for both schemes for a simplified one-dimensional idealistation of the problem and a full two-dimensional turbulent calculation. Finally, an ad-hoc technique is presented for adjusting the under-relaxation factors, used in the solution of the algebraic approximations to the differential equations, to maintain stability and improve the convergence rate.

Chapter 5 describes validation of the model with six sets of experimental data obtained from various sources. These cover three cases of flow in a non-compressing model engine, in which the effects of swirl and a piston bowl are examined, two cases in a motored compressing engine both with and without a cavity in the cylinder head which is equipped with a single central valve, and lastly, comparisons with instantaneous heat flux measurements in a motored high-swirl engine with an axisymmetric cavity piston bowl but with the usual off-axis inlet valve arrangement. Finally, the simple theories of squish and swirl, described in chapter 2, are compared with predictions using the present calculation method.

In chapter 6, predictions of the effects of swirl on the flow structure in simple cylindrical-cavity piston bowls both with

and without lips are described. Also, the predicted flow structures for five different re-entrant bowl pistons are analysed in depth for conditions approximating as closely as possible those found in engines.

Finally, in chapter 7, the achievements of this study are reviewed and suggestions are made for improvements and extensions.

CHAPTER 2

SURVEY OF PREVIOUS RESEARCH

2.1 Introduction

This chapter deals with both experimental and theoretical studies of in-cylinder flows in motored engines by previous researchers. There are a number of aspects of these flows, such as for example, the intake-generated structure, squish and swirl, that can be treated in relative isolation and most studies have focussed on such specific features. Many researchers have found similar behaviour for certain of these flow phenomena, often in very different engines; where areas of agreement are found, these are indicated. There is a further body of literature concerned with fuel sprays and the combustion process; these have been omitted.

Section 2.2 of the chapter deals primarily with intake generated flow and turbulence and the subsequent compression and expansion process. This catagorisation is not exclusive however, and other aspects of the flow are reported where included in the same publication. The bulk air movements known as squish and swirl have long been identified as being of major importance, especially in Diesel engines, and both experimental studies and simple analytical tools relating to these are described in section 2.3. Measurements of the flow in axisymmetric engine cylinders are important for the validation of the predictive model developed in this thesis and are described in section 2.4. Finally, section 2.5 presents a detailed examination of multi-dimensional in-cylinder flow models developed by other researchers. One and zero dimensional models are excluded from this survey, but a summary of such models is given by Watkins (1977).

2.2 Experimental Studies of Air-Motion and Turbulence

One of the first attempts to study in-cylinder air-motion was that of Lee (1939) who introduced feathers into the intake of a motored 4-stroke engine equipped with a glass cylinder and cylinder head to permit photography. It was observed that the air motion created during intake persisted throughout compression but was suppressed soon after the start of the expansion stroke. A shrouded valve was found to cause rotation (swirl) that remained throughout the cycle.

Molchanov (1953) used a hot-wire anemometer (HWA) to measure velocities in an engine with a cylindrical disc chamber (flat cylinder head and piston). The engine was motored at 900 rev/min and results were obtained at the probe locations shown in fig. 2.1. The highest velocities were recorded near the valve and reached a maximum after 60^{o} of inlet valve opening but subsequently decayed until 30^{o} after inlet valve closure, thereafter remaining approximately constant. An apparent increase in the turbulence level near TDC of the compression stroke was noted (a similar trend was found by Witze (1976c) for a similar combustion chamber geometry but later dismissed by him as being the result of an incorrect calibration (Witze, 1979)). Compression ratio was found to have little effect on either the mean or turbulent velocities, however the insertion of anular (squish) inserts resulted in large increases in turbulence levels.

A similar cylindrical combustion chamber was used by Semenov (1958) (fig. 2.2) who extracted mean and turbulent velocities from HWA measurements by time-averaging over 24^{o} crank-angle intervals

and subsequently ensemble averaging over 20-40 engine cycles. The signal was also passed through a band-pass filter to give the spectral composition of the turbulent fluctuations. Semenov concluded that the large spatial velocity variations which he observed reflect the jet-like character of the incoming flow and the associated high velocity gradients are the main source of turbulence. Both the mean and turbulent velocities decayed during the initial part of compression, thereafter remaining relatively constant for the rest of the stroke. The energy-containing turbulent eddies were mostly in the 1 to 3 kHz frequency range during intake although during compression there was a shift toward the low-frequency part of the spectrum. The integral or macro length-scale was estimated to be of the order 1.8 to 2.2 mm during intake. The mean velocities at TDC of the compression stroke were reduced by 20% with an increase of compression ratio from 4 to 9.5, and varied with the square of the engine speed.

HWA measurements were made by Arnold et al (1972) in a motored engine with a hemispherical cylinder head and flat piston crown, shown in fig. 2.3. Both stationary and traversing probes were used to obtain measurements at points a, b and c. His results indicate a peak inlet velocity of the order 35 m/s from a stationary probe at point a with the hot-wire oriented to measure the resultant of the radial and tangential components. The mean velocities generally decreased through the latter part of valve opening and during compression although further maxima were obtained with some orientations of a masked inlet valve. In all cases however, the motion decayed during the 40^{o} crank-angle prior to TDC and remained at a low level throughout expansion. During exhaust, two maxima, lower than those during intake, were measured, and these were attributed to gas expansion through the

valve before BDC and expulsion by the piston after BDC.

James (1972) derived mean and turbulent velocities from instantaneous HWA measurements made within a simple cylindrical combustion chamber and a bowl-in-head configuration. The latter geometry and the probe positions are shown in fig. 2.4. Spacers were fitted between the cylinder head and block to investigate the effects of compression ratio. Filters were used to obtain the energy spectrum within the range 90 to 5800 Hz, the signal being time-averaged over 10^{o} crank-angle intervals and ensemble-averaged over 22 cycles. The mean velocities generally decayed throughout the compression stroke, an effect which was attributed to the extraction of energy from the mean flow by the turbulence. Before TDC, a squish velocity of 6 m/s was observed with a compression ratio of 8.88:1 and TDC piston-head clearance of 1.5 mm at 1500 rev/min for the bowl-in-head geometry. No indication of squish was found at the lower compression ratios due to the higher piston-head clearances, although reverse squish (an outward radial flow from the combustion bowl after TDC) was observed during the period 20^{o}-30^{o} ATDC. The mean velocity at TDC varied linearly with engine speed for both disc and bowl-in-head geometries. The turbulent velocity decreased by about 50% from IVC to TDC at 1450 rev/min in the cylindrical disc chamber but stayed virtually constant at the lower speed of 700 rev/min. Most of the turbulence energy was confined to frequencies below 700 Hz.

Dent and Salama (1975a, 1975b) have made velocity measurements in engines with a wedge combustion chamber of 9:1 compression ratio and in a "Heron" chamber of 8.9:1 compression ratio, shown in figs. 2.5 and 2.6 respectively. HWA was used, the temperature-corrected signal being time-averaged over 10^{o} crank-angle

intervals and ensemble averaged for 70 to 370 cycles. Results are reported for engine speeds varying between 1000 and 3500 rev/min. It was found that both mean and turbulent velocities peaked during inlet and subsequently decayed until inlet valve closure, the relative turbulence intensity (the turbulent velocity normalised by the mean velocity) remaining approximately constant during this time. In the wedge chamber, both mean and turbulent velocities increased during the compression period as a result of squish-induced motion but decayed in the 20^{o} immediately prior to TDC, an effect attributed to viscous dissipation and the increased surface to volume ratio. In the Heron chamber, where squish is not strong, the gas velocity decayed continuously from inlet valve closure until TDC of compression. The variation of the energy spectrum during the cycle for the wedge chamber showed a similar trend to that found by Semenov (1958), that is, high frequency (1-2 kHz) turbulence being generated during intake with a shift toward the lower frequencies (0.7 - 1kHz) during compression. The micro length-scale* was estimated to lie between 0.2 and 0.6 mm for both chambers at 1000 rev/min and re-analysis of the data of Semenov (1958) and James (1972), which covers compression ratios of 4:1 to 9.5:1, showed their data to lie in the range 0.2 to 0.5 mm. Further investigation using a Ricardo E6 (variable compression ratio) engine showed a reduction in spatial microscale with increasing compression ratio. In the Heron chamber the macro length-scale was found to be 3 to 4 times larger than the micro-scale at TDC.

*The macro length-scale is representative of the size of turbulent eddies that are generated by the mean flow. Eddies of this size are responsible for the Reynolds stresses (see section 3.6) and turbulent transport of the flow properties. Dissipation of turbulence occurs in the smaller (micro length-scale) eddies.

Lancaster (1976) measured instantaneous velocity at the spark-gap location of a cylindrical disc combustion chamber using a tri-axial HWA. Three orthogonal velocity components (axial, radial and tangential) were simultaneously recorded for a range of engine speeds, volumetric efficiencies and compression ratios for both shrouded and non-shrouded valves. The continuous signal was analysed in three different ways: firstly, by ensemble averaging over 100 engine cycles; secondly, by applying a stationary analysis such that the signal was time-averaged over a 45^{o} interval from one engine cycle, and thirdly, using a non-stationary analysis whereby the ensemble-averaged velocity is subtracted from the instantaneous value and the remaining data are time-averaged over 45^{o}. The purpose of these last two methods is to eliminate cycle-to-cycle variations in the calculation of the turbulent velocity (see section 3.6).

The main findings of the study are as follows:

1. The turbulent velocity showed a strong correlation with mean velocity during most of the cycle, except for the period immediately after IVC for the shrouded valve where the turbulence intensity dropped with the termination of the jet flow through the valve although the mean velocity remained high due to swirl.
2. Both mean and turbulent velocities showed a linear increase with engine speed for the non-shrouded valve during most of the compression period. Variations in volumetric efficiency produced an inconclusive result and it was thought that changes in the flow structure had occurred. No significant effects of compression ratio on either mean or turbulent velocities were observed.

3. The turbulence intensities derived from the three different averaging procedures showed considerable variation. The high rate-of-change of mean velocity for the shrouded valve invalidates the use of averaging over a 45^{o} interval but the more slowly-varying non-shrouded valve data showed the turbulence intensities from the stationary and non-stationary analysis to be consistently below those from ensemble averaging. The differences, up to 35%, are indicative of the level of cycle-to-cycle variations.
4. The energy spectrum was obtained for the shrouded valve during the period 45^{o} BTDC to TDC using both stationary and non-stationary analyses. In the case of the former, 80% of the energy was contained in frequencies below 1 kHz and 98% below 5 kHz whilst for the latter, 70% was found in frequencies below 1 kHz. The fraction of turbulence energy at the high frequencies was found to reach a maximum near the end of intake and the beginning of compression, shifting towards the lower frequencies during compression. These results support the theory that turbulence is generated during intake and decays during compression and is in agreement with the findings of Semenov (1958), James (1972) and Dent and Salama (1975a, 1975b).
5. The turbulence was found to be anisotropic during intake but tended towards isotropy during compression.

Velocity measurements were made in a motored engine by Tindal et al (1974) with two different piston crowns having either a flat top or a part-spherical recess. By inserting L-shaped probe holders through a central hole in the cylinder head, HWA velocity measurements were recorded at $r/R_0 = .37$, .63 and .92 (where r = radial distance and R_0 = bore/2). A cam mechanism allowed the probe to follow the piston down the stroke to a predetermined position and remain

stationary until it was raised in front of the piston returning on the upward stroke. Three positions were available and additional fixed probes in the cylinder head allowed measurements in the combustion space as shown in fig. 2.7. Vertical and horizontal probe orientations were used to measure the resultant of tangential and radial components, and, axial and radial components respectively.

In the disc chamber, an unmasked valve used in conjunction with an inlet port having no strong directional influence resulted in large cycle-to-cycle variations in gas motion. At $r/R_0 = .92$, the vertical and horizontal probes measured peak inlet velocities of 47 m/s and 43 m/s respectively at 60^0 ATDC falling to 6 m/s and 5 m/s at IVC. The velocities during compression cannot be deduced easily as the data is presented with an ordinate of Reynolds number (which varies with the gas properties).

A suitably oriented masked valve reduced cycle-to-cycle variations and produced a swirl that persisted throughout compression with a progressive tendency towards solid body rotation at the outer radii. Calculations based upon the measured profiles seemed to indicate an increase in angular momentum between IVC and TDC. This anomalous result is attributed to axial variations in the swirl profile at TDC (the radial velocity was assumed zero at all times) when data from only one plane was used to calculate the angular momentum.

Measurements with a vertical probe at r = .7 in ($r/R_0 = .37$) that penetrated .25 in into a shallow piston bowl .75 in deep x 2.2 in diameter at TDC showed increased velocities at the end of compression over those in the disc chamber. An increase from 36 m/s to 61 m/s was observed when the compression ratio was increased from 6.7:1 to 10:1 by varying the piston-cylinder head clearance. Squish velocities

would be low in this engine even for the 10:1 compression ratio (of the order 5 m/s based upon the Fitzgeorge and Allison (1963) analysis, described later), as the TDC clearance gap was .25 in and a velocity of 30 m/s measured in a vertical plane was attributed to the generation of secondary motions within the bowl as the piston moved towards TDC.

Measurements of instantaneous velocity were made by Witze (1976a) at the spark plug position in a Wisconsin L-head engine (fig. 2.8) with a compression ratio of 7.25:1 and motored at 2000 rev/min using a platinum-iridium hot wire operating at 750^{o}C. The cylinder pressure, used to calculate the gas temperature (required for correction of the hot-wire signal), was measured with a diaphram pressure transducer placed in the side of the cylinder head. However, a subsequent analysis of the results revealed that the probe mounting device had caused interference and the well in which the probe was located became charged with gas during the compression stroke which was subsequently expelled during expansion, causing spurious velocities to be measured by the hot-wire.

An addendum (Witze, 1976b) indicates peak mean velocities during intake (110^{o} ATDC), compression (20^{o} BTDC) and exhaust (BDC) of 11 m/s, 11 m/s and 7 m/s. The relative turbulence intensity remained virtually constant throughout the cycle at a value of approximately .5. The micro length-scale varied between .3 mm at BDC to .8 mm at TDC, reducing to .3 mm at BDC on the expansion stroke. These values are in broad agreement with Semenov (1958), Lancaster (1976) and Dent and Salma (1975a, 1975b).

A comparison between HWA and LDA measurements has been made by Witze (1978) in a Wisconsin L-head engine modified for optical

access and motored at 600 rev/min. This work is of especial interest as it provides a direct comparison, between the two alternative methods of velocity measurement in a compressing engine.

The HWA data were obtained using a platinum-iridium wire, calibrated in ambient air for wire temperatures of 350°C and 500°C and oriented parallel to the cylinder axis such that it was responsive mainly to the tangential (swirl) and radial velocity components, the latter being assumed negligibly small. Gas temperature within the cylinder was calculated from pressure transducer measurements.

The tangential velocity component was measured using LDA operated in backscatter mode through a quartz window, shown in fig. 2.9. Solid particle seeding (NaCl of nominal .6 μm diameter or T_iO_2 of .2 μm diameter) was introduced via the inlet port.

A comparison between both sets of hot-wire measurements and the LDA results is shown in fig. 2.10. Both HWA and LDA data are in excellent agreement for both mean and turbulent velocities during induction, the maxima being 80 m/s and 10 m/s respectively. At 260° crank-angle (80° ABDC on the compression stroke) the HWA and LDA turbulent velocity measurements start to differ, a trend that continues until at 20° ATDC the LDA, HWA (500°C) and HWA (350°C) measurements indicate turbulent velocities of 2 m/s, 6 m/s and 12 m/s respectively. The mean velocities show a similar trend, although not to such a great extent, the corresponding values being 20 m/s, 33 m/s and 40 m/s. The difference between the HWA results at different hot-wire operating temperatures is indicative of the temperature sensitivity of this instrument and Witze has attributed the disagreement to spatial variations in temperature caused by flow from the (assumed) cooler valve prechamber region or by the proximity of the probe to the cooler walls.

Main Findings of Experimental Studies

1. High velocities through the intake valve generate considerable turbulence. The wide range of engine configurations and probe positions prevents typical values being assigned to the mean velocity although the relative turbulence intensity is usually about .5 during this period. In simple disc chambers, both mean and turbulent velocities decay during compression but in engines with a piston bowl or bowl-in-head, further bulk air movement and turbulence are created around TDC.
2. Intake turbulence is generated within the frequency range 1 to 5 kHz but during compression there is a downwards shift and most of the turbulence energy ends up in frequencies below 1 kHz.
3. Macro and Micro length-scales are found to be in the ranges 1.8 to 2.2 mm and .2 to .8 mm respectively for a number of different engine configurations.
4. Mean and turbulent velocities increase in an approximately linear fashion with engine speed, and are insensitive to changes in compression ratio, at least for disc-chamber engines.
5. Non-directed ports and/or non-shrouded valves produce higher cycle-to-cycle variations in air motion than directed ports and/or shrouded valves.
6. At the temperatures and pressures encountered in motored engines, HWA requires special care in interpreting the signal to avoid erroneous results during the compression period: also required is a probe mounting that does not cause additional air movement.

7. The use of ensemble-averaging in deriving turbulent velocities will lead to higher apparent turbulence levels being measured than are truly prevailing, due to the cycle-to-cycle variations appearing as additional 'turbulence'.

2.3 Studies of Swirl and Squish

Swirl may be generated within the engine cylinder by virtue of the valve being offset from the cylinder axis and/or by suitable design of the geometry of the inlet tract. There can be large variations in engine performance with different inlet configurations (for the same volumetric efficiency) and the full implications of alternative induction systems are not too well understood, although the total angular momentum input during the intake period, the spatial distribution of the incoming tangential velocity, the flow structure generated within the cylinder and the inlet turbulence structure are all contributory factors. This study (and survey) does not consider the modes of generation of swirl but rather its interaction with the in-cylinder flow.

The term "squish" is applied to the inward radial movement of the gas between the piston crown and cylinder head as the piston approaches TDC, in engines of either piston-bowl or bowl-in-head configuration. (A "reverse-squish" process also occurs as the piston commences the downwards stroke after TDC). It is an important aspect of the air motion as the bulk air movement and turbulence generated by the squish action not only create air motion within the bowl but are also responsible for the redistribution of such properties as swirl momentum.

Studies of Swirl

In an early investigation of in-cylinder air motion in a motored engine with a toroidal-bowl piston, Dicksee (1940) interpreted the changes in wet paint markings on piston and cylinder head surfaces, caused by the air movement. A recognition of the effects on air motion within the piston bowl due to the interaction between swirl and squish, an aspect largely neglected by many subsequent researchers, is adequately demonstrated by the following quotation from this reference: "From these experiments, it appears that when squish alone is the source of air movement the air flow in the chamber partakes of a simple toroidal movement. The addition of a swirl however, changes the nature of the movement and with a swirl of compartively feeble proportions the toroidal movement disappears completely and a movement of an entirely different nature takes its place". This statement is based, in part, upon the observance of an "equator" (a horizontal line in the paint markings in the bowl), from which Dicksee inferred that a double toroidal vortex structure can exist in the bowl when swirl is present. As will be shown later, this inference is supported by the findings of the present study.

A method for calculating in-cylinder swirl in engines with axi-symmetric piston bowls was presented by Fitzgeorge and Allison (1963), using a quasi-steady analysis whereby an ordinary differential equation for the rate-of-change of angular momentum of the cylinder gas is integrated to yield the variation of an equivalent solid-body rotational speed over the engine cycle. Surface friction is ignored. The instantaneous angular momentum flux through the valve is required as an input to the calculation and this information is extracted from steady-state measurements of the swirl-generating properties of the

valve/port assembly, obtained by blowing air through the port and measuring the rotational speed of a paddle-wheel vane anemometer mounted in the liner. Results from these calculations show that during intake the angular momentum of the cylinder gas increases as a result of the inflow, whilst after the inlet valve has closed, this momentum is displaced into the piston bowl and the speed of rotation increases due to the decreasing equivalent radius of gyration of the cylinder/piston-bowl combination, which causes the swirl to reach a maximum at TDC. No comparisons with experimental data are given.

Refinements have been made to the Fitzgeorge and Allison method by Dent and Derham (1974), Davies and Kent (1979) and others by including the effects of friction using empirical formulae for turbulent flow over flat plates. Dent and Derham have presented a comparison between results using this approach and hot-wire measurements of swirl velocity in a piston bowl for three different engine configurations, namely, naturally aspirated and supercharged with a plain inlet valve and naturally aspirated with a masked inlet valve.

The experimental engine had a bore and stroke of 10.16 cm x 10.48 cm, compression ratio of 16:1 and a shallow combustion bowl of 5.33 cm diameter and 1.2 cm depth. The engine speed was varied between 500 and 1500 rev/min. The problems of directional ambiguity usually associated with the HWA were overcome by using a probe with three mutually perpendicular wires and mounted .7 to 1 cm on top of the piston. Pockets were machined in the cylinder head to avoid collision at TDC (although Witze's (1976a) experience indicates that this practice may introduce spurious signals). Additional two-wire probes were mounted on top of the piston to measure the squish and swirl velocity components. The relative axial velocity between the probe and gas was assumed zero near TDC (a reasonable assumption as the probe is mounted close to, and moving with, the piston). A total of 5 probes at radii of 1.27, 2.54, 3.18

3.49 and 3.81 cm were used. Corrections to the HWA signal for pressure and temperature were made using measurements from a pressure transducer and a resistance thermometer thatutilised one wire of a three wire probe.

Results at 1000 rev/min for the plain inlet valve show that for the period 60^{o} ATDC on intake to TDC of compression, solid body rotation exists in the cylinder; this is based on measurements from 4 of the probes. The combination of naturally aspirated with a masked inlet valve (rotated to give the highest swirl) and the plain inlet valve with supercharge (1.7 bar manifold pressure) resulted in swirl velocity increases of 25% and 60% respectively at TDC. The swirl speed was found to increase in an approximately linear fashion with engine speed. The predicted swirl speed throughout the cycle, including the "spin-up" effect at TDC, was in excellent agreement with the measurements for the three test cases examined.

Anasuma and Obokata (1972) measured and predicted the decay of air swirl in an engine with a flat-top piston, the incoming air entering tangentially at the cylinder radius through a side-valve. The swirl velocity was measured in two ways: firstly, from analysis of high speed photography of a high voltage spark discharge between two electrodes, and secondly, using HWA. The latter should not be relied upon however, as corrections for pressure and temperature were neglected*. Spark discharge measurements of the swirl velocity

*Hassan and Dent (1969) and Dent and Derham (1972) have shown that in the absence of an experimental calibration at the temperature and pressures encountered during compression, not only should a semi-empirical calibration, such as that of Davies and Fisher (1964), be used but also a further temperature-loading correction based on the work of, for example, Hilpert (1933) or Collis and Williams (1959).

profile at 3 axial stations have been used to determine the decay of swirl momentum. During the period BDC to TDC, decays of 40%, 60% and 66% were recorded for engine speeds of 1000, 600 and 300 rev/min respectively. It can be deduced from the presented profiles that the BDC swirl ratios (= swirl speed/engine speed) were 11.4, 17.7 and 16.8 at these three speeds. There are exceptionally high values, exceeding those found in most engines by a factor of 2 to 4 and are almost certainly due to the odd inlet system used (see e.g. Tindal and Williams (1977) for details of the swirl-producing characteristics of more typical inlet ports).

The theoretical aspect of their work involved solving numerically the one-dimensional incompressible form of the tangential momentum equation for the swirl velocity, allowing for spatial variations in the radial direction only but ignoring the effects of piston and cylinder head surfaces and all convective transport, i.e. zero radial velocity was assumed. The viscosity was fictictiously increased above the nominal molecular value to 'account for' turbulence and this resulted in a rapid decay of angular momentum. These predictions should however be interpreted with caution as no special account was taken of friction at the boundaries, except to set the swirl velocity to zero. It is difficult to draw any conclusions from this work because of the absence of calibration for the HWA experiments, the untypical swirl conditions for the spark discharge measurements and the unrealistic modelling in the case of the predictions.

In a subsequent paper, Anasuma and Obokata (1973) have solved numerically the two-dimensional stream-function~vorticity formulation

of the Navier-Stokes equations for the axial and tangential velocities and the radial momentum equation, again assuming incompressible flow. An initial solid-body rotation was assumed and calculations were then made of the distribution of swirl and stream-function within the cylinder. Turbulence was ignored.

A complementary experiment photographed the movement of aluminium powder in a swirling water flow inside a rotating cylinder that was impulsively stopped at the start of the experiment. Near the corner that would correspond to the piston~cylinder-wall interface, a small recirculation was observed at $t^* = 10.3$ (t^* is non-dimensional time given by $t^* = tv_0/R_0$ where t = time, v_0 is the tangential velocity at $t = 0$ and at the outer cylinder radius, R_0). A comparison between the photography and predicted lines of iso-stream function show the same qualitative trend although the secondary flow occurs much earlier ($t^* = 0.1$ to $t^* = 2$) in the latter whilst at $t^* = 10$, the predicted recirculation has decayed considerably and is centred at $r = .6R_0$ and approximately mid-way between the top (cylinder head) and bottom (piston) surfaces.

As with their previous work (Anasuma and Obokata, 1972) it is difficult to draw any conclusions that relate to swirl in engine cylinders because the conditions for both their experiments and predictions differ too greatly from such flows.

Studies of Squish

Alcock and Scott (1962) reported experiments in which the motion of cotton tufts was recorded using high-speed photography in a motored engine with a toroidal piston bowl. No evidence of squish was found prior to TDC, but this was possibly attributable to leakage past the piston which would be considerably greater in a motored rather than a fired engine because of higher piston/cylinder clearances in the former. However, the results did indicate "a very definite outward or reversed squish just after TDC". This reverse-squish phenonema is in agreement with the findings of Woods and Ghirlando (1975), reported later, and this study.

The first theory of squish is apparently due to Fitzgeorge and Allison (1963) who divided the cylinder into two regions shown in fig. 2.11, separated by the line AA. Flow between these regions is assumed to be one-dimensional, determined solely by the mass continuity requirement, ignoring pressure and density variations within the cylinder. Calculations using this approach show that for typical bowl-in-piston geometries, the squish velocity reaches a maximum between 8^{o} BTDC to 2^{o} BTDC and increaseswith reduction in both TDC clearance and radius of the piston bowl. Fig. 13 of appendix 4 shows a typical variation of squish velocity near TDC.

Dent and Derham (1974) and Derham (1972) have measured squish velocities using HWA in the experiments previously described in the "Studies of Swirl" section. Predictions of squish velocity using the Fitzgeorge and Allison method are in good agreement with the measurements before TDC for 3 engine speeds of 500, 1000 and 2500 rev/min with maxima of 8, 17 and 27 m/s. At TDC however, the measurements show values of 12, 23 and 34 m/s whilst the predictions are zero. The

reason for this discrepancy is not stated, although it is possible that air movement caused by the wells machined into the cylinder head to accept the probes are responsible.

Shimamoto and Akiyama (1970) investigated both experimentally and theoretically the effects on the squish velocity of both heat-transfer and leakage past the piston. The measurements were made in an engine of 16:1 compression ratio with a bore and stroke of 85 mm x 93 mm with two variants of piston bowl, shown in fig. 2.12,and with TDC clearances of 1 mm and 2.5 mm. The squish velocity was calculated from the change in inductance of a solenoid with the movement of .4 mm diameter needle passing through its centre, the movement resulting from the deflection of a thin plate normal to the flow direction and sensitive to the dynamic pressure. This apparatus is shown in fig. 2.13. A major criticism of the experimental method is that the probe was shielded by the side of the bowl during the important period 15^{o} BTDC to TDC. Their measurements show the peak squish velocity to occur at 18^{o} BTDC which is almost certainly in error, as measurements from other sources (e.g. Woods and Ghirlando (1975)) and predictions of various degrees of sophistication show the maximum at least 10^{o} nearer to TDC. By taking measurements at axial positions of 1.2, 1.9, 3 and 4 mm, a (hypothetical) radial velocity at the piston surface was estimated from spatial extrapolation (although it would be expected that the true value is zero actually at the surface). Subsequent results, which use this extrapolated value, show the peak squish velocity to occur at about 8^{o} BTDC although it is not obvious how this shift of the peak occurs if, as stated, the probe was shielded by the piston during the last stages of compression.

The effect of gas leakage on the squish velocity was estimated in the following way: it was assumed that the instantaneous leakage past the piston could be calculated according to an isentropic orifice relationship for sonic flow (see equation 4. 62)) and that subtraction of the leakage mass flow rate from the mass flow rate out of the clearance volume into the piston bowl calculated from the continuity requirement (as in the Fitzgeorge and Allison (1963) method) gave the net mass flow rate through the plane AA in fig. 2.11. The sonic flow orifice equation requires a value of effective area and this was obtained by matching the solution of this equation, which when integrated over a cycle would give the leakage per cycle, with measurements (presumably from blowby data, although this is not stated). The leakage volume per cycle at 1500 rev/min was found to be 1.6% of the swept volume and the decrease in maximum squish velocity was subsequently calculated as 1% for this leakage rate increasing to about 3% for a leakage of 2.5%.

The model used to investigate the effect of heat transfer on the squish velocity assumed that cooling of the gas during compression in the two regions separated by the line AA in fig. 2.11 (hatched and unhatched zones) may be determined independently from a calculation of the heat transfer through the surfaces bounding each zone. Thus, the increased cooling of the hatched zone gas as the piston approaches TDC, that results from the higher surface area/volume ratio, serves to decrease the squish velocity than would be obtained under either adiabatic conditions or uniform cooling of the total cylinder gas. The heat transfer coefficient was calculated according to Woshni's equation (Woshni, 1967) and was assumed the same for both regions. The instantaneous pressure and temperature, required to

evaluate the Woschni equation, were computed from a polytropic relationship (pV^n = constant). At 1500 rev/min the decrease in maximum squish velocity due to the differential heat transfer was calculated as 6% and variations in the TDC clearance of 1 mm to 2.5 mm and piston bowl/cylinder diameter ratio of .45 to .55 produced negligible changes in this value.

A comparison between the plate deflection measurements, described earlier, and the calculated squish velocity with both leakage and heat-transfer effects included shows good agreement for both piston bowls with a 1 mm TDC clearance and for the .55 bowl/cylinder diameter-ratio configuration with 2.5 mm clearance. These values are generally 7-10% lower than the value calculated without losses. This conflicts with the measurement-theory comparisons of Dent and Derham (1974) who found equally good agreement although neglecting losses.

Woods and Ghirlando (1975) have presented a more comprehensive theory that those already cited for the calculation of squish velocity that includes the effects of:

(i) leakage past the piston,

(ii) heat transfer,

(iii) friction at the cylinder head and piston surfaces,

(iv) gas inertia,

(v) a sloping piston crown and

(vi) the inclusion of the 'dead' volume between the top ring and piston crown.

This was achieved by solving simultaneously the unsteady one-dimensional continuity, momentum and energy equations in the annular gap between the piston crown and cylinder head. The effect of skin friction at the walls was included in the analysis as a body force characterised by a coefficient of friction, as is the practice for pipe flow, and whilst the heat transfer modelling was unspecified it was stated

that both terms had negligible influence and all results presented exclude them. A partially open boundary at the outer radius allowed for leakage past the piston.

Predictions of squish velocity at 6000 and 12000 rev/min, a 0.5 mm TDC clearance gap and without leakage are in agreement with the simpler Fitzgeorge and Allison (1963) method at the lower speed with only minor differences at the higher speed. One fundamental difference between these alternative models however, is that the more sophisticated Woods and Ghirlando analysis predicts a non-zero velocity at TDC as a result of the gas inertia (although not large enought to account for the high velocities measured by Dent and Derham, 1974). Variations in the leakage gap from 0 to 0.5 mm showed a strong influence on the squish velocity when compared with the no-leakage calculation. A 0.1 mm gap reduced the maximum velocity by a factor of 3 and reversed the direction between 6^{o}BTDC to TDC. It is however difficult to relate a leakage gap to engine conditions unless the leakage flow rate is integrated over a complete engine cycle and compared with measured leakage data (as Shimamoto and Akiyama, 1970).

A complementary experimental program used HWA to measure the squish velocity in both flat-top and piston-bowl configurations (fig. 2.14). The probe was located at a radius of 25.4 mm (bowl radius) and various axial depths of .51, 1.78, 3.05 and 4.32 mm. Gas pressure and temperature, for correction of the HWA signal, were measured with a piezo-electric transducer and a resistance thermometer.

With the flat-top piston, both theory and experiment gave negligible squish velocities (< 2 m/s) at all probe depths for the period 60^{o} BTDC to 60^{o}ATDC at 1000 rev/min. However, at 2500 rev/min the measurements show considerable scatter after TDC with a

maximum velocity of 30 m/s, attributed to the generation of a corner vortex. The presence of a bowl increased the velocities, with maxima of 9 m/s and 32 m/s measured after TDC for a 0.5 mm bumping clearance and speeds of 1000 and 2500 rev/min. The activity detected by the HWA after TDC with the flat piston at 2500 rev/min was apparent at all speeds with the bowl geometry, plausibly attributed to reverse squish. The calculated values of squish velocity were generally higher than those measured by a factor of 2 to 3. The reason for this discrepancy is not known.

Main findings of the studies of swirl and squish

1. Swirl is generated by the intake process and persists throughout the engine cycle.
2. Although the momentum of the gas decays after IVC due to wall friction, the swirl speed in a combustion chamber of smaller diameter than the cylinder increases during the compression stroke because of the decreasing equivalent radius of gyration of the cylinder~bowl combination.
3. The interaction of swirl and squish can dramatically alter the flow structure near TDC of compression.
4. Relatively simple models, aided by steady flow data of the swirl-producing characteristics of the inlet assembly, are reasonably successful in predicting the variation of an equivalent solid-body rotational speed of the gas through the engine cycle.
5. The squish phenomena in engines with combustion bowls is confirmed by a number of experimentalists and there is also some evidence of a reverse squish effect after TDC.

6. Calculation of the squish velocity based upon two alternative models, one requiring the satisfaction of the continuity equation and the other satisfying continuity, momentum and energy for the one-dimensional flow in the clearance gap, indicate that the effects of gas inertia are negligible for engine speeds up to 6000 rev/min.
7. Comparisons between these models and experimental squish velocities, and, estimates of the effects of both heat transfer and leakage past the piston are conflicting. It is not known whether this is due to inadequacies of the theoretical models or measuring inaccuracies.

2.4 Experimental Studies in Axisymmetric Engines

Measurements in axisymmetric idealisations of real engines are useful in providing a means of validating predictions from the model described in this thesis. Three such sets of data of adequate quality appear to exist and are described below whilst detailed comparisons between predictions and experiment are left until Chapter 5.

Witze (1976c) has made HWA measurements in a specially constructed axisymmetric engine operating on a 4-stroke cycle by using a central cam-operated valve serving for both intake and exhaust. Two variants of the engine are considered here, shown in fig. 2.15, both having a flat-topped piston and in one case a

flat cylinder head and in the other, a bowl-in-head configuration, formed by introducing an annular insert between the head and block. The hot-wire probe, oriented to measure the resultant of the axial and radial velocity components, was positioned .75 ins and .47 ins from the symmetry axis and the cylinder head surface as indicated. Although the probe was located well away from any surface, so avoiding wall-proximity effects, the data suffer from the same temperature sensitivity and calibration uncertainties of Witze's earlier measurements. The original data, with which complementary predictions were published by the author and others (Gosman et al, 1978b) and presented in section 5.3, were subsequently corrected by Witze (1979).

The original and corrected data for the flat cylinder head case are shown in fig. 2.16. The revised data shows a peak inlet velocity of 42 m/s and a corresponding turbulent velocity of 19 m/s at the mid-stroke position. The probe position is immediately downstream of the inlet valve, and these values reflect the jet-like nature of the incoming flow. Both velocities decrease during the remainder of induction with only a slight rise prior to TDC during compression. The difference between the original and corrected data during compression is similar to the HWA~LDA comparisons of Witze (1978) and underline the uncertainties of HWA correction methods during compression. The revised data are more plausible, on the basis that there are no geometric features to promote substantial bulk air motion and other experimental evidence indicates a decay during compression for this type of chamber. The velocity decay continues through expansion until just before BDC in the exhaust stroke when there is a steeprise in the mean velocity to 20 m/s with a corresponding turbulent velocity of 2 m/s. The turbulence values are lower than those found during intake because the probe is now

located in the upstream region of the valve outflow, and as will be seen in section 5.3 where the predictions for this case are described, the turbulence generation is localised at the valve orifice.

The uncorrected data for the bowl-in-head configuration (corrected data are not available for this case) are shown in fig. 2.17. There is a similar trend to the no-bowl geometry during intake with maximum mean and turbulent velocities of 40 m/s and 19 m/s. During compression, the indicated peak mean and turbulent velocities are 65 m/s and 35 m/s although bearing in mind the difference between the uncorrected and corrected data for the previous case, these maxima should be disregarded. The exhaust period shows an initially oscillatory behaviour for both quantities, and as will be seen later, this is a result of reverse flow into the cylinder. After BDC on the exhaust stroke, the behaviour is similar to the disc chamber.

Morse et al (1978) have used an axisymmetric engine with a glass cylinder for making detailed in-cylinder velocity measurements using LDA. Although non-compressing, the engine can be operated with different cylinder heads so that the effects of alternative inlet configurations can be studied. Results have been reported for an open pipe inlet (Watkins (1977), Yianneskis (1977) and Gosman et al (1978c)) and a permanently-open poppet valve, the base of which is flush with the cylinder head (Yianneskis (1977) and Morse et al (1978)). Variants of the basic geometry also include vanes inserted in the inlet to give the incoming air a pre-swirl and a piston with a simple cylindrical bowl. The important dimensions of the engine are given in fig. 2.18 and the results described here have been obtained at 200 rev/min with the valve inlet as shown.

Mappings in the cylinder of the ensemble average $\overline{v}_n(\theta)$ and rms turbulent $\overline{v'^2(\theta)}^{1/2}$ velocities have been derived from the measured

instantaneous velocity $\hat{v}(\theta)$. For measurement purposes, the crank-angle represented by θ is an interval of finite-size ($\theta - \delta\theta/2$ to $\theta + \delta\theta/2$). The choice of $\delta\theta$, is of necessity a compromise between accuracy which demands $\delta\theta$ as small as possible and data acquisition rate which requires $\delta\theta$ large and its influence on the results has been quantified by Morse (1977). This work shows that, for the applications considered, the mean velocities are only slightly affected with variation in $\delta\theta$ within the range 1^o to 30^o but the turbulence levels are substantially over estimated when the rate-of-change of mean velocity is high for large $\delta\theta(>10^o)$. The measurements reported here have been made with $\delta\theta = 10^o$.

The results are plotted in the form of profiles of axial velocity, turbulence intensity, and where appropriate, swirl velocity at various axial stations, and streamlines. The more detailed profiles are presented in section 5.2 and are used for a quantitative comparison with predictions obtained using the method described in this thesis. The streamlines provide an overall view of the flow structure and are described below for two configurations with a flat-top piston both with and without inlet swirl vanes.

Measurements without swirl

Fig. 2.19 shows experimentally-derived streamlines for 4 crank-angles during the cycle. At 36^o, the intake process is well established and two entrainment eddies are formed either side of the incoming jet. The main recirculationg in the cylinder seems to effect the angle of inflow such that at 90^o the jet has a higher radial velocity component than suggested by the valve entrance angle.

The corner vortex is reduced in size, probably as a result of the higher intake velocities at this time which also cause the air to impinge on the cylinder wall. The deflection of the intake jet at the wall results in a further small eddy forming above the piston. This trend continues and at 144^{o} this weak eddy has increased in size whilst the main recirculation fills over half the cylinder. During expansion, at 270^{o}, the intake-induced structure has disappeared and a sink-like flow is observed.

Measurements with swirl

Measurements have been taken with inlet vanes angled at 15^{o} and 30^{o} to the axis of the cylinder. The higher pre-swirl case (30^{o} vanes) was found to have the more dramatic effect on the flow and is reported briefly here. Fig. 2.20 shows the streamlines for this case. At 36^{o} the flow is similar to the no-swirl configuration in respect of the two eddies either side of the jet but an additional weak eddy has also formed behind the valve. At 90^{o}, the structure varies considerably from the no-swirl counterpart in that the main recirculation is distorted both behind the valve due to the aforementioned additional eddy and near the piston. The wall vortex, previous apparent as a result of jet impingement, is not formed. The picture at 144^{o} is similar to that at 90^{o} although "stretched" by the piston motion. The flow at 270^{o} is nearly identical to the no-swirl case, the intake-induced motions having been suppressed.

Heat Transfer

Dao (1972) and Dao et al (1973) have reported measurements of instantaneous heat flux at 4 radial locations on the cylinder head surface in a motored engine with both disc-chamber and cylindrical piston bowl geometries. The measuring positions and bowl shape are shown in fig. 2.21. The objective of this work was to investigate the influence of gas motion on the heat flux, the former being determined by the shape of the piston and the inlet swirl level, which was generated using a masked valve.

The experimental engine was a single cylinder Fairbanks-Morse diesel of 3.125 ins bore and 4 ins stroke giving a total piston displacement of 30.7 in^3. The inlet was connected to a pressurised tank so that the engine could be supercharged up to 1.4 bar. The cylinder head was modified to accept a valve containing the heat flux measuring assembly, the other valve being used for both intake and exhaust. Strictly, this violates axial symmetry and it is possible that some features evidencedin the measurements are due to three-dimensional effects. Instantaneous gas temperature measurements were made using a pair of thin thermistors deposited on both faces of a pyrex disc of .00511 ins thickness and .375 ins diameter. The resistance variations of the thermistors were measured using two Wheatstone bridges, the outputs of which were fed to an electrical analog simulating the thermal properties of the disc. Measurement of the current through the first resistor of the analog circuit gave a signal proportional to the instantaneous heat flux.

Results with a disc chamber showed strong influence of the gas motion on the heat flux. For weak swirls with an unshrouded valve, the heat fluxes were irregular and showed large cycle-to-cycle

variations. For strong swirls (IVC swirl ratio of 7.3), two flow regimes were inferred to exist adjacent to the cylinder head surface: in the annular region extending from .8 ins to 1.46 ins radius, the heat flux traces were less spiky and reproducible from cycle-to-cycle, thus indicating a regular gas motion, whilst in the central region, cycle-to-cycle variations were apparent, indicating large cyclic variations in the gas motion (Tindal et al (1974) found similar cycle-to-cycle variations for weak swirls).

Fig. 2.22 shows the variation of heat flux at the 4 measuring positions during the period 60° BTDC to 60° ATDC with the cavity piston, an IVC swirl ratio of 7.3 at 900 rev/min and manifold pressure of 1.36 bar. These indicate maxima near TDC with irregularities probably resulting from squish induced effects. The presence of a piston bowl enhanced the heat fluxes by about 25% in the annular region, 100% at the outer radius of the bowl and about 10% in the central zone when compared with the disc chamber results, as shown in fig. 2.23.

2.5 Multi-Dimensional Theoretical Studies

The first attempt to devise a multi-dimensional prediction scheme for the flow induced by a piston reciprocating within a cylinder was that of Watkins (1973) who solved numerically the governing differential conservation equations of mass, momentum and energy. The Eulerian form of the differential equations was transformed into

a co-ordinate frame that allowed the finite-difference grid used for their solution to expand and contract in the axial direction so that the cylinder head and piston surface coincided with the first and last axial grid lines respectively at all times in the cycle, thereby improving resolution at TDC than would otherwise be obtained with a more conventional fixed grid arrangement. The transformed differential equations were cast into fully implicit finite-difference form, so avoiding the 'Courant-Friedrichs-Lewy' (CFL) stability requirement (Courant et al, 1967). Cell Reynolds Number restrictions were removed by using a hybrid of donor cell (upwind) and central differencing to approximate the spatial derivatives. Axial symmetry was assumed and there were no ports or valves.

Results for compression and expansion of the gas with initial conditions of zero velocity and a uniform pressure field show the formation of an annular vortex as the piston moves towards TDC, which is a consequence of the build up in pressure towards the cylinder head and the action of shear stresses in retarding the fluid adjacent to the cylinder wall. The vortex persists even when the piston comes momentarily to rest at TDC but the flow very quickly reverts to nearly one-dimensional behaviour during expansion.

Gosman and Watkins (1976a,1976b) have incorporated a turbulence model into the above procedure that solves two additional differential equations for the kinetic energy (k) and the dissipation rate (ε) of the turbulence. Heat transfer predictions were compared with the empirical correlations of Elser (1954), Annand (1970) and Woschni (1967) and the effects of engine speed, compression ratio and bore/stroke ratio were investigated for a closed cylinder configuration. Comparisons between predictions from the RPM (an acronym of Reciprocating Piston Motion) method and the empirical correlations showed the Nusselt

Number derived from the former to be below the latter by a factor of two, plausibly attributed to the higher turbulence levels generated by intake, squish and combustion found in the engines from which the empirical correlations were derived. It was also observed that the spatial variation of gas temperature at certain periods of the cycle could allow heat fluxes of opposite sign to co-exist, indicating that heat transfer estimates based upon a bulk-mean gas temperature could be grossly in error on occasions. An increase in engine speed from 2000 to 3000 rev/min resulted in a two-fold increase in heat transfer rate although with a reduction in speed the changes were not so dramatic. Similarly, increases in compression ratio from 10:1 to 14:1 and 14:1 to 18:1 produced a 50% increase in heat-transfer rate in each case. Variations in the bore/stroke ratio of .8, 1. and 1.2 showed negligible change in predicted heat transfer rates.

Gosman and Watkins (1976b) have also made predictions using the above-described method for a motored engine equipped with a single, centrally-located valve represented by an annular opening, the area of which was allowed to vary in a realistic fashion, so permitting the simulation of intake and exhaust. A boundary condition of pressure was prescribed in the port, from which the mass flow rate was calculated using an orifice relationship. The incoming air was assumed to enter the cylinder at a prescribed angle to the cylinder head and values typical of engines were assigned to the upstream turbulence quantities and temperature during intake.

A strong recirculation was found to develop soon after the start of the intake stroke which remained during compression, although reduced in strength as a result of wall friction. After TDC the vortex was quickly supressed and a virtually one-dimensional flow remained until EVO. A sink-flow structure was apparent for the entire exhaust stroke. The turbulence at a position near the valve showed high values

during intake as a result of the shear between the entering jet and the fluid already in the cylinder. As the recirculation region was established, the jet-generated turbulence was transported by convection and diffusion and maximum values were then found near the centre of the vortex whilst the level near the symmetry axis was low. It was observed that the turbulence energy diminished at a much slower rate than the mean velocity, evidenced by high values of intensity around TDC of compression. During exhaust, turbulence was again generated by shear near the valve although the effect was localised due to the outward movement of the fluid. The peaks during intake and exhaust were of comparabable size. Heat-transfer during compression and expansion was found to be about twice that predicted for a cylinder with no valve.

Watkins (1977) has made predictions for both laminar and turbulent flows in a non-compressing engine and compared them with experimental data. For the latter, LDA measurements were made in the plexiglass-cylinder engine already described (Morse et al, 1978) at an engine speed of 10 rev/min and with a central, open-pipe inlet. The peak Reynolds Number at the inlet was of the order 640 and the flow was considered both laminar and incompressible; a consequence of the latter is that the inlet mass flow-rate may be calculated from the piston displacement. Boundary conditions for the axial and radial velocity distributions at inlet, which closely determine the form of the incoming jet and consequently the flow structure within the cylinder, were obtained from two sources: experimental profiles were used for the axial velocity, but the radial velocity could not be measured and the profiles during intake were therefore assumed to follow those predicted during exhaust, the latter being "fed-back" during the subsequent induction stroke.

A comparison between the predictions and measurements shows that the main features of the flow, that is, the spread of the jet near the piston and a recirculation zone along the cylinder wall are reasonably well predicted (typically -25% to + 8% error in axial velocity in the case of the jet), but the weaker motions, specifically a small eddy apparent in the experimental data in the corner of the cylinder head/wall is not predicted at all. This is attributed to errors in the strong recirculation,arising from uncertainties in the inlet conditions, having a significant effect on the weaker regions of the flow.

Comparisons have been made for the mean and turbulent velocities at a position close to the single central valve with the experimental data of Witze (1976c) for the flat cylinder head case, described in section 2.4. Fig. 2.24 shows the predicted and experimental mean and turbulent velocities for this case and whilst the comparisons could not be described as good, the trends during inlet and exhaust are similar (Note that the peaks of both velocities during compression for the experimental data are incorrect for reasons previously given, Fig. 2.16 shows the amended results). This particular example should not however be used to judge the performance of the predictive method as there are differences between the experimental and theoretical "engines" of bore/stroke ratio, compression ratio (1 and 14 respectively for the predictions and, .92 and 10.7 for the experimental engine) and valve geometry, the Witze engine having a moving poppet valve and the predictions representing the flow as entering through an annulus in the cylinder head as described earlier. Predictions in the present study for the same case are presented later in this thesis using the correct dimensions and a more realistic treatment

for the valve which confirm that the aforementioned inconsistencies affect the quality of the results.

An early variant of the computer code developed by Watkins has been used by Chong et al (1976) who have reported flow and heat transfer predictions in an axisymmetric engine assuming laminar flow conditions. The flow induced by both a flat-topped piston and a simple cylindrical cavity in the piston have been simulated, in the latter case by "masking" a portion of an expanding/contracting grid; this latter method unfortunately results in a piston bowl whose depth varies with piston position. A coarse (10 axial x 5 radial) computational grid was used. The engine speed was varied between 10 and 1000 rev/min and the compression ratio between 6:1 and 13:1.

At engine speeds below 100 rev/min with the flat-topped piston configuration, a toroidal vortex was observed during compression which was subsequently suppressed during expansion; this compares favourably with the motions predicted by Watkins (1973) for similar circumstances. At higher speeds, a (nearly) one-dimensional axial flow was found during compression and expansion. The heat transfer predictions will not be discussed for two reasons: firstly, studies by Watkins (1977) indicate that the 10 x 5 grid used is inadequate to calculate wall heat transfer (20 x 20 has been found to be the absolute minimum) and secondly, Chong et al appear to have made an error in obtaining the heat transfer rates from the predicted temperature.

It is also difficult to draw any conclusions from the above author's piston-bowl predictions because of the coarseness of the grid and the time-varying dimensions of the bowl. All that can be stated is that the direction of rotation of the squish induced recirculation in the bowl at TDC is opposite in sense to that found

in the present work for a similar geometry (Gosman and Johns, 1978a).

Griffen et al (1976) have obtained numerical solutions to the Navier-Stokes equations in a plane two-dimensional piston/cylinder arrangement. An identical co-ordinate transformation to that of Watkins (1973) was used to cast the partial differential equations for continuity, momentum and thermal energy into the more flexible expanding/contracting co-ordinate frame already mentioned. A turbulence model was not included. The complete 4-stroke cycle has been simulated, although the valve representation is relatively crude, using only 1 grid point in the cylinder head for inhaling and expelling fluid and assuming that the 'valves' are of fixed area and open and close instantaneously at BDC and TDC. Spatial resolution within the cylinder is limited due to the coarse (10 axial x 9 radial) finite-difference grid.

A variant of the time-dependent, predictor-corrector scheme of MacCormack (1969) was used to solve the non-conservative form of the governing equations. The explicit nature of this scheme requires the time-step (δt) to satisfy the CFL stability criterion (Courant et al, 1967), i.e.:

$$\delta t < \left(\frac{\delta x}{v_f + v_a}\right)_{min}$$

where δx is the grid spacing and v_f and v_a are respectively the local fluid and sonic velocities. The implications of the CFL time step limit are discussed in section 4.5 . A further limitation and a severe constraint on the size of geometry and operating condition also arises from the central differencing practices employed for spatial

derivatives. In this case, numerical stability and accuracy requirements dictate that the cell Reynolds number (Re) should remain of the order unity, i.e.

$$Re = \frac{\rho v_f \delta x}{\mu} \sim 1$$

where ρ and μ are respectively the fluid density and viscosity. The fore-mentioned authors have chosen to satisfy this latter criteria by specifying a 'thimble-sized' engine (8mm bore x 9mm stroke) and an ambient pressure of 0.01 atmosphere: the time step then required to satisfy the CFL condition is of the order $.02^{o}$ crank angle.

Flow-field predictions with the cell Reynolds number restriction ignored (Re = 10,000) are presented at various stages throughout a 4-stroke cycle but numerical instabilities are apparent in the solution in the form of an oscillatory velocity field as a consequence. As a result of these instabilities, little can be deduced from the results except that the flow is nearly one-dimensional in regions away from the boundaries during compression and expansion.

In a companion paper, Diwakar et al (1976) have solved the inviscid form of the governing equations, so removing the cell Reynolds number restriction but otherwise using the same numerical method and grid arrangement as Griffen et al (1976). In this instance, normal ambient conditions of pressure and density are assumed and the engine is "full-scale" although the bore and stroke are not stated. The engine speed is 600 rev/min.

Calculations were started at TDC of the intake stroke and the incoming air entered with only an axial velocity component. By the mid-stroke position, a single vortex was formed and this structure persisted throughout compression until TDC at which time it was "squashed" due to the reduced piston/cylinder head clearance. Recirculation was suppressed during the early stages of expansion although at BDC the

single vortex was again apparent. At 20^{o} ABDC, with the exhaust valve open, the vortex had reversed in direction and flow was directed towards the exhuast valve. At the end of the exhaust stroke (TDC), the authors have interpreted the flow structure as having recirculation zones in the corners, although the coarseness of the grid precludes a proper assessment. Unfortunately, the plots of the velocity fields are scaled according to the maximum value at each time-step and it is therefore not possible to deduce either if, or by how much, the strength of the vortex decreases during compression and expansion when both valves are closed. However, in view of the neglect of turbulence, a slip boundary condition (in conformity with the inviscid assumption) and a coarse grid and valve representation it is doubtful whether these results mirror reality.

A comparison has also been made by Diwakar et al between the flow field predictions from the viscous calculations of Griffen et al (1976) and those assuming inviscid flow. These results are interesting in that they represent two limiting assumptions of high (Re $\sim$ 1) and zero viscosity respectively. The two structures are very different, the former depending largely on the piston motion and being essentially one-dimensional during compression whilst the latter shows a single dominant vortex. Neither assumption is realistic although the flow resulting from the zero viscosity (infinite Re) calculations is probably closer to a turbulent flow, as it would be expected that the latter is relatively insensitive to Reynolds number. However, the neglect of turbulence, where the stresses arising from molecular viscosity are augmented by additional turbulent stresses, is not justified.

Three-dimensional inviscid flow calculations in an engine cylinder have been made by Griffen et al (1978) using the same numerical method as Griffen et al (1976) and Diwaker et al (1976) but with a cylindrical-polar co-ordinate system. It was found that an additional

artificial viscosity term was needed in the momentum equations to avoid numerical instabilities. A computational grid of 10 (axial) x 15 (radial) x 9 (circumferential) grid lines was used with inlet and exhaust valves represented by 3 (radial) x 3 (circumferential) grid lines each. The valves were diametrically opposed and the resulting symmetry required calculation in only half (π radians) of the cylinder. Both radial and swirl velocities were specified as zero at the valve.

The velocity field in the axial - radial plane of the valves is similar to the structure found in the two-dimensional (plane) calculations of Diwakar et al (1976) and the intake-generated recirculation persists until TDC of compression. The magnitudes of the velocities in the radial-circumferential plane are stated to be considerably lower than those in the axial-radial plane (which would be expected with a zero swirl boundary condition at the valve) although different velocity scalings preclude a quantitative comparison.

Boni et al (1976) have made predictions of the flow and combustion of methane in an axially symmetric divided-chamber stratified charge engine. The Arbitrary Lagrangian-Eulerian (ALE) numerical method of Hirt et al (1974) was used to solve conservation equations for 5 species, momentum (axial and radial) and energy.

Considerable flexibility of geometry is possible with the ALE method and a partially-implicit formulation of the governing equations allows flows of all speeds to be computed without the CFL time-step restriction. However, there remain a number of restrictions on the maximum allowable time-step (δt), that result from the explicit flux treatment of the scheme. These are:

$$\delta t < \min \left\{ \left| \frac{8\nu}{3}\left(\frac{1}{\delta z^2} + \frac{1}{\delta r^2}\right)\right|^{-1}, \quad f\,\frac{\delta z}{v_1}, \quad f\,\frac{\delta r}{v_2} \right\}$$

where ν is the kinematic viscosity; δz, δr and v_1, v_2 are respectively the grid spacings and velocity components in the axial and radial directions and $f = \frac{2\alpha_0}{1+\alpha_0^2}$ where α_0 is a measure of the donor-cell proportion in the finite-difference formulation of the mass conservation equation ($\alpha_0 = 0$ and $\alpha_0 = 1$ correspond to central and donor cell differencing respectively).

A further consequence of the differencing practices employed is that adjacent nodes may become decoupled under certain flow conditions (Amsden and Hirt, 1973). This results in two (nearly) independent solutions for adjacent grid lines and is manifest as a spatially oscillatory solution. In the case of the momentum equations, oscillations appear in the velocity field and these are apparent in the predictions of Boni et al adjacent to the cylinder wall. Although the authors are unsure whether this phenomena is of numerical or hydrodynamic origin, similar behaviour has not been observed either experimentally or theoretically in engine cylinders by other researchers and the evidence indicates the former.

The fore-mentioned hydrodynamic oscillations are not apparent in a later publication (Boni, 1978) where an improved differencing scheme (the scheme itself is not stated) has been incorporated into the same computational procedure as Boni et al (1976). Predictions using this method of the flow in a Honda CVCC prechamber engine at 6000 rev/min are shown in fig. 2.25 at TDC of compression. A grid of 25 axial x 10 radial lines was used and turbulence was not included. Fig. 2.25 shows a quite plausible behaviour with single vortices in both pre and main chambers. The authors state however, that the latter vortex is greater in size than that observed by Tabacznski et al (1970) or Daneshyar et al (1973) and this is attributed to numerical errors introduced by the coarse grid adjacent to the boundary.

Calculations of the flow and heat transfer in a prechamber engine geometry have also been made by the author and described by Gosman et al (1979). In this instance, a plane two-dimensional idealisation was used to represent the three-dimensional 'Howerd' chamber geometry. The applicability of this idealisation is clearly open to question, but it is possible that the results may be at least qualitatively correct. The governing equations were solved in a general curvilinear orthogonal coordinate frame using the computational grid shown in fig.2.26. The grid was obtained using the methods described in appendix 1 .

Figs. 2.27 and 2.28 show respectively the predicted velocity and turbulence intensity fields during the compression and expansion phases, starting with the fluid at rest. These calculations roughly simulate a motored engine of 10:1 compression ratio operating at 1500 rev/min.

At 30^{o} ABDC the motion in the main chamber is essentially one-dimensional apart from where the flow contracts into the prechamber throat, while in the prechamber itself it simply expands again. The turbulence levels at this stage are very low and are not plotted. By mid-stroke (90^{o} ATDC) however the inflow to the prechamber is much stronger and separates at the throat walls to form two eddies on either side of the jet, the lower one being the larger of the two. Turbulence generation is particularly strong in the shear layers of the throat as is signalled by the maximum value of 0.8 occurring adjacent to the entry lip.

Substantial increases in both velocity and turbulence levels are apparent by 30^{o} BTDC where the lower eddy has enlarged and a small eddy has appeared in the main chamber. By TDC however the prechamber contains just one eddy and the turbulence has decreased, both effects presumably being a consequence of the gradual reduction in the inflow rate as the piston approaches the top of the stroke.

As the piston descends, the prechamber structure quickly alters to one of a simple sink flow, as shown by the results for 90^{o} ABDC. The outflowing gas enters the main chamber in the form of a jet which entrains the surrounding fluid and impinges almost normally onto the piston, producing appreciable turbulence in the process. By BDC the jet has produced a large eddy which fills the main chamber space, while inertia effects have caused a small vortex to appear in the prechamber. The general level of turbulence has decayed due to the smaller shearing rates prevailing.

Calculations of the flow and combustion in a divided-chamber stratified-charge engine have been made by Syed and Bracco (1979), the purpose of which was to assess the applicability of a two-equation turbulence model to the combustion process. The computations were divided into three stages, namely: (1) compression after IVC to ignition, (2) ignition to the end of combustion and (3) the end of combustion to EVO. During periods (1) and (3) the flow properties were assumed uniform but different in the prechamber and mainchamber, thus, the integration of ordinary differential equations (odes) yielded the temporal variations of mass, temperature and pressure. During period (2), partial differential equations for mass, momentum, energy, species, turbulence energy (k) and turbulence energy dissipation rate (ε) were solved to give the spatial (2-d) and temporal variation of the flow properties.

At the time of ignition the velocities were assumed zero and values of species mass fraction and temperature for the main chamber and prechamber were given by the solution of the odes whilst k and ε were ascribed values extrapolated from the experimental data of Witze (1977). This last practice is open to question, as the Witze data

relates to an engine with substantially different combustion chamber and valve geometry and is known to be in error (Witze, 1978). The specification of k and ε in the prechamber is even more difficult in the absence of data and the authors chose initially to use the same values as the main chamber. This led to very fast flame speeds and these values were subsequently reduced to accord with measured flame speeds. In the absence of any guiding information, these difficulties are appreciated.

No-slip boundary conditions were applied to the momentum equations whilst zero gradients were assumed for species and temperature. Heat transfer was accounted for in a rather ad hoc fashion by reducing the heat of combustion of the fuel. This seems an unnecessary simplication as there are better methods readily available for use in conjunction with the $k-\varepsilon$ turbulence model for incorporating wall heat transfer as will be outlined in Chapter 4 of the present thesis. Boundary conditions for k and ε were prescribed according to Launder and Spalding (1974). Combustion was assumed to follow a one-step irreversible reaction.

Experimental studies have also been made by the same authors in an engine of 8.25 cm bore and 11.4 cm stroke with a compression ratio of 8.4:1 and a prechamber to total clearance volume of 14%. A flat transparent cylinder head to permit photography and a flat-top piston were used to approximate two dimensionality as far as possible. The main chamber fuel was injected early in the compression stroke at 140^{o} BTDC via a diesel-type pump with an impinging jet nozzle in an effort to obtain a fine spray and complete evaporation and mixing near to TDC. Additional fuel was injected into the prechamber by a

second pump at 102^{o} BTDC. Tests were run at 1050 and 1550 rev/min, with two throat areas of .705 and 1.1 cm^2 and at rich and lean fuellings. An assessment of the degree of homogeneity and uniformity of the fuel/air mixture was not possible and occasional flaring in the main chamber suggests that local rich pockets or liquid fuel were present. It was also observed that considerable cycle-to-cycle variations occured with lean prechamber fuellings.

The flame front in the computations is characterised by high temperature gradients (evidenced in plotting as close contours) and these are compared with photographic records of the combustion process. After combustion was initiated in the prechamber (in both the engine and computations) the jet passed through the throat and into the main chamber. The jet velocity reached a maximum when the flame first appeared in the main chamber and then decreased rapidly as it progressed through the latter. The increase in flame speed is plausibly attributed to high levels of turbulence in the throat, generated by the localised shear stresses, as a result of the outflow preceeding the flame front. As this turbulence was convected, diffused and dissipated in the main chamber, the flame speed reduced rapidly.

The main findings of this study are that the k-ε turbulence model was superior to an assumption of constant diffusivities used in an earlier work (Gupta et al, 1978) in the prediction of flame propagation although the flame speed and spread were sensitive to both the initial and boundary conditions for k and ε.

Assessment of Theoretical Investigations

The features of the models described can be classified in three groups: firstly, capability of representing geometric aspects which include a moving piston, prechamber, piston bowl, valve etc.; secondly, the extent to which the flow equations solved represent physical reality, i.e. in respect of treatment of turbulence, boundary conditions etc. and lastly, the numerical aspects such as stability limits on time-step and cell Reynolds number. These features vary greatly between the models discussed and are summarised in table 2.1 for the most recent publication of each researcher(s). Also included for reference is the model used in this study.

A few general points are made below concerning the more important aspects:

1. The constraints that a cell Reynolds number restriction imposes are severe.
2. Explicit features of differencing schemes that lead to time-step stability criteria are apparently inefficient because of the small time-steps required. However, a true assessment of the relative merits of explicit and implicit schemes cannot be made unless computer times from two identical computer codes (in terms of equations solved, grids etc.) but with different differencing schemes, are compared.
3. The grids used by some researchers, notably Griffen et al (1976) Diwakar et al (1976) and Chong et al (1976) were too coarse to permit accurate prediction of the flow and heat transfer.
4. The incorporation of turbulence using a two-equation model has been shown by Gosman and Watkins (1976a, 1976b) and Watkins (1977) to be important in calculating both the flow and wall

heat transfer and by Syed and Bracco (1979) to strongly influence the combustion process.

5. With the exception of Boni et al (1978) and this study, the geometry flexibility allowed by the various computational methods is very limited.
6. Detailed quantitative comparisons between calculations and experiment are non-existent, with the exception of Watkins (1977) and this study.

2.6 Closure

In this chapter both experimental and theoretical studies by previous researchers have been reviewed. Certain features of in-cylinder flows have been identified as being of particular importance, namely, the intake-induced flow and subsequent compression, swirl and squish. These have been reviewed in detail and areas of agreement and disagreement between the various researchers indicated. Measurements in axisymmetric engines are of special importance as, at the present, they can provide the only means of experimental verification of the theoretical model used in this study. Three sets of such experiments relating to both the flow and heat transfer in such engines have been described. Finally, models of in-cylinder flow processes used by other researchers have been reviewed and the modelling and numerical features of each indicated. There is a lack of detailed validation of these models, due in part to

the inflexibility of the models in predicting flows in even simple engine geometries (e.g. those with moving valves and bowl-in-head or piston bowl configurations) but also because few experimentalists have made comprehensive and accurate measurements in axisymmetric engines.

CHAPTER 3

THE CO-ORDINATE FRAME AND DIFFERENTIAL EQUATIONS

3.1 Outline of Path

The purpose of this chapter is to assemble the differential equations that govern the flow and heat transfer in a form suitable for the present study. Firstly, in section 3.2, the peculiarities of practical diesel engine combustion chambers are discussed and the possible ways in which these may be incorporated into a viable computational scheme are examined. This section provides the framework upon which the subsequently derived equations are based.

Section 3.3 describes a curvilinear orthogonal Eulerian co-ordinate system in detail including definitions of geometric quantities and operators used in the manipulation of the differential equations. Sections 3.4 and 3.5 present respectively the instantaneous and ensemble-averaged versions of the governing differential equations in curvilinear orthogonal co-ordinates. The equations at this stage contain unknown turbulence correlations and section 3.6, the turbulence model, discusses the alternative 'levels' of turbulence model that may be employed, and how additional equations may be derived to calculate the turbulence properties (which are of interest in their own right). Section 3.7 describes the wall boundary conditions for all equations. In section 3.8, the mean flow equations of section 3.5, are closed using the results of section 3.6.

Section 3.9 derives formulae that are used to transform the differential equations,previously presented in Eulerian form, into a more flexible co-ordinate frame that moves in a manner determined by the motion of the piston. The equations for all variables are, at this stage, transformed into a final form.

3.2 Computational Considerations of Diesel Combustion Systems

The general partial differential equations that govern fluid flow and heat transfer, often referred to as the 'Navier-Stokes' and 'energy' equations, are too complicated for analytic solutions except in idealised situations; for the present problem, a numerical method of solution must be accepted. It is still early in the history of detailed in-cylinder computations, yet a solution protocol is emerging that does appear to possess certain advantages.

Before discussing the main features of such procedures, it is worthwhile examining the characteristics of in-cylinder flows. Firstly, they have a time-varying domain of solution, governed by the position of the piston. Secondly, virtually all commercial diesel combustion systems have certain complex geometric features, such as piston bowls or prechambers, used to promote air motion and hence enhance mixing and combustion. Finally, some means of intake and exhaust must be provided and here there are many alternatives such as poppet valves, sleeve valves, rotary valves, piston-controlled porting etc. On the last two aspects, this study focusses on idealised axisymmetric configurations with centrally-located piston bowls and axisymmetric representations of poppet valves or orifices, however the method is capable of extension to fully three-dimensional

configurations, the sole difficulties here being increased computing requirements and accurate representation of the complex chamber topography.

As with the majority of numerical solution schemes for pdes, the present method uses a computational grid superimposed upon the flow field and the values of the dependent variables of the differential equations are obtained at the intersection of the grid lines (or at intermediate locations, depending on the variable). The various ways in which the incorporation of the features of practical combustion systems into a viable computational procedure may be accomplished are discussed below.

One approach to the problem of moving boundaries, adopted by Hirt et al (1970), has been to cause the grid to move with the mean flow in a Lagrangian fashion. The method has proved powerful in solving, for example, free-surface problems such as fluid slopping in a tank. A major disadvantage however, is that in complicated flows, particularly those exhibiting recirculation, severe mesh distortion can prevent a solution being obtained; for this reason it is not thought a wise choice for the present application. Eulerian methods on the other hand, suffer from problems of resolution when applied to flows with moving boundaries if there are large differences between the maximum and minimum sizes of the solution domain. In the present context, if adequate resolution is provided at BDC this would invariably be inadequate at TDC, whilst, if sufficient grid lines are disposed between the cylinder head and piston top at TDC the grid density in this region would be unnecessarily high at BDC. The use of an Eulerian co-ordinate frame under these circumstances could at best be described as inefficient. The alternative to fully

Lagrangian or Eulerian schemes is to provide a specification of grid movement so that all grid lines remain disposed between the cylinder head and piston top at all times and further, that their distortion is controlled; as the piston motion is known, this is a simple task. Other researchers (Watkins (1973), Boni et al (1976) and Diwakar et al (1976)) have reached the same conclusion.

Turning attention now to the complicated geometry of the combustion chamber, the optimum scheme, if there is an optimum, is not quite so obvious. Referring to fig. 1.1, the possible ways of incorporating such shapes into different co-ordinate frames, together with the attributes of the alternative methods, are given below.

1. Rectilinear co-ordinate frame (fig. 3.1a)

This choice leads to the simplest form of the governing differential equations. Different geometries can be represented relatively easily although the approximation of curved surfaces using "stepped" grids is poor. Further, selective concentration of grid nodes in such regions (required in order to resolve the wall boundary layers) is not possible without introducing nodes elsewhere where they are not needed, and the boundary conditions are no longer easy to apply.

2. Curvilinear orthogonal co-ordinate frame (fig. 3.1b)

The complexity of the differential equations when formulated in this frame is intermediate between rectilinear (1) and non-orthogonal (3) formulations. The flexibility of the frame allows good approximation of curved boundary surfaces and easy application of boundary conditions. However some shapes may not be ideally

suited to orthogonal meshes (see appendix 1), notably those having non-orthogonal boundaries, and the orthogonality requirement sometimes presents non-optimum disposition of the grid nodes. Finally, a procedure is required to obtain the co-ordinate frame.

3. Non-orthogonal co-ordinate frame (fig. 3.1c)

The complexity of differential equations in this frame is greater than (1) or (2). On the other hand, it offers total flexibility and good approximation of boundary surfaces. Some means of co-ordinate frame generation is needed, but this can be relatively simple since orthogonality is not required.

4. Orthogonal co-ordinate directions in non-orthogonal computational mesh

An example of this approach is the ICED-ALE (Implicit Continuous-Fluid Eulerian - Arbitrary Lagrangian-Eulerian) method of Hirt et al (1974) which solves the governing equations in a Cartesian co-ordinate frame on a computing mesh which is non-orthogonal. However, the algorithm presented is semi-explicit and therefore requires the satisfaction of a time-step stability criterion, as previously mentioned in chapter 2.

The development of an implicit method using a similar arrangement was explored by the author, in which the SIMPLE algorithm (described in section 4.3) was to be used to solve the difference equations. However, although promising in some respects, this approach was finally abandoned due to the complexity and extreme length of the difference approximations to the differential equations, which could lead to excessive computing times.

5. Finite-element methods

Although researched by many groups, finite-element methods have not yet gained the popularity for fluid flow problems that they enjoy, almost exclusively, for theoretical stress and vibration analysis. A brief review of the published technical achievements of finite-element methods suggests that they have not reached the stage where they could be applied to the present problem.

Summary of Methods

Method 1, although simple, is not well suited to configurations involving boundary curvature for the reasons indicated and would require considerable testing to quantify the effects of "stepped" boundaries. Haselman and Westbrook (1978) have used this method to approximate a circular flow field, and using fine grids (40 x 40), have found a 5% angular momentum decay per swirl revolution attributable to the boundary treatment even though a "free-slip" boundary condition was imposed. This decay rate, due solely to the numerical method, would prove unacceptable in engine situations, where high rates of rotation are found in piston bowls near TDC.

Method 2 is much more flexible in respect of locating grid lines and imposing boundary conditions and requires little extra computational effort; it does however require that curvilinear orthogonal grids can be generated easily and efficiently.

Method 3 is the most general, but is probably unnecessarily so for the geometries considered. It is the most expensive computationally of the first three and again some means of grid generation must be provided.

In view of a total lack of experience with methods 4 and 5 it would seem unwise to attempt an ambitious problem such as the in-cylinder flow as an introduction to the techniques.

In the light of the above considerations, the co-ordinate frame finally chosen has the following characteristics:

1. Rectilinear and expanding/contracting with the piston motion between the cylinder head and piston top.
2. Curvilinear-orthogonal in the piston bowl and translating with the piston motion.
3. Axisymmetric.

A typical example generated using the method described in appendix 1 is shown in fig. 3.2.

3.3 The Co-Ordinate System

Fig. 3.3 illustrates a portion of a curvilinear orthogonal co-ordinate frame. The mutually-orthogonal co-ordinate directions ζ_1, ζ_2 and ζ_3 are defined with respect to an axial (z), radial (r) and circumferential (θ) co-ordinate frame such that the ζ_1-ζ_2 plane lies in the r-z plane and is a constant ζ_3 surface whilst the ζ_3 direction is identical with the θ direction, the angle of revolution about the r=0 axis. Lines of ζ_1 = constant and ζ_2 = constant are characterised by surfaces of revolution about the r=0 axis whilst ζ_3 = constant represents a plane.

The equations to be presented assume axial symmetry, and within this constraint, all variations in the ζ_3 direction are assumed zero.

Before the conservation equations can be formulated, further definition of the co-ordinate frame is needed. Sufficient information is provided by a knowledge of the orientation of either the ζ_1 or ζ_2 directions with the r or z axes and the radii of curvature r_1, r_2 and r_3. On the former aspect an angle β is defined, between the ζ_1 direction and the r = 0 axis; it follows that the angle between the ζ_2 direction and the r = 0 axis is 90 + β.

The distance between nearby points within the co-ordinate frame, ds, is related to the metric coefficients ℓ_1, ℓ_2 and ℓ_3 and increments in ζ_1, ζ_2 and ζ_3 by:

$$(ds)^2 = (\ell_1 d\zeta_1)^2 + (\ell_2 d\zeta_2)^2 + (\ell_3 d\zeta_3)^2 \qquad (3.1)$$

Although variations in the ζ_3 direction are not accounted for, this does not preclude the existance of a metric coefficient, ℓ_3, which is in fact equal to the radial distance, r. In general, both the grid orientation and the metric coefficients vary throughout the field, and for the present application, the latter may also vary with time (as described in section 3.9).

Four identities that aid the manipulation of the differential equations, and relate the radii of curvature to the metric coefficients, are:

$$\begin{aligned}
-\ell_2 \frac{\partial}{\partial\zeta_1}\left(\frac{1}{\ell_2}\right) &= \frac{1}{\ell_2}\frac{\partial\ell_2}{\partial\zeta_1} = \frac{\ell_1}{r_2} \\
-\ell_1 \frac{\partial}{\partial\zeta_2}\left(\frac{1}{\ell_1}\right) &= \frac{1}{\ell_1}\frac{\partial\ell_1}{\partial\zeta_2} = \frac{\ell_2}{r_1} \\
-\ell_3 \frac{\partial}{\partial\zeta_1}\left(\frac{1}{\ell_3}\right) &= \frac{1}{\ell_3}\frac{\partial\ell_3}{\partial\zeta_1} = \frac{\ell_1 \sin\beta}{r_3} \\
-\ell_3 \frac{\partial}{\partial\zeta_2}\left(\frac{1}{\ell_3}\right) &= \frac{1}{\ell_3}\frac{\partial\ell_3}{\partial\zeta_2} = \frac{\ell_2 \cos\beta}{r_3}
\end{aligned} \qquad (3.2)$$

A further equation that is required is the divergence operator, ∇, defined as:

$$\nabla.\underline{w} = \frac{1}{\ell_1\ell_2\ell_3}\left[\frac{\partial}{\partial\zeta_1}(\ell_2\ell_3 w_1) + \frac{\partial}{\partial\zeta_2}(\ell_1\ell_3 w_2)\right] \qquad (3.3)$$

Here, $\underline{w}$ is a vector quantity and its components in the ζ_1 and ζ_2 directions are w_1 and w_2. Equation 3.3 may be rewritten using the identities 3.2 , to produce a form involving the radii of curvature and the grid orientation, that is:

$$\nabla.\underline{w} = \left(\frac{1}{\ell_1}\frac{\partial w_1}{\partial\zeta_1} + \frac{w_1}{r_2}\right) + \left(\frac{1}{\ell_2}\frac{\partial w_2}{\partial\zeta_2} + \frac{w_2}{r_1}\right)$$

$$+ \frac{1}{r_3}(w_1 \sin\beta + w_2\cos\beta) \qquad (3.4)$$

Both forms are used in the differential equations.

3.4 Instantaneous Conservation Equations

The equations are presented here without proof; further details concerning their derivation may be found in a publication by Gosman et al (1969). Vinokur (1974) also derived the conservation equations, in this instance in a more general non-orthogonal co-ordinate system, although of more interest, a set of equations in a curvilinear orthogonal co-ordinate frame with temporal changes of the metric coefficients is also presented, and this latter aspect is a generalisation of the equations resulting from the co-ordinate transformations of section 3.9. The Eulerian form of the curvilinear-orthogonal equations are also presented by Humphrey (1978)

in general tensor notation and have been derived from the cartesian form by Pope (1978). Although the general tensor form of the equations is more compact, it is not used here so as to preserve clarity and highlight the nature of the additional terms that arise through co-ordinate curvature. In the equations, the symbols have the following meanings: $\hat{\rho}$ is the fluid density; $\hat{v}_1$, $\hat{v}_2$ and $\hat{v}_3$ are the velocity components in the ζ_1, ζ_2 and ζ_3 directions respectively; $\hat{\tau}$ is the stress tensor for a Newtonian fluid, whose components are defined by equations 3.15 and μ is the laminar viscosity; $\hat{h}$ is the stagnation enthalpy defined by:

$$\hat{h} = \hat{C}_p \hat{T} + \Sigma \frac{\hat{v}_i^2}{2} \tag{3.5}$$

$\hat{T}$ stands for absolute temperature, $\hat{\lambda}$ is the thermal conductivity and $\hat{C}_p$ is the specific heat defined as $\hat{C}_p = \frac{\tilde{h}}{\hat{T}}$ where $\tilde{h}$ is the instantaneous static enthalpy and $\hat{p}$ stands for pressure.

Conservation of mass

$$\frac{\partial \hat{\rho}}{\partial t} + \frac{1}{\ell_1 \ell_2 \ell_3} \{\frac{\partial}{\partial \zeta_1}(\ell_2 \ell_3 \hat{\rho} \hat{v}_1) + \frac{\partial}{\partial \zeta_2}(\ell_1 \ell_3 \hat{\rho} \hat{v}_2)\} = 0 \tag{3.6}$$

Conservation of momentum - direction 1

$$\frac{\partial(\hat{\rho}\hat{v}_1)}{\partial t} + \frac{1}{\ell_1 \ell_2 \ell_3} \{\frac{\partial}{\partial \zeta_1} [\ell_2 \ell_3 (\hat{\rho}\hat{v}_1 \hat{v}_1 - \hat{\tau}_{11})] + \frac{\partial}{\partial \zeta_2} [\ell_1 \ell_3 (\hat{\rho}\hat{v}_2 \hat{v}_1 - \hat{\tau}_{12})]\}$$

$$+ \frac{1}{\ell_1} \frac{\partial \hat{p}}{\partial \zeta_1} - \frac{1}{r_2} [\hat{\rho}\hat{v}_2^2 - \hat{\tau}_{22}] - \frac{\sin\beta}{r_3} [\hat{\rho}\hat{v}_3^2 - \hat{\tau}_{33}] + \frac{1}{r_1} [\hat{\rho}\hat{v}_2 \hat{v}_1 - \hat{\tau}_{12}] = 0 \tag{3.7}$$

Conservation of momentum - direction 2

$$\frac{\partial}{\partial t}(\hat{\rho}\hat{v}_2) + \frac{1}{\ell_1\ell_2\ell_3}\{\frac{\partial}{\partial\zeta_1}[\ell_2\ell_3(\hat{\rho}\hat{v}_1\hat{v}_2 - \hat{\tau}_{21})] + \frac{\partial}{\partial\zeta_2}[\ell_1\ell_3(\hat{\rho}\hat{v}_2\hat{v}_2 - \hat{\tau}_{22})]\}$$

$$+ \frac{1}{\ell_2}\frac{\partial\hat{p}}{\partial\zeta_2} - \frac{1}{r_1}[\hat{\rho}\hat{v}_1^2 - \hat{\tau}_{11}] - \frac{\cos\beta}{r_3}[\hat{\rho}\hat{v}_3^2 - \hat{\tau}_{33}] + \frac{1}{r_2}[\hat{\rho}\hat{v}_1\hat{v}_2 - \hat{\tau}_{21}] = 0 \tag{3.8}$$

Conservation of momentum - direction 3

$$\frac{\partial}{\partial t}(\hat{\rho}\hat{v}_3) + \frac{1}{\ell_1\ell_2\ell_3}\{\frac{\partial}{\partial\zeta_1}[\ell_2\ell_3(\hat{\rho}\hat{v}_1\hat{v}_3 - \hat{\tau}_{31})] + \frac{\partial}{\partial\zeta_2}[\ell_1\ell_3(\hat{\rho}\hat{v}_2\hat{v}_3 - \hat{\tau}_{32})]\}$$

$$+ \frac{1}{r_3}[\sin\beta\,(\hat{\rho}\hat{v}_1\hat{v}_3 - \hat{\tau}_{31}) + \cos\beta(\hat{\rho}\hat{v}_2\hat{v}_3 - \hat{\tau}_{32})] = 0 \tag{3.9}$$

Conservation of energy

$$\frac{\partial}{\partial t}(\hat{\rho}\hat{h}) + \frac{1}{\ell_1\ell_2\ell_3}\{\frac{\partial}{\partial\zeta_1}[\ell_2\ell_3\hat{\rho}\hat{v}_1\hat{h}] + \frac{\partial}{\partial\zeta_2}[\ell_1\ell_3\hat{\rho}\hat{v}_2\hat{h}]$$

$$- \frac{\partial}{\partial\zeta_1}[\frac{\ell_2\ell_3}{\ell_1}\frac{\hat{\lambda}}{\hat{C}_p}\frac{\partial\hat{h}}{\partial\zeta_1}] - \frac{\partial}{\partial\zeta_2}[\frac{\ell_1\ell_3}{\ell_2}\frac{\hat{\lambda}}{\hat{C}_p}\frac{\partial\hat{h}}{\partial\zeta_2}]\}$$

$$- \frac{\partial\hat{p}}{\partial t} - \frac{1}{\ell_1\ell_2\ell_3}\{\frac{\partial}{\partial\zeta_1}[\frac{\ell_2\ell_3}{\ell_1}(\hat{\mu} - \frac{\hat{\lambda}}{\hat{C}_p})\frac{\partial}{\partial\zeta_1}(\Sigma\frac{\hat{v}_i^2}{2})]$$

$$+ \frac{\partial}{\partial\zeta_2}[\frac{\ell_1\ell_3}{\ell_2}(\hat{\mu} - \frac{\hat{\lambda}}{\hat{C}_p})\frac{\partial}{\partial\zeta_2}(\Sigma\frac{\hat{v}_i^2}{2})]\} = 0 \tag{3.10}$$

The temperature, density and pressure are linked by an equation of state; the ideal gas relationship is used here, but this is not essential to the analysis:

$$\hat{\rho} = \hat{Q}\hat{p} \tag{3.11}$$

where $$\hat{Q} = \frac{1}{R\hat{T}} \tag{3.12}$$

The normal and shear stress components for a compressible flow are given in general form (see e.g. Goldstein (1957)) by:

$$\hat{\tau}_{ii} = \hat{\mu}\ \{\ 2[\frac{1}{\ell_i}\frac{\partial \hat{v}_i}{\partial \zeta_i} + \frac{\hat{v}_j}{\ell_i \ell_j}\frac{\partial \ell_i}{\partial \zeta_j} + \frac{\hat{v}_k}{\ell_k \ell_i}\frac{\partial \ell_i}{\partial \zeta_k}] - \frac{2}{3}\nabla.\hat{\underline{v}}\} \tag{3.13}$$

and:

$$\hat{\tau}_{ij} = \hat{\mu}\ \{\ \frac{\ell_j}{\ell_i}\frac{\partial}{\partial \zeta_i}(\frac{\hat{v}_j}{\ell_j}) + \frac{\ell_i}{\ell_j}\frac{\partial}{\partial \zeta_j}(\frac{\hat{v}_i}{\ell_i})\} \tag{3.14}$$

Using equations 3.2 relating the gradients of metric coefficient to the radii of curvature, the components of the stress tensor can be written as:

$$\hat{\tau}_{11} = \hat{\mu}\ \{2[\frac{1}{\ell_1}\frac{\partial \hat{v}_1}{\partial \zeta_1} + \frac{\hat{v}_2}{r_1}] - \frac{2}{3}\nabla.\hat{\underline{v}}\ \}$$

$$\hat{\tau}_{22} = \hat{\mu}\ \{2[\frac{1}{\ell_2}\frac{\partial \hat{v}_2}{\partial \zeta_2} + \frac{\hat{v}_1}{r_2}] - \frac{2}{3}\nabla.\hat{\underline{v}}\}$$

$$\hat{\tau}_{33} = \hat{\mu}\ \{\frac{2}{r_3}\ [\hat{v}_1 \sin\beta + \hat{v}_2 \cos\beta] - \frac{2}{3}\nabla.\hat{\underline{v}}\} \tag{3.15}$$

$$\hat{\tau}_{21} = \hat{\tau}_{12} = \hat{\mu}\ \{\frac{1}{\ell_2}\frac{\partial \hat{v}_1}{\partial \zeta_2} - \frac{\hat{v}_1}{r_1} + \frac{1}{\ell_1}\frac{\partial \hat{v}_2}{\partial \zeta_1} - \frac{\hat{v}_2}{r_2}\ \}$$

$$\hat{\tau}_{31} = \hat{\tau}_{13} = \hat{\mu}\ \{\frac{1}{\ell_1}\frac{\partial \hat{v}_3}{\partial \zeta_1} - \frac{\hat{v}_3 \sin\beta}{r_3}\}$$

$$\hat{\tau}_{32} = \hat{\tau}_{23} = \hat{\mu}\ \{\frac{1}{\ell_2}\frac{\partial \hat{v}_3}{\partial \zeta_2} - \frac{\hat{v}_3 \cos\beta}{r_3}\ \}$$

Equations 3.6 to 3.10 are exact and are equally applicable to both laminar and turbulent flows, however, they are not solved in the form presented for the reason indicated below.

3.5 Ensemble-Averaged Conservation Equations

The numerical method of solution employed to solve the equations calculates the value of each dependent variable at discrete locations throughout the field defined by the co-ordinate mesh. The flow in engine cylinders is highly turbulent and the important properties of the turbulence have small time and length scales, for example, the characteristic dimension of the eddies responsible for the decay of turbulence in engines is less than .5mm (Dent and Salama 1975b). To resolve detail of this order is impossible and resort is therefore made to the determination of averaged values of the variable in question in which the averaging process removes explicit reference to the small-scale motions. This is done by first replacing the instantaneous values of the variables (designated by the $\hat{\phi}$ symbol) by the sum of an ensemble-average value ($\overline{\phi}$) and a variation (ϕ') about this value, i.e. typically:

$$\hat{\rho} = \overline{\rho} + \rho' \ , \qquad \hat{v}_i = \overline{v}_i + v_i' \qquad \text{etc.}$$

The application of this technique to steady flows, is well established, however there are implications when applied to unsteady processes that merit additional consideration and these are discussed in the next section.

The replacement of the instantaneous quantities in equations 3.6 to 3.10 by a mean and fluctuating component and ensemble averaging the result (see Watkins, 1977) produces the following:

Conservation of mass

$$\frac{\partial \overline{\rho}}{\partial t} + \frac{1}{\ell_1 \ell_2 \ell_3}\left\{\frac{\partial}{\partial \zeta_1}\left[(\ell_2 \ell_3(\overline{\rho v_1} + \overline{\rho' v_1'})\right] + \frac{\partial}{\partial \zeta_2}\left[\ell_1 \ell_3(\overline{\rho v_2} + \overline{\rho' v_2'})\right]\right\} = 0 \quad (3.16)$$

Conservation of momentum - direction 1

$$\frac{\partial}{\partial t}\left(\overline{\rho v_1} + \overline{\rho' v_1'}\right) + \frac{1}{\ell_1 \ell_2 \ell_3}\left\{\frac{\partial}{\partial \zeta_1}\left[\ell_2 \ell_3(\overline{\rho v_1}\,\overline{v}_1 + (\overline{\rho v_1' v_1'} - \overline{\tau}_{11}) + 2\overline{v}_1\,\overline{\rho' v_1'}\right.\right.$$

$$\left. + \overline{\rho' v_1' v_1'}\right] + \frac{\partial}{\partial \zeta_2}\left[\ell_1 \ell_3(\overline{\rho v_2}\,\overline{v}_1 + (\overline{\rho v_2' v_1'} - \overline{\tau}_{21}) + \overline{v}_2\overline{\rho' v_1'} + \overline{v}_1\overline{\rho' v_2'} + \overline{\rho' v_1' v_2'})\right]\Big\}$$

$$+ \frac{1}{\ell_1}\frac{\partial \overline{p}}{\partial \zeta_1} - \frac{1}{r_2}\left[\overline{\rho v_2 v_2} + (\overline{\rho v_2' v_2'} - \overline{\tau}_{22}) + \overline{2 v_2 \rho' v_2'} + \overline{\rho' v_2' v_2'}\right]$$

$$- \frac{\sin\beta}{r_3}\left[\overline{\rho v_3 v_3} + (\overline{\rho v_3' v_3'} - \overline{\tau}_{33}) + \overline{2 v_3 \rho' v_3'} + \overline{\rho' v_3' v_3'}\right]$$

$$+ \frac{1}{r_1}\left[\overline{\rho v_2 v_1} + (\overline{\rho v_2' v_1'} - \overline{\tau}_{21}) + \overline{v_2 \rho' v_1'} + \overline{v_1 \rho' v_2'} + \overline{\rho' v_2' v_1'}\right] = 0 \quad (3.17)$$

Terms involving the ensemble-average of a single fluctuating quantity are, by definition, zero. The stress tensor components have been grouped with certain fluctuating quantities for which the reason will become apparent after the turbulence model has been discussed. Note also that $\hat{\tau}$ may be replaced directly by $\overline{\tau}$ as it contains no products of fluctuating quantities, ignoring fluctuations of laminar viscosity which could be caused by, for example, temperature fluctuations

which are in any case usually negligibly small in unreacting turbulent flows.

Conservation of momentum - direction 2

$$\frac{\partial}{\partial t}(\overline{\rho v}_2 + \overline{\rho' v_2'}) + \frac{1}{\ell_1\ell_2\ell_3}\{\frac{\partial}{\partial \zeta_1}[\ell_2\ell_3(\overline{\rho v}_1\overline{v}_2 + (\overline{\rho v_1' v_2'} - \overline{\tau}_{12}) + \overline{v}_2\overline{\rho' v_1'}$$

$$+ \overline{v}_1\overline{\rho' v_2'} + \overline{\rho' v_1' v_2'})] + \frac{\partial}{\partial \zeta_2}[\ell_1\ell_3(\overline{\rho v}_2\overline{v}_2 + (\overline{\rho v_2' v_2'} - \overline{\tau}_{22})$$

$$+ 2\overline{v}_2\overline{\rho' v_2'} + \overline{\rho' v_2' v_2'})]\} + \frac{1}{\ell_2}\frac{\partial \overline{p}}{\partial \zeta_2}$$

$$- \frac{1}{r_1}[\overline{\rho v}_1\overline{v}_1 + (\overline{\rho v_1' v_1'} - \overline{\tau}_{11}) + 2\overline{v}_1\overline{\rho' v_1'} + \overline{\rho' v_1' v_1'}]$$

$$- \frac{\cos\beta}{r_3}[\overline{\rho v}_3\overline{v}_3 + (\overline{\rho v_3' v_3'} - \overline{\tau}_{33}) + 2\overline{v}_3\overline{\rho' v_3'} + \overline{\rho' v_3' v_3'}]$$

$$+ \frac{1}{r_2}[\overline{\rho v}_1\overline{v}_2 + (\overline{\rho v_1' v_2'} - \overline{\tau}_{12}) + \overline{v}_1\overline{\rho' v_2'} + \overline{v}_2\overline{\rho' v_1'} + \overline{\rho' v_1' v_2'}] = 0 \qquad (3.18)$$

Conservation of momentum - direction 3

$$\frac{\partial}{\partial t}(\overline{\rho v}_3 + \overline{\rho' v_3'}) + \frac{1}{\ell_1\ell_2\ell_3}\{\frac{\partial}{\partial \zeta_1}[\ell_2\ell_3(\overline{\rho v}_1\overline{v}_3 + (\overline{\rho v_1' v_3'} - \overline{\tau}_{13}) + \overline{v}_3\overline{\rho' v_1'}$$

$$+ \overline{v}_1\overline{\rho' v_3'} + \overline{\rho' v_1' v_3'})] + \frac{\partial}{\partial \zeta_2}[\ell_1\ell_3(\overline{\rho v}_2\overline{v}_3 + (\overline{\rho v_2' v_3'} - \overline{\tau}_{23}) + \overline{v}_3\overline{\rho' v_2'}$$

$$+ \overline{v}_2\overline{\rho' v_3'} + \overline{\rho' v_2' v_3'})]\}$$

$$+ \frac{1}{r_3}[\sin\beta(\overline{\rho v}_1\overline{v}_3 + (\overline{\rho v_1' v_3'} - \overline{\tau}_{13}) + \overline{v}_1\overline{\rho' v_3'} + \overline{v}_3\overline{\rho' v_1'} + \overline{\rho' v_1' v_3'})$$

$$+ \cos\beta(\overline{\rho v}_2\overline{v}_3 + (\overline{\rho v_2' v_3'} - \overline{\tau}_{23}) + \overline{v}_2\overline{\rho' v_3'} + \overline{v}_3\overline{\rho' v_2'} + \overline{\rho' v_2' v_3'})] = 0 \qquad (3.19)$$

Conservation of energy

Ignoring fluctuations of laminar viscosity, thermal conductivity and specific heat, the ensemble averaged stagnation enthalpy equation is:

$$\frac{\partial}{\partial t}(\overline{\rho h}) + \frac{1}{\ell_1\ell_2\ell_3}\{\frac{\partial}{\partial \zeta_1}[\ell_2\ell_3(\overline{\rho v_1 h} + \overline{\rho v_1' h'} + \overline{v_1 \rho' h'} + \overline{h\rho' v_1'} + \overline{\rho' v_1' h'})]$$

$$+ \frac{\partial}{\partial \zeta_2}[\ell_1\ell_3(\overline{\rho v_2 h} + \overline{\rho v_2' h'} + \overline{v_2 \rho' h'} + \overline{h\rho' v_2'} + \overline{\rho' v_2' h'})]$$

$$- \frac{\partial}{\partial \zeta_1}[\frac{\ell_2\ell_3}{\ell_1}\overline{\frac{\lambda}{C_p}\frac{\partial h}{\partial \zeta_1}}] - \frac{\partial}{\partial \zeta_2}[\frac{\ell_1\ell_3}{\ell_2}\overline{\frac{\lambda}{C_p}\frac{\partial h}{\partial \zeta_2}}]\} - \frac{\partial \overline{p}}{\partial t}$$

$$- \frac{1}{\ell_1\ell_2\ell_3}\{\frac{\partial}{\partial \zeta_1}[\frac{\ell_2\ell_3}{\ell_1}(\overline{\mu} - \frac{\overline{\lambda}}{\overline{C_p}})\frac{\partial}{\partial \zeta_1}(\Sigma \frac{\overline{v_i^2}}{2} + k)]$$

$$+ \frac{\partial}{\partial \zeta_2}[\frac{\ell_1\ell_3}{\ell_2}(\overline{\mu} - \frac{\overline{\lambda}}{\overline{C_p}})\frac{\partial}{\partial \zeta_2}(\Sigma \frac{\overline{v_i^2}}{2} + k)]\} = 0 \qquad (3.20)$$

where $$\overline{h} = \overline{C_p T} + \Sigma \frac{\overline{v_i^2}}{2} + k \qquad (3.21)$$

$$(k = \Sigma \frac{\overline{v_i'^2}}{2})$$

Equations 3.16 to 3.20 are as complete and exact as the instantaneous equations in two dimensions and are equally insoluble because the averaging process has given rise to new unknowns like $\overline{\rho v_1' v_2'}$. Before a solution can be effected, further equations for these unknowns must be found in order to form a closed set. The process of formulating equations for the unknown correlations is termed 'turbulence modelling' and forms the subject of the next section.

3.6 The Turbulence Model

Physics of the Turbulence Process

Turbulent flows contain a spectrum of eddy sizes and strengths from the largest, generated by the action of the mean flow, to the smallest, dominated by viscous effects. The larger eddies are often referred to as 'energy containing' and they extract energy from the mean flow at a rate equal to the work done by the mean rate of strain against the Reynolds stresses ($-\overline{\rho v_i' v_j'}$ terms). (Strictly speaking, the energy containing eddies are not the largest, although the more permanent larger eddies contain up to 20% of the total kinetic energy (Hinze, 1959)). Turbulence in this part of the size spectrum exhibits an anisotropic (directionally dependent) structure as the Reynolds stresses and mean strain rates depend upon the mean flow. Viscous effects on these eddies are small if a turbulent Reynolds number, defined as $Re_\lambda = v'\lambda/\nu$ where v' is a fluctuating velocity, λ is a typical length scale (intermediate between the largest and smallest eddies and termed the Taylor microscale) and ν is the kinematic viscosity, is reasonably high ($Re_\lambda > 30$) (Bradshaw, 1971). At the lower end of the size spectrum, the smallest eddies exhibit an isotropic structure, which is statistically independent of the mean flow and the largest eddies. The small eddies are supplied energy from the larger ones (this exchange process is called the "energy cascade") which is subsequently dissipated into heat by the action of viscosity. The process is not of course quite this simple, as large eddies are affected to some extent by viscosity and the small eddies do contain some energy, yet this picture does provide a broad view of the modes of generation and destruction of turbulence.

Turbulence is also convected and diffused in the mean flow. It would seem reasonable therefore that any turbulence model that purports to being realistic would at least attempt to incorporate these phenomena.

The mathematical representation of turbulence quantities

As indicated in the previous section the instantaneous value of some dependent variable of the flow, denoted $\hat{\phi}$, can be represented mathematically by an average value, $\overline{\phi}$, upon which a fluctuating component, ϕ', has been superimposed, i.e.

$$\hat{\phi} = \overline{\phi} + \phi' \tag{3.22}$$

For a statistically stationary or 'steady' flow, it is usual to define $\overline{\phi}$ as being a time-averaged value (see e.g. Hinze, 1959) as:

$$\overline{\phi}(\underline{x}_0) = \underset{t_0 \to \infty}{\text{Limit}} \frac{1}{2t_0} \int_{t=-t_0}^{t=t_0} \phi(\underline{x}_0, t)\,dt \tag{3.23}$$

If the flow is non-stationary or unsteady, an ensemble-averaged value is defined as:

$$\overline{\phi}(\underline{x}_0,\ t) = \underset{m \to \infty}{\text{Limit}} \frac{1}{2m+1} \sum_{n=-m}^{n=m} \phi(\underline{x}_0, nt_0+t) \tag{3.24}$$

Here, if the flow is not cyclically repeating temporarally, n stands for the number of identically repeated experiments and if the flow is cyclically repetative then n is the number of cycles; t is the time after the start of each experiment or cycle of period t_0 and $\underline{x}_0$ is some fixed point in space. It is possible to determine experimentally both the ensemble averaged and fluctuating components using these expressions (the latter quantity by subtracting the mean from the instantaneous value). However, when applied to

"cyclic" process that exhibit cycle-to-cycle variations, as is the case in IC engines, the measured turbulence quantity will be larger than the true value, that is, the cycle-to-cycle variations appear as an additional or apparent turbulence. This, at least in theory, can be overcome by using a mixed ensemble/time average (Lancaster, 1976, and, Woods and Ghirlando, 1975). If $\hat{\phi}$ is defined as:

$$\hat{\phi} = \overline{\phi}_n + \overline{\phi}_t + \phi' \tag{3.25}$$

where $\overline{\phi}_n$ is the ensemble averaged value and $\overline{\phi}_t$ is a time-averaged value over some short time interval for the n'th cycle after $\overline{\phi}_n$ has been subtracted, then $\overline{\phi}_t$ represents the cycle-to-cycle variation of the mean velocity (see fig. 3.4). In practice, the determination of $\overline{\phi}_t$ is difficult as the crank-angle "window" over which the value of $\hat{\phi}$ is averaged is of necessity large (Lancaster used 45^o), and over which period the "constant" time-averaged value certainly varies considerably.

A distinction should here be drawn between experiment and cycle-averaged quantities in the context of the differential equations. If it is assumed that because the motions inside the reciprocating engine are cyclic (ignoring cycle-to-cycle variations), then $\overline{\Phi}$ is by definition a cycle-averaged value, thus precluding the use of the equations for anything other than a cyclic solution (Watkins, 1977). It is therefore expedient to consider $\overline{\Phi}$ as being experiment-averaged which does not restrict the use of the method to a cyclically-steady operating condition.

Density Fluctuations

Equations 3.16 to 3.20 contain some terms of the form $\overline{\rho' v_i'}$ and $\overline{\rho' h'}$. The replacement of these by calculable quantities is difficult and uncertain (Syed, 1977), although in the absence of combustion, they are in any case probably much smaller than the other correlations. Their role in combustion calculations however, could prove to be significant (Libby and Bray, 1977). They are ignored in the present analysis. An alternative proposed by Favre (1969) is to work with mass-averaged variables. It has been shown by Pope (1976) others that when this is done the resulting equations are the same and as the ensemble-averaged versions with the above-mentioned terms omitted. However the extraction of the ensemble-average variables from the mass averaged ones still requires the modelling of the $\overline{\rho' \phi'}$ terms.

Choice of a Turbulence Model

A variety of models exist for incorporating the effects of turbulence into fluid flow calculations. The alternative modelling approaches may be summarised as follows:

(1) The 'turbulent' or 'eddy' viscosity concept approximates the turbulent transport of momentum in the mean flow equations by the product of a turbulent viscosity (μ_t) and a gradient of mean velocity (see equations 3.29 and 3.30). The turbulent viscosity is related to turbulent length (ℓ_t) and velocity (v_t) scales (Prandtl, 1925, 1945) via the relationship:

$$\mu_t = \bar{\rho} \ell_t v_t \qquad (3.26)$$

these latter quantities being either specified or calculated from differential equations.

(2) The turbulent viscosity approximation may be dispensed with by solving differential equations for the Reynolds stresses themselves. This requires the solution of 6 pdes if all stress components are non-zero and an additional pde for the length scale (see e.g. Rotta, 1951). In certain classes of flow, characterised by small velocity gradients, the mean flow transport terms of the Reynolds stress pdes may be approximated in an algebraic fashion, thereby reducing the number of differential equations (see e.g. Ying, 1971).

(3) Large eddy simulation (LES) is a 3-d, time-dependent calculation of the large-scale turbulence field. Modelling is necessary only for turbulence of scales smaller than the computational grid spacing. Unlike (1) and (2) above, the large-scale turbulence does not need modelling, this being required only for the small-scale turbulence which is much more universal (isotropic) in character and may be modelled in terms of the local large-scale field. The length scales of the subgrid-scale turbulence are determined by the grid size and not by a modelled equation, thus, the method simulates directly all of the turbulence greater than the grid size (see e.g.Reynolds, W.C., 1978).

The above options are listed in increasing order of complexity (and computational expense). The condition of small velocity gradients, required for the algebraic approximation to the Reynolds-stress model in (2), is not fulfilled for the flow in engine cylinders. The alternative in this case is a solution of 7 pdes in addition to the mean flow equations - a task not to be taken lightly. LES, (3) above, appears attractive as the flow in engine cylinders is time-dependent

and most configurations of interest are 3-d. However this form of modelling is still at an embryonic stage and the indications are that the required computer resources can be enormous (see e.g. Saffman, 1977). It therefore seems reasonable that unless the class of models outlined in (1) are, through careful validation, found to be inadequate, or such time as advances in computers and further model development make (2) and (3) more attractive, that the simpler models are worthy of exploitation.

Focussing attention then on the class of models in (1), Prandtl (1945) has suggested that the velocity scale is well represented by the square root of the turbulent kinetic energy, $k(=1/2\ \Sigma\ \overline{v_i'^2})$. This definition implies isotropy in the larger scale turbulent motions, no distinction being made between the three normal components of Reynolds stress. The turbulent viscosity is then given by:

$$\mu_t = \rho \ell_t k^{1/2} \tag{3.27}$$

Both ℓ_t and k may be determined from the solution of differential transport equations. Other two-equation models have been proposed (see e.g. Launder and Spalding, 1972), the most popular being that of Jones and Launder (1972) which solves pdes for the turbulence energy and its dissipation rate, $\varepsilon\ (=k^{3/2}/\ell_t)$. Other variables related to k and ℓ_t may be substituted for ε although this quantity is favoured because of the relative simplicity of the ε equation. This model would therefore seem a reasonable choice for the present and does have the advantage of being well documented, at least, for steady flows.

Turbulent Kinetic-Energy Equation

A differential equation for the conservation of turbulent kinetic energy may be derived by multiplying the momentum equation for $\hat{v}_i$ by its respective fluctuating component v_i', then summing over i and ensemble-averaging. The process has been carried out in detail by Watkins (1977) and others; the result is:

$$
\begin{aligned}
\text{I} \quad & \frac{\partial}{\partial t}(\overline{\rho} k) \\
\text{II} \quad & + \frac{1}{\ell_1 \ell_2 \ell_3} \left\{ \frac{\partial}{\partial \zeta_1}(\ell_2 \ell_3 \overline{\rho v}_1 k) + \frac{\partial}{\partial \zeta_2}(\ell_1 \ell_3 \overline{\rho v}_2 k) \right. \\
\text{III} \quad & \left. + \frac{\partial}{\partial \zeta_1}\left[\frac{\ell_2 \ell_3}{\ell_1} \overline{\rho v_1'(k + \frac{p'}{\overline{\rho}})}\right] + \frac{\partial}{\partial \zeta_2}\left[\frac{\ell_1 \ell_3}{\ell_2} \overline{\rho v_2'(k + \frac{p'}{\overline{\rho}})}\right] \right\} \\
\text{IV} \quad & \left\{ \begin{array}{l}
+ \overline{\rho v_1' v_1'} \left(\frac{1}{\ell_1} \frac{\partial \overline{v}_1}{\partial \zeta_1} + \frac{\overline{v}_2}{r_1} \right) + \overline{\rho v_2' v_2'} \left(\frac{1}{\ell_2} \frac{\partial \overline{v}_2}{\partial \zeta_2} + \frac{\overline{v}_1}{r_2} \right) \\
+ \overline{\rho v_3' v_3'} \left(\frac{\overline{v}_1 \sin\beta + \overline{v}_2 \cos\beta}{r_3} \right) + \overline{\rho v_1' v_2'} \left(\frac{1}{\ell_2} \frac{\partial \overline{v}_1}{\partial \zeta_2} - \frac{\overline{v}_1}{r_1} + \frac{1}{\ell_1} \frac{\partial \overline{v}_2}{\partial \zeta_1} - \frac{\overline{v}_2}{r_2} \right) \\
+ \overline{\rho v_1' v_3'} \left(\frac{1}{\ell_1} \frac{\partial \overline{v}_3}{\partial \zeta_1} - \frac{\overline{v}_3 \sin\beta}{r_3} \right) + \overline{\rho}\, \overline{v_2' v_3'} \left(\frac{1}{\ell_2} \frac{\partial \overline{v}_3}{\partial \zeta_2} - \frac{\overline{v}_3 \cos\beta}{r_3} \right)
\end{array} \right. \\
\text{V} \quad & - \Sigma \left\{ \overline{\frac{p'}{\ell_i} \frac{\partial v_i'}{\partial \zeta_i}} \right\} \\
\text{VI} \quad & + \Sigma \mu \left\{ \overline{\frac{1}{\ell_j} \frac{\partial v_i'}{\partial \zeta_j}^2} \right\} \\
\text{VII} \quad & - \Sigma \frac{1}{\ell_i} \frac{\partial}{\partial \zeta_i} \left\{ \frac{\mu}{\ell_i} \frac{\partial k}{\partial \zeta_i} \right\} = 0
\end{aligned}
\tag{3.28}
$$

Terms I and II represent the rate of change and convection by the mean flow of k respectively.

Term III describes the transport of k by the fluctuating velocities, which has been assumed by Prandtl (1945), Kolmogorov (1942) and others to be a diffusion process. The pressure diffusion part of this term (proportional to p'/ρ) is neglected on the evidence of measured turbulence energy budgets which balance without it (Bradshaw, Cebeci and Whitelaw, 1977). Term III is modelled as:

$$- \frac{1}{\ell_1 \ell_2 \ell_3} \{ \frac{\partial}{\partial \zeta_1} (\frac{\ell_2 \ell_3}{\ell_1} \frac{\mu_t}{\sigma_k} \frac{\partial k}{\partial \zeta_1}) + \frac{\partial}{\partial \zeta_2} (\frac{\ell_1 \ell_3}{\ell_2} \frac{\mu_t}{\sigma_k} \frac{\partial k}{\partial \zeta_2}) \}$$

where σ_k is a turbulent Prandtl number.

Term IV consists of products of stresses and mean strain rates and represents the generation rate of turbulence energy. A general form of the Boussinesq approximation (Boussinesq, 1877) for a compressible flow may be used to express the stress components in terms of the mean strain rate (Hinze, 1959):

$$- \overline{\rho v_i' v_i'} = 2\mu_t \{ \frac{1}{\ell_i} \frac{\partial \overline{v}_i}{\partial \zeta_i} + \frac{\overline{v}_j}{\ell_i \ell_j} \frac{\partial \ell_i}{\partial \zeta_j} + \frac{\overline{v}_k}{\ell_k \ell_i} \frac{\partial \ell_i}{\partial \zeta_k} \} - \frac{2}{3} (\overline{\rho}\, k + \mu_t \nabla . \underline{\overline{v}}) \qquad (3.29)$$

and

$$- \overline{\rho}\, \overline{v_i' v_j'} = \mu_t \{ \frac{\ell_j}{\ell_i} \frac{\partial}{\partial \zeta_i} (\frac{\overline{v}_j}{\ell_j}) + \frac{\ell_i}{\ell_j} \frac{\partial}{\partial \zeta_j} (\frac{\overline{v}_i}{\ell_i}) \} \qquad (3.30)$$

Using these expressions, the generation rate may be written as:

$$G_t = \mu_t \{ 2\left(\frac{1}{\ell_1}\frac{\partial \bar{v}_1}{\partial \zeta_1} + \frac{\bar{v}_2}{r_1}\right)^2 + 2\left(\frac{1}{\ell_2}\frac{\partial \bar{v}_2}{\partial \zeta_2} + \frac{\bar{v}_1}{r_2}\right)^2$$

$$+ 2\left(\frac{\bar{v}_1 \sin\beta + \bar{v}_2 \cos\beta}{r_3}\right)^2 + \left(\frac{1}{\ell_2}\frac{\partial \bar{v}_1}{\partial \zeta_2} - \frac{\bar{v}_1}{r_1} + \frac{1}{\ell_1}\frac{\partial \bar{v}_2}{\partial \zeta_1} - \frac{\bar{v}_2}{r_2}\right)^2$$

$$+ \left(\frac{1}{\ell_1}\frac{\partial \bar{v}_3}{\partial \zeta_1} - \frac{v_3 \sin\beta}{r_3}\right)^2 + \left(\frac{1}{\ell_2}\frac{\partial \bar{v}_3}{\partial \zeta_2} - \frac{v_3 \cos\beta}{r_3}\right)^2$$

$$- 2\nabla.\underline{\bar{v}} \left(\bar{\rho} k + \mu_t \nabla.\underline{\bar{v}} \right) \qquad (3.31)$$

Term V is also a production term, in this case due to the interaction between the fluctuating pressure and the fluctuating velocities. Little is known about the term although Bray (1974) suggests that it is negligible for low Mach number reacting flows; it is therefore neglected here.

Term VI represents the dissipation of turbulence energy and is replaced by $\bar{\rho}\varepsilon$, the dissipation rate ε being the dependent variable of its own transport equation as mentioned earlier.

Noting that $k^{1/2}$ and $k^{3/2}/\varepsilon$ are respectively a characteristic velocity and length scale of the turbulent field, dimensional analysis yields the following relation for the turbulent viscosity:

$$\mu_t = C_\mu \bar{\rho} \frac{k^2}{\varepsilon} \qquad (3.32)$$

where C_μ is an empirical coefficient, usually ascribed a constant value.

Term VII represents the transport of k by molecular diffusion and may be combined with the modelled form of term III to give:

$$- \frac{1}{\ell_1\ell_2\ell_3}\{\frac{\partial}{\partial\zeta_1}(\frac{\ell_2\ell_3}{\ell_1}\ \frac{\mu_{eff}}{\sigma_k}\frac{\partial k}{\partial\zeta_1}) + \frac{\partial}{\partial\zeta_2}(\frac{\ell_1\ell_3}{\ell_2}\frac{\mu_{eff}}{\sigma_k}\frac{\partial k}{\partial\zeta_2})\}$$

where the effective viscosity, μ_{eff}, is the sum of the turbulent and laminar viscosities, i.e.:

$$\mu_{eff} = \mu_t + \mu \tag{3.33}$$

The final term of the k equation may be written as:

$$\frac{\partial}{\partial t}(\bar{\rho}k) + \frac{1}{\ell_1\ell_2\ell_3}\{\frac{\partial}{\partial\zeta_1}(\ell_2\ell_3\bar{\rho}\ \bar{v}_1 k) + \frac{\partial}{\partial\zeta_2}(\ell_3\ell_1\bar{\rho}\ \bar{v}_2 k)$$

$$- \frac{\partial}{\partial\zeta_1}(\frac{\ell_2\ell_3}{\ell_1}\frac{\mu_{eff}}{\sigma_k}\frac{\partial k}{\partial\zeta_1}) - \frac{\partial}{\partial\zeta_2}(\frac{\ell_1\ell_3}{\ell_2}\ \frac{\mu_{eff}}{\sigma_k}\frac{\partial k}{\partial\zeta_2})\}$$

$$- G_t + \bar{\rho}\epsilon = 0 \tag{3.34}$$

Dissipation Equation

An exact equation for ϵ can be derived by taking a derivative of the equation for v_i' with respect to ζ_ℓ, multiplying by $\frac{2\mu}{\ell_\ell}\frac{\partial v_i'}{\partial\zeta_\ell}$ and ensemble averaging (see e.g. Watkins, 1977). The result, in general form, is:

$$\text{I} \quad \frac{\partial}{\partial t}(\bar{\rho}\epsilon) + \frac{1}{\ell_1\ell_2\ell_3}\{\frac{\partial}{\partial\zeta_1}(\ell_2\ell_3\overline{\rho v}_1\epsilon) + \frac{\partial}{\partial\zeta_2}(\ell_1\ell_3\overline{\rho v}_2\epsilon)$$

$$\text{II} \quad + \frac{\partial}{\partial\zeta_1}(\frac{\ell_2\ell_3}{\ell_1}\overline{\rho v_1'\epsilon}) + \frac{\partial}{\partial\zeta_2}(\frac{\ell_1\ell_3}{\ell_2}\overline{\rho v_2'\epsilon})\}$$

$$\text{III} \quad + 2\mu\{\frac{1}{\ell_\ell}\frac{\partial\bar{v}_j}{\partial\zeta_\ell}\ \frac{1}{\ell_\ell}\overline{\frac{\partial v_i'}{\partial\zeta_\ell}\frac{1}{\ell_j}\frac{\partial v_i'}{\partial\zeta_j}} + \frac{1}{\ell_j}\frac{\partial\bar{v}_i}{\partial\zeta_j}\frac{1}{\ell_\ell}\overline{\frac{\partial v_i'}{\partial\zeta_\ell}\frac{1}{\ell_\ell}\frac{\partial v_i'}{\partial\zeta_\ell}}\}$$

$$\text{IV} \quad + 2\mu \left\{ \frac{1}{\ell_\ell} \frac{\overline{\partial v_i'}}{\partial \zeta_\ell} \frac{1}{\ell_\ell} \frac{\partial v_j'}{\partial \zeta_\ell} \frac{1}{\ell_j} \frac{\partial v_i'}{\partial \zeta_j} + \frac{\mu}{\rho} \left(\frac{\overline{\partial^2 v_i'}}{\ell_j \partial \zeta_j \ell_\ell \partial \zeta_\ell} \right)^2 \right\}$$

$$\text{V} \quad - \frac{\overline{2\rho\varepsilon}}{\ell_j} \frac{\partial v_j'}{\partial \zeta_j} - \frac{\overline{\rho}\varepsilon}{\ell_\ell} \frac{\partial \overline{v}_\ell}{\partial \zeta_\ell}$$

$$\text{VI} \quad + \frac{2\mu}{\rho} \frac{1}{\ell_i} \frac{\partial}{\partial \zeta_i} \left(\frac{1}{\ell_\ell} \frac{\overline{\partial v_i'}}{\partial \zeta_\ell} \frac{1}{\ell_\ell} \frac{\partial p'}{\partial \zeta_\ell} \right) + \frac{2\mu \partial^2 \overline{v}_i}{\ell_\ell \partial \zeta_\ell \ell_j \partial \zeta_j} \frac{\overline{v_j'} \frac{\partial v_i'}{\partial \zeta_\ell}}{\ell_\ell}$$

$$- s_\mu = 0 \qquad (3.35)$$

where s_μ contains terms involving gradients of molecular viscosity, mean density and fluctuating pressure.

Term II describes the transport of ε by the fluctuating velocities and is modelled in the same fashion as the similar term in the k equation:

$$- \frac{1}{\ell_1 \ell_2 \ell_3} \left\{ \frac{\partial}{\partial \zeta_1} \left(\frac{\ell_2 \ell_3}{\ell_1} \frac{\mu_{eff}}{\sigma_\varepsilon} \frac{\partial \varepsilon}{\partial \zeta_1} \right) + \frac{\partial}{\partial \zeta_2} \left(\frac{\ell_1 \ell_3}{\ell_2} \frac{\mu_{eff}}{\sigma_\varepsilon} \frac{\partial \varepsilon}{\partial \zeta_2} \right) \right\}$$

Term III expresses the augmentation of the dissipation rate by the mean motion, which Launder and Spalding (1972) have modelled as:

$$2\mu \left\{ \frac{1}{\ell_\ell} \frac{\partial \overline{v}_j}{\partial \zeta_\ell} \frac{1}{\ell_\ell} \frac{\overline{\partial v_i'}}{\partial \zeta_\ell} \frac{1}{\ell_j} \frac{\partial v_i'}{\partial \zeta_j} + \frac{1}{\ell_j} \frac{\partial \overline{v}_i}{\partial \zeta_j} \frac{1}{\ell_\ell} \frac{\overline{\partial v_i'}}{\partial \zeta_\ell} \frac{1}{\ell_\ell} \frac{\partial v_i'}{\partial \zeta_\ell} \right\}$$

$$= - C_1 \frac{\varepsilon}{k} \overline{\rho} \, \overline{v_i' v_j'} \frac{1}{\ell_j} \frac{\partial \overline{v}_i}{\partial \zeta_j}$$

Term IV represents the decay of the dissipation rate and is assumed to be proportional to the dissipation rate itself divided by

the decay time scale of the turbulence, k/ε, (Hanjalic, 1970), thus:

$$2\mu \{ \frac{1}{\ell_\ell} \overline{\frac{\partial v_i'}{\partial \zeta_\ell} \frac{1}{\ell_\ell} \frac{\partial v_j'}{\partial \zeta_\ell} \frac{1}{\ell_j} \frac{\partial v_i'}{\partial \zeta_j}} + \frac{\mu}{\rho} \left(\overline{\frac{\partial^2 v_i'}{\ell_j \partial \zeta_j \ell_\ell \partial \zeta_\ell}} \right)^2 \}$$

$$= C_2 \bar{\rho} \frac{\varepsilon^2}{k}$$

Term V contains the product of dissipation rate and (a) the divergence of the fluctuating velocity and (b) the divergence of the mean velocity. The former is assumed negligible and is neglected while the latter is retained.

Term VI contains unknown correlations of gradients of fluctuating pressure and velocity; these, together with the remaining terms in s_μ are neglected for high Reynolds number flows.

The final form of the ε equation is then:

$$\frac{\partial}{\partial t}(\rho\varepsilon) + \frac{1}{\ell_1 \ell_2 \ell_3} \{ \frac{\partial}{\partial \zeta_1}(\ell_2 \ell_3 \bar{\rho} \bar{v}_1 \varepsilon) + \frac{\partial}{\partial \zeta_2}(\ell_1 \ell_3 \bar{\rho} \bar{v}_2 \varepsilon)$$

$$- \frac{\partial}{\partial \zeta_1} \left(\frac{\ell_2 \ell_3}{\ell_1} \frac{\mu_{eff}}{\sigma_\varepsilon} \frac{\partial \varepsilon}{\partial \zeta_1} \right) - \frac{\partial}{\partial \zeta_2} \left(\frac{\ell_1 \ell_3}{\ell_2} \frac{\mu_{eff}}{\sigma_\varepsilon} \frac{\partial \varepsilon}{\partial \zeta_2} \right) \}$$

$$- C_1 \frac{\varepsilon}{k} G_t + C_2 \bar{\rho} \frac{\varepsilon^2}{k} - \bar{\rho}\varepsilon \nabla . \underline{\bar{v}} = 0 \qquad (3.36)$$

The values assigned to the various empirical constants that appear in the turbulence equations are given in table 3.1 and are taken from Gosman and Pun (1974).

3.7 Wall Boundary Conditions

These are two important features that distinguish near-wall regions from other parts of the flow field: firstly, there are steep gradients of most of the flow properties, and secondly, the turbulent Reynolds number is low so that the effects of molecular viscosity can influence the production, dissipation and transport of turbulence energy. In addition, the presence of the wall influences the eddy structure so that the small scale turbulence is no longer isotropic. Within the framework of the method already described, these effects can in principle be accounted for, the former, by using closely spaced grids to resolve the gradients and the latter, by modifying the turbulence model so that low Reynolds number phenomena are more accurately modelled (see e.g. Jones and Launder, 1972). However, unless detail near the wall is of special interest it is impractical to use this approach. The alternative is to 'bridge' the near wall region by using semi-empirical relationships for the dependent variables based upon the (nearly) universal functions of the dimensionless distance normal to the wall, y^+, defined as:

$$y^+ = \frac{\rho v_\tau y}{\mu} \tag{3.37}$$

where the 'friction velocity' v_τ is given by:

$$v_\tau = \left(\frac{\tau_w}{\rho}\right)^{1/2} \tag{3.38}$$

τ_w being the wall shear stress and y the normal distance.

It is important to note that the experimental data used to determine the 'law of the wall' are, with few exceptions, for steady, one-dimensional flows. The use of these formulae for unsteady

recirculating flows is difficult to justify on any grounds apart from the absence of any feasible alternative. It could however be reasonably argued that in engine cylinders, wall effects will be of secondary importance on the interior flow structure although highly important in determining, for example, wall heat transfer.

The parameter y^+ has been used by Tennekes and Lumley (1973), Reynolds, A.J. (1974) and others to correlate experimentally-determined flow properties near the wall. In engineering calculations, the buffer layer ($5 < y^+ < 30$) may be dispensed with by extending the viscous and inertial sublayers to a common boundary at $y^+ = 11.63$. In the inertial sublayer (now defined as $y^+ > 11.63$) the velocity variation may be described by a logarithmic relationship (Schlichting, 1968), i.e.:

$$\overline{v} = \frac{v_\tau}{\kappa} \ell n(Ey^+) \tag{3.39}$$

where E and κ are experimentally determined constants given in table 3.1. In both the viscous ($y^+ < 11.63$) and inertial sublayers, the shear stress is calculated from the product of effective viscosity μ_{eff} and tangential velocity gradient $\frac{\partial \overline{v}}{\partial y}$, i.e,:

$$\tau_w = \mu_{eff} \frac{\partial \overline{v}}{\partial y} \tag{3.40}$$

for $y^+ < 11.63$ the turbulent viscosity is assumed zero and μ_{eff} may be replaced by μ whilst for $y^+ > 11.63$, μ_t is considerably greater than μ and the latter may be assumed negligible.

Near a wall, the transport equation for the turbulent kinetic energy 3.34 reduces to a balance between the local production and

dissipation of k (Launder and Spalding, 1972) to give:

$$\mu_t\left(\frac{\partial \overline{v}}{\partial y}\right)^2 = \rho\varepsilon \tag{3.41}$$

The velocity gradient and dissipation rate may be replaced from equation 3.40 and 3.32 to give:

$$\tau_w = C_\mu^{1/2}\ \rho k = \rho v_\tau^2 \tag{3.42}$$

Hence, it follows from equation 3.39:

$$\tau_w = \frac{\rho C_\mu^{1/4} k^{1/2} \overline{v}\ \kappa}{\ell n(Ey^+)} \tag{3.43}$$

Here, it should be noted that the tangential velocity, $\overline{v}$, is the resultant of either $\overline{v}_1$ and $\overline{v}_3$ or $\overline{v}_2$ and $\overline{v}_3$ depending upon the boundary under consideration. Typically, for a ζ_2 = constant boundary, this is:

$$\overline{v} = (\overline{v}_1^2 + \overline{v}_3^2)^{1/2} \tag{3.44}$$

The resultant shear stress, evaluated from either equation 3.40 or 3.43 depending upon the value of y^+, must therefore be resolved into the two co-ordinate directions, as follows:

$$\tau_{21} = \tau_w \frac{\overline{v}_1}{\overline{v}}$$

$$\tau_{23} = \tau_w \frac{\overline{v}_3}{\overline{v}} \tag{3.45}$$

where τ_{21} and τ_{23} are the components of shear stress in directions 1 and 3 respectively at a ζ_2 = constant boundary.

The boundary condition for the dissipation rate is obtained in the following way: the turbulent viscosity is replaced in equation 3.40 from 3.32 to give:

$$\tau_w = \frac{C_\mu \rho k^2}{\varepsilon} \frac{\partial \overline{v}}{\partial y} \tag{3.46}$$

Substituting for y^+ in equation 3.39 and differentiating gives:

$$\frac{\partial \overline{v}}{\partial y} = \frac{v_\tau}{\kappa y} \tag{3.47}$$

The velocity gradient may now be eliminated between equations 3.46 and 3.47, i.e.:

$$\varepsilon = \frac{C_\mu \rho k^2}{\kappa y} \cdot \frac{v_\tau}{\tau_w} \tag{3.48}$$

Finally, v_τ and τ_w may be replaced in equation 3.48 from 3.39 and 3.43 to yield:

$$\varepsilon = \frac{C_\mu^{3/4} \, k^{3/2}}{\kappa y} \tag{3.49}$$

The generation rate of k is evaluated using the calculated shear stress, such that:

$$G = \tau_w \frac{\partial \overline{v}}{\partial y} \tag{3.50}$$

Typically, for a ζ_2 = constant boundary:

$$G = \tau_{21} \{ \frac{1}{\ell_2} \frac{\partial \overline{v}_1}{\partial \zeta_2} - \frac{\overline{v}_1}{r_1} \} + \tau_{23} \{ \frac{1}{\ell_2} \frac{\partial \overline{v}_3}{\partial \zeta_2} - \frac{\overline{v}_3}{r_3} \cos\beta \} \tag{3.51}$$

An expression for the heat flux at the boundary, $\dot{q}_w$, can be developed from dimensional considerations (Reynolds, A.J., 1974), which in the absence of kinetic heating, pressure gradients, mass transfer and surface roughness is:

$$\dot{q}_w = - \frac{\mu\, y^+}{\sigma_h} \{ \frac{1}{\kappa} \ell n\ (Ey^+) + P \}^{-1} \frac{dT_w}{dy} \qquad (3.52)$$

where $\frac{dT_w}{dy}$ is the normal temperature gradient. The term, P, expresses the contribution of the laminar sublayer to the total resistance and the function and here is due to Jayatillaka (1969); it is:

$$P = 9\{ \frac{\sigma_\ell}{\sigma_h} - 1 \} \{ \frac{\sigma_\ell}{\sigma_h} \}^{-1/4} \qquad (3.53)$$

For $y^+ < 11.63$ the heat flux is evaluated from:

$$\dot{q}_w = - \frac{\mu}{\sigma_\ell} \frac{dT_w}{dy} \qquad (3.54)$$

3.8 Modelled Form of the Mean Flow Equations

The modelling of the Reynolds stress terms in the ensemble-averaged momentum equation has already been indicated in the previous section. The additional terms appearing in the energy equation (3.20) are of the form $\overline{\rho}\ \overline{v_i' h'}$ and represent additional fluxes due to turbulence. Following Launder and Spalding (1972) and others, these are modelled as a diffusion process, typically:

$$\overline{\rho}\ \overline{v_i' h'} = - \frac{1}{\ell_i} \frac{\mu_t}{\sigma} \frac{\partial \bar{h}}{\partial \zeta_i} = - \frac{\mu_t}{\ell_i} \{ \frac{1}{\sigma_h} \frac{\partial \bar{h}}{\partial \zeta_i} + (1 - \frac{1}{\sigma_h}) \frac{\partial}{\partial \zeta_i} (\Sigma \frac{\bar{v}_i^2}{2}) + (\frac{1}{\sigma_k} - \frac{1}{\sigma_h}) \frac{\partial k}{\partial \zeta_i} \} \qquad (3.55)$$

where

$$\bar{h} = \overline{c_p T} + \Sigma \frac{\bar{v}_i^2}{2} + k \qquad (3.56)$$

The equation of state for the ensemble averaged properties may be written as:

$$\overline{\rho} = \overline{Q}\ \overline{p} \tag{3.57}$$

where $$\overline{Q} = \frac{1}{R\overline{T}} \tag{3.58}$$

The foregoing differential equations for all variables can be written in a general form as:

$$\frac{\partial}{\partial t}(\overline{\rho\phi}) + \frac{1}{\ell_1\ell_2\ell_3}\left\{\frac{\partial}{\partial\zeta_1}(\ell_2\ell_3\ \overline{\rho}\ \overline{v}_1\overline{\phi}) + \frac{\partial}{\partial\zeta_2}(\ell_1\ell_3\overline{\rho}\ \overline{v}_2\overline{\phi})\right.$$

$$\left. - \frac{\partial}{\partial\zeta_1}\left(\frac{\ell_2\ell_3}{\ell_1}\Gamma_\phi\ \frac{\partial\phi}{\partial\zeta_1}\right) - \frac{\partial}{\partial\zeta_2}\left(\frac{\ell_1\ell_3}{\ell_2}\Gamma_\phi\ \frac{\partial\phi}{\partial\zeta_2}\right)\right\} = s_\phi \tag{3.59}$$

where ϕ represents $\overline{v}_1$, $\overline{v}_2$, $\overline{v}_3$, $\overline{h}$, k, ε or in the case of mass conservation, unity. The definitions of the associated turbulent diffusivity, Γ_ϕ, and source term, s_ϕ, are given in table 3.2.

3.9 Equations for Moving Co-ordinate Frame

The equations assembled so far in this chapter are for an Eulerian co-ordinate frame. As discussed in section 3.2, a more flexible system is required that expands and contracts between the cylinder head and piston top and translates with the piston within the piston bowl. Transformation formulae have been derived by Watkins (1973) for the case of a reciprocating flat-topped piston which requires the expanding/contracting feature but the particular

form of the chosen transformation is not sufficiently general for the present application. Nevertheless, a modified form of the derivation employed by Watkins can be used here.

Firstly, new independent variables ζ_1' and ζ_2' are introduced which are functions of the Eulerian co-ordinates and time, viz:

$$\begin{aligned} \zeta_1' &= f_1(\zeta_1,\zeta_2,t) \\ \zeta_2' &= f_2(\zeta_1,\zeta_2,t) \end{aligned} \tag{3.60}$$

from which it follows from differential calculus that:

$$\begin{aligned} d\zeta_1' &= \frac{\partial\zeta_1'}{\partial\zeta_1} d\zeta_1 + \frac{\partial\zeta_1'}{\partial\zeta_2} d\zeta_2 + \frac{\partial\zeta_1'}{\partial t} dt \\ d\zeta_2' &= \frac{\partial\zeta_2'}{\partial\zeta_1} d\zeta_1 + \frac{\partial\zeta_2'}{\partial\zeta_2} d\zeta_2 + \frac{\partial\zeta_2'}{\partial t} dt \end{aligned} \tag{3.61}$$

A variable ϕ can be expressed in either co-ordinate system as:

$$\phi(\zeta_1,\zeta_2, t) = \phi(\zeta_1',\zeta_2', t) \tag{3.62}$$

Or, in differential form:

$$\frac{\partial\phi}{\partial\zeta_1} d\zeta_1 + \frac{\partial\phi}{\partial\zeta_2} d\zeta_2 + \frac{\partial\phi}{\partial t} dt = \frac{\partial\phi}{\partial\zeta_1'} d\zeta_1' + \frac{\partial\phi}{\partial\zeta_2'} d\zeta_2'$$

$$+ \frac{\partial\phi}{\partial t} dt \tag{3.63}$$

Inserting relations 3.61 into 3.63 gives:

$$\frac{\partial\phi}{\partial\zeta_1} d\zeta_1 + \frac{\partial\phi}{\partial\zeta_2} d\zeta_2 + \frac{\partial\phi}{\partial t} dt = \frac{\partial\phi}{\partial\zeta_1'} \frac{\partial\zeta_1'}{\partial\zeta_1} d\zeta_1 + \frac{\partial\phi}{\partial\zeta_1'} \frac{\partial\zeta_1'}{\partial\zeta_2} d\zeta_2$$

$$+ \frac{\partial\phi}{\partial\zeta_1'} \frac{\partial\zeta_1'}{\partial t} dt + \frac{\partial\phi}{\partial\zeta_2'} \frac{\partial\zeta_2'}{\partial\zeta_1} d\zeta_1 + \frac{\partial\phi}{\partial\zeta_2'} \frac{\partial\zeta_2'}{\partial\zeta_2} d\zeta_2 + \frac{\partial\phi}{\partial\zeta_2'} \frac{\partial\zeta_2'}{\partial t} dt + \frac{\partial\phi}{\partial t} dt \tag{3.64}$$

By inspection, the general transformation formulae between the two frames are given by:

$$\frac{\partial \phi}{\partial \zeta_1} \rightarrow \frac{\partial \phi}{\partial \zeta_1'} \frac{\partial \zeta_1'}{\partial \zeta_1} + \frac{\partial \phi}{\partial \zeta_2'} \frac{\partial \zeta_2'}{\partial \zeta_1}$$

$$\frac{\partial \phi}{\partial \zeta_2} \rightarrow \frac{\partial \phi}{\partial \zeta_1'} \frac{\partial \zeta_1'}{\partial \zeta_2} + \frac{\partial \phi}{\partial \zeta_2'} \frac{\partial \zeta_2'}{\partial \zeta_2} \tag{3.65}$$

$$\frac{\partial \phi}{\partial t} \rightarrow \frac{\partial \phi}{\partial \zeta_1'} \frac{\partial \zeta_1'}{\partial t} + \frac{\partial \phi}{\partial \zeta_2'} \frac{\partial \zeta_2'}{\partial t} + \frac{\partial \phi}{\partial t}$$

The specification of f_1 and f_2 (equations 3.60) determine the nature of correspondence between the (ζ_1,ζ_2,t) and $(\zeta_1',\zeta_2',\ t)$ co-ordinate systems. Watkins (1973), defined f_1 and f_2 as:

$$\zeta_1' = f_1 = \frac{z}{z_H}\ , \qquad \zeta_2' = f_2 = r \tag{3.66}$$

where z is the axial co-ordinate, z_H is the instantaneous distance between the cylinder head and piston top and r the radial co-ordinate. This specification ensures that the solution domain, defined in the new $(\zeta_1',\zeta_2',\ t)$ co-ordinate frame, is always bounded in the axial direction by the cylinder head and piston top.

The specification of f_1 and f_2 employed here is:

$$\zeta_1' = f_1 = \frac{1}{\ell_1'} \{ \ell_1 \zeta_1 - X_1 \}$$

$$\zeta_2' = f_2 = \frac{1}{\ell_2'} \{ \ell_2 \zeta_2 - X_2 \} \tag{3.67}$$

Here, $\ell_1'(t)$ and $\ell_2'(t)$ are time-varying metric coefficients whilst $X_1(t)$ and $X_2(t)$ are the instantaneous displacements from a time-varying reference position $(\zeta_1(t),\ \zeta_2(t))$ to the co-ordinate point $(\zeta_1,\ \zeta_2')$. Distances, ds', in the (ζ_1',ζ_2',t) system are related to the metric

coefficients ℓ_1' and ℓ_2' in a similar fashion to their Eulerian counterparts:

$$(ds')^2 = (\ell_1' d\zeta_1')^2 + (\ell_2' d\zeta_2')^2 + (\ell_3' d\zeta_3)^2 \tag{3.68}$$

(note that $\ell_3 = \ell_3'$)

The differentials of equations 3.67 with respect to ζ_1, ζ_2 and t are:

$$\frac{\partial \zeta_1'}{\partial \zeta_1} = \frac{\ell_1}{\ell_1'}$$

$$\frac{\partial \zeta_1'}{\partial \zeta_2} = 0$$

$$\frac{\partial \zeta_1'}{\partial t} = -\frac{1}{\ell_1'}\left\{\frac{\partial X_1}{\partial t} + \zeta_1' \frac{\partial \ell_1'}{\partial t}\right\}$$

$$\frac{\partial \zeta_2'}{\partial \zeta_1} = 0 \tag{3.69}$$

$$\frac{\partial \zeta_2'}{\partial \zeta_2} = \frac{\ell_2}{\ell_2'}$$

$$\frac{\partial \zeta_2'}{\partial t} = -\frac{1}{\ell_2'}\left\{\frac{\partial X_2}{\partial t} + \zeta_2' \frac{\partial \ell_2'}{\partial t}\right\}$$

Inserting the above expressions into the general transformation formulae 3.65 yields the particular form:

$$\frac{\partial \phi}{\partial \zeta_1} \rightarrow \frac{\ell_1}{\ell_1'}\frac{\partial \phi}{\partial \zeta_1'}$$

$$\frac{\partial \phi}{\partial \zeta_2} \rightarrow \frac{\ell_2}{\ell_2'}\frac{\partial \phi}{\partial \zeta_2'}$$

$$\frac{\partial \phi}{\partial t} \rightarrow \frac{\partial \phi}{\partial t} - \left\{\left(\frac{\partial X_1}{\partial t} + \zeta_1' \frac{\partial \ell_1'}{\partial t}\right)\frac{1}{\ell_1'}\frac{\partial \phi}{\partial \zeta_1'}\right.$$

$$\left. + \left(\frac{\partial X_2}{\partial t} + \zeta_2' \frac{\partial \ell_2'}{\partial t}\right)\frac{1}{\ell_2'}\frac{\partial \phi}{\partial \zeta_2'}\right\} \tag{3.70}$$

Applying these to the general transport equation 3.59 gives:

$$\frac{\partial(\overline{\rho\phi})}{\partial t} - (\frac{\partial X_1}{\partial t} + \zeta_1' \frac{\partial \ell_1'}{\partial t})\frac{1}{\ell_1'} \frac{\partial(\overline{\rho\phi})}{\partial \zeta_1'} - (\frac{\partial X_2}{\partial t} + \zeta_2' \frac{\partial \ell_2'}{\partial t})\frac{1}{\ell_2'} \frac{\partial(\overline{\rho\phi})}{\partial \zeta_2'}$$

$$+ \frac{1}{\ell_1\ell_2\ell_3} \{\frac{\ell_1}{\ell_1'} \frac{\partial}{\partial \zeta_1'}(\ell_2\ell_3\overline{\rho v_1\phi}) + \frac{\ell_2}{\ell_2'} \frac{\partial}{\partial \zeta_2'}(\ell_1\ell_3 \overline{\rho v_2\phi})$$

$$- \frac{\ell_1}{\ell_1'} \frac{\partial}{\partial \zeta_1'}(\frac{\ell_2\ell_3}{\ell_1}\Gamma_\phi \frac{\ell_1}{\ell_1'} \frac{\partial\overline{\phi}}{\partial \zeta_1'}) - \frac{\ell_2}{\ell_2'} \frac{\partial}{\partial \zeta_2'}(\frac{\ell_1\ell_3}{\ell_2}\Gamma_\phi \frac{\ell_2}{\ell_2'} \frac{\partial\overline{\phi}}{\partial \zeta_2'}) \} - s_\phi' = 0 \qquad (3.71)$$

Noting that:

$$- (\frac{\partial X_1}{\partial t} + \zeta_1' \frac{\partial \ell_1'}{\partial t})\frac{1}{\ell_1'} \frac{\partial(\overline{\rho\phi})}{\partial \zeta_1'} = - \frac{1}{\ell_1'\ell_2\ell_3} \frac{\partial}{\partial \zeta_1'} \{\ell_2\ell_3(\frac{\partial X_1}{\partial t} + \zeta_1' \frac{\partial \ell_1'}{\partial t})\overline{\rho\phi}\}$$

$$+ \frac{\overline{\rho\phi}}{\ell_1'\ell_2\ell_3} \frac{\partial}{\partial \zeta_1'} \{\ell_2\ell_3(\frac{\partial X_1}{\partial t} + \zeta_1' \frac{\partial \ell_1'}{\partial t})\} \qquad (3.72)$$

and:

$$- (\frac{\partial X_2}{\partial t} + \zeta_2' \frac{\partial \ell_2'}{\partial t})\frac{1}{\ell_2'} \frac{\partial(\overline{\rho\phi})}{\partial \zeta_2'} = - \frac{1}{\ell_1\ell_2'\ell_3} \frac{\partial}{\partial \zeta_2'} \{\ell_1\ell_3(\frac{\partial X_2}{\partial t} + \zeta_2' \frac{\partial \ell_2'}{\partial t})\overline{\rho\phi}\}$$

$$+ \frac{\overline{\rho\phi}}{\ell_1\ell_2'\ell_3} \frac{\partial}{\partial \zeta_2'} \{\ell_1\ell_3(\frac{\partial X_2}{\partial t} + \zeta_2' \frac{\partial \ell_2'}{\partial t})\} \qquad (3.73)$$

the 2nd and 3rd terms of equation 3.71 may be replaced to give:

$$\frac{\partial}{\partial t}(\overline{\rho\phi}) + \frac{\overline{\rho\phi}}{\ell_1'\ell_2\ell_3} \frac{\partial}{\partial \zeta_1'} \{\ell_2\ell_3(\frac{\partial X_1}{\partial t} + \zeta_1' \frac{\partial \ell_1'}{\partial t})\} + \frac{\overline{\rho\phi}}{\ell_1\ell_2'\ell_3} \frac{\partial}{\partial \zeta_2'}\{\ell_1\ell_3(\frac{\partial X_2}{\partial t} + \zeta_2' \frac{\partial \ell_2'}{\partial t})\}$$

I II III

$$+ \frac{1}{\ell_1'\ell_2\ell_3} \{\frac{\partial}{\partial \zeta_1'}(\ell_2\ell_3 \overline{\rho v_1\phi}) - \frac{\partial}{\partial \zeta_1'}\{\ell_2\ell_3(\frac{\partial X_1}{\partial t} + \zeta_1' \frac{\partial \ell_1'}{\partial t})\overline{\rho\phi}\}$$

IV V

$$- \frac{\partial}{\partial \zeta_1'}\left(\frac{\ell_2 \ell_3}{\ell_1'} \Gamma_\phi \frac{\partial \overline{\phi}}{\partial \zeta_1'}\right)\}$$

VI

$$+ \frac{1}{\ell_1 \ell_2' \ell_3}\left\{\frac{\partial}{\partial \zeta_2'}\left(\ell_1 \ell_3 \overline{\rho v_2 \phi}\right) - \frac{\partial}{\partial \zeta_2'}\left\{\ell_1 \ell_3 \left(\frac{\partial X_2}{\partial t} + \zeta_2' \frac{\partial \ell_2'}{\partial t}\right)\overline{\rho \phi}\right\}\right.$$

VII VIII

$$- \frac{\partial}{\partial \zeta_2'}\left(\frac{\ell_1 \ell_3}{\ell_2'} \Gamma_\phi \frac{\partial \overline{\phi}}{\partial \zeta_2'}\right)\} - s_\phi' = 0 \qquad (3.74)$$

IX

The radii of curvature in the (ζ_1, ζ_2, t) co-ordinates remain unchanged after transformation to the (ζ_1', ζ_2', t) system, thus:

$$\frac{1}{\ell_2 \ell_3} \frac{\partial}{\partial \zeta_1}(\ell_2 \ell_3) = \frac{1}{\ell_2 \ell_3} \frac{\partial}{\partial \zeta_1'}(\ell_2 \ell_3) = \frac{1}{\ell_2' \ell_3'} \frac{\partial}{\partial \zeta_1'}(\ell_2' \ell_3')$$

$$\frac{1}{\ell_1 \ell_3} \frac{\partial}{\partial \zeta_2}(\ell_1 \ell_3) = \frac{1}{\ell_1 \ell_3} \frac{\partial}{\partial \zeta_2'}(\ell_1 \ell_3) = \frac{1}{\ell_1' \ell_3'} \frac{\partial}{\partial \zeta_2'}(\ell_1' \ell_3') \qquad (3.75)$$

This allows terms II and III of 3.74 to be rewritten as:

$$II + III = \frac{\overline{\rho \phi}}{\ell_1' \ell_2' \ell_3'}\left\{\frac{\partial}{\partial \zeta_1'}\left[\ell_2' \ell_3'\left(\frac{\partial X_1}{\partial t} + \zeta_1' \frac{\partial \ell_1'}{\partial t}\right)\right] + \frac{\partial}{\partial \zeta_2'}\left[\ell_1' \ell_3'\left(\frac{\partial X_2}{\partial t} + \zeta_2' \frac{\partial \ell_2'}{\partial t}\right)\right]\right\} \qquad (3.76)$$

The quantities $\frac{\partial}{\partial \zeta_1'}\left(\frac{\partial X_1}{\partial t} + \zeta_1' \frac{\partial \ell_1'}{\partial t}\right)$ and $\frac{\partial}{\partial \zeta_2'}\left(\frac{\partial X_2}{\partial t} + \zeta_2' \frac{\partial \ell_2'}{\partial t}\right)$ are the spatial variations of the co-ordinate frame velocities in directions ζ_1 and ζ_2 respectively, thus, upon integration with respect to their

co-ordinate directions, terms II and III represent the convective flux of $\overline{\rho\phi}$ resulting solely from co-ordinate frame movement. Integration of terms II and III with respect to ζ_1' and ζ_2' and subsequent addition results in the surface integral of the normal velocity, v_n, at the surface, a, of a closed but variable volume, V, bounded between the limits of integration, that is:

$$\frac{\overline{\rho\phi}}{\ell_1'\ell_2'\ell_3'}\left\{\int_{\zeta_1'}^{\zeta_1'+d\zeta_1'} \frac{\partial}{\partial\zeta_1'}\{\ell_2'\ell_3'(\frac{\partial X_1}{\partial t} + \zeta_1' \frac{\partial \ell_1'}{\partial t})\}\, d\zeta_1' + \right.$$

$$\left.\int_{\zeta_2'}^{\zeta_2'+d\zeta_2'} \frac{\partial}{\partial\zeta_2'}\{\ell_1'\ell_3' (\frac{\partial X_2}{\partial t} + \zeta_2' \frac{\partial \ell_2'}{\partial t})\}\, d\zeta_2'\right\} = \frac{\overline{\rho\phi}}{V} \iint_a v_n da \qquad (3.77)$$

where $\iint_a$ denotes integration over the surface.

The Leibnitz formula for differentiating an integral (Bird et al, 1960) may be used to express the RHS of equation 3.77 in a more convenient form:

$$\frac{\overline{\rho\phi}}{V} \iint_a v_n da = \frac{\overline{\rho\phi}}{V} \frac{\partial}{\partial t} \iiint_V dV = \frac{\overline{\rho\phi}}{V} \frac{\partial V}{\partial t} = \frac{\overline{\rho\phi}}{\ell_1'\ell_2'\ell_3'} \frac{\partial}{\partial t}(\ell_1'\ell_2'\ell_3') \qquad (3.78)$$

where $\iiint_V$ denotes integration over the volume V.

Terms I, II and III may now be combined to give:

$$\frac{\partial}{\partial t}(\overline{\rho\phi}) + \frac{\overline{\rho\phi}}{\ell_1'\ell_2'\ell_3'} \frac{\partial}{\partial t}(\ell_1'\ell_2'\ell_3') = \frac{1}{\ell_1'\ell_2'\ell_3'} \frac{\partial}{\partial t}(\ell_1'\ell_2'\ell_3'\overline{\rho\phi}) \qquad (3.79)$$

Terms V and VIII express the variations in directions ζ_1 and ζ_2 of the product of area, co-ordinate frame velocity and $\overline{\rho\phi}$. If the resultant velocity of the co-ordinate frame at the location (ζ_1', ζ_2') is specified to be v_g in the axial (z) direction, then the components in the co-ordinate directions are:

$$\frac{\partial X_1}{\partial t} + \zeta_1' \frac{\partial \ell_1'}{\partial t} = v_g \cos\beta \tag{3.80}$$

and:

$$\frac{\partial X_2}{\partial t} + \zeta_2' \frac{\partial \ell_2'}{\partial t} = - v_g \sin\beta$$

Terms IV and V may now be combined to give:

$$\frac{1}{\ell_1'\ell_2'\ell_3'} \frac{\partial}{\partial \zeta_1'} \{\ell_2'\ell_3'\overline{\rho}(\overline{v}_1 - v_g \cos\beta)\overline{\phi}\} \tag{3.81}$$

similarly, the combination of terms VII and VIII gives:

$$\frac{1}{\ell_1'\ell_2'\ell_3'} \frac{\partial}{\partial \zeta_2'} \{ \ell_1'\ell_3' \overline{\rho}(\overline{v}_2 + v_g \sin\beta)\overline{\phi}\} \tag{3.82}$$

Defining fluid velocities relative to the co-ordinate frame, $\tilde{v}_1$ and $\tilde{v}_2$, as:

$$\tilde{v}_1 = \overline{v}_1 - v_g \cos\beta$$

$$\tilde{v}_2 = \overline{v}_2 + v_g \sin\beta \tag{3.83}$$

the general transport equation can be written in the new co-ordinate system as:

$$\frac{1}{\ell_1'\ell_2'\ell_3'} \{ \frac{\partial}{\partial t}(\ell_1'\ell_2'\ell_3' \overline{\rho\phi}) + \frac{\partial}{\partial \zeta_1'} (\ell_2'\ell_3' \overline{\rho\tilde{v}_1\phi}) + \frac{\partial}{\partial \zeta_2'}(\ell_1'\ell_3' \overline{\rho\tilde{v}_2\phi})$$

$$- \frac{\partial}{\partial \zeta_1'}(\frac{\ell_2'\ell_3'}{\ell_1'} \Gamma_\phi \frac{\partial\overline{\phi}}{\partial \zeta_1'}) - \frac{\partial}{\partial \zeta_2'}(\frac{\ell_1'\ell_3'}{\ell_2'} \Gamma_\phi \frac{\partial\overline{\phi}}{\partial \zeta_2'})\} = s_\phi' \tag{3.84}$$

It should be noted that the two major differences between equation 3.84 and its Eulerian counterpart 3.59 are firstly, that the time-dependent term now contains the rate-of-change of volume and secondly, the convective terms use the velocity of the fluid relative to the co-ordinate frame instead of the absolute fluid velocity.

Transformation of the source terms for each variable in table 3.2 produces the result summarised in table 3.3.

3.10 Closure

In this chapter, alternative schemes have been discussed for formulating the differential equations that govern the flow and heat transfer in engine cylinders. The formulation that has been selected uses a translating curvilinear-orthogonal co-ordinate frame to accommodate the complex shape of the piston bowl and an expanding/contracting rectilinear co-ordinate frame in the region bounded by the piston top and cylinder head. The differential equations have been presented in instantaneous and ensemble-averaged forms for the curvilinear orthogonal co-ordinate frame and a co-ordinate transformation has been described that allows it to move in a prescribed time-varying fashion. A turbulence model which employs two additional differential equations for the kinetic energy of turbulence and its dissipation rate has been selected to allow the mean flow equations to be closed and the wall boundary conditions for all differential equations have been given.

CHAPTER 4

THE NUMERICAL SOLUTION PROCEDURE

4.1 Introduction

This chapter is concerned with numerical aspects of the method. Section 4.2 describes the disposition of variables within the computational grid and how the general transport equation may be integrated in both space and time, for both scalars and velocities, to give general finite difference equations.

The method used to link the momentum, continuity and energy equations is fundamental to the whole procedure and is described in section 4.3 together with a technique for making overall adjustments to the pressure field to improve both speed of convergence and numerical stability.

In section 4.4, the method of incorporating the boundary conditions into the numerical method for no-slip boundaries and inlet/exhaust apertures is described. The stability and accuracy of alternative differencing schemes are examined in section 4.5 within the context of both idealised 1-d and full 2-d problems. The effects of both grid spacing and time step are quantified.

Section 4.6 indicates the differences between the strong and weak conservation forms of the differential equations and the relevance of this to co-ordinate systems with curvature. The finite-difference forms of the source terms of all equations particular to the present problem, which include curvature terms in the momentum equations and the pressure-work term in the energy equation, are given.

A method is also presented for improving the stability of the method when high swirl rates prevail.

In section 4.7,an heuristic scheme for improving the stability and convergence of the method is described. This is achieved by dynamically adjusting the under-relaxation factorsof the various equations according to the variation of the residual sources.

4.2 Differencing of the General Transport Equation

Fig. 4.1 illustrates a portion of the computational grid. The scalar quantities of pressure, enthalpy, density, turbulence kinetic energy, dissipation rate and viscosity, and the v_3 velocity are calculated at the points denoted by capitals - NSEWP etc. and are surrounded by an imaginary control volume or cell as shown. Following the practice of Harlow and Welch (1965) and Caretto et al (1972) the v_1 and v_2 velocities are displaced in the ζ_1 and ζ_2 directions to the points nsew on the face of the "scalar" cell as are the control volumes of the former (the term scalar is not strictly correct, the exception being the v_3 velocity, but to differentiate between variables located at the point P and the displaced velocities, this terminology will be retained). This has two advantages: firstly, the velocities are in a convenient position to calculate the convective flux across the cell boundaries, and secondly, they lie between the pressures, so providing a straightforward evaluation of the important pressure gradient term in the momentum equations.

The derivation of the finite-difference equations uses the finite-volume approach of Gosman et al (1969) whereby each term of the differential equations is integrated over the surrounding control volume and in time. The integration of the general transport equation 3.84 for a quantity ϕ located at P can be expressed as*:

$$\frac{1}{\delta t}\int_{t}^{t+\delta t}\Big\{\int_{V_p}\frac{\partial}{\partial t}(\ell_1\ell_2\ell_3\rho\phi)\,d\zeta_1\,d\zeta_2$$

$$+\int_{\zeta_{2,s}}^{\zeta_{2,n}}\ell_2\ell_3\Big\{\rho\tilde{v}_1\phi-\frac{\Gamma_\phi}{\ell_1}\frac{\partial\phi}{\partial\zeta_1}\Big\}_w^e\,d\zeta_2$$

$$+\int_{\zeta_{1,w}}^{\zeta_{1,e}}\ell_1\ell_3\Big\{\rho\tilde{v}_2\phi-\frac{\Gamma_\phi}{\ell_2}\frac{\partial\phi}{\partial\zeta_2}\Big\}_s^n\,d\zeta_1$$

$$-\int_{V_p}\ell_1\ell_2\ell_3\,s_\phi\,d\zeta_1\,d\zeta_2\Big\}\,dt=0 \qquad (4.1)$$

where $\int_{V_p}$ denotes integration over the scalar control volume surrounding P.

*To preserve clarity, the overbars (-) and primes (') are dropped henceforth and it should be assumed that all dependent variables are ensemble averaged and all independent variables refer to the (ζ_1', ζ_2', t) co-ordinate system unless stated otherwise.

The first term may be approximated as:

$$\frac{1}{\delta t}\int_{t}^{t+\delta t}\int_{V_p}\frac{\partial}{\partial t}(\ell_1\ell_2\ell_3\rho\phi)d\zeta_1\, d\zeta_2\, dt$$

$$\approx \frac{(\ell_1\delta\zeta_1\ell_2\delta\zeta_2\ell_3\rho\phi)^n - (\ell_1\delta\zeta_1\ell_2\delta\zeta_2\ell_3\rho\phi)^o}{\delta t}$$

$$= \frac{(V_p\rho\phi)^n - (V_p\rho\phi)^o}{\delta t} \qquad (4.2)$$

where the superscripts n and o denote the new and old time levels respectively, separated by the time interval δt and V_p is the cell volume per radian. The second and third terms of equation 4.1 represent the convective and diffusive inflow/outflow of ϕ across the cell faces in the ζ_1 and ζ_2 directions. Focussing attention on the first, this may be differenced spatially as:

$$\int_{\zeta_{2,s}}^{\zeta_{2,n}} \ell_2\ell_3 \left\{\rho\tilde{v}_1\phi - \frac{\Gamma_\phi}{\ell_1}\frac{\partial\phi}{\partial\zeta_1}\right\}_w^e d\zeta_2 = F_{\zeta_1}$$

$$\approx a_{se/ne}\left\{\rho\tilde{v}_1\phi_e - \frac{\Gamma_\phi(\phi_E-\phi_P)}{(\ell_1\delta\zeta_1)_{E/P}}\right\}_e$$

$$- a_{sw/nw}\left\{\rho\tilde{v}_1\phi_w - \frac{\Gamma_\phi(\phi_P-\phi_W)}{(\ell_1\,\delta\zeta_1)_{P/W}}\right\}_w \qquad (4.3)$$

where the a's are areas given by, for example:

$$a_{sw/nw} = (\ell_2\delta\zeta_2\ell_3)_w \qquad (4.4)$$

The appearance of a '/' in a subscript indicates that evaluation is between the points indicated, thus $(\ell_1 \delta\zeta_1)_{E/P}$ is the distance between points E and P. The term $\frac{1}{\ell_1} \frac{\partial\phi}{\partial\zeta_1}$ is differenced as:

$$\frac{1}{\ell_1} \frac{\partial\phi}{\partial\zeta_1} \Big|_e = \frac{\phi_E - \phi_P}{(\ell_1 \delta\zeta_1)_{E/P}}$$

$$\frac{1}{\ell_1} \frac{\partial\phi}{\partial\zeta_1} \Big|_w = \frac{\phi_P - \phi_W}{(\ell_1 \delta\zeta_1)_{P/W}} \qquad (4.5)$$

Defining cell-boundary Peclet numbers as:

$$Pe_e = \frac{(\rho\tilde{v}_1)_e (\ell_1 \delta\zeta_1)_{E/P}}{\Gamma_e}$$

$$Pe_w = \frac{(\rho\tilde{v}_1)_w (\ell_1 \delta\zeta_1)_{P/W}}{\Gamma_w} \qquad (4.6)$$

equation 4.3 may be written as:

$$F_{\zeta_1} \approx a_{se/ne} (\rho\tilde{v}_1)_e \left\{ \phi_e - \frac{\phi_E - \phi_P}{Pe_e} \right\}$$

$$- a_{sw/nw} (\rho\tilde{v}_1)_w \left\{ \phi_w - \frac{\phi_P - \phi_W}{Pe_w} \right\} \qquad (4.7)$$

The cell-boundary densities and diffusivities are evaluated assuming a linear variation between their nearest neighbours, typically:

$$\rho_e = f_1 \rho_p + (1 - f_1) \rho_E$$

$$\Gamma_e = f_1 \Gamma_p + (1 - f_1) \Gamma_E \qquad (4.8)$$

where f_1 is a spatial weighting factor, given by:

$$f_1 = \frac{(\ell_1 \delta\zeta_1)_{E/e}}{(\ell_1 \delta\zeta_1)_{E/P}} \tag{4.9}$$

By expressing the cell-face values of ϕ as:

$$\begin{aligned} \phi_e - \frac{\phi_E - \phi_P}{Pe_e} &= (1 - \alpha_e)\phi_E + \alpha_e \phi_P \\ \phi_w - \frac{\phi_P - \phi_W}{Pe_w} &= \alpha_w \phi_W + (1 - \alpha_w)\phi_P \end{aligned} \tag{4.10}$$

equation 4.3 becomes:

$$\begin{aligned} F_{\zeta_1} \approx\ & a_{se/ne}(\rho\tilde{v}_1)_e \{ (1 - \alpha_e)\phi_E + \alpha_e \phi_P \} \\ & - a_{sw/nw}(\rho\tilde{v}_1)_w \{ \alpha_w \phi_W + (1 - \alpha_w)\phi_P \} \end{aligned} \tag{4.11}$$

The quantities α_e and α_w are weighting factors to be defined later.

The time level at which the various quantities in this term are to be evaluated has not as yet been specified and to complete the integration a temporal weighting factor η is introduced such that:

$$\frac{1}{\delta t} \int_t^{t+\delta t} F_{\zeta_1} dt = F_{\zeta_1, t} \approx \eta F_{\zeta_1}^n + (1 - \eta) F_{\zeta_1}^o \tag{4.12}$$

The final form of the second term of equation 4.1 is then given by:

$$F_{\zeta_1,t} \approx \eta a^n_{se/ne}(\rho\tilde{v}_1)^n_e \{(1-\alpha^n_e)\phi^n_E + \alpha^n_e\,\phi^n_p\}$$

$$- \eta a^n_{sw/nw}(\rho\tilde{v}_1)^n_w \{\alpha^n_w\phi^n_W + (1-\alpha^n_w)\phi^n_p\}$$

$$+ (1-\eta)a^o_{se/ne}(\rho\tilde{v}_1)^o_e \{(1-\alpha^o_e)\phi^o_E + \alpha^o_e\,\phi^o_p\}$$

$$- (1-\eta)a^o_{sw/nw}(\rho\tilde{v}_1)^o_w \{\alpha^o_w\phi^o_W + (1-\alpha^o_w)\phi^o_p\} \qquad (4.13)$$

The third term of equation 4.1 is treated in a similar fashion, resulting in:

$$\frac{1}{\delta t}\int_t^{t+\delta t}\int_{\zeta_{1,w}}^{\zeta_{1,e}} \ell_1\ell_3 \left\{\rho\tilde{v}_2\phi - \frac{\Gamma_\phi}{\ell_2}\frac{\partial\phi}{\partial\zeta_2}\right\}^n_s d\zeta_1\,dt$$

$$= F_{\zeta_2,t} \approx \eta a^n_{nw/ne}(\rho\tilde{v}_2)^n_n \{(1-\alpha^n_n)\phi^n_N + \alpha^n_n\,\phi^n_P\}$$

$$-\eta a^n_{sw/se}(\rho\tilde{v}_2)^n_s \{\alpha^n_s\phi^n_S + (1-\alpha^n_s)\phi^n_P\}$$

$$+ (1-\eta)a^o_{nw/ne}(\rho\tilde{v}_2)^o_n \{(1-\alpha^o_n)\phi^o_N + \alpha^o_n\phi^o_P\}$$

$$- (1-\eta)a^o_{sw/se}(\rho\tilde{v}_2)^o_s \{\alpha^o_s\phi^o_S + (1-\alpha^o_s)\phi^o_P\} \qquad (4.14)$$

The form of the last term of equation 4.1 depends upon the variable under consideration and for the present, will be represented by:

$$\frac{1}{\delta t}\int_t^{t+\delta t}\int_{V_p} s_\phi dV dt = S_\phi \qquad (4.15)$$

Adding the constituent terms and substituting $\dot{m} = \rho a\tilde{v}$, the final form of the general transport equation is:

$$\frac{(V_p\rho\phi)_p^n - (V_p\rho\phi)_p^o}{\delta t}$$

$$+ \{ \eta(1-\alpha_e^n)\dot{m}_e^n\phi_E^n + (1-\eta)(1-\alpha_e^o)\dot{m}_e^o\phi_E^o\}$$

$$- \{\eta\alpha_w^n\dot{m}_w^n\phi_W^n + (1-\eta)\alpha_w^o\dot{m}_w^o\phi_W^o\}$$

$$+ \{\eta(1-\alpha_n^n)\dot{m}_n^n\phi_N^n + (1-\eta)(1-\alpha_n^o)\dot{m}_n^o\phi_N^o \}$$

$$- \{\eta\alpha_s^n\dot{m}_s^n\phi_S^n + (1-\eta)\alpha_s^o\dot{m}_s^o\phi_S^o \}$$

$$+ \eta\{\alpha_e^n\dot{m}_e^n - (1-\alpha_w^n)\dot{m}_w^n + \alpha_n^n\dot{m}_n^n - (1-\alpha_s^n)\dot{m}_s^n \} \phi_P^n$$

$$+ (1-\eta) \{\alpha_e^o\dot{m}_e^o - (1-\alpha_w^o)\dot{m}_w^o + \alpha_n^o\dot{m}_n^o - (1-\alpha_s^o)\dot{m}_s^o\} \phi_P^o$$

$$- S_\phi = 0 \qquad (4.16)$$

This equation can be written in more compact form as:

$$A_p^n\phi_p^n = \Sigma_c A_c^n\phi_c^n + \Sigma_c A_c^o\phi_c^o + A_p^o\phi_p^o + S_\phi \qquad (4.17)$$

where the subscript c denotes summation over the surrounding points NSEW and the coefficients are given by:

$$A_N^n = -\eta(1-\alpha_n^n)\dot{m}_n^n$$

$$A_S^n = \eta\alpha_s^n\dot{m}_s^n$$

$$A_E^n = -\eta(1-\alpha_e^n)\dot{m}_e^n$$

$$A_W^n = \eta\alpha_w^n\dot{m}_w^n$$

$$A_N^o = -(1-\eta)(1-\alpha_n^o)\dot{m}_n^o$$

$$A_S^o = (1-\eta)\alpha_s^o\dot{m}_s^o \qquad (4.18)$$

$$A_E^o = -(1-\eta)(1-\alpha_e^o)\dot{m}_e^o$$

$$A_W^o = (1-\eta)\alpha_w^o\dot{m}_w^o$$

$$A_P^n = \eta\{\alpha_e^n\dot{m}_e^n - (1-\alpha_w^n)\dot{m}_w^n + \alpha_n^n\dot{m}_n^n - (1-\alpha_s^n)\dot{m}_s^n\} + \frac{(V_p\rho)^n}{\delta t}$$

$$A_P^o = -(1-\eta)\{\alpha_e^o\dot{m}_e^o - (1-\alpha_w^o)\dot{m}_w^o + \alpha_n^o\dot{m}_n^o - (1-\alpha_s^o)\dot{m}_s^o\} + \frac{(V_p\rho)^o}{\delta t}$$

Treatment of Momentum Equations

The integration of equation 4.1 when it is taken to be one of the momentum equations differs from its scalar counterpart in that

the control volume is split between two half scalar cells (see fig. 4.1). Thus, for example, the first term for the direction-1 equation is integrated as:

$$\frac{1}{\delta t}\int_{t}^{t+\delta t}\int_{V_w}\frac{\partial}{\partial t}(\ell_1\ell_2\ell_3\rho\phi)\,d\zeta_1\,d\zeta_2\,dt$$

$$= \frac{1}{\delta t}\left[\{(V_{wnw/wsw/sw/nw}\rho_w\phi_w)^n + (V_{nw/sw/s/n}\rho_p\phi_w)^n\}\right.$$

$$\left. - \{(V_{wnw/wsw/sw/nw}\rho_w\phi_w)^o + (V_{nw/sw/s/n}\rho_p\phi_w)^o\}\right] \qquad (4.19)$$

where for example $V_{wnw/wsw/sw/nw}$ is the volume bounded by the subscripted vertices and ϕ stands for v_1.

The mass flow rates in the ζ_1 direction, which arise from the integration of the second term of equation 4.1, are evaluated assuming a linear variation between neighbouring velocities, typically:

$$\dot{m}_w = \rho_w a_{wsw/wnw}\frac{(\tilde{v}_{1,ww}+\tilde{v}_{1,w})}{2} \qquad (4.20)$$

with a similar assumption for the cell face Peclet numbers:

$$Pe_w = \rho_w\frac{(\tilde{v}_{1,ww}+\tilde{v}_{1,w})}{2}\,\frac{(\ell_1\delta\zeta_1)_{w/ww}}{\Gamma_w} \qquad (4.21)$$

In the ζ_2 direction, the mass flow rates are obtained from a summation of the various contributions; for the south cell face this is:

$$\dot{m}_{sw} = a_{wsw/sw} \{ \rho_{SW} f_2 + \rho_W(1-f_2)\} \tilde{v}_{2,wsw}$$

$$+ a_{sw/s} \{\rho_S f_2 + \rho_p(1-f_2)\} \tilde{v}_{2,s} \qquad (4.22)$$

The quantity f_2 is a spatial weighting factor whose specification provides a linear variation of scalar variables between SW to W and S to P, and is defined in a similar fashion to f_1, that is:

$$f_2 = \frac{(\ell_2 \delta\zeta_2)_{P/s}}{(\ell_2 \delta\zeta_2)_{P/S}} \qquad (4.23)$$

The ζ_2 direction Peclet number is calculated from:

$$Pe_{sw} = \frac{\rho_{sw} \tilde{v}_{2,sw} (\ell_2 \delta\zeta_2)_{ssw/w}}{\Gamma_{sw}} \qquad (4.24)$$

where ρ_{sw} is obtained from a weighted average of surrounding values:

$$\rho_{sw} = f_1 \{\rho_{SW} f_2 + \rho_W(1-f_2)\} + (1-f_1) \{ \rho_S f_2 + \rho_p(1-f_2)\} \qquad (4.25)$$

with a similar expression for Γ_{sw}. $\tilde{v}_{2,sw}$ is also a weighted average, in this case of $\tilde{v}_{2,wsw}$ and $\tilde{v}_{2,s}$:

$$\tilde{v}_{2,sw} = f_1 \tilde{v}_{2,wsw} + (1-f_1)\tilde{v}_{2,s} \qquad (4.26)$$

When cast in the form of equation 4.17, the ζ_1 direction momentum equation is:

$$A_w^n v_{1,w}^n = \sum_c A_c^n v_{1,c}^n + \sum_c \dot{A}_c^o v_{1,c}^o + A_w^o v_{1,w}^o + S_{v_1} \qquad (4.27)$$

where the summation convention is over points ww-e-ssw-nnw and the coefficients are given by analogous relationships to 4.18 except with the changes already indicated.

Similar reasoning applied to the integration of the direction-2 momentum equation produces:

$$A_s^n v_{2,s}^n = \Sigma_c A_c^n v_{2,c}^n + \Sigma_c A_c^o v_{2,c}^o + A_s^o v_{2,s}^o + S_{v_2} \tag{4.28}$$

The finite-difference equations for v_1 and v_2 may be rearranged so that the dependent variables are the velocities relative to the co-ordinate frame, that is, $\tilde{v}_1 = v_1 - v_g\cos\beta$ and $\tilde{v}_2 = v_2 + v_g\sin\beta$. The advantage of this is that as the relative velocity is needed more often during the computations, it is more efficient to work with it directly. When this is done the equation becomes:

$$A_w^n \tilde{v}_{1,w}^n = \Sigma_c A_c^n \tilde{v}_{1,c}^n + \Sigma_c A_c^o \tilde{v}_{1,c}^o + A_w^o \tilde{v}_{1,w}^o + S'_{v_1} \tag{4.29}$$

where the 'source' term is now:

$$S'_{v_1} = S_{v_1} + \Sigma_c A_c^n (v_g\cos\beta)_c^n + \Sigma_c A_c^o (v_g\cos\beta)_c^o$$

$$- A_w^n (v_g\cos\beta)_w^n + A_w^o (v_g\cos\beta)_w^o \tag{4.30}$$

and similarly for the ζ_2 direction momentum equation:

$$A_s^n \tilde{v}_{2,s}^n = \Sigma_c A_c^n \tilde{v}_{2,c}^n + \Sigma_c A_c^o \tilde{v}_{2,c}^o + A_s^o \tilde{v}_{2,s}^o + S'_{v_2} \tag{4.31}$$

where:

$$S'_{v_2} = S_{v_2} - \Sigma_c A_c^n (v_g\sin\beta)_c^n - \Sigma_c A_c^o (v_g\sin\beta)_c^o$$

$$+ A_s^n (v_g\sin\beta)_s^n - A_s^o (v_g\sin\beta)_s^o \tag{4.32}$$

4.3 Solution of the Momentum, Continuity and Energy Equations

For low Mach number flows and in the absence of combustion, the linkage between the energy equation and the continuity and momentum equations is relatively weak on a local basis, although the overall changes in temperature and pressure are important for a gas undergoing compression. The velocity field is however strongly dependent upon small spatial variations (in comparison with the mean level) of pressure. The technique used to link the momentum and continuity equations, due to Chorin (1968) and Caretto et al (1972) is an iterative "guess and correct" procedure. The method is often referred to as the SIMPLE algorithm, standing for Semi-Implicit Method for Pressure-Linked Equations. The first step in deriving the equations is to express each dependent variable ϕ in terms of an approximation, labelled (ϕ^*), and a correction value, denoted (ϕ'), thus:

$$p = p^* + p' \tag{4.33}$$

$$\rho = \rho^* + \left(\frac{\partial \rho}{\partial p}\right)_T p' = \rho^* + Qp' \tag{4.34}$$

$$\tilde{v}_1 = \tilde{v}_1^* + \tilde{v}_1' \qquad \tilde{v}_2 = \tilde{v}_2^* + \tilde{v}_2' \tag{4.35}$$

If the momentum equations are solved with the approximate pressure field p^* inserted then the velocity and pressure fields satisfy e.g. for direction-1:

$$A^n_{w,v_1}\tilde{v}^*_{1,w} = \sum_c A^n_{c,v_1}\tilde{v}^*_{1,c} + \sum_c A^o_{c,v_1}\tilde{v}^o_{1,c} + A^o_{w,v_1}\tilde{v}^o_{1,w}$$

$$+ R_{w,v_1} - \{ \eta a^n_{nw/sw}(p^*_p - p^*_w) + (1-\eta)a^o_{nw/sw}(p^o_p - p^o_w)\} \qquad (4.36)$$

where the pressure gradient contribution to the source term has been extracted, so that:

$$S'_{v_1} = R_{w,v_1} - a_{nw/sw}(p_p - p_w) \qquad (4.37)$$

The superscript (n) has been dropped and those variables with (*), (') or without superscript refer implicitly to the advanced time-level value. The subscript v_1 has been attached to the coefficients to associate them with this particular momentum component. The 'correct' velocity and pressure fields will satisfy

$$A^n_{w,v_1}\tilde{v}_{1,w} = \sum_c A^n_{c,v_1}\tilde{v}_{1,c} + \sum_c A^o_{c,v_1}\tilde{v}^o_{1,c} + A^o_{w,v_1}\tilde{v}^o_{1,w}$$

$$+ R_{w,v_1} - \{ \eta a^n_{nw/sw}(p_p - p_w) + (1-\eta)a^o_{nw/sw}(p^o_p - p^o_w)\} \qquad (4.38)$$

Subtracting equation 4.36 from the above gives a relation between the velocity and pressure corrections thus:

$$A^n_{w,v_1}\tilde{v}'_{1,w} = \sum_c A^n_{c,v_1}\tilde{v}'_{1,c} - \eta a^n_{nw/sw}(p'_p - p'_w) \qquad (4.39)$$

If it is assumed that:

$$\left| \sum_c A^n_{c,v_1}\tilde{v}'_{1,c} \right| \ll \left| \eta a^n_{nw/sw}(p'_p - p'_w) \right|$$

then the correction velocity can be written in terms of the correction pressures as:

$$\tilde{v}'_{1,w} = \frac{-\eta a^n_{nw/sw}(p'_p - p'_W)}{A^n_{w,v_1}} \tag{4.40}$$

hence, from 4.35:

$$\tilde{v}_{1,w} = \tilde{v}^*_{1,w} - \frac{\eta a^n_{nw/sw}(p'_p - p'_W)}{A^n_{w,v_1}} \tag{4.41}$$

From similar reasoning, the equivalent result for the ζ_2 direction is:

$$\tilde{v}_{2,s} = \tilde{v}^*_{2,s} - \frac{\eta a^n_{sw/se}(p'_p - p'_S)}{A^n_{s,v_2}} \tag{4.42}$$

The expressions4.41 and 4.42 together with equation 4.34, which links the density and pressure corrections, may be inserted into the finite-difference form of the mass conservation equation to yield an equation for the p'. Before this is done however, a further temporal weighting factor, κ, will be introduced, having the same significance as η but applying only to the continuity equation. This allows a different temporal weighting for the various equations, the reason for which will become apparent later.

The finite-difference form of the continuity equation is obtained by setting $\phi = 1$ and $S_\phi = \Gamma_\phi = 0$ into the integrated form of equation 4.1, which, after substitution of equations 4.41, 4.42 and 4.34 is:

$$\frac{(V_p Q p'_p)^n}{\delta t}$$

$$+ \kappa\, a^n_{nw/ne} \left\{ \tilde{v}^*_{2,n} Q p'_n - \eta \rho^*_n \frac{a_{nw/ne}}{A^n_{n,v_2}} (p'_N - p'_p) \right\}$$

$$- \kappa\, a^n_{sw/se} \left\{ \tilde{v}^*_{2,s}\, Q p'_s - \eta \rho^*_s \frac{a^n_{sw/se}}{A^n_{s,v_2}} (p'_p - p'_S) \right\}$$

$$+ \kappa a^n_{se/ne} \left\{ \tilde{v}^*_{1,e} Q p'_e - \eta \rho^*_e \frac{a^n_{se/ne}(p'_E - p'_p)}{A^n_{e,v_1}} \right\}$$

$$- \kappa\, a^n_{sw/nw} \left\{ \tilde{v}^*_{1,w} Q p'_w - \eta \rho^*_w \frac{a^n_{sw/nw}}{A^n_{w,v_1}} (p'_p - p'_W) \right\}$$

$$= - \left\{ \frac{(V_p \rho^*)^n - (V_p \rho)^o}{\delta t} \right\} + \{ -\kappa \dot{m}^*_n - (1-\kappa) \dot{m}^o_n$$

$$+ \kappa \dot{m}^*_s + (1-\kappa) \dot{m}^o_s - \kappa \dot{m}^*_e - (1-\kappa) \dot{m}^o_e + \kappa \dot{m}^*_w + (1-\kappa) \dot{m}^o_w \} \qquad (4.43)$$

Defining a cell face Mach number as:

$$Ma^2 = \frac{\tilde{v}^* Q}{\rho^* D_v} \qquad (4.44)$$

where, for example:

$$D_{v,n} = \frac{\eta a^n_{nw/ne}}{A^n_{n,v_2}} \qquad (4.45)$$

and noting that the RHS of equation 4.43 is the local mass imbalance,

denoted by $S_{p'}$, the equation for p' can be rewritten as:

$$\frac{(V_p Q p'_p)^n}{\delta t}$$

$$+ \kappa Q\tilde{v}^*_{2,n}\, a^n_{nw/ne} \left\{ p'_n - \frac{p'_N - p'_p}{Ma^2_n} \right\}$$

$$- \kappa Q\tilde{v}^*_{2,s}\, a^n_{sw/se} \left\{ p'_s - \frac{p'_p - p'_S}{Ma^2_s} \right\}$$

$$+ \kappa Q\tilde{v}^*_{1,e}\, a^n_{se/ne} \left\{ p'_e - \frac{p'_E - p'_P}{Ma^2_e} \right\}$$

$$- \kappa Q\tilde{v}^*_{1,w}\, a^n_{sw/nw} \left\{ p'_w - \frac{p'_p - p'_W}{Ma^2_w} \right\}$$

$$= S_{p'} \qquad (4.46)$$

By analogy with equation 4.10, the cell face values of p' are replaced by, for example:

$$p'_n - \frac{p'_N - p'_p}{Ma^2_n} = (1-\alpha_n)p'_N + \alpha_n p'_p \qquad (4.47)$$

resulting in a final form of the p' equation as:

$$\frac{(V_p Q p'_p)^n}{\delta t}$$

$$+ \kappa Q \tilde{v}^*_{2,n} \; a^n_{nw/ne} \; \{(1-\alpha_n)p'_N + \alpha_n p'_p\}$$

$$- \kappa Q \tilde{v}^*_{2,s} \; a^n_{sw/se} \; \{\alpha_s p'_S + (1-\alpha_s)p'_p\}$$

$$+ \kappa Q \tilde{v}^*_{1,e} \; a^n_{se/ne} \; \{(1-\alpha_e)p'_E + \alpha_e p'_p\}$$

$$- \kappa Q \tilde{v}^*_{1,w} \; a^n_{sw/nw} \; \{\alpha_w p'_W + (1-\alpha_w)p'_p\} = S_{p'} \qquad (4.48)$$

The above equation may be written in analogous form to 4.17, that is:

$$A^n_p p'_p = \sum_c A^n_c p'_c + S_{p'} \qquad (4.49)$$

where the coefficients are:

$$A^n_N = - \kappa Q \tilde{v}^*_{2,n} \; a^n_{nw/ne} \; (1-\alpha_n)$$

$$A^n_S = \kappa Q \tilde{v}^*_{2,s} \; a^n_{sw/se} \; \alpha_s$$

$$A^n_E = - \kappa Q \tilde{v}^*_{1,e} \; a^n_{se/ne} \; (1-\alpha_e)$$

$$A^n_W = \kappa Q \tilde{v}^*_{1,w} \; a^n_{sw/nw} \; \alpha_w$$

$$A_p^n = \frac{(V_p Q)^n}{\delta t}$$

$$+ \kappa Q \tilde{v}^*_{2,n} \, a^n_{nw/ne} \, \alpha_n - \kappa Q \tilde{v}^*_{2,s} \, a^n_{sw/se} (1-\alpha_s)$$

$$+ \kappa Q \tilde{v}^*_{1,e} \, a^n_{se/ne} \, \alpha_e - \kappa Q \tilde{v}^*_{1,w} \, a^n_{sw/nw} (1-\alpha_w)$$

$$S_{p'} = - \{ \frac{(V_p \rho^*)^n - (V_p \rho)^o}{\delta t} \} + \{ -\kappa \dot{m}^*_n - (1-\kappa) \dot{m}^o_n$$

$$+ \kappa \dot{m}^*_s + (1-\kappa) \dot{m}^o_s - \kappa \dot{m}^*_e - (1-\kappa) \dot{m}^o_e + \kappa \dot{m}^*_w + (1-\kappa) \dot{m}^o_w \} \qquad (4.50)$$

Overall Pressure Adjustment Procedure

A method that has been found to improve the convergence of the numerical method is to adjust the overall pressure level before making the much smaller local adjustments required to achieve a local continuity balance. Following the practice of Watkins (1977) an overall pressure correction, p", is defined in a similar fashion to the local pressure correction (equation 4.34) as:

$$\rho = \rho^* + Qp" \qquad (4.51)$$

Replacing n by κ in equation 4.16, setting $\phi = 1$, $\Gamma = 0$, $S_\phi = 0$ and summing over the entire solution domain gives:

$$\sum_F \frac{(V\rho)^n_p - (V\rho)^o_p}{\delta t} + \kappa \sum_b \dot{m}^n_b + (1-\kappa) \sum_b \dot{m}^o_b = 0 \qquad (4.52)$$

where $\sum_F$ and $\sum_b$ denote summations over the whole field and boundaries (inlets and exhausts) respectively (Note that the summation of $\dot{m}$'s is also over the entire field except that the sum of all "internal" mass flows is zero, the net effect being due solely to the boundaries). Substituting the correct density from equation 4.51 into equation 4.52 yields:

$$\sum_F \frac{(V^n\rho^*)_p - (V\rho)^o_p}{\delta t} + p'' \sum_F \frac{V^n_p Q}{\delta t}$$

$$+ \kappa \sum_b \dot{m}^*_b + (1-\kappa) \sum_b \dot{m}^o_b + \kappa p'' \sum_b Q\, a_A v_A = 0 \qquad (4.53)$$

where quantities a_A and v_A are the areas and velocities at the apertures. Rearrangement of equation 4.53 gives an expression for the overall pressure adjustment:

$$p'' = \frac{-\{\sum_F \frac{(V^n\rho^*)_p - (V\rho)^o_p}{\delta t} + \kappa \sum_b \dot{m}^*_b + (1-\kappa) \sum_b \dot{m}^o_b\}}{\sum_F \frac{V^n_p Q}{\delta t} + \kappa \sum_b Q\, a_A\, v_A} \qquad (4.54)$$

The improvement in performance achieved with this adjustment scheme is demonstrated by fig. 4.2 which shows the variation of $\log_{10}$(mass residual), a quantity representative of the degree of convergence of the continuity equation, for a typical calculation with and without it. It is clear that the rate of convergence, indicated by the gradient, is superior when the overall pressure adjustment is operative, the residuals from the two schemes differing by 1 order of magnitude at 30 iterations and the differential increasing thereafter.

A variant of this scheme which provides for simultaneous adjustment of the pressure and temperature by invoking overall energy conservation, detailed by Watkins (1977), has not been found to given any further advantages over the more simple pressure adjustment described here.

Local Velocity and Pressure Adjustment

The procedure for this is as follows: first, the two momentum equations ($\tilde{v}_1$ and $\tilde{v}_2$) are solved with the guessed velocity and pressure fields; their solution provides the $\tilde{v}_1^*$ and $\tilde{v}_2^*$ velocities and the quantities D_v (equation 4.45) used to calculate the coefficients of the p' equation. The solution of the p' equation provides firstly a correction to the pressure field, for subsequent re-use in the momentum equations and secondly, using the linearised form of the momentum equations 4.41 and 4.42 , a correction to the velocity field such that continuity is satisfied; the densities are also updated at this stage (equation 4.34). The remaining equations for v_3, h, k and ε are then solved, so completing the iterative cycle. The steps are summarised below:

1. Iterate on the $\tilde{v}_1$ momentum equation.
2. " " " $\tilde{v}_2$ momentum equation.
3. " " " p" and p' equations.

   Correct $\tilde{v}_1$, $\tilde{v}_2$, p and ρ.
4. Iterate on the v_3 equation.
5. " " " h equation.

   Correct ρ and $\partial\rho/\partial p$.

6. Iterate on the k equation.
7. " " " ε equation.
8. Check for convergence: if not converged return to step 1, otherwise start the next time step.

Solution of the Finite-Difference Equations

The set of simultaneous equations for each variable is solved using a form of block iteration. The equations for the grid nodes on each ζ_1 = constant or ζ_2 = constant line are assembled into a tri-diagonal matrix by temporarily assuming that values on neighbouring lines are known, as in the Gauss-Seidal method. The tri-diagonal matrix is solved in an implicit fashion using the Thomas algorithm, a particular form of Gaussian elimination (see appendix 2). Adajcent lines are treated in a similar fashion until the whole field has been scanned. Full convergence of the calculation is not required and a few scans, typically 3, of the above procedure suffices.

Convergence Criteria

The solution is assumed to have converged when the sum of the normalised absolute residuals for the $\tilde{v}_1$, $\tilde{v}_2$ and p' equations have fallen below a specified level, usually 10^{-3}. Experience has shown that if the aforementioned equations have converged adequately then the remaining equations, namely those for v_3, h, k and ε, have also converged. Referring to the general finite-difference

equation 4.17 the sum of the absolute residuals for the field R_ϕ is given by:

$$R_\phi = \sum_F \left| \sum_c A_c^n \phi_c^n + \sum_c A_c^o \phi_c^o + A_p^o \phi_p^o + S_\phi - A_p^n \phi_p^n \right| \qquad (4.55)$$

Normalisation of R_ϕ for the pressure correction and momentum equations requires a reference mass and momentum respectively. For the former this quantity, denoted $N_{p'}$, is given by:

$$N_{p'} = \rho.\max(v_m, |v_{F,max}|, |v_I|) \qquad (4.56)$$

where ρ is a time varying density at a reference location in the field (The location chosen is not important as the spatial variations of density are small) and v_m, $|v_{F,max}|$ and $|v_I|$ are respectively the mean piston velocity, the absolute value of the maximum fluid velocity in the field and the absolute instantaneous piston velocity. The normalisation momentums, $N_{\tilde{v}_1}$ and $N_{\tilde{v}_2}$ are defined in terms of the same quantities, i.e.:

$$N_{\tilde{v}_1} = N_{\tilde{v}_2} = \rho.\max(v_m^2, v_{F,max}^2, v_I^2) \qquad (4.57)$$

A further convergence criterion is also applied, in this instance to the rate-of-change of the v_1 and v_2 velocities at a location in the centre of the flow field. Convergence is assumed if $|v_1^{i-1} - v_1^i|$ and $|v_2^{i-1} - v_2^i|$ are both less than 10^{-3}, where superscripts i-1 and i refer to values on successive iterations.

If either of the above criteria are satisfied, it has been found that values for all variables at the chosen location differ by approximately 10^{-3} or better from those on the previous iteration and convergence is assumed.

4.4 Boundary Conditions

Wall Boundary Conditions

For each variable, the coefficient A_c in equation 4.17 that would normally link the internal grid node to that at the boundary is set to zero and appropriate terms that invoke the boundary conditions described in section 3.7 are inserted into a linearised form of the source term S_ϕ, given by:

$$S_\phi = S_I \phi^n + S_E \tag{4.58}$$

where the subscripts I and E refer to the implicit and explicit contributions respectively. A sufficient condition for stability is that S_I is negative (Gosman and Pun, 1974).

Momentum Equations

The resultant wall shear stress, τ_w, is evaluated from either equation 3.40 or 3.43 depending on the value of y^+. The components of τ_w, denoted generally by τ_{ij} and given by equations 3.45 are calculated and the term $\tau_{ij} \cdot a_c$, where a_c is the cell face area over which τ_{ij} acts, is inserted into the linearised source term (equation 4.58).

ε Equation

The value of ε at the near wall grid node, denoted ε_w, is evaluated from equation 3.49. To ensure ε remains fixed at this value, S_I and S_E of the linearised source term (equation 4.58) are ascribed the following values:

$$S_I = L$$

$$S_E = L.\varepsilon_w$$

where L is a large number, typically 10^{30}.

k Equation

The usual expression for the shear stress contribution to the generation rate that would act in a direction tangential to the boundary (see table 3.3) is replaced by equation 3.50, τ_w being evaluated according to the y^+ value.

h Equation

The wall heat flux $\dot{q}_w$ is calculated from equation 3.52 or 3.54 according to the y^+ criteria. The temperature gradient $\frac{dT_w}{dy}$ is evaluated from:

$$\frac{dT_w}{dy} = \frac{T_p - T_w}{y_p}$$

where T_w and T_p are the temperatures of the wall and gas at the internal grid node adjacent to the wall respectively.

The quantity $\dot{q}_w.a_c$ is added into the linearised source term (equation 4.58).

p' Equation

The normal velocity at the boundary is prescribed and this requires that the normal gradient of p' is zero, i.e. $\frac{\partial p'}{\partial y} = 0$. This is done by setting the appropriate A_c in equation 4.49 to zero.

Inlet/Exhaust Boundary Conditions

In order to simulate complete engine cycles, a treatment is needed for the intake and exhaust processes. It is accepted that in "real" engines, valves offset from the centreline of the cylinder play an important role, together with the shape of the inlet tract, in generating both swirl and turbulence and that an axisymmetric representation is not capable of accurately modelling these effects. Nevertheless, there are important reasons why a valve should be included in the simulation: firstly, there are measurements available in motored engines with axisymmetric valves that can be used for the very necessary validation of the prediction method, and secondly, it is expected that the two-dimensional valve representation will provide some insight into real engine phenomena.

The measurements available for validation, described in chapter 2,apply to engines with very different types of valve. Morse et al (1978) have used an annular orifice in a fixed position and flush with the cylinder head whilst the engine of Witze (1976c) is equipped with a moving poppet valve. Boundary conditions for the in-cylinder calculation must be provided somewhere, and the choice as to where is balanced between what is realistic and what is

computationally possible, within reasonable limits. The arguments against extending the calculation through the valve opening and into the inlet tract are the difficulty in fitting a computational grid to what is invariably a complex 3-d geometry and the prohibitive additional grid requirement, necessary to adequately resolve the detail. The alternative is to specify or calculate the fluxes of each variable entering or leaving the cylinder at the valve opening. This can be achieved if the instantaneous mass flow rate, $\dot{m}$, through the valve can be calculated, and if the values of the various turbulence quantities, temperature etc. are known in the manifold and their spatial distribution across the valve can be prescribed.

If the engine speed is sufficiently low that compressibility can be ignored then $\dot{m}$ can be calculated according to the amount of fluid displaced by the piston (Watkins, 1977). This is not generally the case however and resort is therefore made to determining $\dot{m}$ from a compressible-flow orifice-type of equation that relates $\dot{m}$ to the pressure drop across the valve, as in cycle program analyses (see e.g. Whitehouse et al, 1962). The equation used depends upon the flow regime prevailing at the valve orifice, which in turn depends upon the pressure ratio between the cylinder and manifold. For subsonic flow, which requires:

$$\frac{p_d}{p_u} > \left(\frac{2}{\gamma+1}\right)^{\frac{\gamma}{\gamma-1}} \tag{4.59}$$

$\dot{m}$ is given by:

$$\dot{m} = \frac{dm}{dt} = A_{eff}\, \rho_u \left\{\gamma R T_u \frac{2}{\gamma-1} \left(\frac{p_d}{p_u}\right)^{2/\gamma} \left(1-\left(\frac{p_d}{p_u}\right)^{\frac{\gamma-1}{\gamma}}\right)\right\}^{1/2} \tag{4.60}$$

and for sonic flow:

$$\frac{p_d}{p_u} \leq \left(\frac{2}{\gamma+1}\right)^{\frac{\gamma}{\gamma-1}} \tag{4.61}$$

$\dot{m}$ is obtained from:

$$\dot{m} = \frac{dm}{dt} = A_{eff}\rho_u \left\{ \gamma RT_u \left(\frac{2}{\gamma+1}\right)^{\frac{\gamma+1}{\gamma-1}} \right\}^{1/2} \tag{4.62}$$

where A_{eff} is the effective area and the subscripts u and d refer to upstream and downstream conditions respectively. Sonic flow through the valve orifice is rarely encountered in motored engines and usually only exists during the initial stages of exhaust blowdown in fired engines, however allowance is nevertheless made for its occurence in the calculations. The manifold conditions of pressure and temperature are here assumed to be constant with time although better account may be taken of their temporal variation either by using a "filling-and-emptying" type of calculation (Johns, 1975) which assumes the manifolds to be of finite volume and linked to atmosphere by another orifice or by solving the 1-d unsteady continuity, momentum and energy equations that govern the manifold wave action (Benson et al, 1969).

Equations 4.60 and 4.62 are integrated numerically using a forth-order Runga-Kutta method over the same time interval employed for the main finite-difference equations but before the latter are solved. An implicit assumption in this approach is that the cylinder temperature remains constant over the interval of integration (typically 1^o-3^o) as equations 4.60 and 4.62 are not solved simultaneously with the energy equation. The temperature changes during intake and exhaust are not appreciable for motored engines, typically $1^oK/3^o$ crank angle. With a gas temperature of approximately

$300^{o}K$, the error thereby introduced into the calculation of the mass flow rate, $E_{\dot{m}}$, as a result of this assumption is estimated to be:

$$E_{\dot{m}} = |1 - \{\frac{300}{301}\}|^{1/2} \times 100 = .17\%$$

The mass inflow or outflow , δm, obtained from the integration of equations 4.60 and/or 4.62 is used to calculate the velocity through the valve from:

$$v = \frac{\delta m}{\rho_u A_{eff}} \tag{4.63}$$

The specification of the spatial distribution of all variables in the incoming flow depends upon the specific application and is described in this context in a later chapter.

Application to Specific Geometries

The Engine of Morse et al (1978)

The grid employed for the fixed-orifice engine of Morse et al (fig. 2.18) is shown in fig. 4.3 for the flat-topped and bowl-in-piston configurations. Uniformly spaced grids are used in the axial direction in the cylinder and piston bowls but grid lines have been concentrated around the inlet in the radial direction to improve the resolution in this region. It can be seen that this unavoidably produces excessively fine grids elsewhere in the field, for example, adjacent to the wall of the piston bowl. Boundary conditions are specified in the plane indicated.

The Engine of Witze (1976c)

The additional complication of valve movement in this geometry (see fig. 2.15) requires a different form of grid. In the first numerical simulation of this experiment,Watkins (1977) assumed the flow to enter in the plane of the cylinder head and the valve to be represented by fixed grid lines such that the orifice area was not time-varying. The density of the incoming flow was adjusted according to the ratio of (true instantaneous valve area)/(value area defined by fixed grid lines) to procure correct mass and momentum flow rates.

The approach adopted here is to accommodate the protrusion of the valve into the cylinder by inserting a fixed number of additional axial grid lines between the valve and cylinder head and to apply the boundary conditions along the cylindrical surface extending from the periphery of the valve to the edge of the valve seat. This process is illustrated in figs. 4.4 and 4.5 which show respectively the grids used for the flat cylinder head and bowl-in-head configurations. The valve head is always represented by the same grid line, thus the grid lines in the cylinder head either side of the valve head grid line expand and contract with the valve motion. The aforementioned additional grid lines are only operative when the valve is open. At the instant of valve opening, values of the dependent variables need to be prescribed along the newly-inserted grid lines. In the case of h, ρ, k and ε, there are ascribed the values on the grid line adjacent to the cylinder head immediately prior to valve opening whilst the v_1, v_2 and v_3 velocities are set to zero.

4.5 Stability and Accuracy of Alternative Differencing Schemes

This section examines the properties of alternative ways of differencing the general transport equation although special emphasis will be placed on the momentum and continuity equations as they are strongly coupled and the stability, accuracy and convergence of their solution procedure determines the performance of the method as a whole. The factors affecting the performance are: firstly, the ways in which the equations are linked although this aspect has largely been determined (see section 4.3), and secondly, the specification of the parameters α, η and κ in the finite-difference equations. It is toward determining a suitable combination of the latter that attention is now turned.

Before examining specific schemes, it is worthwhile discussing the effect of these above-mentioned parameters on the relative magnitudes of certain terms of the finite-difference equations*.

1. The factor α determines the relative importance of the convection and diffusion terms. The most widely used specifications are:

   (a) $\alpha = \frac{1}{2}$ Central differencing (as derived from a Taylor series)

   (b) $\alpha = 1$ $Pe > 0$ } Upwind differencing (first proposed by Hellums and Churchill, 1961).
   $\alpha = 0$ $Pe < 0$ }

   (c) A combination of (a) and (b).

*To preserve clarity, the discussion here relates to equally spaced grids. The results are equally applicable to non-uniform grids with the inclusion of appropriate weighting factors.

2. The quantities η and κ define the temporal differencing of terms in the momentum and continuity equations respectively. There are three widely used alternatives, these being:

   (a) $\eta(\kappa) = 0$ Explicit (evaluation using 'old' time level values)

   (b) $\eta(\kappa) = \frac{1}{2}$ Time-centered or Crank-Nicholson (an average of 'old' and 'new' time-level values).

   (c) $\eta(\kappa) = 1$ Implicit (reliance on 'new' time-level values).

The alternatives in (1) and (2) produce a large number of permutations and a detailed study of the possibilities is clearly a major undertaking (in fact the problem can be taken still further by providing different temporal weightings for the convection and diffusion terms (Runchal, 1977)). A further hindrance in the evaluations of these alternative schemes is that analytically derived expressions and criteria for accuracy and stability are difficult, if not impossible, for the coupled equations and resort is therefore made to simple analytic tools and numerical testing. These latter methods can however provide considerable insight into the performance of the overall scheme and it will be demonstrated that results obtained in a simple one-dimensional analysis are at least qualitatively applicable to a full two-dimensional solution.

Spatial Differencing

Studies by Spalding (1972) and Raithby and Torrance (1974) have shown that the use of solely central or upwind differencing can cause erroneous results if proper account is not taken of the value of the Peclet number (equation 4.6). By obtaining an analytical solution to the particular case of the 1-d steady form of the transport equation, i.e.:

$$\frac{d\phi}{dz} = \frac{1}{Pe} \frac{d^2\phi}{dz^2} \tag{4.64}$$

it has been demonstrated by Spalding (1972) that a specification of:

$$\alpha_e = - \{e^{-Pe/2} - 1\}^{-1} \tag{4.65}$$

with a similar expression for α_w (equation 4.10) produces identical numerical and analytic solutions for ϕ_P(this does not imply an exact solution for the 2-d case). An alternative to the direct use of this expression, which involves the time-consuming evaluation of an exponential, is a piecewise fit of central and upwind differencing schemes. This is:

$$\alpha_e = \begin{cases} \frac{1}{2} + \frac{1}{Pe} & \text{for } |Pe| \leq 2 \\ 1 & \text{for } Pe > 2 \\ 0 & \text{for } Pe < -2 \end{cases} \tag{4.66}$$

This scheme enhances the stability of the numerical method by virture of the presence of positive coefficients in the finite-difference equation 4.17, thus the coefficient matrix is always diagonally dominant (Roach, 1972).

The accuracy of this scheme can however be poor under certain conditions when it is used for multi-dimensional flows. Errors arise when the grid is not aligned with the dominant flow direction and they are propagated in a direction normal to the flow. Thus, recirculating flows or an inappropriate grid orientation in uni-directional flows can produce solutions substantially in error. This problem has been recognised by Raithby (1976) among others, who proposed a two-dimensional 'skew' scheme that takes better account of the upstream direction. Although encouraging, it was noted by Raithby that under certain flow conditions the matrix of coefficients could become non-diagonally dominant and numerical stability could not therefore be guaranteed. However, further work in this area should result in improved spatial differencing schemes.

Temporal Differencing Schemes - Assessment of Stability

Explicit schemes involve a stability requirement that the Courant number $(v_f+v_a)\delta t/\delta x$ should remain less than unity (Courant et al, 1967). In the context of the present problem, assuming the following engine and computational conditions:

- 1000 rev/min
- Peak inlet velocity (v_f) of 100 m/s
- Sonic velocity (v_a) at 300^o K = 347 m/s
- Radial grid spacing in 9 cm bore engine with 30 equally spaced radial grid lines = 1.5 mm

would require less than 0.02^o crank angle steps for the Courant number to equal unity. This is clearly unacceptable and for this reason alone explicit schemes can be rejected.

The most popularly-employed alternatives remaining are the fully-implicit and time-centred formulations. A formal stability analysis of the coupled finite-difference equations arising in the present study is extremely difficult but the examination of a single equation is feasible and can yield useful qualitative information. The analysis presented below is, in essence, similar to that attributed to Von-Neuman and published by O'Brian et al (1951) whereby the propagation of errors can be expressed in terms of an 'amplification factor', which describes their growth or diminution as the solution proceeds. The equation examined is the one-dimensional form of the mass conservation equation (3.16) with the features of the present problem. This equation is:

$$\frac{\partial}{\partial t}(\ell_1 \rho) + \frac{\partial}{\partial \zeta_1}(\rho \tilde{v}_1) = 0 \tag{4.67}$$

The time-centred approximation is obtained by setting $\kappa = 1/2$ and, when continuity is satisfied, $p' = 0$ in equation 4.49 to give:

$$\frac{(\ell_1 \rho)^n - (\ell_1 \rho)^o}{\delta t} + \frac{1}{2} \{\{(\rho \tilde{v}_1)_e^n + (\rho \tilde{v}_1)_e^o\} - \{(\rho \tilde{v}_1)_w^n + (\rho \tilde{v}_1)_w^o\}\} = 0 \tag{4.68}$$

If a sinusoidal specification of piston motion is made, i.e.:

$$z_H = A_o + A_1(1 + \cos t) \tag{4.69}$$

where z_H is the instantaneous distance between the cylinder head and piston top, A_o is the TDC 'bumping clearance' and $2A_1$ is the stroke, the density/volume relationship may be written as:

$$(z_H \rho)^n = (z_H \rho)^o \tag{4.70}$$

from which it follows:

$$\frac{\rho^o}{\rho^n} = \frac{A_o+A_1(1 + \cos t \cos \delta t - \sin t \sin \delta t)}{A_o + A_1(1 + \cos t)} \tag{4.71}$$

The specification of $(\ell_1)^n$ and $(\ell_1)^o$ determine the local relative movement of the grid lines. If those quantities are equal, as they are in the piston-bowl region, then they can be replaced by a constant, δz. Substituting this value and the density relationship, equation 4.71, into 4.68 gives, after rearrangement:

$$(\tilde{v}_{1,e} - \tilde{v}_{1,w})^n = C_1(t) + C_2(t)\ (\tilde{v}_{1,e} - \tilde{v}_{1,w})^o \tag{4.72}$$

where:

$$C_1(t) = - \frac{2\delta z}{\delta t} A_1 \left\{ \frac{\cos t\ (1- \cos \delta t) + \sin t \sin \delta t}{A_o + A_1(1 + \cos t)} \right\}$$

$$C_2(t) = - \frac{A_o+A_1(1 + \cos t \cos \delta t - \sin t \sin \delta t)}{A_o + A_1(1 + \cos t)} \tag{4.73}$$

If an error, E, which may arise through roundoff or other numerical approximation is now introduced into the solution such that:

$$(\tilde{v}_{1,e} - \tilde{v}_{1,w})^o = (\tilde{v}_{1,e} - \tilde{v}_{1,w})^o_C + E^o \tag{4.74}$$

where the subscript C denotes the correct solution, then the error at the new time level, E^n, will be given by:

$$E^n = C_2(t)E^o \tag{4.75}$$

Noting that C_2 is always negative, the error at time level $t + m\delta t$ is given by:

$$E^m = |E^{m-1}|(-1)^m C_2(t + m\delta t) \qquad (4.76)$$

The quantity $C_2(t + m\delta t)$ may be regarded as an error amplification factor, relating the magnitude of errors on successive time steps. Inserting the values $A_1/A_0 = 10$ which corresponds to a compression ratio of 21:1 and $\delta z = A_1/10$ into expression 4.73 and 4.76, fig. 4.6 shows $(-1)^m C_2(t + m\delta t)$ plotted against non-dimensional time, t^*, defined as $t^* = t/t_0$ where t_0 is the time for 1 cycle, with δt equivalent to 3^o, 6^o and 12^o increments. There are three points to note: firstly the magnitudes of C_2 before and after TDC ($t^* = .5$) are less than and greater than unity respectively, indicating that errors would be attenuated and amplified either side of TDC; secondly, the variation is oscillatory in nature, due to the $(-1)^m$ term (although for clarity, successive solutions are only shown for the start of the 6^o case); and thirdly, the magnitude of C_2 increases with increasing δt after TDC and decreases with increasing δt before TDC. The solution of equation 4.74 is shown in fig. 4.7 in which $(\tilde{v}_{1,e} - \tilde{v}_{1,w})^n$ is plotted over 1 cycle. As expected, the solution is oscillatory with an increasing amplitude during the period $t^* = .5$ to $t^* = 1$ (although not shown, the oscillations are damped during the period $t^* = 1$ to $t^* = 1.5$ on the successive cycle ($|C_2| < 1$)) also, the amplitude of oscillation increases with increasing time step. Similar performance of the Crank-Nicholson scheme has been found by Wood (1974) and, Patankar and Baliga (1978). This behaviour is often termed 'inaccurate' and not 'unstable', however whatever the terminology, it is clearly unacceptable.

The fully implicit scheme is unconditionally stable. If sufficiently small time steps, of the order 1^o-2^o, can be used, then the choice

between implicit and time-centred schemes will depend upon their relative accuracy (which will be examined below); for larger time intervals however the latter must be rejected on grounds of stability.

Temporal Differencing Schemes - Assessment of Accuracy

The existence of an analytic solution for the coupled one-dimensional momentum, continuity and energy equations provides a basis for comparing the accuracy of alternative differencing schemes. The solution, obtained by Watkins (1973), requires that the v_2 and v_3 velocities are zero, the boundaries are adiabatic and the piston is slow moving such that the density, molecular viscosity and thermal conductivity are spatially uniform. The governing differential equations are then:

Continuity

$$\frac{\partial}{\partial t}(\ell_1 \rho) + \frac{\partial}{\partial \zeta_1}(\rho \tilde{v}_1) = 0 \tag{4.77}$$

Momentum - direction 1

$$\frac{\partial}{\partial t}(\ell_1 \rho v_1) + \frac{\partial}{\partial \zeta_1}(\rho \tilde{v}_1 v_1) = \frac{\partial}{\partial \zeta_1}\left(\frac{\mu}{\ell_1}\frac{\partial v_1}{\partial \zeta_1}\right) - \frac{\partial p}{\partial \zeta_1} \tag{4.78}$$

Thermal energy

$$\frac{\partial}{\partial t}(\ell_1 \rho h) + \frac{\partial}{\partial \zeta_1}(\rho \tilde{v}_1 h) = \frac{\partial}{\partial \zeta_1}\left(\frac{1}{\ell_1}\frac{\mu}{\sigma_\ell}\frac{\partial h}{\partial \zeta_1}\right) + \ell_1 \frac{\partial p}{\partial t}$$

$$- v_g \frac{\partial p}{\partial \zeta_1} \tag{4.79}$$

with the density being solely a function of piston displacement, z_H, i.e.:

$$\rho = \frac{(\rho z_H)_I}{z_H} \tag{4.80}$$

Here, the subscript I denotes an initial condition. The solution gives the spatial variation of velocity and pressure as:

$$v_1 = \xi \frac{dz_H}{dt} \tag{4.81}$$

$$p = p_0(t) - \frac{(\rho z_H)_I}{2} \xi \frac{d^2 z_H}{dt^2} \tag{4.82}$$

where the pressure at the cylinder head, $p_0(t)$, is given by:

$$P_0(t) = P_{0,I} \{\frac{z_{H,I}}{z_H}\}^{\gamma} \tag{4.83}$$

and the temperature $T_0(t)$ as:

$$T_0(t) = T_I \{\frac{z_{H,I}}{z_H}\}^{\gamma-1} \tag{4.84}$$

Here, $\xi(=z/z_H)$ is a time-independent, dimensionless axial co-ordinate varying linearly between zero at the cylinder head to unity at the surface of the piston.

To be representative of the type of grid used for calculations with piston bowls, a one-dimensional 'hybrid' grid, shown in Fig. 4.8(a), has been used for the accuracy assessment of the numerical method. This has the feature of a block of grids that translate without relative movement in the manner of a piston bowl, and, an expanding/contracting portion between the (imaginary) piston surface and the cylinder head.

The assessment considers first the variation of velocity error with grid spacing and time-step using the analytic solution for the axial pressure variation (equation 4.82) to evaluate the momentum equation pressure gradient. Both fully implicit ($\eta = 1$) and time-centred ($\eta = 1/2$) formulations are examined. The evaluation of the error, E_v, has in each case been made at a point midway between the cylinder head and piston surface, interpolation being used where necessary and is defined as:

$$E_v = \{\frac{v_1 - v_{1,C}}{v_{H,max}}\} \times 100$$

where v_1 and $v_{1,C}$ are respectively the numerical and analytic solutions for the absolute axial velocity and $v_{H,max}$ is the maximum piston velocity.

Figs. 4.9 to 4.12 show the velocity error for both differencing schemes for three different time-steps, equivalent to 2^o, 1^o and $.5^o$* crank-angle increments and three different grids of ($N_1 = 3, N_2 = 3$), ($N_1 = 6$, $N_2 = 6$) and ($N_1 = 12$, $N_2 = 12$) , where N_1 and N_2 are the number of grid lines in the cylinder and 'bowl' regions respectively (see fig.4.8a). The error is plotted against non-dimensional time. Considering first the fully-implicit scheme, the error reduces with time-step (fig. 4.9) and has a maximum value before TDC. The variation of error with grid size, shown in fig. 4.10, exhibits no obvious trend, the intermediate size of grid apparently gives the least errors, however, the coarsest grid does produce the highest error.

*These time-steps have been chosen to minimise any oscillations associated with time-centred schemes.

Turning now to the time-step variation of error for the time-centred scheme, shown in fig. 4.11, the results for the three time steps are virtually identical for the entire cycle, they are also one order of magnitude greater than those of the fully implicit formulation. The variation of error with grid spacing, fig. 4.12, does not show any definite trend.

It would seem that the momentum equation is best satisfied using fully implicit differencing and that this scheme does possess the desirable feature of the error reducing with time step.

Retaining the implicit momentum equation differencing, figs. 4.13 to 4.20 show the behaviour of the velocity and pressure error with grid spacing and time-step for both implicit ($\kappa = 1$) and time-centred ($\kappa = 1/2$) differencing of the continuity equation when both equations are solved. The pressure error, E_p, is evaluated at the same position as E_v and defined in a similar fashion, i.e.:

$$E_p = \{\frac{p - p_c}{p_{max}}\} \times 100$$

where p and p_c are respectively the numerical and analytic pressure solutions and p_{max} is the pressure at the time of maximum piston acceleration.

Considering first the implicit scheme, the velocity error decreases with refinement in the time-step (fig. 4.13) whilst the pressure error (fig. 4.14) shows no discernable trend except for $t^* = 1$ where the error increases with decreasing time-step. It should be noted that the level of velocity error is below that resulting from a solution of the momentum equation with the analytic pressure field. This, and similar results for the time-centred scheme suggests that the continuity equation enforces a correct (or nearly so)

velocity solution, the errors being 'swept' into the pressure field. Fig. 4.15 indicates that the velocity errors are independent of grid size. However, the pressure error (fig. 4.16) shows a reduction with grid spacing at all times of the cycle.

The time-centred scheme shows a reduction of error with time step (fig. 4.17) and, as would be expected from the result of the stability analysis, also exhibits the characteristic oscillatory behaviour. The velocity errors here are two orders of magnitude lower than those of the implicit formulation. Again, the errors appear in the pressure solution, shown in fig. 4.18, these being of the same order as those of the implicit differencing and showing the same trend. There is no definite trend in the variation of velocity error with grid spacing (fig. 4.19) although the pressure errors (fig. 4.20) decrease considerably at all times in the cycle.

The results of this analysis may be summarised as follows:

Solution of momentum equation only

(1) The implicit formulation produces errors one order of magnitude lower than those found with the time-centred scheme. The errors decrease with time-step for the former but are independent of time-step in the case of the latter.

Solution of momentum (implicit differencing) and continuity equations

(1) Velocity errors for the implicit and time-centred continuity differencing are respectively one and three orders of magnitude lower than those associated with the solution of the momentum equation in isolation and in both cases reduce with time-step refinement.

(2) Pressure errors for both schemes are of the same order and in both cases reduce with grid refinement.

(3) Oscillatory behaviour, characteristic of the time-centred scheme, is apparent in the velocity solutions.

Application to a Two-Dimensional Turbulent Flow

Results from the one-dimensional analysis indicate that, for the equations examined, a combination of time-centred continuity and implicit momentum equation differencing gives the best solution provided small time-steps are used to minimise the inherent oscillatory nature of this scheme. However, although the velocity errors of this scheme are two orders of magnitude lower than those found with the implicit continuity formulation, the errors associated with the latter are not large (less than 0.5% for the 2^{o} time-step (fig. 4.13)) and both schemes are therefore worthy of further investigation. Toward this end, results are presented below for a full two-dimensional, turbulent simulation of a piston bowl configuration, although the parametric testing is of necessity more limited due to the increased computer requirements. The results shown are for one cycle (BDC → TDC → BDC) with the simple piston bowl geometry illustrated in fig. 4.8b with initial conditions of zero velocities, including swirl, and spatially uniform fields of turbulence energy and dissipation values, typical of those generated during the intake process. The effects examined are: (a) time-step dependence of the time-centred continuity/implicit momentum* equation scheme, (b) grid dependence

*Implicit differencing is used throughout for the turbulence and energy equations.

of the time-centred continuity/implicit momentum equation scheme and (c) a comparison of the time-centred continuity/implicit momentum and fully implicit schemes for the same grid and time step. The axial and radial velocity components and the turbulence energy are plotted for each case for a location in the centre of the piston bowl.

Figs. 4.21 and 4.22 show the mean velocity and turbulence energy respectively using the time-centred continuity equation differencing for crank-angle increments of 1^{o} and 3^{o} and with a grid of (9 x 18)/(9 x 9)*. The velocities are similar except for the period immediately before and after TDC (t^{*} = .5) at which time the effects of squish are strongly felt in the bowl, resulting in high temporal and spatial velocity gradients. The turbulence energy is increased for the small time increment and this is probably associated with the evaluation of the generation term in this equation which consists primarily of products of velocity gradients, and as already seen, these are reduced for the coarser time step.

The effect of grid refinement on the mean and turbulent velocities, shown in figs. 4.23 and 4.24 for grids of (9 x 18)/(9 x 9), (14 x 28)/(14 x 14) and (19 x 38)/(19 x 19) for the 3^{o} crank-angle step, is similar to time-step refinement in that finer grid spacing enhances the maxima and minima, which is in turn reflected in increased turbulence levels. In essence, the coarser grid tends to smooth the steep spatial gradients, this effect being most pronounced around TDC.

---

*The format $(N_1 \times N_3)/(N_2 \times N_4)$ corresponds to:

N_1 = no. of axial grid lines in the cylinder.
N_2 = " " " " " " " piston bowl.
N_3 = " " radial " " " " cylinder.
N_4 = " " " " " " " piston bowl.

Axial velocity predictions from the two differencing schemes are shown in fig. 4.25 for the (9 x 18)/(9 x 9) grid and using a 1^{o} time increment. The radial velocity and turbulence energy are not shown as the two schemes produce indistinguishable results.

The results of this investigation are summarised below:

(1) Both grid and time-step refinement enhance the solution of the momentum and turbulence equations for the time-centred continuity differencing scheme. It is probable that this is also true for the implicit differencing of this equation (bearing in mind the similar performance found in the one-dimensional analysis), although this should be confirmed by further investigation.

(2) Differences in the solution using the time-centred and implicit continuity equation differencing are minimal for the test case examined.

The conclusion is therefore that unless small time-steps are a necessity (e.g. for a combustion calculation) the implicit scheme is preferred on grounds of stability.

4.6 Differencing of the Source* Terms

The differencing of the source terms for all equations, with the exception of the pressure gradient in the momentum equations, is dealt with here. Many of these terms are similar in form, in which case only a representative example will be given. Some of the

*The term is used here loosely to include all constituent parts of S_{ϕ} in the general transport equation (4.17).

terms however are unique to the present problem and make significant contributions to their respective conservation equations. For example, the interaction of the v_3 (swirl) velocity with the v_1 and v_2 fields can be of major importance, affecting both the flow structure and the stability of the method for even moderate swirl rates and the pressure-work term in the energy equation is also extremely important in the calculation of the temperature, thus these terms are dealt with separately.

Before examining individual terms, the difference between the 'strong' and 'weak' conservation forms of the differential equations will be discussed. The one-dimensional continuity and general transport equation in strong conservation form for an Eulerian co-ordinate system are:

$$\frac{\partial \rho}{\partial t} + \frac{\partial (\rho v)}{\partial z} = 0 \tag{4.85}$$

$$\frac{\partial (\rho \phi)}{\partial t} + \frac{\partial}{\partial z}(\rho v \phi) - \frac{\partial}{\partial z}(\Gamma \frac{\partial \phi}{\partial z}) - s_\phi = 0 \tag{4.86}$$

The time-dependent and convective terms of the full differential equations presented in chapter 3 are of this type and the subsequent differencing ensures that, when ϕ is a scalar, conservation prevails on a local and hence overall basis. If alternatively the general transport equation is rewritten as:

$$\phi \{\frac{\partial \rho}{\partial t} + \frac{\partial}{\partial z}(\rho v)\} + \rho \frac{\partial \phi}{\partial t} + \rho v \frac{\partial \phi}{\partial z} - \frac{\partial}{\partial z}(\Gamma \frac{\partial \phi}{\partial z}) - s_\phi = 0 \tag{4.87}$$

then the bracketed term is zero (from continuity) giving the weak conservation form:

$$\rho \frac{\partial \phi}{\partial t} + \rho v \frac{\partial \phi}{\partial z} - \frac{\partial}{\partial z}(\Gamma \frac{\partial \phi}{\partial z}) - S_\phi = 0 \qquad (4.88)$$

Unless especial care is taken in the differencing of this equation the numerical scheme will be non-conservative.

The curvature terms in the curvilinear orthogonal momentum equation, of the general form $\frac{\rho v_i v_j}{r_k}$, which serve to redistribute momentum between the three co-ordinate directions, should ideally be conservatively differenced. This is not easy to arrange because a curvature term in one equation does not have a direct counterpart in another. A method proposed by Vinokur (1974) is superior to the scheme presented here in that it takes account of the finite size of the cell and results in conservative differencing. This method has been extended by Watford (1978) to include viscosity terms. This scheme is not used here as a not inconsiderable amount of further work would be needed before a viable computer code could be produced, but it is worthy of further investigation.

The main curvature terms are of two types, namely centrifugal and Coriolis, of the general forms $\rho v_i^2/r_k$ and $\rho v_i v_j/r_k$ $(i \neq j)$ respectively. The former enter the calculation in an explicit fashion and for high values of v_i and/or low radii of curvature can be important contributors to the local momentum balance, reducing the dependence on surrounding cells and sometimes causing numerical instability. A linearisation method used by Gosman et al (1975), provides a means of suppressing this effect. For ease of explanation, if $\cos \beta$ is taken to be unity, then the term involving the swirl velocity (v_3) in the radial momentum equation (3.19) is $\frac{\rho v_3^2}{r_3}$. The suggested linearised implicit form of this term is:

$$\frac{\rho v_3^2}{r_3}\left(1 + \frac{f}{v_3}\left(v_2^i - v_2^{i+1}\right)\right) \tag{4.89}$$

where f is an under-relaxation factor and superscript i refers to the ith iteration. The additional contribution, which is zero for a converged solution ($v_2^i = v_2^{i+1}$), attempts to anticipate the effect of perturbations of the v_2 velocity on the convection of v_3 momentum in the radial direction as the solution proceeds. A value of f = .3 has been found to give good results.

For the direction-1 momentum equation, the terms to be approximated are:

$$\frac{\rho v_2^2}{r_2} + \frac{\sin\beta \rho v_3^2}{r_3} - \frac{\rho v_2 v_1}{r_1}$$

The constituent parts of these terms are calculated according to the following specification:

$$\rho = f_1 \rho_W + (1-f_1)\rho_P \tag{4.90}$$

$$v_2 = f_1 \frac{(v_{2,wnw} + v_{2,wsw})}{2} + (1-f_1)\frac{(v_{2,n} + v_{2,s})}{2} \tag{4.91}$$

where f_1 is defined in equation 4.9.

$$v_3 = f_1 v_{3,W} + (1-f_1)v_{3,P} \tag{4.92}$$

$$r_2 = f_1 \frac{(r_{2,wnw} + r_{2,wsw})}{2} + (1-f_1)\frac{(r_{2,n} + r_{2,s})}{2} \tag{4.93}$$

$$r_3 = f_1 r_{3,W} + (1-f_1)r_{3,P} \tag{4.94}$$

The curvature terms in the direction 2 and 3 momentum equations are differenced in similar fashion.

The remaining source terms for all the differential equations, with the exception of the pressure work term in the energy equation, are of 3 general types, i.e.:

$$\text{I} \qquad \frac{1}{\ell_1}\frac{\partial\phi}{\partial\zeta_1} \quad \text{or} \quad \frac{1}{\ell_2}\frac{\partial\phi}{\partial\zeta_2} \tag{4.95}$$

$$\text{II} \qquad \frac{1}{\ell_1}\frac{\partial}{\partial\zeta_1}\left(\frac{1}{\ell_1}\frac{\partial\phi}{\partial\zeta_1}\right) \quad \text{or} \quad \frac{1}{\ell_2}\frac{\partial}{\partial\zeta_2}\left(\frac{1}{\ell_2}\frac{\partial\phi}{\partial\zeta_2}\right) \tag{4.96}$$

$$\text{III} \qquad \frac{1}{\ell_1}\frac{\partial}{\partial\zeta_1}\left(\frac{1}{\ell_2}\frac{\partial\phi}{\partial\zeta_2}\right) \quad \text{or} \quad \frac{1}{\ell_2}\frac{\partial}{\partial\zeta_2}\left(\frac{1}{\ell_1}\frac{\partial\phi}{\partial\zeta_1}\right) \tag{4.97}$$

The above terms are differenced in the fashion indicated below. Only the first of each example is given as differencing of the other follows similar rules.

$$\text{I} \qquad \frac{1}{\ell_1}\frac{\partial\phi}{\partial\zeta_1} = \frac{\phi_e - \phi_w}{(\ell_1\delta\zeta_1)_{e/w}} \tag{4.98}$$

where

$$\phi_w = f_1\phi_W + (1-f_1)\phi_P \tag{4.99}$$

with a similar expression for ϕ_e and f_1 is defined by equation 4.9.

$$\text{II} \qquad \frac{1}{\ell_1}\frac{\partial}{\partial\zeta_1}\left(\frac{1}{\ell_1}\frac{\partial\phi}{\partial\zeta_1}\right) = \frac{1}{(\ell_1\delta\zeta_1)_{e/w}}\left\{\frac{\phi_E - \phi_P}{(\ell_1\delta\zeta_1)_{E/P}} - \frac{\phi_P - \phi_W}{(\ell_1\delta\zeta_1)_{P/W}}\right\} \tag{4.100}$$

$$\text{III} \qquad \frac{1}{\ell_1}\frac{\partial}{\partial\zeta_1}\left(\frac{1}{\ell_2}\frac{\partial\phi}{\partial\zeta_2}\right) = \frac{1}{(\ell_1\delta\zeta_1)_{e/w}}\left\{\frac{\phi_{ne} - \phi_{se}}{(\ell_2\delta\zeta_2)_{ne/se}} - \frac{\phi_{nw} - \phi_{sw}}{(\ell_2\delta\zeta_2)_{nw/sw}}\right\} \tag{4.101}$$

Here, ϕ_{ne}, ϕ_{se}, ϕ_{nw} and ϕ_{sw} are obtained from a weighted average of the 4 surrounding values, typically

$$\phi_{sw} = f_1\{ \phi_{SW}f_2 + \phi_W(1-f_2) \} +(1-f_1)\{ \phi_S f_2 + \phi_P(1-f_2)\} \quad (4.102)$$

Formulation of the Pressure-Work Term

This source term is dominant in the energy equation for a gas undergoing compression and its correct formulation is fundamental to the accurate calculation of gas temperature and heat transfer. The following relationship that connects the pressure and temperature changes to piston displacement, i.e.:

$$\frac{T^n}{T^o} = \left(\frac{p^n}{p^o}\right)^{\frac{\gamma-1}{\gamma}} = \left(\frac{V^o}{V^n}\right)^{\gamma-1} \quad (4.103)$$

for circumstances of isentropic flow , may be used as a basis for the assessment of alternative differencing schemes. The one-dimensional form of the energy equation 4.79 , with the exact solution for density, velocity and pressure inserted is used to test the numerical solution. The solution of this differential equation should have the following properties when solved with an initial condition of a uniform temperature field and adiabatic boundary conditions for the process of compression and expansion (BDC → TDC → BDC):

1. Reversibility (The temperature fields at the start of compression and the end of expansion should be identical).

2. Accuracy (the temperatures should be spatially uniform and near to those given by eqn. (4.103) throughout the cycle).

Before a proposal is made for a scheme that satisfies the above criteria, the shortcomings of expressing the terms on the RHS of equation 4.79 as simple central differences and the alternative scheme used by Watkins (1977) will be examined when used for a 'hybrid'-type grid as defined earlier in section 4.5.

When expressed in central finite-difference form, equation 4.79 is:

$$\frac{C_p}{\delta t}\{(\rho \ell_l T)_p^n - (\rho \ell_l T)_p^o\} + C_p\{(\rho \tilde{v}_l)_e^n T_E^n - (\rho \tilde{v}_l)_w^n T_W^n\}$$

$$= \ell_{l,p}^n \left\{\frac{(p)_p^n - (p)_p^o}{\delta t}\right\} - v_g(p_e^n - p_w^n) \qquad (4.104)$$

Substituting the exact solutions for v_l (and $\tilde{v}_l$), p and ρ from equations 4.81, 4.82 and 4.80 into 4.104 the result for the hybrid grid ($N_1 = 2$, $N_2 = 3$ and δt equivalent to 10^o crank-angle) is shown in fig. 4.26. This scheme fails miserably, being irreversible and totally inaccurate with large spatial temperature gradients and will be discarded henceforth.

Turning now to the scheme used by Watkins for a simple expanding/contracting grid (i.e., without a piston bowl), when expressed in finite-differences for the hybrid grid it is:

$$\frac{C_p}{\delta t}\{(\rho \ell_1 T)_p^n - (\rho \ell_1 T)_p^o\} + C_p\{(\rho \tilde{v}_1)_e^n T_E^n - (\rho \tilde{v}_1)_w^n T_W^n\}$$

$$= \frac{1}{\delta t}\{(\ell_1 p)_p^n - (\ell_1 p)_p^o\} - \{[v_g(\frac{p^n+p^o}{2})]_e - [v_g(\frac{p^n+p^o}{2})]_w\} \quad (4.105)$$

The condition of reversibility and accuracy can be examined by summing equation 4.105 over all control volumesin the field to give:

$$\frac{C_p}{\delta t}\{(\rho z_H T)^n - (\rho z_H T)^o\}$$

$$= \frac{1}{\delta t}\{(z_H p)^n - (z_H p)^o - (z_H^n - z_H^o)\ (\frac{p^n+p^o}{2})\} \quad (4.106)$$

Noting that continuity requires $(\rho z_H)^n = (\rho z_H)^o$ and $p = \rho RT$, the ratio of temperatures on successive time steps can be written as:

$$\frac{T^n}{T^o} = \frac{1 - (\frac{\gamma-1}{2\gamma})\ (1 + \frac{z_H^n}{z_H^o})}{1 - (\frac{\gamma-1}{2\gamma})(1 + \frac{z_H^o}{z_H^n})} = f(z_H^n,\ z_H^o) \quad (4.107)$$

Reversibility may be tested for by examining a situation where $z_H^o \to z_H^n \to z_H^o$ in which case it is required that $T^o \to T^n \to T^o$. This condition may be expressed as:

$$\frac{T^n}{T^o} \cdot \frac{T^o}{T^n} = f(z_H^n,\ z_H^o) \cdot f(z_H^o,\ z_H^n) = 1 \quad (4.108)$$

By interchanging T^n, T^o and z_H^n, z_H^o in equation 4.107 to give:

$$\frac{T^o}{T^n} = \frac{1 - (\frac{\gamma-1}{2\gamma})(1 + \frac{z_H^o}{z_H^n})}{1 - (\frac{\gamma-1}{2\gamma})(1 + \frac{z_H^n}{z_H^o})} = f(z_H^o,\ z_H^n) \quad (4.109)$$

it can easily be verified that the reversibility condition is satisfied.

The accuracy of the scheme can be examined by expressing the analytic solution and finite-difference approximation as power series and comparing coefficients. Replacing z_H^o/z_H^n by (1-b) where $b = (z_H^n - z_H^o)/z_H^n$ and $|b| << 1$, the power series expansion of the analytic expression (4.84) is:

$$\frac{T^n}{T^o} = \left(\frac{z_H^o}{z_H^n}\right)^{\gamma-1} = 1 + \sum_{n=1}^{\infty} \frac{b^n(-1)^n \sum_{m=0}^{n-1} (\gamma-1-m)}{n!} \qquad (4.110)$$

The Watkins formulation (4.106) arranged as a power series is:

$$\frac{T^n}{T^o} = 1 + \sum_{n=1}^{\infty} b^n \left\{1 - \gamma \sum_{m=1}^{n} \left(\frac{1-\gamma}{2}\right)^{m-1}\right\} \qquad (4.111)$$

Assuming a value $\gamma=1.4$, the first 3 coefficients of equations 4.110 and 4.111 are compared in table 4.1. The coefficients are identical up to b^2, thereafter differing, but with the value of b substantially less than unity and proportional to time step, the error is small in practice. Using the exact solutions for $\tilde{v}_1$, ρ and p the temperature solution for the Watkins scheme (4.105) when used with the hybrid gird is shown in fig. 4.27. The results are much better than those of equation (4.104) but there are spatial temperature gradients, the temperature being less than the analytic solution near the cylinder head and greater, by about 40^oK, at the piston, thus this scheme has also been rejected for the present application.

A scheme that does satisfy all of the foregoing criteria has been discovered by trial and error. It is possible in this instance to demonstrate that the scheme is reversible and produces small temperature errors, but the assessment of spatial uniformity

must again rely on a numerical test. The proposed formulation is:

$$\frac{C_p}{\delta t}\{(\rho\ell_1 T)_p^n - (\rho\ell_1 T)_p^o\} + C_p\{(\rho\tilde{v}_1)_e^n T_E^n - (\rho\tilde{v}_1)_w^n T_W^n\}$$

$$= \{\frac{p_p^n - p_p^o}{\delta t}\}\ \ell_{1,p}^o\ (\frac{\rho^o}{\rho^n})^{1/2} \qquad (4.112)$$

The condition of reversibility and accuracy can be examined, as in the case of the Watkins scheme, by summing equation (4.112) over all control volumes in the field to give:

$$\frac{C_p}{\delta t}\{(\rho z_H T)^n - (\rho z_H T)^o\} = \{\frac{p^n - p^o}{\delta t}\}\ z_H^o(\frac{\rho^o}{\rho^n})^{1/2} \qquad (4.113)$$

Replacing p by ρRT gives:

$$\frac{T^n}{T^o} = \frac{1 - (\frac{\gamma-1}{\gamma})(\frac{z_H^n}{z_H^o})^{1/2}}{1 - (\frac{\gamma-1}{\gamma})(\frac{z_H^o}{z_H^n})^{1/2}} \qquad (4.114)$$

Interchanging z_H^o, z_H^n and T^o, T^n it may be shown that the reversibility criterion(4.108) is satisfied. Replacing z_H^o/z_H^n by (1-b) equation (4.114) may be expressed as a power series (see appendix 3). This is:

$$\frac{T^n}{T^o} = 1 - \frac{\alpha b}{1-\alpha^2} + \sum_{n=1}^{\infty}(\frac{-\alpha^2}{1-\alpha^2})^n b^n\{1 - (\frac{\alpha}{1-\alpha^2})b\}$$

$$-(\frac{\alpha}{1-\alpha^2})\sum_{n=1}^{\infty} b^{n+1}\{\sum_{m=1}^{n}\frac{(\frac{1}{2})(\frac{3}{2})\cdots(\frac{1}{2}+m-1)}{m!}(\frac{-\alpha^2}{1-\alpha^2})^{n-m}\} \qquad (4.115)$$

where:

$$\alpha = \frac{\gamma-1}{\gamma} \qquad (4.116)$$

A comparison between the coefficients for this series in table 4.1 shows that this scheme is identical with the Watkins and analytic solutions up to b^2 and closer to the latter in b^3. The improvement over the Watkins scheme in overall accuracy is marginal but of more importance, there are no spatial temperature gradients, as shown by a numerical test with the same hybrid grid and time step as before. The maximum temperature error during the compression and expansion cycle was found to be .117%.

The same performance has been found for a two-dimensional test case with adiabatic boundary conditions and this scheme is therefore employed here.

4.7 The Dynamic Control of Stability and Convergence

It became apparent during the initial calculations of the flow in piston bowl geometries that stability of the numerical method could not be guaranteed near TDC of compression, which is a period of intense flow activity. In such cases, the residuals (equation 4.55) of the equations would either increase monotonically (diverge) or simply "wander" about some mean level with no obvious trend. Apart from the overall pressure adjustment scheme and the modifications for controlling the effect of the swirl source terms already described, the only means left to control stability and convergence is to use under-relaxation in the solution procedure. Under-relaxation is introduced into the iterative solution of the general difference equation 4.17 as follows:

$$A_P^n \phi_P^n = \sum_c A_c^n \{ f\phi_c^{n,i} + (1-f)\phi_c^{n,i-1} \} + \sum_c A_c^o \phi_c^o + S_\phi \qquad (4.117)$$

where the superscript i denotes the i'th iteration and f is an under-relaxation factor defined in the range $0 < f < 1$. After rearrangement, new coefficients for A_p, A_c^o and S_ϕ are given by:

$$A_p^n \rightarrow \frac{A_p^n}{f} \; , \; A_c^o \rightarrow \frac{A_c^o}{f} \qquad (4.118)$$

and $$S_\phi \rightarrow \frac{S_\phi}{f} + \left(\frac{1-f}{f}\right) \sum_c A_c^n \phi_c^{n,i-1}$$

It is common practice to specify different values of f for the various variables but to retain these same values for the duration of the calculations. This was found to be inadequate in the present circumstances as demonstrated later, so a new scheme was therefore devised with two objectives: firstly, to ensure that the iteration scheme remains stable at all times, and secondly, to maximise the convergence rate. These two requirements are usually conflicting and as it was considered that a slowly converging solution was better than one that diverged, the emphasis has been on stability. The optimum values for the under-relaxation factors differ according to the flow conditions. For example, it was found during single cycle calculations, where the piston was implusively started at BDC, compressing the gas until TDC, followed by expansion to BDC, that for the initial stages of the compression stroke and the latter part of the expansion stroke when the rates-of-change of the various flow properties is relatively low, high values of f (typically .5 to .7) could be used, resulting in high convergence rates. Conversely, near TDC, steep gradients and high rates-of-change (especially when swirl is present) requires low values of f(.1 to .3) to even maintain stability. These differing requirements cannot be met by fixed

values of under-relaxation factor, the penalties being either numerical instability or slow convergence depending upon the values chosen.

It was observed that high convergence rates could often be obtained with the under-relaxation factors set at a level at the limit of numerical stability. It was also found that once a solution had started to diverge, as signaled by an increase in the residuals of one or more of the equations, that convergence could be re-established by immediately reducing the under-relaxation factors. The most sensitive equations in this respect are those for the v_1 and v_2 velocities and the pressure field. The scheme described below for automatic adjustment of the under-relaxation factors incorporates these observations.

Designating residuals on successive iterations as R_ϕ^{i-2}, R_ϕ^{i-1} and R_ϕ^i where the subscript ϕ may stand for v_1 or v_2 and introducing under-relaxation factor adjustment parameters β_1, β_2 and β_3 with magnitudes slightly greater than unity, slightly less than unity and substantially less than unity respectively, the criteria employed for adjusting the f's are as follows:

1. Convergence - slight increase required to under-relaxation factors

$$\begin{aligned}
&\text{(a) If } R_{v_1}^{i-2} > R_{v_1}^{i-1} > R_{v_1}^{i} \quad : \quad f_{v_1} \to \beta_1 f_{v_1} \\
&\text{(b) If } R_{v_2}^{i-2} > R_{v_2}^{i-1} > R_{v_2}^{i} \quad : \quad f_{v_2} \to \beta_1 f_{v_2} \\
&\text{(c) If (a) or (b)} \quad : \quad f_{p'} \to \beta_1 f_{p'}
\end{aligned} \tag{4.119}$$

2. Stability limit - slight decrease required to under-relaxation factors

$$\begin{aligned}
&\text{(a) If } R_{v_1}^{i-2} > R_{v_1}^{i} < R_{v_1}^{i} \text{ or } R_{v_1}^{i-2} < R_{v_1}^{i-1} > R_{v_1}^{i} : \; f_{v_1} \to \beta_2 f_{v_1} \\
&\text{(b) If } R_{v_2}^{i-2} > R_{v_2}^{i-1} < R_{v_2}^{i} \text{ or } R_{v_2}^{i-2} < R_{v_2}^{i-1} > R_{v_2}^{i} : \; f_{v_2} \to \beta_2 f_{v_2}
\end{aligned} \tag{4.120}$$

3. Divergence - substantial decrease required to under-relaxation factors

$$\begin{aligned}
&\text{(a) } \underline{\text{If}} \quad R_{v_1}^{i-2} < R_{v_1}^{i-1} < R_{v_1}^{i} \quad : \quad f_{v_1} \rightarrow \beta_3 f_{v_1} \\
&\text{(b) } \underline{\text{If}} \quad R_{v_2}^{i-2} < R_{v_2}^{i-1} < R_{v_2}^{i} \quad : \quad f_{v_2} \rightarrow \beta_3 f_{v_2} \qquad (4.121) \\
&\text{(c) } \underline{\text{If}} \quad \text{(a) } \underline{\text{AND}} \text{ (b)} \quad : \quad f_{p'} \rightarrow \beta_3 f_{p'}
\end{aligned}$$

The values assigned to the various control parameters are:

$\beta_1 = 1.03, \qquad \beta_2 = .95, \qquad \beta_3 = .5$

f_{min} (minimum allowable value) = .1

f_{max} (maximum " ") = .7 (except for p' where $f_{max} = 1.$)

f_{ref} (starting value) = .5

The performance of the scheme may be assessed by reference to figs. 4.28 to 4.30 which show the variations of both the v_1 and v_2 residuals and, f_{v_1} and f_{v_2} at different stages during the computation of an engine cycle. This particular engine had a simple piston bowl (fig. 4.8b) and engine speed, compression ratio and initial BDC swirl ratio of 1400 rev/min, 14:1 and 7.3 respectively.

Near BDC, shown in fig. 4.28, convergence is rapid for both the v_1 and v_2 equations, so the scheme causes the under-relaxation factors to be increased and by 18 iterations the normalised residuals are of the order 10^{-4}. At approximately the mid-stroke position, fig. 4.29, differing performance of the residuals for the two variables is observed: thus,divergence of the v_1 equation commences at 7 iterations which causes the scheme to immediately reduce the value of f_{v_1} to f_{min}. Convergence is re-established by 12 iterations and apart

from a slight "hiccup" at 20 iterations, the calculation is thereafter otherwise convergent. A much more complex situation is shown in fig. 4.30, which is at 2^{o} BTDC and where physically, angular momentum is being convected into the piston bowl by the action of squish. The strong inter-relationship between the swirl velocity and the radial (v_2) momentum equation is a threat to stability, a fact mirrored by the performance of the latter equation. The f's, which start in this case at the value remaining from the previous time-step (if these values are less than the reference value, they are taken in preference) are increased initially, but at 30 iterations the residuals of the v_2 equation start to increase, bringing an immediate reaction from the scheme such that f_{v_2} is reduced to f_{min} (note the effect of the v_2 divergence on the v_1 residuals). The reduction in f_{v_2} restores convergence until at 48 iterations the residuals of both equations increase simultaneously, probably exacerbated by the now high value of f_{v_1}. All under-relaxation factors are here reduced (although not shown, $f_{p'}$ is also reduced to f_{min}) and convergence is eventually restored by 70 iterations, although at a slower rate than previously (indicated by the slope).

The improvement that the scheme offers over more conventional fixed under-relaxation factors is adequately described by fig. 4.31 which shows the variation of the number of iterations at each time-step to achieve a converged solution on the one hand with fixed values of $f_{v_1} = f_{v_2} = .3$ and $f_{v_1} = f_{v_2} = .5$ and on the other with the dynamic adjustment scheme described. The same convergence criteria have been used in each case. With $f_{v_1} = f_{v_2} = .3$, convergence is achieved throughout the cycle but the number of iterations to convergence at each time-step is consistently above the number for the dynamic adjustment scheme. With $f_{v_1} = f_{v_2} = .5$, the results are virtually identical with the dynamic adjustment scheme except for the period $\pm 10^{o}$ of TDC. Within

the period 7^{0} BTDC to TDC convergence of the solution with fixed under-relaxation factors could not be achieved within 200 iterations, and although not divergent, the solution showed no tendency to converge either. This test has been made with less stringent conditions than that used for the results of figs. 4.28 to 4.30 in that swirl was absent. If the previously described problem had been attempted with fixed under-relaxation factors, it is probable that divergence leading to numerical failure would have resulted.

4.8 Closure

In this chapter, the differential equations of chapter 3 have been approximated with finite-difference expressions and the solution method has been described.

The method of incorporating the boundary conditions into the solution procedure for both no-slip walls and inlet/exhaust apertures has been detailed. Variants of the basic grid to accommodate both moving and fixed valves have been presented.

Alternatives for both spatial and temporal differencing have been discussed with particular emphasis on the latter and different schemes have been examined within the framework of both one and two-dimensional problems. The accuracy and stability properties of each scheme have been quantified and recommendations have been made based upon the results of this work.

The differencing of certain source terms peculiar to the in-cylinder flow problem and the curvilinear orthogonal grid has been dealt with and appropriate recommendations have been made.

Finally, a novel scheme for controlling the convergence and stability of the numerical procedure has been described. This scheme, which adjusts the under-relaxation factors in a fashion determined by the immediate history of the solution, has been demonstrated to be superior to the more traditional fixed under-relaxation factor methods.

CHAPTER 5

VALIDATION OF THE PREDICTION METHOD

5.1 Introduction

In the previous chapter differencing schemes were devised which accorded reasonably well with analytical solutions for velocity, pressure and temperature for one-dimensional isentropic compression-expansion.

In the absence of further analytical solutions, validation of other features of the model must rely on comparison with experiment. This latter course is not without difficulty for a number of reasons: firstly, a vast amount of detailed information may be derived from the model but this is reflected in a requirement for an equally detailed specification of both initial and boundary conditions in the experiments; secondly, a validation test should ideally examine just one aspect of the model if there are not to be subsequent difficulties in pinpointing the source of any disparity between theory and experiment; thirdly, in spite of careful experimentation, there are always uncertainties in the experiments themselves, exemplified by the HWA calibration difficulties of Witze (1976c, 1979), described in chapter 2, and finally, evaluation of the actual modelling (as distinct from numerical approximation) is difficult if not impossible, as the results of sector 4.5 indicate that grid and time-step independent solutions are difficult to obtain using economical specifications of these parameters. The outlook for validation is not quite as bleak as suggested by these observations, but an appreciation of the afore-mentioned limitations is necessary in drawing realistic conclusions from the comparisons presented.

The measurements in axisymmetric engines of various kinds described in section 2.4 are used as a basis for evaluating the present method as described in subsequent sections. A detailed comparison of axial velocity, turbulence intensity and where appropriate, swirl velocity profiles for the non-compressing glass-cylinder engine of Morse et al (1978) is presented in section 5.2. Three cases are considered and these include the effects of the introduction of a piston bowl and swirl. In section 5.3, comparisons are made with the single-point HWA measurements of Witze (1976c, 1979) in a compressing engine with both flat and bowl-in-head configurations. Predictions of instantaneous heat flux at 4 radial positions on the cylinder head are compared with measurements of Dao et al (1973) in section 5.4. It will be recalled from chapter 2 that the engine in which these measurements were performed is not truly axisymmetric, having a single off-set valve used for both inlet and exhaust. However, the axisymmetric piston-bowl and quality of the experiments warrants inclusion in this chapter. Finally, in section 5.5, the simple theories of squish and swirl for bowl-in-piston chamber configurations due to Fitzgeorge and Allison (1963) are compared with calculations using the present method for an engine with a cylindrical piston bowl. The computer run times, computational time step and total number of grid cells used for each test case are given in table 5.1.

5.2 Cases (1) to (3) - Comparison with the Measurements of Morse et al

This section presents three sets of detailed comparisons with experiment for the non-compressing, axisymmetric, glass-cylinder engine fitted with a fixed, central valve, positioned flush with the cylinder-head such that the air enters and leaves via an annulus angled at 60^{o} to the latter. The arrangement is shown in fig. 2.18 and is described in section 2.4. The test cases cover the following configurations and conditions:

case 1 - Flat top piston without swirl (Morse et al, 1978)

case 2 - " " " with " (" " " ")

case 3 - Cylindrical cavity piston without swirl (Yianneskis,1977)

Details of the computations are given below.

Specification of Inlet Conditions

The mass flow rate is calculated according to the method described in section 4.4, although a subsequent analysis of the results has shown that at the engine speed of 200 rev/min the pressure drop across the valve orifice is negligibly small, and a specification based on the instantaneous piston displacement and the assumption of incompressible flow would probably be quite adequate, the differences between these alternative methods being at most about 3%. The equation (4.60) for the mass flow rate requires a value of discharge coefficient ; in the absence of a pressure drop-flow relationship for this port a typical value of .6 was assigned.

The greatest uncertainty lies in the specification of the axial and radial velocity components at the orifice plane. Examination of the experimental streamlines (figs. 2.19 and 2.20 for the no-swirl and swirl cases repectively) shows that early in the intake process at 36^{o} the flow leaving the orifice has a higher axial component than suggested by the inclination of the orifice passage whilst at 144^{o} the angle of the streamlines close to the valve indicates a higher radial component. The reason for this is probably that the short length of the annular passage (7 mm) is insufficient to cause the flow to align with its walls and the exit angle is therefore partly determined by the steep angle of the external valve surface. It is also apparent from figs. 2.19 and 2.20 that the inclination of the streamlines is strongly affected by the primary recirculation in the cylinder. It was not thought justified to include these effects into the predictions and the results presented here are based on a constant inlet angle of 60^{o}. A further uncertainty is the shape of the inlet velocity profile. In the calculations presented here, uniform profiles have been assumed for both axial and radial components, however recently available measurements of the former at a distance of 0.5 mm from the cylinder head (fig. 5.20) show this is not the case; more will be said of the effects of this disparity later.

It was observed in the measurements that, during intake, the turbulence downstream of the inlet annulus is considerably higher than that at the orifice itself, thus indicating that much of the turbulence is generated in the shear layers of the jet inside the cylinder; the inlet boundary conditions for turbulence energy and dissipation rate were therefore assigned small values of $10^{-5}\ m^2/s^2$ and $10^{-5}\ m^2/s^3$ respectively.

Other Computational Details

The large orifice area and slow rotational speed of the engine ensure nearly isothermal and isobaric operation and it is therefore not strictly necessary to solve the energy equation. For completeness, this equation was included, with the gas temperature at the valve and surface temperature (all surfaces) prescribed as $313^{o}K$ and $325^{o}K$ respectively. The ambient gas pressure was specified as 10^{5} N/m^{2}. In the cylinder, the initial gas temperature and pressure were assumed uniform and equal to the values at the valve.

The grids for the flat top and cylindrical bowl pistons have already been described in section 4.4 and are shown in fig. 4.3. For cases (1) and (3), the differential equation for the swirl was not solved.

Cyclic Dependence

The behaviour of the flow after "start-up" is governed by both the initial and boundary conditions. If the former differ greatly from the conditions that would otherwise prevail under cyclic operation and the effect of the boundary conditions on the flow is small, then the start-up transient will be longer than if the situation were reversed.

These calculations were started at TDC and predictions at this crank-angle position on subsequent cycles indicate that the velocities are small, so the assumption of zero initial velocities is reasonable. Subsequently, the flow structure is strongly governed by the intake jet and it would therefore be expected that cyclic operation would be reached quickly.

Fig. 5.1 shows, for case 1 at a position just downstream of the valve, the variation over 2½ cycles of the axial and radial velocity components, normalised by the mean piston speed. There are no perceptible differences between the maxima produced during induction on the 3 successive cycles shown and less than 1% difference between the minimum values of the radial velocity on cycles 1 and 2: hence it may be concluded that for calculations without swirl (cases 1 and 3), the second cycle adequately represents cyclic operation.

When the flow is swirling however, the rotation persists throughout the cycle with not insignificant levels of residual angular momentum carrying over to the start of intake on the next cycle. Thus, the effects of the initial conditions, which here include the specification of no swirl, persist for longer until the latter builds up to the appropriate level.

Fig. 5.2 shows 3 cycles of the variation of the normalised axial, radial and swirl velocities for the swirling flow of case 2. at the same position as before. The initial cycle-to-cycle differences in the maxima during intake in both axial and radial velocities are about 3%, the radial velocity minima during exhaust vary by 13% and an increase of about 15% in swirl velocity is observed between cycles 1 and 2. The progressive increase in swirl speed is illustrated more dramatically in fig. 5.3, which shows the variation of the same quantities at a position near the piston,

For the swirling flow calculations, it would seem that three cycles should be computed before it can be reasonably assumed that the solution is no longer dependent on the initial conditions.

Case 1 - Flat Top Piston Without Swirl

Fig. 5.4 shows the predicted velocity field in the form of velocity vectors* at 36^{o}, 90^{o}, 144^{o} and 270^{o}; the corresponding experimental streamlines are shown in fig. 2.19.

At 36^{o}, the overall flow structure is reasonably well predicted. Specifically, areas of agreement are: the existence and correct sense of rotation of recirculation zones centred at (a) and (b); the position of the centre of (b) and the location of the stagnation point (zero streamline in fig. 2.19) on the axis. Features not predicted so well are the position of the centre of vortex (a) and its axial extent, the discrepancies in the calculations apparently being caused by higher radial velocities immediately downstream of the inlet.

The experimental and predicted flow fields at the mid-stroke position (90^{o}) show slightly better agreement in that the length of vortex (a) is now about the same. The eddy centred at (b) is also well-predicted although at (c) the small recirculation zone observed in the measurements has not appeared in the predictions.

Agreement is better at 144^{o} at (c) although the measurements indicate a larger recirculation zone (examination of the numerical values of the predictions shows only small negative axial velocities adjacent to the wall at (c)). Other features of the flow, which include the vortices at (a) and (b) and the inclination of the vectors

*The velocities are plotted in the form of arrows indicating the direction, determined from the resultant of the axial and radial components, whilst their length is scaled linearly with the magnitude. The same scaling is used at each crank-angle and a reference vector is included to indicate the scaling factor. This format is retained throughout the remainder of this thesis.

In addition, regions of special interest in the flow field have been labelled (a), (b), (c) etc. in the figures for ease of reference in the text.

and streamlines throughout the field are generally in good agreement.

At the mid-stroke position during exhaust (270^{o}), with the exception of a weak predicted residual eddy at (a) which is not seen in the measurements, the sink-like appearance of the flow compares well.

Figs. 5.5 to 5.8 show comparisons for the same case between the axial mean ($\overline{v}_1$) and turbulent ($v_1^{**} = \overline{v_1'^2}^{1/2}$) velocity profiles, normalised by the mean piston speed, at a number of axial positions and the same crank-angles as previously. At 36^{o} (fig. 5.5) the axial velocity at z = 10 mm is in reasonable agreement with the measurements with co-incident radial positions of the peak at r = 24 mm although the value is under-predicted by about 25%. The peak negative value is 40% higher than that measured at r = 15 mm but is in better agreement nearer the axis. The peak turbulence intensity is 30% lower than the measurements and the predicted profile is much flatter.

At z = 20 mm, the predicted axial velocity shows a relatively flat profile for r > 22 mm and the negative velocities close to the wall (r > 30 mm) evidenced in the measurements are not predicted at all (hence the under-prediction of the length of the recirculation zone (a) in fig. 5.4.) The difference between the measured and predicted profiles suggests that the former retains a jet-like structure for a greater distance than the latter. The turbulence shows the calculated values to be about 50% of the measured ones at r = 23 mm although for r < 15 mm both mean and turbulent velocities are in better agreement. At z = 30 mm, the comparison is considerably better than nearer the cylinder head, probably because the flow close to the piston is influenced more by the piston motion than the inlet jet.

At 90^{o} (fig. 5.6), the peak inlet velocity at z = 10 mm is again under-predicted, in this instance by about 30%. Towards the axis (r <15 mm) agreement is good but at the outer radii (r > 33 mm) the measured negative axial velocities are not predicted at all. The turbulent velocity shows a flatter profile than the measurements, the latter reflecting the jet-like structure and steeper gradients of the mean velocity. At z = 20 mm the positions of the mean velocity peaks in both measurements and predictions have shifted radially outward by about 4 mm and the level of agreement is about the same as at z = 10 mm. The measured peak turbulence level close to the wall is not predicted at all and the differences are substantial for r > 17 mm. In view of the discrepancies at z = 10 mm and z = 20 mm the mean velocity agreement at z = 30 mm is surprisingly good, the peak values differing by about 15% with a similar level of agreement for r < 23 mm. The turbulence levels are again poorly predicted however, being only about 30% of the measured values. Bearing in mind the poor upstream correlation, this is not unexpected. The position of the peak mean velocity at z = 40 mm shows the predictions to have a higher axial component nearer the wall. This is again evidenced at z = 50 mm where a negative axial velocity is observed in the measurements, signalling the existence of the recirculation zone at (c) in fig. 5.4 that does not appear in the predictions until later in the cycle.

At 144^{o} (fig. 5.7) the z = 10 mm mean velocity profile shows the predicted position of the peak to be much nearer the wall than in the measurements and the negative axial velocities adjacent to the wall in the latter are not apparent although towards the axis (r <15 mm) agreement is better. The turbulence velocity peak at r = 24 mm is under-predicted by 50% but for r <20 mm, agreement is

better. The mean velocity profiles at z = 20 mm agree well: the peak is within 5% and for r < 20 mm, differences of the order 15% are observed. The two small turbulence peaks between r = 20 mm and the wall are not apparent in the predictions although agreement is virtually exact for r <20 mm. The z = 30 mm mean velocity profile does not correspond to that measured and although the position of zero axial velocity at r = 22 mm is co-incident, the errors in the positive and negative values either side are between 20% and 50%. The turbulence maxima for r > 20 mm are not predicted although at the inner radii agreement is better. At z = 40 mm errors in the peak mean velocity at r = 30 mm and at the axis are about 25%. The measured turbulence shows high values adjacent to the wall which are not apparent in the calculated profiles past z = 40 mm. At z = 50 mm, although there are differences in mean velocity at r = 18 mm, the peak at r = 28 mm and the centreline value agree well. The negative velocity adjacent to the wall at z = 60 mm and z = 70 mm is under-predicted, thus, the strength of the predicted recirculation at (c) in fig. 5.4 is weaker than that measured.

At the mid-stroke position (270^{o}) during exhaust (fig. 5.8) errors in the mean velocity peak of the z = 10 mm profile are about 25%, increasing to 50% at the axis. The flow is virtually one-dimensional and the level of agreement for both mean and turbulent velocities improves progressively nearer the piston.

Case 2 - Flat Top Piston With Swirl

This case differs from that previously described in that a differential equation for the swirl velocity is solved in addition to those for the remaining variables. The swirl boundary condition at the annulus was obtained by spatially discretising the profiles shown in fig. 5.14 measured at a distance of 0.5 mm from the cylinder head at 36^{o}, 90^{o} and 144^{o} crank-angles, to obtain values at the grid lines, and linearly interpolating in time. The swirl velocity at the valve was assumed to be zero at TDC, BDC and throughout the exhaust stroke. In this context, it should be noted that as the high velocities through the valve during exhaust invoke the upwind feature of the differencing scheme, the boundary conditions at the valve are effectively de-coupled from the solution in the cylinder.

Fig. 5.9 shows the predicted flow structure for comparison with the experimental streamlines of fig. 2.20. At 36^{o}, the eddies at (a) and (b) are similar to the predictions without swirl although there are differences near the piston at the region (d) where the large vortex centred at (b) is distorted by swirl. The axial length of recirculation zone (a) is in better agreement than the no-swirl case, although at (e), the weak vortex observed in the measurements is not apparent. At 90^{o}, the distortion of vortex (b) near the piston at (d) is well predicted although the weak but large measured eddy at (e) is hardly discernable in the calculations. At 144^{o}, the structure is similar although "stretched" and agreement is good apart from region (e). It is interesting that the absence of the weak recirculation observed at (c) in the no-swirl case is correctly predicted. The flow at 270^{o} is virtually one-dimensional except close to the valve and piston for both calculations and measurements.

A detailed comparison between the measured and predicted axial velocity and turbulence intensity profiles is presented in figs. 5.10 to 5.13. At 36^{o} (fig. 5.10), the general level of agreement is similar to the previous case. The velocity peak at z = 10 mm is under-estimated by 15% and the reverse flow observed in the measurements from r = 28 mm to the wall only extends from r = 32 mm in the predictions. At the centreline, a negative velocity is predicted instead of the small positive value measured as already indicated by under-prediction of the vortex length (e) in fig. 5.9. The calculated turbulence profile shows the now-characteristic flat appearance instead of the well defined peak of the measurements, the maximum of the former being about 60% of the latter. At z = 20 mm, the mean velocity agreement is quite good near the axis, although between r = 20 mm and the wall the predicted profile is smooth instead of the jet-like appearance of the measurements. The measured and calculated mean velocity profiles are of similar shape at z = 30 mm but from r = 20 mm to the axis, the latter has a steeper gradient such that the centreline velocity is negative instead of positive. The turbulence profiles here show good correlation.

At the mid-stroke position (fig. 5.11), agreement of the mean velocity at z = 10 mm is poor: the reverse flow adjacent to the wall is not predicted, the peak is under-estimated by some 30% and displaced radially outwards, whilst at the axis, a large negative velocity is predicted instead of a small positive value. The well-defined peak of the measured turbulence is replaced in the predictions by a smooth flat profile although two small maxima at r = 22 mm and r = 34 mm are evidenced in the latter. The predicted turbulence profiles at z = 3 mm show these maxima to be generated near the inlet and subsequently convected downstream although the measurements

here show only a single maximum. The calculated peak value here is only 20% below that measured. Two well defined maxima are also apparent in the measurements but much further downstream at z = 20 mm and their positions correspond to the shear layers on either side of the point of maximum velocity. It would seem that the predicted jet has expanded much more rapidly than the measurements indicate. The mean velocity profile at z = 30 mm is in better agreement than at z = 10 mm or z = 20 mm although the peak is still under-predicted by some 20%. The small measured positive velocity at the centreline indicates that the experimentally observed recirculation zone extends at least 30 mm from the cylinder head whereas the predicted length is less than 10 mm. At z = 40 mm and z = 50 mm agreement of the mean velocity is good with the exception of the centreline value at the latter position. It is no surprise that the turbulence levels at the outer radii (r >15 mm) are under-predicted in view of the poor upstream correspondence.

At 144^{o} (fig. 5.12), the mean velocity is in poor agreement with the measurements: the substantial reverse flow of the latter adjacent to the wall is not predicted, the peak jet velocity is only 40% of that measured and displaced radially outwards by 10 mm whilst the centreline value is twice the magnitude and of opposite sign. The turbulence shows a similarly poor correlation although the profiles at z = 3 mm suggest that sufficient turbulence is generated near the valve (the peak is under-estimated by about 20%) but is subsequently either dissipated too rapidly or diffused radially at a greater rate than occurs in the measurements. It appears that the predictions have a higher radial velocity than in the experiments; this is not however due to the swirl as the same trend was in evidence in the no-swirl calculations. Further downstream, the agree-

ment improves and from z = 50 mm to z = 80 mm the comparison is quite good with the exception of the centreline velocity near the piston. The turbulence shows reasonable correlation for r < 15 mm and z > 40 mm but agreement is poor at the outer radii where the measurements still show the influence of the intake jet.

Agreement at 270^{o} (fig. 5.13) is worse than the no-swirl case, with substantially over-estimated velocities for r < 15 mm from z = 20 mm to z = 50 mm. At z = 3 mm, where the influence of the valve is strongly felt, the peak mean velocity is over-estimated by 20% but the turbulence is too high by a factor of 4.

Fig. 5.14 shows a comparison between the measured and predicted swirl velocity profiles. The 36^{o} profiles compare favourable with the measurements with errors generally much less than 20%, with the exception of the region between r = 25 mm and the wall at z = 10 mm. At 90^{o}, the effects of the large intake-induced recirculation centered at (b) (fig. 5.9) can clearly be seen in that angular momentum is transported radially inwards to region (d) and the subsequent "spin-up" effect results in peak swirl velocities close to the centreline. Although there are areas of disagreement, notably at z = 10 mm and z = 50 mm the trends are otherwise well predicted. The calculated profiles at z = 30 mm and z = 50 mm show a greater decay of swirl velocity from r = 25 mm to the wall than is measured although this is probably due to the poorly-predicted intake jet. The 144^{o} profiles show better agreement close to the wall but the measurements for r < 15 mm at z = 20 mm and z = 30 mm are only about 50% of those in the calculations. It will be recalled that the predicted axial velocity was in poor agreement in this region, and the high negative values calculated probably account for the increased transport of angular momentum with the associated higher

swirl velocities. Near the centreline ($r < 10$ mm) for $z > 50$ mm the measurements show steeper gradients than the calculations. At 270^{o}, agreement is good for all profiles.

Case 3 - Cylindrical Piston Bowl Without Swirl

A set of measurements obtained by Yianneskis (1977), not described in chapter 2, are available for a simple cylindrical piston bowl inserted in the same configuration as Cases 1 and 2, without swirl. The dimensions of the bowl are shown in fig. 2.18 and the geometry and operating conditions are otherwise identical to case 1.

Experimental streamlines are not available for this case and the predicted velocity field, shown in fig. 5.15, may be compared with the no-bowl calculations of fig. 5.4. At all crank-angles, the influence of the bowl on the overall flow pattern is seen to be negligible, which is not surprising in view of the absence of compression and the high piston-cylinder-head TDC clearance. The only observation that can be added to the description of case 1 is that the flow within the bowl is relatively unaffected by intake and remains one-dimensional throughout the cycle although as will be seen below, quantitative agreement is not as good as case 1.

A detailed comparison of the axial velocity and turbulence intensity profiles for this case is shown in figs. 5.16 to 5.19. Agreement of the mean velocity is worse than the no-bowl case at 36^{o}: at $z = 10$ mm, the predicted peak value of the intake jet is only 50% of that measured and the reverse flow extending from $r = 29$ mm to the wall is not predicted. The comparison is better

near the axis but further downstream at z = 20 mm, whilst the measurements have retained their jet-like appearance, the calculations show a flat profile with no sign of either the peak at r = 24 mm or the negative axial velocities between the centreline and r = 17 mm. The turbulence maximum is under-predicted by 40% at z = 10 mm although on both sides of the jet, agreement is much better. However, the predicted turbulence decays more rapidly than is indicated by the measurements, a trend also apparent in the previous predictions, such that at z = 20 mm, the predicted turbulence level is only 20% of that measured. In the bowl, the mean velocity shows neither axial nor radial variations (with the exception of the gradients at the surface) and the absence of any appreciable stresses near the centre is reflected in low turbulence levels there. Agreement of both mean and turbulent velocities is good at the entrance of the bowl but towards the bottom, calculated values of the latter are only about 30% of the measurements.

At 90^{o} (fig. 5.17), agreement of the shape of the mean velocity profile is reasonable at z = 10 mm although the peaks of both quantities are under-estimated, in the case of the turbulence, by 50%. Further downstream, the correlation deteriorates: at z = 30 mm for example, the peak predicted velocity is only 35% of that measured and the position of the latter is about 5 mm closer to the wall. The position of zero axial velocity is displaced by a similar amount to the peak value and the magnitude of the reverse flow at the centreline is half that of the measurements. The turbulence is also under-predicted and shows a flat profile instead of the double maxima of the measurements. At z = 50 mm and z = 55 mm, the mean velocity agrees better, probably because this region of the flow is influenced more strongly by the piston motion than the intake jet, although it is still under-predicted, as is the turbulence. In the

bowl, agreement is quite good for both quantities, with the essentially one-dimensional velocity profile as earlier in the cycle and low turbulence levels.

At 144^{o} (fig. 5.18) the same comments apply as at 90^{o}. During exhaust (fig. 5.19), agreement is better than induction with errors in the mean and turbulent velocities up to 25% and 50% respectively.

Assessment of Cases 1, 2 and 3

Errors in the predictions may originate from any of three major sources; namely, specification of the valve boundary conditions, numerical errors and inadequacies of the turbulence model although it is extremely difficult to isolate the relative influence of each because of the complexity of the flow and cost limitations on grid refinement. Further, it has been assumed up to now that the measurements are without errors; this is not the case and more will be said of this later.

There are assumed features of the mean flow boundary conditions at the valve which are know to be incorrect: firstly, the assumption of a uniform profile, and secondly, the specification of a constant estimated exit flow angle. Measurements of axial velocity at $z = .5$ mm for case 1, shown in fig. 5.20, indicate a maximum value at approximately the mid-point of the valve. The variation over the orifice is not insubstantial although it is unlikely that profile specification errors are as important as the flow direction. Unfortunately measurements of the radial velocity component are not available and

therefore the behaviour of the inlet angle during intake must remain an unknown. Attempts to estimate the angle from the measured downstream flow can be misleading as the effects of the primary recirculation in the cylinder on the jet are strong.

The grid dependence tests for a closed cylinder and cylindrical piston bowl geometry described in section 4.5 showed that fine grids and small time-steps enhance the maxima and minima in both mean and turbulent velocities, or conversely, coarse grids and long time-steps have a smoothing effect. It was also mentioned in section 4.5, in the context of differencing schemes, that false-diffusion errors are worst when the mean flow direction is oriented at an angle of 45^{o} to the grid. It would seem that for the entire intake period, these particular experiments and predictions have all the ingredients for maximising these numerical errors in the important inlet region: the flow is jet-like with a well defined peak and steep velocity gradients, and oriented at about $45^{o} \pm 20^{o}$ to the grid, which in turn, is too coarse to adequately resolve a flow of this nature. A trend observed in all cases is that the predicted velocity decay of the jet is too rapid and the initially well defined peak soon deteriorates into a flatter profile; this is in keeping with the nature of the numerical errors. The turbulence, in general, is under-predicted and unlikely to account for the higher calculated spreading rate.

It is improbable that the low values of turbulence boundary conditions specified at the inlet are the cause of the poor agreement of the turbulence profiles as the measured axial turbulence intensity at z = .5 mm (fig. 5.20) is much lower than the levels

found further downstream, indicating that most of the turbulence is generated in the shear layers of the jet. Also, the z = 3 mm profiles of figs. 5.11 and 5.12 show that nearly adequate turbulence levels are generated close to the valve in the predictions but the subsequent dissipation and/or diffusion is too rapid. The numerical errors already described apply equally to the turbulence, but here, there are further uncertainties in the calculation of both the convective transport and production of turbulence because of the numerical smearing of the mean velocity.

Turning now to the experiments, there are two factors that serve to increase the measured turbulence levels above their true values. The first is cycle-to-cycle variations, the effect of which was discussed earlier in section 3.6. The measurements of Lancaster (1976), described in section 2.2, showed that for a cylindrical disc chamber geometry, the "turbulence" may be augmented by up to 35% due to cyclic variations in the flow. Unfortunately without a continuous signal (as is obtained with HWA) it is impossible to estimate the magnitude of this effect and it can only be stated that cyclic variations will invariably be present in these data and the true turbulence will be less than that measured, but by how much is not known.

The other source of error is introduced not by the measurements but by the subsequent processing and results from the use of a finite-sized crank-angle window over which the measurements are averaged. Unlike cycle-to-cycle variations, the magnitude of this effect is more easily determined by simply processing the same data with different size windows. Morse et al (1978) state that the differences in mean and turbulent velocities using 1^0 and 10^0 windows

(10^{0} was used for all measurements in the cases examined here) were of the order 3% and 15% respectively. However, these differences are only found near the axis and the jet edge where, at certain parts of the cycle, the variation of mean velocity and count rate are large. Typically, the turbulence errors would be lower (Morse et al (1978) have estimated 10%).

One final point not so far mentioned is the deviation from isotropy of the turbulence. An assumption invoked in the development of the turbulence model is that the axial, radial and swirl fluctuating components are equal, but a limited number of measurements of all three components (Morse et al, 1978) indicate that this is not the case in practice. Typically, at the mid-stroke position, the maxima of the radial and swirl components at z = 10 mm for case 2 gave values of 75% and 60% of the axial component. If these measurements were averaged to produce a single value of the turbulent velocity (and strictly speaking, this is the quantity that should be compared with the calculated turbulent velocity), this would be about 80% of the axial component and agreement with the predictions would be correspondingly better.

In summary, the major features of a very complicated flow structure are reasonably well predicted although a detailed quantitative comparison has revealed errors in the intake jet which subsequently affect the rest of the flow. A number of factors have been identified as sources of error, some of which are beyond the control of both experimentalist and theoretician, such as cyclic variations; but others, namely, grid dependence and crank-angle broadening are correctable.

5.3 Cases (4) and (5) - Comparison with the Data of Witze

The section describes a comparison between the flow calculations and single point mean and turbulent velocity data derived from HWA measurements in the single valve, axisymmetric engine configuration of Witze (1976c), described in section 2.4. Calculations have been performed for both flat and cylindrical-bowl cylinder heads although it will be recalled that the HWA signal processing method used for the latter is likely to be incorrect (see fig. 2.16 for a comparison between the original and amended data for the flat cylinder head geometry). This is unfortunate as it makes a comparison during the compression period questionable for this case, but does nevertheless allow a reasonable assessment to be made during the intake and exhaust phases.

Fig. 4.4 and 4.5 show the computational grids used for both cases. In order to improve the resolution of the intake jet near the valve, grid lines have been concentrated in the cylinder head with additional moving grid lines introduced between the cylinder-head and valve when the latter is open, in the manner described in section 4.4. The valve lift is specified according to fig. 5.21, taken from Witze (1976c).

The specification of the inlet flow angle presents the same problems as cases (1) to (3) but in this exercise, there was no guiding information in the form of detailed measurements, and in the absence of any feasible alternative, the air was assumed to enter at the valve seat-angle of 45^{o}. Similarly, no pressure-drop~flow data was available for the valve/port assembly and the effective area, required for the calculation of the mass flow rate, was calculated as the product of the time-varying geometric area extending from the periphery of the valve to the valve seat and an assumed constant discharge coefficient of .6.

The ambient pressure and temperature were specified as 10^5 N/m^2 and 310^{o}K whilst the cylinder head, wall and piston temperatures were assigned the values 400^{o}K, 350^{o}K and 325^{o}K. The measurements for case 1 indicated that much of the turbulence is generated inside the cylinder and the values of turbulence energy and dissipation rate at inlet were therefore assigned small values of 10^{-5} m^2/s^2 and 10^{-5} m^2/s^3 respectively. For both the geometry variants the engine speed is 1500 rev/min.

Calculations were started at TDC with the valve open and a uniform pressure and temperature equal to the ambient values. Both axial and radial velocity components, the turbulence energy and dissipation rate were initially set to zero.

Case 4 - Compression of 4-Stroke Engine with Flat Cylinder Head

Figs. 5.22 and 5.23 show respectively the velocity and turbulence fields at crank-angles of 60^o, 120^o, 180^o, 360^o, 540^o and 630^o (0^o and 360^o correspond to TDC during valve-overlap and TDC of compression). The velocity fields are plotted in the same format as before whilst the turbulence is presented as contours of iso-turbulence intensity (= $\sqrt{2/3k}/\bar{v}_H$, where $\bar{v}_H$ is the mean piston speed).

At 60^o, the intake jet generates two toroidal vortices of considerable strength, and in many respects, quite similar to the structure in the non-compressing engine. High levels of turbulence are produced at the valve and where the jet impinges at the wall and this turbulence is subsequently transported downstream into

the main eddy in the cylinder. The eddy adjacent to the cylinder head remains essentially unchanged in shape throughout intake although its centre shows a progressive tendency to move nearer the cylinder head as the piston approaches BDC; the primary recirculation grows to fill the cylinder. The turbulence levels at the valve decay during the latter stages of intake until at BDC (180^{o}), the maximum is found in the centre of the cylinder. Both mean and turbulent velocities decay during compression until at TDC (360^{o}), only very weak residual recirculation is observed in the clearance space with low turbulence levels. During expansion, the motion decays still further until EVO (470^{o}) at which time air enters the cylinder as pressure in the latter has fallen below the ambient value. The inflow is such that by BDC (540^{o}) both a definite flow structure and reasonably high turbulence levels are evident. It is interesting that the structure of the mean flow is quite different from that produced during the intake stroke. This is probably because the velocities are substantially lower and the weak jet is entrained by its own recirculation zone such that it follows a path into the cylinder-head ~ wall corner and then along the wall. This structure breaks down soon after BDC by explusion of the gas through the valve by the piston, resulting in a flow of sink-like appearance for the entire exhaust stroke, of which the structure at 630^{o} is typical. Substantial turbulence is again generated at the valve but the effects are localised.

A comparison between the measured and calculated mean* and turbulent velocities at the position marked 'X' in fig. 2.15 is shown in fig. 5.24. Also shown are the mean velocities at positions

*Defined as the absolute value of the resultant of the axial and radial velocity components.

displaced 1.27 mm (.05 in) of the nominal probe position in both the axial and radial directions; this is included to give an indication of the errors that would be introduced by a mis-positioned probe or an incorrect inlet flow-angle specification. During intake, the measurements and predictions are in reasonable agreement, with the exception of the initial stages where the latter show a steeper rise and a local maximum at about 60^{o}. Judging by the calculated velocities at the surrounding positions, the probe is positioned in a region of extremely high shear and it must be regarded as fortuitious that the measured and predicted peaks agree to within 5% as even a slight deviation from the 45^{o} inlet flow angle or a mis-positioned probe would have produced very different results. The turbulence peak is under-predicted by about 30% although the trend is otherwise very similar. Both measured and predicted mean velocities show a slight rise during the early stages of compression but subsequently decay until exhaust valve opens. The measured turbulence level shows a similar trend to the mean velocity but the calculated values decay continuously after the intake maximum. Near BDC, the calculated mean velocity shows a small initial peak from the gas inflow followed by a much larger peak at the mid-stroke position as the gas is expelled by the piston. For some reason, the measured peak occurs just after BDC with a subsequent decay until TDC. The measured turbulence shows a similar peak but the calculations retain a relatively constant level during this phase.

Case 5 - Compressing 4-Stroke Engine with Bowl-in-Head

Figs. 5.25 and 5.26 show the velocity and turbulence fields at various crank-angles through the cycle. At 60^{o}, the structure near the valve is very similar to that found in the flat cylinder-head geometry with vortices (a) and (b) on either side of the intake jet. Impingement of the jet occurs on the side face of the cylinder-head, causing further impingement on the piston, which eventually results in a strong eddy in the outer clearance space (c). As in Case 4, the intake process generates high turbulence which is convected into this eddy. At 90^{o}, the eddy (c) has extended with the piston motion whilst (b) is distorted by the inward radial growth of the former such that at 120^{o} a further weak vortex (d) is formed just above the piston near the axis. Production of turbulence at the valve remains high during this period. By BDC, intake has finished and the residual flow pattern, although similar to that earlier, is much weaker and turbulence in the cylinder has decayed. At 210^{o}, outflow through the valve is observed just before the valve closes and there is a further decay of both mean and turbulent velocities which continues throughout compression until at TDC there is little air movement within the bowl and a turbulence intensity maximum of .5. The high bowl-to-cylinder diameter ratio of .67 results in negligible squish effects (Fitzgeorge and Allison, 1963). At the mid-stroke position during expansion (450^{o}) the flow is virtually one-dimensional until the valve opens such that at 510^{o}, an initial inflow directed radially outward across the face of the cylinder head again creates high turbulence at the valve entrance. By BDC (540^{o}) the inflow has created a structure identical to that found during induction

with the associated turbulence convected into the cylinder. As the piston moves towards TDC, so the gas is expelled and a flow of sink-like appearance is formed at the valve with high localised turbulence, comparable in magnitude to that of intake. At TDC (720^{o}) a weak eddy is observed in the bowl and the turbulence levels are low.

A comparison between the single point mean and turbulent velocity measurements is shown in fig. 5.27. During intake the predicted mean velocity is 30% higher than that measured, although it should be remembered that this experimental data is uncorrected and the revised results for the flat cylinder-head case resulted in a 10 m/s increase in the peak value (see fig. 2.16). In contrast, the turbulence maximum is under-predicted by 30%. The behaviour of the predictions just after BDC is probably caused by the change in flow structure resulting from the outflow just before valve closing. The compression period should be ignored in view of uncertainties about the data.

In view of the complexity of the exhaust phase flow structure, with an initial inflow directed radially across the face of the cylinder head (510^{o}), followed by a flow of intake-like appearance with two eddies (540^{o}) and eventually outflow (630^{o}), the variations in both the mean and turbulent velocities are in reasonable agreement. The magnitude of the mean velocity just before BDC (540^{o}) is under-predicted as is the peak during gas explusion at approximately 650^{o}, but the phasing is essentially correct for both quantities. The reason for the discontinuity in the measured turbulence at 430^{o} is not known as the valve has not yet opened and there are no obvious reasons why the flow should be disturbed.

Assessment of cases 4 and 5

The probable sources of error identified for cases (1) to (3) will also apply to this engine. An effort has been made to reduce the numerical errors in these calculations however by using a high concentration of grid lines in the cylinder head to resolve the intake flow. Resolution elsewhere in the field suffers as a consequence (see, for example, 180^{o} in fig. 5.24 where the vector plot shows poor definition in the cylinder) but as the influence of the primary eddy in the cylinder on the velocities at the measuring position is probably small compared with the intake jet, this is of secondary importance.

Unlike the non-compressing engine, the accurate calculation of the pressure and temperature are important here, as the difference between the cylinder and ambient pressure determines the mass inflow or outflow and hence the velocity boundary conditions at the valve. Although pressure measurements through the cycle are not available, it is likely that pressures are calculated reasonably correctly as the maximum values at TDC are within 7% of those quoted by Witze (1976c) for both configurations.

The generally good agreement between the measured and predicted flow structures for cases (1) to (3) suggests that these flow patterns may also be correct. Bearing in mind the complexity of the flow structure, in one case with no less than four co-existing toroidal vortices, the overall agreement is good. However, without measurements elsewhere in the cylinder it is impossible to judge whether such agreement would be universal or is confined to the measuring position.

5.4 Case(6)- Comparison with the Data of Dao et al

This section describes a comparison between the measurements of Dao et al (1973), described in section 2.4, and predictions of the instantaneous heat flux at 4 locations on the cylinder head of a motored engine with a simple cylindrical piston bowl. The engine dimensions and measuring positions are shown in fig.2.21 and the computational grid in fig. 5.28. The calculations were started at BDC with an imposed solid body swirl structure equivalent to a swirl ratio (SR) of 7.3, estimated from an equation taken from the reference cited, that is:

$$SR = a\left(\frac{N}{30}\right)^{b-1}\left(\frac{CR-1}{CR}\right)$$

where a and b are constants that depend on the shroud angle of a masked valve and assigned the values 4.89 and 1.14 for the 90^{o} shroud used, N is the engine speed (900 rev/min) and CR is the compression ratio (14:1). The axial and radial velocity components,and the turbulence energy and dissipation rate were assumed to be zero at BDC. This is obviously not the case and the sole justification for this practice is that in the absence of any better information, the early inlet valve closing at 35^{o} ABDC will allow sufficient time before TDC for the decay of the intake generated structure to levels much lower than those produced by subsequent squish effects. This decay process during the early stages of compression has been confirmed experimentally by a number of investigators, described in section 2.2, and was also observed in the bowl-in-head computations of case 5, although squish effects were negligible in the latter case. The gas temperature and pressure at BDC were assumed uniform and assigned the values $311^{o}K$ and 1.2×10^{5} N/m^{2}. The piston and cylinder-wall temperatures were assumed constant through the calculation and assigned typical

values of $320^{o}K$ and $333^{o}K$. The instantaneous cylinder-head temperature was measured however, and this was approximated in the calculation by specifying a time-varying sinusoidal variation between the limits $328^{o}K$ and $356^{o}K$ at BDC and TDC respectively. These surface temperatures cannot be too far in error as the predicted maximum cylinder pressure was subsequently calculated as 37.1×10^{5} N/m^{2} whilst the measurements varied between 35.5×10^{5} N/m^{2} and 37.5×10^{5} N/m^{2}.

Before discussing the heat flux predictions, it is instructive to examine the calculations of the flow field near TDC. Fig. 5.29 shows the predicted flow structure at a number of crank angles between 30^{o} BTDC to 30^{o} ATDC; these are plotted in the form of velocity vectors and contours of iso-swirl velocity and turbulence intensity (the latter is normalised by the mean piston speed as usual) with the iso-values equally spaced. At 30^{o} BTDC, the velocity vector field shows the start of squish effects and the gas displaced from between the clearance space passes along the side face of the piston bowl. This contrasts with calculations without swirl or with low swirl levels where a dominant toroidal vortex is formed within the bowl (see appendix 4). The swirl iso-values show an essentially solid-body rotation in the bowl. Considerable turbulence is generated between the piston top and cylinder head by the squish and the shear stresses associated with gradients of swirl velocity; high levels are also found in the bowl, in this case augmented by the transport of turbulence from the squish region.

The structure at 15^{o} BTDC shows an increase in the squish velocities and localisation of the maximum swirl velocity near the lip of the piston. This latter phenomena results from convection of angular momentum radially inwards by the squish motion from the

outer radii with the associated "spin-up" effect. The turbulence shows maxima at the lip and in the centre of the bowl and the structure suggests that the high levels in the latter result primarily from convection of the turbulence produced in the clearance space, although examination of the turbulence structures at 6^{o} BTDC and TDC, when convective transport by the squish is small, revealsincreased maximum values. One must therefore conclude that at this stage most of the bowl turbulence is produced in the bowl itself, probably from shear stresses associated with the swirl as the axial and radial velocities are low. The 6^{o} BTDC structure is otherwise very similar to that at 15^{o} BTDC with negligible axial and radial velocities towards the centre of the bowl and a swirl maximum near the lip. The effect of the squish flow along the piston side-face on the convective transport of swirl momentum can be seen at TDC, where the maximum swirl velocity contour extends almost to the bottom of the bowl.

At 6^{o} ATDC, reverse-squish flow into the clearance space can be seen. The swirl and turbulence structures are much the same as those at TDC although with a slight decay in the levels of both. At 12^{o} ATDC the reverse squish flow is observed to break away near the lip and impinge on the cylinder head with a corresponding increase in the turbulence in this region. At 15^{o} ATDC and 18^{o} ATDC the picture is similar, with a small reverse-squish induced vortex at the lip and extremely high localised turbulence adjacent to the cylinder head. The nearly equal spacing of the swirl iso-vels and the absence of any appreciable axial variation indicates solid body rotation within the bowl. At 24^{o} ATDC, the formation of a second eddy in the clearance space results from the deflection of the reverse squish flow by impingement on the cylinder head. The turbulence levels have decayed slightly, whilst the swirl shows much the same structure as

before although the transport of swirl momentum into the clearance space has reduced the velocities in the bowl.

A comparison between the measured and calculated heat fluxes at the 4 radial positions on the cylinder-head is shown in fig. 5.30 for the period 60^{o} BTDC to 60^{o} ATDC. At the innermost radius (r = .37 ins) the peak value is predicted well but the experimental trace shows two features not in evidence in the calculations: firstly, an initial maximum occurs around 10^{o} BTDC such that there is a phase difference between the predictions and measurements (this is not an error in plotting as the experimental trace was carefully reproduced from Dao (1972)) and secondly, two peaks exist. The reason for this behaviour of the experimental trace is unclear, as the effects of squish and reverse squish are not felt this close to the centre-line although three-dimensional effects, such as circumferential variations in the swirl velocity cannot be ruled out.

At the two radii near the piston lip (r = .75 ins and r = .88 ins) the increased heat transfer rates are accurately predicted, although at r = .88 ins the value is over-estimated slightly. This increase results from the high turbulence levels adjacent to the surface both before and after TDC. Both measurements show the existence of two spikes near TDC and Dao et al (1973) have attributed these to squish and reverse squish. This is probably correct and although the predictions do not have the same spiky appearance, a slight discontinuity is observed at about 15^{o} ATDC which corresponds to the occurrence of high, reverse-squish induced, turbulence levels adjacent to the cylinder head.

At r = 1.3 ins, agreement is excellent although the spike observed in the measurements at approximately 20^{o} ATDC, probably due to reverse squish effects reaching the outer radii, is not predicted.

Assessment of Case 6

Apart from the minor discrepancies already mentioned, these predictions compare favourably with the experiments. The heat transfer is a sensitive indicator of the accuracy of most of the flow properties, as its evaluation depends on the gas temperature and heat transfer coefficient, the latter quantity being derived from the local turbulence levels, which in turn are strongly dependent upon the velocity field.

There are however uncertainties arising from both the initial conditions and the flow structure produced by the off-set valve. For the former, the assumption of zero turbulence and the axial and radial velocity components at BDC are unrealistic, but it is unlikely that this introduces any significant errors because of the decay process during compression and the strength of the squish-induced motions, as already indicated. However, a recent analysis of intake generated swirl structures by the author, not reported in this thesis, seems to indicate that, in contrast with the turbulence and axial and radial velocities, whatever swirl structure is produced during induction remains relatively intact during compression. Thus, if the structure produced by the valve is strongly three-dimensional and the assumption of a solid-body swirl rotation is wrong, the effects would persist until TDC, although in the absence of any velocity measurements it is impossible to quantify any such errors.

Nevertheless, there are two factors that contribute to these calculations conforming with the limits of both the modelling and the numerical method. Firstly, the flow in the clearance space around TDC is nearly one-dimensional and it will be recalled from chapters 3 and 4 that the boundary conditions are based upon a one-dimensional analysis of the near-wall region. Secondly, the relative simplicity of the flow and the high number of grid lines packed into the clearance space possibly result in a grid independent solution (although it should be stated that grid dependence tests have not specifically examined this aspect). If these observations are correct, then it is reasonable to assume that under ideal conditions, the heat-transfer model is capable of accurately calculating the surface heat transfer. Conditions elsewhere, for example in the bowl, are not as ideal as in the clearance space, and it should not be assumed that agreement here would be as good.

5.5 Comparison with the Simple Theories of Squish and Swirl

Comparisons are here made with the simple theories of squish and swirl due to Fitzgeorge and Allison (1963), described in section 2.3 Although not a true validation test in the sense that these theories represent only a simplified picture of the in-cylinder processes, there is some evidence, (for example, Dent and Derham, 1974), that reasonable agreement with experiment can sometimes be obtained with them. The details and results of these comparisons were published by Gosman and Johns (1978a) and reference is made to appendix 4 which includes a copy of this paper. The main findings of this exercise are given below:

1. Agreement with the simple theory of squish is good, and the assumptions of one-dimensional flow, negligible influence of heat transfer and essentially uniform pressure and density fields throughout the cylinder are confirmed as being correct.
2. A reverse squish phenomena, not mentioned by Fitzgeorge and Allison, that creates a strong recirculation in the clearance space after TDC is observed (see fig.3 in appendix 4). Experimental evidence of this has been reported by Woods and Ghirlando (1975) and Dicksee (1940).
3. The finite-difference calculations do not agree with the closed-cycle part of the Fitzgeorge and Allison swirl analysis. The assumption used by the latter authors, and others,that an initial solid-body rotation persists through the compression period is reasonable (evidenced in the iso-swirl velocity contours of case (6)) but the decay of swirl momentum between BDC and TDC is found to be high, at least for high swirl rates (5 ~ 10); typically, the angular momentum at TDC is between .5 and .7 of the initial value at BDC. Modifications to the basic theory by Dent and Derham (1974) and Davies and Kent (1979) to account for surface friction using empirical formulae for turbulent flow over flat plates should be used if these losses are to be accounted for.

5.6 Closure

In this chapter, comparisons have been made between calculations using the theoretical model described in chapters 3 and 4 and experimental data for a number of engine configurations. The experimental data were chosen not for their diversity, as might at first seem the case, but because they represent the only available data in axisymmetric engines (at the time of writing) of adequate quality and approaching somewhere near the desired level of specification of geometry, boundary conditions etc.

There are a number of lessons to be learnt from this validation exercise:

(1) The existing theoretical model and numerical solution method is capable of producing predictions for very complicated flows in a variety of engines. These show good qualitative agreement with the measurements and under favourable conditions, reasonable quantitative agreement.

(2) The greatest area of uncertainty in the modelling is the turbulence although implementation of the existing model to give solutions free from numerical errors has not yet proved possible. Judging by the measurements of the three velocity components of case 2, the isotropy assumption employed in the derivation of the turbulence energy equation appears to be incorrect.

(3) This exercise has highlighted areas where further work is needed, namely, (a) the elimination of uncertainties in the valve boundary conditions, (b) the removal or reduction of grid dependence and false-diffusion errors and (c) signal processing methods that do not introduce additional "turbulence".

(4) The features of the method that allow solutions of the flow and heat transfer in piston bowls of complex shape have not been tested and data is urgently required to alleviate this deficiency.

CHAPTER 6

APPLICATION TO PRACTICAL ENGINE CONFIGURATIONS

6.1 Introduction

The validation exercise described in the previous chapter examined a number of engine configurations and effects of governing parameters, but, until such time as data is available for a wider range of conditions in compressing engines, more comprehensive testing is not possible. The absence of data does not however preclude parametric studies of swirl level, bowl shape etc. since the comparisons thus far suggest that the prediction method yields results which are at least qualitatively correct; such studies should themselves provide guidance for further experimental work.

Towards this end, section 6.2 of the present chapter describes briefly flow predictions in simple cylindrical piston bowls, both with and without lips, and at various levels of swirl. A more comprehensive study of bowl geometry effects is described in section 6.3, where the flow structures in five different re-entrant bowl configurations are analysed in depth, for conditions approximating as far as possible those found in operating engines, although necessarily within the overall constraint of an axisymmetric calculation.

6.2 Predictions of the Effects of Swirl for Pistons with Cylindrical Bowls

This section summarises the results of a preliminary investigation into the effects of initial (BDC) swirl level on the flow

structure during compression and expansion in a simple cylindrical piston bowl both with and without a protruding rectangular-sectioned lip at entry. Details and results of this analysis were reported by Gosman and Johns (1978a)(see appendix 4) and for brevity, only the more significant features and findings are given here.

The geometry and important dimensions of the engine are shown in fig. 6.1. Six conditions and configurations were analysed; in each case one cycle was computed in the absence of swirl the latter being subsequently imposed as a solid-body rotation at BDC of the second cycle with the swirl ratio (SR) varied between 0 and 10. The initial conditions at the start of the first cycle and boundary conditions for the remaining variables were specified as for case (6) of section 5.4,i.e. zero axial and radial motion and uniform values of k, ε and T. The grids used for each geometry are shown in fig. 6.2 and although they are too coarse for quantitative predictions, they are believed to be adequate for a qualitative indication of the flow structure. The lip form and initial swirl ratio for each case are given below:

Case Number	1	2	3	4	5	6
Swirl Ratio	0	1	5	10	0	5
No Lip	✓	✓	✓	✓		
Lip					✓	✓

The calculations were performed in the manner already described for all but one case (no lip, SR = 0) which was continued until cyclic operation was reached; this took 8 cycles. It was noted for this latter case that the flow structure around TDC

on the first cycle was indistinguishable from that on subsequent cycles when plotted, although a more detailed examination revealed quantitative differences. The reason for this is that the residual gas motion from a compression-expansion sequence decays considerably during the subsequent compression process such that around TDC, the flow is governed by squish and not by the immediate history of the flow. Thus, the single-cycle calculations of cases (2) to (6) are reasonably representative of closed-cylinder cyclic operation (although it should be stressed that in the absence of intake, the swirl would decay continuously unless re-introduced each cycle).

The main findings of this exercise are summarised below (note that figure numbers refer to appendix 4) whilst a more detailed analysis of TDC flow structures is deferred until the next section.

Base-Case - Cylindrical Bowl, No Swirl (figs. 3 and 4)

(1) At BDC, considerable gas motion remains from the previous cycle but this is suppressed through the compression period and is not evident past 45^{o} BTDC.

(2) By 21^{o} BTDC, squish effects induce a single toroidal vortex in the bowl which intensifies during the remainder of compression to TDC.

(3) After TDC, a reverse-squish phenomena produces a strong recirculation zone in the clearance space between the piston and cylinder-head.

Effect of Swirl Level (figs. 6 to 8)

(4) Increasing BDC swirl results in a progressively more complex flow structure in the bowl, with, for SR = 1, a small vortex formed near the bottom of the bowl in addition to the primary vortex, changing to two contra-rotating vortices of approximately equal size for SR = 5 and then to two co-rotating vortices for SR = 10.

Effect of Lip (figs. 9 and 10)

(5) The lipped bowl produces a similar structure to the cylindrical cavity piston of case (1) for SR = 0, but at SR = 5 although two contra-rotating vortices are also observed they are rotating in an opposite sense to those found in the cylindrical bowl at the same swirl ratio.

This study both confirms a number of experimentally-observed phenomena (to be identified below) and demonstrates the importance of swirl on the TDC flow structure. The formation of a toroidal vortex prior to TDC when swirl is not present and the existence of strong reverse-squish after TDC is in agreement with the experiments of Dicksee (1940) and Woods and Ghirlando (1975). The qualitative effects of swirl were identified by Dicksee (1940), who deduced that a double vortex structure is formed when swirl is present (see section 2.3) and although the bowl geometry used here differs from the toroidal bowl he investigated, they do serve to underline the importance of swirl on the TDC flow.

6.3 Predictions for Practical Re-entrant Bowl Configurations

This section describes calculations in re-entrant bowl pistons typical of current designs, as shown in fig. 1.1. All of the bowl configurations investigated have been employed in engines and test-bed results of smoke, specific fuel consumption and equivalent nitrogen oxide are reported by Middlemiss (1978). The interested reader may wish to attempt to relate the changes in engine performance noted in the forementioned paper with the predicted flow structure obtained here for each case; however, in the absence of information from either source about the mixing and combustion processes, this is not an easy task and will not be attempted here. What is described, are both the common features and differences between the flow structures produced by the various designs. As with the swirl-level investigation described in section 6.2, these do not yet exist quantitative experimental data to support these calculations.

Problems associated with calculations in practical engine configurations

Firstly, it must be remembered that these calculations do not include the fuel air mixing and combustion processes, and as such, they do not provide a complete picture of the in-cylinder events. Secondly, in addition to the errors introduced by the turbulence modelling and numerical method of solution already discussed in chapter 5, two further uncertainties arise in

attempts to simulate real engines. The first stems from the three-dimensional valves and piston bowl. Results of a study by Brandl et al (1979) using an engine with the usual off-axis inlet valve and with the axis of the piston bowl offset from the cylinder axis by a similar amount to the engines investigated by Middlemiss, indicate circumferential variations in swirl velocity of the order of 30% near the periphery of an open-chamber piston bowl and a strongly three-dimensional flow structure within the bowl. It is likely that differences of this order also exist between these axisymmetric calculations and the real engine processes.

The second problem is arrving at initial (BDC) fields for the three velocity components and the various turbulence parameters for use in the calculations. The results of the previous section indicate that the initial axial and radial velocities and the turbulence energy and its dissipation rate are relatively unimportant in determining the TDC flow, however this is not true for the swirl velocity. In the absence of any swirl velocity measurements the practice followed here has been to use the Fitzgeorge and Allison (1963) method, described in section 2.3, to calculate the swirl momentum at BDC on the start of the compression stroke and to then assume a solid-body structure. The only departure between the Fitzgeorge and Allison method and that used here is that a more accurate filling-and-emptying cycle simulation program (Johns, 1975) was employed to calculate the mass inflow through the valve instead of the "perfect-displacement" assumption.

Geometry Details

Of the five different bowl configurations investigated four have been run in engines of otherwise identical design, whilst the fifth, although employed in an engine differing slightly from the others in all major details (bore, stroke, speed etc.) is included because of the particularly interesting flow structure it produces near TDC.

The bowls are classified according to the numbering system of fig. 1.1 and the important details of each are given below:

Bowl	1.11	1.2	1.12	1.3	1.15*
Throat dia.(mm)	31.5	31.5	31.5	40.6	39.2
Flank angle	50^{o}	20^{o}	70^{o}	90^{o}	45^{o}
Rounded lip	✓	✓			
Straight-sided lip			✓	✓	✓

*Not illustrated in fig. 1.1

Details of the engines are given below:

Bowls 1.11, 1.2, 1.12 and 1.3

Bore - 91.4 mm

Stroke - 127 mm

TDC clearance - .127 mm

Con-rod length - 223 mm

Compression ratio - 21:1

Speed - 1400 rev/min

BDC swirl ratio - 3.3

Bowl 1.15

Bore - 98.4 mm

Stroke - 89 mm

TDC clearance - .127 mm

Con-rod length - 225 mm

Compression ratio - 15.5:1

Speed - 1428 rev/min

BDC swirl ratio - 2.02

Computational Details

Curvilinear-orthogonal grids were generated for each bowl volume using the method described in appendix 1. The complete grids for each configuration are shown in figs. 6.3 to 6.7. Grid refinement tests were not undertaken for this exercise and these results are therefore only believed to be qualitatively correct. The computational time step was set at 1^{o}. The calculations were started at BDC with the initial conditions prescribed in the same fashion as in the previous section with the exception of the swirl, which was imposed at the start of the calculation.

The output from each run is shown graphically in the same format as before, that is, in the form of velocity vectors and contours of iso-swirl velocity and iso-turbulence intensity. The changes that occur in the flow structure around TDC are adequately displayed by plots at crank-angles of 30^{o}, 15^{o} and 6^{o} BTDC, TDC and 6^{o}, 15^{o} and 30^{o} ATDC although difficulties in reading the magnetic tape used to store the data for the 1.2 bowl at 6^{o} ATDC prevented this information from being plotted.

Predictions for the 1.11 Bowl Configuration

At 30^{o} BTDC (fig. 6.8a), the squish process induces a flow directed around the piston lip and into the bowl, which detaches from the underside of the lip just inside the bowl and forms a small recirculation zone there. The swirl velocity contours show the effects of transport of angular momentum radially inwards from the clearance space, which results in increased swirl velocities in the entrance of the bowl from the "spin-up" effect and an axial variation that is characteristic of all of the present calculations. This trend of higher rotational speeds above the piston before TDC is confirmed experimentally by Brandl et al (1979), who also found the opposite behaviour after TDC, that is, the gas in the bowl rotates faster; the present predictions are also in agreement with this latter finding, as will be seen later. Turbulence is generated near the lip from the stresses associated with the squish-induced jet and a local maximum is found there.

At 15^{o} BTDC, the flow follows the contour of the curved lip and a single dominant toroidal vortex is formed in the bowl. It should be noted that the direction of rotation of this vortex is opposite in sense to that found in no-swirl calculations (see fig. 11 of appendix 4 which shows the TDC structure of this bowl in the absence of swirl). The reason for this is that in the presence of swirl, the radially-inward squish jet is unable to reach the axis because of the opposing centrifugal force and is constrained to flow around the corner. The swirl velocity field shows a much increased and more localised maximum value in the mouth of the bowl and the effects of swirl momentum transport by the squish along the bowl wall are evidenced by high values there; elsewhere in the bowl, the increases are not so dramatic. The

turbulence also shows increased values and extending over a greater area than previously. The high turbulence levels near the axis are probably caused by the curvature of the flow as the gas from the main squish-induced vortex is deflected by the cylinder head.

A further eddy has formed in the mouth of the bowl by 6^{o} BTDC (fig. 6.8b), a feature found in all of the calculations, and is created by the strong squish at this stage, the maximum squish velocity occurring at about 5^{o} BTDC. The sense of rotation of this eddy is the same as the single toroidal vortex found in no-swirl calculations and is generated by the same mechanism. The effect of this eddy is to attenuate the recirculation of the primary vortex near the cylinder head and produces a relatively stagnant region near the axis. Squish effects continue to dominate the swirl structure in the bowl entrance as signalled by an increased maximum value and a radially-inwards shift in its location. Turbulence levels in the bowl are generally about the same as at 15^{o} BTDC with the exception of regions adjacent to the lip where high values and high gradients are found.

The picture is similar at TDC, although the small lip-eddy has been distorted by the primary vortex and a further weak eddy has appeared near the axis at the bottom of the bowl. Both the swirl and turbulence fields exhibit the same structure as before, the former having increased slightly in value with the position of the maximum moved further inwards, whilst the latter has decreased in value. Swirl velocities in the bowl are generally about three times those at 30^{o} BTDC.

The squish-induced lip-eddy disappears quickly after TDC and a sink-like flow into the clearance space is observed at 6^{o} ATDC (fig. 6.8c). The primary vortex is still apparent but considerably reduced in strength. The reverse-squish flow has increased the radial extent of the maximum swirl velocity contour and its value is about half that at TDC. Interestingly, the flow near the axis is virtually solid body in structure for the entire distance between the cylinder head and bottom of the piston. It would seem that in the absence of any appreciable axial and radial velocities, the swirl soon reverts to its equilibrium structure of solid body rotation. The position of the turbulence maximum has shifted into the clearance space adjacent to the lip and is produced by the reverse-squish flow around the lip and not by transport of the pre-TDC squish-generated turbulence, as this trend continues long after TDC.

The squish-induced primary vortex has virtually disappeared by 15^{o} ATDC (A feature found in all of the predictions is that recirculation in the bowl ceases fairly quickly after TDC). The region of solid-body rotation has extended radially, and the experimentally-observed trend, mentioned previously, of higher rotational speeds in the bowl is evidenced in the predictions by the low swirl velocities in the clearance space. This post-TDC "spin-down" effect is a reverse mechanism of the pre-TDC "spin-up". The turbulence maximum has decreased slightly, but the trend of high reverse-squish-generated turbulence adjacent to the lip continues.

The picture is similar at 30^{o} ATDC (fig. 6.8d) although, somewhat surprisingly, the maximum swirl velocity in the bowl has increased slightly. The only explanation that can be offered for this is that swirl momentum from the curved region of the bowl

has been transported inwards as a result of the outflow from the bowl and the decreasing radius has caused a swirl speed increase.

Predictions for 1.2 Bowl Configuration

This bowl differs from the previous case by having a 30^{o} steeper angle side wall. The overall picture at 30^{o}BTDC (fig. 6.9a) is very similar to the 1.11 bowl calculations in both structure and magnitude, with the exception of the flow around the lip which shows a more pronouced detachment due to the steeper angle of the wall. Unlike the previous predictions, the flow does not re-attach at the corner but at the bottom of the bowl so that at 15^{o} BTDC, two eddies are formed in the curved part of the bowl. This finding suggests that for a given lip radius, swirl rate etc. there is a minimum value of flank angle, probably somewhere between the 50^{o} and 20^{o} values used here, that will allow a single main squish-induced toroidal vortex to initially form in the bowl and that a further decrease in flank angle will cause two such eddies to be created.

With the exception of the two-eddy structure the flow is much the same as the 1.11 bowl predictions at 6^{o} BTDC and TDC (fig. 6.9b), with the formation of an additional squish-induced vortex in the mouth and the appearance of a weak recirculation zone towards the bottom of the bowl near the axis, which incidentally occurs earlier in the present case. The post-TDC behaviour also follows a similar pattern to that seen previously (note that no plots are available for 6^{o} ATDC) with the exception of the slight increase in swirl speed between 15^{o} and 30^{o} ATDC observed in the previous example.

Predictions for the 1.12 Bowl

This bowl differs from the 1.11 and 1.2 configuration, firstly by having a 70^{o} flank-angle and secondly, a straight-sided lip with a sharp outer edge.

At 30^{o} BTDC (fig. 6.10a) the flow shows identical trends and similar values for all quantities to those seen previously. By 15^{o} BTDC however, the flow into the bowl shows a small recirculation at the lip, a behaviour contrary to immediate intuition as the bowl flank is inclined less than, for example, the 1.11 bowl, whose flow had re-attached at this stage. The answer lies in the sharp edge of the lip as compared with the smooth curvature of the previous versions, which allowed the gas to flow smoothly along the side wall of the bowl. The structure is otherwise quite similar to the 1.11 bowl with the initial formation of a single strong, clockwise-rotating primary vortex. Both the swirl and turbulence levels are slightly higher (5-10%) than those observed in the other configurations.

By 6^{o} BTDC (fig. 6.10b) the now-familiar eddy has formed in the mouth of the bowl and the swirl shows the characteristic high maximum value approximately mid-way between the lip and axis. The turbulence however has a similar structure to 15^{o} BTDC, although with reduced levels. This contrasts with previous calculations which showed slightly increasing values before TDC and a maximum located near the lip. At TDC, high inward radial velocities are found near the cylinder head and the turbulence maximum has increased dramatically. The reason for this phenomena can possibly be explained in the following way: in the calculation with curved-lip bowls (1.11 and 1.2) the lip curvature acts in a similar fashion to a diffuser, thus, the squish flow leaving the clearance

space experiences a region of increasing area at the edge of the bowl and although the maximum squish velocity occurs at about 5^{o} BTDC, the diffusion effect will be most pronounced at this stage as the clearance gap is small. The net effect of a curved lip on this aspect of the flow is to increase the effective bowl diameter with the associated reduction in squish velocity. On the other hand, no such diffusion occurs with a sharp-edged lip and the squish velocities are not attenuated. It should be remembered that the production of turbulence depends upon the magnitude of the velocity gradients and it is probable that these reach a maximum value somewhere between the time of maximum squish velocity and TDC.

At 6^{o} ATDC (fig. 6.10c), much higher reverse squish velocities are seen at the lip than with previous bowl configurations; this also seems to be a feature common to sharp-edged lips as will be seen later in a similar configuration. The trends at 15^{o} ATDC and 30^{o} ATDC (fig. 6.10d) are much the same as those found previously, with virtually solid body rotation extending to half the bowl radius and a local turbulence maximum adjacent to the lip in the clearance space.

Predictions for the 1.3 Bowl

This open-chamber bowl could be classified as having a 90^{o} flank-angle, although to avoid excessive bowl depth while preserving the same compression ratio, the throat is of larger diameter than for the previous calculations.

At 30^{o} BTDC (fig. 6.11a), both the turbulence generated at the lip and the swirl velocities are lower than in the earlier case because of the reduced squish velocities that result from the increased bowl diameter, thus illustrating the merits of the re-entrant design. The swirl velocity contours also show a less localised structure with the maximum value extending to the cylinder wall, although the axial variation above the piston occurs as before.

By 15^{o} BTDC, the primary vortex has appeared in the bowl cavity and a small eddy has formed just inside adjacent to the lip, where the flow has separated and reattached. Although the swirl maximum is now more localised the values are considerably lower than in any of the previous calculations.

At 6^{o} BTDC and TDC (fig. 6.11b), the structures are quite similar to the 1.12 (70^{o} flank-angle, sharp-edged lip) predictions and show the same trend of decreasing turbulence immediately prior to TDC followed by a substantial increase at TDC.

The post-TDC behaviour (figs. 6.11c and 6.11d) is also very similar to the 1.12 bowl in all respects, including the occurrence of high reverse-squish velocities. Both the swirl and turbulence levels remain lower than those of previous calculations.

Predictions for the 1.15 Bowl

This configuration differs from those analysed previously in a number of geometry details, already described at the start of this section, and a lower BDC swirl ratio of 2.02.

At 30^{o} BTDC (fig. 6.12a) the characteristic squish-generated structure is observed, with localised maxima of both swirl and turbulence levels near the lip. By 15^{o} BTDC, two eddies have formed in the bowl, but unlike previous calculations, they are of approximately similar size. The mechanism that has produced this flow pattern should not be confused with the two-eddy structure found in the 1.2 bowl (fig. 6.9a), the latter being caused by the flow detaching from the steep wall, but rather by the same mechanism that produced the lip-eddy of the same rotational sense in all the other bowls immediately prior to TDC. The reason for this is probably the reduced centrifugal forces opposing the squish, that are associated with the lower swirl ratio, allow the formation of a stronger counter-clockwise rotating vortex (as evidenced in the no-swirl calculations of appendix 4) than would be obtained with a higher initial swirl.

At 6^{o} BTDC and TDC the counter-clockwise rotating vortex dominates, with the other pushed toward the bottom of the bowl. The swirl and turbulence fields show similar trends to previous calculations.

The dominant vortex disappears quickly after TDC and by 6^{o} ATDC only a weak clockwise recirculation is observed in the bowl. Characteristic of sharp-edged lips, the reverse-squish velocities are high. The subsequent behaviour is otherwise much the same as the post-TDC performance of previous predictions.

Assessment of Curved Bowl Predictions

These calculations demonstrate that the flow structure in axisymmetric representations of piston-bowl chambers typical of

current design can be analysed using the method developed in this study. The results suggest that apparently minor variations in the geometry and/or operating condition can produce dramatic changes in the behaviour of the flow. A few general observations can be made concerning these calculations; it should not be assumed that these observations will apply to conditions far removed from those used here, for example, very high or low initial swirl levels.

(1) It is usual for the squish to provoke a clockwise-rotating toroidal vortex by 15^{o} BTDC and a second eddy of counter-clockwise rotation immediately before TDC, although the flank-angle, lip shape and swirl ratio can alter the proportions and timing of each.

(2) A reverse-squish phenomena is observed and is found to be more intense in bowls with straight-sided rather than curved lips.

(3) The squish motion prior to TDC transports swirl momentum into the bowl, increasing the swirl velocities in the latter, which are found to reach a maximum at, or just before TDC. Also observed are an axial variation in swirl velocity, with higher values nearer the cylinder head, and a localised maximum between the lip and cylinder axis.

(4) After TDC, the swirl momentum is transported back into the clearance space and lower swirl velocities are then found above the piston. Solid body rotation, without appreciable axial variation, is then observed in a substantial portion of the bowl.

(5) The squish process generates considerable turbulence near the lip prior to TDC and this is subsequently transported into the bowl. Curved and straight-sided lips exhibit a different behaviour, turbulence levels in the former increasing steadily before TDC, whilst in the latter, a decay is observed immediately before TDC followed by an increase in localised lip-turbulence at TDC.

(6) All of the configurations analysed indicate that a localised turbulence maximum is created just above the piston by the reverse-squish and the predictions of section 5.4 show that this is responsible for increasing the heat transfer rates in this region.

6.4 Closure

In this chapter, flows in various piston bowl configurations and conditions have been examined. Analysis of the flow in cylindrical cavity pistons agrees qualitatively with the experimentally observed phenomena of squish and reverse squish and the finding that swirl has a strong effect on the TDC flow.

The calculations in curved bowls show that the flow structure prior to TDC is extremely complicated and that minor geometry changes can produce substantial changes to the flow as can swirl level and possibly other parameters. Nevertheless, a number of features of commonality in the different flow patterns have been identified.

Quantitative comparison with experimental data has not yet been possible, but the behaviour of the flow seems plausible and does agree at a qualitative level with a number of experimental investigations.

CHAPTER 7

SUMMARY AND CONCLUSIONS

7.1 Summary of Achievements and Findings

A computational procedure has been developed to predict the gas motion in diesel engine cylinders equipped with piston bowls typical of current design. This has been achieved by formulating the differential conservation equations governing the flow in a general curvilinear-orthogonal axisymmetric co-ordinate frame that allows the solution domain to be always bounded by the cylinder head, cylinder wall and piston surfaces and solving numerically algebraic finite-difference approximations to the transformed equations. Within this framework, the following features have been included: a contemporary two-equation turbulence model, swirl, and a fixed orifice or a moving poppet valve through which air may be inhaled and expelled.

The accuracy of alternative finite-difference schemes has been examined and the effects of grid size and time step determined by comparing numerical and analytical solutions for the case of one-dimensional compression-expansion. A similar, but more limited exercise has been carried out for a two-dimensional turbulent flow in a simple cylindrical-cavity piston-bowl configuration. A stability analysis has also been undertaken for time-centred differencing of the one-dimensional continuity equation which has indicated the nature and effect of time-step on stability. The one-dimensional analysis shows that the time-centred scheme produces a more accurate solution than the fully-implicit formulation for the velocity although the level of error for both schemes is low. In two-dimensional calculations, differences between the schemes are negligible and implicit differencing

is therefore preferred on grounds of stability. The time-centred scheme may be used if small (1^{o}) time-steps can be tolerated, but larger steps invariably result in an oscillatory solution. A scheme for adjusting the under-relaxation factors, used to control convergence and stability, has been proposed and shown to be superior to the usual practice of specifying fixed values of these parameters.

The above work has resulted in a numerical scheme that, at least for all calculations described in this thesis and others not included, remains stable and convergent, however, it must also be concluded that for complex recirculating turbulent flows, solutions independent of the effects of grid size and time-step cannot be obtained for economical specifications of these quantities.

Comparison between the calculations and six experiments have been described which include: detailed profiles of mean and turbulent velocities in a non-compressing engine both with and without swirl and a piston bowl, single point mean and turbulent velocities in a compressing engine with a moving poppet valve in both bowl-in-head and flat cylinder head configurations and instantaneous heat fluxes at four positions on the cylinder-head of a high-swirl cavity-piston compressing engine. These results show that the calculations are generally in reasonable agreement with the measurements. In all cases, trends have been correctly predicted although a detailed examination has, on occasions, revealed substantial numerical differences. Various reasons have been suggested to account for the observed discrepancies in chapter 5, which include numerical smearing, certain assumptions used in the turbulence model, inadequate specification of inlet boundary conditions and errors in the measurements and subsequent data-processing.

In chapter 6, the flow structure around TDC has been examined for both simple cylindrical-cavity piston-bowls and five different re-entrant bowl configurations. Results for the former show that swirl strongly effects the flow structure, with higher initial swirl rates producing a progressively more complex flow pattern at TDC. In the case of the latter, variations in the bowl flank-angle, lip shape and initial swirl ratio resulted in substantial changes in the flow structure. With a shallow-angle piston bowl side-wall, a single clockwise-rotating toroidal vortex was formed initially, but with a steeper angle the flow detached at the edge of the lip, resulting in a two eddy structure within the bowl. The effects of both curved and sharp-edged lips were also examined. Here, differences were observed both before and after TDC, with the gas flowing smoothly around the curved lip but detaching from the sharp lip to produce an additional small eddy prior to TDC and a stronger reverse-squish flow after TDC. It is hoped that these or similar calculations will provide guidance for future experimental work.

7.2 Improvements and Extensions

Improvements

(i) Reduction of Storage

Various arguments can be marshalled against wastage of computer storage, e.g. cost, portability to smaller machines etc. and it must generally be regarded as undesirable. The current implementation of the computer code uses two-dimensional storage with direct-addressing of array elements, i.e. typically, a variable $\phi_{i,j}$

is addressed as PHI(I,J) where i(I) and j(J) refer to a particular location in the field at the co-ordinates z(I), r(J). Although conceptually very simple, this system is not particularly efficient when used with a variable number of grid lines in either or both of the co-ordinate directions. In the context of the present application, storage is wasted in the region between the side wall of the piston bowl and the cylinder wall. Typically, this amounts to 200 array locations per variable and, with a total of 45 two-dimensional arrays, the wasted storage is 72 k bytes. There are two relatively simple ways of eliminating this unused space, both using one-dimensional storage for all variables and indirect-addressing of array elements as described below.

The first and simpler of the two methods, addresses a two-dimensional array element $\phi_{i,j}$ in a one-dimensional fashion as PHI(IS(J)+I); this process is illustrated in fig. 7.1 for a small but representative grid (the randomly-distributed number 1 to 18 shown within the grid should be ignored for the present). In fig. 7.1, the main point to note is that one-dimensional storage allows the use of 'J' lines of variable length, thus, the redundant storage contained in the J=3 and J=4 lines in the upper figure has been eliminated. The method of computing the address, given by IS(J)+I, is very similar to that undertaken by the compiler for a two-dimensional array, the only difference being that IS(J) is a constant in the latter case and equal to one of the dimensions of the array. Accessing the surrounding grid cells at points N, S, E and W is achieved by inserting the appropriate I and J into the address formula; typically for a North cell ($\phi_{i,j+1}$), this is PHI(IS(J+1)+I). The values contained in the array IS can be regarded as the start addresses of each J line and the numerical values for this example are shown in fig. 7.1.

The second method of indirect-addressing is more complicated but offers greater flexibility as to the positioning of grid cells within the solution domain and is ideally suited to handling geometries with many discontinuities. In this case, the concept of I, J addressing is dispensed with and each grid cell is allocated a unique integer number (K), as shown within the grid of fig. 7.1 (in this example, $1 < K < 18$). The ordering of these numbers is unimportant. Address arrays are then defined, LN(K), LS(K), LE(K) and LW(K) as containing the cell number to the North, South, East and West of cell 'K', e.g. for the grid of fig. 7.1, LN(13) = 11 and LE(5) = 17. The variables contained in the surrounding cells are then accessed as PHI(LN(K)), PHI(LS(K)) etc. An additional 8 integer arrays are also needed to access the surrounding velocity components (it will be recalled that these are located at the cell boundaries) and to indicate when a cell boundary is also a physical boundary of the domain; this is done in an identical fashion to the scalar cell addressing. The differencing schemes and solution method already described in this thesis could be used without modification, and if this indirect-addressing technique were used in conjunction with the grid-matching method developed in section 5.3 of appendix 1 for generating curvilinear-orthogonal grids in discontinuous regions of complex shape, it would provide a powerful method for handling, for example, the prechamber engine configuration described by Gosman et al (1979) and summarised in chapter 2 where conventional direct-addressing was used.

In addition to the storage savings that would be obtained from either of the indirect-addressing methods outlined, it may be

possible to further reduce the storage per variable by using lower precision for storage of certain variables. At present,double precision on an IBM machine is used (8 bytes = 64 bits per variable), giving accuracy to approximately 14 significant figures. Attempts to use single precision throughout resulted in roundoff errors sufficient to prevent convergence. The use of selective double precision may however prove fruitful; for example, it was found that if double precision was used for all variables involved in the calculation of the pressure field (recall it is the small spatial variations of pressure that drive the velocities obtained from the momentum equations) that a much better solution was obtained. Thus, it may not be possible to halve the storage, but some savings can almost certainly be made. These comments do not however apply to all computers; in particular CDC machines use a 60 bit word length for single precision (giving identical accuracy to IBM double precision) which cannot easily be reduced.

(ii) Reduction of cpu Time

Methods for reducing the cpu time are not so obvious, as the present version of the computer code has already been optimised to improve its speed. One idea, used by Butler et al (1978), is to delete grid lines in the contracting portion of the grid as the piston approaches TDC and to subsequently reinsert them as the piston descends and the grid expands. This is not a particularly difficult task, the main criterion being that rezoning of the control volumes must be conservative, that is, there should be no sources or sinks

of any of the conserved properties artifically introduced as a consequence of the rezone. One unfortunate effect of rezoning however would be to diffuse properties in the axial direction as a result of averaging, thus a certain amount of numerical smearing would occur. It is likely that the spatially integrated squish velocity (integrated along the line AA in fig. 2.11) would be the same between the conventional and rezoned solutions, as the indications are this quantity depends solely on satisfaction of the continuity equation (with the possible exception of extremely high-speed engines (> 10,000 rev/min)) but the axial gradients of squish velocity would be reduced from the effects of both rezone smearing and the reduced number of grid lines. It was seen in chapter 4 that coarser grids tend to reduce the velocity gradients and hence the turbulence levels. Deletion of grid lines would therefore need careful testing to determine the effect on the solution of the turbulence equations. The required programming effort is small however and is certainly worthy of further investigation.

Further improvements at reducing cpu time can only come about by using a more efficient algorithm for linking the momentum and continuity equations, probably of the non-iterative variety, and/or by running on one of the new-generation array processors such as the CRAY 1, for which this type of program is ideally suited.

(iii) Non-orthogonal Co-ordinates

As indicated in appendix 1, orthogonal grids may not be suited to some geometries, specifically, those with non-orthogonal corners or highly concave regions, the resulting mesh being non-

orthogonal or sparse in these regions. A non-orthogonal co-ordinate system would provide much greater freedom in the choice of grid density and positioning although the computational time would invariably increase as a result of the extra terms appearing in the governing equations that express the effects of departures from orthogonality. An alternative to using a fully non-orthogonal system throughout would be to use a combination of rectilinear, orthogonal-curvilinear and non-orthogonal co-ordinate frames with each grid cell in the flow field flagged to indicate which system it belongs to. Thus, the computer could detect quickly which co-ordinate system has been assigned to each grid cell and only the relevant terms would be evaluated.

(iv) Local Grid Refinement and Adapative Grids

It was mentioned in chapter 4 that research into more accurate methods of differencing the differential equations has not yet provided a scheme that fulfills the two important criteria of diagonal dominance and conservation. An alternative approach to improving the accuracy of finite-difference calculations is suggested below.

The proposed method relies on the fact that errors generally diminish with reduction in grid size, but that fine grids are usually only required in certain regions of the flow field. Within the constraint of the type of grid described so far, this is not possible, as refinement in one region of the field

invariably produces unwanted and usually unnecessary refinement elsewhere because in i, j space the grid is topologically rectangular i.e. each mesh point is always connected to its four nearest neighbours. However, if it were possible to refine a grid locally, that is, to subdivide a single grid cell into (say) a 4 x 4 mesh, then the advantages of a fine mesh could be obtained without incurring the associated penalties throughout the field.

As an illustration of where local grid refinement should be useful Case 1 of chapter 5 will be used. It was noted that the intake jet crossed the rectilinear grid at an angle of $45^{o} \pm 20^{o}$ and the calculated expansion of the jet was greater than that measured, which was attributed in part to false-diffusion errors, and the turbulence energy was consequently underpredicted. Figs. 7.2a and 7.2b show respectively the flow structure at 90^{o} during intake for case 1 (computed with the conventional grid arrangement) and a proposed improved computational grid that has been locally refined along the lines discussed above. Here it can be seen that the grid has been refined in regions where false diffusion errors are expected to be greatest, special attention being given to the intake jet.

It is often not known á priori how the calculated flow structure will develop as the solution proceeds, thus, the refined grids may be initially misplaced, or alternatively, required in different regions of the flow at different times as the structure changes. A logical extension of this concept would be to allow the additional grids available for refinement to be disposed according to the nature of the solution itself, such that regions of refinement would be determined from some specified criteria that depends upon the solution. This could take the form of a weighting function, evaluated at each grid cell in the field, with refinement

applied in the regions where the value of the weights is greatest. For example to procure refinement in regions of maximum false diffusion, the weighting function might take the form: | mass flux x sin 2θ| where the mass flux is evaluated at the cell face and θ is the local orientation of the flow to the mesh. Other weighting criteria could also be evolved: for example, in a combustion calculation, the refinement criterion could be based upon gradients of temperature or concentration such that the position of the flame front could be located and the grid there subsequently refined to improve definition. More generally, this method could be used whenever events occur on length scales much smaller than the scale of the solution domain.

As yet nothing has been said about detailed implementation of the foregoing ideas and this is by no means a trivial task. Although much of the work already described in this thesis, that is, the differential equations, finite-difference approximations etc. could be used with little or no change, with the exception of the line-by-line solution procedure which would require a more general Gaussian-elimination as the coefficient matrix for a single line that employs grid refinement can no longer be forced into tri-diagonal form, much careful thought is needed before a computer code could be assembled. Work by the author has indicated that a viable method, which makes extensive use of a more general indirect-addressing technique to that previously described may be used successfully, although the penalty for such flexibility is a vast increase in the quantity of integer storage (of the order 80 additional arrays, dimensioned to the total number of grid cells in the field) used for the addressing if conventional high-level language programming methods used. However by introducing machine-dependent operations into the program, these overheads can be reduced to manageable proportions.

For example, on a CDC machine, which uses are 60 bit word for the storage of each integer, by introducing two simple and extremely fast operations, 5 integers (whose value must be less than $2^{12}-1=4095$) can be easily packed into a single word, thereby reducing the integer storage requirement by a factor of 5.

This concept is certainly worth persuing, at least in two dimensions, to determine whether or not the hoped-for improvements would be realised in practice.

Extensions

(i) Three-dimensionality

The differential equations, differencing practices and many features of the solution method described in chapters 3 and 4 are readily extendable to three dimensions. However, this is not a step to be taken lightly in engine calculations for two reasons: firstly, because of the increases in both storage and cpu time, the cost of operating such a code will be substantially higher than the 2-d version and secondly, if a 3-d computer code is to be useful, it must embody features of practical interest, such as piston bowls or valves offset from the cylinder axis. In view of the grid-dependence of the solution found for the two-dimensional calculations in chapter 4, it is improbable however that quantitative results could be relied upon in three dimensions with the differencing practices currently used. Nevertheless, it is likely that useful qualitative information could be derived from such a program.

To illustrate how the method may be extended to cater for practical 3-d configurations three examples are described below. It should be noted that the methods suggested for the following engine configurations use no new concepts, such as non-orthogonal co-ordinate systems, but only different applications of the ideas already developed in this thesis.

Example 1 - Flat cylinder head, no valves, offset piston bowl of complex shape

Such a geometry is shown in fig. 7.3. As with the piston-bowl calculations already described, the solution domain can be divided into two components, namely, a translating region in the bowl and an expanding/contracting region between the piston surface and cylinder head. If the piston bowl is circular (although this is not a constraint on the method) then a curvilinear orthogonal grid can be employed in the r-z plane within the bowl in the manner used for the calculations of chapter 6. Outside the bowl however, the non-coincidence of the bowl and cylinder axes requires a further curvilinear-orthogonal grid to be generated in the r-θ plane. In this case, an analytic transformation exists for a pair of non-concentric circles (Kober, 1957) although other transformations may also be used. An example of such a grid is shown in fig. 7.3*. The resulting grid therefore consists of two general curvilinear-orthogonal regions, the first in the piston bowl (r-z plane) and the second in

*This grid was produced using the method of Watford (1978).

the cylinder (r-θ plane). Thus, expansion and contraction in the rectilinear (r-z) plane of the co-ordinate frame between the piston surface and cylinder head is identical to that already used whilst the piston bowl portion similarly translates as before.

Example 2 - Flat cylinder head and piston surfaces, single offset protruding poppet valve

This configuration is shown in fig. 7.4. The grid required for this configuration is essentially the same as that suggested for the expanding/contracting region in example 1, but with the valve protruding into the cylinder in an identical fashion to that described in chapters 4 and 5 used for simulating the experiments of Witze (1976c). The boundary conditions, which would almost certainly have to come from experiment for any given port configuration (although spatially resolved steady-state measurements of the 3 velocity components at different valve lifts and pressure-differentials may be adequate), would be provided at the surface of the cylindrical region extending from the periphery of the valve to the cylinder head, as shown in fig. 7.4. As with the moving-valve calculations of chapter 5, a constant number of grid lines could be retained between the cylinder head and valve when the latter is open to improve resolution, these contracting to a line in the plane of the cylinder head and becoming inoperative when the valve is closed.

Example 3 - Uniflow scavenged two-stroke; inlet~piston-controlled porting, exhaust~offset poppet valve in cylinder head, flat cylinder head and piston surfaces

This example is intended to illustrate how an engine with fairly complicated porting can be analysed using a combination of techniques. The geometry and proposed grid are shown in fig. 7.5. The cylinder contains a port belt used for intake that is uncovered before the piston reaches BDC and remains open until closed by the piston during compression. At BDC, the bottom of the port belt and the piston surface are co-incident. In the cylinder head, a poppet valve is used for exhaust which may or may not be offset from the cylinder axis. In fig. 7.5(a) the piston is at BDC with the exhaust valve still partially open and the port belt fully exposed. The grid line at C remains fixed to the top of the port belt whilst the latter is open and a constant number of grid lines are used between A and B and between C and D. At the start of compression, fig. 7.5(b), the exhaust valve is closed and the grid lines between A and B are co-incident at the cylinder head surface whilst in the port belt, the grid lines between C and D are compressing. As the port closes, all grid lines between C and D become co-incident at the piston surface as is fig. 7.5(c). During expansion, as the valve and port open, the reverse procedure is adopted and the grid lines between A-B and C-D reappear.

(ii) Fuel Sprays

Numerous methods have been developed to analyse fuel sprays, ranging from simple algebraic formulae that relate the

distance travelled by the spray tip to certain characteristics of the injection system and time (see e.g. Hay and Jones (1972) for a survey of 12 such correlations) to calculations of the heat and mass transfer and trajectory of a single droplet (Borman and Johnson, 1962) and more sophisticated models which take account of the spray growth and heat and mass transfer within the mixing region (Adler and Lyn, 1971). Unfortunately, the vast majority of these methods cannot easily be incorporated into the framework of the multi-dimensional calculation method already described.

An alternative approach, which in principle is capable of including most of the important phenomena that occur in the two-phase fuel-air mixing process, is an extension of single-droplet calculation methods to a multi-droplet calculation (Gosman and Johns, 1980). In this method, the spray is represented by a statistical sample of discrete droplet 'parcels' that eminate from the zone of atomisation with specified initial sizes, velocities and temperatures; these are subsequently 'tracked' in a Lagrangian fashion as they traverse through, and heat up and vaporise in the gas flow, by solving appropriate conservation equations of mass, momentum and energy. Each parcel consists of a number of identical, non-interacting fuel drops and the behaviour of the entire parcel is characterised by that of a single member. Full two-way interactions between the gas and liquid phases are allowed for in the following way: as the droplets traverse the flow field, the gas temperature, fuel vapour concentration and velocities, used in the solution of ordinary differential equations for the droplet behaviour, are obtained from the gas phase solution at the grid cell in which the droplet parcel

currently resides; at the same time, fields of 'sources' of mass, momentum and energy, that expresses the interaction between the phases, are assembled and subsequently used explicitly in the gas phase calculation.

Results for a two-dimensional (pintle-type nozzle) hollow-cone spray calculation using this method show that strong interactions occur between the phases, the greatest effects being confined to regions around the injector. To illustrate this point, figs. 7.6 and 7.7 show the predicted flow and concentration fields and the fuel spray dispersion at TDC (taken from Gosman and Johns, 1980). These figures represent respectively, a solution in which the effect of the droplets on the gas has been ignored and full two-way interactions. It is however concluded that considerable further work is needed in such areas as the behaviour of multi-component fuel droplets at the thermodynamic critical point and the specification of reliable initial conditions before the model can be deemed truly predictive.

(iii) Ignition

Modelling of the ignition process is a prerequisite to modelling combustion and is dependent upon whether the fuel is spark or compression ignited. The former case is easier to analyse in that the location and timing of the spark are known. In the absence of an ignition model, the practice adopted by Ahmadi-Befrui et al (1980) is to specify a burning rate over a few degrees of crank-angle for the fuel in the grid cell at the spark gap position; the resulting temperature increase and depletion of the fuel subsequently

initiates combustion in the surrounding grid cells and throughout the field. In this context, the use of local grid refinement, as previously described, should prove to be a worthwhile method of resolving the small length scale of the initial flame.

Compression-induced ignition is more difficult to analyse and model. It is known from high-speed photography (Shiozaki et al, 1980) that combustion is often initiated simultaneously in different regions of the cylinder and a model that claims to be realistic must therefore allow for this. The ignition delay period in diesel engines is conventionally thought to consist of a physical delay, during which fuel evaporates and mixes with the surrounding air, and a chemical delay, in which time the fuel undergoes complex chemical reactions; analysis is complicated by the fact that the two occur simultaneously. Very little is known about the detailed reactions leading to autoignition although Garner et al (1961) found that for four different hydrocarbon fuels, peroxides and aldehydes were formed during the delay period and reached their peak concentration at the start of combustion. They also found that for high cetane number fuels the peak concentration of these intermediate compounds occurred earlier than with fuels of low cetane number. Henein and Bolt (1969) and others have investigated the effect of cetane number (CN) on the duration of the delay period and found that petrol (CN = 18) has a longer ignition delay than diesel fuel (CN = 57.5). Similar observations have been reported by Stringer et al (1971) for the autoignition of several fuels in a continuous flow system. The preignition reactions may be considered in two stages: in the first, slow reactions occur and intermediate compounds are formed; when these have reached some critical

concentration, fast reactions are initiated, leading to autoignition and combustion. Furthermore, the rate of the physical processes such as evaporation increase with fuel volatility, thus, if physical processes determined the duration of the delay period, the ignition delay for petrol would be shorter than that for diesel. As this is not the case, it must be concluded that the delay is chemically-controlled (Henein, 1976).

Attempts to calculate the duration of the ignition delay are usually based upon an Arrhenius-type relationship. The starting point is to assume that the formation rate of intermediate compounds is governed by an expression of the form:

$$\frac{d[IC]}{dt} = k\,[F]^n\,[O_2]^m \qquad (7.1)$$

where k is the reaction velocity, [IC], [F] and $[O_2]$ are the concentrations of the intermediate compounds, fuel and oxygen, and n and m are the order of the reaction with respect to the fuel and oxygen. The reaction velocity is usually expressed as:

$$k = C_1 e^{-E_a/R_o T} \qquad (7.2)$$

where C_1 = constant, E_a is the global activation energy, R_o is the universal gas constant and T is the gas temperature. If it is further assumed that the fuel and air will only ignite within narrow limits of stoichometry, then the ratio of fuel and oxygen concentrations is fixed and equation 7.1 can be written as:

$$\frac{d[IC]}{dt} = C_2 e^{-E_a/R_o T} \qquad (7.3)$$

The conventional approach to evaluating the ignition delay is to simply replace equation (7.3) by an expression containing an empirical

constant (A) which must be determined experimentally and depends upon the shape of the combustion chamber, fuel-injection characteristics etc. typically:

$$\text{ignition delay} = Ae^{E_a/R_oT} \tag{7.4}$$

The above method is inadequate for multi-dimensional calculations for two reasons: firstly, equation 7.4 requires a constant that can only be obtained from engine tests, and secondly, it provides no information as to where ignition occurs in the combustion chamber. An alternative approach that is more compatible with multi-dimensional models is outlined below.

A conservation equation for the formation of the intermediate compounds can be written as:

$$\frac{\partial}{\partial t}(\rho\chi) + \frac{\partial}{\partial x_i}(\rho v_i \chi) - \frac{\partial}{\partial x_i}(\Gamma \frac{\partial \chi}{\partial x_i}) = s_\chi \tag{7.5}$$

Here, χ is the mass fraction of intermediate compounds and s_χ is the net generation-destruction rate of χ (to preserve clarity, this equation has not been written in general curvilinear-orthogonal co-ordinates). The generation rate of χ (s_χ) is evaluated from equations such as 7.1 and 7.2. Equation 7.5 is solved only after the start of injection and the occurrence of ignition would subsequently be detected by scanning the field of χ's to determine if the concentration of intermediate compounds is greater than some specified value, χ_{ig}, that is, if

$$\chi(x_i, t) > \chi_{ig}$$

then combustion would start at that position in the combustion chamber. It would be expected that once combustion had started in

a particular grid cell that it would spread quickly throughout the remainder of the field due to the exponential relationship with temperature.

Such a model incorporates both the chemical and physical components of the delay period. The quantities C_1 in equation 7.2 and χ_{ig} must first be determined but these should be constant for a particular fuel.

(iv) Combustion

The development of engine combustion models has, in the past, been hampered by a lack of temporally and spatially resolved information about the flow, temperature and concentration fields. As a consequence, numerous methods have evolved to circumvent these problems (see e.g. Blizzard and Keck (1974) and Grigg and Syed (1970) who address the problems of homogeneous charge petrol and diesel spray combustion respectively).

Multi-dimensional calculation methods offer an opportunity to construct combustion models that may be solved simultaneously with the flow field.At the present, there appear to be two schools of thought as to the way this should be done, both apparently giving plausible results. One method used (Ahmadi-Befuri et al(1980)) is to assume that the combustion rate is governed by the rate-of-mixing of the fuel and oxygen such that the former is proportional to the dissipation time-scale (k/ε) (Magnussen and Hjertager (1976)). The second approach assumes the chemical kinetics to be the rate-controlling process. Both methods solve one or more differential

equations similar to 7.5, the differences being in the specification of the source term.

It is probable that both mechanisms are simultaneously operative and each is rate-controlling at different stages in the overall process. It is also likely that for the hetrogeneous combustion in diesel engines, the turbulent mixing model is more appropriate. At the present however, it is too early to make a reasonable assessment of the two alternative approaches.

REFERENCES

Adler, D. and Lyn, W.T., (1971), "The Steady Evaporation and Mixing of a Spray in a Gaseous Swirl", Int. J. Heat and Mass Transfer, 14, p. 793.

Ahmadi-Befrui, B., Gosman, A.D. and Watkins, A.P., (1980), "Multidimensional Modelling of Turbulent Combustion in an Axisymmetric Homogeneous-Charge Engine", Oral presentation at SAE Congress, Detroit, Feb. 1980.

Alcock, J.F. and Scott, W.M., (1962), "Some More Light on Diesel Combustion", Proc. Auto. Div. of I. Mech. E., 1962-63, 25.

Allen, D.N. de G. and Southwell, R.V., (1955), "Relaxation Methods Applied to Determine the Motion in Two Dimensions of a Viscous Fluid past a Fixed Cylinder", Quart. J. Appl. Math., vol. 8, No. 2, p. 129.

Amsden, A.A. and Hirt, C.W., (1973), "YAQUI: An Arbitrary Lagrangian-Eulerian Computer Program for Fluid Flow at all Speeds", Los Alamos Sci. Labs. rpt. LA5100.

Anasuma, T. and Obokata, T., (1972), "Decay of Air Swirl Motion in an Engine Cylinder", JARI tech. memo., No. 10.

Anasuma, T. and Obokata, T., (1973), "Decay of Air Swirl Motion in an Engine Cylinder", JARI tech. memo., No. 15.

Annand, W.J.D., (1970), "Instantaneous Heat Transfer Rates to the Cylinder Head Surface of a Small Compression-Ignition Engine", Proc. I. Mech. E., vol. 185.

Arnold, M.J., Tindall, M.J. and Williams, T.J., (1972), "Measurement of Induction Gas Velocities in a Reciprocating Engine Cylinder", SAE 720115.

Benson, R.S. and Foxcroft, J.S., (1969), "Non-Steady Flow in I.C. Engine Inlet and Exhaust Systems", Proc. I. Mech. E., vol. 184, pt. 3G(1).

Bird, R.B., Stewart, W.E. and Lightfoot, E.N. (1966), Transport Phenomena, Wiley, New York.

Blizzard, N.C. and Keck, J.C.,(1974), "Experimental and Theoretical Investigation of Turbulent Burning Model for Internal Combustion Engines", SAE 740191.

Boni, A.A., Chapman, M., Cook, J.L. and Schneyer, G.P., (1976), "Computer Simulation of Combustion in a Stratified Charge Engine", Proc. 16th Symp. (Int.) on Comb.

Boni, A.A.,(1978), "Numerical Simulation of Flame Propagation in Internal Combustion Engines: A Status Report", SAE 780316.

Borman, G.L. and Johnson, J.H., (1962), "Unsteady Vaporisation Histories and Trajectories of Fuel Drops Injected into Swirling Air", SAE 598C.

Boussinesq, V.J. (1877), Memo pres. par div. savants a l'acad. Sci. Paris, 23, p. 46.

Bradshaw, P., (1971), An introduction to turbulence and its measurement, Pergamon Press.

Bradshaw, P., Cebeci, T. and Whitelaw, J.H., (1977), "Engineering Calculation Methods for Turbulent Flow", Imperial College Aero. Tech. Note 77-102, 1977.

Brandl, E.F., Reverencic, I., Cartellieri,W. and Dent, J.C., (1979), "Turbulent Air Flow in the Combustion Bowl of a DI Diesel Engine and its Effect on Engine Performance", SAE 790040.

Bray, K.N.C., (1974), "Kinetic Energy of Turbulence in Flames", Univ. of Southampton, AASU rpt. 332.

Butler, T.D., Cloutman, L.D., Dukowicz, J.K., Ramshaw, J.D. and Kreiger, R.B., (1978), "Towards a Comprehensive Model for Combustion in a Direct-Injection Stratified-Charge engine", Proc. General Motors Res. Labs. Symp. on Comb. Modelling in Reciprocating Engines, Nov. 1978.

Caretto, L.S., Gosman, A.D., Patankar, S.V., Potter, R. and Spalding, D.B., (1972), "Two Numerical Procedures for Three-Dimensional Recirculating Flows", Proc. Int. Conf. on Num. Methods in Fluid Dynamics, Paris.

Chong, M.S., Milkins, E.E. and Watson, H.C., (1976), "The Prediction of Heat and Mass Transfer during Compression and Expansion in I.C. Engines", SAE 760761.

Chorin, A.J., (1968), "Numerical Solution of the Navier-Stokes Equations", Math. Comp., 22, p. 745.

Chow, L.C. and Tien, C.L., (1978), "An Examination of Four Differencing Schemes for some Elliptic-Type Convective Equations", Num. Heat Transfer, Vol. 1, p. 87.

Collis, R.C. and Williams, M.J., (1959), "Two-Dimensional Convection from Heated Wires at Low Reynolds Numbers", J. Fluid Mech., Vol. 6, 1959.

Courant, R., Friedrichs, K. and Lewy, H., (1967), "On the Partial Difference Equations of Mathematical Physics", IBM Journal 2, 1967.

Curnow, H.J., (1976), "The Comparison of Computer Speeds using Synthetic Benchmark Programs",Central Computer Agency, Civil Service Department, TSD Memo. No. 5064, Issue 5, Nov. 1976.

Daneshyar, H., Fuller, D.E. and Deckker, B.E.L., (1973), "Vortex Motion Induced by the Piston of an Internal Combustion Engine", Int. J. Mech. Sci.

Dao, K., (1972), "Heat Transfer with Cyclic Pressure Variations in Piston Engines", Ph.D. Thesis, Univ. of Wisconsin.

Dao, K., Uyehara, O.A. and Myers, P.S., (1973), "Heat Transfer Rates at Gas-Wall Interfaces in a Motored Piston Engine", SAE 730632.

Davies, P.O.A.L. and Fisher, M.J., (1964), "Heat Transfer from Electrically Heated Cylinders", Proc. Roy. Soc. A., vol. 280, 1964.

Davies, G.C. and Kent, J.C., (1979), "Comparison of Model Calculations and Experimental Measurements of the Bulk Cylinder Flow Processes in a Motored PROCO Engine", SAE 790290.

Dent, J.C. and Derham, J.A., (1972), "A Method for Checking the Consistency of Velocity Computations from Hot Wire Anemometer Measurements in Variable Density Flows", J. of Phys. E: Scientific Instruments, Vol. 5, (1972).

Dent, J.C. and Derham, J.A., (1974), "Air Motion in 4-Stroke Direct Injection Diesel Engine", Proc. I. Mech. E., Vol. 188, 1974.

Dent, J.C. and Salama, N.S., (1975a), "Turbulence Structure in the Spark Ignition Engine", Paper no. C83/75, I. Mech. E. Conf. on Comb. in Engines, Cranfield.

Dent, J.C. and Salama, N.S., (1975b), "The Measurement of Turbulence Characteristics in an Internal Combustion Engine Cylinder", SAE 750886.

Derham, J.A., (1972), "Air Motion in a Four-Stroke Direct Injection Diesel Engine", Ph.D. Thesis, Loughborough Univ. of Technology.

Dicksee, C.B., (1940), The High-Speed Compression Ignition Engine, Blackie and Son.

Diwakar, R., Anderson, J.D. Jnr., Griffen, M.D. and Jones, E., (1976), "Inviscid Solutions of the Flowfield in an Internal Combustion Engine", AIAA Journal, Vol. 14, No. 12.

Elser, K., (1954), "Der Instationaire Warmeubergung in Diesel Motoren", Mitt. Inst. Thermodyn., No. 15, Zurich, 1954.

Favre, A., (1969), "Statistical Equations of Turbulent Gases, Problems of Hydrodynamics and Continuum Mechanics", Soc. of Industrial and Appl. Math., p. 231.

Fitzgeorge, D. and Allison, J.L., (1963), "Air Swirl in a Road Vehicle Diesel Engine", Proc. I. Mech. E. (Auto. Div.), Vol. 25, 1962-3.

Garner, F.H., Morton, F. and Saundy, J.B., (1961),J. Inst. Petrol, 47, p. 175.

Goldstein, S., (1957), Modern Developments in Fluid Dynamics, Oxford Univ. Press.

Gosman, A.D., Pun. W.M., Runchal, A.K., Spalding, D.B. and Wolfstein, M., (1969), Heat and Mass Transfer in Recirculating Flows, Academic Press, London.

Gosman, A.D. and Pun, W.M., (1974) Lecture notes for a course entitled "Calculation of Recirculating Flows", Imperial College, Mech. Eng. Dept. rpt., Nov. 1974.

Gosman, A.D., Koosinlin, M.L., Lockwood, F.C. and Spalding, D.B., (1975), "Transfer of Heat in Rotating Systems", Imperial College, Mech. Eng. Dept., rpt., HTS/75/12.

Gosman, A.D. and Watkins, A.P., (1976a), "Calculation of Turbulent Heat Transfer in a Closed Piston/Cylinder System", Imperial College, Mech. Eng. Dept. rpt., March 1976.

Gosman, A.D. and Watkins, A.P., (1976b), "Simulation of Flow and Heat Transfer during a Four-Stroke Motored Engine Cycle", Imperial College, Mech. Eng. Dept. rpt., March 1976.

Gosman, A.D. and Johns, R.J.R., (1978a), "Development of a Predictive Tool for In-Cylinder Gas Motion in Engines", SAE 780315.

Gosman, A.D., Johns, R.J.R. and Watkins, A.P., (1978b), "Assessment of a Predictive Method for In-Cylinder Processes in Reciprocating Engines", General Motors Res. Labs. Symp. on Comb. Modelling in Reciprocating Engines, Nov. 1978.

Gosman, A.D., Melling, A., Whitelaw, J.H. and Watkins, A.P., (1978c), "Axisymmetric Flow in a Motored Reciprocating Engine", Proc. I. Mech. E., Vol. 192, No. 11.

Gosman, A.D., Johns, R.J.R., Tipler, W. and Watkins, A.P., (1979), "Computer Simulation of In-Cylinder Flow, Heat Transfer and Combustion: a Progress Report", Proc. 13th CIMAC Conf., Vienna, 1979.

Gosman, A.D. and Johns, R.J.R., (1980), "The Computer Analysis of Fuel-Air Mixing in Direct-Injection Engines", SAE 800091.

Griffen, M.D., Anderson, J.D. Jnr. and Diwakar, R., (1976), "Navier-Stokes Solutions of the Flowfield in an Internal Combustion Engine", paper 76-403, AIAA 9th Fluid and Plasma Dynamics Conf., San Diego.

Griffen, M.D., Diwakar, R., Anderson, J.D. Jnr. and Jones, E., (1978), "Computational Fluid Dynamics applied to Flows in an Internal Combustion Engine", paper 78-57, AIAA 16th Aerospace Sciences meeting, Huntsville, Alabama.

Grigg, H.C. and Syed, H.M., (1970), "The Problem of Predicting Rate of Heat Release in Diesel Engines", Proc. Symp. on Diesel Engine Combustion, I. Mech. E., April 1970.

Gupta, H.C., Steinberger, R.L. and Bracco, F.V., (1978), "Combustion in a Divided-Chamber, Stratified-Charge, Reciprocating Engine: Initial Comparisons of Calculated and Measured Flame Propagation", Proc. 17th Symp. (Int.) on Comb.

Hanjalic, K., (1970), "Two-Dimensional Asymmetric Turbulent Flow in Ducts", Ph.D. Thesis, University of London.

Harlow, F.H. and Welch, J.E., (1965), "Numerical Calculation of Time-Dependent Viscous Incompressible Flow of Fluid with a Free Surface", Phys. of Fluids, 8, p. 2182.

Haselman, L.C. and Westbrook, C.K., (1978), "A Theoretical Model for Two-Phase Fuel Injection in Stratified Charge Engines", SAE 780318.

Hassan, H. and Dent, J.C., (1969), "Correction for Temperature Loading and High Gas Pressure Effects for the Constant Temperature Hot Wire Anemometer", British J. Appl. Phys. (J. Phys. D), Vol. 2, 1969.

Hay, N. and Jones, P.L., (1972), "Comparison of the Various Correlations for Spray Penetration", SAE 720776.

Hellums, J.D. and Churchill, S.W. (1961), "Computation of Natural Convection by Finite Difference Methods", Int. Dev. Heat Transfer, pt. 1, p. 985.

Henein, N.A. and Bolt, J., (1969), "Correlation of Air Charge Temperature and Ignition Delay for Several Fuels in a Diesel Engine", SAE 690252.

Henein, N.A., (1976), "Analysis of Pollutant Formation and Control and Fuel Economy in Diesel Engines", Prog. Energy Comb. Sci., Vol. 1, p. 165.

Hilpert, R., (1933), Forsch. Geb. Ingwes., 4.

Hinze, J.O., (1959), Turbulence, McGraw-Hill, New York.

Hirt, C.W., Cook, J.L. and Butler, T.D., (1970), "A Lagrangian Method for Calculating the Dynamics of an Incompressible Fluid with a Free Surface", J. Comp. Phys., 5, p. 103.

Hirt, C.W., Amsden, A.A. and Cook, J.L., (1974), "An Arbitrary Lagrangian-Eulerian Computing Method for all Flow Speeds", J. Comp. Phys., 14, no. 3.

Householder, A.S., (1964), The Theory of Matrices in Numerical Analysis, Blaisdell, New York.

Humphrey, J.A.C., (1978), "Numerical Calculation of Variable Property Flows in Curvilinear Orthogonal Co-ordinates", Can. J. of Chem. Eng., Vol. 56, Oct. 1978 and Imperial College, Fluids Section rpt.

James, E.H., (1972), "Investigations of Turbulent Flow in the Combustion Chamber of a Spark-Ignition Engine", Ph.D. Thesis, Loughborough University of Technology.

Jayatillaka, C.V.L., (1969), "The Influence of Prandtl Number and Surface Roughness on the Resistance of the Laminar Sub-Layer to Momentum and Heat Transfer", Progress in Heat and Mass Transfer, Vol. 1, Pergamon Press, London.

Johns, R.J.R., (1975), "The Filling and Emptying Cycle Simulation Program for Direct and Indirect Injection Diesel Engines", Perkins Engines rpt. RE/1860/R14.

Jones, W.P. and Launder, B.E., (1972a) "The Prediction of Laminarisation with a Two-Equation Model of Turbulence", Int. J. of Heat and Mass Transfer, 15, p. 301.

Jones, W.P. and Launder, B.E., (1972b), "The Calculation of Low-Reynolds-Number Phenomena with a Two Equation Model of Turbulence", Int. J. Heat and Mass Transfer, Vol. 16, p. 1119, also Imperial College, Mech. Eng. Dept. rpt. HTS/72/13.

Kahn, I.M. and Wang, C.H.T., (1973), "Factors Affecting Emissions of Smoke and Gaseous Pollutants from Direct Injection Diesel Engines", Lucas Eng. Review, Vol. 6, No. 2, Nov. 1973.

Kober, H., (1957), Dictionary of Conformal Representations, Dover Publications Inc.

Kolmogorov, A.N., (1942), "Equations of Turbulent Motion of an Incompressible Turbulent Flow", Izv. Akad. Nauk SSSR Ser. Phys. VI, No. 1-2, 56.

Lancaster, D.R., (1976), "Effect of Engine Variables on Turbulence in a Spark-Ignition Engine", SAE 760159.

Launder, B.E. and Spalding. D.B., (1972) Mathematical Models of Turbulence, Academic Press, London.

Launder, B.E. and Spalding, D.B., (1974), "The Numerical Computations of Turbulent Flows", Computer Methods in Appl. Mech. and Eng., Vol. 3, 1974.

Lee, D.W., (1939), "A Study of Air Flow in Engine Cylinders", NACA rpt. No. 653.

Libby, P.A. and Bray, K.N.C., (1977), "Variable Density Effects in Premixed Turbulent Flames", AIAA Vol. 15, No. 8, p. 1186.

Lyn, W.T., (1963), "Study of Burning Rate and Nature of Combustion in Diesel Engines", Proc. 9th Symp. (Int.) on Comb., p. 1069.

MacCormack, R.W., (1969), "The Effect of Viscosity on Hypervelocity Impact Cratering", AIAA paper 69-354.

Magnussen, B.F. and Hjertager, H., (1976) "On the Mathematical Modelling of Turbulent Combustion with Special Emphasis on Soot Formation and Combustion", Proc. 16th Symp. (Int.) on Comb.

Middlemiss, I.D., (1978), "Characteristics of the Perkins 'Squish Lip' Direct Injection Combustion System", SAE 780113.

Molchanov, L.K., (1953), "On the Problem of Gas Motion and Combustion in a Light Fuel Engine", Trudy Makovwkogo Automil' No-Dorozhnogo Instituta, Autatransizdat, Moscow, 17.

Morse, A.P., (1977), "The Effect of Crank-Angle Broadening on Laser-Doppler Measurements in Reciprocating Engines", Imperial College, Mech. Eng. Dept. rpt. FS/77/18.

Morse, A.P., Whitelaw, J.H.and Yianneskis, M., (1978), "The Influence of Swirl on the Flow Characteristics of a Reciprocating Piston-Cylinder Assembly", Imperial College, Mech. Eng. Dept. rpt. FS/78/41.

O'Brian, G.G., Hyman, M.A. and Kaplan, S., (1951), "A Study of the Numerical Solution of Partial Differential Equations", J. Math. Phys.,29,p. 223.

Patankar, S.V. and Baliga, B.R., (1978), "A New Finite-Difference Scheme for Parabolic Differential Equations", Num. Heat Transfer, Vol. 1, p. 27.

Pope, S.B., (1976), "The Calculation of the Flow Behind Bluff Bodies with and without Combustion", Ph.D. Thesis, University of London.

Pope, S.B., (1978), "The Calculation of Turbulent Recirculating Flows in General Orthgonal Co-ordinates", J. Comp. Phys., 26, p. 197.

Prandtl, L., (1925), "Bericht uber Untersuchungen zur Ausgebildeten Turbulenz", ZAMM, 5, 136.

Prandtl, L., (1945), "Uber ein Neus Formelsystem fur die Ausgebildete Turbulenz", Nachrichten von der Akad. der Wissenschaft in Gottingen.

Raithby, G.D. and Torrance, K.E., (1974), "Upstream-weighted Differencing Schemes and their Application to Elliptic Problems involving Fluid Flow", Computers and Fluids, 2, p. 191.

Raithby, G.D., (1976), "Skew Upstream Differencing Schemes for Problems involving Fluid Flow", Comp. Meth. Appl. Mech. Eng., 9, p. 153.

Reynolds, A.J., (1974), Turbulent Flows in Engineering, Wiley, London.

Reynolds, W.C., (1976), "Computation of Turbulent Flows", Annual Review of Fluid Mechanics, 8, p. 183.

Reynolds, W.C., (1978), "Modelling of Fluid Motions in Engines - An Introductory Overview", Proc. General Motors Res. Labs., Symp. on Comb. Modelling in Reciprocating Engines, Nov. 1978.

Roach, P.J., (1972), Computational Fluid Dynamics, Hermosa Publishers, Albequerque, New Mexico.

Rotta, J., (1951), "Statstiche Theorie nicto-moglner Turbulenz", Zeitsch. f. Physik, Bd. 129, p. 547 and Bd. 131, p. 51.

Runchal, A.K., (1977), "Comparitive Criteria for Finite-Difference Formulations for Problems of Fluid Flow", Int. J. Num. Methods in Eng., 11, p. 1667.

Saffman, P.G., (1977), "Problems and Progress in the Theory of Turbulence", Structure and Mechanisms of Turbulence II, Lecture Notes in Physics 76, Springer Verlag, Berlin.

Schlichting, H., (1968), Boundary-Layer Theory, McGraw-Hill, 6th Edition.

Semenov, E.S., (1958), "Studies of Turbulent Gas Flow in Piston Engines", Otedelenie Technicheskikh Nauk, 8 and NACA tech. Trans. F97, 1963.

Shimamoto, Y. and Akiyama, (1970), "A Study of Squish in Open Combustion Chambers of a Diesel Engine", Bull. of JSME, Vol. 13, No. 63.

Shiozaki, T., Suzuki, T. and Shimoda, M., (1980), "Observation of Combustion Process in D.I. Engine via High Speed Direct and Schlieren Photography", SAE 800025.

Spalding, D.B., (1969), "The Prediction of Two-Dimensional Steady Turbulent Flows", Imperial College, Heat Transfer Section rpt. EF/TN/A/16.

Spalding, D.B., (1972), "A Novel Finite-Difference Formulation for Differential Expressions involving both First and Second Derivatives", Int. J. Num. Methods in Eng., 4, p. 551.

Starkman, E.S. and Newhall, H.K., (1967), "Direct Spectroscopic Determination of Nitric Oxide in Reciprocating Engine Cylinders", SAE 670122.

Stringer, F.W., Clarke, A.E. and Clarke, J.S., (1971), "Spontaneous Ignition of Hydrocarbon Fuels in a Flowing System", Lucas Eng. Rev., Vol. 5, No. 2, Nov. 1971.

Syed, S.A., (1977), "Experimental and Theoretical Investigation of a Horizontal Free Turbulent Diffusion Flame", Ph.D. Thesis, University of London.

Syed, S.A. and Bracco., (1979), "Further Comparisons of Computed and Measured Divided-Chamber Engine Combustion", SAE 790247.

Tabaczynski, R.J., Hoult, D.P. and Keck, J.C., (1970), "High Reynolds Number Flow in a Moving Corner", J. Fluid Mech., 42.

Tennekes, H. and Lumley, J.L., (1973), A First Course in Turbulence, M.I.T. Press.

Tindal, M.J., Williams, T.J. and El Khafaji, A.H.A., (1974), "Gas Flow Measurements in Engine Cylinders", SAE 740719.

Tindal, M.J. and Williams, T.J., (1977), "An Investigation of Cylinder Gas Motion in the Direct Injection Diesel Engine", SAE 770405.

Vinokur, M., (1974), "Conservation Equations of Gas Dynamics in Curvilinear Co-ordinate Systems", J. Comp. Phys., 14(2), p. 105.

Watford, R.W., (1978), "A Method for Orthogonalizing Meshes in Plane Regions and its Application to Discrete Fluids Mechanics Problems", Imperial College, Fluids Section rpt. FS/78/43.

Watkins, A.P., (1973), "Calculation of Flow and Heat Transfer in the Combustion Chamber of a Reciprocating Engine", M.Sc. Thesis, University of London.

Watkins, A.P., (1977), "Flow and Heat Transfer in Piston Cylinder Assemblies", Ph.D. Thesis, University of London.

Whitehouse, N.D., Stotter, A., Goudie, G.O. and Prentice, B.W., (1962), "A Method of Predicting some Aspects of the Performance of a Diesel Engine using a Digital Computer", Proc. I. Mech. E., 176, p. 195.

Witze, P.O., (1976a), "Hot-Wire Measurements of the Turbulence Structure in a Motored Spark-Ignition Engine", AIAA paper no. 76-37, AIAA 14th Aerospace Sciences Conf., Washington.

Witze, P.O., (1976b), "Revised figures for AIAA paper no. 76-37", Private Communication, 1976.

Witze, P.O., (1976c), "Preliminary Hot-Wire Measurements in a Motored Engine with an Axisymmetric Cylinder Geometry", Private Communication.

Witze, P.O., (1977), "Measurements of the Spatial Distribution and Engine Speed Dependence of Turbulent Air Motion in an I.C. Engine", SAE 770220.

Witze, P.O., (1978), "Application of Laser Velocimetry to a Motored Internal Combustion Engine", 3rd Int. Workshop on Laser Velocimetry, Purdue University, 1978.

Witze, P.O., (1979), Revised figures for Witze (1976c), Private Communication.

Wood, W.L., (1974), "Marginal Stability: Experiments with the Diffusion Equation", Finite Element Symposium, Atlas Computer Laboratory.

Woods, W.A. and Ghirlando, R., (1975), "Radial Flow in an Engine Cylinder near the End of Compression", Paper No. C82/75, I. Mech. E. Conf. on Comb. in Engines, Cranfield.

Woschni, G., (1967), "A Universally Applicable Equation for the Instantaneous Heat Transfer Coefficient in the Internal Combustion Engine", SAE 670931.

Yianneskis, M., (1977), "Flow Patterns in Internal Combustion Engines", M.Sc. Thesis, University of London.

Ying, W.M.,(1971), "Fully-Developed Flow with Swirl in Non-Circular Ducts", Ph.D. thesis, University of London.

Zeldovich, Ya. B., Sadovnikov, P. Ya and Frank-Kumenetskii, D.A., (1947), "Oxidation of Nitrogen in Combustion", Acad. of Sci., USSR, Moscow-Leningrad.

NOMENCLATURE

A	coefficient of finite difference equation
A_o	TDC clearance
A_1	amplitude of oscillation
a	area
b	$(z_H^n - z_H^o)/z_H^n$
C_1, C_2, C_μ	turbulence model constants
C_p	specific heat at constant pressure
D	$\partial v/\partial p$
E	turbulence model constant or error
E_a	global activation energy
F	cell face flux
f	spatial weighting factor or under-relaxation factor
G_t	generation rate of turbulence energy
h	stagnation enthalpy
k	turbulent kinetic energy
ℓ	metric coefficient or length scale
Ma	Mach number
$\dot{m}$	mass flow rate
N	normalising quantity
$N_1..N_4$	number of grid lines
P	laminar sublayer resistance
Pe	Peclet number
p	pressure
Q	$(\partial\rho/\partial p)_T$
$\dot{q}$	heat flux
R	momentum equation source term in finite-difference expression with pressure gradient contribution subtracted, residual or gas constant

R_0	cylinder radius
Re	Reynolds number
r	radial co-ordinate or radius of curvature
S	source term in finite difference equation
S_I, S_E	implicit and explicit contributions to S
s	source term in differential equation or distance
s_μ	source term in equation 3.35
T	temperature
t	time
t*	non-dimensional time
t_0	period of oscillation
V	volume
v	velocity
v_a	speed of sound
v_I	instantaneous piston velocity
v_m	mean piston velocity
v_n	normal velocity on ensemble average velocity
v_0	reference velocity
v_τ	friction velocity
w	a vector quantity
X	displacement
x	Cartesian co-ordinate
y	normal distance from boundary
z	axial co-ordinate

Greek Symbols

α	spatial weighting function
β	angle between ζ_1 co-ordinate direction and r = 0 axis or under-relaxation factor adjustment parameter
Γ	turbulent diffusivity
γ	ratio of specific heats
∇	divergence operator
δ	increment
ϵ	dissipation rate of turbulence energy
ζ	curvilinear orthogonal co-ordinate
η	temporal weighting factor
θ	circumferential co-ordinate or crank angle
κ	turbulence model constant or temporal weighting factor
λ	thermal conductivity or Taylor macro length-scale
μ	dynamic viscosity
ν	kinematic viscosity
ξ	dimensionless axial co-ordinate
ρ	density
Σ	summation
σ	Prandtl or Schmidt number
τ	stress
τ_w	wall shear stress
ϕ	a dependent variable
$\overline{\phi}_n$	ensemble averaged value
$\overline{\phi}_t$	time-averaged value - $\overline{\phi}_n$
ϕ'	turbulent fluctuation of ϕ
χ	mass fraction

Subscripts

A	aperture
b	boundary
C	correct
c	any of NSEW, nsew etc.
d	downstream
E	explicit
eff	effective
F	field
f	fluid
g	grid
H	piston
h	stagnation enthalpy
I	initial or implicit
i,j,k,ℓ	co-ordinate directions
ig	ignition
ℓ	laminar
k	turbulence energy
max	maximum
min	minimum
o	cylinder head or reference
P,N,S,E,W	points-of-the-compass notation for grid points
n,s,e,w	
p'	pressure correction
ref	reference
t	turbulent or time
u	upstream

v_i	the i'th component of velocity
w	wall
ε	turbulence energy dissipation rate
ζ_1,ζ_2,ζ_3 1,2,3	co-ordinate directions
ϕ	pertaining to ϕ
-	(underbar) vector quantity

Superscripts

i	iteration
m	time step
n	new time-level
o	old time-level
^	instantaneous
-	(overbar) ensemble averaged
'	fluctuating, (ζ_1',ζ_2',t) co-ordinate system, local correction or modified source term
"	overall correction
+	dimensionless
~	relative to the co-ordinate frame
*	prevailing
**	rms turbulent fluctuation

APPENDIX 1

IMPERIAL COLLEGE OF SCIENCE AND TECHNOLOGY,

FLUIDS SECTION,

MECHANICAL ENGINEERING DEPARTMENT,

LONDON. SW7 2BX

A SIMPLE METHOD FOR GENERATING CURVILINEAR-ORTHOGONAL GRIDS FOR NUMERICAL FLUID MECHANICS CALCULATIONS

A.D. Gosman and R.J.R. Johns

FS/79/23

ABSTRACT

A method is described for producing curvilinear-orthogonal grids suitable for use in numerical calculations of fluid mechanics problems, based on the finite-difference solution of a set of Laplace equations for the physical co-ordinates of the grid. Also described is a technique for treating complex configurations with discontinuous boundaries, involving decomposition into subregions, generation of independent grids for each and then merging into a final, continuous grid for the whole region. The capabilities of the method are illustrated by examples of grids generated for design calculations of flows in reciprocating engines.

Index

1. Introduction

Information about the flow and temperature fields in the complex geometrical configurations found in heat exchangers, nuclear fuel assemblies, gas-turbine and diesel-engine combustion chambers, diffusers, furnaces etc. is of major interest to engineers and designers. Over the past two decades, numerous computer-based prediction methods for such problems have been in the course of development, based on the numerical solution of the governing differential equations of motion and convective transport. However, perhaps more by accident than design, these methods have for the most part been developed thus far within the restrictive framework of computing meshes conforming to simple-orthogonal co-ordinate frames such as the Cartesian and cylindrical-polar systems. As a consequence, the utility of these procedures has been restricted to problems having boundaries which conform to these systems, i.e. to rectangles and circles or sectors thereof whereas few practical configurations, including those just cited, are of this form. The main drawbacks in applying methods based on the simple co-ordinate frames to such configurations are inefficient use of grid mesh points and difficulties in resolving wall boundary layers.

The possibility has long been recognised of formulating numerical solution methods in the context of general curvilinear-orthogonal co-ordinates (see, e.g. Ref.[1]), thus allowing a much greater degree of flexibility and virtually eliminating the problems just mentioned. The present authors and their colleagues have pursued this approach in connection with a variety of problems, including Diesel engine air flow analysis [2], tube heat exchanger performance [3] and analysis of flow in non-circular ducts [4] .and are of the view that it can endow the finite-difference

technique with very nearly the same geometrical flexibility as the more recent finite element method, at perhaps smaller cost.

One of the arguments often marshalled against the use of curvilinear-orthogonal computing grids is that they are difficult to generate. The purpose of the present report is to demonstrate that this is not the case: in particular, it describes a simple method for producing curvilinear-orthogonal meshes for arbitrary simply-connected regions as well as an extension to this which allows more complex, discontinuous regions to be treated. Also presented are techniques to compute certain geometrical properties of the mesh that are typically needed for the finite-difference fluid-mechanics calculations.

2. Contents

In the remainder of this report, section 3 reviews previous work by other researchers on the generation of non-orthogonal, orthogonal and conformal (a subset of orthogonal) meshes. The associated equations and transformations are outlined and the advantages and disadvantages of the alternative approaches are discussed. Sections 4 and 5 respectively detail the method devised here to generate curvilinear-orthogonal grids, and present some sample results for two practical configurations that arise in diesel engine combustion chamber analyses.

3. Previous Research

In recent years, numerical techniques have been devised for solving the differential equations of fluid mechanics when written in terms of general curvilinear-orthogonal (see e.g. Gosman et al [5])

and non-orthogonal (see e.g. Cusolo and Orlandi [6]) co-ordinate systems, thereby allowing a much greater range of boundary configurations to be efficiently handled that has previously been possible. Each approach has its pros and cons, but these will not be discussed here, for the present concern is with the generation of the computing meshes which both require, with special emphasis on the orthogonal systems.

Applications of non-orthogonal co-ordinates for the solution of flow problems are few, primarily because of the complexity of the resulting equations, especially in three dimensions. Amsden and Hirt [7] employ a non-orthogonal grid in their Arbitrary Langrangian-Eulerian (ALE) finite-difference method [8] for fluid flow calculations. The iterative technique they devised for generating the required grids involves initially prescribing a regular mesh and then systematically distorting it such that the exterior nodes are caused to move to the boundaries of the solution domain while the interior nodes are moved to positions given by weighted means of the co-ordinates of their nearest neighbours. The magnitude and direction of the weighting is adjustable so as to prevent excursions of the mesh outside the solution domain as may happen, for example, at convex boundaries. The method is effective and economical, but is restricted to non-orthogonal mesh generation as orthogonality is not prescribed at the boundaries. It is analogous, as will be seen later, to numerical solution of differential equations for the physical co-ordinates of the mesh.

Thom and Apelt [1] were amongst the earliest researchers to produce conformal meshes for fluid mechanics calculations,

equivalent to a potential flow solution for the problem under study. Two alternative methods of generating such meshes were evolved, namely a 'direct' one involving solution of differential equations for the stream function (ψ) field and the orthogonal velocity potential (ϕ) field on a regular Cartesian x~y mesh and an inverse method requiring solution of equations for the x and y co-ordinates on a regular $\psi \sim \phi$ mesh.

In the direct approach, ψ is obtained from an appropriate finite-difference approximation to the Laplace equation:

$$\frac{\partial^2 \psi}{\partial x^2} + \frac{\partial^2 \psi}{\partial y^2} = 0 \qquad (1)$$

in which ψ has known values on two opposing boundaries and zero normal derivative on the other pair. Then, the conjugate function ϕ is found by, for example, integrating the Cauchy-Riemann equations, i.e.

$$\phi_2 - \phi_1 = - \int_1^2 \frac{\partial \psi}{\partial x} dy = \int_1^2 \frac{\partial \psi}{\partial y} dx \qquad (2)$$

Finally, interpolation is used to obtain the x-y co-ordinates of the intersections of the iso-ϕ and iso-ψ lines.

On the other hand, their inverse method involving solution of the Laplace equation for one of the physical co-ordinates, i.e.:

$$\frac{\partial^2 y}{\partial \psi^2} + \frac{\partial^2 y}{\partial \phi^2} = 0 \qquad (3)$$

and integration of the Cauchy-Riemann equations to obtain the other:

$$x_2 - x_1 = \int_1^2 \frac{\partial x}{\partial \phi} d\phi = - \int_1^2 \frac{\partial y}{\partial \psi} d\phi \qquad (4)$$

gives the x and y co-ordinates of intersecting ψ and ϕ lines directly. This approach however has a drawback which is described below.

(5)

The determination of a field of x-y co-ordinates which correspond to prescribed values of ψ or ϕ is equivalent to the mapping process illustrated in fig. 1, where an arbitrary region R in the physical (x-y) plane is transformed into the rectangle R' in the transformed (ψ-ϕ) plane: thus, the point (x_1,y_1) maps to (ϕ_1,ψ_1), (x_2,y_2) to (ϕ_1,ψ_2), (x_3,y_3) to (ϕ_2,ψ_2) and (x_4,y_4) to (ϕ_2,ψ_1). Specification of the physical co-ordinates of the boundaries and the limits on one of the transformed co-ordinates (say ψ_2-ψ_1) is sufficient to determine the other interval (ϕ_2-ϕ_1). Conversely, if (ϕ_2-ϕ_1), (ψ_2-ψ_1) and three of the boundaries in the physical plane are specified, the other physical boundary is a function of the solution. Thus, in Thom and Apelts inverse solution method, the initial specification of a regular ψ-ϕ mesh determines the final shape of the geometry considered as either x or y are functions of the solution and it was noted that the location of grid points on the boundary, which determine the locus of the boundary, sometimes differed from that desired.

This problem was circumvented by Hung and Brown [9] , who used essentially the same method of inverse solution but devised a method for automatically adding or deleting mesh lines in one direction such that the potential (ϕ_2-ϕ_1) was determined as part of the solution. Hung and Brown also examined the accuracy of the final solution by evaluating a residual based upon the satisfaction of the Cauchy-Riemann equations and found the greatest errors where the mesh is coarsest in the physical plane.

Winslow [10] started from the two Laplace equations for the potential and stream function of an irrotational flow:

$$\frac{\partial^2\phi}{\partial x^2} + \frac{\partial^2\phi}{\partial y^2} = 0$$

$$\frac{\partial^2\psi}{\partial x^2} + \frac{\partial^2\psi}{\partial y^2} = 0 \qquad (5)$$

but obtained the inverse form of these by using the general transformations:

$$\frac{\partial\phi}{\partial x} = -\frac{1}{J}\frac{\partial y}{\partial\psi} \quad , \quad \frac{\partial\psi}{\partial x} = \frac{1}{J}\frac{\partial y}{\partial\phi}$$

$$\frac{\partial\phi}{\partial y} = \frac{1}{J}\frac{\partial x}{\partial\psi} \quad , \quad \frac{\partial\psi}{\partial y} = -\frac{1}{J}\frac{\partial x}{\partial\phi} \tag{6}$$

where the Jacobian J of the transformation is given by:

$$J = \frac{\partial x}{\partial\psi}\frac{\partial y}{\partial\phi} - \frac{\partial x}{\partial\phi}\frac{\partial y}{\partial\psi} \tag{7}$$

to yield:

$$\alpha\frac{\partial^2 x}{\partial\phi^2} - 2\beta\frac{\partial^2 x}{\partial\phi\partial\psi} + \gamma\frac{\partial^2 x}{\partial\psi^2} = 0$$

$$\alpha\frac{\partial^2 y}{\partial\phi^2} - 2\beta\frac{\partial^2 y}{\partial\phi\partial\psi} + \gamma\frac{\partial^2 y}{\partial\psi^2} = 0 \tag{8}$$

Here α, β and γ, which are related to the metric coefficients of the transformation, are the quadratic functions:

$$\alpha = \left(\frac{\partial x}{\partial\psi}\right)^2 + \left(\frac{\partial y}{\partial\psi}\right)^2$$

$$\beta = \frac{\partial x}{\partial\phi}\frac{\partial x}{\partial\psi} + \frac{\partial y}{\partial\phi}\frac{\partial y}{\partial\psi} \tag{9}$$

$$\gamma = \left(\frac{\partial x}{\partial\phi}\right)^2 + \left(\frac{\partial y}{\partial\phi}\right)^2$$

Equations (8) and (9) were approximated by finite-difference expressions on a triangular mesh in the ϕ~ψ plane and solved for the physical coordinates. The grids generated by Winslow were non-orthogonal however, as fixed points were chosen to locate the vertices of the triangles at boundaries.

In connection with the above approach, it should be noted that orthogonality requires satisfaction of the Cauchy-Riemann equations which,

under a general transformation become:

$$\frac{\partial x}{\partial \psi} = a \frac{\partial y}{\partial \phi}$$
$$\frac{\partial y}{\partial \psi} = - a \frac{\partial x}{\partial \phi} \qquad (10)$$

where a is the aspect ratio given by:

$$a^2 = \frac{\gamma}{\alpha} \qquad (11)$$

Thus for an orthogonal mesh, equations (8) reduce to:

$$\frac{\partial^2 x}{\partial \phi^2} + a^2 \frac{\partial^2 x}{\partial \psi^2} = 0$$
$$\frac{\partial^2 y}{\partial \phi^2} + a^2 \frac{\partial^2 y}{\partial \psi^2} = 0 \qquad (12)$$

and the central terms in the original versions are therefore redundant. It should also be noted that conformality of the transformation dictates that the aspect ratio is unity and under these circumstances equations (12) reduce to the true Laplacian.

Pope [11] used equations (12) to generate curvilinear-orthogonal meshes for use in the calculation of flow in curved diffusers. The aspect ratio was calculated by integrating the Cauchy-Riemann equations along a selected boundary in the transformed plane; e.g., for a ϕ_1 = constant boundary, a is obtained from:

$$a = - \frac{1}{(y_2 - y_1)} \int \frac{\partial x}{\partial \phi} d\psi \qquad (13)$$

Boundary conditions are required for both x and y at all locations on the perimeter and these were determined from (i) a specification of the boundary loci (i.e. $f(x,y) = 0$) and (ii) by integrating the appropriate conjugate function (eqs. 10). Equations (12) were approximated by a simple five-point finite-difference scheme and

the resulting equations were solved iteratively using a line-by-line method.

Barfield [12] presented a method for producing nearly-orthogonal curvilinear meshes in a least-squares sense, subject to the constraint that mesh lines are matched to specified points around the perimeter of the region. This was achieved by deriving fourth-order equations for the co-ordinates, viz:

$$w_2 \frac{\partial^4 x}{\partial^2\psi\partial^2\phi} + w_1\left(\frac{\partial^2 x}{\partial\phi^2} + a^2 \frac{\partial^2 x}{\partial\psi^2}\right) = 0$$

$$w_2 \frac{\partial^4 y}{\partial^2\psi\partial^2\phi} + w_1\left(\frac{\partial^2 y}{\partial\phi^2} + a^2 \frac{\partial^2 y}{\partial\psi^2}\right) = 0 \qquad (14)$$

where w_1 and w_2 are arbitrarily specified weights. It was found that with $w_1 = 1$ and $w_2 = 0$ (that is, equivalent to eqs. 12) and a prescribed value of a, that meshes would occasionally "spill-over" across convex boundaries, as would be expected from earlier remarks. However, the absence of an orthgonality prescription at the boundaries resulted in non-orthogonal meshes.

Also described by Barfield is a technique to link "sub-regions" together at common boundaries to obtain mappings of more complex shapes; a similar approach is employed in the present work.

A technique for obtaining curvilinear orthogonal grids was developed by Watford [13] which, unlike the methods described so far, allows a strong measure of control over the locations of either the ψ or ϕ grid lines. This is achieved by first generating a non-orthogonal mesh using an explicit algebraic transformation which may be specified so as to optimise the disposition of the chosen set grid lines and then transforming to an orthogonal mesh by finding the orthogonal trajectories of the other set. The latter only requires

non-iterative solution of ordinary differential equations which is a further advantage of the method.

4. Description of the Present Procedure

4.1 Selection of the co-ordinate equations to be solved

As previously mentioned, the generation of an orthogonal mesh can be accomplished either by solving equations (5) for ϕ and ψ on a regular x-y mesh and then interpolating to obtain the x,y co-ordinates of the iso-ϕ and iso-ψ lines or by solving the inverse equations (8) for x and y directly. The latter method has been chosen on the basis that it avoids the need for interpolation of the ϕ-ψ solution. A conformal mesh with the attendant problems already mentioned, notably the tendency for the mesh to stray outside the boundaries, seems undesirable, and experience has shown that this tendency is only partially alleviated by going to a non-conformal mapping with constant aspect ratio. Accordingly, the maximum flexibility will be procured by allowing the aspect ratio to vary from point to point, in a manner which will be determined as part of the mesh generation: thus the basis for the method will be equations (8).

Equation (8) may be expressed in finite-difference form using second-order central differences on a mesh in the transformed plane with uniform* but different spacings $\Delta\psi$ and $\Delta\phi$ in the respective co-ordinate directions as:

*Variable mesh spacing could be used to alter the local grid density, but second-order accuracy would be lost and in any case the same effect can be achieved by the grid selection procedure to be described later.

$$\alpha \left\{\frac{x_E - 2x_P + x_W}{\Delta\phi^2}\right\} + \gamma\left\{\frac{x_N - 2x_P + x_S}{\Delta\psi^2}\right\} = 0 \qquad (15)$$

where the NSEW-P notation is shown in fig. 2. The associated functions (9) for α and γ are also approximated by central differences:

$$\begin{aligned} \alpha &= \left\{\frac{x_N - x_S}{2\Delta\psi}\right\}^2 + \left\{\frac{y_N - y_S}{2\Delta\psi}\right\}^2 \\ \gamma &= \left\{\frac{x_E - x_W}{2\Delta\phi}\right\}^2 + \left\{\frac{y_E - y_W}{2\Delta\phi}\right\}^2 \end{aligned} \qquad (16)$$

Equation (15) may be expressed in the form:

$$A_P x_P = A_N x_N + A_S x_S + A_E x_E + A_W x_W \qquad (17)$$

where the coefficients are given by:

$$\begin{aligned} A_N = A_S &= (x_E - x_W)^2 + (y_E - y_W)^2 \\ A_E = A_W &= (x_N - x_S)^2 + (y_N - y_S)^2 \end{aligned} \qquad (18)$$

An equation similar to (17) may be derived with y as the dependent variable, whose coefficients are also defined by (18). Interlinkage between the equations exists via the coefficients and also the boundary conditions, as described below.

4.2 Boundary Conditions

In essence, the boundary conditions require that the co-ordinate lines linking boundary locations to internal grid points should be orthogonal to the boundary. The method used here to impose this requires only that the boundary be specified in the physical plane

in terms of a discrete or continuous specification of its co-ordinates x^B, y^B, i.e.:

$$f(x^B, y^B) = 0 \tag{19}$$

The approach adopted is to postulate an initial guess of the co-ordinates of the boundary grid nodes and to then refine them by successive iteration on the equations expressing the orthogonality condition. The procedure will be described in conjunction with fig. 3, where $P(x^P,y^P)$ is a typical internal mesh point, $P(x^B,y^B)$ is the 'correct' location of the adjacent boundary point and $P(x^{B*}, y^{B*})$ is an estimate of the latter location. The method requires that the form of the boundary equation (19) is continuous and explicit in the first derivative over the region of interest. This is arranged for situations where the boundary is specified as discrete points by fitting a piecewise parametric cubic polynomial [14] to the (x^B, y^B) boundary co-ordinates, this equation having a continuous first derivative over its length.

The slope of the boundary curve $(\frac{dy}{dx})_{B*}$ evaluated at the approximate nodal location (x^{B*}, y^{B*}) is used to obtain equations for straight lines passing through the internal grid point and the 'correct' location, viz:

$$y^P = - (\frac{dy}{dx})^{-1}_{B*} x^P + C \tag{20}$$

$$y^B = - (\frac{dy}{dx})^{-1}_{B*} x^B + C \tag{21}$$

The points $P(x^B, y^B)$ and $P(x^{B*}, y^{B*})$ are linked, to first-order accuracy, by the equation:

$$(\frac{dy}{dx})_{B*} = \frac{y^{B*} - y^B}{x^{B*} - x^B} \tag{22}$$

Eliminating c between (20) and (21) and y^B using (22), a better approximation is obtained for the coordinate point x^B via

the iteration formula:

$$x^B = \frac{y^{B*} - y^P - x^{B*}\left(\frac{dy}{dx}\right)_{B*} - x^P\left(\frac{dy}{dx}\right)^{-1}_{B*}}{-\left(\frac{dy}{dx}\right)_{B*} - \left(\frac{dy}{dx}\right)^{-1}_{B*}} \qquad (23)$$

This equation may be used to make further refinements to x^B in an iterative fashion. The value of y^B is obtained from the boundary specification, i.e. equation (19). In the case of a horizontal boundary (y = constant), for which $\left(\frac{dy}{dx}\right)^{-1}_B$ is infinite, the latter is replaced by a large number, typically 10^{30}, which effectively sets $x^B \simeq x^P$, the correct solution. For a vertical or near-vertical boundary, equation (23) is replaced by a similar one for y^B, which is arrived at in an analogous fashion.

4.3 Overall solution procedure

There exist a variety of methods available for solving the equation set represented by (17), (23) and their counterparts for y_p, given any boundary configuration (19). The method must perforce be iterative, due to the nature of the boundary treatment outlined above, plus the fact that the equations are non-linear. The method employed here is of the block-iterative variety: specifically, iteration by lines is employed in the Gauss-Seidel manner, as described by Ames [15]. In this, eqn. (17) and its counterpart for y_p are solved alternatively and repeatedly along constant-ϕ and constant-ψ grid lines, the solution being made possible by forcing the equations into a tri-diagonal form, with terms relating to neighbouring lines simply evaluated from prevailing information and temporarily taken as known. After each iteration the x^B and y^B are updated using the boundary formulae and the whole process is repeated until convergence is obtained. Solution

of the tri-diagonal systems is achieved by the simple Gaussian elimination procedure often referred to as the Thomas algorithm also described by Ames [15].

4.4 Accuracy, stability and convergence

The differencing practices employed here for equations (8) and (9) yield a coefficient matrix for the discretised versions (17) which is unconditionally diagonally dominant: this property is known to be a sufficient condition for convergence of a linear system of algebraic equations (see, e.g. Ames [15]), i.e. ones for which the A's are constant. Although the latter is not the case here, experience has shown that the procedure adopted still works satisfactorily without recourse to such measures as under-relaxation.

The accuracy of the solutions obtained can be defined in the present context in terms of the degree of orthogonality of the curvilinear mesh. This is evaluated at each mesh intersection by fitting an equation of the form:

$$y = f(x) = Ax^2 + Bx + C \tag{24}$$

to the intersecting co-ordinate lines in the physical plane and then deducing the angle from:

$$\cos\theta = \frac{1 - (\frac{\partial f}{\partial x})_\phi (\frac{\partial f}{\partial x})_\psi}{(1 + (\frac{\partial f}{\partial x})^2_\phi)^{\frac{1}{2}} (1 + (\frac{\partial f}{\partial x})^2_\psi)^{\frac{1}{2}}} \tag{25}$$

The coefficients A, B and C in eqn. (24) are determined from the requirement that $f(x)$ passes through the intersection point and the adjacent nodes lying on the grid line in question. This method of determining θ is of the same order as the differencing scheme.

Fig. 4 shows the orthogonality error E in degrees at two locations within a 40 x 40 mesh plotted against the number of iterations for a section of curved duct whose shape is shown in fig. 6. The two locations correspond to an inner grid point in the centre of the field ($\psi = \psi_{max}/2$, $\phi = \phi_{max}/2$) and the point at which the maximum value of error in the entire field occurs. In general the location of the latter can and does vary as the solution proceeds. At 250 iterations, a converged solution has been reached and this shows that the inner mesh location has a residual error of less than 1^{o} whilst the maximum error, which occurs at the top right and bottom left regions of the duct where the mesh is relatively sparse, is of the order 3^{o}. The coincidence of the two curves up to approximately 150 iterations indicates that the maximum error in the field occurs at the inner mesh location until a converged solution is approached, that is, the position of maximum error moves from the centre toward the boundary as the solution progresses.

Fig. 5 shows the variation of error with mesh spacing at the central mesh point, with the four results shown being obtained using 40 x 40, 30 x 30, 20 x 20 and 10 x 10 grids, corresponding to $\Delta\phi = \Delta\psi = .25, .33, .5$ and 1 respectively. This diagram confirms that the error decreases with mesh refinement according to an equation of the form:

$$E = K\Delta^{n} \tag{26}$$

where $n \sim 1.7$. The present scheme is therefore of the usual central difference accuracy i.e. approximately 2nd order ($n = 2$), the slight discrepancy probably being caused by the lower accuracy of the boundary solution: no doubt this could be improved, but this was not regarded as a priority in the present study.

5. Practical Applications of the Method

5.1 The Diesel engine combustion chamber

Situations often arise in practice where the boundary configuration does not strictly fulfill all the criteria which are required for a perfectly-orthogonal mesh. The direct-injection Diesel engine combustion chamber is such a case, in which the criteria that the boundary intersections in the x-y plane corresponding to points (ϕ_1,ψ_1), (ϕ_2,ψ_1), (ϕ_1,ψ_2) and (ϕ_2,ψ_2) (see fig. 1) in the ϕ-ψ plane should be orthogonal, is inviolate. It turns out however that the present method can be used in these circumstances if a certain degree of non-orthogonality in the offending regions can be tolerated in the fluid dynamics calculations. This is usually the case, especially when, as in for example [2], the latter are based on integration over finite volumes surrounding each mesh point, and account therefore can be taken of local non-orthogonality if important.

Fig. 7 shows a 32 x 32 mesh generated for such a geometry. The discrete co-ordinates used to define the boundary shape are shown as crosses on the perimeter. The locations labelled (A) and (B) indicate the non-ideal aspects of this configuration: thus at (A), the boundary intersection angle is approximately 30^0, whilst at (B) this angle is 180^0, i.e. the boundary is continuous. The maximum orthogonality errors in the grid occur in these regions and are 5.9^0 and 9.4^0 respectively. In regions not influenced by the non-orthogonal specification, the errors are of the same order as those for the configuration of fig. 6 with a similar number of grid nodes. The computer time required to generate this grid was 10s on a CDC 7600.

5.2 Grid selection and the calculation of geometric data

In this subsection a technique is described for the selection of a computational grid suitable for fluid dynamics calculations from a mesh generated by the method outlined above, and the associated determination of all of the geometric parameters required for such calculations, viz. the cell face areas, volumes, arc lengths, radii of curvature and local angles with respect to a reference plane. The latter is here taken to be the x-axis, which, for an axially symmetric situation is taken to coincide with the centreline.

The necessity for a grid selection procedure arises because the mesh locations in the physical plane are not known á priori and it is not therefore possible to arrange for them to be concentrated for example, in regions of high boundary curvature as required for the fluid dynamics calculations. The method chosen here to overcome this disadvantage is simply to initially generate an excessively fine grid and then to select from this the grid lines which are suitable for the final mesh as illustrated by fig. 8. This is not a perfect solution by any means, nevertheless, it does offer some degree of control over the mesh disposition and is easy to implement.

Concerning the geometric data, the calculations of these are based on the piecewise parametric cubic polynomial fit [14] to the co-ordinate lines, and have proved to provide an accurate method for the necessary integrations. Fig. 9 shows a selected region of the mesh where the continuous lines have been selected for retention and the dashed lines are to be discarded, i.e. the imaginary fluid mechanics control volume is bounded by the continuous lines with vertices ABCD: for the sake of generality the volume is assumed to be a body of revolution centred on the x axis.

The arc lengths ΔS of the volume boundaries are computed from the following relation:

$$\Delta S = \int \{(\frac{dx}{ds})^2 + (\frac{dy}{ds})^2\}^{1/2} \; ds \tag{27}$$

and cell face areas (ΔA) from:

$$\Delta A = \int y\{(\frac{dx}{ds})^2 + (\frac{dy}{ds})^2\}^{1/2} \; ds \tag{28}$$

where y, dx/ds and dy/ds are evaluated from the cubic polynomial equation, and the limits of integration are defined by the mesh intersections AB, BC, CD and DA.

The volume (V) of the region bounded by ABCD is calculated from:

$$V = \frac{1}{2} \S y^2 \frac{dx}{ds} \cdot ds \tag{29}$$

where § indicates integration around the boundary ABCD.

The radii of curvature r_ψ and r_ϕ shown in fig. 9 are given by:

$$\frac{1}{r_\psi} = \frac{1}{\ell_\psi \ell_\phi} \frac{\partial \ell_\psi}{\partial \phi}$$

and: (30)

$$\frac{1}{r_\phi} = \frac{1}{\ell_\phi \ell_\psi} \frac{\partial \ell_\phi}{\partial \psi}$$

where the metric coefficients ℓ_ψ and ℓ_ϕ are defined by and obtained from, for example:

$$(\ell_\psi)_{BC} = \{(\frac{\partial x}{\partial \psi})^2 + (\frac{\partial y}{\partial \psi})^2\}^{1/2}_{BC} = (\frac{\Delta S}{\Delta \psi})_{BC}$$

$$(\ell_\phi)_{AB} = \{(\frac{\partial x}{\partial \phi})^2 + (\frac{\partial y}{\partial \phi})^2\}^{1/2}_{AB} = (\frac{\Delta S}{\Delta \phi})_{AB} \tag{31}$$

Here ΔS_{AB} is for example the arc length along the ψ = const. line between grid points A and B. The above formulae allow a relatively

simple finite difference approximation to be obtained for the mean radii of curvature in terms of the arc lengths joining the vertices, thus:

$$r_{\psi} = \frac{(\Delta S)^2}{\Delta S_{BC} - \Delta S_{DA}}$$

$$r_{\phi} = \frac{(\Delta S)^2}{\Delta S_{AB} - \Delta S_{CD}} \qquad (32)$$

where:

$$(\Delta S)^2 = \frac{1}{4} \{\Delta S_{BC} + \Delta S_{DA}\} \{\Delta S_{AB} + \Delta S_{CD}\} \qquad (33)$$

5.3 Problems requiring multiple mappings: prechamber engine configuration

Certain classes of problems involve complex geometrical configurations such as the Diesel engine combustion prechamber depicted in fig. 10(a), for which the combination of boundary discontinuities and far-from-rectangular shape make mapping into a single rectangular region inappropriate. In this section a method is described whereby such configurations are subdivided into a number of subregions, grids being generated independently for each of these subregions and the interfaces or junctions between them matched to produce continuous grid lines in the physical plane for the entire region. For the example of fig. 10, this approach is equivalent to the mapping of the original configuration of (a), R, to the transformed region of (b), R', where the shape of the latter now conforms more logically to the problem than would a simple rectangle. Points of correspondence between the

x-y and ψ-ϕ planes are indicated in the diagram. This mapping, if attempted directly, is difficult, primarily because it is not known á priori which grid lines map to which boundary.

The generation of the individual grids for the subregions ABCI, IJGH and JDEF is performed in the manner indicated earlier, yielding the result shown in fig. 11. Fig. 12 shows the interface region between these grids in more detail. Although it is possible to formulate the discretised fluid mechanics equations so as to allow solution across these interfaces with their discontinuous grid lines, the organisation of such calculations is considerably simplified if lines are made continuous. Linear interpolation is therefore used to generate additional grid lines in one or both of the adjacent regions in such a way as to procure continuity. The final selected grid, which has been employed for fluid dynamics calculations described in [16], is shown in fig. 13 and a magnification of the junction region is given in fig. 14 showing the now-continuous system. This procedure also lends itself well to interactive computing in conjunction with a graphics terminal.

6. Summary

A simple technique has been described for generating curvilinear-orthogonal meshes to fit complex geometrical configurations and for the deduction therefrom of geometric data required for numerical fluid dynamics calculations based on curvilinear-orthogonal formulations of the equations of motion. The technique relies on direct numerical

solution of Laplace equations for the physical co-ordinates of the grid intersections, with the solution being obtained on a regular rectangular grid in transformed space.

A technique of mapping complex geometries by subdivision into subregions which are subsequently connected has also been described which is both simple and powerful. Both techniques are ideally suited for use on interactive computer graphics systems.

7. Acknowledgement

The authors wish to acknowledge the encouragement and support of the Perkins Engines Co.

8. Nomenclature

A	coefficient of finite-difference equation or area
a	aspect ratio
E	error (degrees)
ℓ	metric coefficient
J	Jacobian (defined by equation 7)
r	radius of curvature
s	path of integration along iso-ψ or iso-ϕ line
S	arc length
V	volume
x	physical co-ordinate
y	" " "

Greek

α	quadratic function (defined by equation 9)
β	" " " " " "
γ	" " " " " "
Δ	increment
∇	Laplacian operator
ψ	transformed co-ordinate
ϕ	" "

Subscripts

ψ	relating to ψ
ϕ	" " ϕ
A,B,C,D	vertices of selected grid
N,S,E,W,P	grid points

Superscripts

P	internal grid point
B	boundary point
*	guessed or intermediate value

9. References

1. Thom, A. and Apelt, C.J. Field Computations in Engineering and Physics. Van Nostrand, 1971.
2. Gosman, A.D. and Johns, R.J.R. "Development of a Predictive Tool for In-Cylinder Air Motion" SAE 780315.
3. Antonopoulos, K., Gosman, A.D. and Issa, R. "Flow and Heat Transfer in Tube Assemblies". Proceedings of 1st International Conference on Laminar and Turbulent Flow. University of Swansea, 1978.
4. Gosman, A.D. and Rapley, C.W. "A Prediction Method for Fully-Developed Flow through Non-Circular Passages". Proceedings of 1st International Conference on Numerical Methods in Laminar and Turbulent Flow, University of Swansea, 1978.
5. Gosman, A.D., Pun, W.M., Runchal, A.K., Spalding, D.B. and Wolfstein, M. Heat and Mass Transfer in Recirculating Flows. Academic Press, 1969.
6. Cusolo, D. and Orlandi, P. "Accuracy in Non-Orthogonal Grid Reference Systems". Proceedings of 1st International Conference on Numerical Methods in Laminar and Turbulent Flow, University of Swansea, 1978.
7. Amsden, A.A. and Hirt, C.W. "A Simple Scheme for Generating General Curvilinear Grids". J. Comp. Phys. 11, 1973, 348-359.
8. Hirt, C.W., Amsden, A.A. and Cook, J.L. "An Arbitrary Lagrangian-Eulerian Computing Method for all Flow Speeds". J. Comp. Phys. 14, 1974, 227.
9. Hung, T.K. and Brown, T.D. "An Implicit Finite-Difference Method for Solving the Navier-Stokes Equations using Orthogonal Curvilinear Co-ordinates". J. Comp. Phys. 23, 1977, 343-363.
10. Winslow, A.M. "Numerical Solution of the Quasilinear Poisson Equation in a Non-Uniform Triangular Mesh". J. Comp. Phys. 2, 1967, 149-172.
11. Pope, S.B. "The Calculation of Turbulent Recirculating Flows in General Orthogonal Co-ordinates". J. Comp. Phys. 26, 1978, 197-217.

12. Barfield, W.D. "An Optimal Mesh Generator for Lagrangian Hydrodynamic Calculations in Two Space Dimensions". J. Comp. Phys. 6, 1970, 417-429.

13. Watford, R.W. "A Method for Orthogonalizing Meshes in Plane Regions, and its Application to Discrete Fluid Mechanics Problems", Imperial College Mech. Eng. Dept. report FS/78/43.

14. McConalogue, D.J. "A Quasi-Intrinsic Scheme for Passing a Smooth Curve through a Discrete Set of Points". The Computer Journal, vol. 13, no. 14, Nov. 1970.

15. Ames, W.F. Numerical Methods for Partial Differential Equations, 2nd ed., Academic Press, New York, 1977.

16. Gosman, A.D., Johns, R.J.R., Tipler, W. and Watkins, A.P., "Computer Simulation of In-Cylinder Flow, Heat Transfer and Combustion: A Progress Report". Proc. 13th CIMAC Conference, Vienna, 1979.

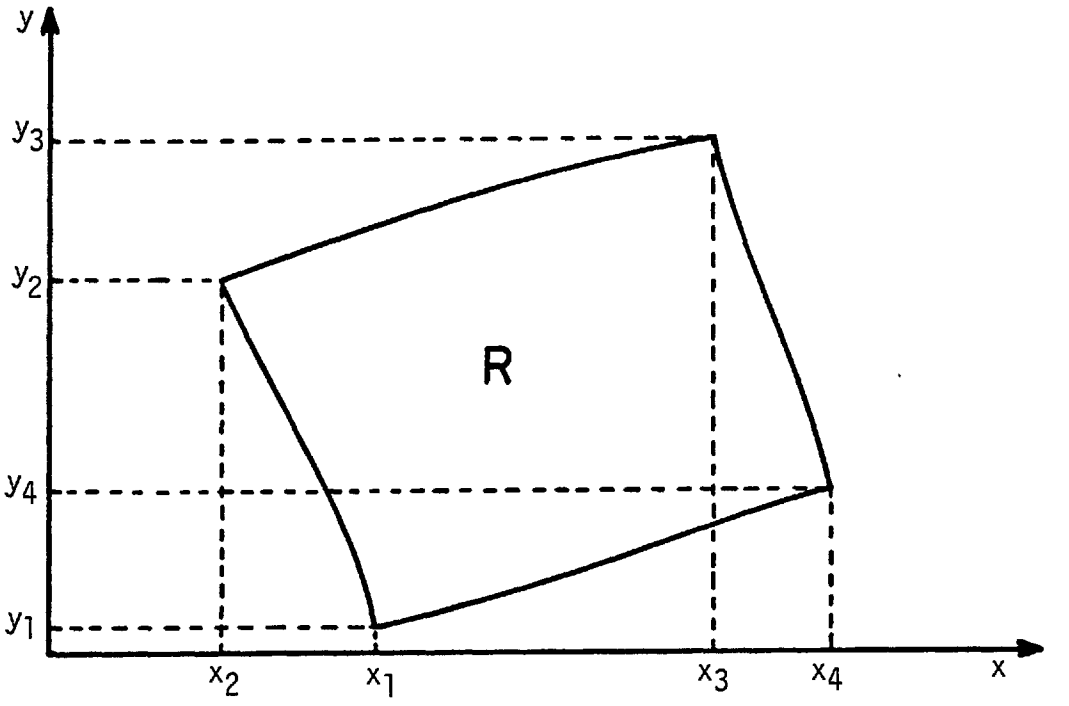

Physical (x-y) plane

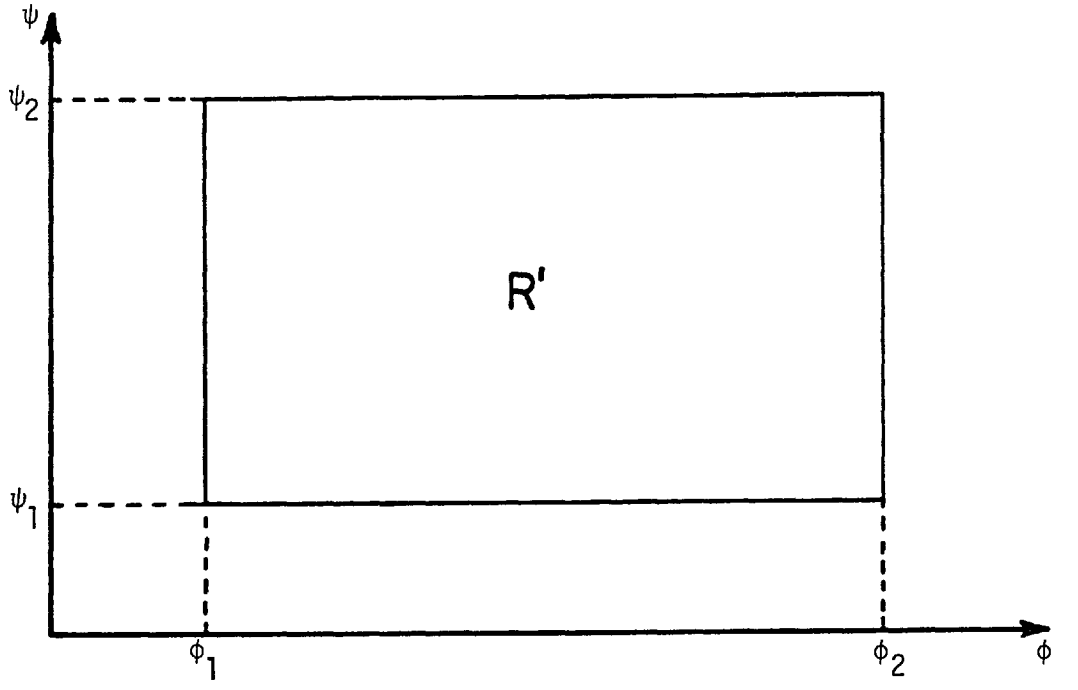

Transformed (ψ-φ) plane

Fig. 1 The mapping process: correspondence between the physical and transformed planes

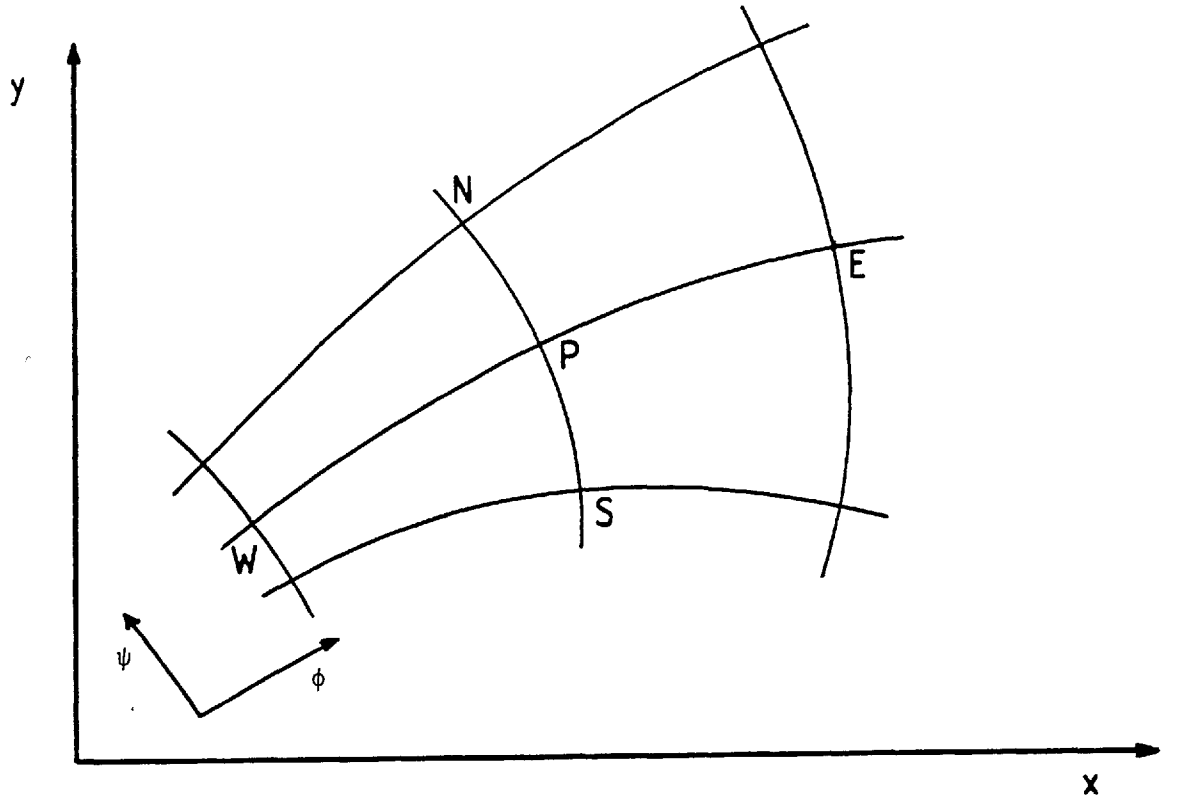

Fig. 2 Grid layout and notation

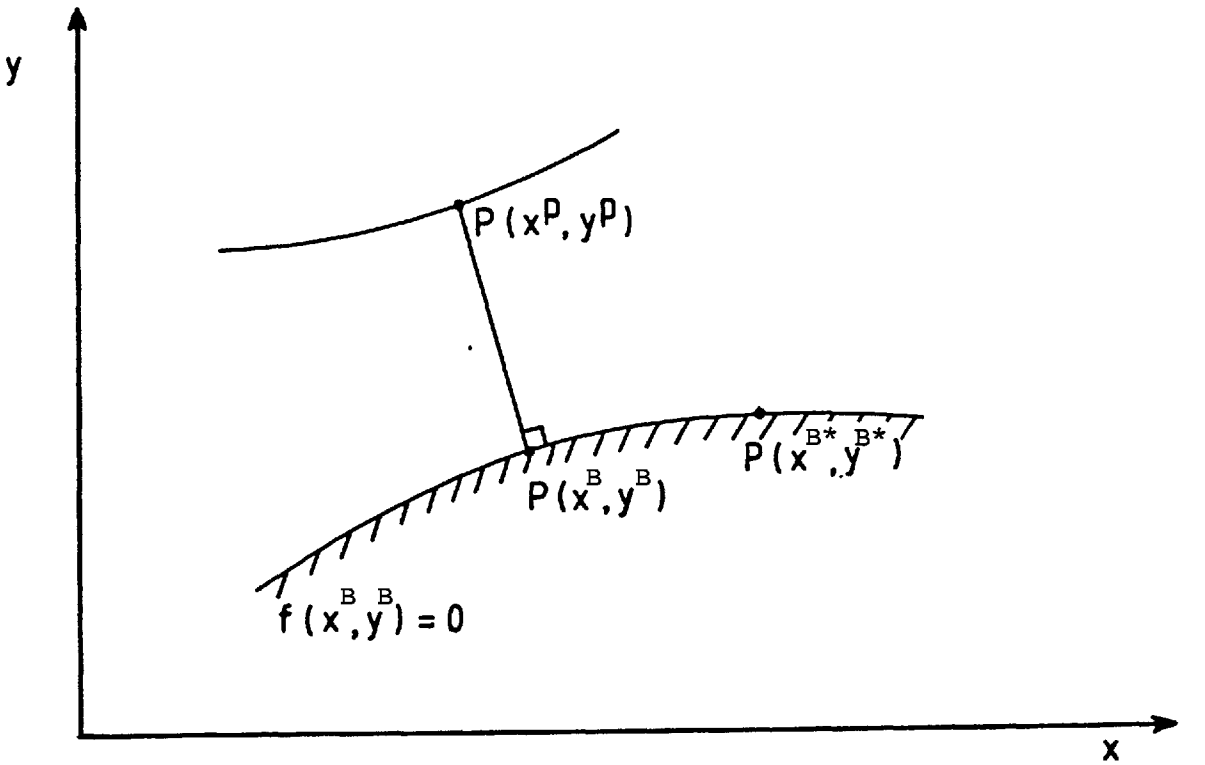

Fig. 3 Boundary calculations: layout and notation

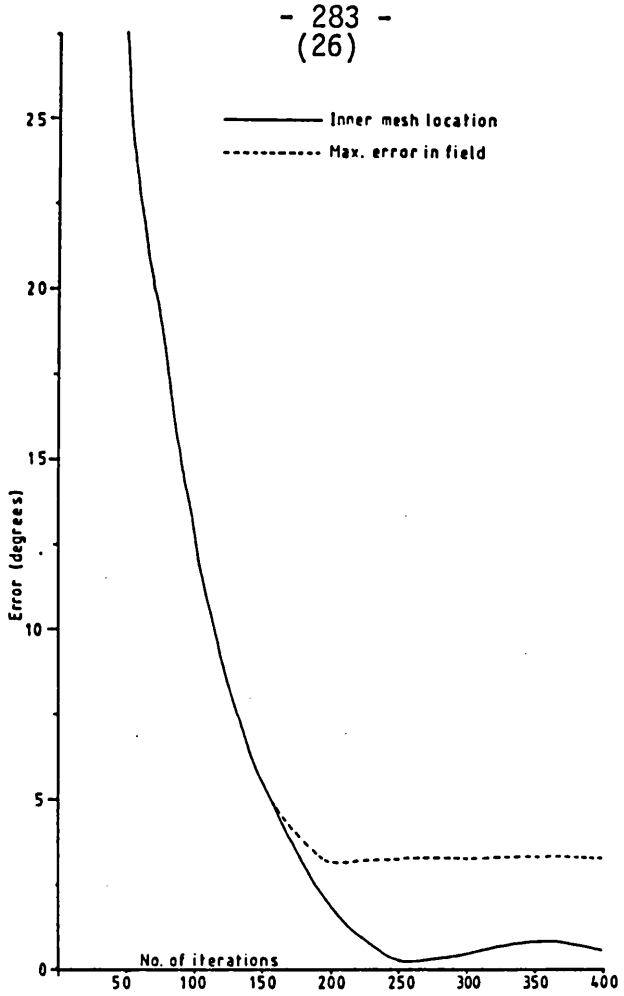

Fig. 4 Variation of orthogonality error with number of iterations for the geometry of fig. 6

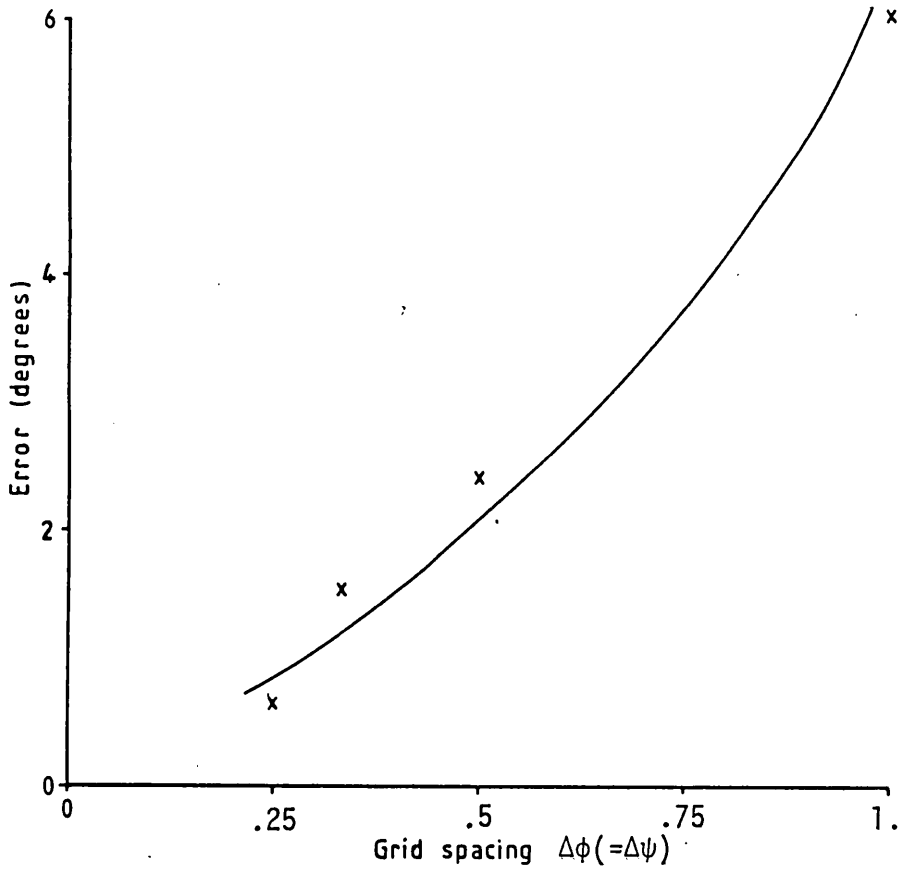

Fig. 5 Variation of orthogonality error with grid spacing for the geometry of fig. 6

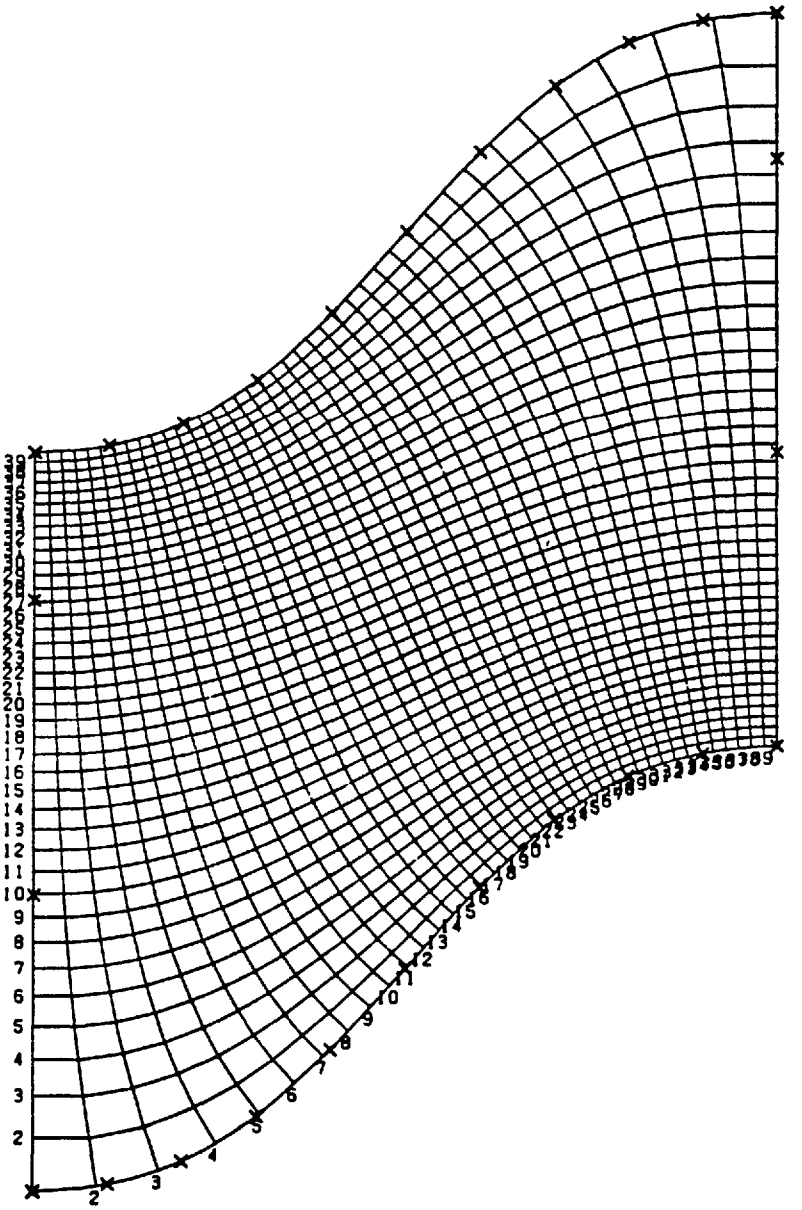

Fig. 6 Orthogonal grid for curved duct

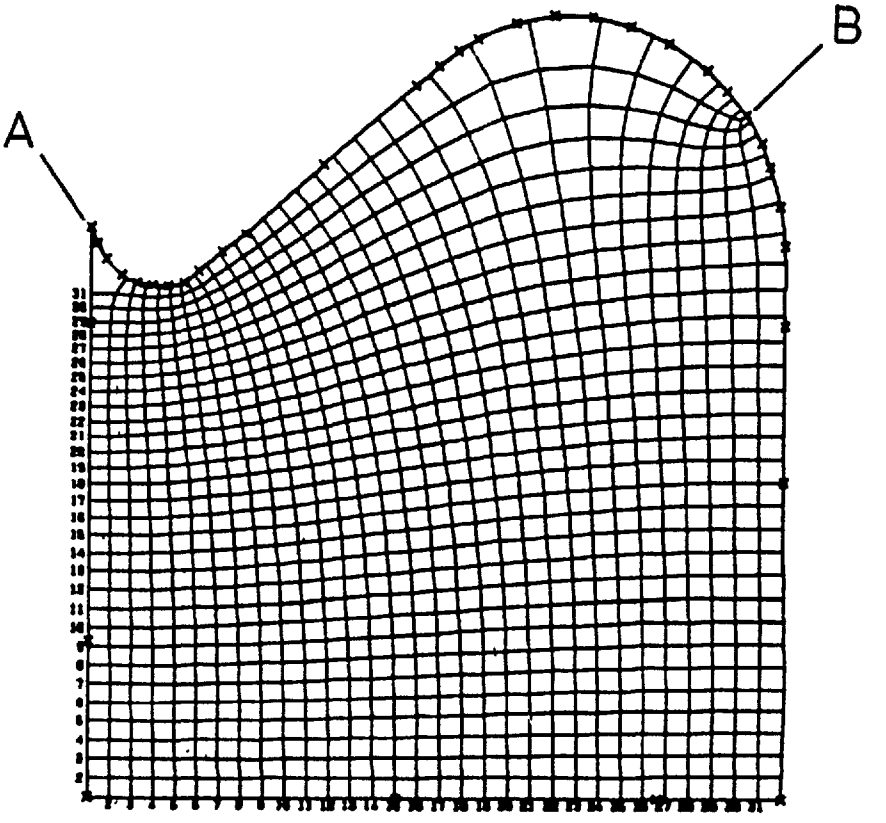

Fig. 7 Diesel piston grid

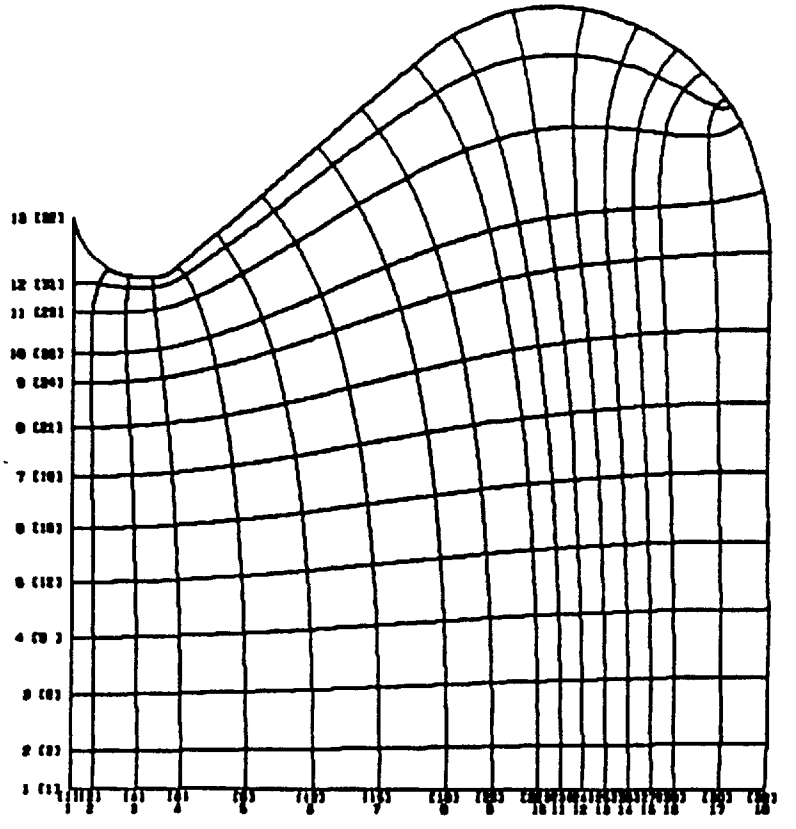

Fig. 8 Selected grid for Diesel piston based on the original grid of fig. 7

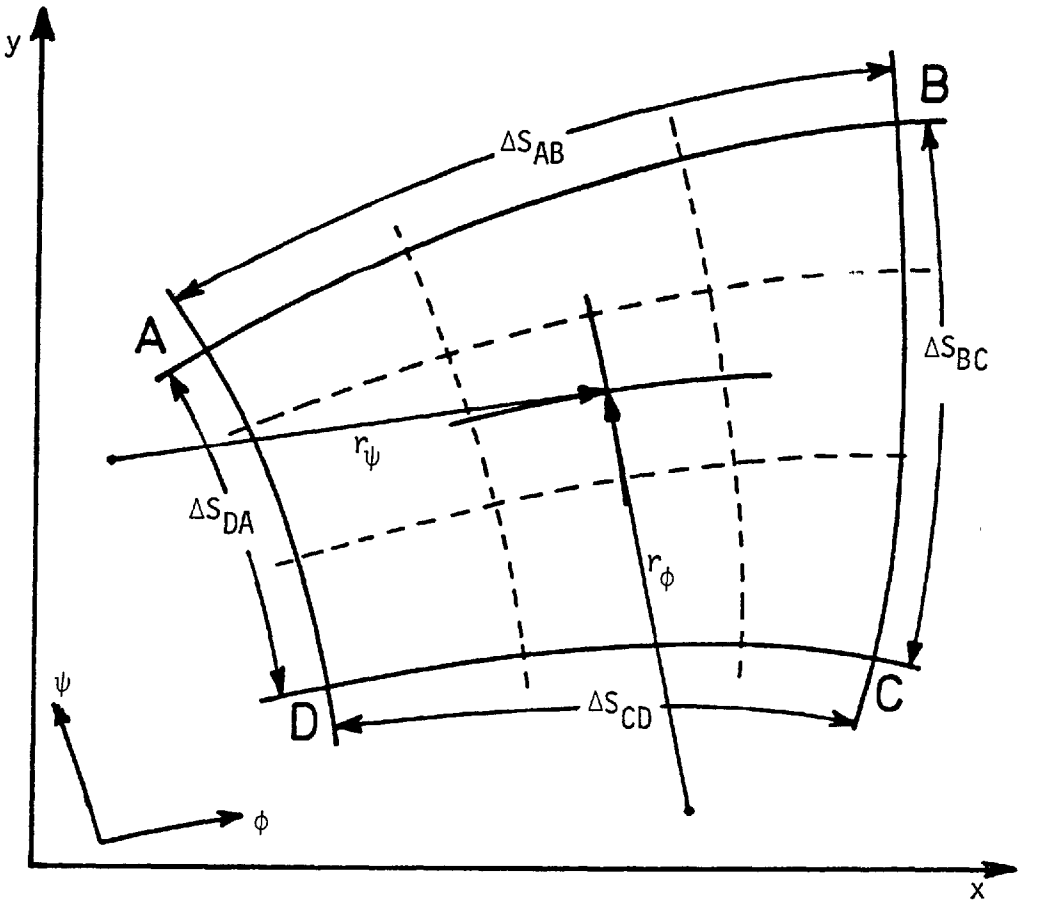

Fig. 9 Grid selection procedure

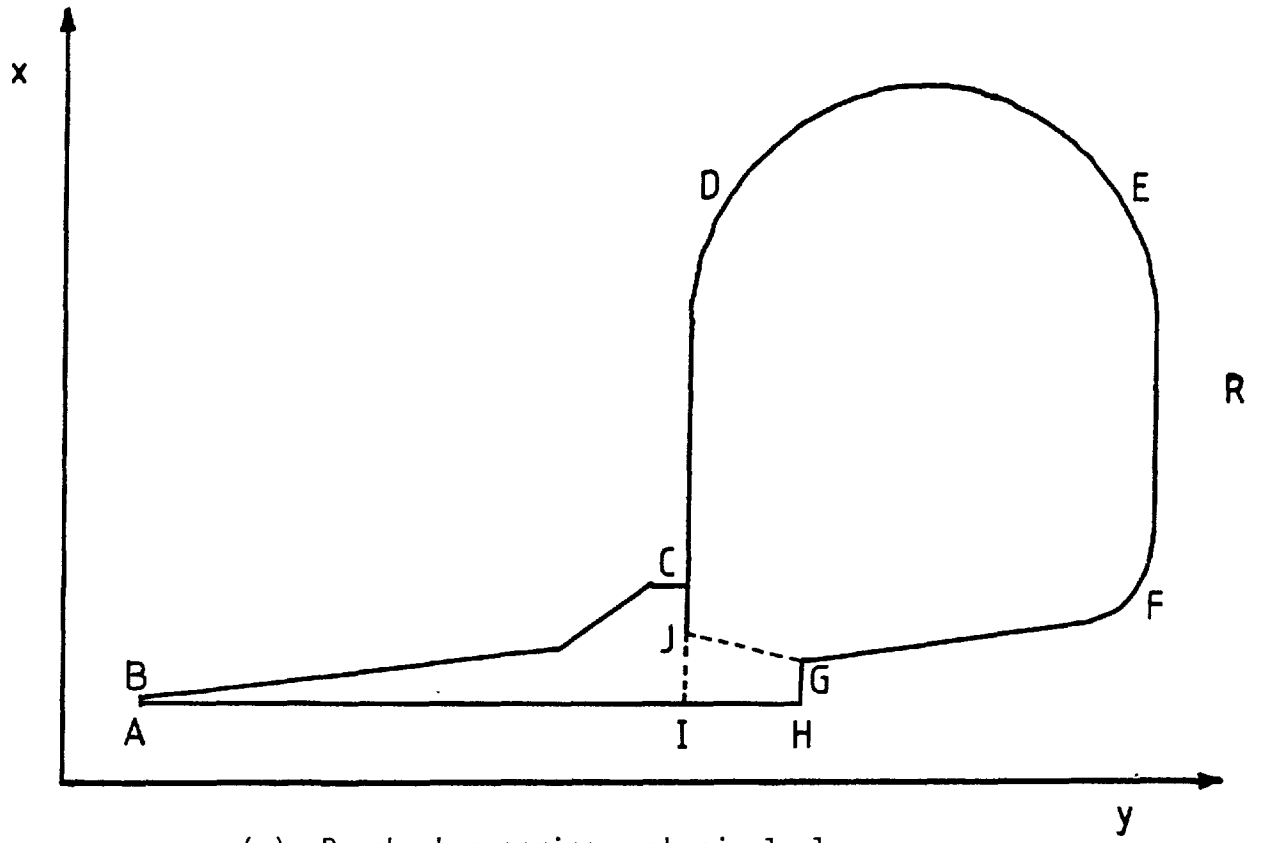

(a) Prechamber engine - physical plane

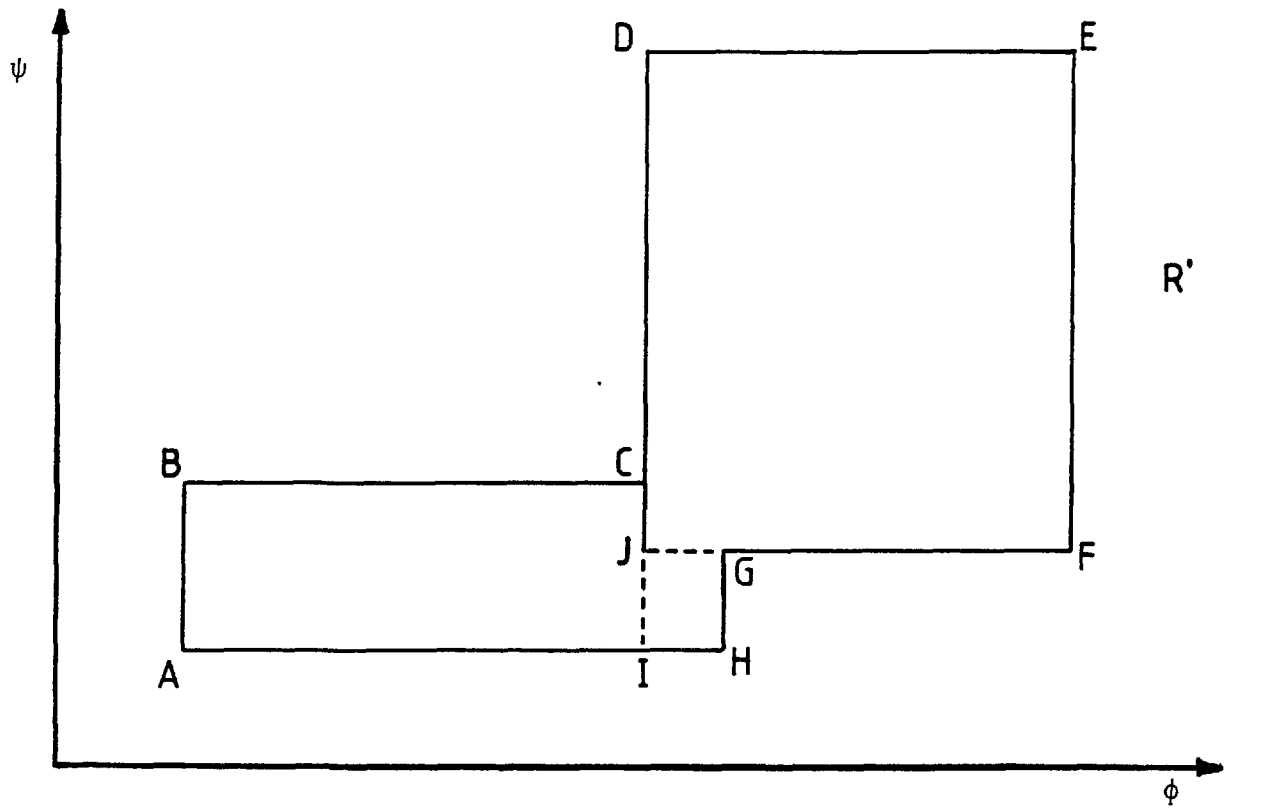

(b) Prechamber engine - transformed plane

Fig. 10 Physical and transformed planes for complex discontinous geometry

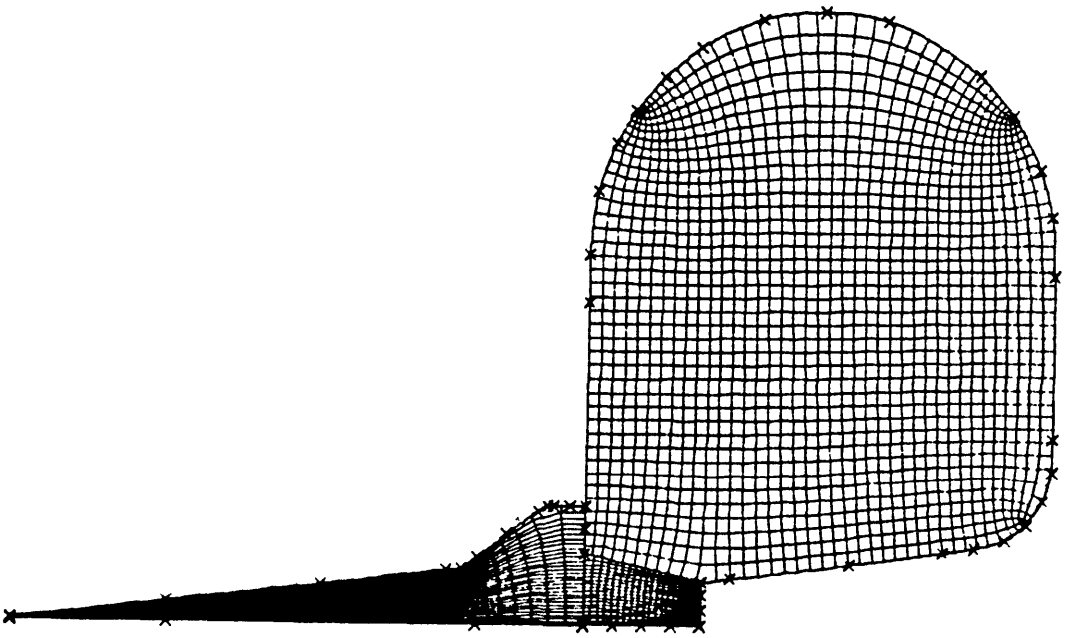

Fig. 11 Division into sub-regions showing independent mappings

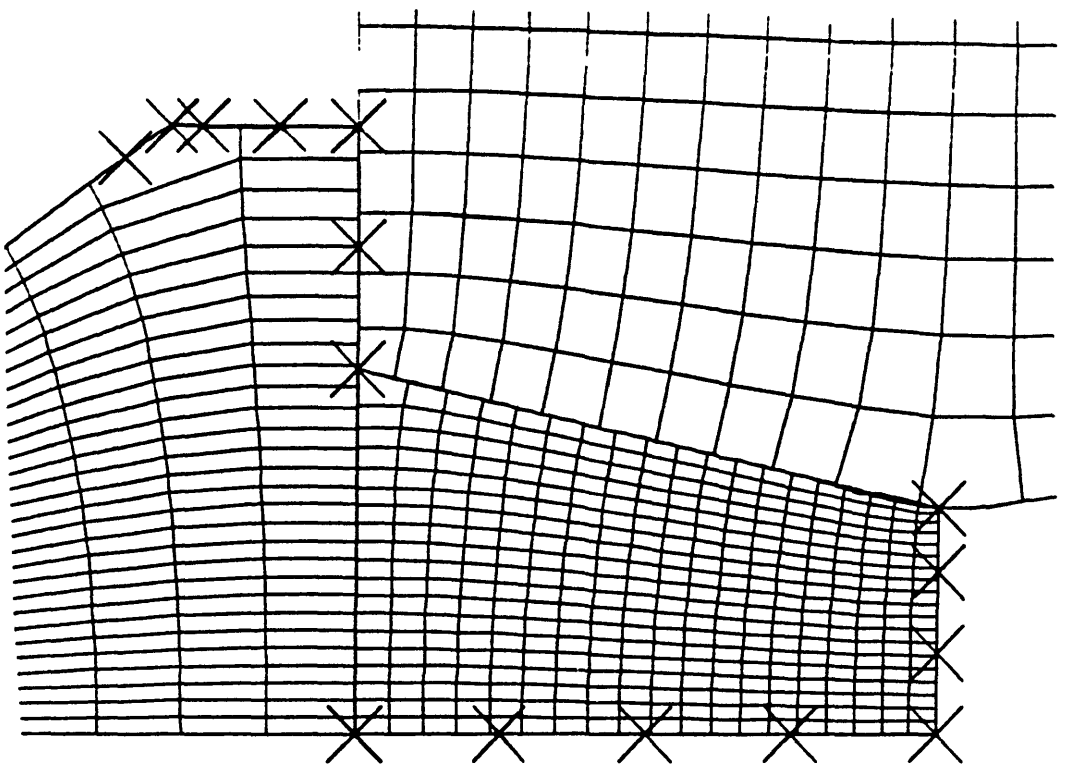

Fig. 12 Magnification of junction region showing discontinuous mesh

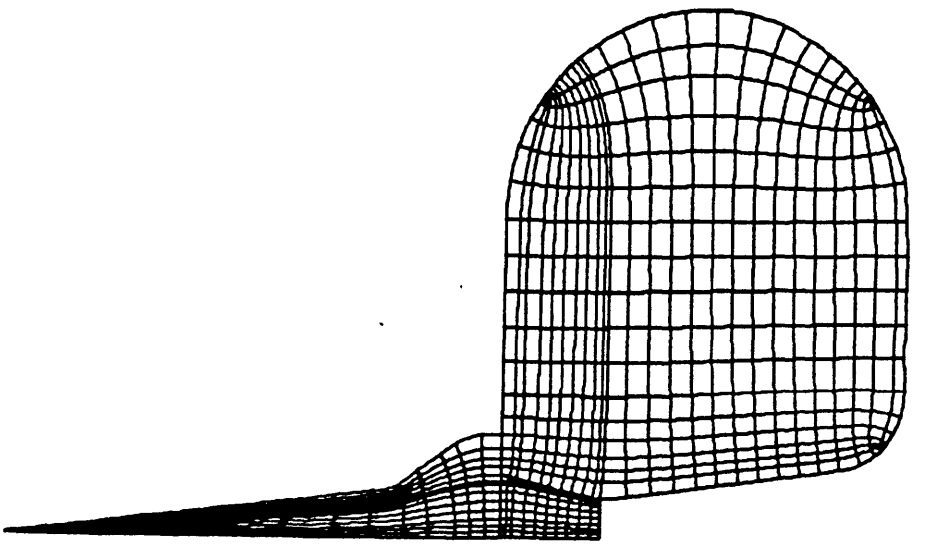

Fig. 13 Result of grid selection

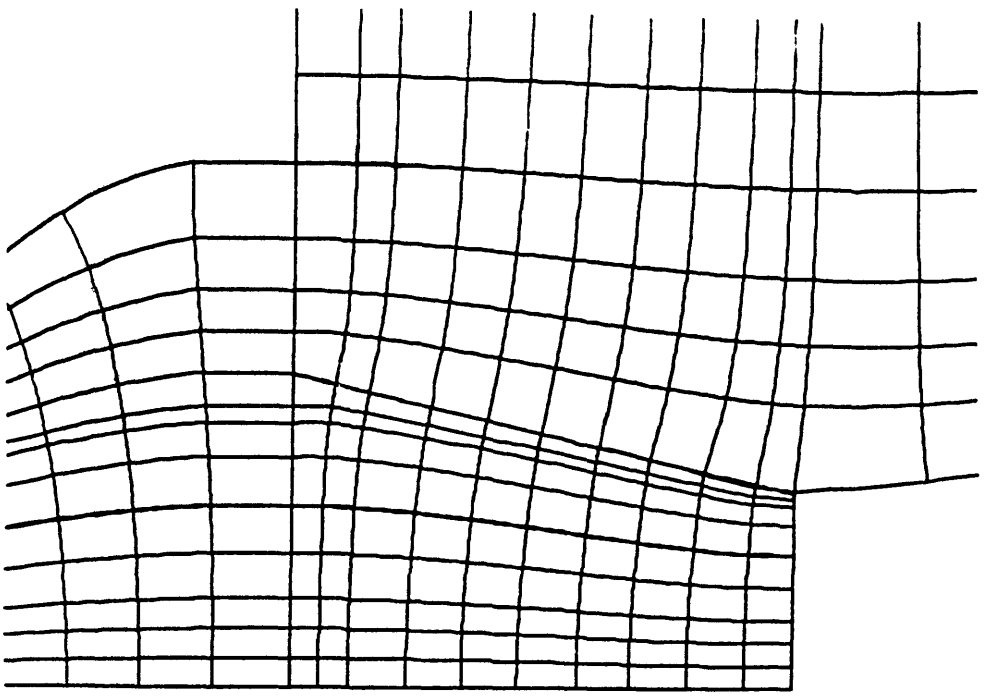

Fig. 14 Magnification of junction region after selection showing continuous mesh

APPENDIX 2

TRI-DIAGONAL MATRIX ALGORITHM (TDMA)

The general finite-difference equation 4.17 and its counterparts for the v_1 and v_2 velocities (4.27 and 4.28) may be expressed in the form:

$$A_P\phi_{ij} = A_N\phi_{i,j+1} + A_S\phi_{i,j-1} + A_E\phi_{i+i,j} + A_W\phi_{i-1,j} + S'_\phi \qquad (A2.1)$$

where the points-of-the-compass notation on the ϕ's have been replaced by the i,j subscripts. Equation A2.1 represents a set of simultaneous algebraic equations equal to the number of values of ϕ in the field to be determined.

If the values of ϕ either side of, for example, line i (i.e. $\phi_{i-1,j}$ and $\phi_{i+1,j}$ for all j) are temporarily regarded as known, then equation A2.1 reduces to:

$$\phi_j = A_j\phi_{j+1} + B_j\phi_{j-1} + C_j \qquad (A2.2)$$

where $$A_j = \frac{A_N}{A_P}, \qquad B_j = \frac{A_S}{A_P}$$

and $$C_j = \frac{(A_E\phi_{i+1,j} + A_W\phi_{i-1,j} + S'_\phi)}{A_P}$$

and the i subscript has been dropped in A2.2. If the ϕ values at the boundaries j = 1 and j = M are known, then, for example:

$$A_1 = B_1 = 0, \; C_1 = \phi_1 \qquad (A2.3)$$

Thus, equation A2.2 represents M-2 equations for which the coefficient matrix is tri-diagonal. The method of solution used here is sometimes

referred to as the Thomas algorithm (Householder, 1964) but is merely a special adaption of the Gaussian elimination procedure, as described below.

If ϕ_j is expressed in terms of ϕ_{j+1} only, thus:

$$\phi_j = A'_j\phi_{j+1} + C'_j \tag{A2.4}$$

then equation A2.2 may be written as:

$$\phi_j = A_j\phi_{j+1} + B_jA'_{j-1}\phi_j + B_jC'_{j-1} + C_j \tag{A2.5}$$

which after rearrangement, becomes:

$$\phi_j = \left(\frac{A_j}{1-B_jA'_{j-1}}\right)\phi_{j+1} + \frac{B_jC'_{j-1} + C_j}{1-B_jA'_{j-1}} \tag{A2.6}$$

Comparison of the coefficients in equations A2.4 and A2.6 gives the recurrence relations:

$$A'_j = \frac{A_j}{1-B_jA'_{j-1}} \quad , \qquad C'_j = \frac{B_jC'_{j-1} + C_j}{1-B_jA'_{j-1}} \tag{A2.7}$$

Using the values for A_1, B_1 and C_1 given by equations A2.3, the recurrence process is started by the values:

$$A'_1 = 0, \qquad C'_1 = \phi_1 \tag{A2.8}$$

and proceeds from j = 2 to M-1.

When the A'_j's and C'_j's have been assembled for the line, the ϕ_j's are determined from equation A2.4.

This process is carried out for each i line in turn by starting at the line adjacent to one boundary (i=2) and marching through the field to the line adjacent to the opposite boundary (i=N-1).

Similar equations to the above can be derived by assuming the ϕ's on adjacent j lines to be known, and the procedure is subsequently repeated for j = 2 to j = M-1.

APPENDIX 3

FORMULATION OF EQUATION 4.114 AS A POWER SERIES

Equation 4.114 is:

$$\frac{T^n}{T^o} = \frac{1 - (\frac{\gamma-1}{\gamma})(\frac{z_H^n}{z_H^o})^{1/2}}{1 - (\frac{\gamma-1}{\gamma})(\frac{z_H^o}{z_H^n})^{1/2}} \qquad \text{(A3.1)}$$

Replacing z_H^o/z_H^n by $(1-b)$ and $(\gamma-1)/\gamma$ by α, equation A3.1 becomes:

$$\frac{T^n}{T^o} = \frac{1 - \alpha(1-b)^{-1/2}}{1 - \alpha(1-b)^{1/2}} \qquad \text{(A3.2)}$$

Multiplying A3.2 by $1 + \alpha(1-b)^{1/2}$ produces, after simplification:

$$\frac{T^n}{T^o} = \frac{1 - \alpha^2 - \alpha b(1-b)^{-1/2}}{1 - \alpha^2 + \alpha^2 b} \qquad \text{(A3.3)}$$

Noting that:

$$(1-b)^{-1/2} = 1 + (-\tfrac{1}{2})(-b) + \frac{(-\frac{1}{2})(-\frac{3}{2})(-b)^2}{2!} + \frac{(-\frac{1}{2})(-\frac{3}{2})(-\frac{5}{2})(-b)^3}{3!} + \ldots \qquad \text{(A3.4)}$$

and:

$$(1 + \frac{\alpha^2 b}{1-\alpha^2})^{-1} = 1 + \frac{(-1)\alpha^2 b}{1-\alpha^2} + \frac{(-1)(-2)}{2!}(\frac{\alpha^2 b}{1-\alpha^2})^2 + \ldots \qquad \text{(A3.5)}$$

equation A3.3 may be expressed as:

$$\frac{T^n}{T^o} = \{1 - (\frac{\alpha}{1-\alpha^2})b \left[1 + \frac{1}{2}b + \frac{\frac{1}{2}\cdot\frac{3}{2}}{2!}b^2 + \frac{\frac{1}{2}\cdot\frac{3}{2}\cdot\frac{5}{2}}{3!}b^3 + \ldots\ldots\right]\}$$

$$\times \{1 - \frac{\alpha^2 b}{1-\alpha^2} + (\frac{\alpha^2 b}{1-\alpha^2})^2 + \ldots\ldots\}$$

$$= \sum_{n=0}^{\infty} (\frac{-\alpha^2 b}{1-\alpha^2})^n - (\frac{\alpha}{1-\alpha^2})b \{1 + \left[\frac{1}{2} - \frac{\alpha^2}{1-\alpha^2}\right]b$$

$$+ \left[\frac{\frac{1}{2}\cdot\frac{3}{2}}{2!} - \frac{\frac{1}{2}\cdot\alpha^2}{1-\alpha^2} + (\frac{\alpha^2}{1-\alpha^2})^2\right]b^2$$

$$+ \left[\frac{\frac{1}{2}\cdot\frac{3}{2}\cdot\frac{5}{2}}{3!} - \frac{\frac{1}{2}\cdot\frac{3}{2}}{2!}\cdot\frac{\alpha^2}{1-\alpha^2} + \frac{1}{2}\cdot(\frac{\alpha^2}{1-\alpha^2})^2 - (\frac{\alpha^2}{1-\alpha^2})^3\right]b^3$$

$$+\ldots\ldots\}$$

$$= \sum_{n=0}^{\infty} (\frac{-\alpha^2 b}{1-\alpha^2})^n - (\frac{\alpha}{1-\alpha^2})b \{1 +$$

$$\sum_{n=1}^{\infty} b^n \{ \sum_{m=1}^{n} \frac{\frac{1}{2}\cdot\frac{3}{2}\cdots(\frac{1}{2}+m-1)}{m!}(\frac{-\alpha^2}{1-\alpha^2})^{n-m}$$

$$+ (\frac{-\alpha^2}{1-\alpha^2})^n\}\}$$

$$= 1 + \sum_{n=1}^{\infty} (\frac{-\alpha^2}{1-\alpha^2})^n b^n \{1 - (\frac{\alpha}{1-\alpha^2})b\}$$

$$- (\frac{\alpha}{1-\alpha^2})b - (\frac{\alpha}{1-\alpha^2}) \sum_{n=1}^{\infty} b^{n+1} \{ \sum_{m=1}^{n} \frac{\frac{1}{2}\cdot\frac{3}{2}\cdot\ldots\cdot(\frac{1}{2}+m-1)}{m!}(\frac{-\alpha^2}{1-\alpha^2})^{n-m}\}$$

(A3.6)

The coefficients of this series for b, b^2 and b^3 are as follows:

b:

$$\frac{-\alpha}{1-\alpha} = -(\gamma-1) \qquad \text{(A3.7)}$$

b^2:

$$\frac{\alpha(2\alpha-1)}{2(1-\alpha)^2} = \frac{1}{2}(\gamma-1)(\gamma-2) \qquad \text{(A3.8)}$$

b^3:

$$\frac{-\alpha(8\alpha^2 - 9\alpha + 3)}{8(1-\alpha)^3} = \frac{-(\gamma-1)(2\gamma^2 - 7\gamma + 8)}{8} \qquad \text{(A3.9)}$$

Taking a value $\gamma = 1.4$, coefficients A3.7 to A3.9 have the numerical values given in table 4.1.

APPENDIX 4

Technical Paper Series

780315

Development of a Predictive Tool for In-Cylinder Gas Motion in Engines

A. D. Gosman and R. J. R. Johns

Imperial College

Congress and Exposition
Cobo Hall, Detroit
February 27-March 3, 1978

Society of Automotive Engineers

SOCIETY OF AUTOMOTIVE ENGINEERS, INC.
400 COMMONWEALTH DRIVE
WARRENDALE, PENNSYLVANIA 15096

780315

Development of a Predictive Tool for In-Cylinder Gas Motion in Engines

A. D. Gosman and R. J. R. Johns
Imperial College

1. BACKGROUND

IT IS GENERALLY accepted that air motion and turbulence in diesel engine cylinders are very influential on the combustion process, as is exemplified by the studies reported in (1,2). Previous work on air motion in diesel engines has analysed two main aspects, namely the induction-induced swirl and the compression-induced squish. Fitzgoerge and Allison (3) developed a method for predicting the end of compression swirl in the bowl of a direct-injection engine. Their flow model consists essentially of two rotating, coaxial cylinders of air, one in the piston bowl and the other in the cylinder: solid body rotation is assumed to prevail in each region. Exchange of angular momentum is postulated to occur between the two regions due to the displacement of the fluid by the piston, and all shear effects are neglected. As a consequence of the lower mean radius of gyration of the piston bowl region, the swirl speed therein increases as TDC is approached. Input data in the form of measurements of the flow rate and swirl level of the incoming air are required by the method, which integrates this information over the induction period to obtain the swirl level at the time of inlet valve closure. Computations are then continued to TDC and comparisons of the TDC swirl levels produced by different port configurations are then possible. This approach was further developed by Dent and Derham (4) to allow for frictional affects at the surfaces of the cylinder and piston. They made comparisons between results from the theory and experiment with which they found acceptable agreement.

Fitzgeorge and Allison also generalised a method due to Loeffler (5) to allow predictions of the squish velocity variation near TDC. This method assumes that the flow in the annulus formed between the piston crown and cylinder head near TDC is one dimensional and in the assumed absence of spatial pressure gradients and frictional affects can be calculated from mass conservation considerations alone. Dent and Derham (4) made comparisons between predictions of the radial velocity distributions in the annulus with this method and experiment

ABSTRACT

A method is described of calculating the flow, temperature and turbulence fields in cylinder configurations typical of a direct-injection diesel engine. The method operates by solving numerically the Navier Stokes equations that govern the flow, together with additional equations representing the effects of turbulence. A general curvilinear-orthogonal grid that translates with the piston motion is used for the calculations in the complex-shaped piston bowl, whilst an expanding/contracting grid is used elsewhere. Predictions are presented showing the evolution of the velocity and turbulence fields during the compression and expansion phases of a motored engine cycle, for various shapes of axisymmetric piston bowl and various initial swirl levels. These results illustrate the strong influence of these factors on the TDC flow structure.

0148-7191/78/0227-0315$02.50

and again quite reasonable agreement was found. Shimamoto and Akyama (6) refined the Fitzgeorge and Allison squish model to allow for leakage past the piston rings and heat transfer from the cylinder wall. They found that the combined affect was most apparent between 20° BTDC and TDC and could decrease the maximum squish velocity by up to 10%.

More recently, the advances made in numerical methods and digital computers have allowed solutions of the Navier-Stokes equations to be obtained for complex flow situations similar in some respects to those encountered in engine cylinders. Watkins (7) obtained finite difference solutions to the flow equations for axisymmetric laminar flow in a closed cylinder equipped with a flat-topped piston, using a novel grid that expands and contracts with the piston motion. Chong et al (8) used an early variant of this method to predict the laminar in-cylinder flow for the case of a piston with a cylindrical bowl, although the accuracy of their predictions was impaired by the particular computational grid which they employed. Diwakar et al (9) made calculations for a plane two-dimensional representation of a piston-in-cylinder arrangement that incorporates a valve: they produced predictions for both inviscid and laminar flows using the explicit finite-difference procedure of MacCormack (10) in conjunction with an expanding/contracting grid. In an extension of the work of (7), Gosman and Watkins (11) included in their model mathematical representations of the effects of turbulence and a centrally located valve operated in a four-stroke cycle. They obtained fair qualitative agreement with experimental data for this situation.

Interest in the development of low-emissions enginees has stimulated work on predictive techniques for divided-chamber spark-ignition designs, although of course the divided-chamber arrangement has been used for some time in in-direct-injection Diesel engines. Boni et al (12) have made predictions for the compression and expansion phases of a spark-ignited prechamber arrangement using a version of the 'ICED-ALE' method of Hirt et al (13) in which the combustion process was represented by a multi-step reaction scheme, but a very crude representation of turbulence effects was employed.

Although the ultimate goal of these developments is a full computer simulation of the in-cylinder processes of reciprocating engines, the path will be a long and difficult one, stretching the capabilities of analyst and computer alike. It is important therefore that the simpler representations are exploited to the maximum degree. Towards this end, in the present study the method of Gosman and Watkins (11) has been extended to allow fairly realistic axi-symmetrical representations of the flow in piston-bowl combustion chamber configurations of the kind commonly found in direct-injection Diesel engines and in certain designs of stratified-charge spark-ignition engines. Predictions are displayed of the flow evolution during the compression and expansion strokes under motored conditions for various bowl configurations and various levels of swirl.

1.1 CONTENTS - Sections 2 and 3 of the paper are devoted to an outline of the method of prediction. Section 2 describes the mathematical problem in terms of the differential equations to be solved and shows how these can be expressed in a form suitable for solution in the presence of arbitrarily-shaped and moving boundaries, while Section 3 presents the finite-difference forms of the equations and describes how these are solved.

Some results obtained with the method are presented in Section 4, which commences with a sequence of plots showing the evolution of the flow and turbulence fields produced by a simple cylindrical bowl in the absence of swirl. There follows selected predictions from parametric studies of the effects of BDC swirl level and piston bowl configuration on the flow structure. Finally, some comparisons are made between the present predictions of squish and swirl velocities and those obtained from the simple theories mentioned earlier. The main conclusions of the study are summarised in Section 5.

2. MATHEMATICAL MODEL

2.1 COORDINATE FRAME AND DIFFERENTIAL EQUATIONS - The present method solves the differential conservation equations governing the flow and heat transfer by numerical, finite-difference means. As is usual with numerical methods for partial differential equations, a computational grid is superimposed upon the flow field and solutions are obtained at the grid line intersections.

The flow domain for a closed cylinder with a bowl-in-piston arrangement such as that of Fig. 1 can conveniently be divided into a disc-shaped region between the plane of the piston crown and the cylinder head, and the region inside the piston bowl. This subdivision allows an arrangement in which a rectilinear grid that expands and contracts with the piston motion in the manner of the original method (11) is used for the outer disc-shaped region, whilst a general curvilinear orthogonal grid is fitted to the often-complex shape of the piston bowl, this latter grid translating with the piston motion. The curvilinear grid is obtained by numerical solution of two coupled Laplace equations for the coordinates of the intersections (14). An example of a complete grid is shown in Fig. 1.

The choice of an orthogonal co-ordinate frame instead of an arbitrary non-orthogonal system was motivated by the relative simplicity of the orthogonal-coordinate form of the governing equations and hence the smaller number of computer operations required to solve them. A further advantage is the ease with which

*Numbers in parentheses designate References at end of paper

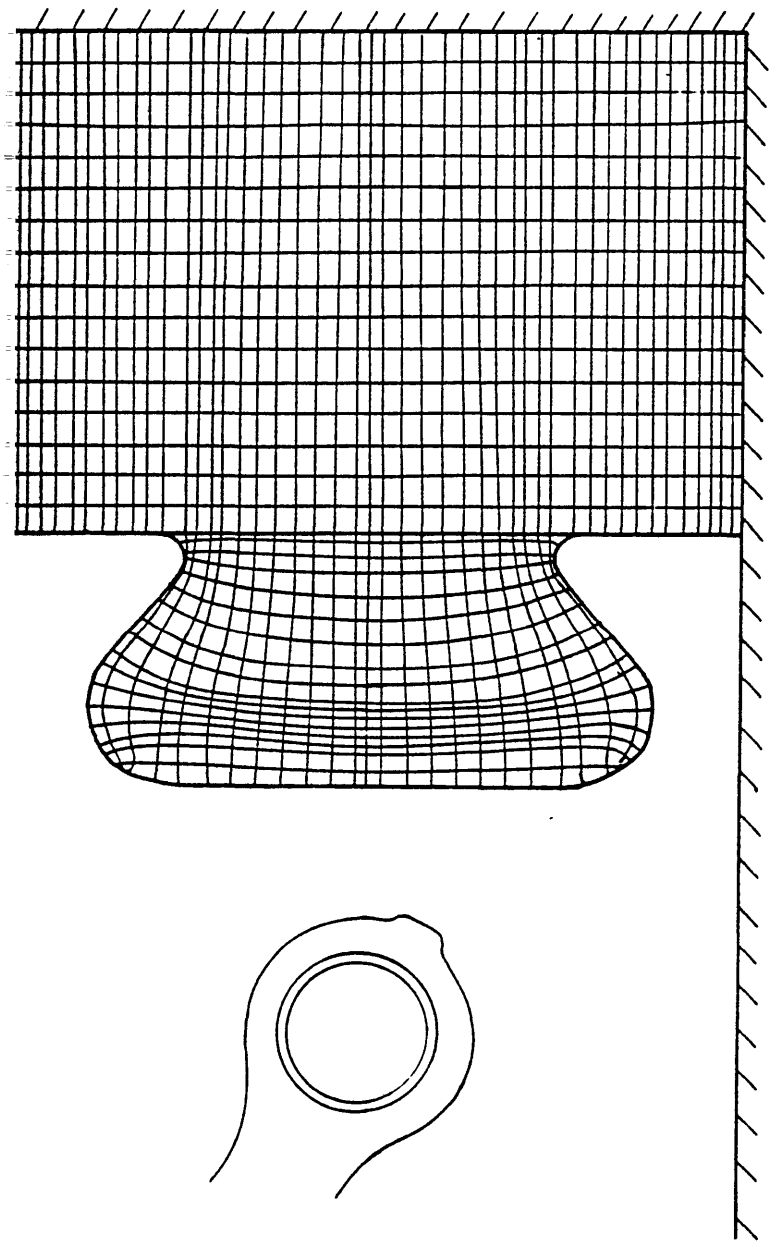

Fig. 1 - A typical grid arrangement

boundary conditions may be imposed. It has been found that curvilinear grids can be easily produced for a wide selection of chamber shapes using methods such as that described in (14).

The flow is assumed to be governed by the ensemble-averaged conservation equations of mass, momentum and energy. Although axial symmetry is assumed, the gas may be swirling. In the absence of turbulence, the problem may then be described by five simultaneous non-linear partial differential equations, the dependent variables being axial velocity* (v_1), radial (or squish) velocity (v_2), circumferential (or swirl) velocity (v_3), pressure (p) and stagnation enthalpy ($h \equiv c_v T + p/\rho + (v_1^2+v_2^2+v_3^2)/2$) where c_v, T and ρ are respectively the constant-volume specific heat, temperature and density of the fluid.

When turbulence is present, as is the case in normal circumstances, information is needed about the turbulence structure (which is of interest in its own right in connection with combustion) and its effects on the 'mean' flow. This information can be obtained by employing a 'turbulence model', which consists of additional equations connecting the turbulent fluxes of mass, momentum and energy to known or calculable quantities. Turbulence modelling is a subject on which much has been written (see e.g. (15)) and available models range in complexity from the simple mixing length theory of Prandtl to the differential equations for the turbulent Reynolds stresses themselves. It is not possible to discuss here the pros and cons of the various options: suffice it merely to state that firstly, whatever model is selected must be capable in principle of realistically representing an unsteady turbulent recirculating flow, and secondly, the model must place minimal additional demands on computing time and storage. The representation that currently seems to best satisfy these requirements is one comprising of two differential equations whose dependent variables are the ensemble-averaged kinetic energy of turbulence (k) and its dissipation rate (ε) (see (12) for further details). Accordingly the 'k-ε' representation has been used in the present study, although it should be stressed that this is only a tentative choice until suitable experimental data emerge to allow a proper assessment.

The resulting, now seven, differential equations may be generalised for compactness into a single equation, written here in terms of a general, moving, curvilinear-orthogonal, axisymmetric coordinate frame:

$$\frac{\partial}{\partial t}(\ell_1 \ell_2 r\rho\phi) + \frac{\partial}{\partial \xi_1}(\ell_2 r\rho \tilde{v}_1 \phi)$$

$$+ \frac{\partial}{\partial \xi_2}(\ell_1 r\rho \tilde{v}_2 \phi) - \frac{\partial}{\partial \xi_1}(\ell_2 r\Gamma_\phi \frac{\partial \phi}{\partial \xi_1})$$

$$- \frac{\partial}{\partial \xi_2}(\ell_1 r\Gamma_\phi \frac{\partial \phi}{\partial \xi_2}) - \ell_1 \ell_2 r s_\phi = 0 \qquad (1)$$

where: ϕ may stand for any of $\tilde{v}_1$, $\tilde{v}_2$, $\tilde{v}_3$, p, h, k and ε, the tilda superscript denoting a velocity relative to that of the coordinate frame; Γ_ϕ and s_ϕ are respectively the 'eddy diffusivity' and 'volumetric source rate' of entity ϕ: t stands for time; ξ_1 and ξ_2 are curvilinear coordinates in planes containing the symmetry axis; and ℓ_1 and ℓ_2 are corresponding metric coefficients, to be defined later.

*The terms "axial" and "radial" are only strictly applicable for the region outside the piston bowl: within the latter v_1 and v_2 are defined along the curvilinear coordinate directions as shown in Fig. 2.

4

Thus, for example, when ϕ is replaced by h, Γ_ϕ has the significance of an eddy conductivity and s_ϕ contains pressure-work and other terms (see, e.g (11)).

In general the metric coefficients, which connect increments of distance ds in the physical plane to increments in the ξ coordinates via:

$$ds^2 = \ell_1 d\xi_1^2 + \ell_2^2 d\xi_2^2 \qquad (2)$$

may be defined in many ways. This flexibility allows the coordinate systems required for the present application to be constructed with ease, as will be explained below.

For the region within the bowl, where the coordinate frame simply translates with the piston, the curvilinear gird is calculated as described earlier and the metric coefficients, which are time-invariant in this case, are then computed from eqn. (2) and the specification that ξ_1 and ξ_2 both range over fixed intervals, taken as unity for convenience. If the instantaneous piston velocity is denoted by v_p, then the relative fluid velocities calculated in this frame are related to absolute ones by:

$$v_1 = \tilde{v}_1 + v_p \cos\theta \qquad (3)$$

$$v_2 = \tilde{v}_2 - v_p \sin\theta$$

where θ is the local angle between the ξ_1 direction and the axis.

The expanding/contracting coordinate frame for the disc-shaped cylinder space is constructed by defining $\xi_1 \equiv (z - z_1)/(z_2 - z_1)$ and $\xi_2 \equiv r/R$, where z is an axial coordinate measured from the cylinder head, z_1 and z_2 are reference planes which may move with time and R is the cylinder radius. The corresponding metric coefficients are then $\ell_1 = z_2 - z_1$ (which is now time-varying) and $\ell_2 = R$. The local absolute fluid velocities are now:

$$v_1 = \tilde{v}_1 + v_g \qquad (4)$$

$$v_2 = \tilde{v}_2$$

where v_g is the local velocity of the coordinate frame.

3. SOLUTION PROCEDURE

3.1 FINITE DIFFERENCE EQUATIONS - The entire region is divided into a number of contrd volumes or "cells" by the grid shown in Fig. 1. Every cell has a single value of each dependent variable associated with it and located at its centre. The velocities v_1 and v_2 are exceptions and these are located at the centres of the lines forming the sides of the cells, as depicted in Fig. 2.

The differential equation (1) is integrated both in space and time to produce an approximate algebraic equation, the limits of integration being $t \to t + \delta t$ where δt is the time increment and $\xi_1 \to \xi_1 + \delta\xi_1$, $\xi_2 \to \xi_2 + \delta\xi_2$ where $\delta\xi_1$ and $\delta\xi_2$ are the lengths of the cell sides. Using the 'NSEWP' notation of Fig. 2, this integrated equation relates the value of the

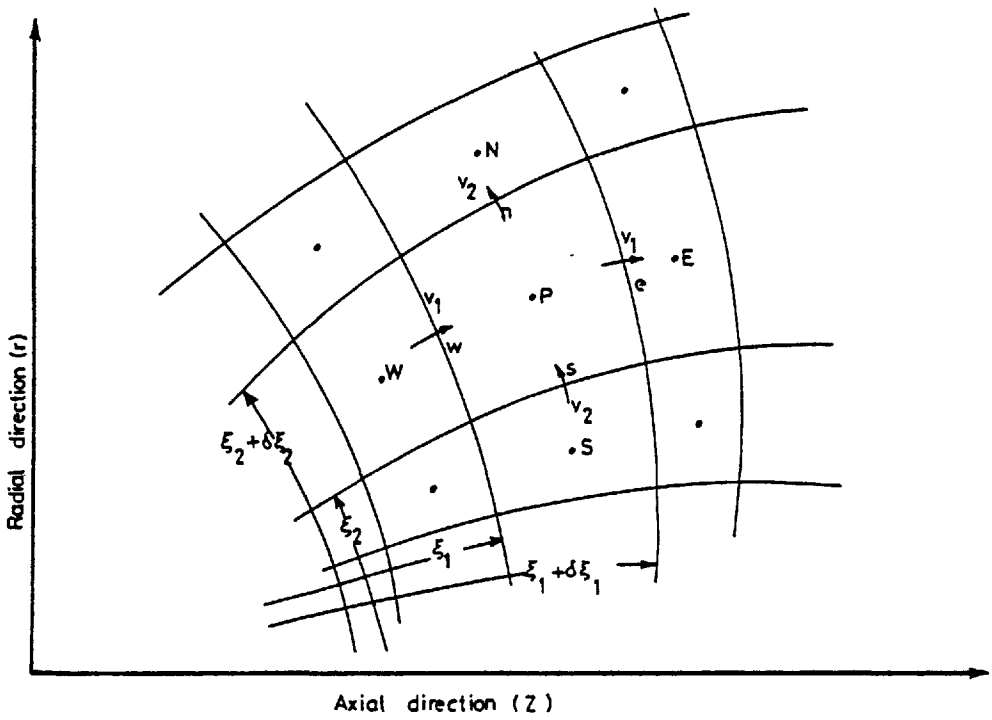

Fig. 2 - Illustration of portion of computational grid and notation

dependent variable at the node P and the advanced time level ϕ_P^n to values at the surrounding grid points NSEW at the same time level and to ϕ_P^o, the previous time level value. This equation takes the form:

$$M_P^n\phi_P^n - M_P^o\phi_P^o + \sum_c A_c^n(\phi_P^n - \phi_c^n) - S_P = 0 \qquad (5)$$

where the superscripts o and n refer to the old and new time levels respectively. The coefficients in equation (5) are defined by:

$$M_P^n = (\rho V)_P^n/\delta t, \quad A_W^n = (\rho\tilde{v}_1 af)_w^n, \quad A_S^n = (\rho\tilde{v}_2 af)_s^n$$

$$A_E^n = -(\rho v_1 af)_e^n, \quad A_N^n = -(\rho\tilde{v}_2 af)_n^n, \quad S_P = \int_{V_P} s_\phi dV \qquad (6)$$

where V_P is the cell volume. The f's in equation (6) are spatial weighting factors which affect accuracy and numerical stability (16). The latter and to some extent the former is enhanced by the following specification:

$$f_w = \begin{cases} (1 + 2/Pe_w)/2, & \text{for } |Pe_w| < 2 \\ 1, & \text{for } Pe_w > 2 \\ 0, & \text{for } Pe_w < -2 \end{cases} \qquad (7)$$

where $Pe_w = (\rho\tilde{v}_1)_2 (\ell_1\delta\xi_1)_w/\Gamma_w$; and similar formulae exist for the remaining f's. Finite-difference equations for the individual dependent variables may be generated from (6) by insertion of the appropriate expressions for the associated Γ_ϕ and s_P.

As a consequence of the above differencing practice, the resulting simultaneous equation set for each variable possesses the property of unconditional diagonal dominance of the coefficient matrix, which is favourable to the iterative method of solution which we employ.

3.2 THE CALCULATION OF PRESSURE - Following the practice of Gosman and Watkins (11), the pressure field is obtained by a 'guess and correct' procedure which invokes the global continuity requirement to set the pressure level and the local continuity condition to establish the distribution. The derivation, which will not be reproduced in detail here, starts from the finite-difference continuity equation (written in this instance in time-centred form) for a cell:

$$M_P^n - M_P^o = \dot{m}_w - \dot{m}_e + \dot{m}_s - \dot{m}_n \qquad (8)$$

where the $\dot{m}$'s represent time-averaged mass flows across the cell boundaries. Substitution for M_P^n from

$$M_P^n = M_P^* + \beta_P\bar{P}' + \gamma_P^*\bar{T}' \qquad (9)$$

and summation over the entire field (denoted by $\sum_P$) yields the following equation for the global pressure adjustment $\bar{P}'$:

$$\bar{P}'\sum_P\beta_P^* = \sum_P[M_P^o + \sum_c\dot{m}_c + M_P^o - M_P^* - \gamma_P^*\bar{T}'] \qquad (10)$$

where $\beta_P \equiv V_P(\partial\rho/\partial P)_T/\delta t$, $\gamma_P \equiv V_P(\partial\rho/\partial T)_P/\delta t$, $\bar{T}'$ is a mean temperature adjustment obtained from solution of the global energy equation, and the asterisk superscript denotes an estimate obtained from the prevailing field values. Equations for the local pressure adjustments P' are derived by combining the finite-difference continuity and momentum equations to yield:

$$M_P^* - M_P^o + \sum_c A_c(P_P' - P_c') + \sum_c\dot{m}_c + \beta_P^*\bar{P}' + \gamma_P^*\bar{T}' = 0 \qquad (11)$$

where the A_c coefficients are linked to the momentum equations (see (11)).

3.3 SOLUTION PROCEDURE - Given the initial values of and boundary prescriptions on all variables, the procedure is to advance an increment of time (i.e. crank angle) δt, estimate the bulk pressure level from eqn. (10) and a like one for $\bar{T}'$ and then commence the local adjustments. The velocities $\tilde{v}_1$ and $\tilde{v}_2$ are first obtained by iterative solution of their respective momentum equations; then eqn. (11) is solved for the local pressure adjustments and corresponding changes are made to the velocities. Following this, the remaining variables are solved for in turn from eqn. (5); and the entire procedure is repeated until the difference equations are satisfied to the required degree, the fields so obtained then representing the 'initial' values for the next time advancement.

As with all finite-difference calculations, the solutions cannot be regarded as representative of the differential equations until the necessary tests have been made of sensitivity to reduction in grid and time intervals. At the time of writing these tests have not been completed and the results shown herein cannot therefore be claimed to be free of numerical errors.

4. RESULTS

4.1 AIR MOTION INDUCED BY COMPRESSION AND EXPANSION IN CYLINDRICAL BOWL WITH NO SWIRL - Fig. 3 shows at various stages in a compression/expansion cycle the predicted flow field for this case in the form of vectors representing the absolute velocities and Fig. 4 displays the corresponding turbulence intensity distributions, plotted as contours of constant $\sqrt{2k/3}/\bar{v}_p$, where $\bar{v}_p$ is the mean piston speed and $\sqrt{2k/3}$ is the ensemble-averaged velocity fluctuation for isotropic turbulence. The cylinder dimensions and wall temperatures were prescribed as typical of current practice and the speed is 1800 rpm. These results were obtained by starting with the piston initially at BDC and the fluid at rest and then performing as many simulated compression/expansion cycles as were necessary to obtain a cyclically-repeating solution, i.e. one representative of steady operating conditions: this was achieved after about eight cycles of piston motion.

Referring first to the mean flow structure in Fig. 3 with the piston at BDC, the residual

6

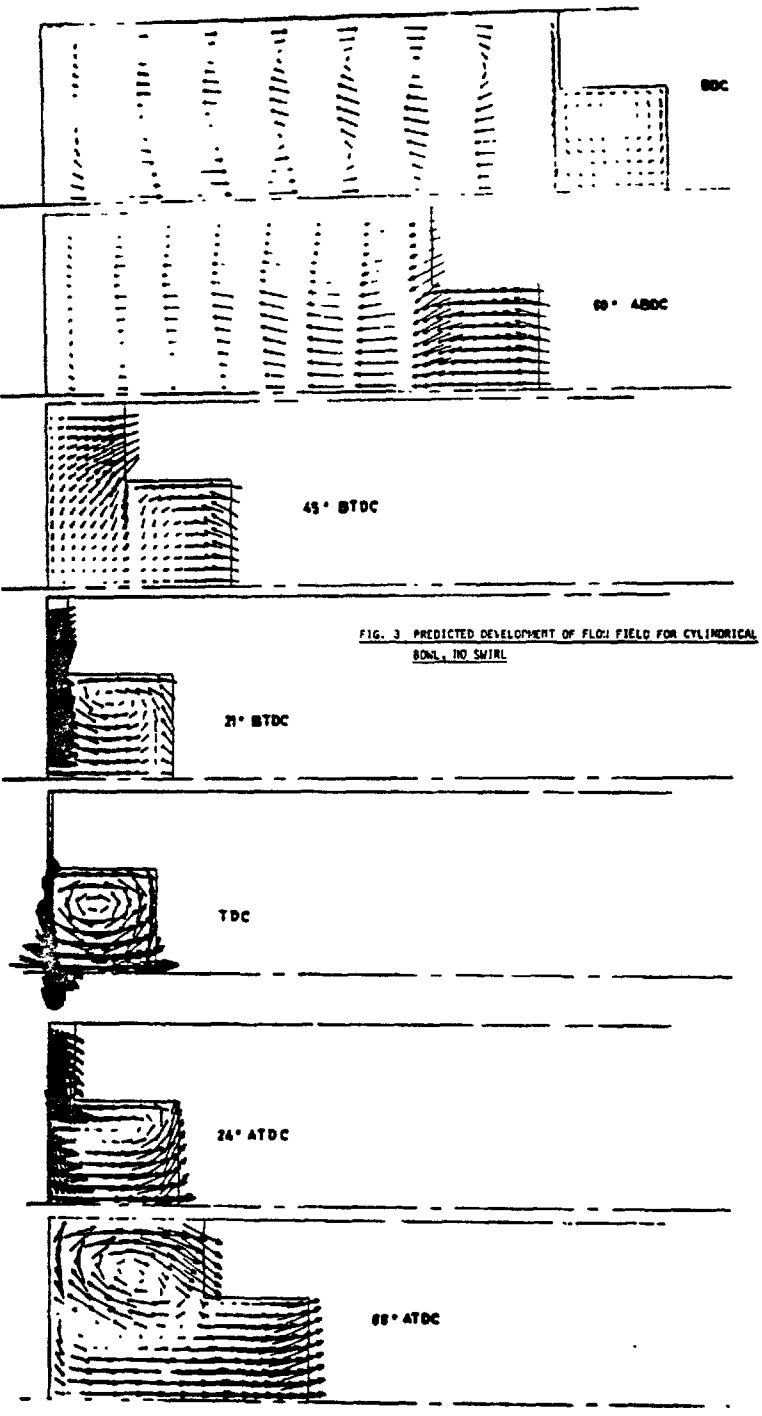

FIG. 3 PREDICTED DEVELOPMENT OF FLOW FIELD FOR CYLINDRICAL BOWL, NO SWIRL

air motion at the end of the expansion stroke of the previous cycle consists essentially of two main toroidal vortices of appreciable strength (the velocity scale is shown in the figure and the mean piston speed is 12 m/s). The first of these is centred near the outer periphery of the cylinder and is formed by a 'reverse squish' phenomenon immediately after TDC, as is revealed in plots later in the sequence. The second recirculation region, nearer the cylinder head, is formed by the compression-induced 'squish' immediately before TDC as will also be seen in later plots. It is interesting to note that both of these vortices have persisted for the entire expansion stroke and they are not suppressed until subsequent compression. A small vortex can also be seen in the bowl. This first appears a few degrees before BDC and is the result of the inertia of the fluid causing it to impinge on the piston bottom as the latter decelerates, the fluid then spreading like a wall jet and inducing the recirculation in the bowl.

The plot at 60° ABDC shows the first-mentioned vortex to have been suppressed completely, due in part to viscous action, (similar predictions obtained by solving the laminar flow equations for the same conditions show the suppression to be slower) but also to the pressure field provoked by the piston motion and the chamber configuration, both of which exert a significant role in maintaining or destroying recirculation. The second vortex closer to the cylinder head has decreased in strength whilst that in the piston bowl has also disappeared. The start of compression-induced squish can be seen from the inwards inclination of the vectors immediately above the piston crown and in the plane of the bowl opening.

At 45° BTDC all residual motion from the previous cycle has gone and the flow is dominated by the developing squish motion. This trend persists, and at 20° BTDC a single squish-induced vortex in the bowl is well established. At TDC the flow is characteristed by high inward radial or squish velocities adjacent to the cylinder head above the piston bowl, high axial velocities into the bowl near the centre-line and a single strong toroidal vortex in the bowl.

At 24° ATDC, with the piston moving outward, the reverse-squish mechanism can be seen, the air in the outer periphery of the bowl spilling out, impinging on the cylinder head, and thence flowing into the clearance space between piston crown and cylinder head where it is again turned by impingement on the cylinder wall and the downward motion of the piston. It is this stage that is critical in the formation of the second strong recirculating zone depicted in the following and initial sequences.

As the piston begins to move to outward, the squish-induced bowl vortex initially remains in the bowl and undergoes stretching but by the next plot in the sequence at 66° ATDC this vortex has been left behind by this stage and the 'reverse squish' vortex is now clearly visible.

The contours of turbulence intensity in Fig. 4 are drawn at the same stages in the cycle as the velocity plots of Fig. 3 to facilitate interpretation. Although the contours at BDC approximate in shape to the mean flow structure, the maximum intensities do not coincide with the recirculation centres. The steepest gradients are adjacent to the cylinder wall due to the thin boundary layers there. At 60° ABDC and 45° BTDC the turbulence level is diminishing, due presumably to reduction in shear generation as the large vortices dissipate and vanish: however in the latter figure a zone of locally-high energy is forming near the edge of the bowl as the squish-induced shear stresses

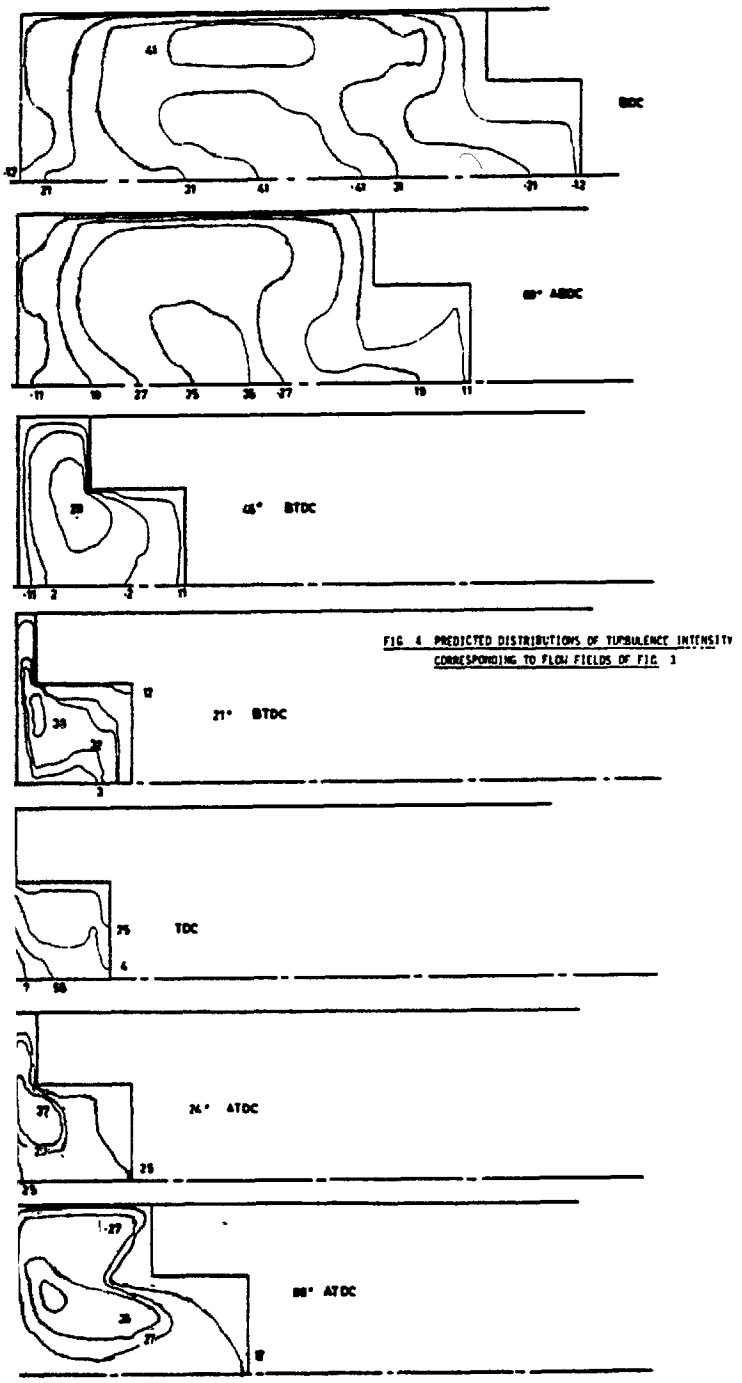

FIG 4 PREDICTED DISTRIBUTIONS OF TURBULENCE INTENSITY CORRESPONDING TO FLOW FIELDS OF FIG 3

there build up. At 21° BTDC, the general turbulence level has risen due to the increasing generation in the shear layers eminating from the edge of the bowl and the transport of the turbulence produced there into the bowl by the vortex motion.

At TDC the turbulence levels are further augmented by squish effects, as would be expected, and the highest values occur near the centre of the cylinder head. It should be noted that the peak intensities at this stage are very large indeed, amounting to around 70% based on the mean piston velocity: however it should also be borne in mind that the local squish velocities considerably exceed $\bar{v}_p$ near TDC (see Fig. 13). At 24° ATDC with the piston moving outward, the turbulence near the centre of the cylinder has rapidly decayed (or has been convected elsewhere) and the reverse squish mechanism serves to generate high levels near the edge of the bowl, which are then convected into the clearance gap: this explains why at 66° ATDC there is a region of high intensity in the gap, although it is not clear why the turbulence levels existing at this time are maintained and indeed augmented throughout the remainder of the expansion phase. The second patch of high turbulence nearer the centre of the cylinder is presumably the result of the generation and transport of turbulence by the squish-generated vortex.

4.3 THE EFFECTS OF SWIRL AND BOWL CONFIGURATION - In this section the predicted flow patterns at TDC are shown for various levels of swirl and different shapes of piston bowl. These results were obtained without the turbulence model incorporated, but experience thus far with the few duplicate calculations that have been made with turbulence simulation suggest that although the magnitudes of the predicted velocities are strongly affected by turbulence, the gross flow structure is not. Comparison of the TDC patterns in Figs. 3 and 5 corroborates this observation.

Figs. 5 to 8 show the TDC structures produced by calculating one cycle without swirl and then imposing different solid-body swirl levels at BDC and performing another cycle of calculation. The swirl ratio S given in these figures is defined as the initial swirl in revolutions/minute divided by the engine speed.

It is immediately apparent from these figures that swirl strongly affects the flow structure. The basic mechanisms are not difficult to understand: for example swirl directly affects the radial velocities by way of a centripetal acceleration; the mass continuity requirement feeds these affects through to the axial velocities; both velocities then further influence the swirl distribution. The magnitude of these effects of course depends upon the swirl rate. However the overall picture is much more complex than that envisaged by Fitzgeorge and Allison and other proposers of simple models, for the interaction with the swirl field of vortices induced by the squish and swirl mechanisms produces distributions of circumferential velocity which are far from the idealised picture of solid-body rotation. At the time of writing analysis of these interactions is incomplete (it is necessary to follow the details of the evolution of all three velocity components over the entire cycle) and no attempt will therefore be made to fully explain the results.

Fig. 6 shows that the effect of low swirl (S = 1) is to provoke near the axis an additional small vortex centred towards the bottom of the bowl and rotating in the opposite sense to the single one which existed at S = 0. One consequence of the appearance of this new vortex is that the direction of fluid motion near the axis is now out of the bowl rather than inwards

8

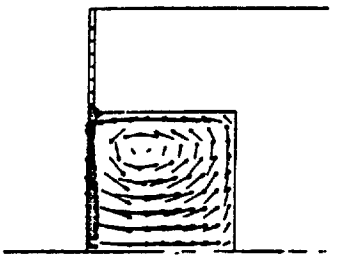

FIG. 5 TDC FLOW FIELD FOR CYLINDRICAL BOWL, NO SWIRL

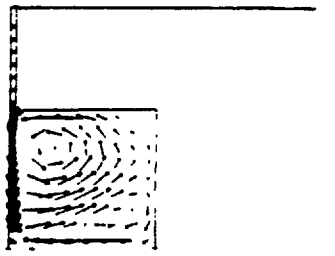

FIG. 6 TDC FLOW FIELD FOR CYLINDRICAL BOWL, S = 1

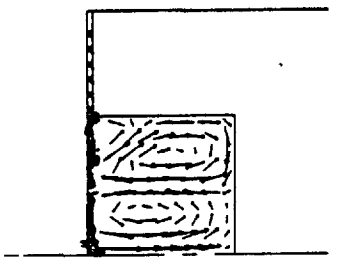

FIG. 7 TDC FLOW FIELD FOR CYLINDRICAL BOWL, S = 5

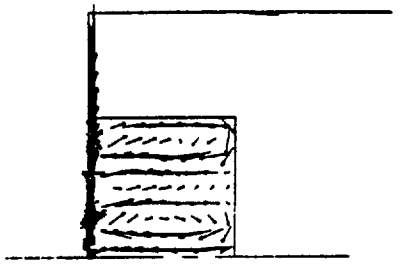

FIG. 8 TDC FLOW FIELD FOR CYLINDRICAL BOWL, S = 10

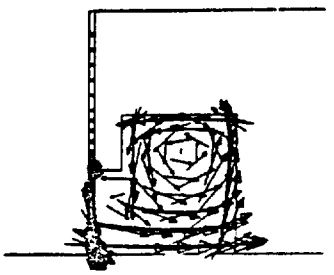

FIG. 9 TDC FLOW FIELD FOR LIPPED BOWL, NO SWIRL

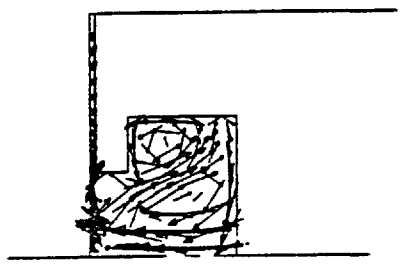

FIG. 10 TDC FLOW FIELD FOR LIPPED BOWL, S = 5

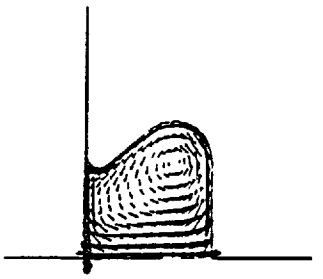

FIG. 11 TDC FLOW FIELD FOR CURVED BOWL, NO SWIRL

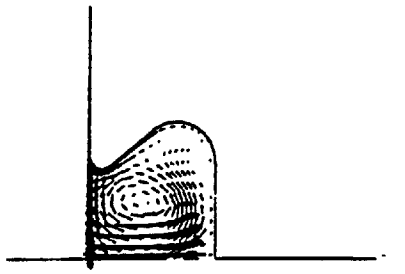

FIG. 12 TDC FLOW FIELD FOR CURVED BOWL, S = 7

as at S = 0. A higher swirl level of S = 5 (Fig. 7), which is a typical value for a diesel engine, produces even more dramatic changes: there are now two main vortices of roughly equal dimensions which are contrarotating, the directions of rotation being opposite to those of Fig. 6. There is a suggestion of a third, smaller vortex near the outer corner of the bowl. At S = 10 (Fig. 8) there is a further dramatic change, for although there are again two strong vortices, the inner one has reverted to the original sense of rotation, thereby producing a region of strong shear between the two.

Figs. 9 and 10 show the TCD flows produced when the shape of the bowl is changed from a simple cylinder to one with a protruding rectangular-sectioned lip. There are strong similarities for S = 0 between the flow pattern of Fig. 9 and that of Fig. 5 although in the former case there is a suggestion of a small eddy adjacent to the top lip. (These and other calculations suggest that, in the absence of swirl, there is invariably a single strong vortex in the bowl rotating in the direction shown). There is likewise a superficial similarity in the prediction for S = 5 in Fig.10 and the corresponding cylindrical bowl predict-

ion of Fig. 7 but closer inspection reveals that the sense of rotation of the eddies is different and the dividing region between them is inclined towards the inner corner of the lipped bowl.

Figs. 11 and 12 show results* for the shape of bowl depicted in Fig. 1, which is probably more characteristic of current designs than the simple cylindrical shape. The cylinder dimensions are again assigned realistic values and the speed in this case is 1400 rpm. Fig. 11 shows the characteristic single strong squish-induced bowl vortex which emerges when no swirl is imparted to the flow. Fig. 12 shows the effect of swirl in this configuration, the initial swirl rate being set at S = 7: in this instance the TDC flow structure is not dissimilar to the S = 0 case, in that there is a single strong vortex. However swirl causes the centre of the vortex to move towards the mouth of the bowl, leaving a region of relatively stagnant fluid where the S = 0 vortex was centred. The differences between the two cases are even more marked prior to TDC: for example at 20° BTDC swirl causes a twin-vortex structure to form similar to that of Fig. 10.

*It should be noted that the vectors in these figures are plotted to a different scale than the earlier ones.

4.3 COMPARISON WITH SIMPLE SQUISH THEORY - The predictions indicate that the basic assumptions underlying the simple squish theory of Fitzgeorge and Allison (3) are reasonable: for example the flow in the clearance gap is closely one dimensional during the last 30 degrees or so before TDC. It is therefore not surprising that the comparisons shown in Fig. 13 between the present predictions for a cylindrical bowl and no swirl and the forementioned theory show close agreement, with the former lying slightly below the latter. The discrepancies can be plausibly attributed to the effects of heat transfer, which were of course simulated in the present analysis but not in the original Fitzgeorge and Allison model.

4.4 COMPARISON WITH SIMPLE SWIRL THEORY - In the light of our earlier observations about the observed departure of the swirl velocity distributions predicted by the present method from the solid-body rotation model on which the Fitzgeorge and Allison (3) method is based, it is not surprising that significant quantitative differences are found to exist in the swirl behaviour predicted by the two methods. Fig. 14 shows comparisons during the latter phase of the

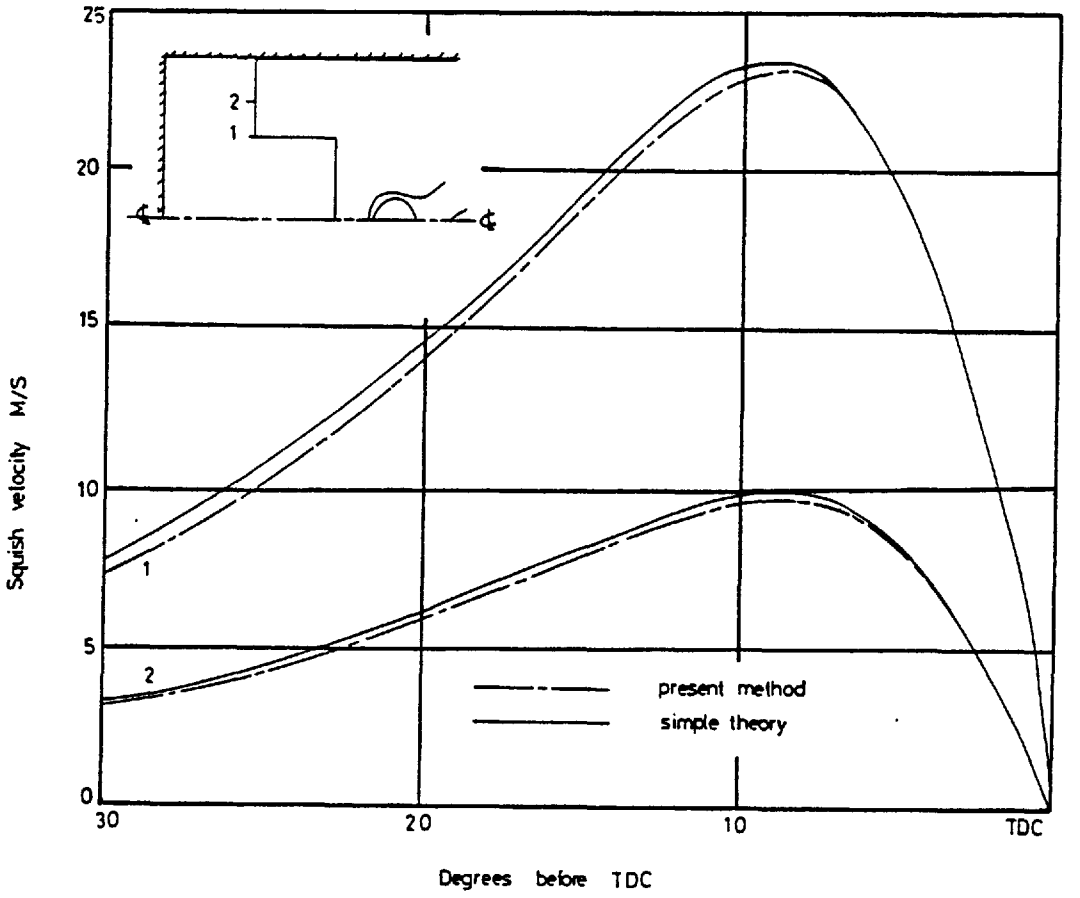

Fig. 13 - Comparison between simple squish theory and the present method

10

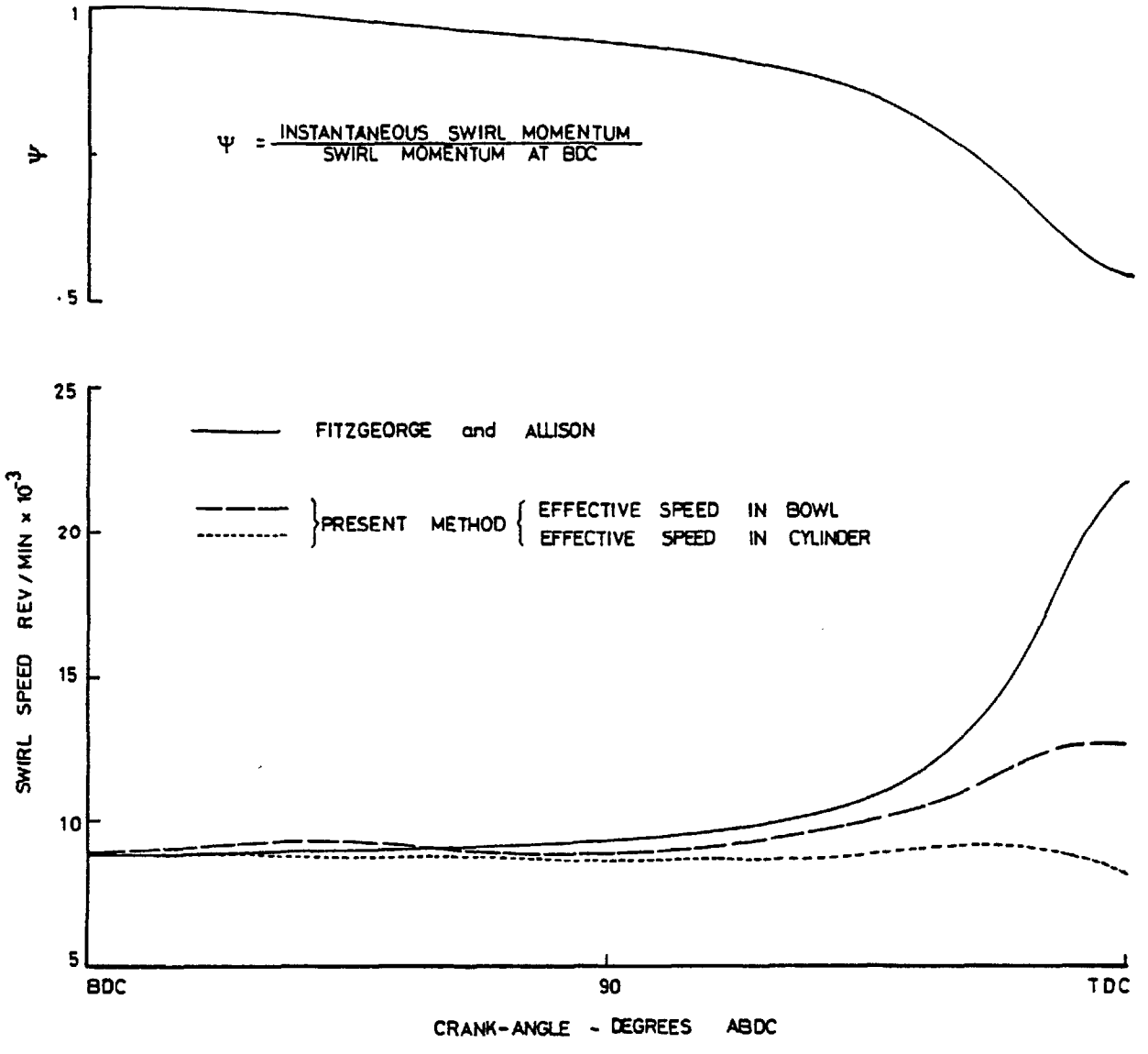

Fig. 14 - Comparison of swirl predictions with simple swirl theory for a cylindrical-bowl piston--BDC swirl rate S = 5, 1800 rpm

compression stroke for the case of a cylindrical-bowl piston at an engine speed of 1800 rpm and an initial BDC swirl rate S = 5. The lower part of the diagram contains the single curve of swirl speed versus crank angle produced by the simple theory, and two curves representing the volume-averaged swirl speed predicted by the present method for the bowl and upper cylinder volumes respectively. The simple method evidently overpredicts the swirl build-up in the bowl as TCD is approached, due in great measure, it is believed, to the neglect of friction. This view is reinforced by the observed decay in the swirl level in the upper cylinder region and also in the total swirl momentum for the chamber, which is plotted in the upper diagram of the figure.

4.5 DISCUSSION - Encouragement can be drawn from the fact that, as these results demonstrate, the present method is capable of solving the large system of coupled non-linear differential equations governing a turbulent, swirling and recirculating flow with heat transfer in cylinder configurations characteristic of those found in many current designs of Diesel and stratified-charge spark-ignition engines. However, although the predictions of the method appear plausible, it still remains to establish its accuracy, a question which, for the present application, is almost inseparably connected with the validity of the mathematical representation of turbulence effects employed.

As to the predictions themselves, in one respect they merely serve to confirm what has already been inferred directly from flow measurements in engines and indirectly from combustion performance; namely that changes in bowl shape or swirl level may have a profound influence on the events in the cylinder. In the present case however it is possible to see in

far more detail than hitherto just what are the in-cylinder flow and turbulence patterns for a particular set of circumstances. Hopefully this information will assist the designer in optimising conditions. For example, it may be that the stagnant region of flow in Fig. 12 is an undersirable feature, and alterations to the bowl shape or swirl characteristics should therefore be made to remove it. The present method may, when sufficiently developed and tested, be used to explore various proposed alterations in order to identify those which show most promise, thereby minimising the amount of time-consuming and expensive experimentation required.

One important drawback of methods which focus only on flow and heat transfer is the the difficulty of making the connection between predictions of these processes and the consequences for combustion, which is after all the process of ultimate interest. Although it is possible on the basis of current knowledge to make some inferences, it is probably preferable to extend the method to incorporate combustion modelling, and work of this kind is currently in progress.

Finally, returning again to the question of testing prediction methods of the present kind, there is an urgent need for reliable and detailed measurements for this purpose. The immediate requirement is strictly for data for axisymmetric configurations, which is virtually non-existent, but even if the axisymmetric constraint is relaxed, there are few, if any, suitable in-cylinder measurements. The reasons for this state of affairs reside mainly in the formidable difficulties of obtaining such measurements, although techniques such as Laser-Doppler Anemometry are showing promise (see e.g. (17)) in overcoming the difficulties. However in planning future experiments it should also be recognised that, like the real flow, computer simulations reflect whatever conditions are imposed on the flow as it enters the cylinder; and it is therefore necessary, as well as measuring within the cylinder itself, to quantify the inlet conditions in as much detail as possible. To be more specific, what is ideally required are measurements over the entire intake process of the distributions in the plane of the valve orifice of the velocity components and the turbulence level and length scale.

5. CONCLUSIONS

The following are the main conclusions to be drawn from the present study:

1. The method here developed is capable of solving the conservation equations governing in-cylinder flow and heat transfer in typical Diesel and stratified-charge configurations with swirl under motoring conditions, but the accuracy of the solutions remains to be assessed.
2. According to the predictions the presence of a bowl provokes, even in the absence of swirl, a complex flow pattern containing at least two strong vortices, one being formed during the approach to TDC by the squish phenomenon and the other in the clearance gap by 'reverse squish' during the initial descent of the piston. The evolution of the turbulence intensity distribution can largely be explained in terms of the flow behaviour, although some features are not yet fully understood.
3. The results presented also demonstrate that changes in piston bowl shape and swirl level may profoundly alter the flow structure.
4. Detailed in-cylinder measurements with well-defined inlet conditions are needed as testing grounds for methods of the present kind.
5. Extension of the method to incorporate combustion modelling is desirable in order to realise its full potential as a design tool, and is in progress.

6. ACKNOWLEDGEMENTS

The authors gratefully acknowledge the encouragement and assistance of the Perkins Engines Co.

7. REFERENCES

1. T.H. Ma, "Effects of cylinder change motion on combustion", Proc. I. Mech. Eng. Conference on Combustion in Engines, (1975).

2. D.R. Lancaster, R.B. Krieger, S.C. Sorenson and W.L. Hull, "Effects of turbulence on spark-ignition combustion", General Motors Research Laboratory report GMR-2061R, (1976).

3. D. Fitzgeorge and J.L. Allison, "Air swirl in a road vehicle diesel engine", Proc. Instn. Mech. Engrs., (A.D.) No. 4, (1962-63).

4. J.C. Dent and J.A. Derham, "Air motion in a four-stroke direct-injection diesel engine", Proc. Instn. Mech. Engrs., Vol. 188OO/74, (1974).

5. B. Loeffler, "Development of an improved automotive diesel combustion system", Trans. Soc. Auto. Engrs, Vol. 62, p. 243, (1954).

6. Y. Shimato and K. Akiyama, "A study of squish in open combustion chambers of a diesel engine", Bull. of JSME, Vol. 13, No. 63, (1970).

7. A.P. Watkins, "Calculation of flow and heat transfer in the combustion chamber of a reciprocating engine", M.Sc. Thesis, University of London, (1973).

8. M.S. Chong, E.E. Milkins and H.C. Watson, "The prediction of heat and mass transfer during compression and expansion in I.C. engines", SAE Trans. 760761, (1976).

9. R. Diwakar, J.D. Anderson, M.D. Griffin and E. Jones, "Inviscid solutions of the flow field in an internal combustion engine", Dept. of Aerospace Engr. Report, Univ. of Maryland, (1976).

10. R.W. MacCormack, "The effect of viscosity in hypervelocity impact cratering", AIAA paper No. 69-354, (1969).

11. A.D. Gosman and A.P. Watkins, "A computer prediction method for turbulent flow and heat transfer in piston/cylinder assemblies", Proc. Symposium on Turbulent Shear Flows, Penn. State Univ., (1977).

12. A.A. Boni, M. Chapman, J.L Cook, and G.P. Schneyer, "Computer simulation of combustion in a stratified charge engine", Proc. Sixteenth International Symposium on Combustion, (1976).

13. C.W. Hirt, A.A. Amsden and J.L. Cook, "An arbitrary Lagrangian-Eulerian computing method for all flow speeds", J. Comp. Phys., Vol. 14, (1974).

14. R.J.R. Johns, "The generation of curvilinear-orthogonal grids for the solution of problems in fluid mechanics", Imperial College, Mech. Eng. Dept. Report, Nov. (1977).

15. B.E. Launder and D.B. Spalding, "Mathematical Models of Turbulence", Academic Press, (1970).

16. G.D. Raithby and K.E. Torrance "Upstream-weighted differencing schemes and their application to elliptic problems involving fluid flow", Computers and Fluids, Vol. 2, (1974).

17. A.D. Gosman, A. Melling, A.P. Watkins and J.H. Whitelaw, "Axisymmetric flow in a motored reciprocating engine", Imperial College Mech. Eng. Dept. Report FS/77/20 (1977). Also to appear in J. Mech. Eng. Sci.

NOMENCLATURE

A	coefficients of finite-difference equation
a	cell-boundary area
c_v	constant-volume specific heat
f	spatial-differencing weighting factor
h	stagnation enthalpy
k	turbulent kinetic energy
ℓ	metric coefficient
M	coefficient of finite-difference equation
$\dot{m}$	mass flow rate
p	pressure
Pe	cell Peclet number
r	radial co-ordinate
S	swirl ratio
s	distance along co-ordinate line
s ,S	source terms in differential and difference equations respectively
T	temperature
t	time
V	cell volume
v	velocity
z	axial co-ordinate

Greek Symbols

$\beta = V_p(\partial\rho/\partial T)_p/\delta t$

$\gamma = V_p(\partial\rho/\partial P)_T/\delta t$

Γ	exchange coefficient
δ	an increment
ε	dissipation rate of turbulent kinetic energy
ϕ	a dependent variable
ρ	density
θ	angle between ξ_1 and z directions
ξ	co-ordinate direction.

Subscripts

C	member of grid cluster
P,N,S,E,W	nodal points of finite-difference grid
n,s,e,w	cell boundary locations on finite-difference grid
ϕ	relating to ϕ
g	relating to the grid
1,2,3	denotes ξ_1, ξ_2 and $\xi_3(\theta)$ directions respectively.

Superscripts

~	a velocity relative to the co-ordinate frame
'	correction
*	approximate or temporary value
n	new time level
o	old time level

Table 2.1 Relative Degrees of Sophistication of In-Cylinder Predictive Models of Previous Researchers

Details of model \ Research Group	1	2	3	4	5	6
1. Differencing scheme						
Time-step stability criteria		✓		✓		
2. Combustion chamber geometry:						
Moving piston	✓	✓	✓	✓		✓
Limited piston bowl shape			✓			
Arbitrary " " "						✓
Limited prechamber "					✓	
Arbitrary " "				✓		✓
3. Inlet/Exhaust valve geometry:						
None			✓	✓	✓	
Orifice of fixed dimensions	✓	✓				✓
Moving poppet valve						✓
4. Turbulence:						
Not included		✓	✓			
Roughly included				✓		
Turbulence model	✓				✓	✓
5. Wall heat transfer:						
Not included		✓		✓		
Roughly included			✓		✓	
Empirically included	✓					✓

Details of model \ Research Group	1	2	3	4	5	6
6. Wall momentum transfer:						
Not included		✓				
Roughly included			✓	✓	✓	
Empirically included	✓					✓
7. Comparison with experiment:						
None		✓	✓	✓		
Some	✓				✓	✓

Research Groups:

1. Watkins (1977)
2. Diwakar et al (1978)
3. Chong et al (1976)
4. Boni et al (1978)
5. Syed and Bracco (1979)
6. Present study

Constant	C_μ	C_1	C_2	κ	E	σ_k	σ_ε	σ_h	σ_ℓ
Value	.09	1.44	1.92	.4187	9.793	1.	$\frac{\kappa^2}{(C_1-C_2)C_\mu^{1/2}}$	.9	.7

Table 3.1 Values of turbulence model constants

Table 3.2 Expressions for turbulent diffusivity and source terms for the curvilinear-orthogonal Eulerian co-ordinate frame

Dependent variable	Γ_ϕ	S_ϕ
$\bar{v}_1$	μ_{eff}	$-\frac{1}{\ell_1}\frac{\partial \bar{p}}{\partial \zeta_1} + \frac{1}{\ell_1\ell_2\ell_3}\{\frac{\partial}{\partial \zeta_1}[\ell_2\ell_3(\mu_{eff}(\frac{1}{\ell_1}\frac{\partial \bar{v}_1}{\partial \zeta_1} + \frac{2\bar{v}_2}{r_1}) - \frac{2}{3}(\bar{\rho}k + \mu_{eff}\nabla.\underline{\bar{v}}))] + \frac{\partial}{\partial \zeta_2}[\ell_1\ell_3\,\mu_{eff}(\frac{1}{\ell_1}\frac{\partial \bar{v}_2}{\partial \zeta_1} - \frac{\bar{v}_1}{r_1} - \frac{\bar{v}_2}{r_2})]\}$ $+\frac{1}{r_2}[\overline{\rho v_2 v_2} - 2\mu_{eff}(\frac{1}{\ell_2}\frac{\partial \bar{v}_2}{\partial \zeta_2} + \frac{\bar{v}_1}{r_2}) + \frac{2}{3}(\bar{\rho}k + \mu_{eff}\nabla.\underline{\bar{v}})]$ $+\frac{\sin\beta}{r_3}[\overline{\rho v_3 v_3} - 2\mu_{eff}(\frac{\bar{v}_1\sin\beta+\bar{v}_2\cos\beta}{r_3}) + \frac{2}{3}(\bar{\rho}k + \mu_{eff}\nabla.\underline{\bar{v}})]$ $-\frac{1}{r_1}[\overline{\rho v_2 v_1} - \mu_{eff}(\frac{1}{\ell_2}\frac{\partial \bar{v}_1}{\partial \zeta_2} - \frac{\bar{v}_1}{r_1} + \frac{1}{\ell_1}\frac{\partial \bar{v}_2}{\partial \zeta_1} - \frac{\bar{v}_2}{r_2})]$
$\bar{v}_2$	μ_{eff}	$-\frac{1}{\ell_2}\frac{\partial \bar{p}}{\partial \zeta_2} + \frac{1}{\ell_1\ell_2\ell_3}\{\frac{\partial}{\partial \zeta_1}[\ell_2\ell_3\,\mu_{eff}(\frac{1}{\ell_2}\frac{\partial \bar{v}_1}{\partial \zeta_2} - \frac{\bar{v}_1}{r_1} - \frac{\bar{v}_2}{r_2})] + \frac{\partial}{\partial \zeta_2}[\ell_1\ell_3(\mu_{eff}(\frac{1}{\ell_2}\frac{\partial \bar{v}_2}{\partial \zeta_2} + \frac{2\bar{v}_1}{r_2}) - \frac{2}{3}(\bar{\rho}k + \mu_{eff}\nabla.\underline{\bar{v}}))]\}$ $+\frac{1}{r_1}[\overline{\rho v_1 v_1} - 2\mu_{eff}(\frac{1}{\ell_1}\frac{\partial \bar{v}_1}{\partial \zeta_1} + \frac{\bar{v}_2}{r_1}) + \frac{2}{3}(\bar{\rho}k + \mu_{eff}\nabla.\underline{\bar{v}})]$ $+\frac{\cos\beta}{r_3}[\overline{\rho v_3 v_3} - 2\mu_{eff}(\frac{\bar{v}_1\sin\beta+\bar{v}_2\cos\beta}{r_3}) + \frac{2}{3}(\bar{\rho}k + \mu_{eff}\nabla.\underline{\bar{v}})]$ $-\frac{1}{r_2}[\overline{\rho v_1 v_2} - \mu_{eff}(\frac{1}{\ell_2}\frac{\partial \bar{v}_1}{\partial \zeta_2} - \frac{\bar{v}_1}{r_1} + \frac{1}{\ell_1}\frac{\partial \bar{v}_2}{\partial \zeta_1} - \frac{\bar{v}_2}{r_2})]$

Dependent variable	Γ_ϕ	S_ϕ
$\bar{v}_3$	μ_{eff}	$-\frac{1}{\ell_1\ell_2\ell_3}\{\frac{\partial}{\partial\zeta_1}(\ell_2\ell_3\mu_{eff}\frac{\bar{v}_3\sin\beta}{r_3}) + \frac{\partial}{\partial\zeta_2}(\ell_1\ell_3\mu_{eff}\frac{\bar{v}_3\cos\beta}{r_3})\}$ $-\frac{1}{r_3}[\sin\beta(\overline{\rho v_1}\bar{v}_3 - \mu_{eff}\frac{1}{\ell_1}\frac{\partial\bar{v}_3}{\partial\zeta_1})$ $+\cos\beta(\rho\overline{v_2v_3} - \mu_{eff}\frac{1}{\ell_2}\frac{\partial\bar{v}_3}{\partial\zeta_2}) + \mu_{eff}\frac{\bar{v}_3}{r_3}]$
1	0	0
$\bar{h}$	$\frac{\mu_{eff}}{\sigma_h}$	$\frac{\partial p}{\partial t} + \frac{1}{\ell_1\ell_2\ell_3}\{\frac{\partial}{\partial\zeta_1}[\frac{\ell_2\ell_3}{\ell_1}\mu_{eff}(1-\frac{1}{\sigma_h})\frac{\partial}{\partial\zeta_1}(\Sigma\frac{\bar{v}_i^2}{2})]$ $+\frac{\partial}{\partial\zeta_2}[\frac{\ell_1\ell_3}{\ell_2}\mu_{eff}(1-\frac{1}{\sigma_h})\frac{\partial}{\partial\zeta_2}(\Sigma\frac{\bar{v}_i^2}{2})]$ $+\frac{\partial}{\partial\zeta_1}[\frac{\ell_2\ell_3}{\ell_1}\mu_{eff}(\frac{1}{\sigma_k}-\frac{1}{\sigma_h})\frac{\partial k}{\partial\zeta_1}] + \frac{\partial}{\partial\zeta_2}[\frac{\ell_1\ell_3}{\ell_2}\mu_{eff}(\frac{1}{\sigma_k}-\frac{1}{\sigma_h})\frac{\partial k}{\partial\zeta_2}]\}$
k	$\frac{\mu_{eff}}{\sigma_k}$	$G_t - \bar{\rho}\varepsilon$
ε	$\frac{\mu_{eff}}{\sigma_\varepsilon}$	$\frac{\varepsilon}{k}(C_1G_t - C_2\bar{\rho}\varepsilon) + \bar{\rho}\varepsilon\,\nabla\cdot\underline{\bar{v}}$

Table 3.3 Source terms in the transformed co-ordinate system

Dependent variable	S_ϕ
$\bar{v}_1$	$-\frac{1}{\ell_1'}\frac{\partial \bar{p}}{\partial \zeta_1'} + \frac{1}{\ell_1'\ell_2'\ell_3'}\{\frac{\partial}{\partial \zeta_1'}[\ell_2'\ell_3'(\mu_{eff}(\frac{1}{\ell_1'}\frac{\partial \bar{v}_1}{\partial \zeta_1'} + \frac{2\bar{v}_2}{r_1})$ $-\frac{2}{3}(\bar{\rho}k + \mu_{eff}\nabla\cdot\underline{\bar{v}}))] + \frac{\partial}{\partial \zeta_2'}[\ell_1'\ell_3'\mu_{eff}(\frac{1}{\ell_1'}\frac{\partial \bar{v}_2}{\partial \zeta_1'} - \frac{\bar{v}_1}{r_1} - \frac{\bar{v}_2}{r_2})]\}$ $+\frac{1}{r_2}[\overline{\rho v_2 v_2} - 2\mu_{eff}(\frac{1}{\ell_2'}\frac{\partial \bar{v}_2}{\partial \zeta_2'} + \frac{\bar{v}_1}{r_2}) + \frac{2}{3}(\bar{\rho}k + \mu_{eff}\nabla\cdot\underline{\bar{v}})]$ $+\frac{\sin\beta}{r_3}[\overline{\rho v_3 v_3} - 2\mu_{eff}(\frac{\bar{v}_1\sin\beta+\bar{v}_2\cos\beta}{r_3}) + \frac{2}{3}(\bar{\rho}k + \mu_{eff}\nabla\cdot\underline{\bar{v}})]$ $-\frac{1}{r_1}[\overline{\rho v_2 v_1} - \mu_{eff}(\frac{1}{\ell_2'}\frac{\partial \bar{v}_1}{\partial \zeta_2'} - \frac{\bar{v}_1}{r_1} + \frac{1}{\ell_1'}\frac{\partial \bar{v}_2}{\partial \zeta_1'} - \frac{\bar{v}_2}{r_2})]$
$\bar{v}_2$	$-\frac{1}{\ell_2'}\frac{\partial \bar{p}}{\partial \zeta_2'} + \frac{1}{\ell_1'\ell_2'\ell_3'}\{\frac{\partial}{\partial \zeta_1'}[\ell_2'\ell_3'\mu_{eff}(\frac{1}{\ell_2'}\frac{\partial \bar{v}_1}{\partial \zeta_2'} - \frac{\bar{v}_1}{r_1} - \frac{\bar{v}_2}{r_2})]$ $+\frac{\partial}{\partial \zeta_2'}[\ell_1'\ell_3'(\mu_{eff}(\frac{1}{\ell_2'}\frac{\partial \bar{v}_2}{\partial \zeta_2'} + \frac{2\bar{v}_1}{r_2}) - \frac{2}{3}(\bar{\rho}k + \mu_{eff}\nabla\cdot\underline{\bar{v}}))]\}$ $+\frac{1}{r_1}[\overline{\rho v_1 v_1} - 2\mu_{eff}(\frac{1}{\ell_1'}\frac{\partial \bar{v}_1}{\partial \zeta_1'} + \frac{\bar{v}_2}{r_1}) + \frac{2}{3}(\bar{\rho}k + \mu_{eff}\nabla\cdot\underline{\bar{v}})]$ $+\frac{\cos\beta}{r_3}[\overline{\rho v_3 v_3} - 2\mu_{eff}(\frac{\bar{v}_1\sin\beta+\bar{v}_2\cos\beta}{r_3}) + \frac{2}{3}(\bar{\rho}k + \mu_{eff}\nabla\cdot\underline{\bar{v}})]$ $-\frac{1}{r_2}[\overline{\rho v_1 v_2} - \mu_{eff}(\frac{1}{\ell_2'}\frac{\partial \bar{v}_1}{\partial \zeta_2'} - \frac{\bar{v}_1}{r_1} + \frac{1}{\ell_1'}\frac{\partial \bar{v}_2}{\partial \zeta_1'} - \frac{\bar{v}_2}{r_2})]$

Dependent variable	S_ϕ
$\overline{v}_3$	$-\frac{1}{\ell_1'\ell_2'\ell_3'}\{\frac{\partial}{\partial\zeta_1'}(\ell_2'\ell_3'\mu_{eff}\frac{\overline{v}_3\sin\beta}{r_3}) + \frac{\partial}{\partial\zeta_2'}(\ell_1'\ell_3'\mu_{eff}\frac{\overline{v}_3\cos\beta}{r_3})\}$ $-\frac{1}{r_3}\{\sin\beta(\overline{\rho v}_1\overline{v}_3 - \mu_{eff}\frac{1}{\ell_1'}\frac{\partial\overline{v}_3}{\partial\zeta_1'}) + \cos\beta(\overline{\rho v}_2\overline{v}_3 - \mu_{eff}\frac{1}{\ell_2'}\frac{\partial\overline{v}_3}{\partial\zeta_2'})$ $+ \mu_{eff}\frac{\overline{v}_3}{r_3}\}$
$\overline{h}$	$\frac{\partial\overline{p}}{\partial t} - v_g\cos\beta\frac{1}{\ell_1'}\frac{\partial\overline{p}}{\partial\zeta_1'} + v_g\sin\beta\frac{1}{\ell_2'}\frac{\partial\overline{p}}{\partial\zeta_2'} +$ $\frac{1}{\ell_1'\ell_2'\ell_3'}\{\frac{\partial}{\partial\zeta_1'}[\frac{\ell_2'\ell_3'}{\ell_1'}\mu_{eff}(1-\frac{1}{\sigma_h})\frac{\partial}{\partial\zeta_1'}(\Sigma\frac{\overline{v}_i^2}{2})]$ $+\frac{\partial}{\partial\zeta_2'}[\frac{\ell_1'\ell_3'}{\ell_2'}\mu_{eff}(1-\frac{1}{\sigma_h})\frac{\partial}{\partial\zeta_2'}(\Sigma\frac{\overline{v}_i^2}{2})]$ $+\frac{\partial}{\partial\zeta_1'}[\frac{\ell_2'\ell_3'}{\ell_1'}\mu_{eff}(\frac{1}{\sigma_k}-\frac{1}{\sigma_h})\frac{\partial k}{\partial\zeta_1'}]$ $+\frac{\partial}{\partial\zeta_2'}[\frac{\ell_1'\ell_3'}{\ell_2'}\mu_{eff}(\frac{1}{\sigma_k}-\frac{1}{\sigma_h})\frac{\partial k}{\partial\zeta_2'}]\}$
k	As table 3.2.
ε	As table 3.2.

where the divergence of velocity and turbulence kinetic energy generation rate are given by:

$$\nabla.\underline{\bar{v}} = \left(\frac{1}{\ell_1'}\frac{\partial \bar{v}_1}{\partial \zeta_1'} + \frac{\bar{v}_1}{r_2}\right) + \left(\frac{1}{\ell_2'}\frac{\partial \bar{v}_2}{\partial \zeta_2'} + \frac{\bar{v}_2}{r_1}\right) + \frac{1}{r_3}\left(\bar{v}_1 \sin\beta + \bar{v}_2 \cos\beta\right)$$

$$G_t = \mu_{eff}\left\{2\left(\frac{1}{\ell_1'}\frac{\partial \bar{v}_1}{\partial \zeta_1'} + \frac{\bar{v}_2}{r_1}\right)^2 + 2\left(\frac{1}{\ell_2'}\frac{\partial \bar{v}_2}{\partial \zeta_2'} + \frac{\bar{v}_1}{r_2}\right)^2 + 2\left(\frac{\bar{v}_1 \sin\beta + \bar{v}_2 \cos\beta}{r_3}\right)^2\right.$$

$$+ \left(\frac{1}{\ell_2'}\frac{\partial \bar{v}_1}{\partial \zeta_2'} - \frac{\bar{v}_1}{r_1} + \frac{1}{\ell_1'}\frac{\partial \bar{v}_2}{\partial \zeta_1'} - \frac{\bar{v}_2}{r_2}\right)^2 + \left(\frac{1}{\ell_1'}\frac{\partial \bar{v}_3}{\partial \zeta_1'} - \frac{\bar{v}_3 \sin\beta}{r_3}\right)^2$$

$$\left. + \left(\frac{1}{\ell_2'}\frac{\partial \bar{v}_3}{\partial \zeta_2'} - \frac{\bar{v}_3 \cos\beta}{r_3}\right)^2\right\}$$

Table 4.1 Comparison of the coefficients in the series for various finite-difference formulations of the energy equation pressure-work term

Scheme	b	b^2	b^3
Analytic	$-(\gamma-1)$	$\frac{1}{2}(\gamma-1)(\gamma-2)$	$-\frac{1}{6}(\gamma-1)(\gamma-2)(\gamma-3)$
	$= -.4$	$= -.12$	$= -.064$
Watkins (1977)	$-(\gamma-1)$	$\frac{1}{2}(\gamma-1)(\gamma-2)$	$-\frac{1}{4}(\gamma^3-4\gamma^2+7\gamma-4)$
	$= -.4$	$= -.12$	$= -.176$
Present study	$-(\gamma-1)$	$\frac{1}{2}(\gamma-1)(\gamma-2)$	$-\frac{1}{8}(2\gamma^3-9\gamma^2+15\gamma-8)$
	$= -.4$	$= -.12$	$= -.106$

Table 5.1 Computer Run Times for Test Cases 1 to 6

Case	Time-step	No. of Grid Cells	Computer Run Time (mins)
1	2^{o}	784	$30/360^{o}$ cycle
2	2^{o}	784	23/ " "
3	2^{o}	1024	29/ " "
4	3^{o}	647	$37/720^{o}$ (4 stroke) cycle
5	3^{o}	455	36/ " " "
6	1^{o}	404	$65/360^{o}$ cycle

The following cpu times relate to an IBM 360/195 running under OS-MVT using the Extended H compiler at the highest level of optimisation (2) and in double precision for both real (R*8) and integer (I*4) variables. These times exclude compilation and loading but include the time for writing information at each crank-angle step (for subsequent analysis and plotting) to magnetic tape; typically, this time is 3 to 6 mins per cycle. Run times are often quoted elsewhere for the CDC 7600; an approximate conversion of x IBM mins = .54 x CDC mins is applicable when the latter is using the FTN compiler at the highest optimisation level (2) (Curnow, 1976).

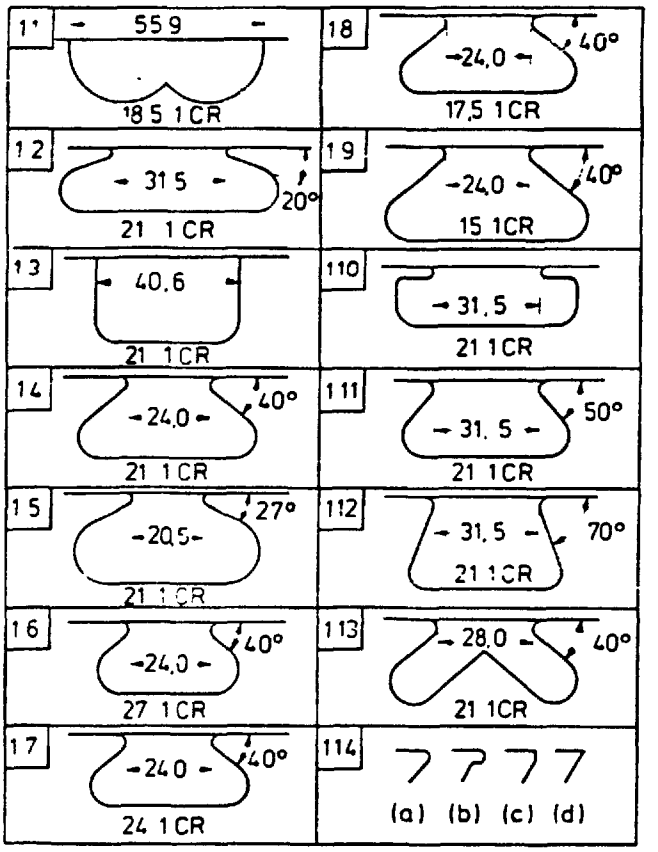

Fig. 1.1 Various designs of re-entrant bowl piston (taken from Middlemiss, 1978)

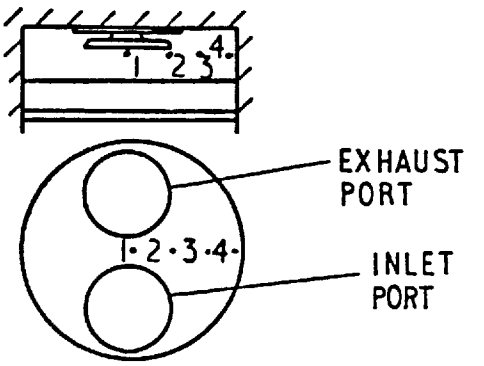

Fig. 2.1 Disc-chamber engine configuration used in the experiments of Molchanov (1953)

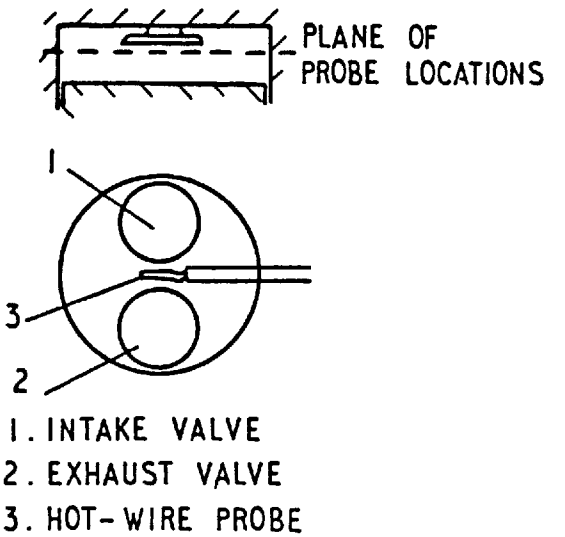

Fig. 2.2 Disc-chamber engine configuration used in the experiments of Semenov (1958)

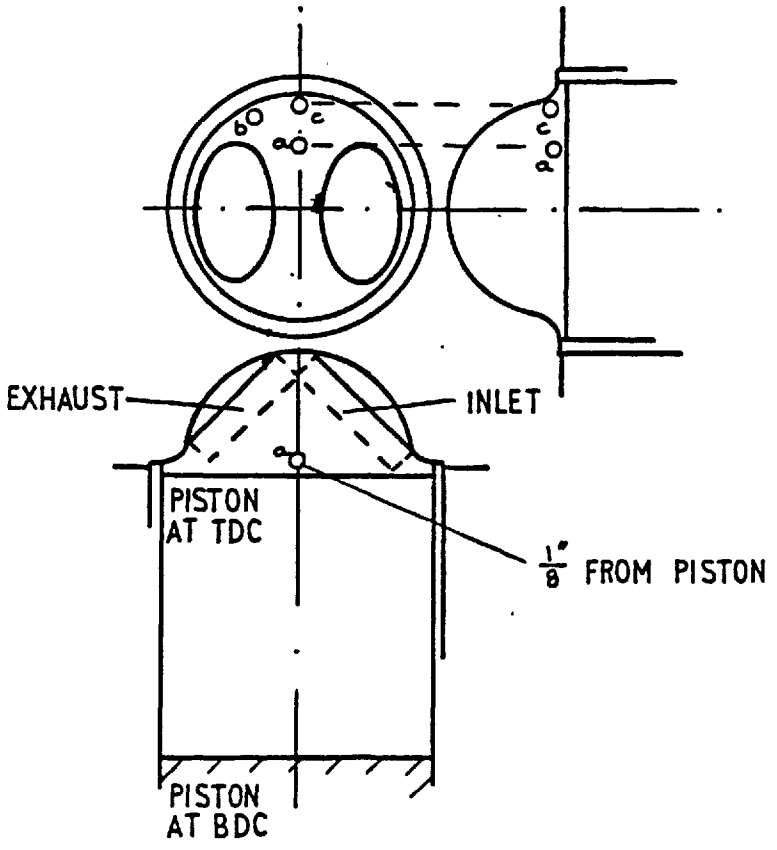

Fig. 2.3 Hemispherical combustion chamber engine configuration and measuring positions used by Arnold et al (1972)

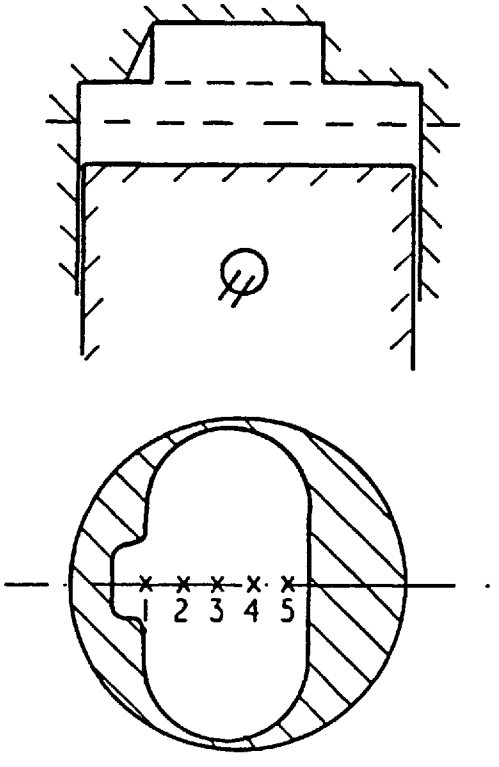

Fig. 2.4 Bowl-in-head engine configuration and measuring positions used by James (1972)

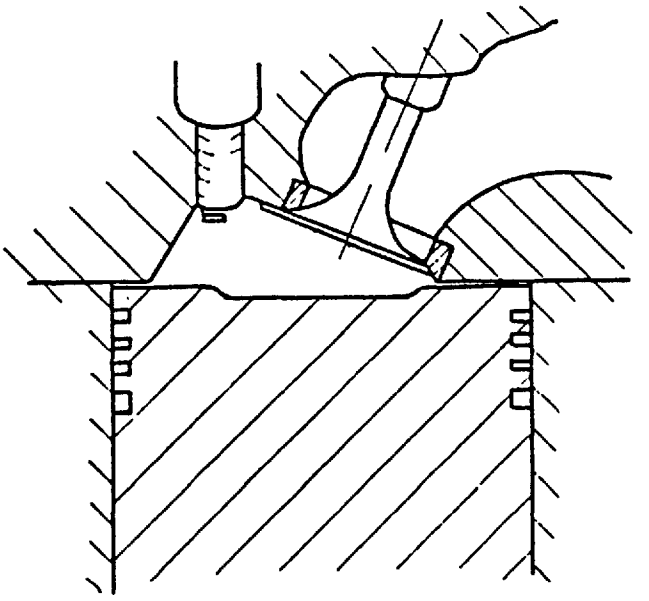

Fig. 2.5 Cross-section of the wedge chamber engine configuration used in the experiments of Dent and Salama (1975a, 1975b)

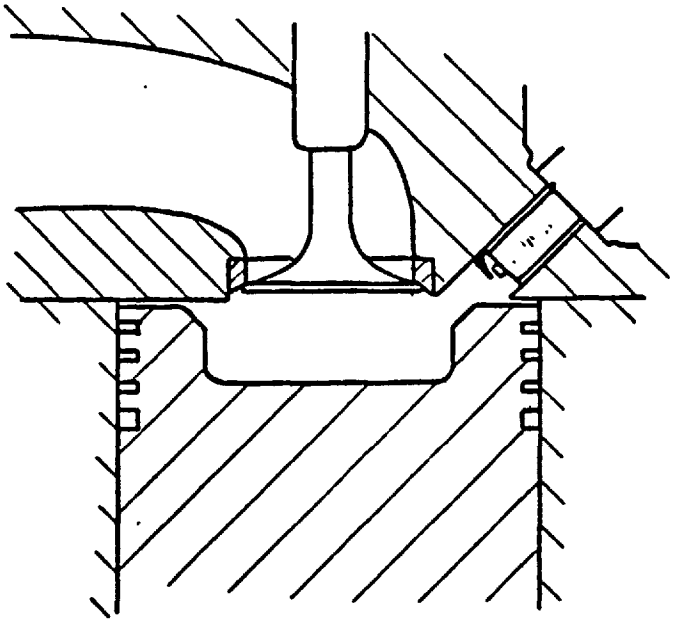

Fig. 2.6 Cross-section of the Heron chamber engine configuration used in the experiments of Dent and Salama (1975a, 1975b)

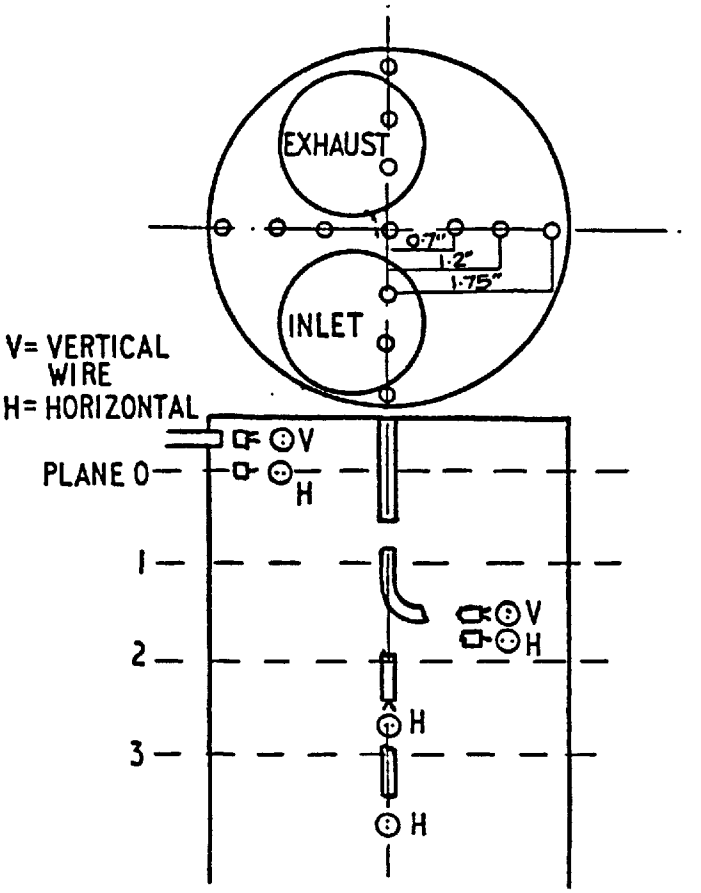

Fig. 2.7 Sketch of the engine configuration and measuring positions used by Tindal et al (1974)

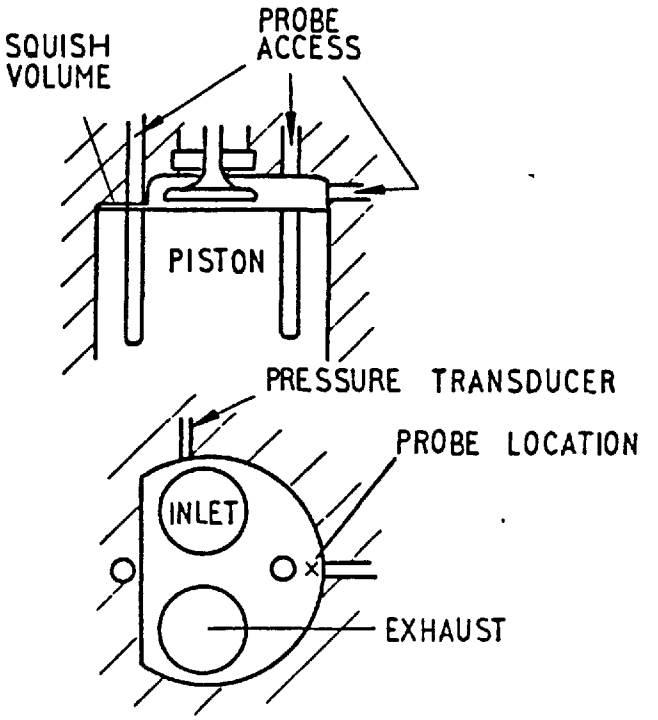

Fig. 2.8 Sketch of the Wisconsin L-head engine used by Witze (1976a, 1976b)

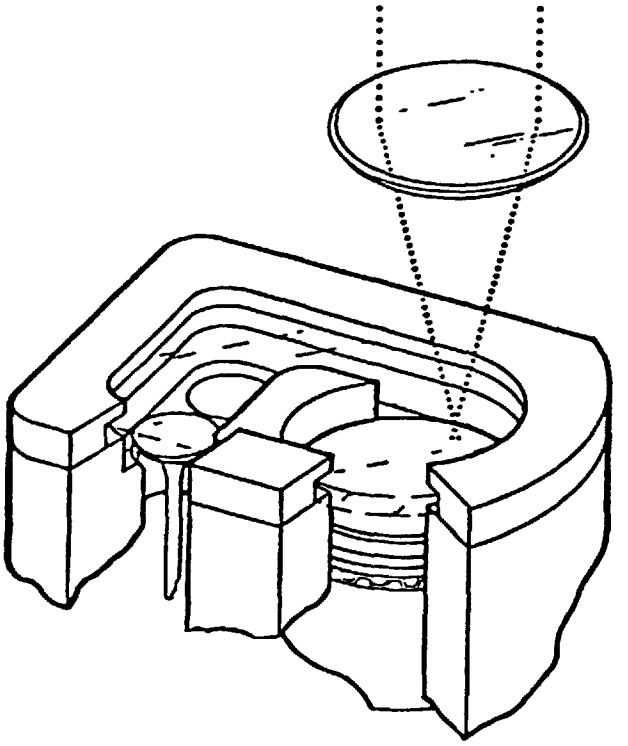

Fig. 2.9 Sketch of the Wisconsin L-head engine with optical access used by Witze (1978)

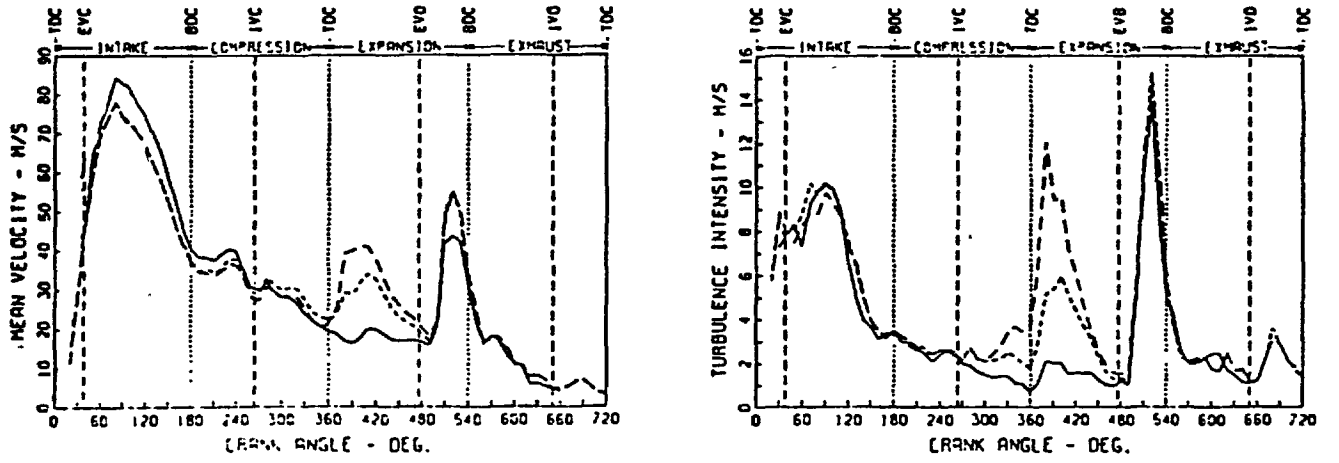

Fig. 2.10 Comparison between LDA (solid line) and HWA results (long dashes ~ 350°C, short dashes ~ 500°C wire temperatures), from Witze (1978)

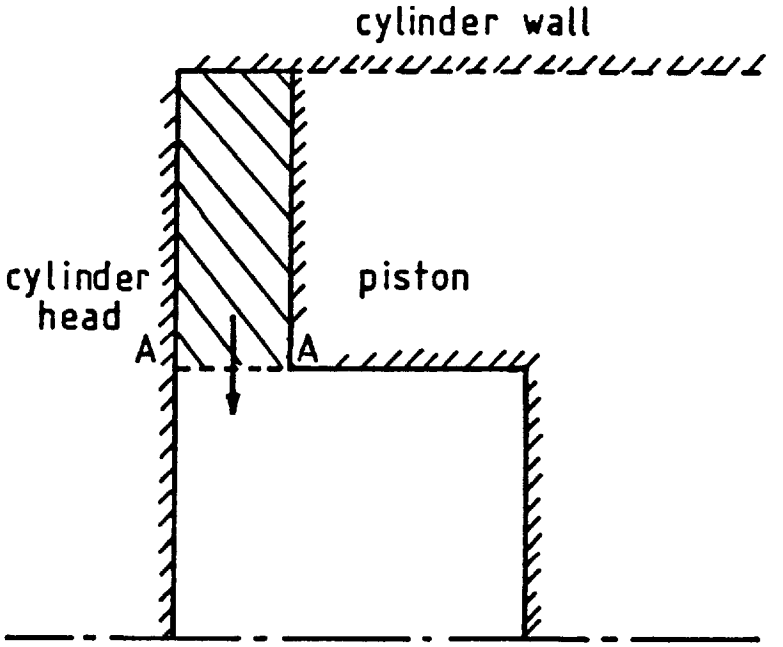

Fig. 2.11 Sketch of the cylinder-piston-bowl idealisation used for the squish studies of Fitzgeorge and Allison (1963)

Fig. 2.12 Open-chamber piston bowls used in the experiments of Shimamoto and Akiyama (1970)

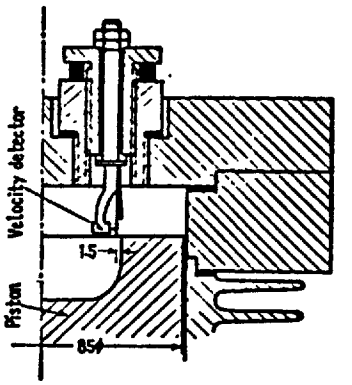

Fig. 2.13 Sketch of the squish velocity measuring apparatus used by Shimamoto and Akiyama (1970)

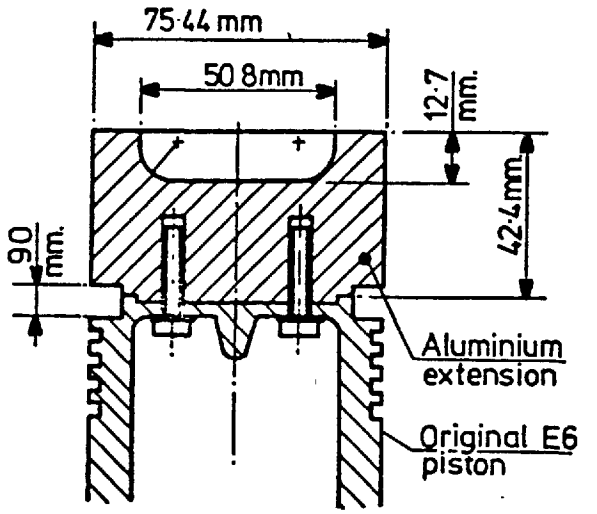

Fig. 2.14 Cross-section of the piston used in the squish studies of Woods and Ghirlando (1975)

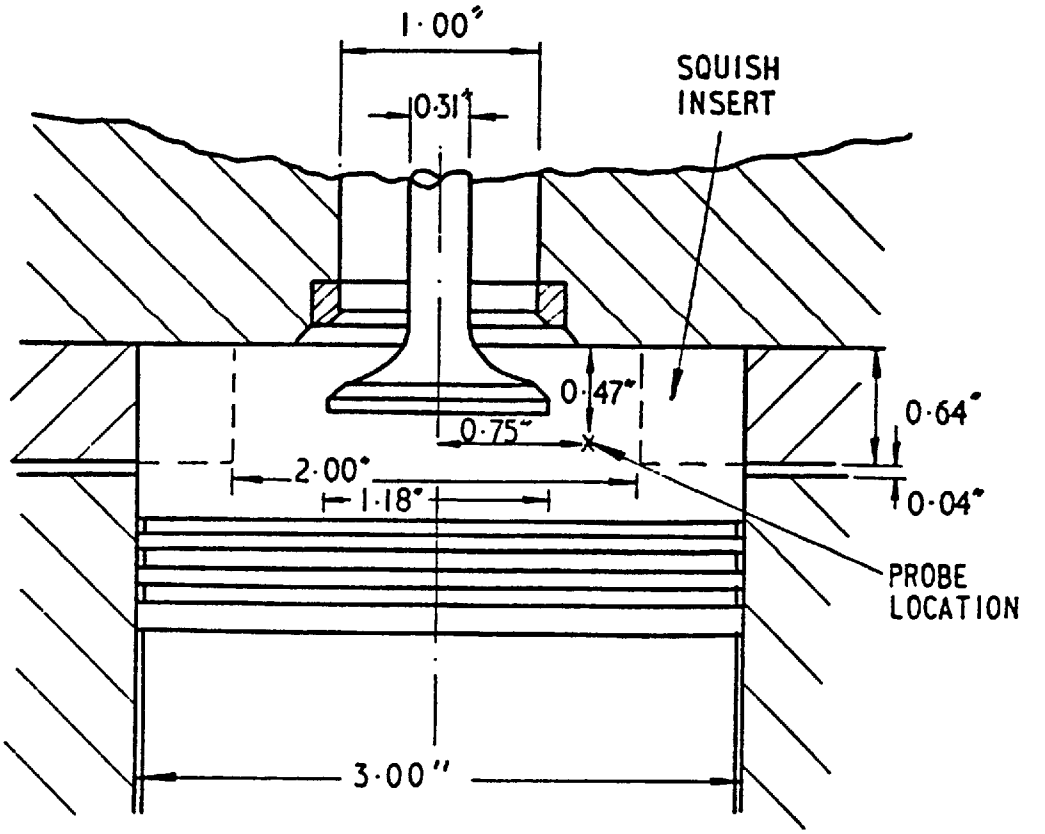

Fig. 2.15 Sketch of the axisymmetric engine used in the experiments of Witze (1976c)

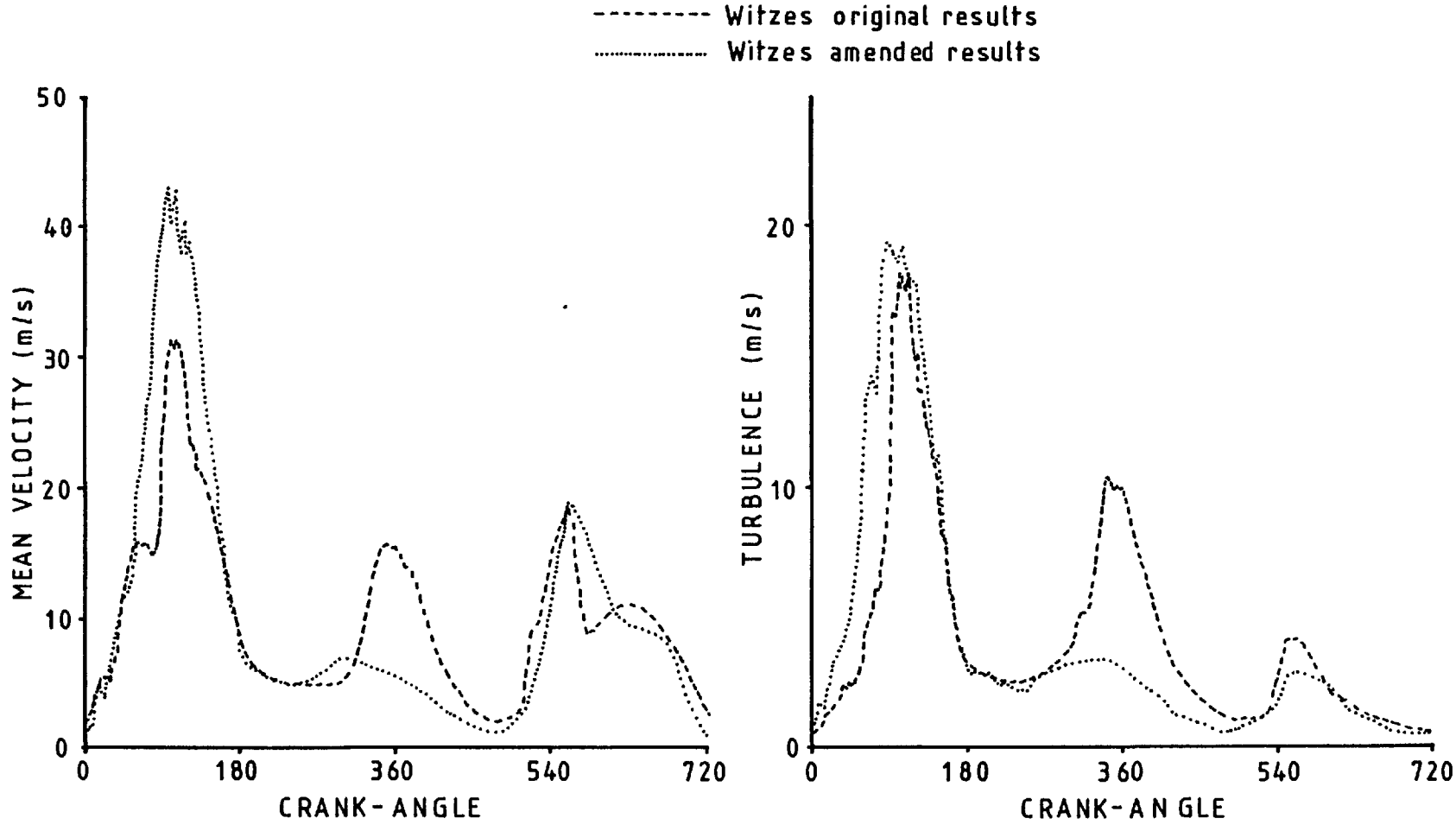

Fig. 2.16 Original and amended mean and turbulent velocities for the axisymmetric disc-chamber engine of Witze (1976c)

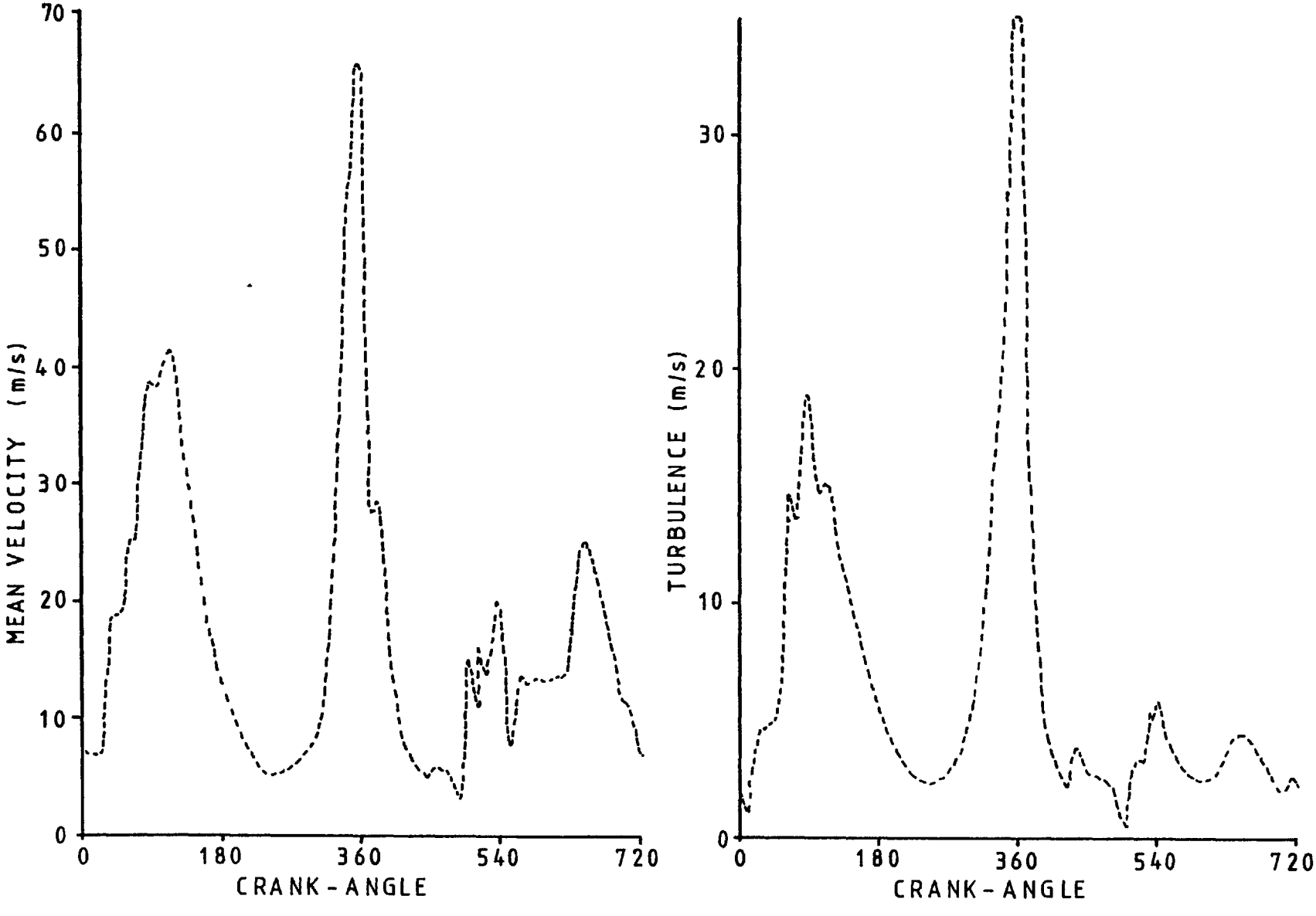

Fig. 2.17 Mean and turbulent velocities for the axisymmetric bowl-in-head geometry of Witze (1976c)

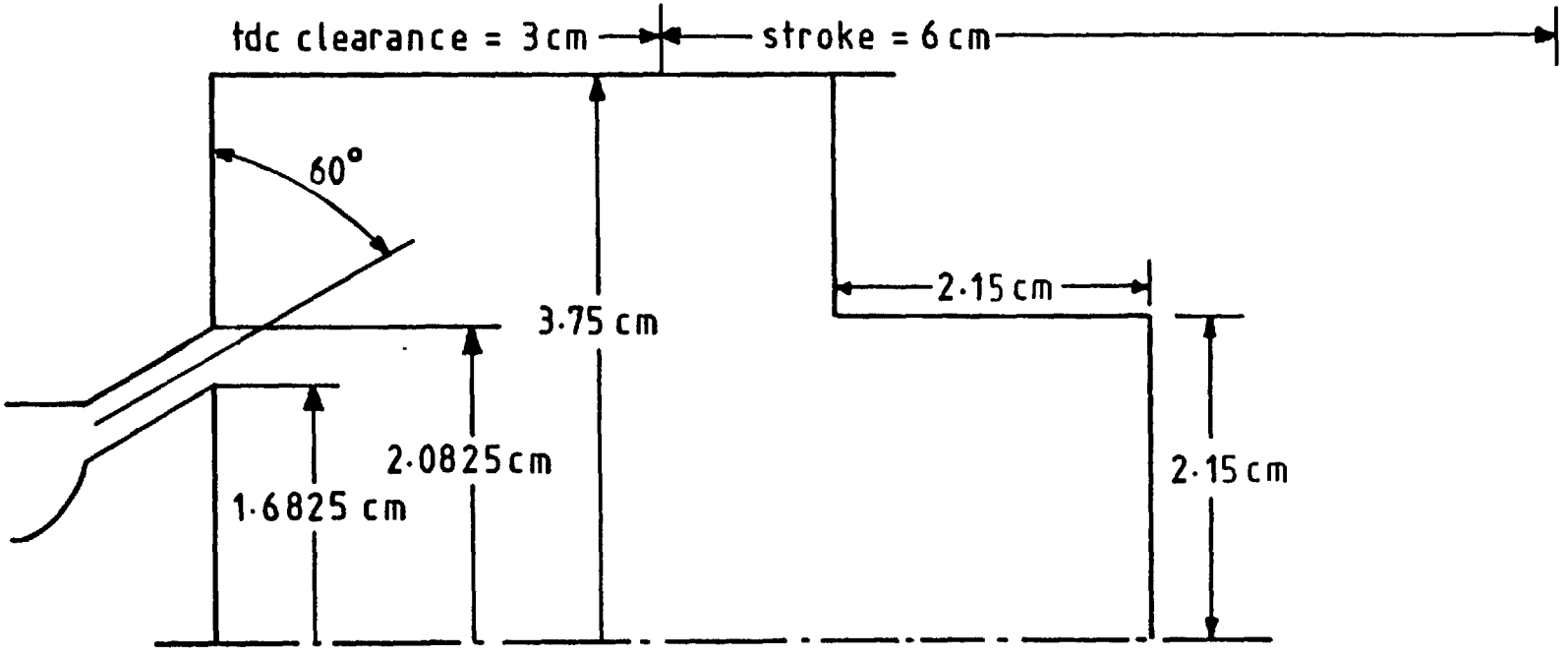

Fig. 2.18 Sketch of the axisymmetric engine used in the study of Morse et al (1978)

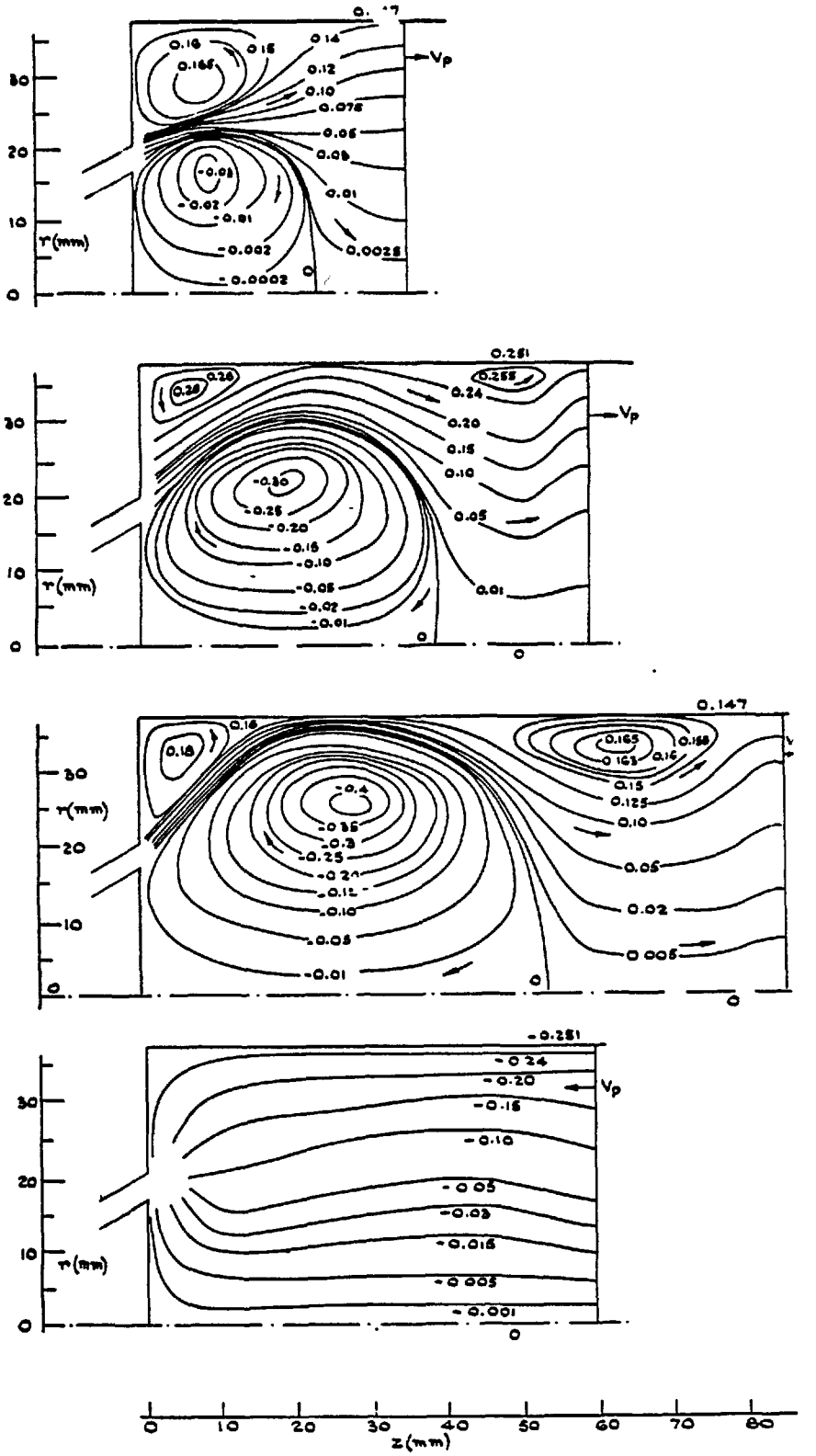

Fig. 2.19 Streamlines for the experiments, without swirl, of Morse et al (1978)

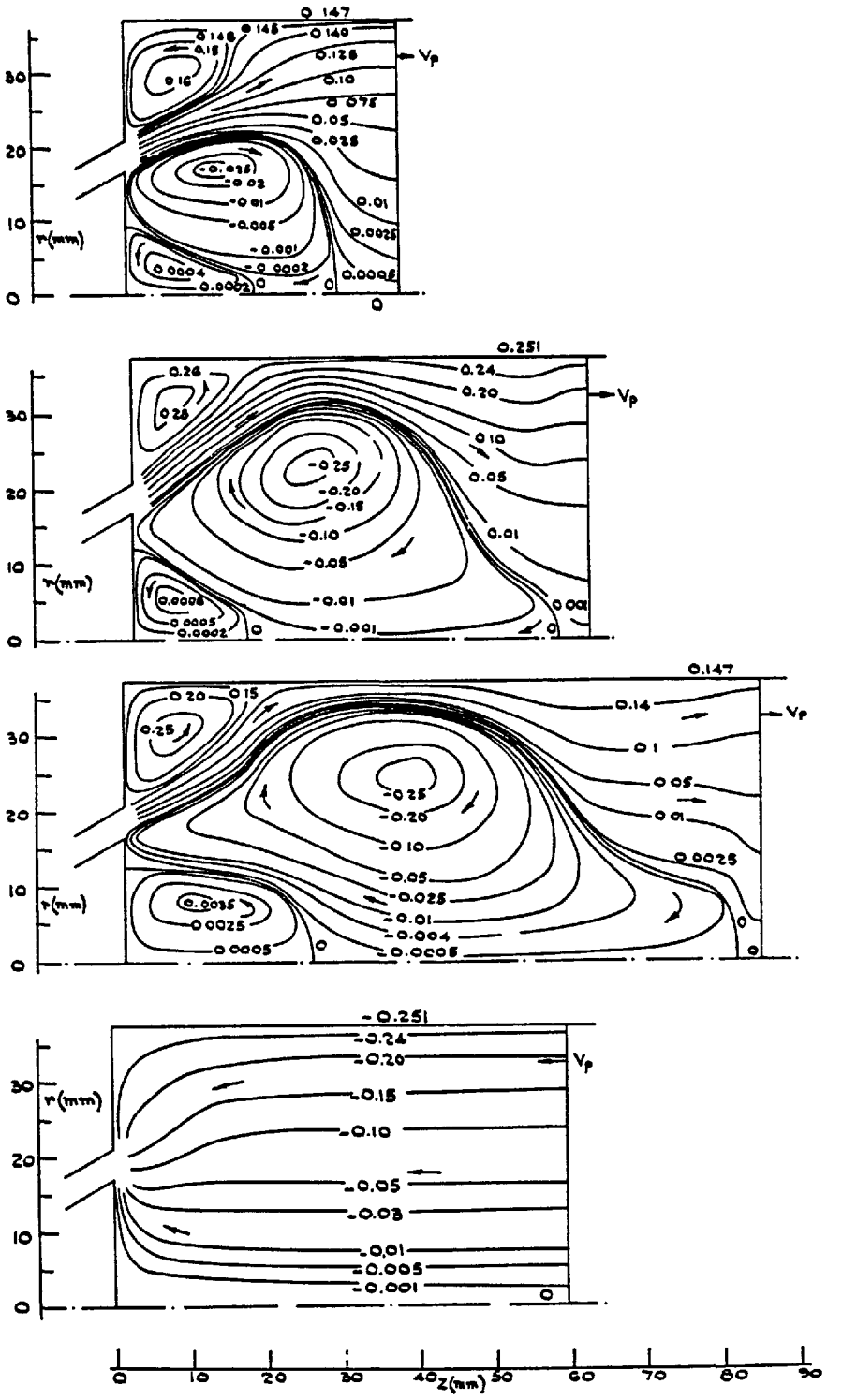

Fig. 2.20 Streamlines for the experiments, with swirl, of Morse et al (1978)

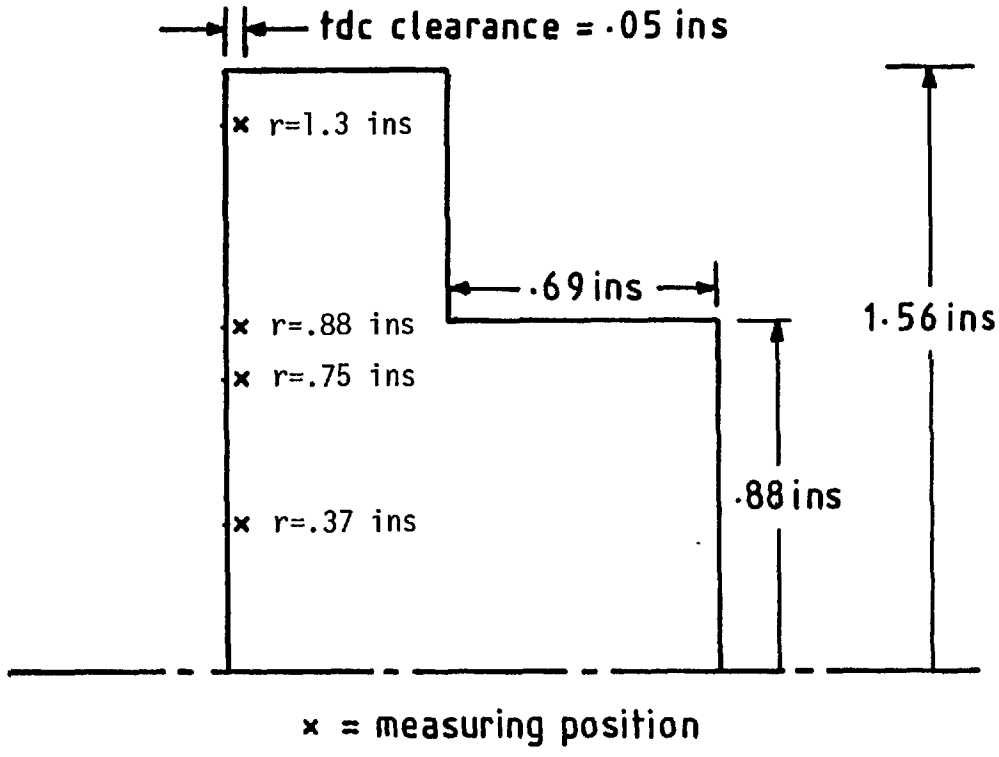

Fig. 2.21 Sketch of the geometry and heat flux measuring locations of the engine configuration of Dao (1972)

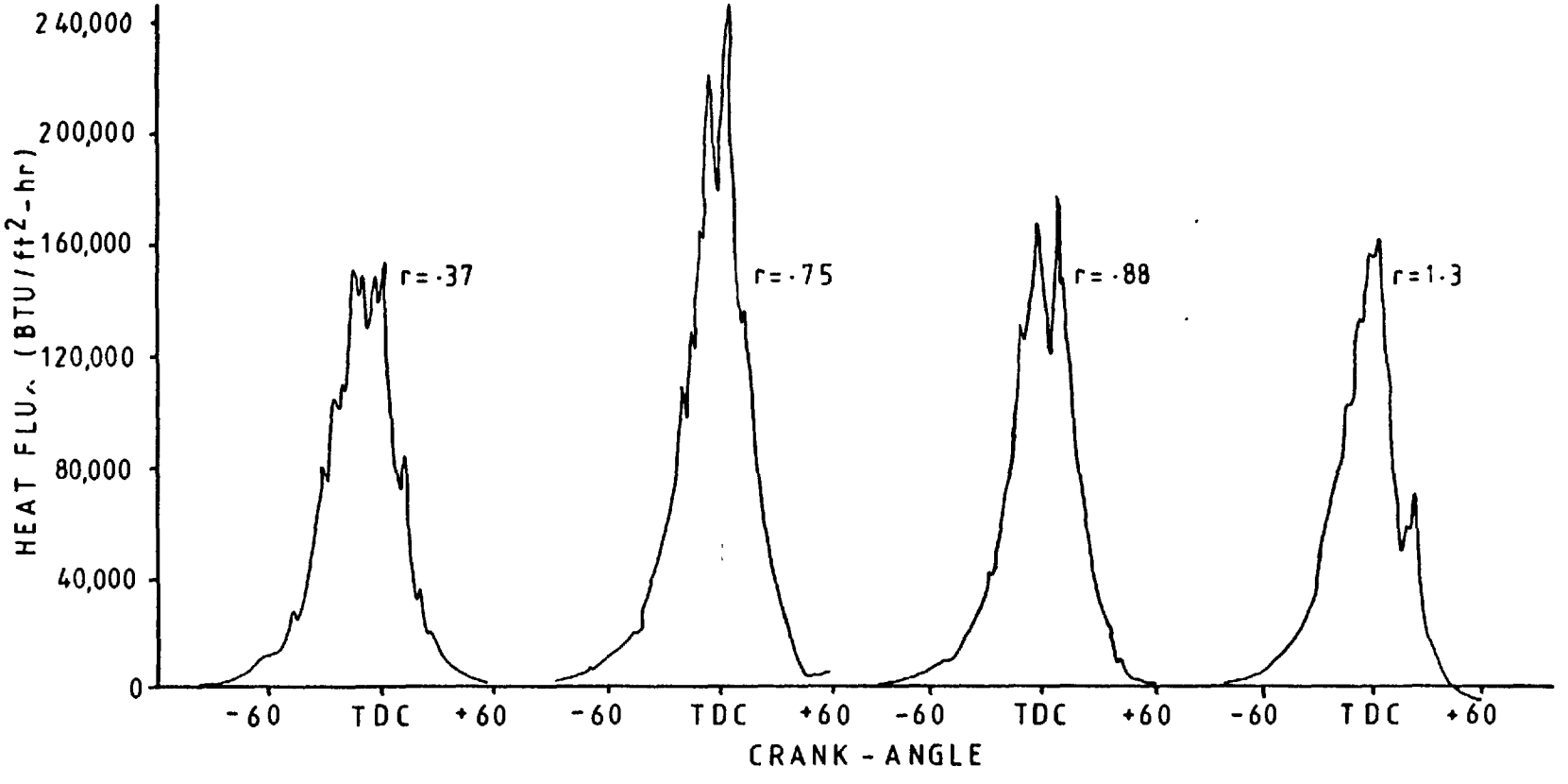

Fig. 2.22 Measurements of instantaneous heat flux from the engine of Dao (1972)

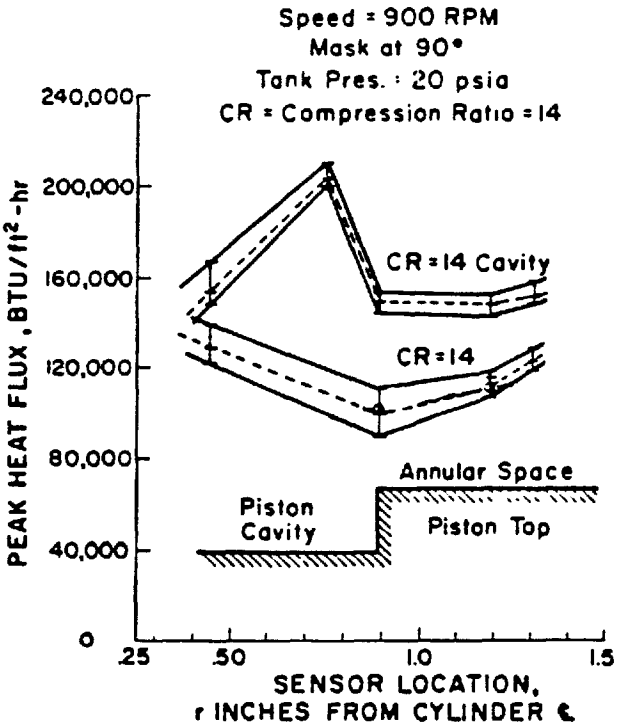

Fig. 2.23 Variation of peak heat flux with radial distance for cavity and flat-top pistons in the engine of Dao (1972)

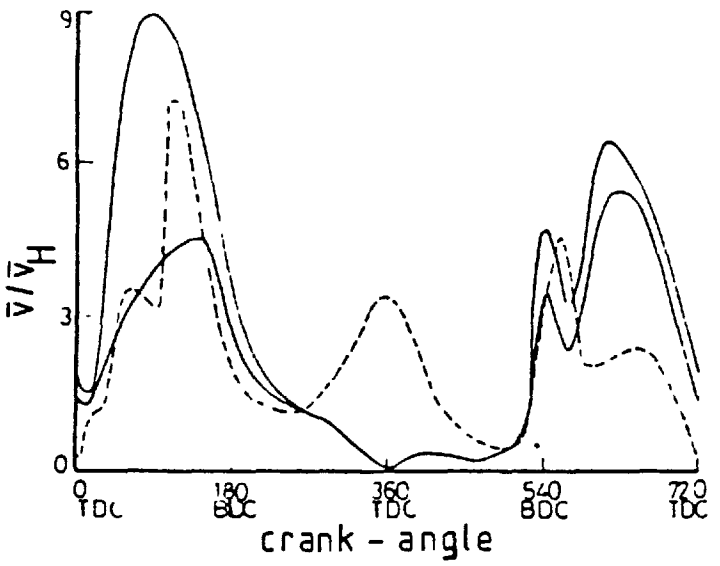

Fig. 2.24 Comparison between measurements (dashed line) and predictions (solid line - two positions) by Watkins (1977) for the experiments of Witze (1976c)

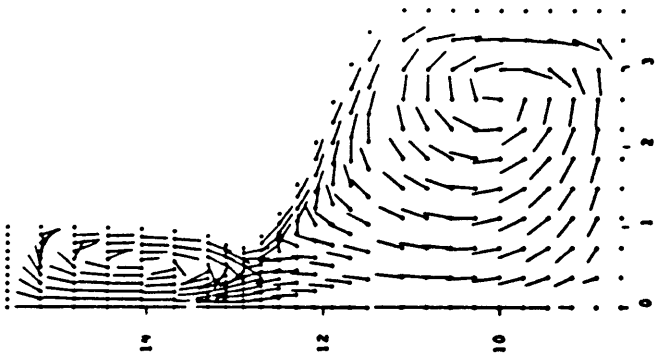

Fig. 2.25 Velocity predictions for the Honda CVCC prechamber engine at TDC by Boni (1978)

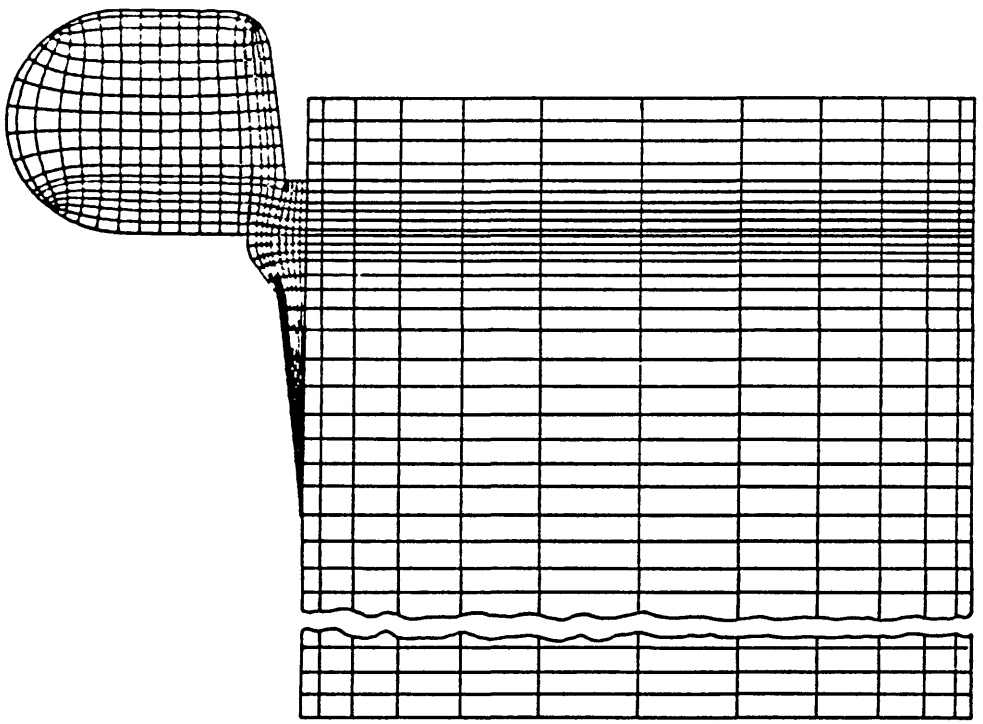

Fig. 2.26 Curvilinear orthogonal grid used for the prechamber engine calculations of Gosman et al (1979)

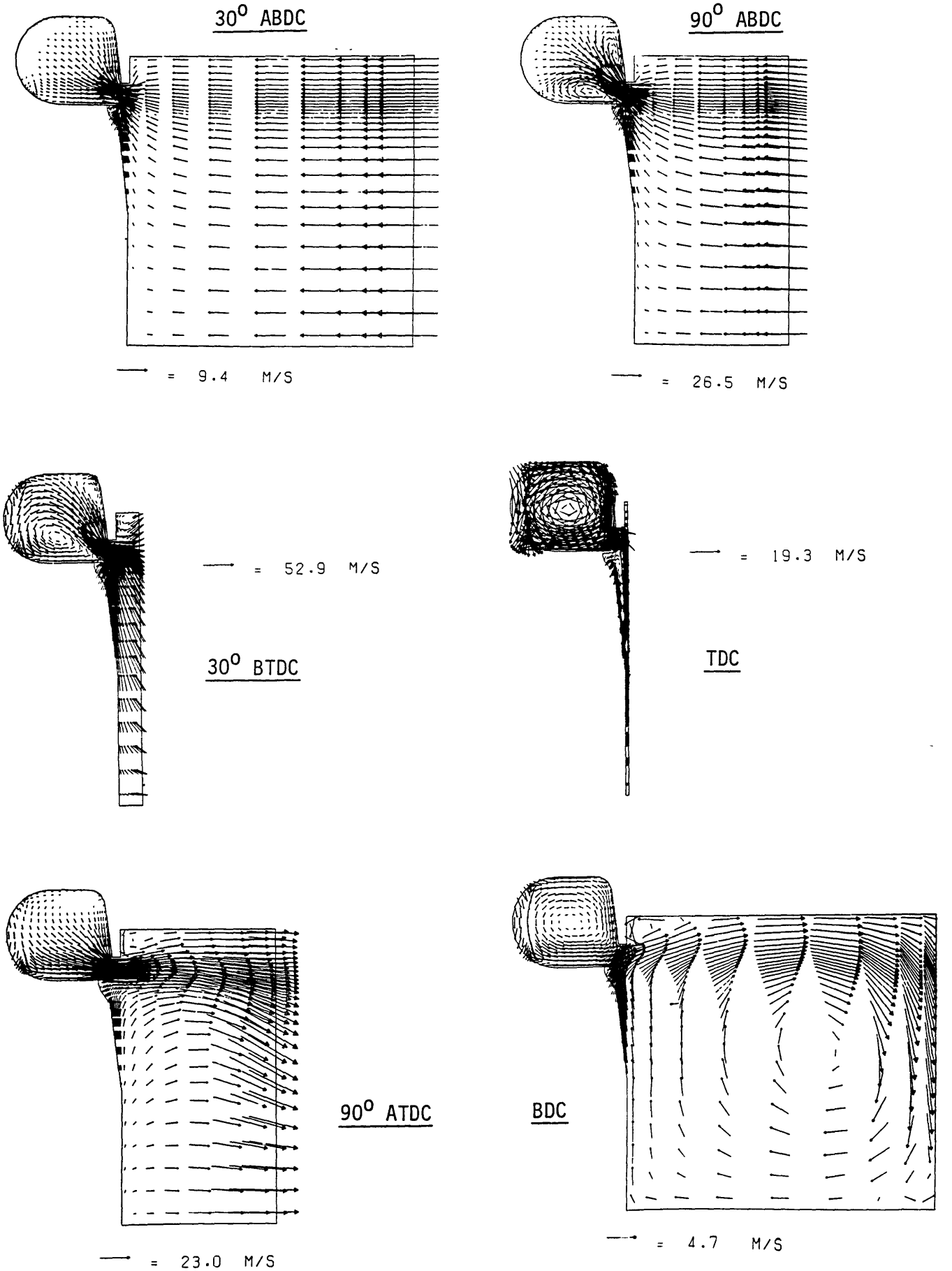

Fig. 2.27 Predicted velocity fields for the prechamber engine configuration of Gosman et al (1979)

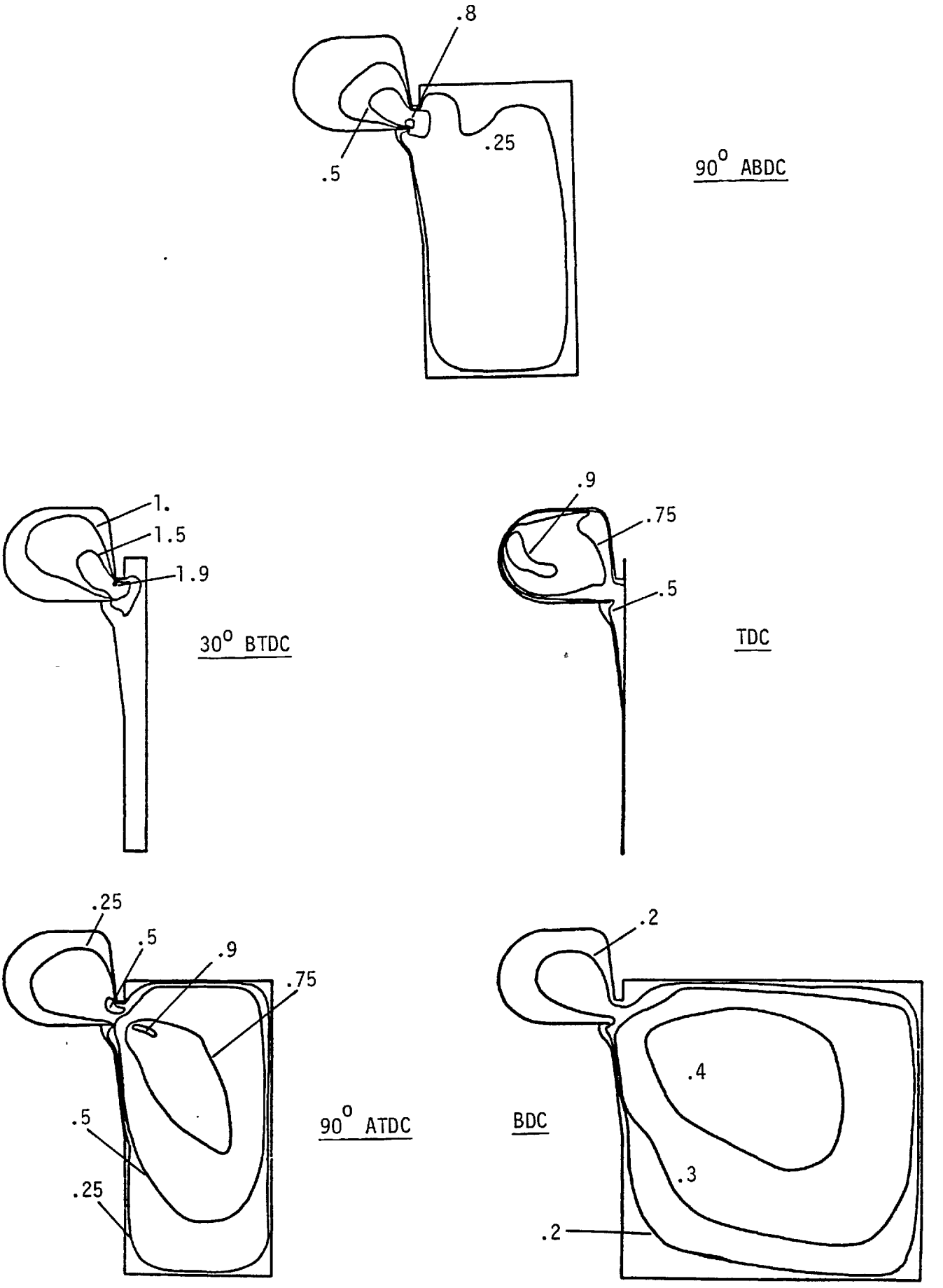

Fig. 2.28 Predicted turbulence intensities for the prechamber engine configuration of Gosman et al (1979)

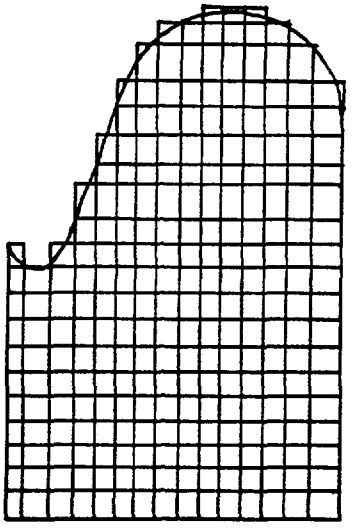

(a) Rectilinear co-ordinate frame

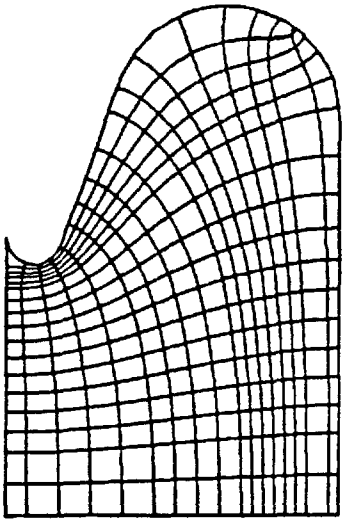

(b) Curvilinear-orthogonal co-ordinate frame

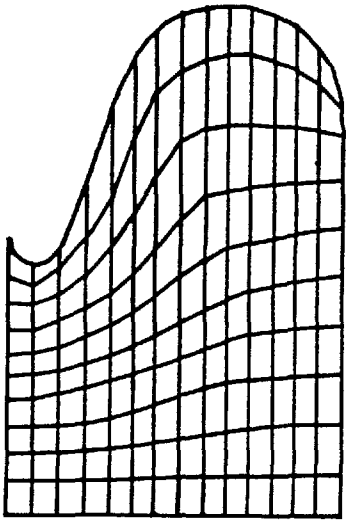

(c) Non-orthogonal co-ordinate frame

Fig. 3.1 Alternative computing meshes for piston-bowls

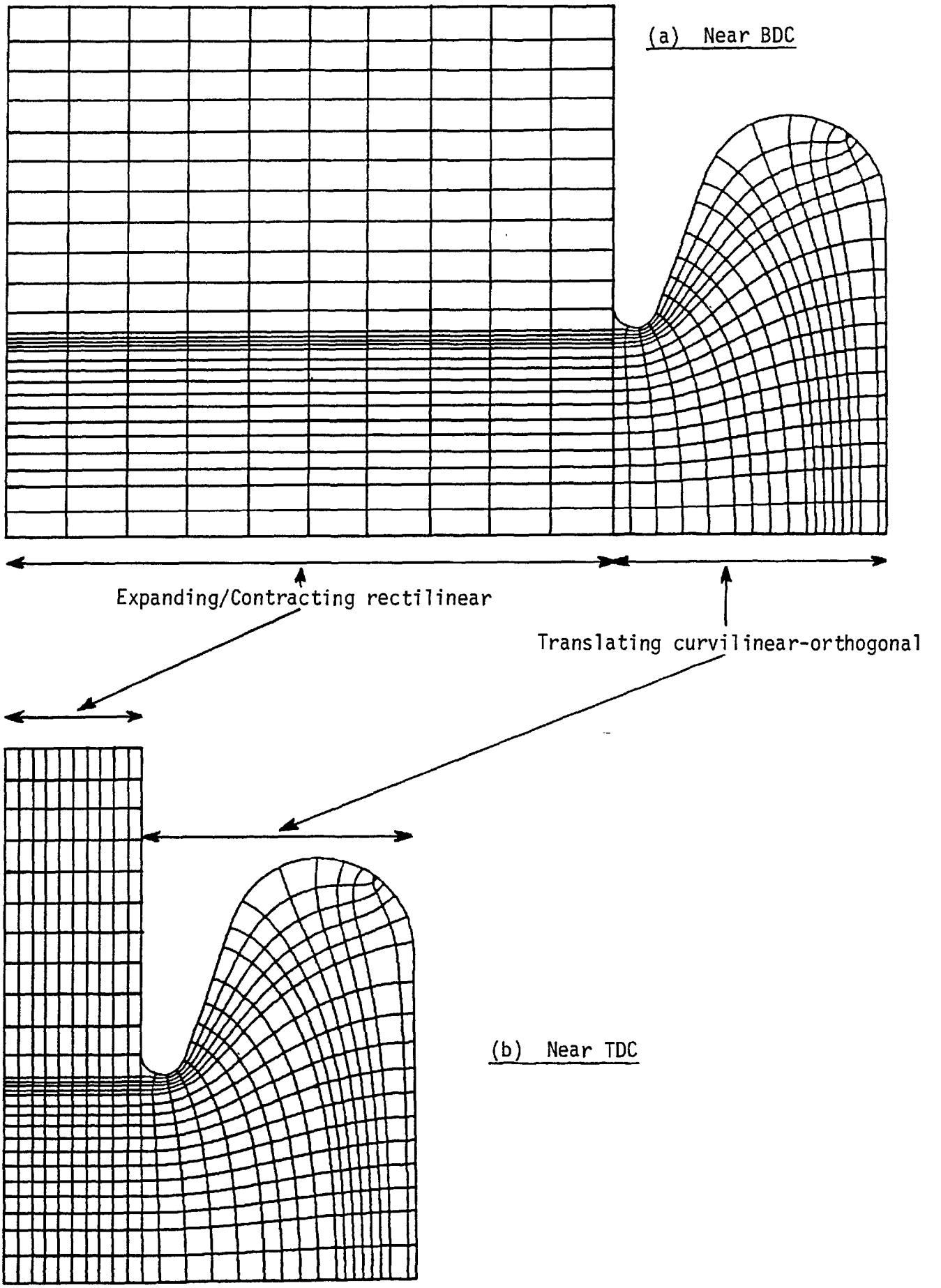

Fig. 3.2 The selected computational grid, showing curvilinear-orthogonal and rectilinear components

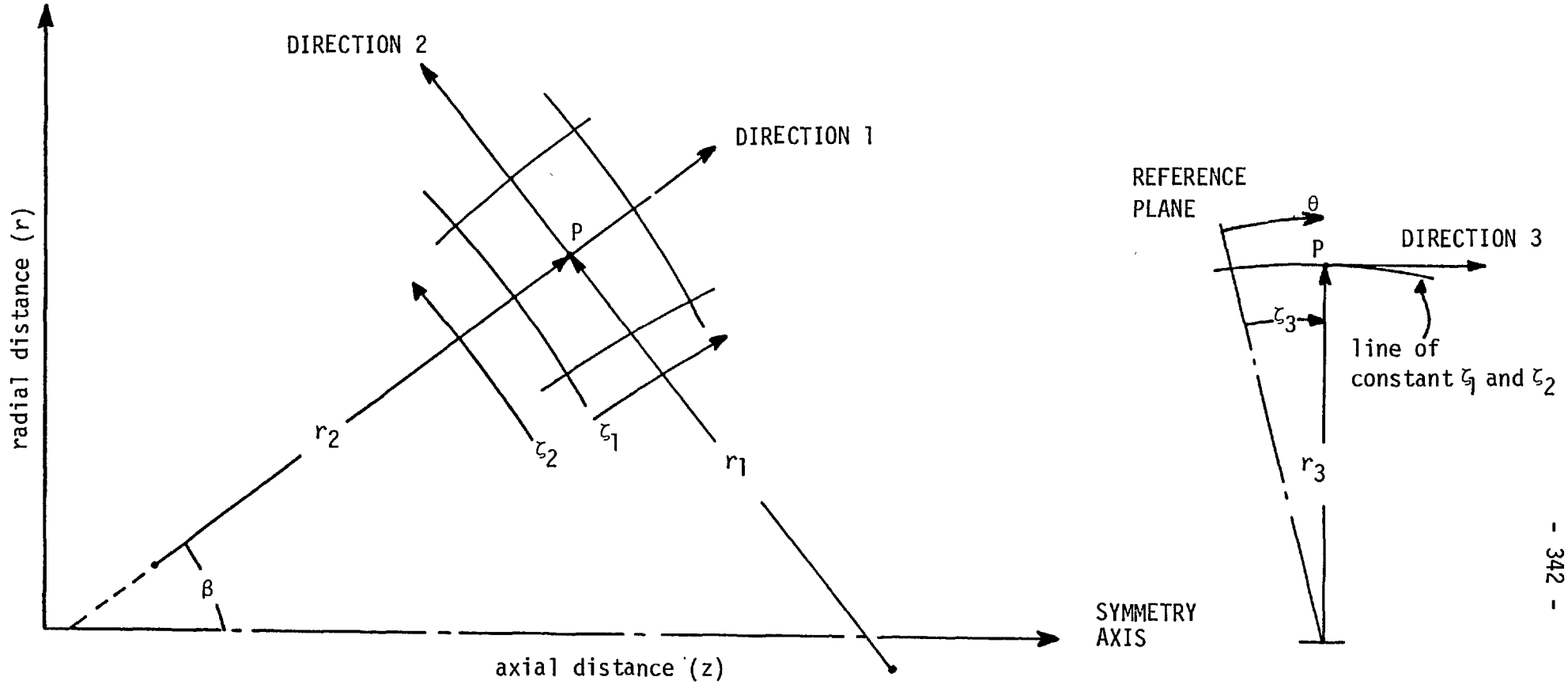

Fig. 3.3 The axisymmetric curvilinear-orthogonal co-ordinate system

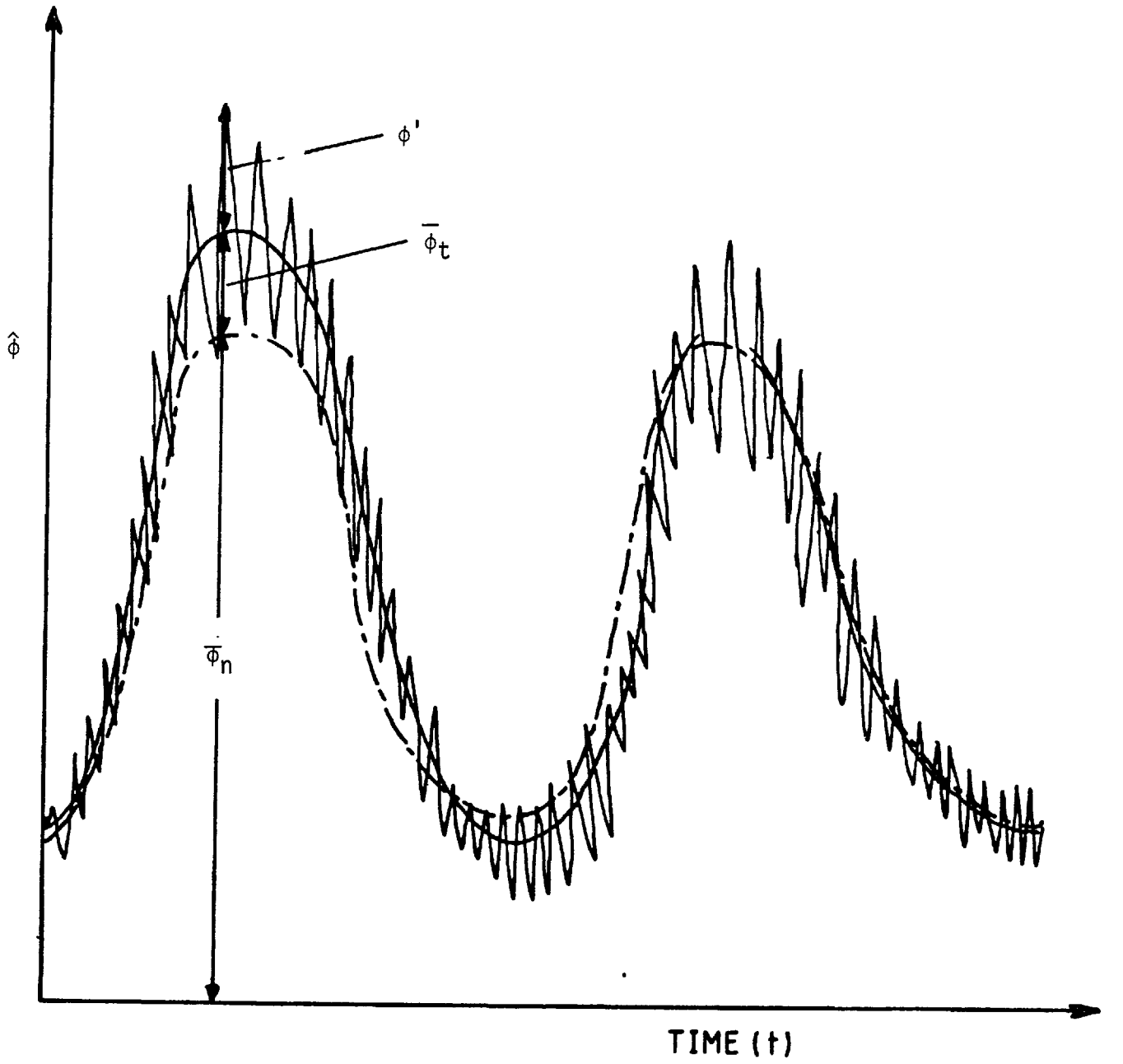

Fig. 3.4 Components of $\hat{\phi}$ (instantaneous ϕ) for a cyclic process with cycle-to-cycle variations

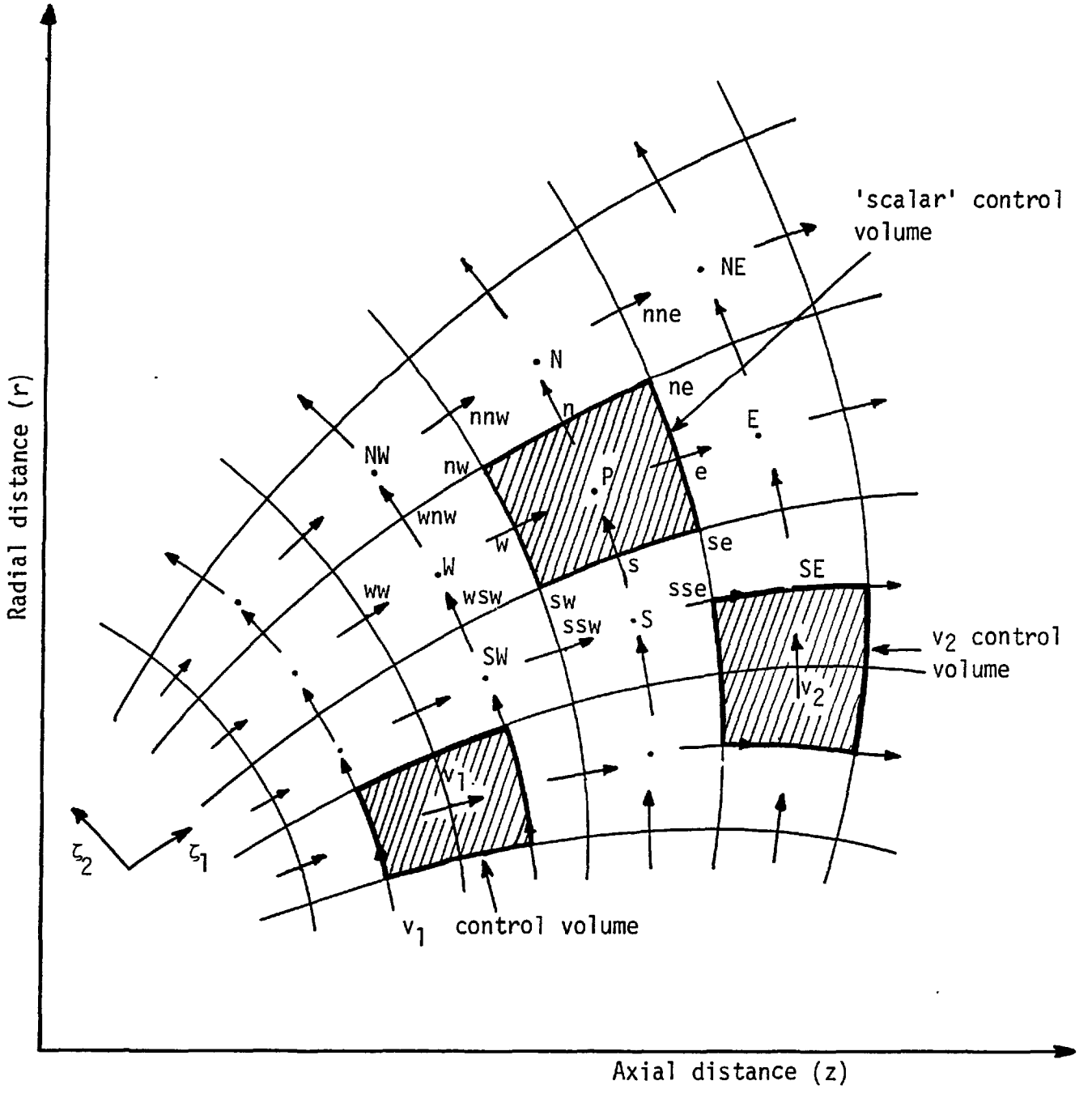

Fig. 4.1 Computational grid showing scalar, v_1 and v_2 control volumes and notation

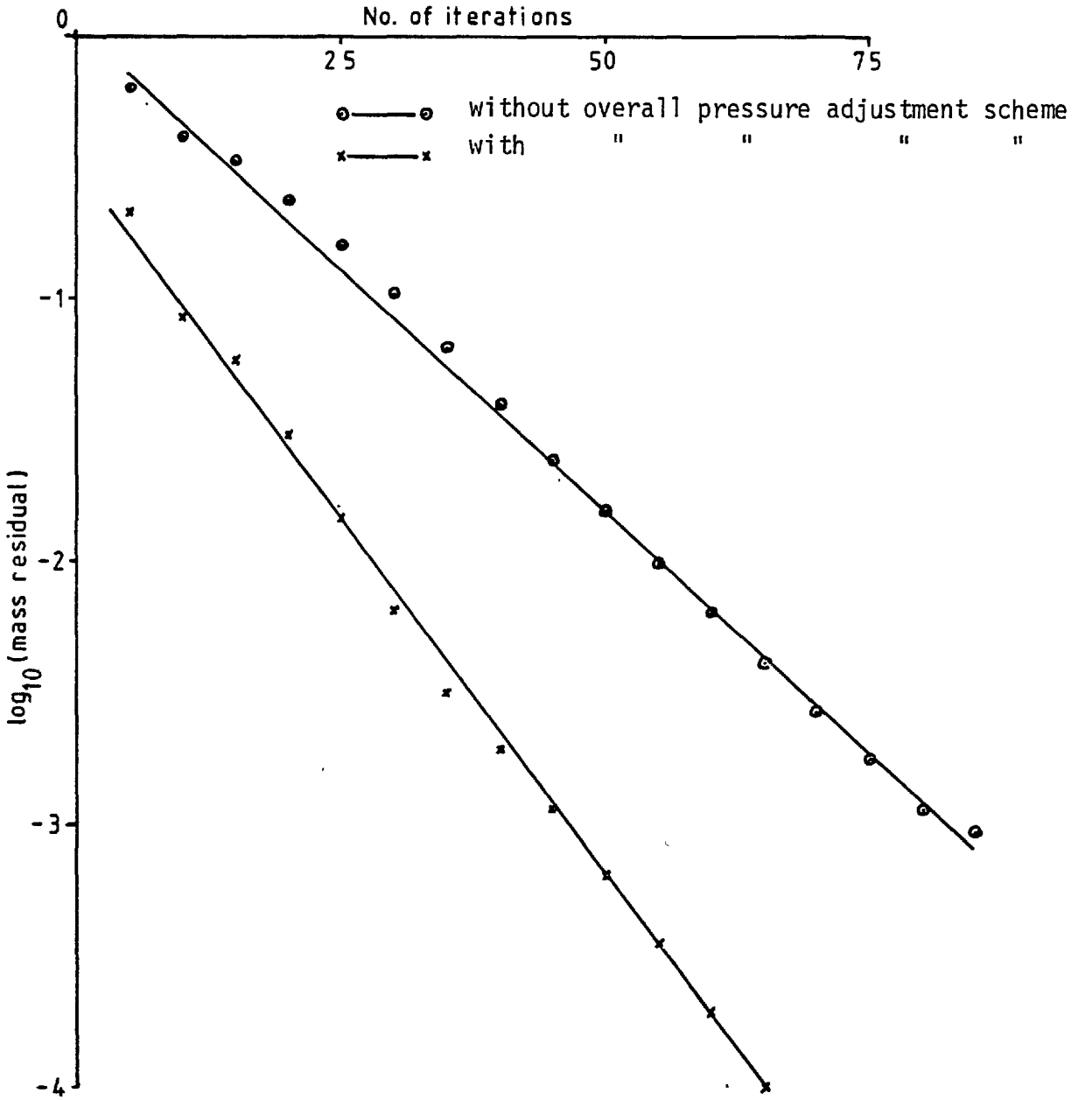

Fig. 4.2 Variation of mass residual with number of iterations with and without overall pressure adjustment scheme

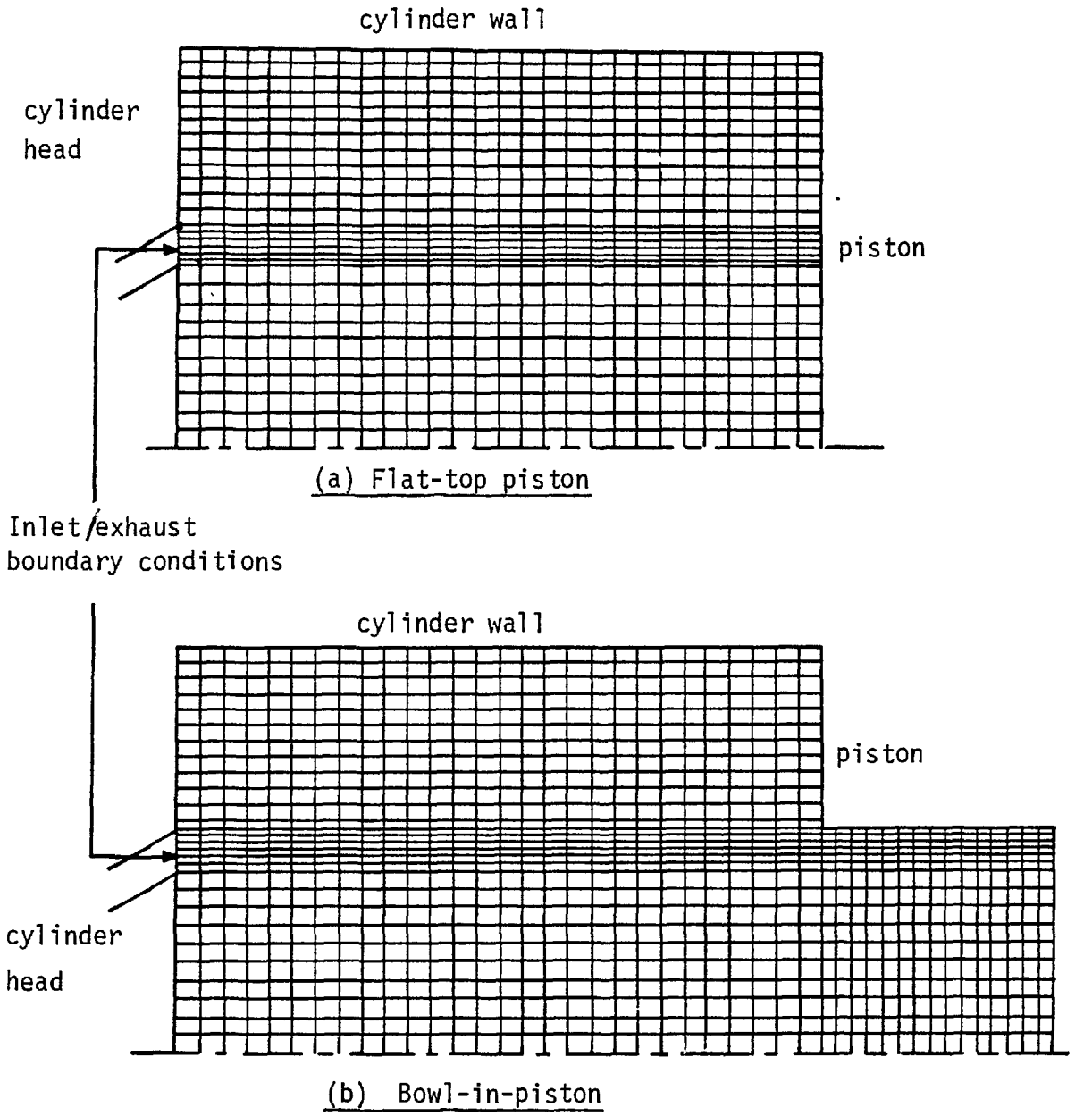

Fig. 4.3 Computational grids used for the simulation of the experiments of Morse et al (1978)

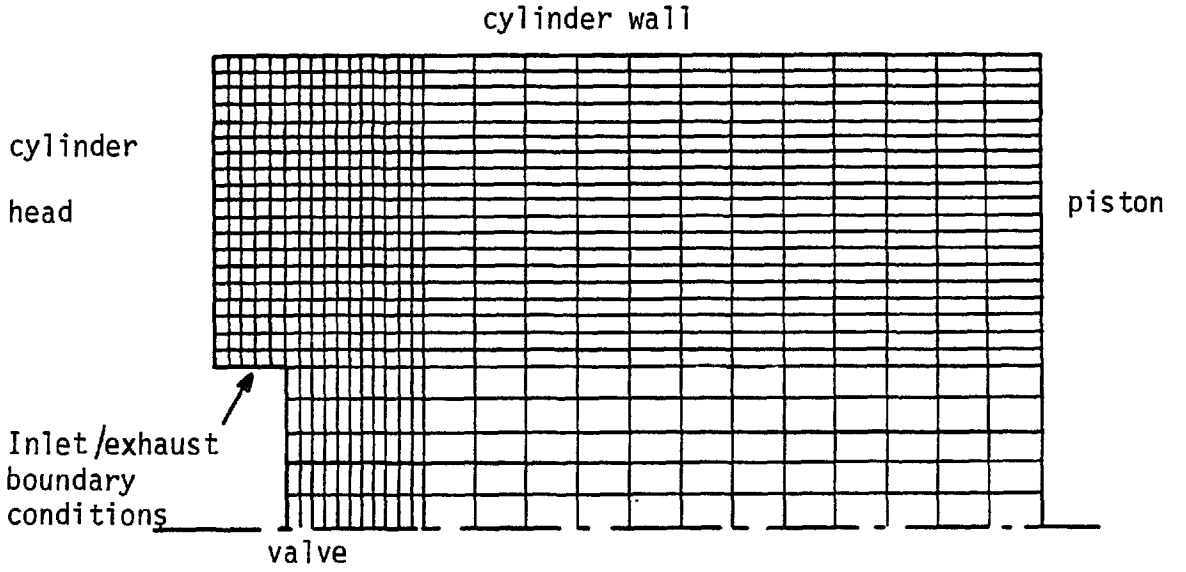

(a) Valve open, near BDC

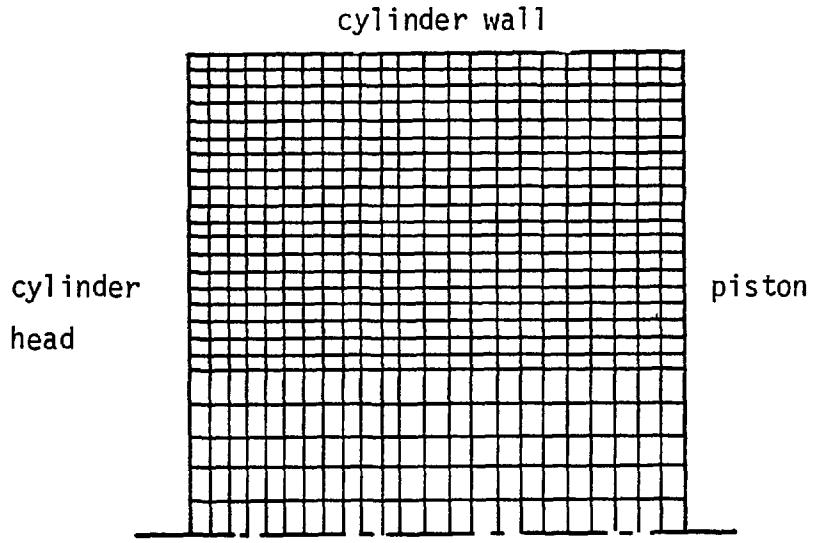

(b) Valve closed, near TDC

Fig. 4.4 Computational grid used for the simulation of the experiments of Witze (1976c), (Flat cylinder head configuration)

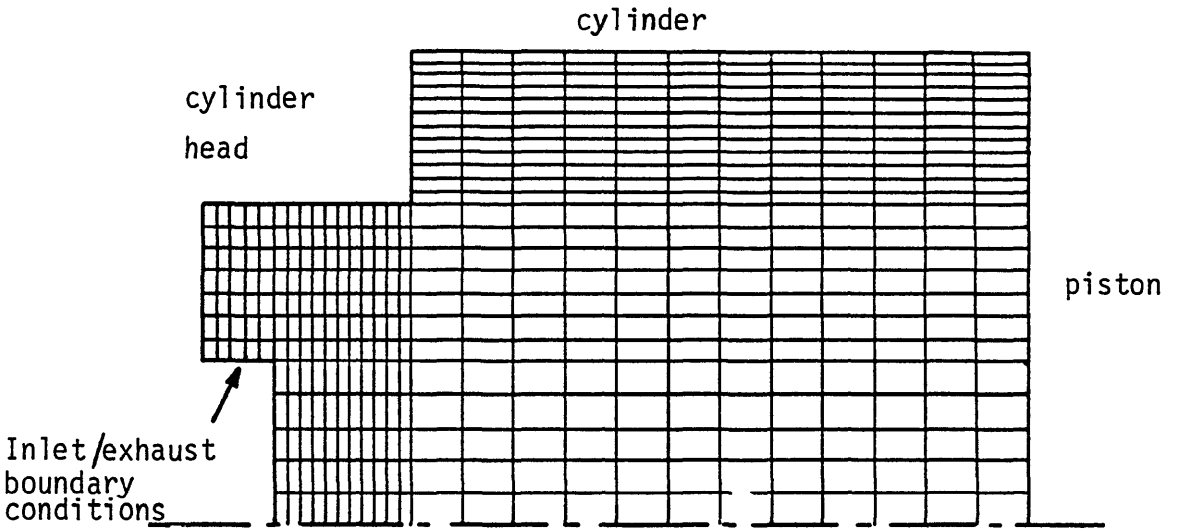

(a) Valve open, near BDC

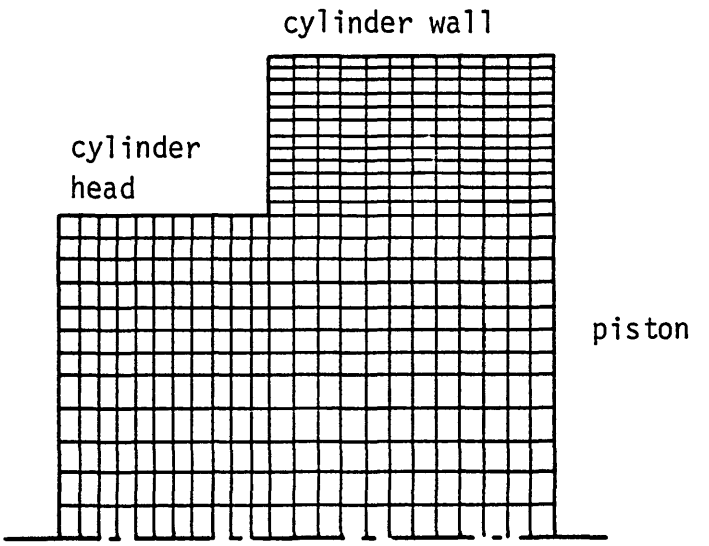

(b) Valve closed, near TDC

Fig. 4.5 Computational grid used for the simulation of the experiments of Witze (1976c), (Bowl-in-head configuration)

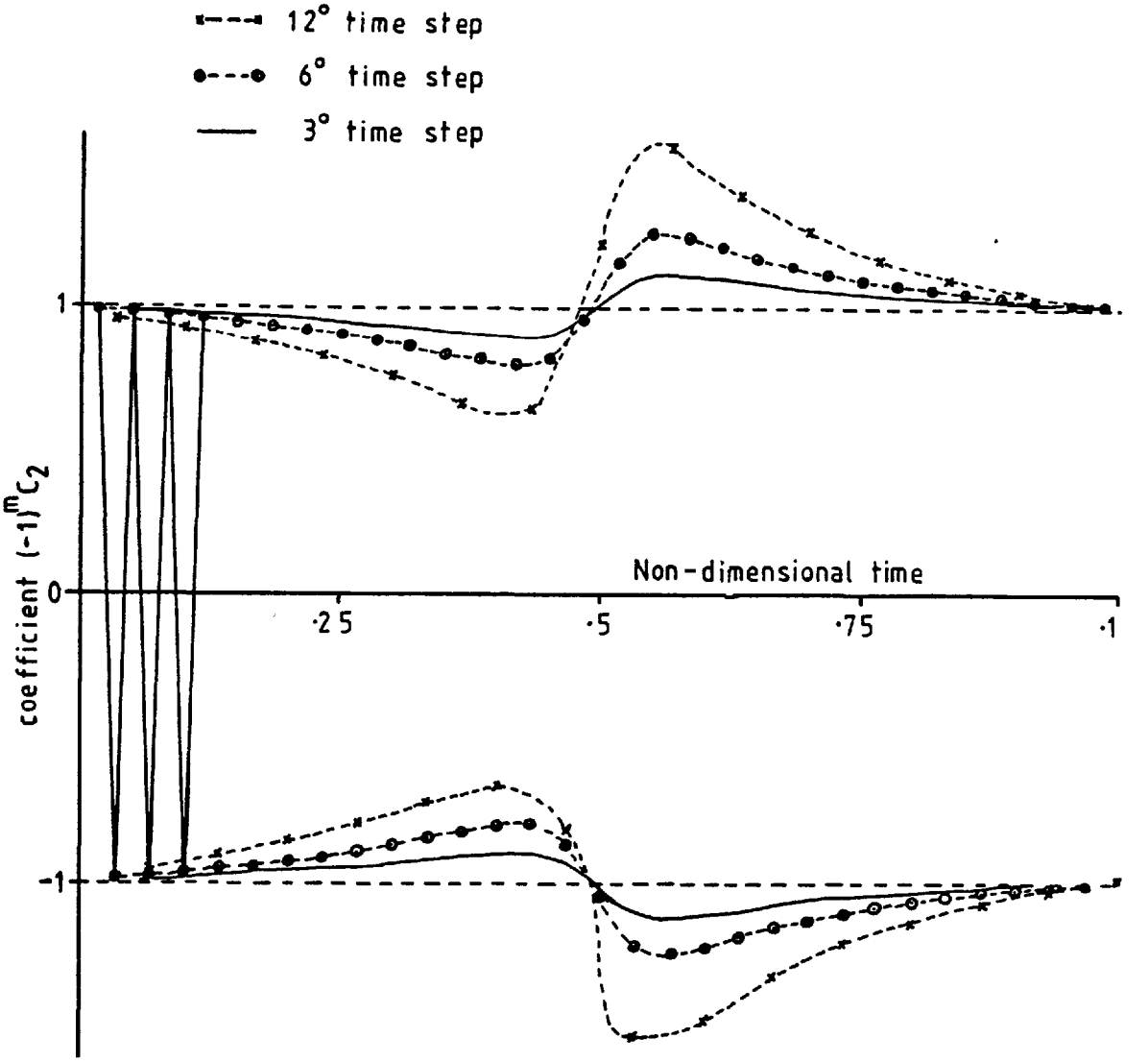

Fig. 4.6 Variation of the coefficient $(-1)^m C_2$ (equation 4.76) over one cycle

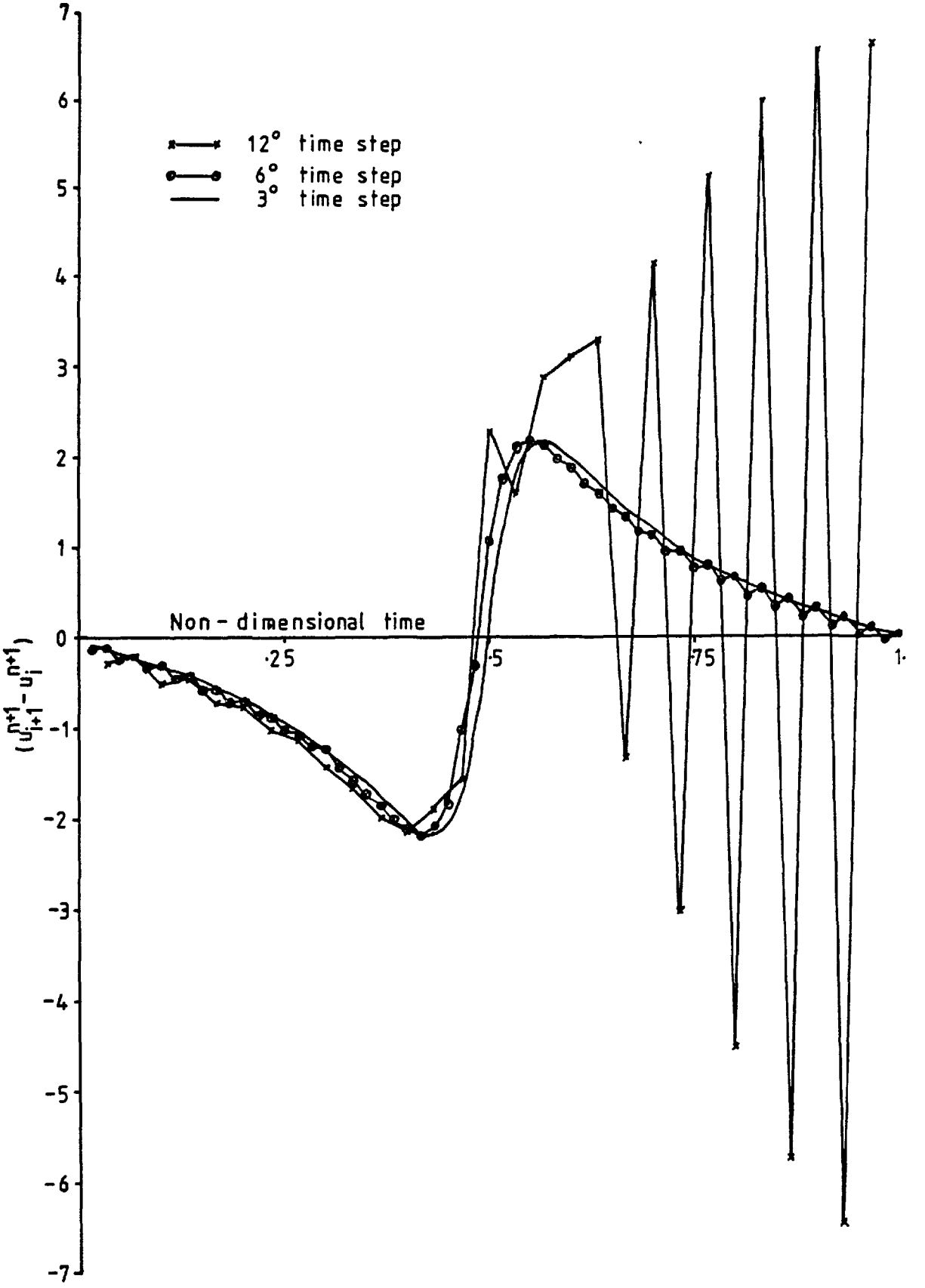

Fig. 4.7 Solution of equation 4.74 over one cycle

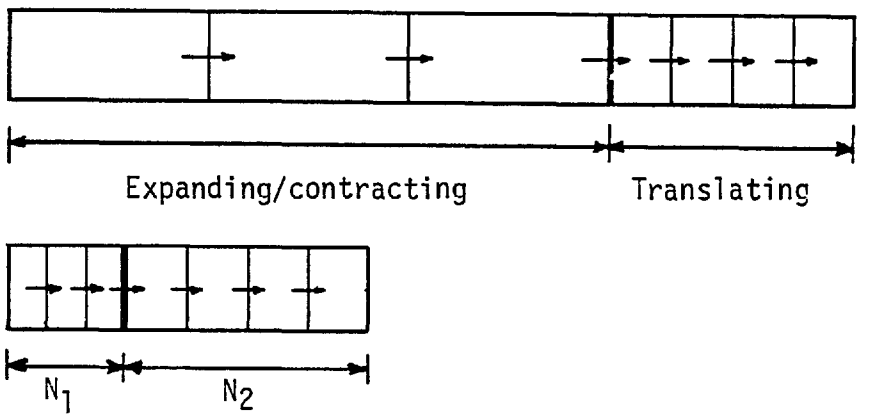

(a) One-dimensional 'hybrid' grid

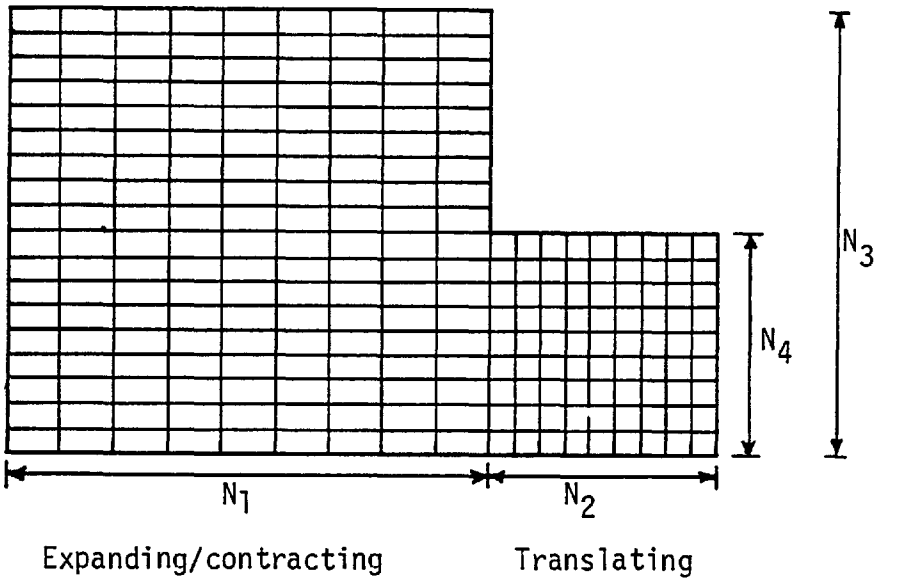

(b) Two-dimensional 'piston-bowl' grid

Fig. 4.8 Computational grids used for the 1-d and 2-d numerical assessment

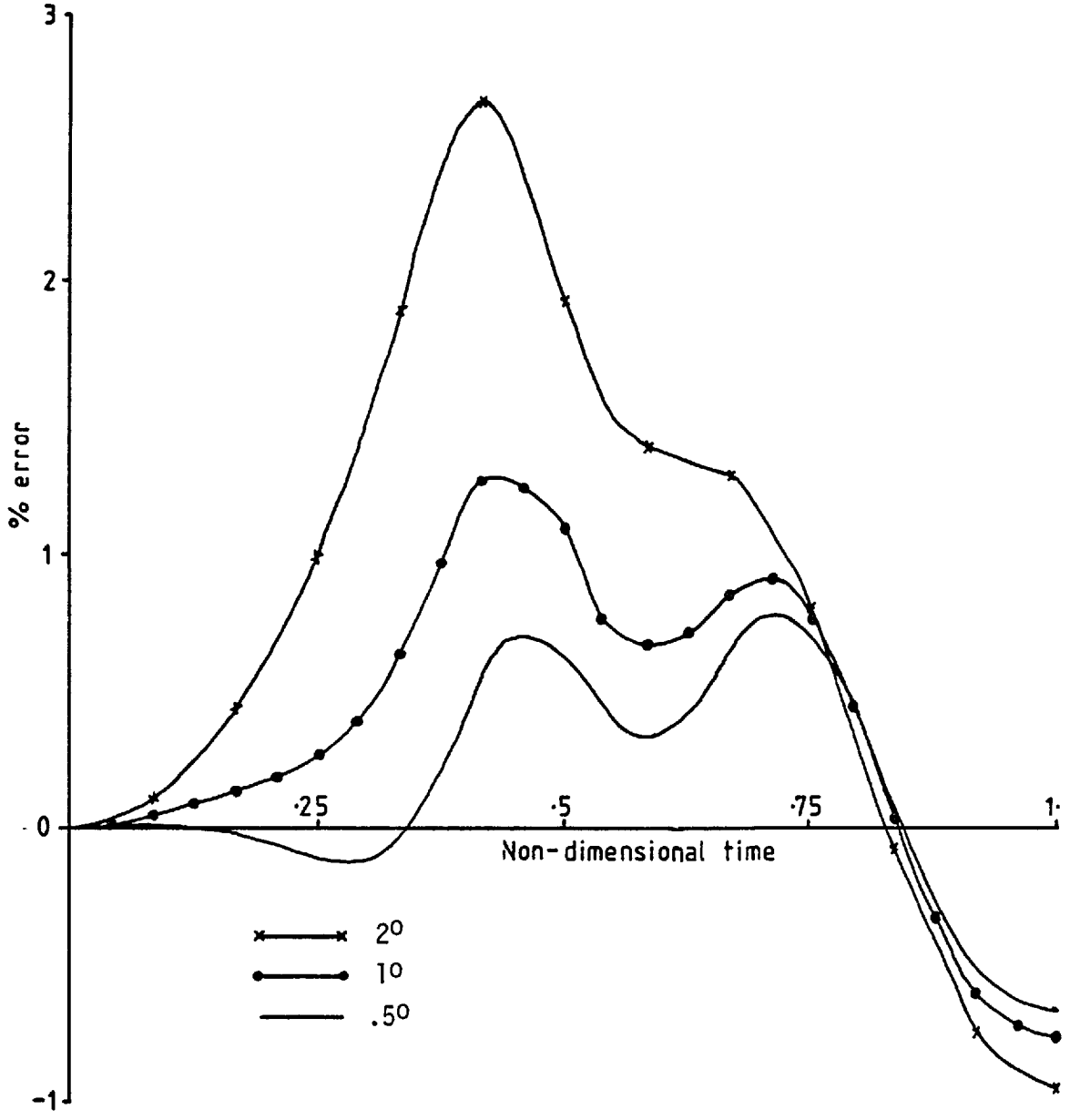

Fig. 4.9 Effect of time-step on velocity error (solution of momentum equation only with implicit differencing; grid ~N_1=N_2=6)

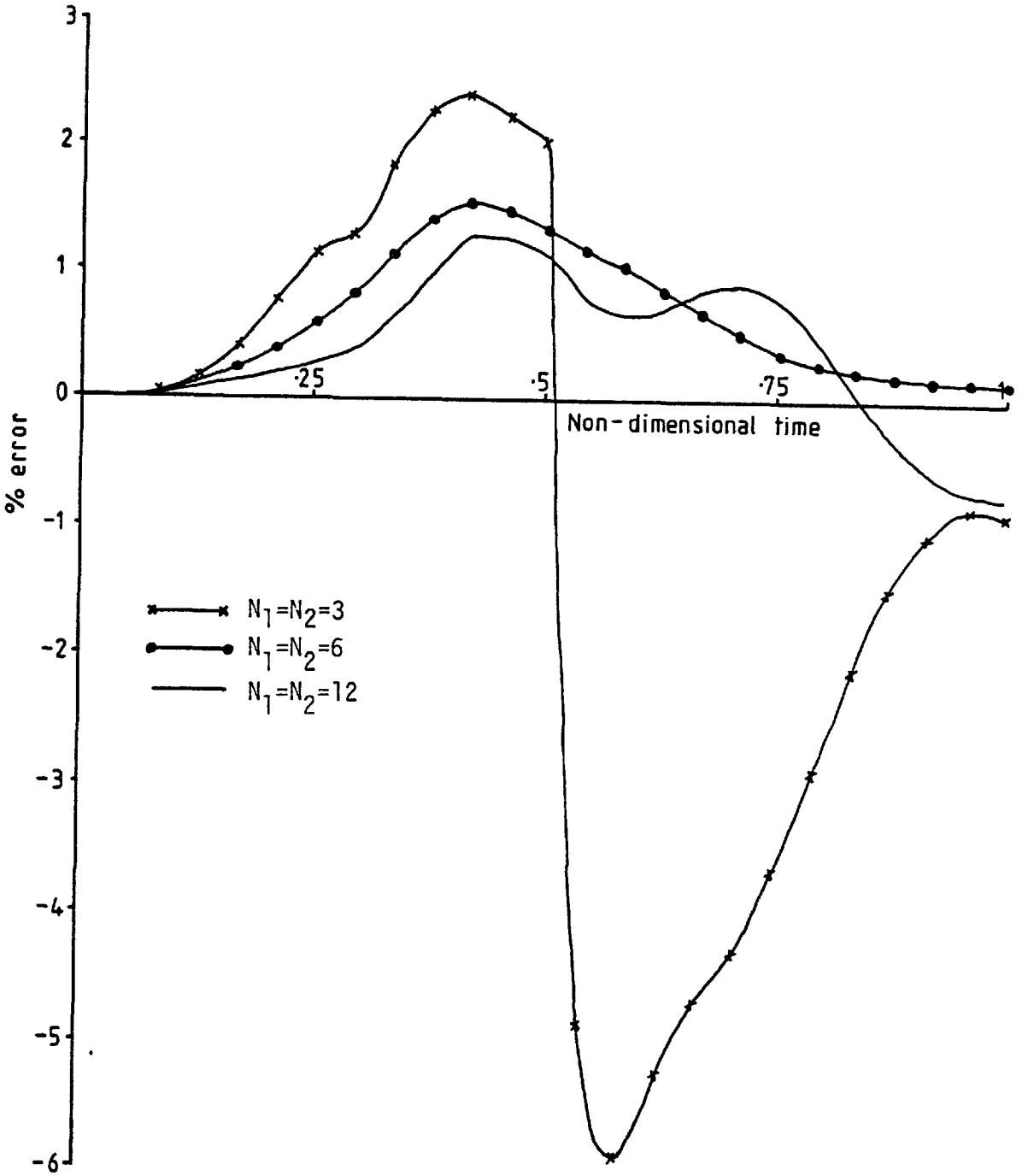

Fig. 4.10 Effect of grid size on velocity error (solution of momentum equation only with implicit differencing; time step ~ 1^{o})

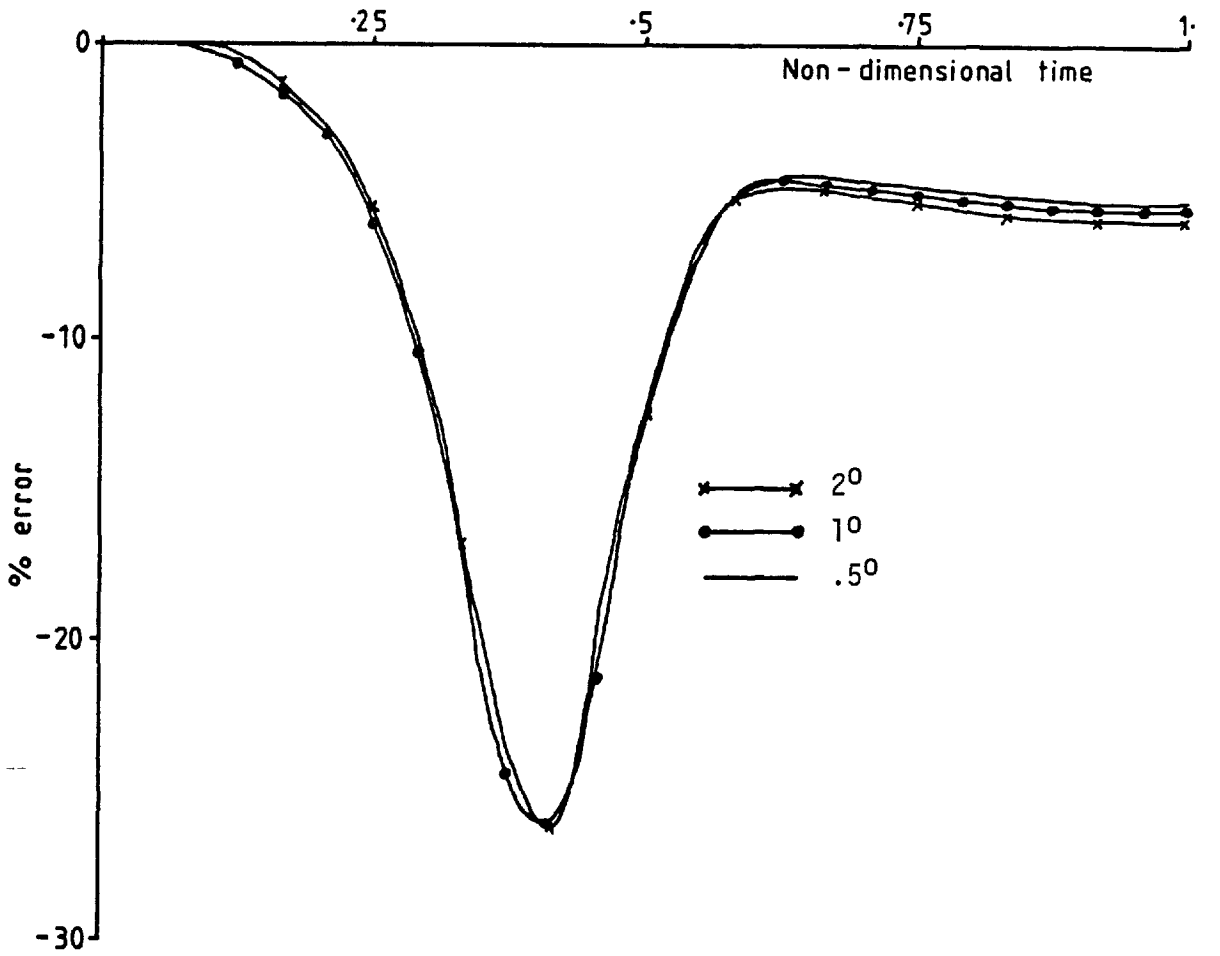

Fig. 4.11 Effect of time-step on velocity error (solution of momentum equation only with time-centred differencing; grid ~ $N_1 = N_2 = 6$)

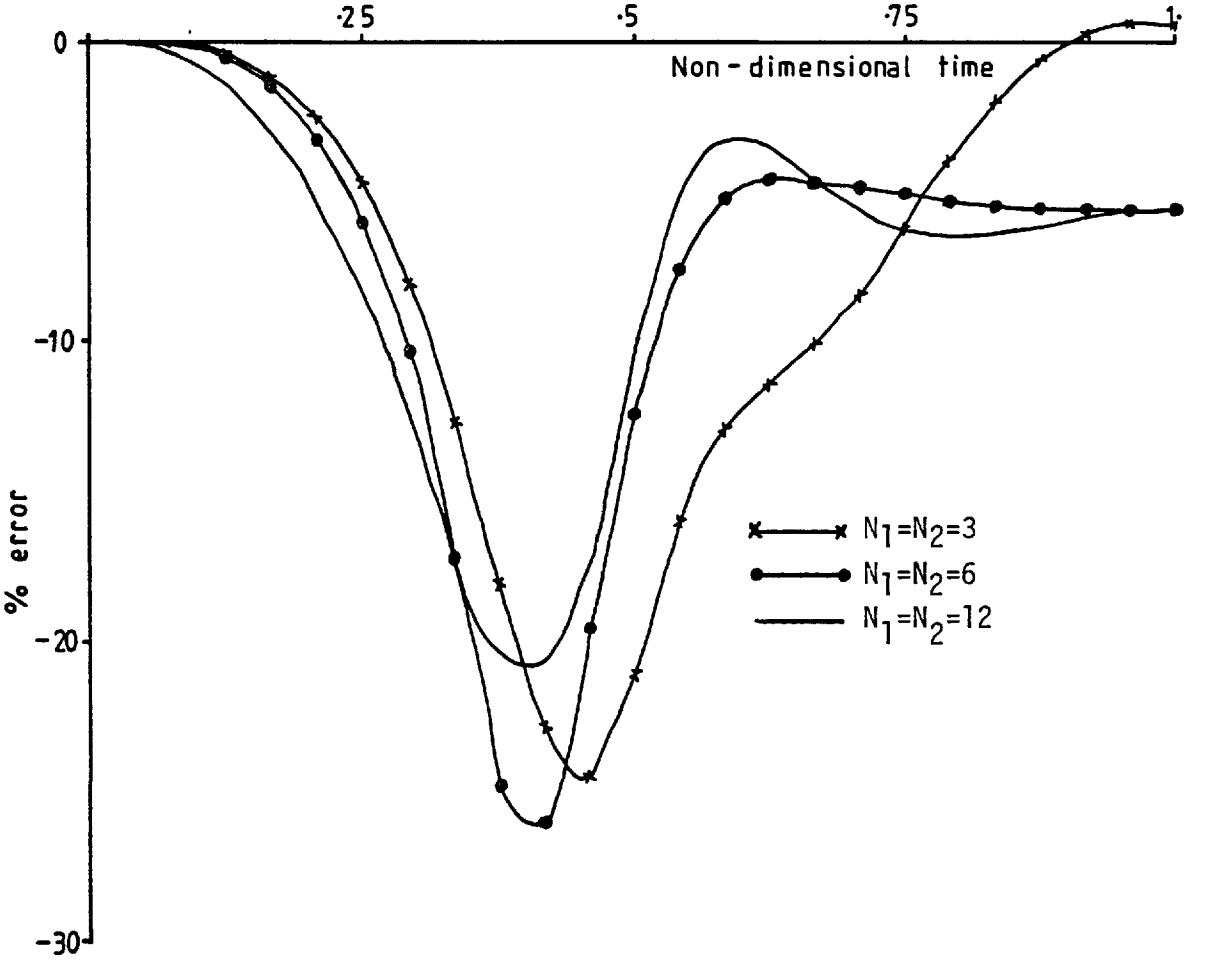

Fig. 4.12 Effect of grid size on velocity error (solution of momentum equation only with time-centred differencing; time step ~ 1^{o})

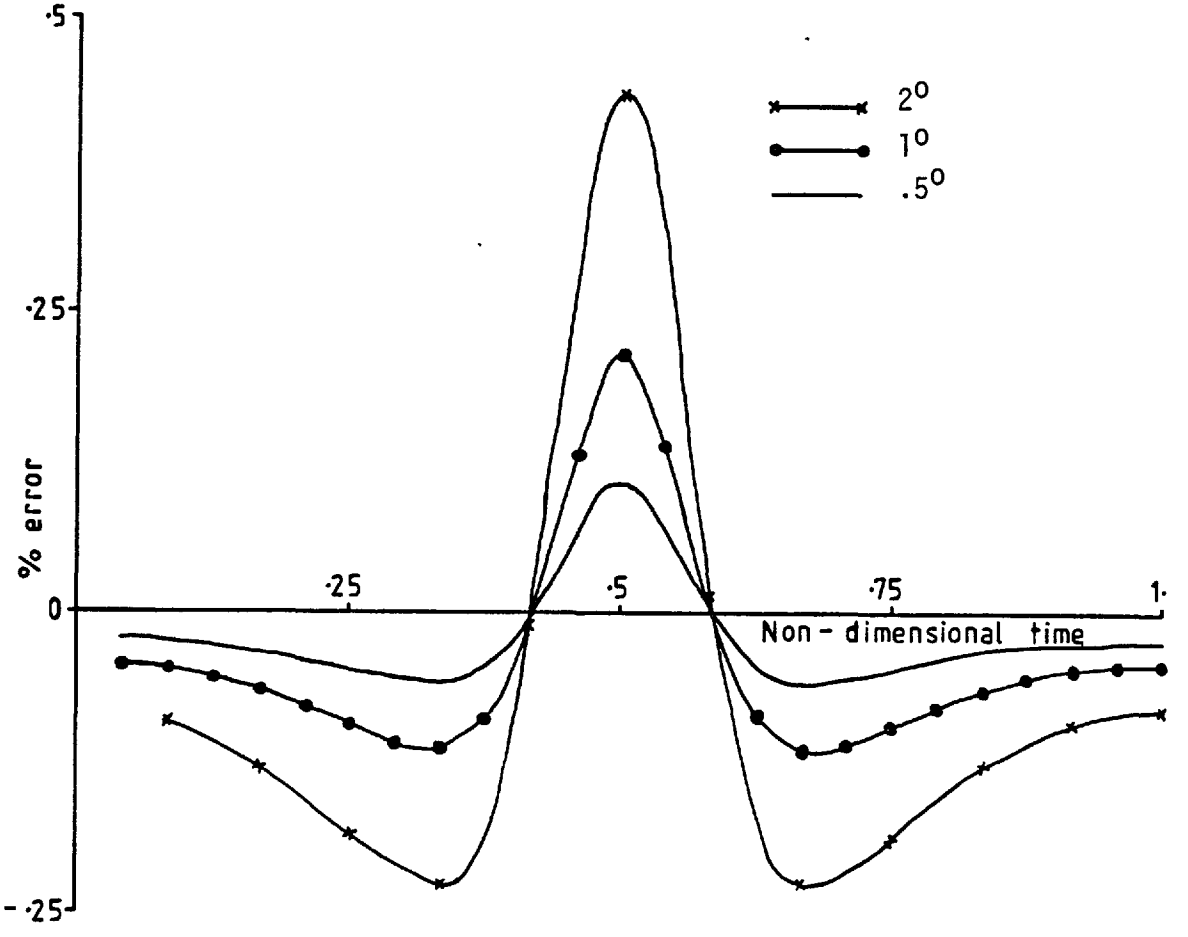

Fig. 4.13 Effect of time-step on velocity error (implicit momentum and continuity equation differencing; grid $N_1=N_2=6$)

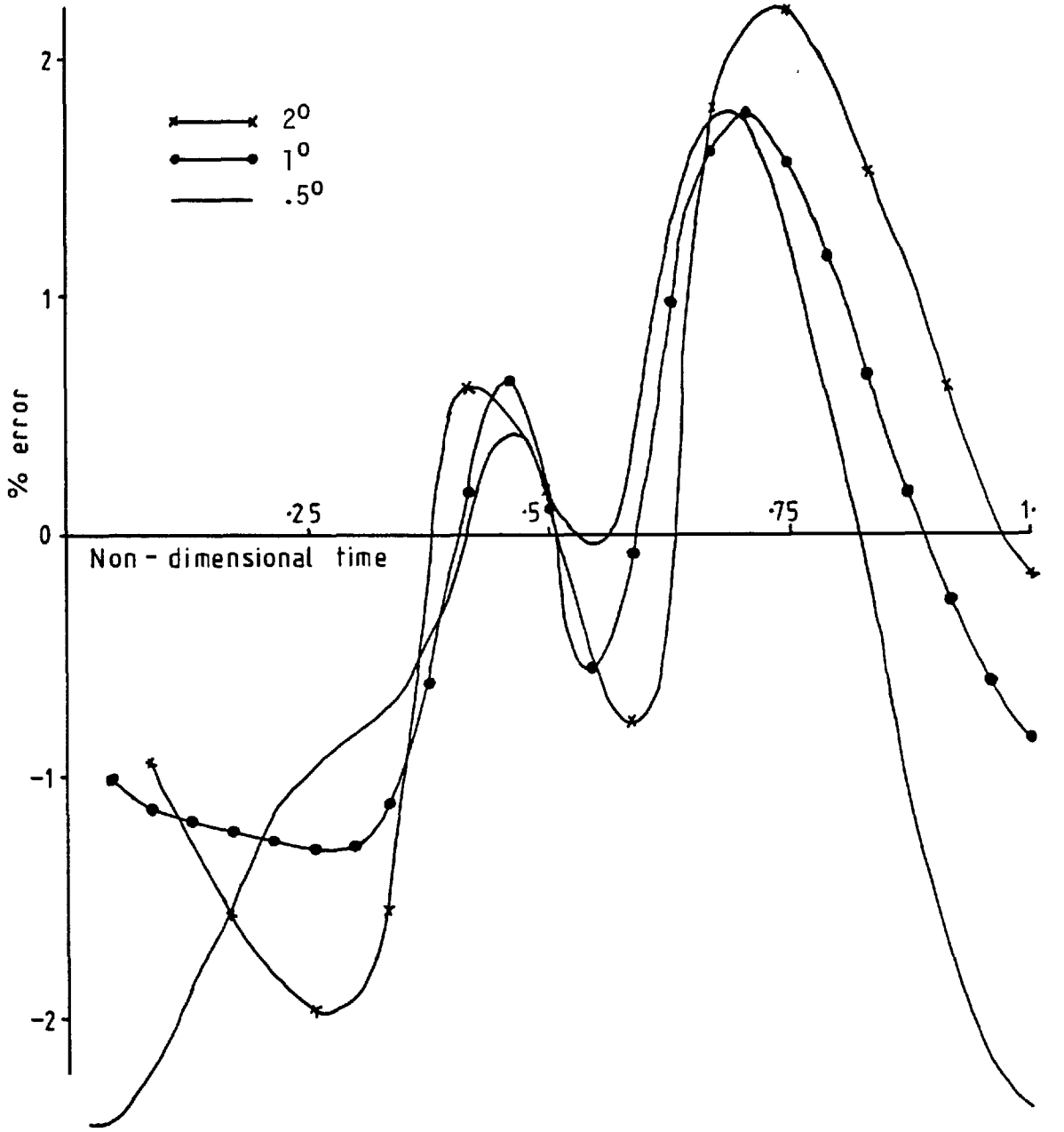

Fig. 4.14 Effect of time-step on pressure error (implicit momentum and continuity equation differencing; grid ~ $N_1=N_2=6$)

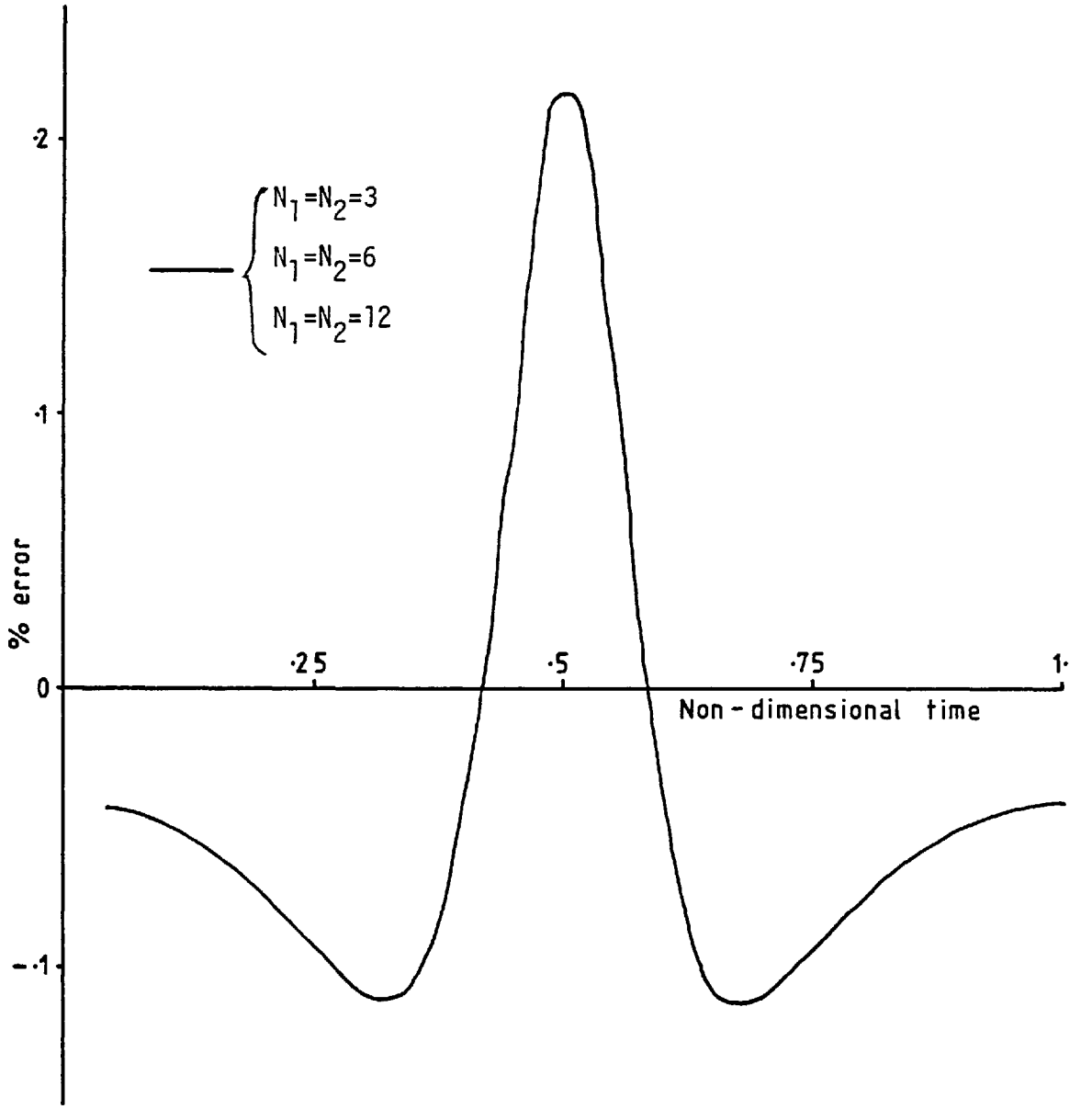

Fig. 4.15 Effect of grid size on velocity error (implicit momentum and continuity equation differencing; time step ~ 1^{o})

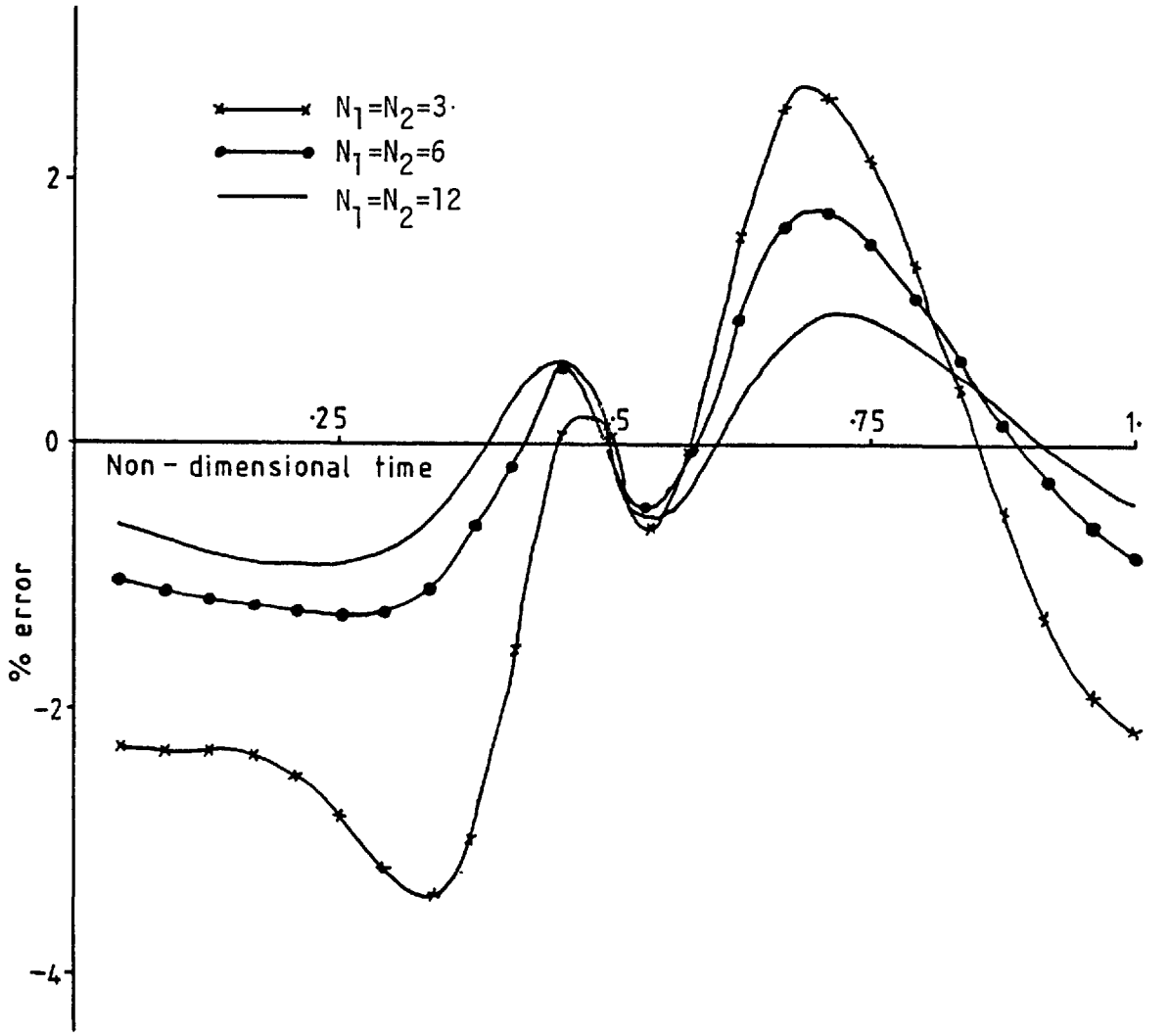

Fig. 4.16 Effect of grid size on pressure error (implicit momentum and continuity equation differencing; time-step ~ 1^{o})

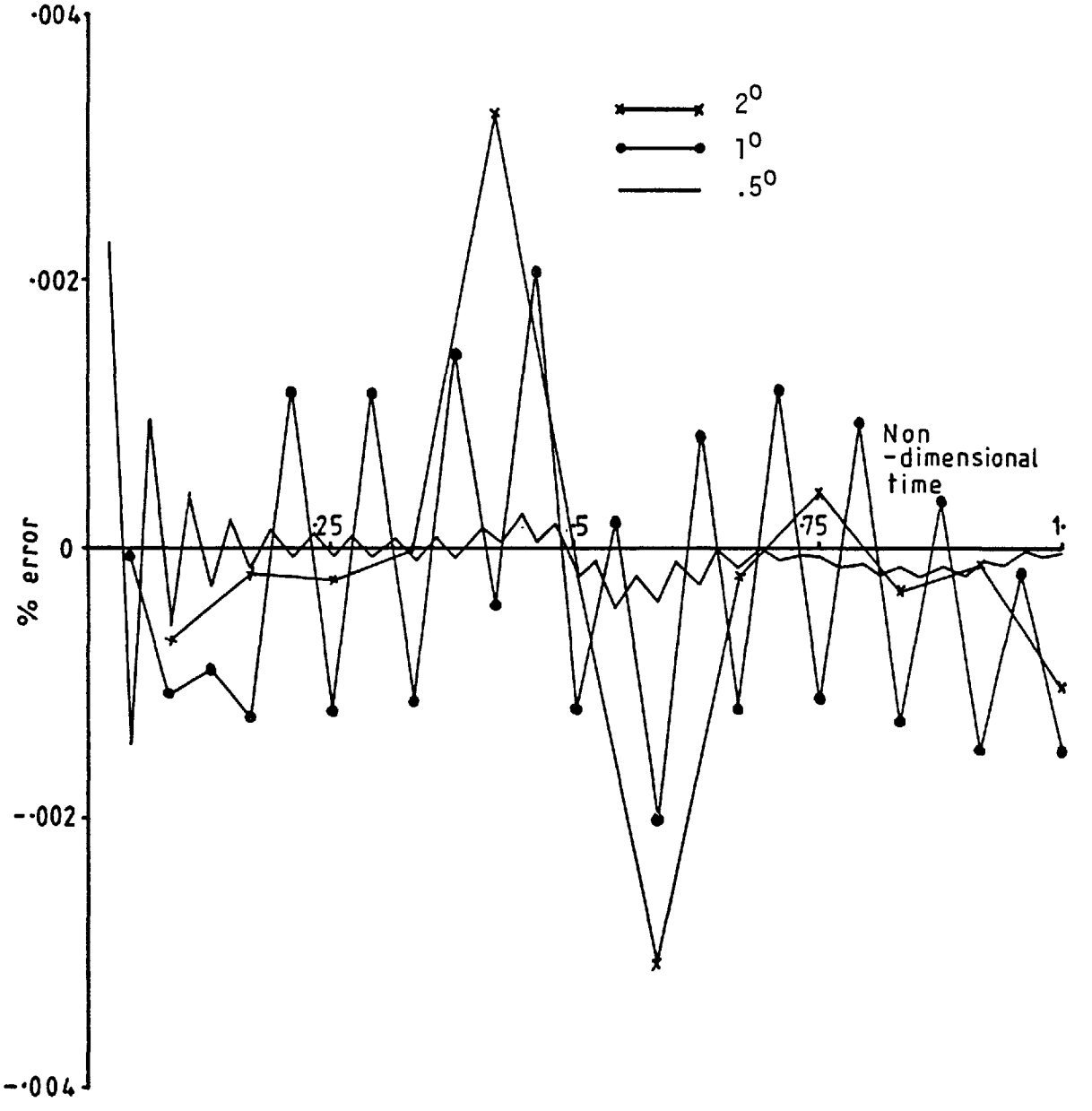

Fig. 4.17 Effect of time-step on velocity error (implicit momentum and time-centred continuity equation differencing; grid ~ $N_1=N_2=6$)

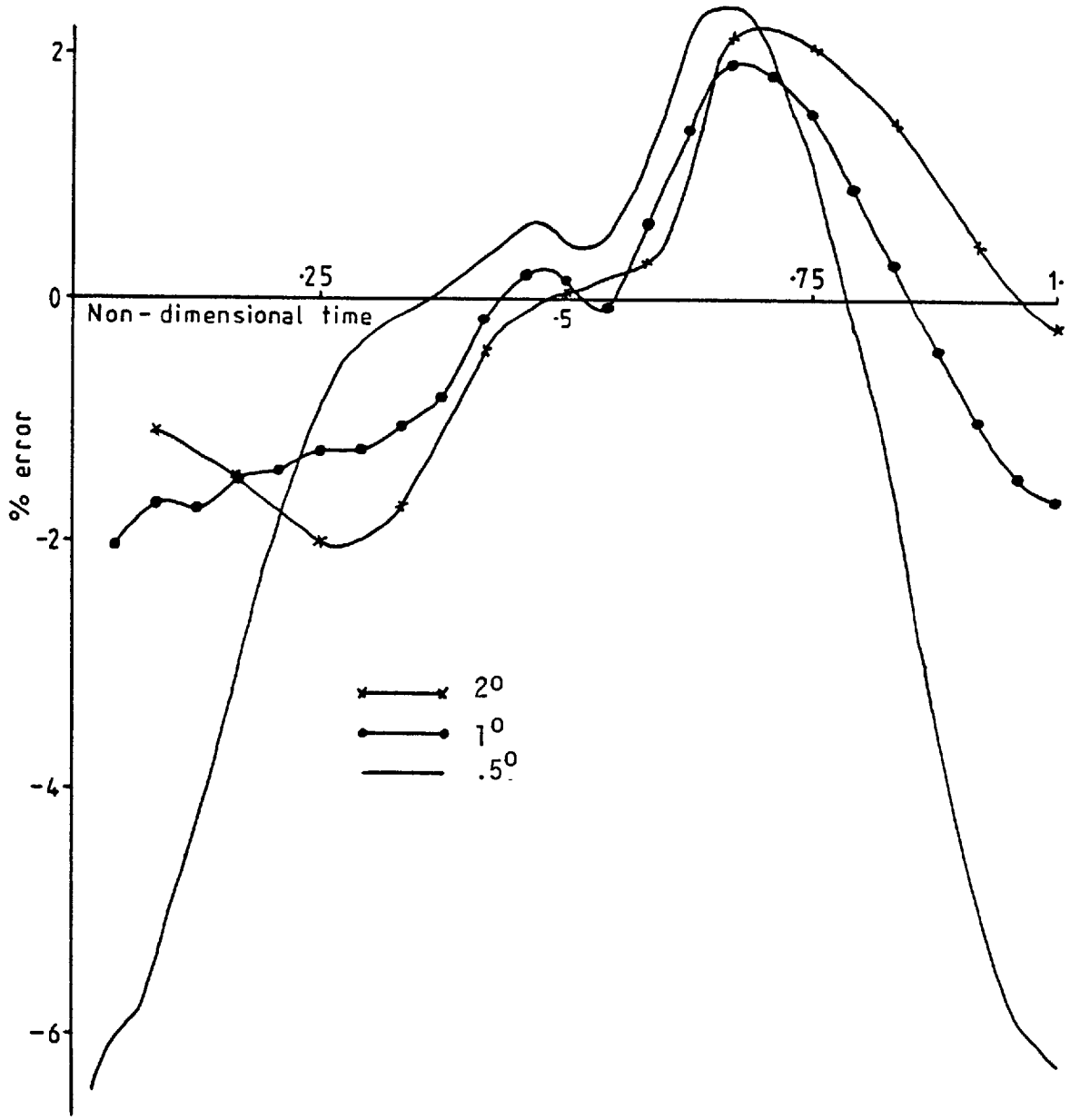

Fig. 4.18 Effect of time-step on pressure error (implicit momentum and time-centred continuity equation differencing; grid ~N_1=N_2=6)

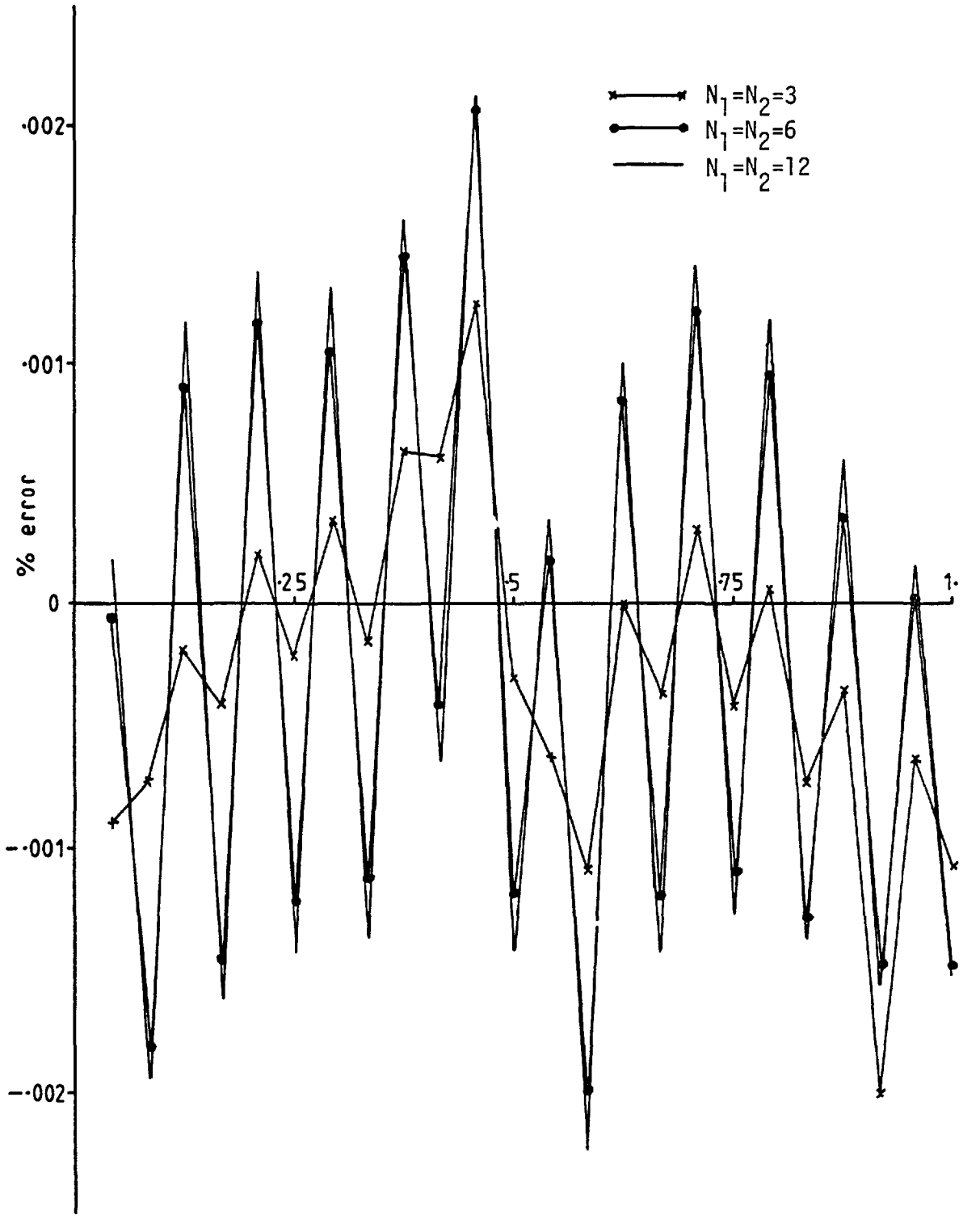

Fig. 4.19 Effect of grid size on velocity error (implicit momentum and time-centred continuity equation differencing; time-step ~1^{o})

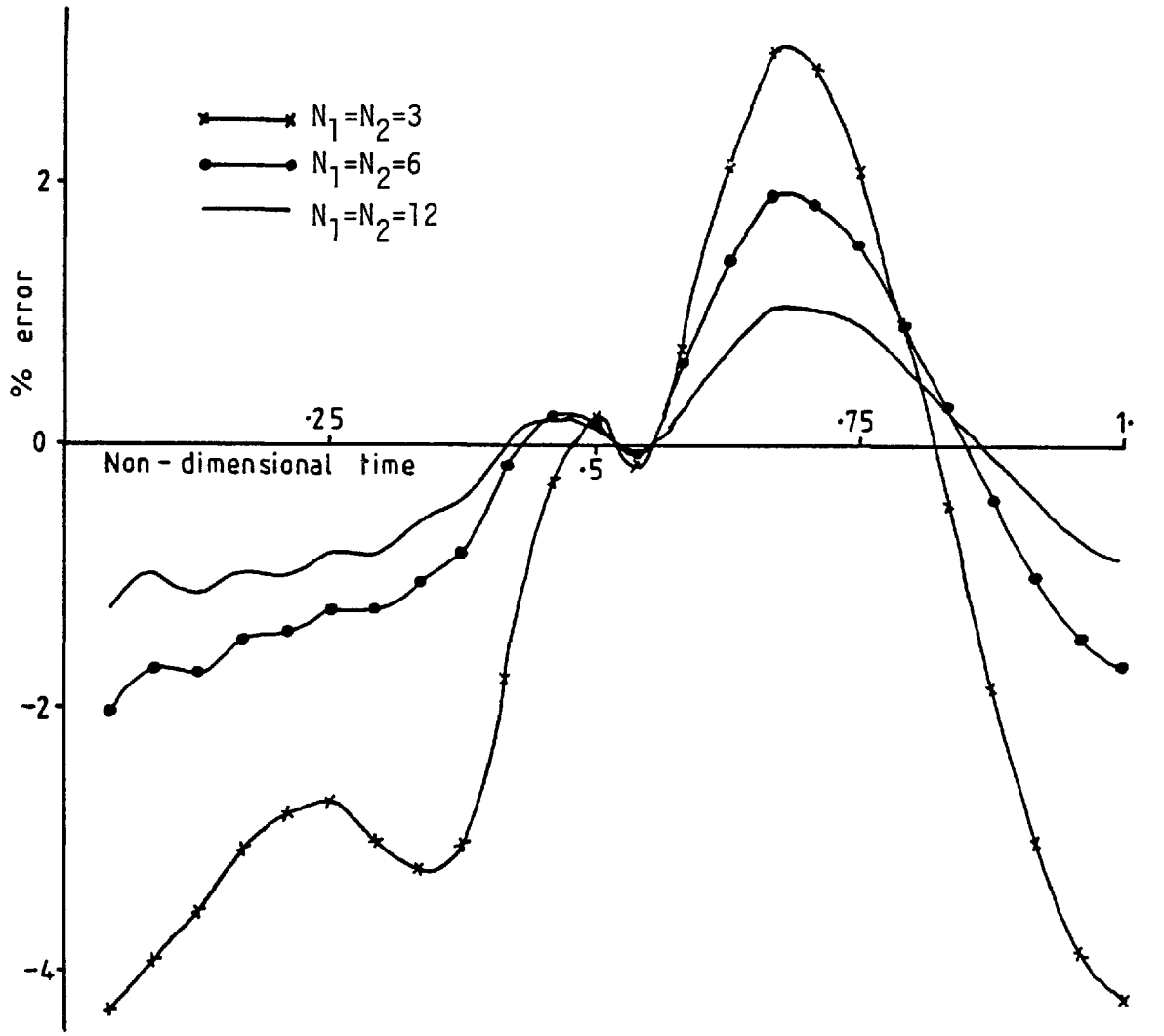

Fig. 4.20 Effect of grid size on pressure error (implicit momentum and time-centred continuity equation differencing; time-step ~ 1^{o})

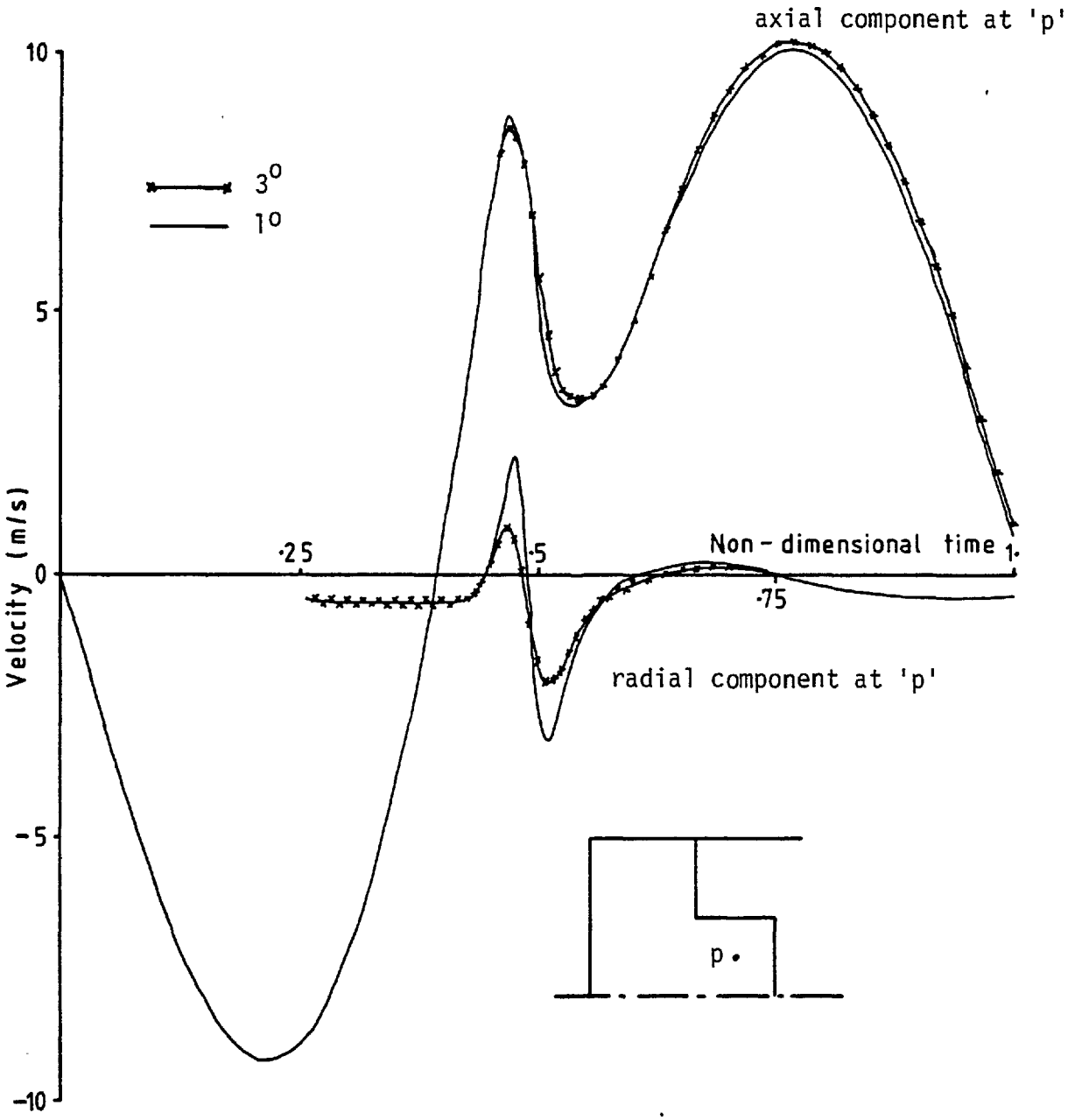

Fig. 4.21 Effect of time-step on the axial and radial velocity components for time-centred continuity equation differencing (grid ~ 9 x 18/9 x 9)

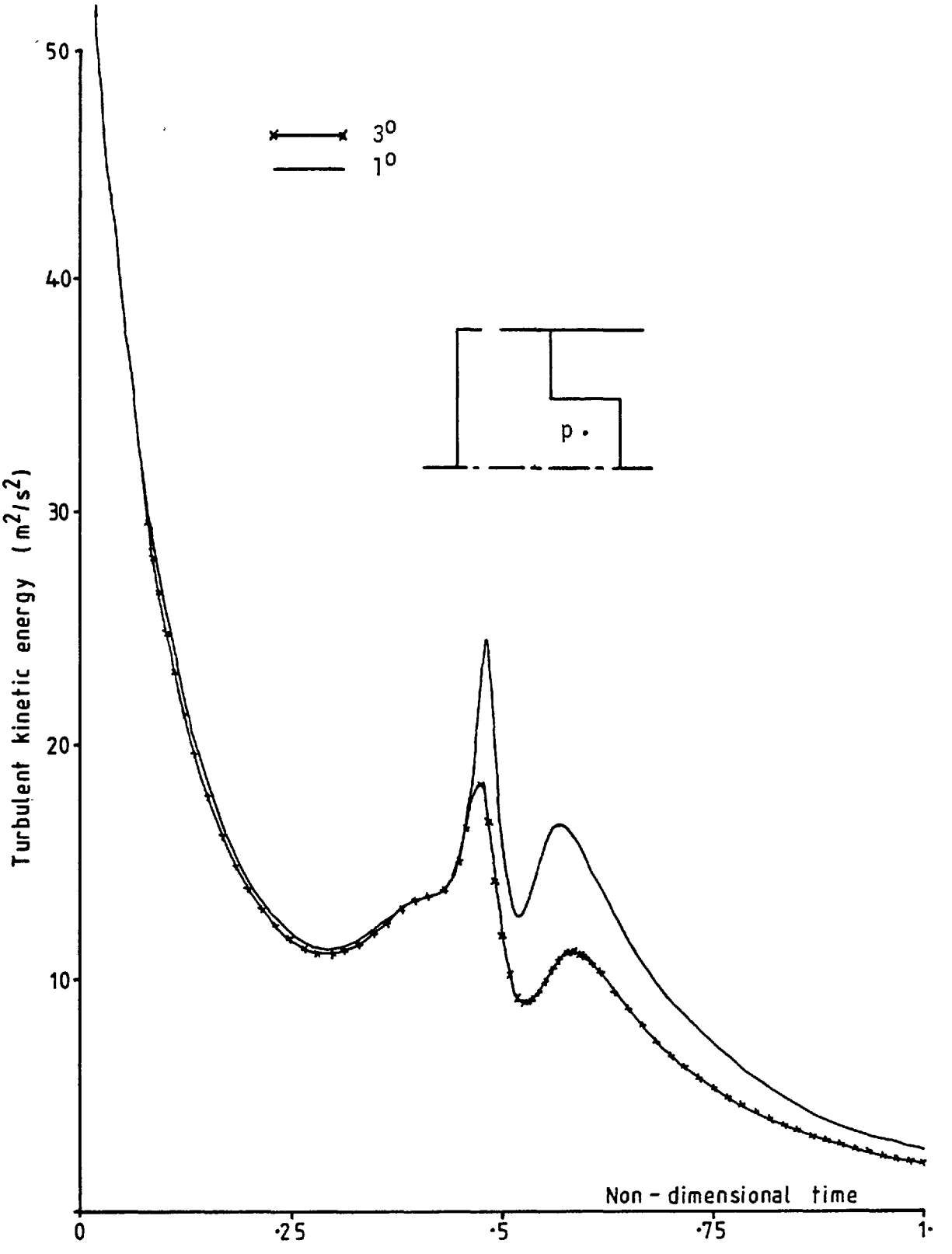

Fig. 4.22 Effect of time-step on the turbulence energy for time-centred continuity equation differencing (grid ~ 9 x 18/9 x 9)

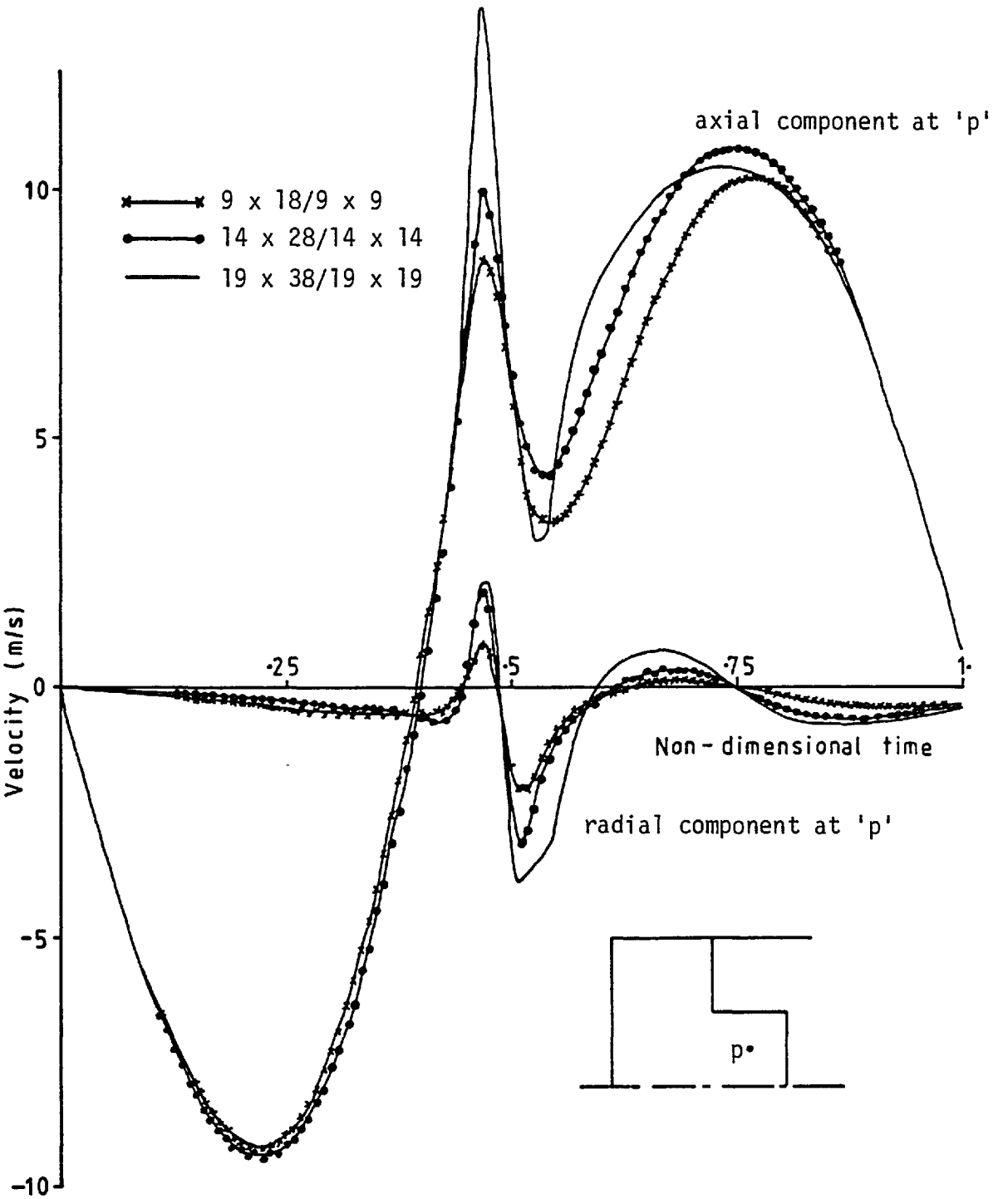

Fig. 4.23 Effect of grid size on the axial and radial velocity components for time-centred continuity equation differencing (time-step ~ 3^{o})

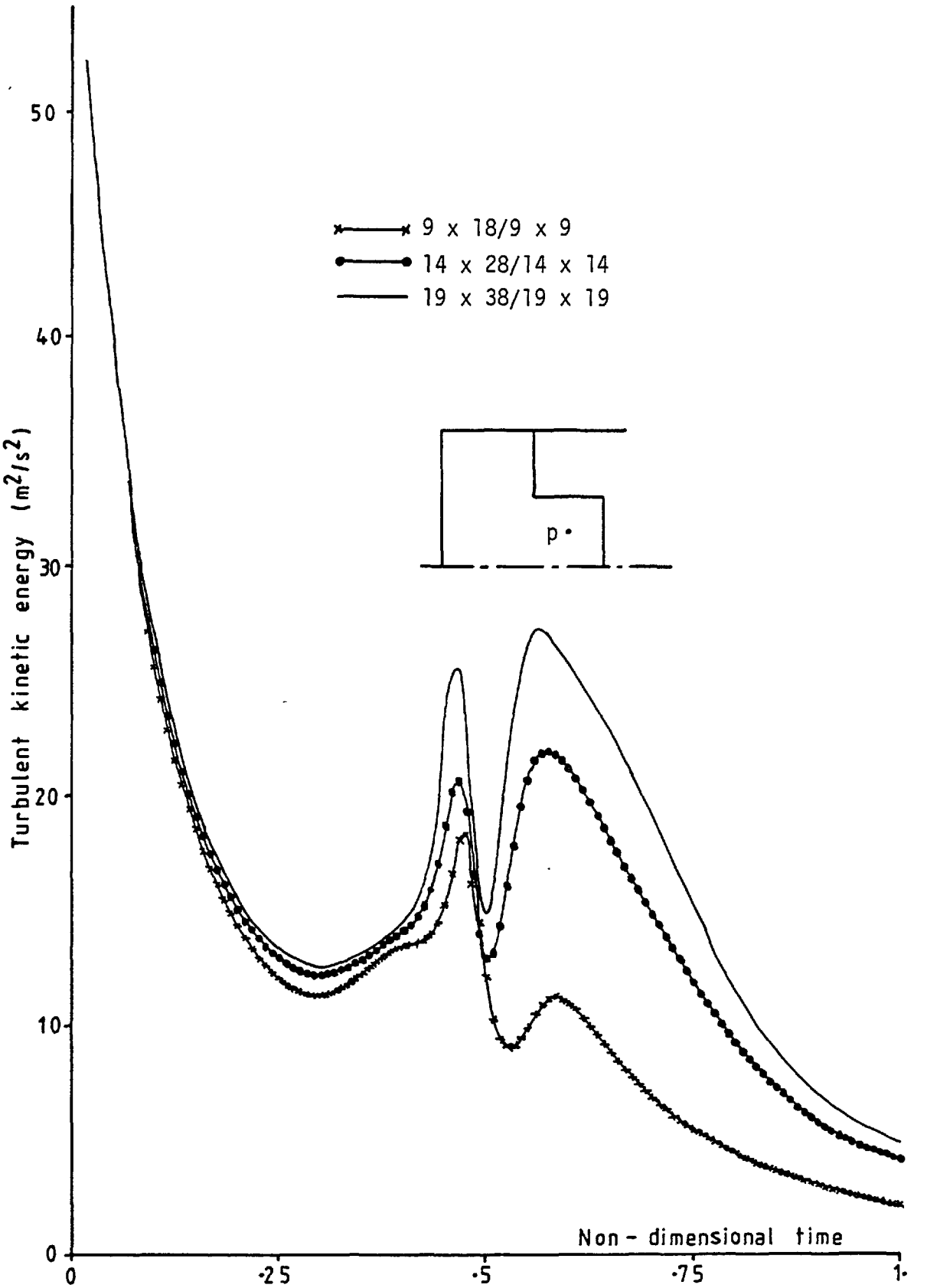

Fig. 4.24 Effect of grid size on the turbulence energy for time-centred continuity equation differencing (time-step ~3°)

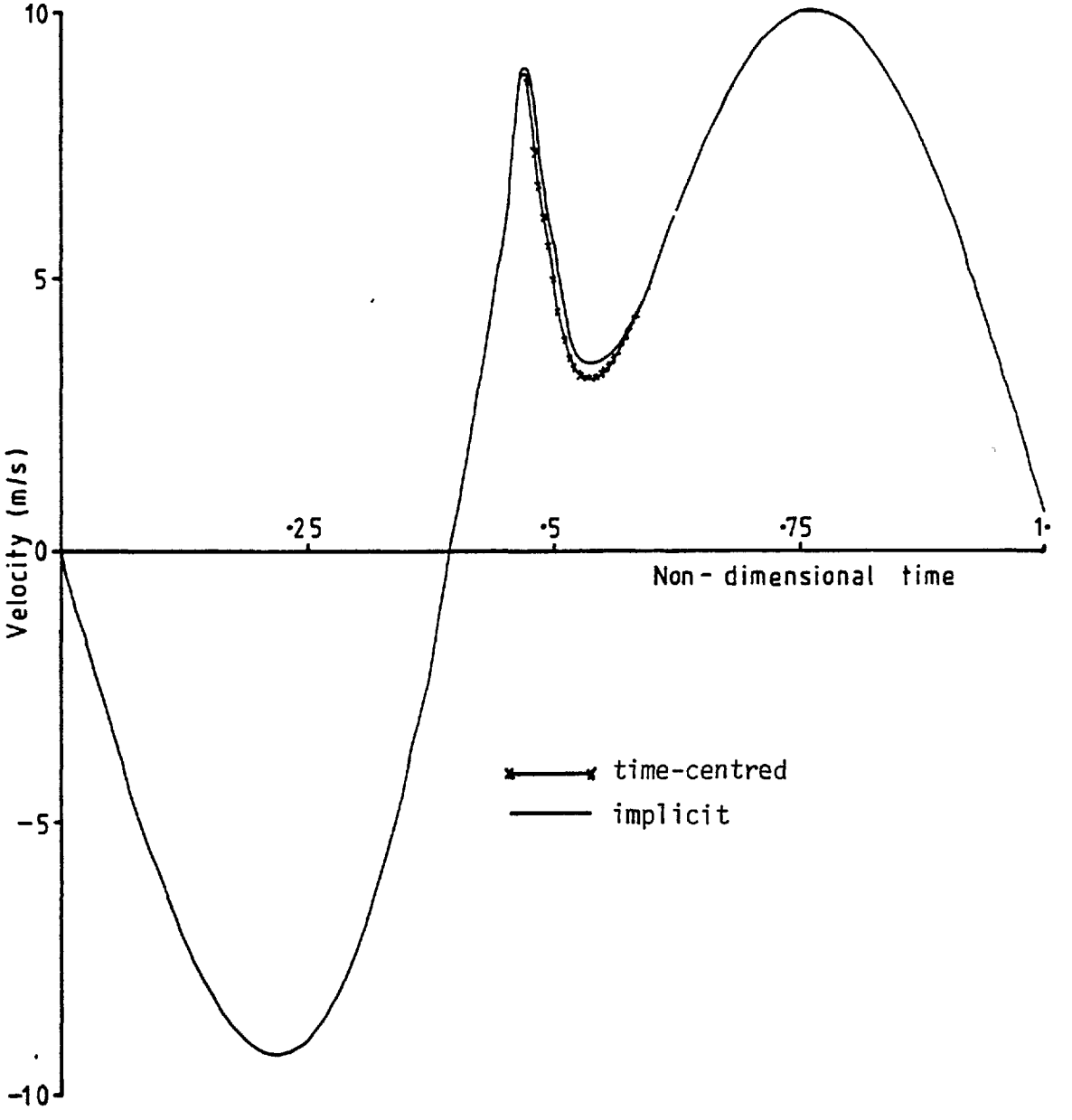

Fig. 4.25 Axial velocity component for implicit and time-centred continuity equation differencing (time-step ~ 1^{o})

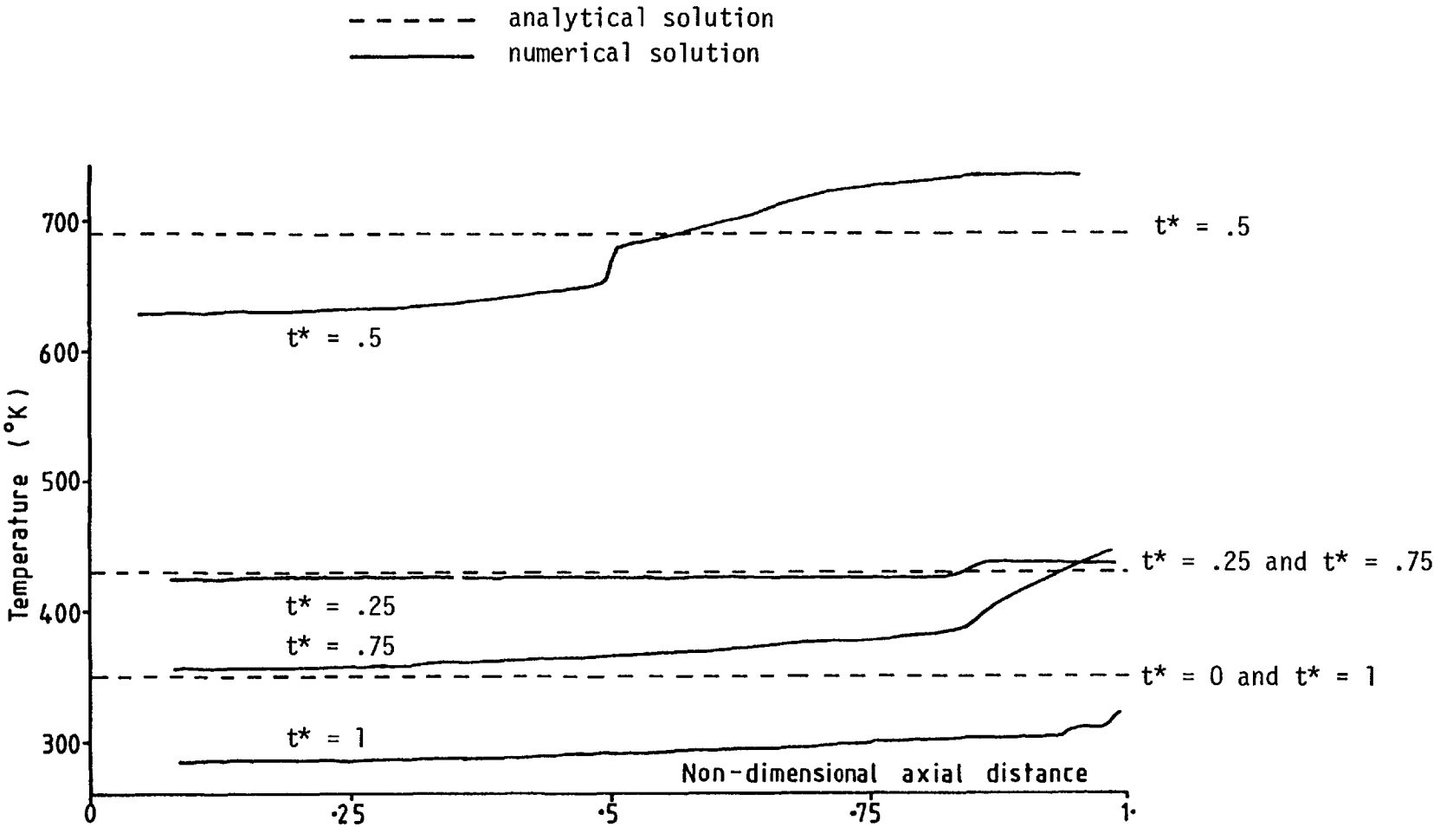

Fig. 4.26 Variation of temperature with axial distance for central differencing of the pressure work term (equation 4.104) when used with the 'hybrid' one-dimensional grid

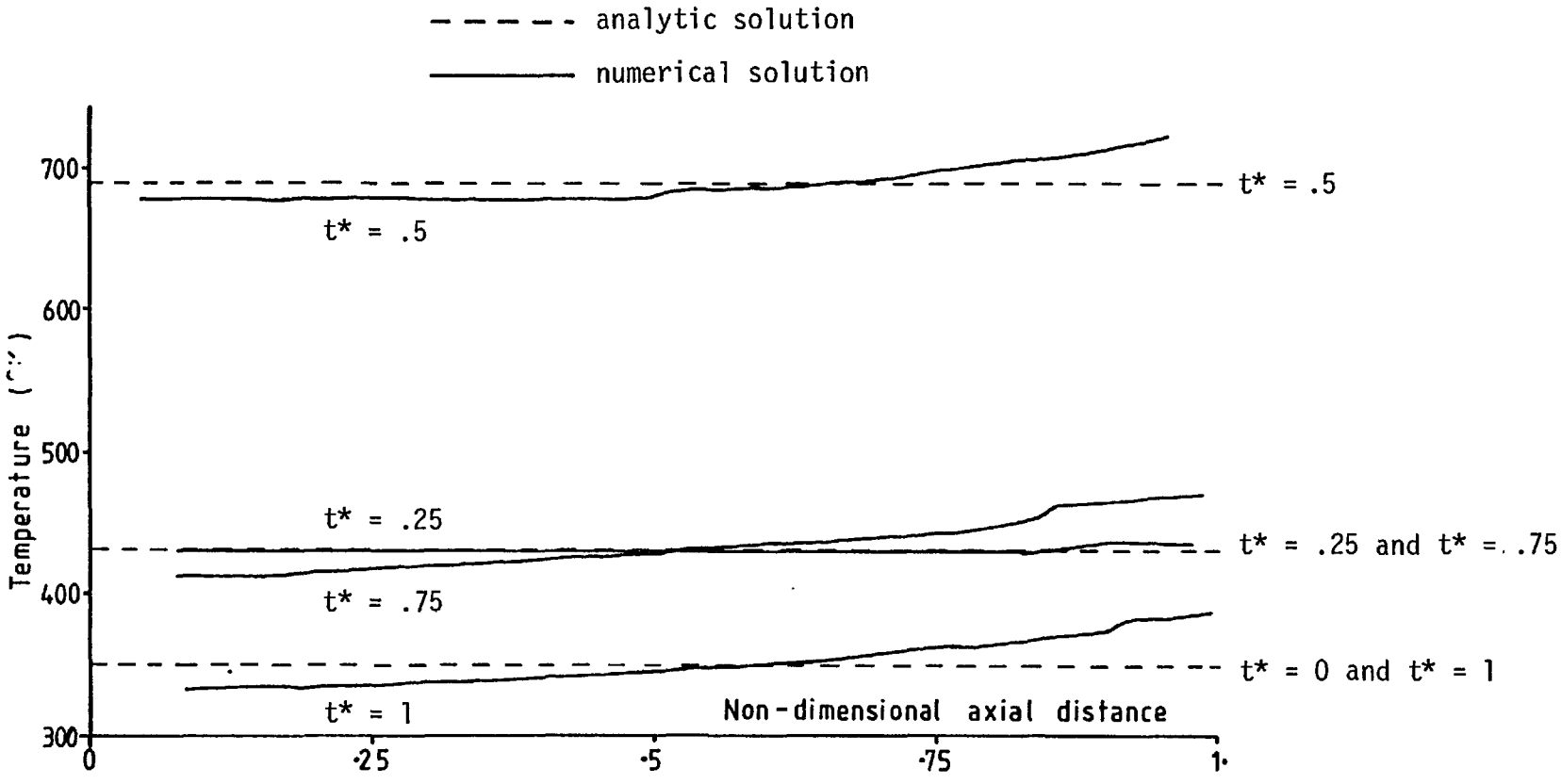

Fig. 4.27 Variation of temperature with axial distance for Watkins formulation of the pressure work term (equation 4.105) when used with the 'hybrid' one-dimensional grid

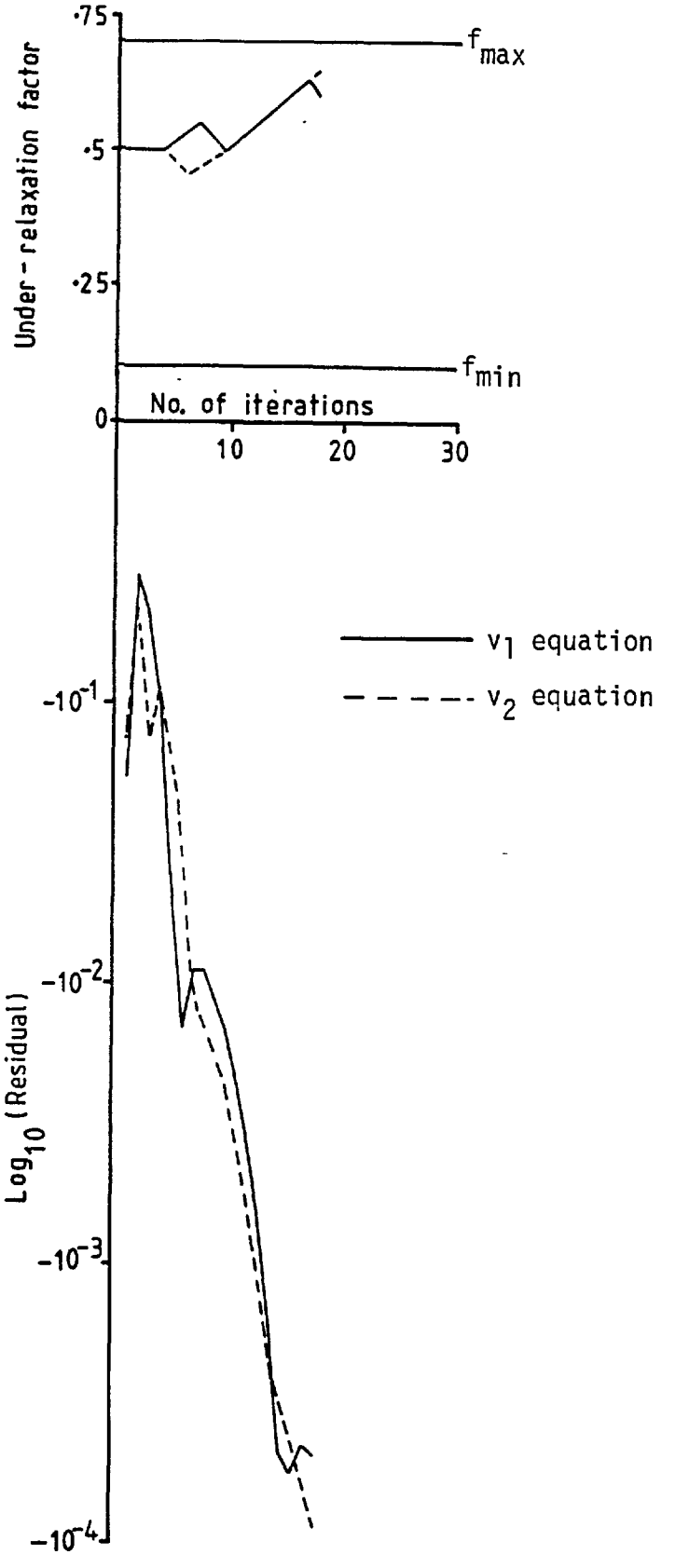

Fig. 4.28 Variation of under-relaxation factors and residuals for the v_1 and v_2 momentum equations near BDC

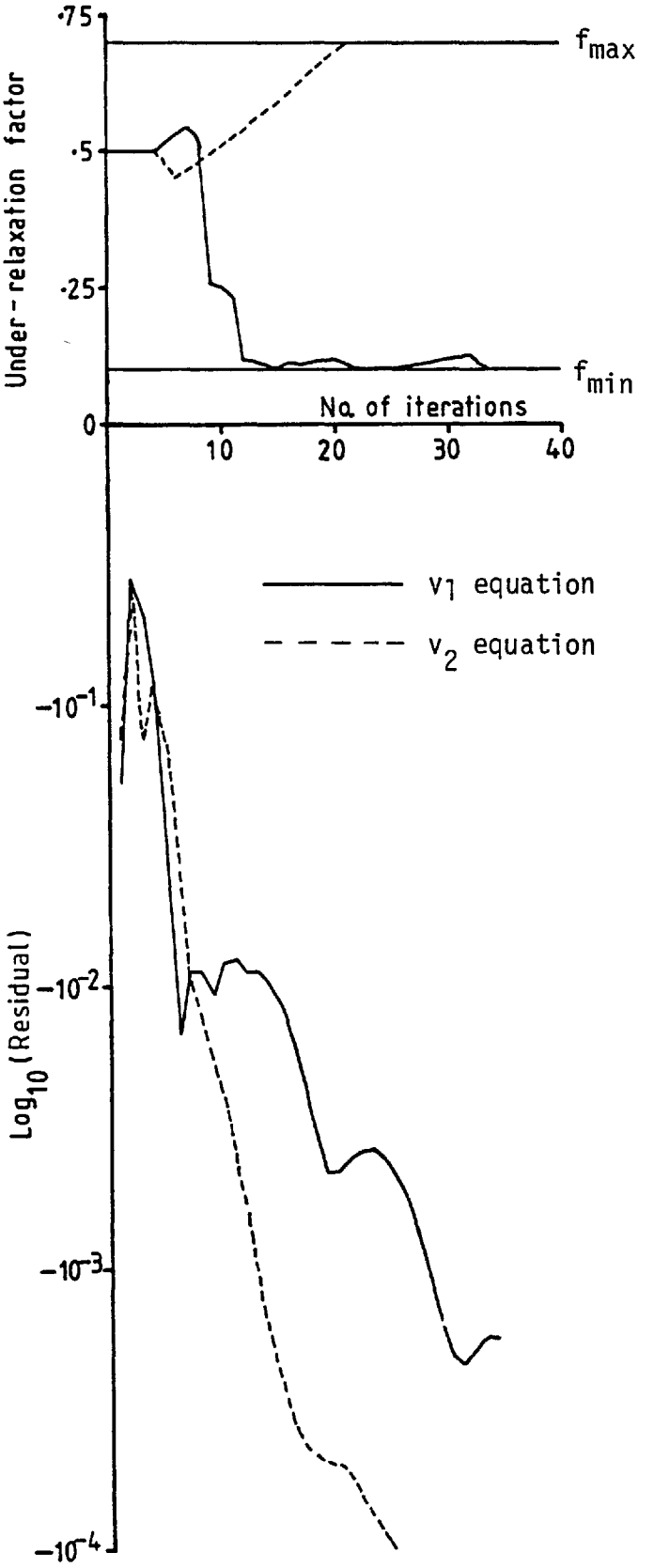

Fig. 4.29 Variation of under-relaxation factors and residuals for the v_1 and v_2 momentum equations near the mid-stroke position

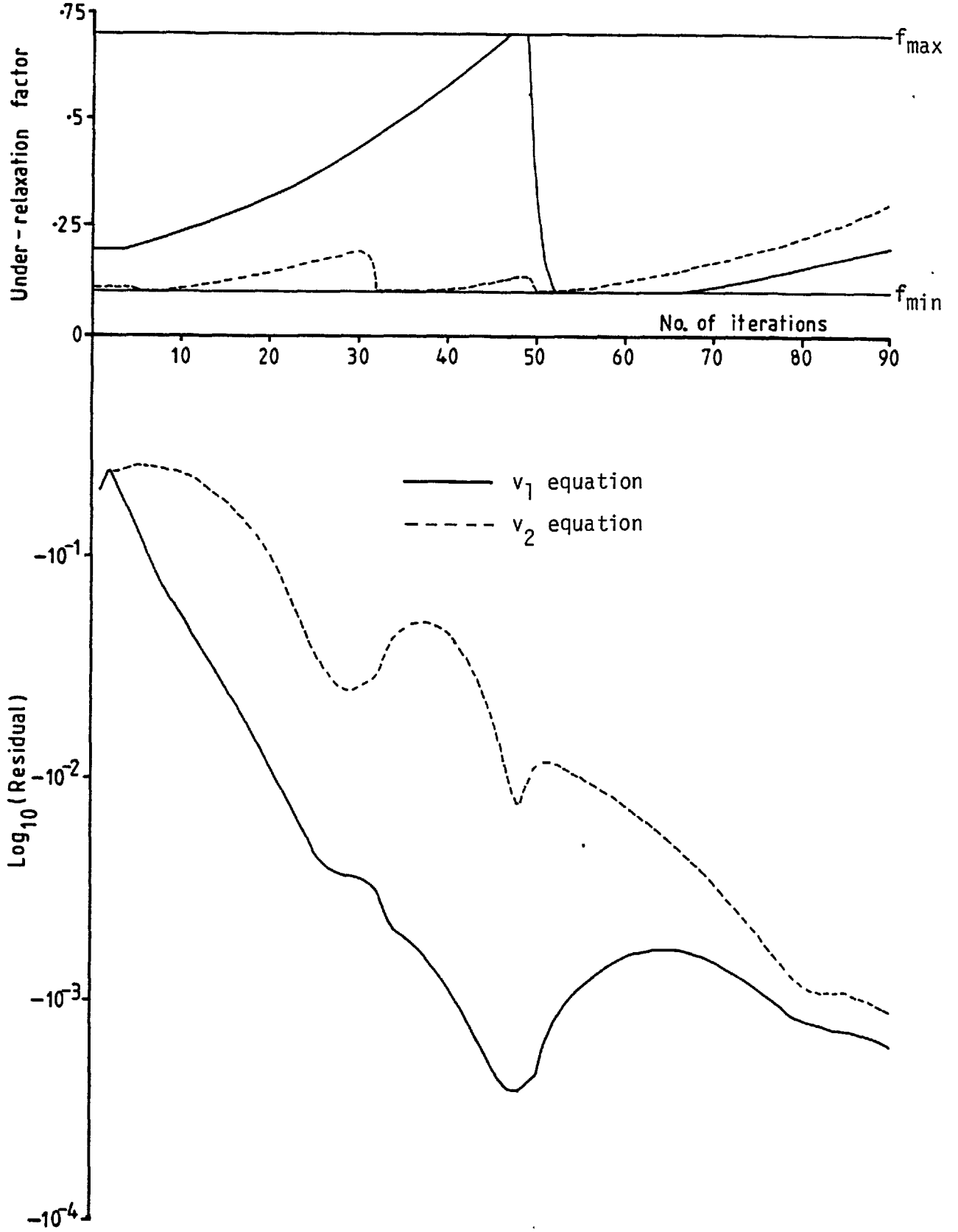

Fig. 4.30 Variation of under-relaxation factors and residuals for the v_1 and v_2 momentum equations near TDC

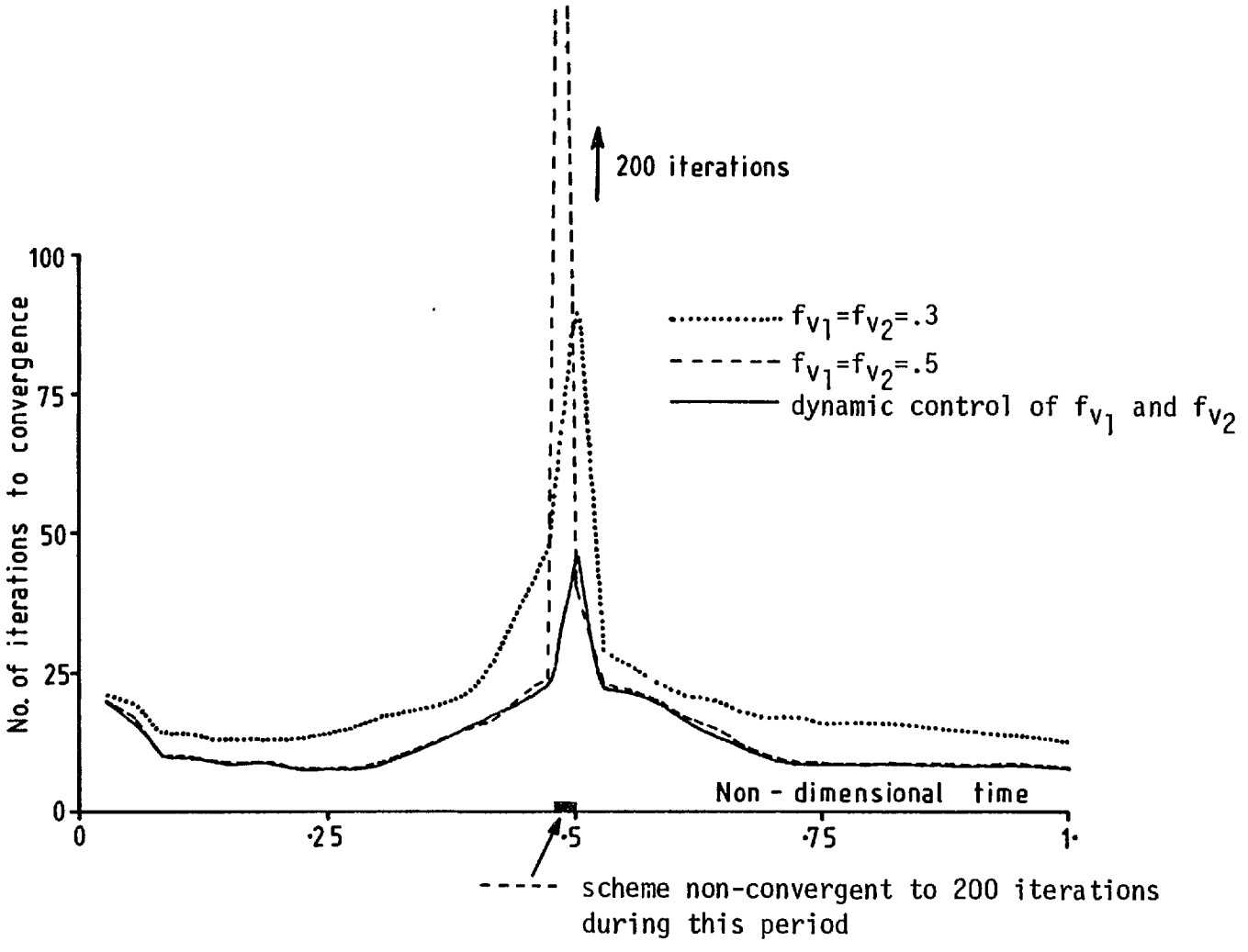

Fig. 4.31 Variation of the number of iterations to convergence with fixed and dynamically-controlled under-relaxation factors

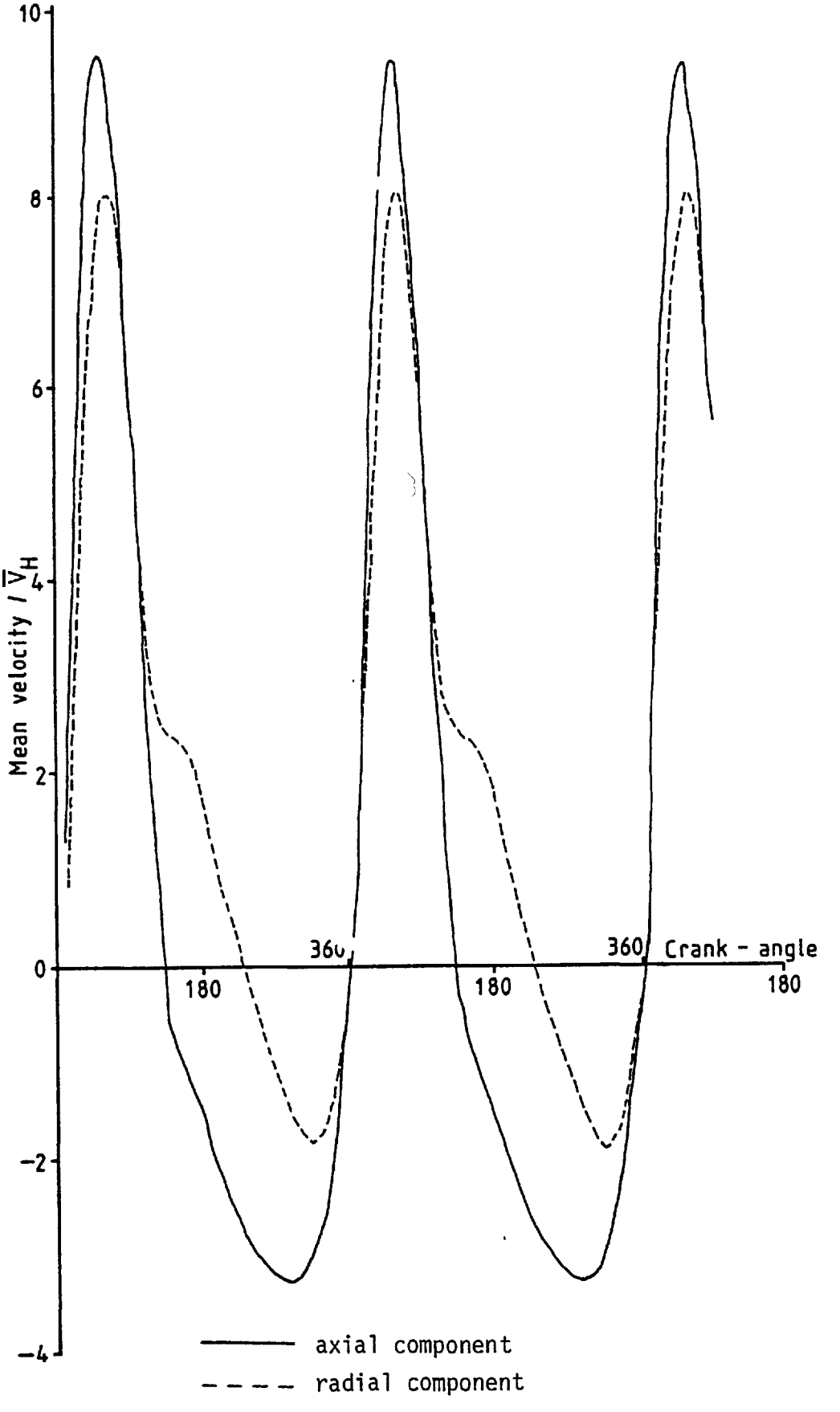

Fig. 5.1 Variation of the axial and radial velocity components at a position near the valve for case 1

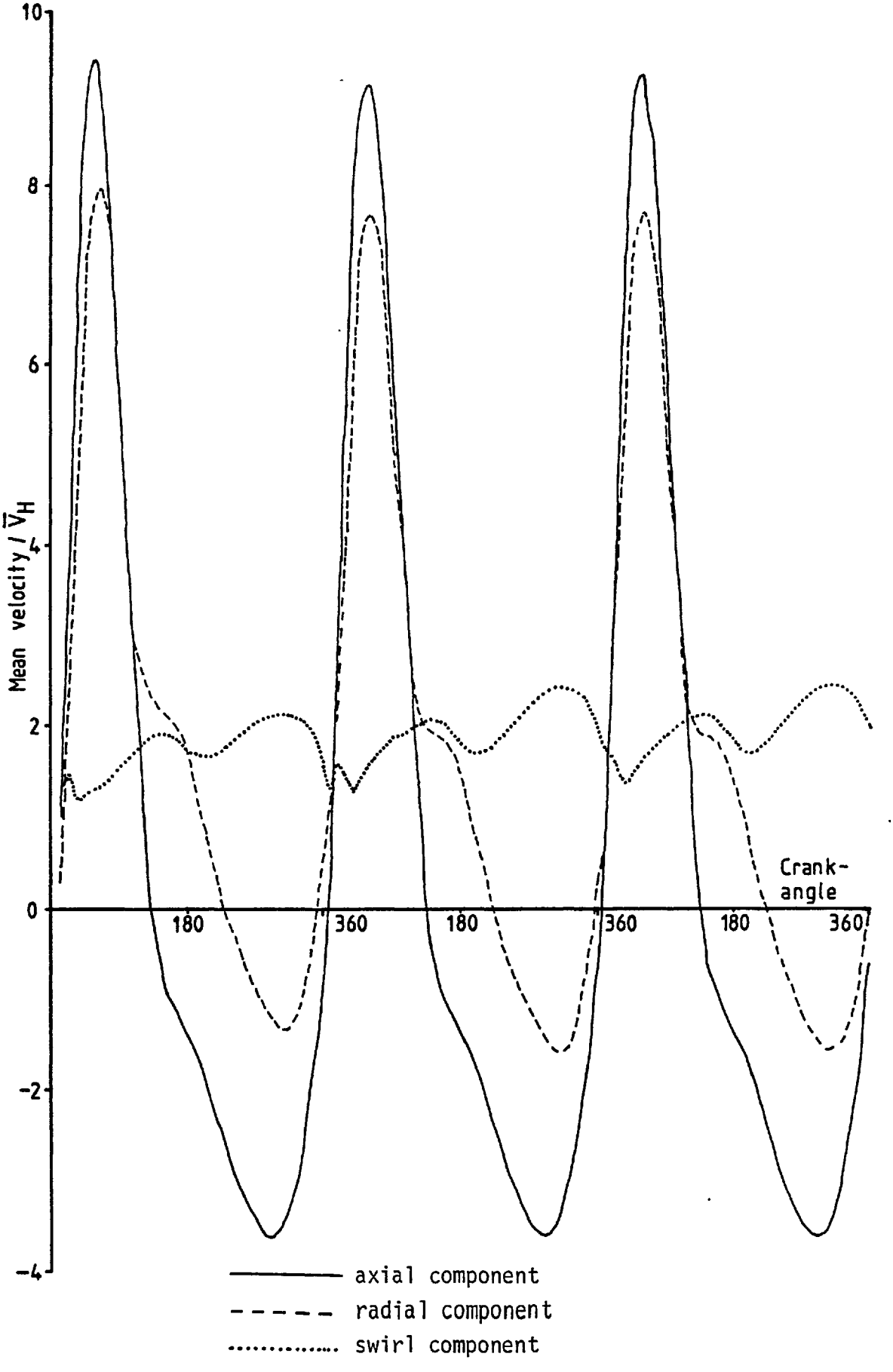

Fig. 5.2 Variation of the axial, radial and swirl velocity components at a position near the valve for case 2

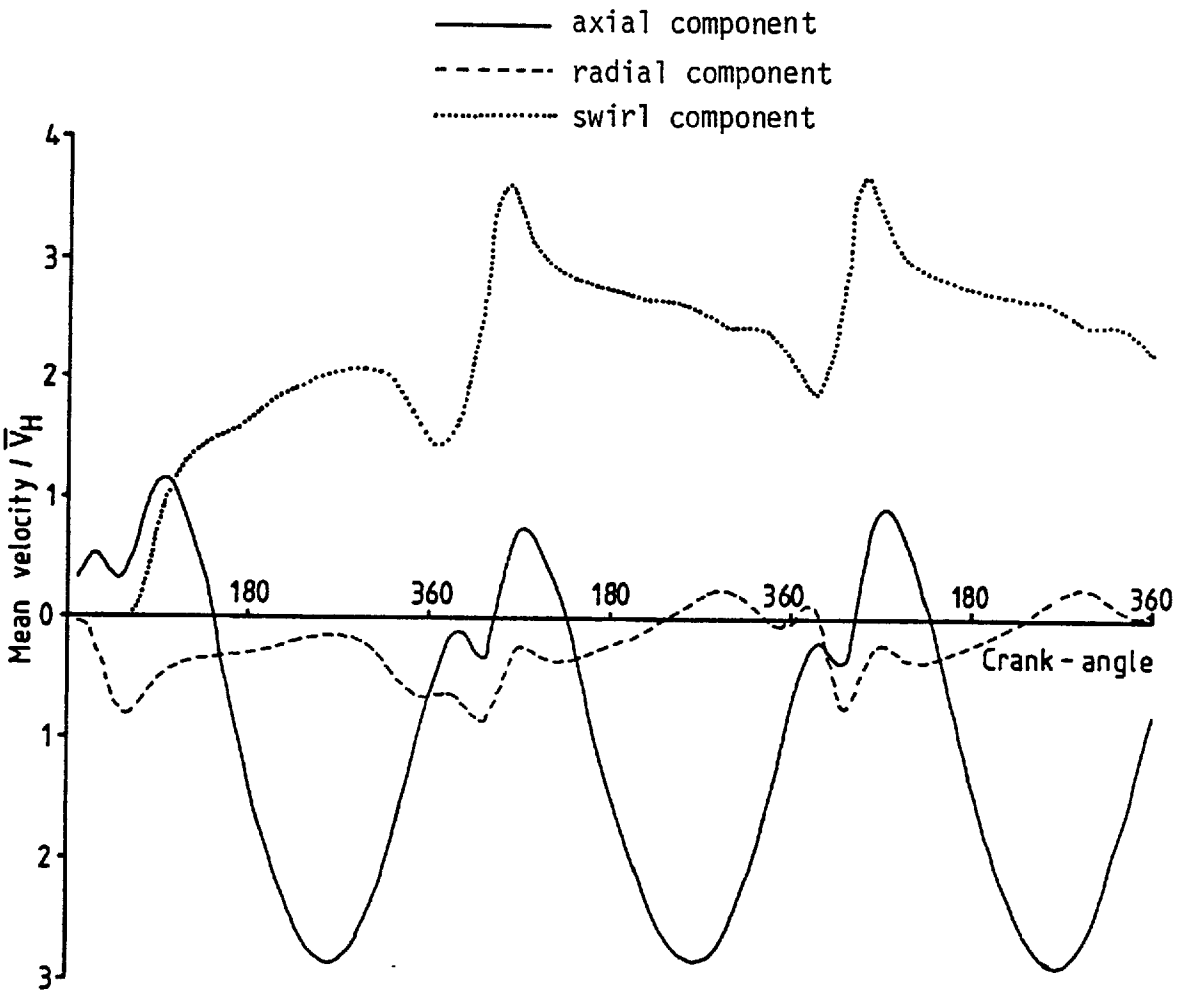

Fig. 5.3 Variation of the axial, radial and swirl velocity components at a position near the piston for case 2

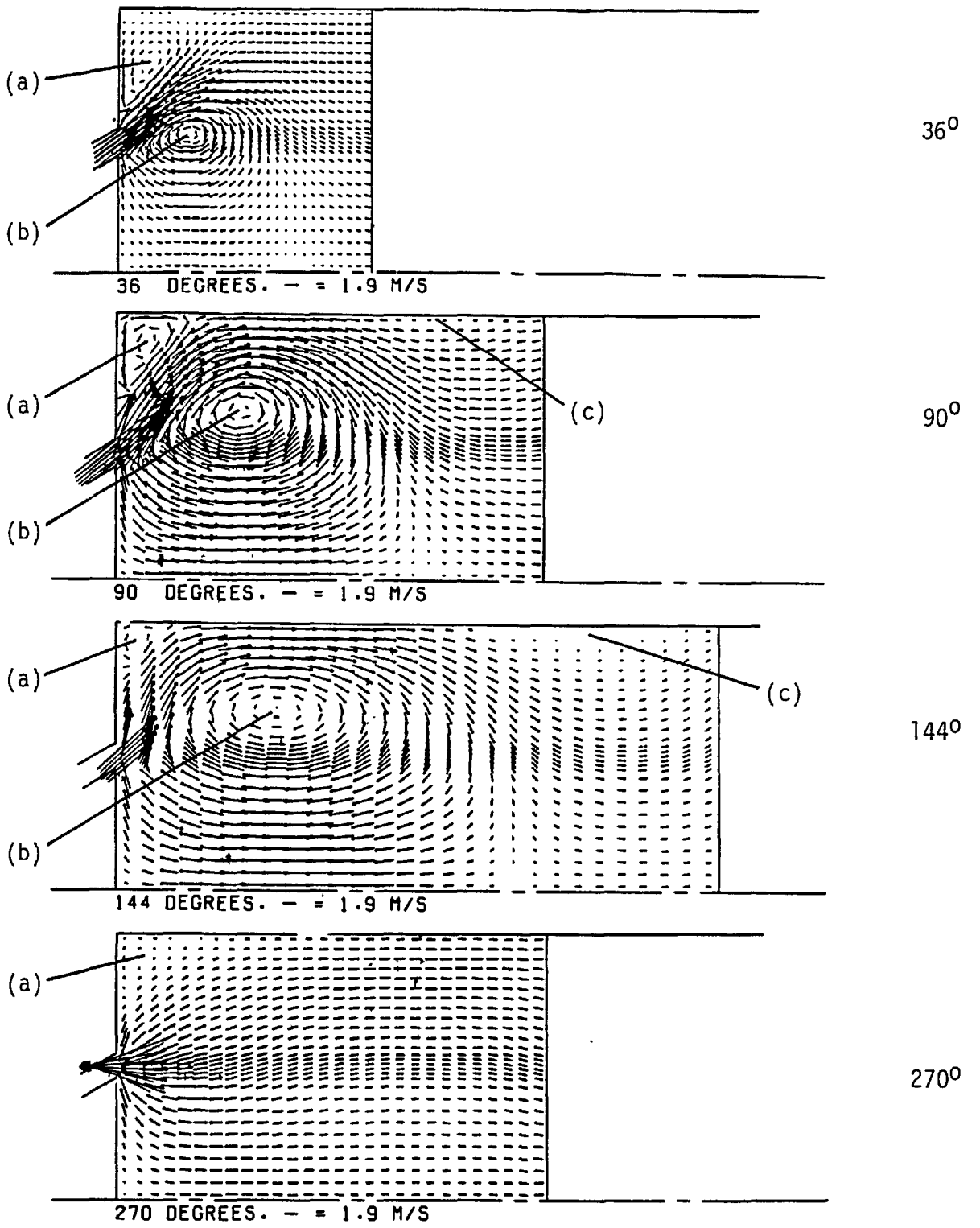

Fig. 5.4 Predicted axial-radial velocity fields for case 1

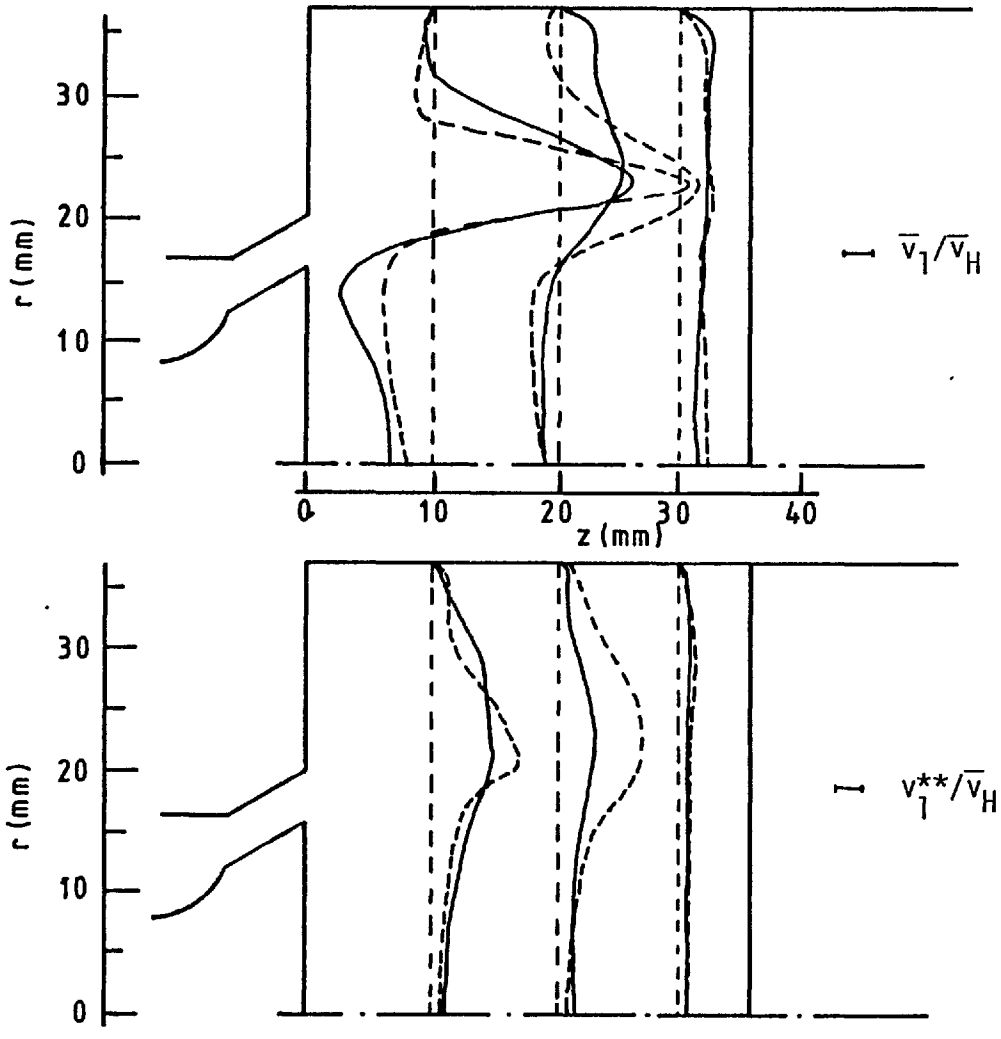

Fig. 5.5 Measured (---) and calculated (—) mean and turbulent axial velocities at 36^o for case 1

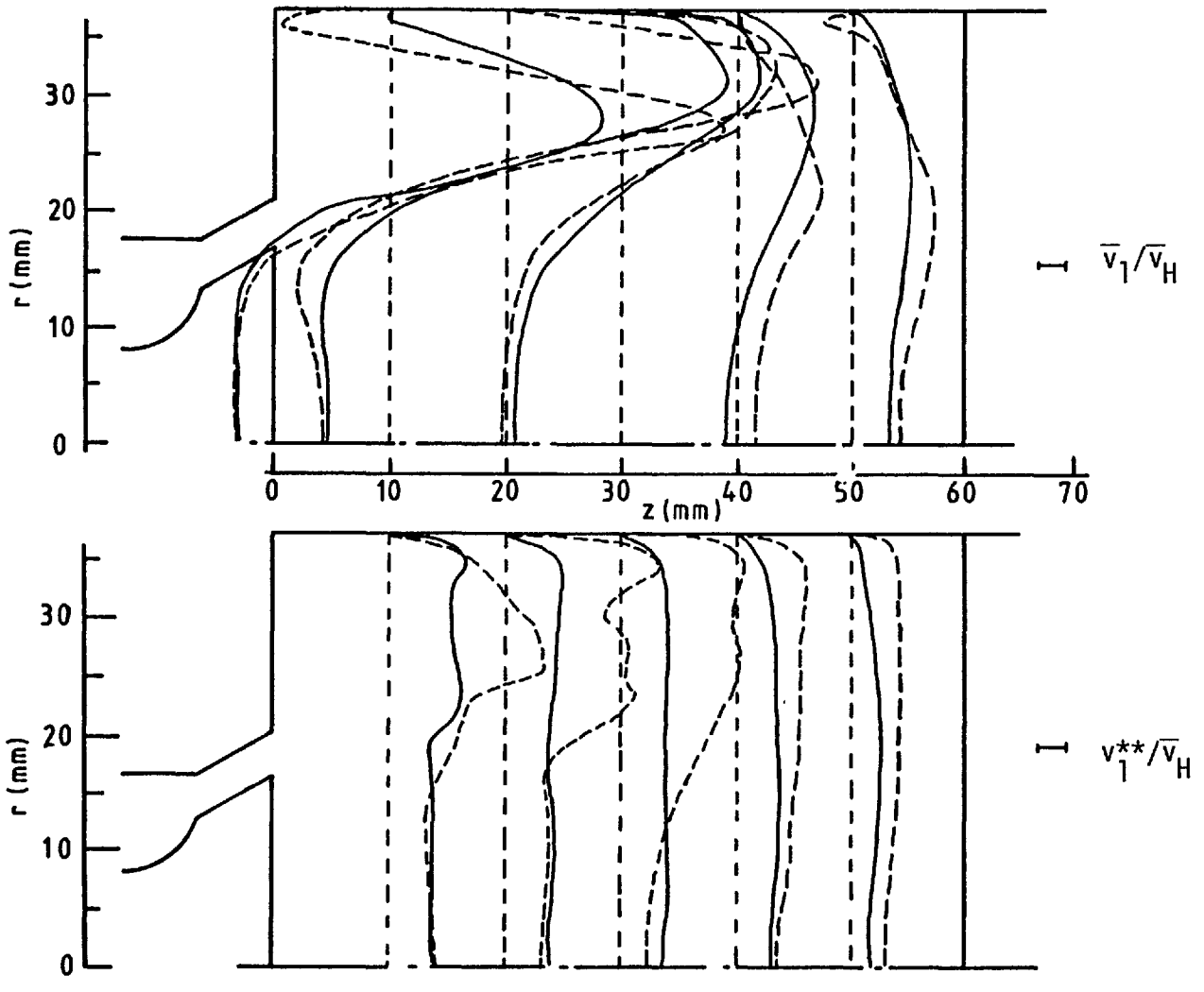

Fig. 5.6 Measured (---) and calculated (——) mean and turbulent axial velocities at 90^0 for case 1

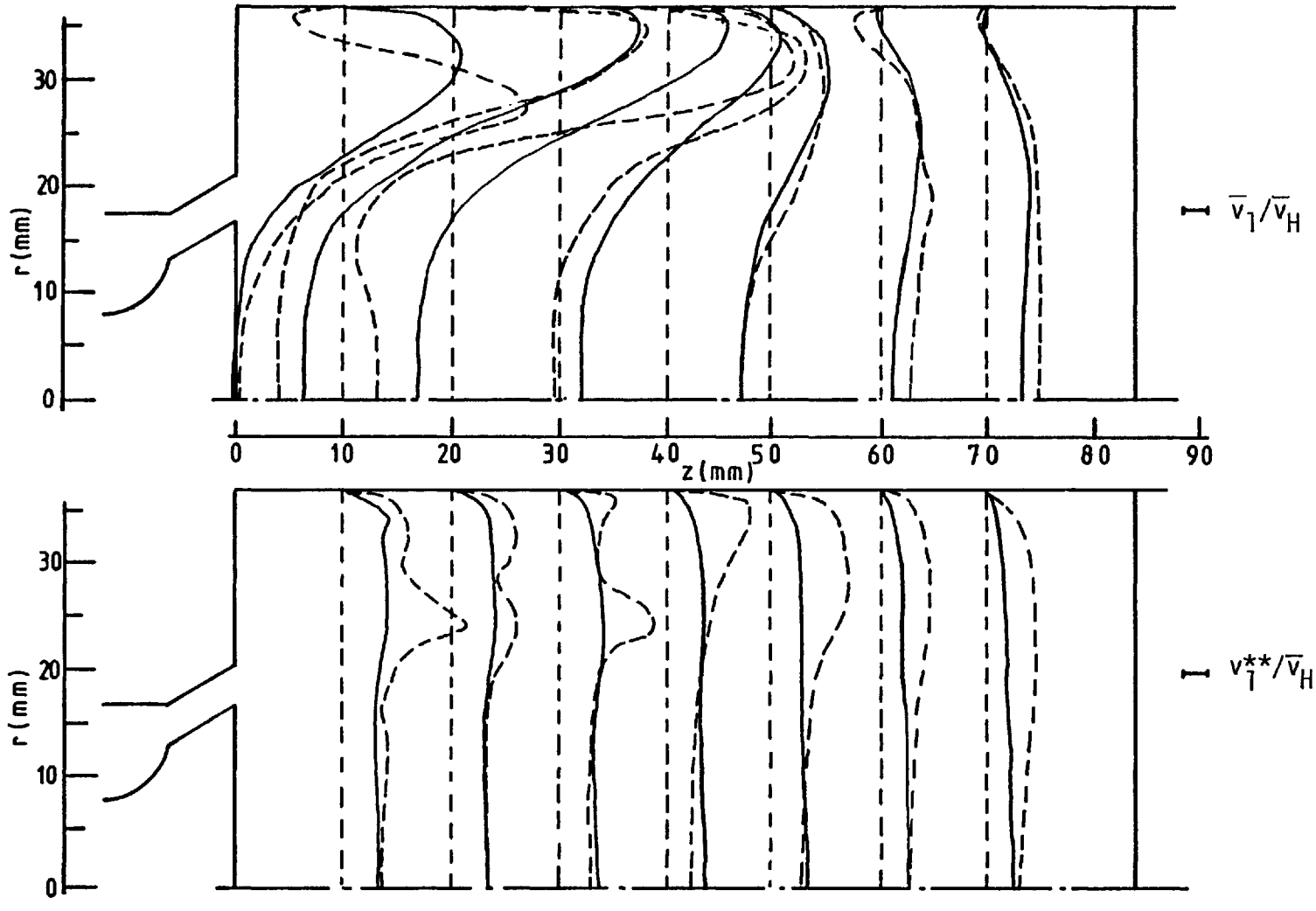

Fig. 5.7 Measured (---) and calculated (——) mean and turbulent axial velocities at 144° for case 1

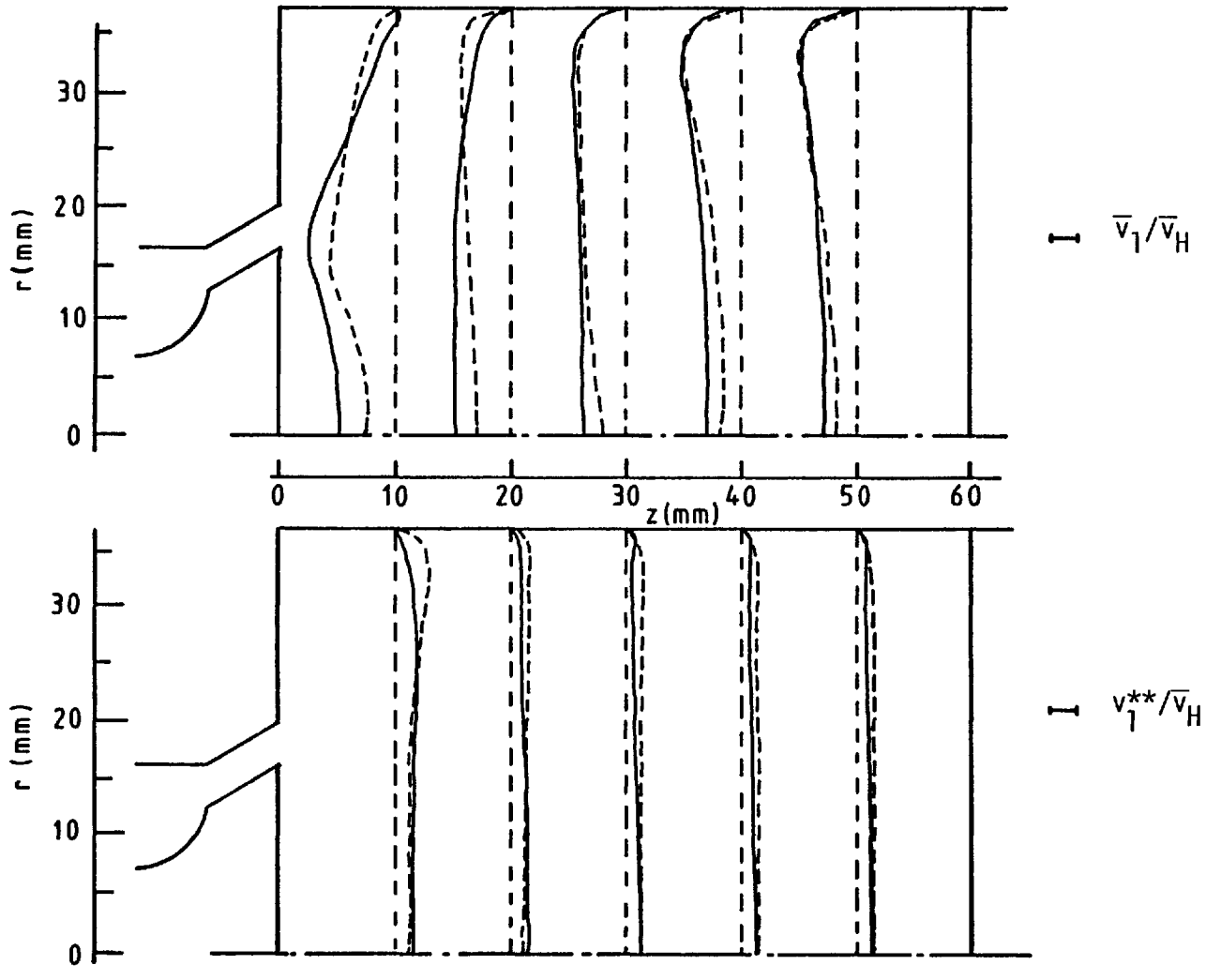

Fig. 5.8 Measured (---) and calculated (——) mean and turbulent axial velocities at 270^{o} for case 1

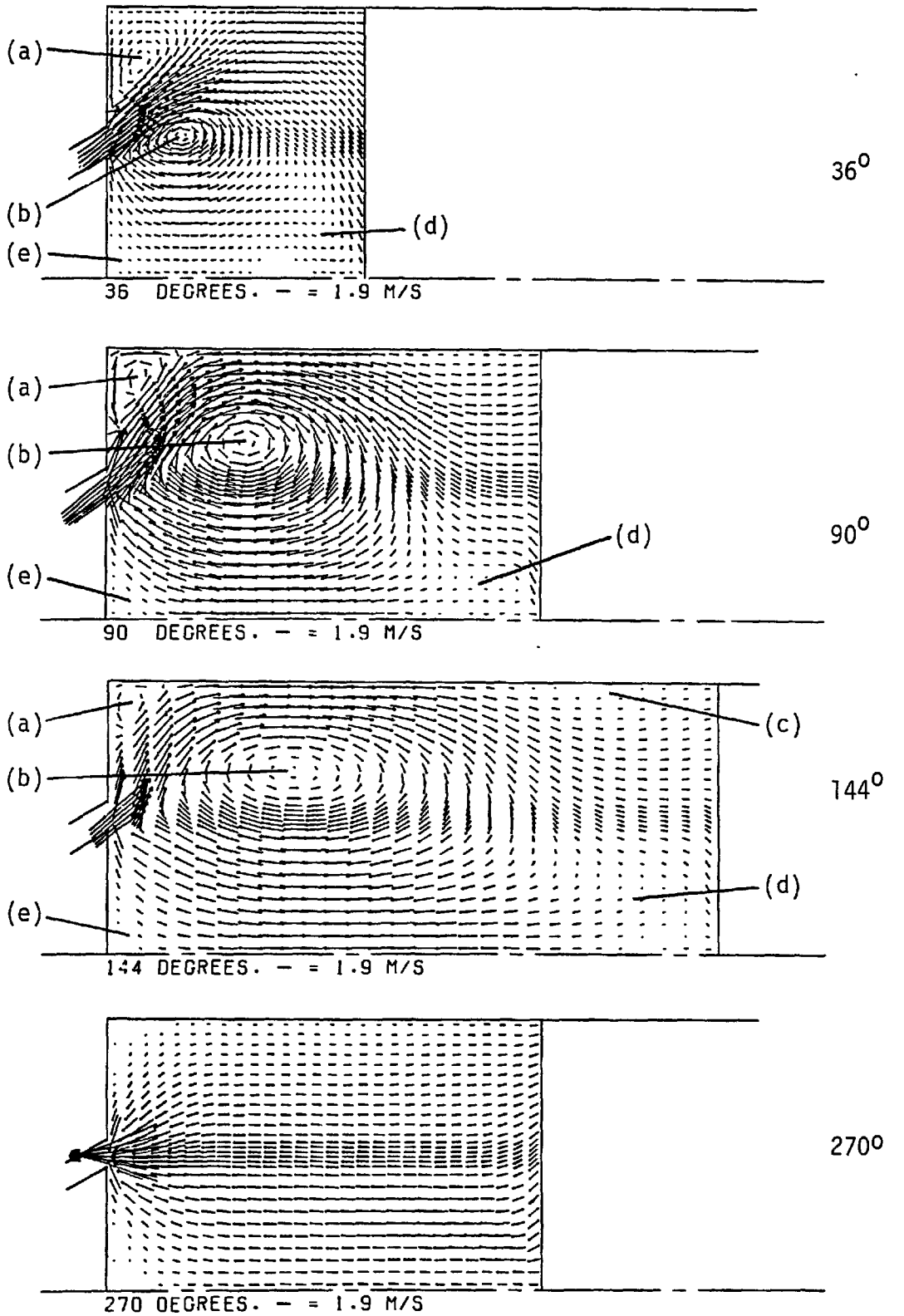

Fig. 5.9 Predicted axial-radial velocity fields for case 2

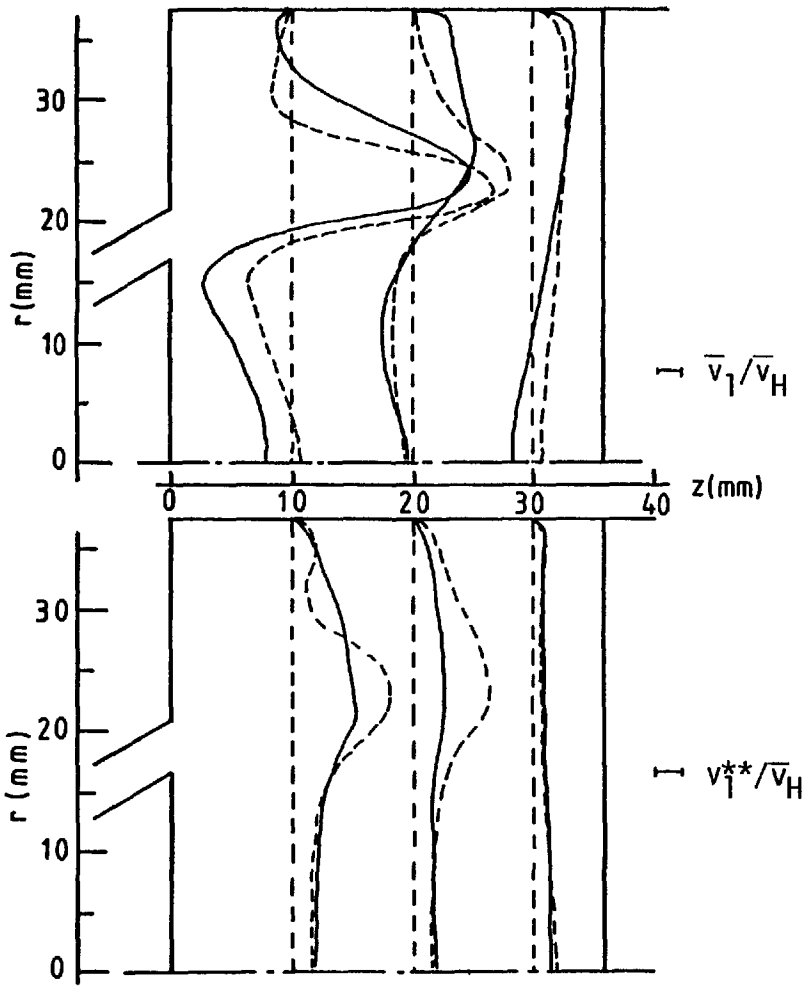

Fig. 5.10 Measured (---) and calculated (—) mean and turbulent axial velocities at 36^{o} for case 2

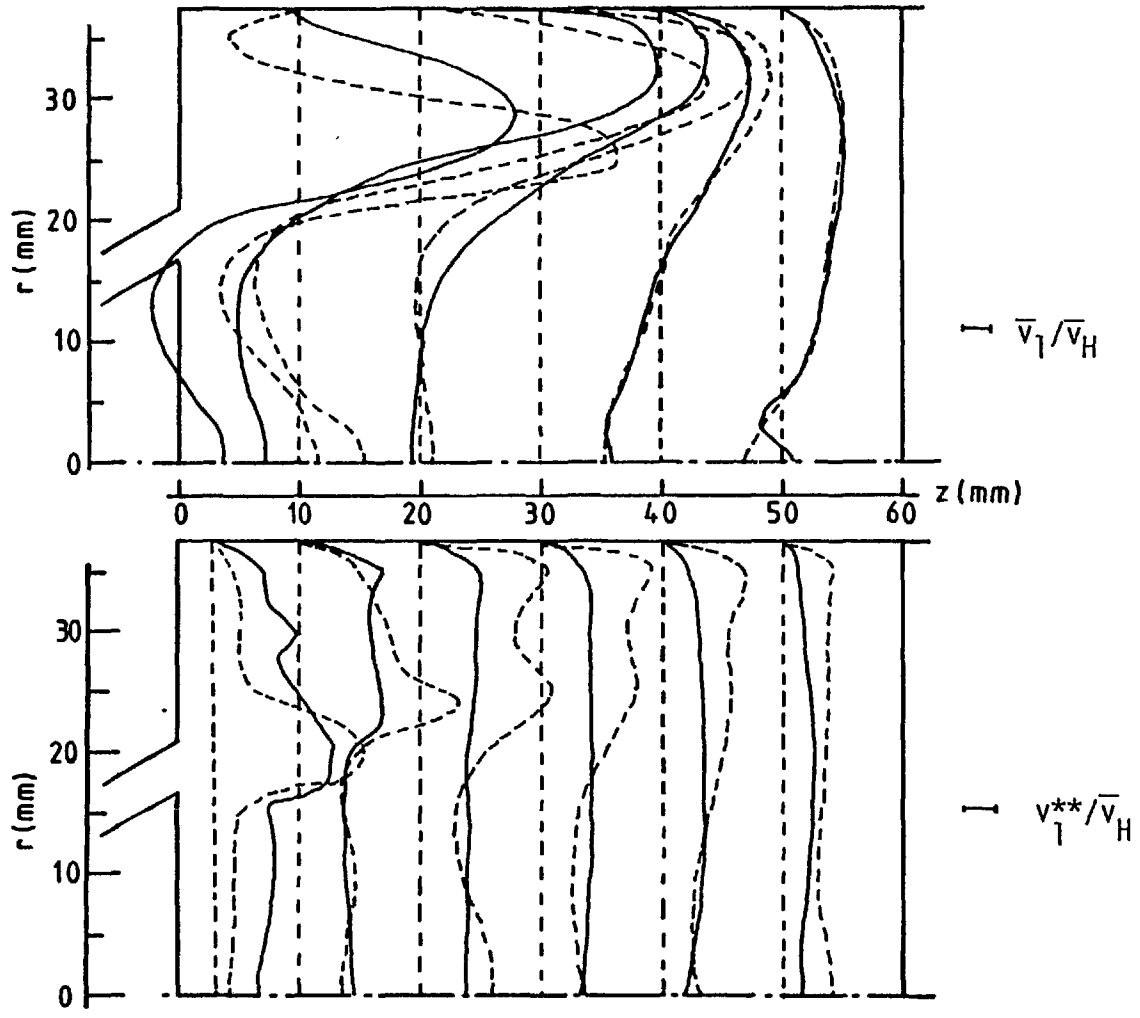

Fig. 5.11 Measured (---) and calculated (—) mean and turbulent axial velocities at 90° for case 2

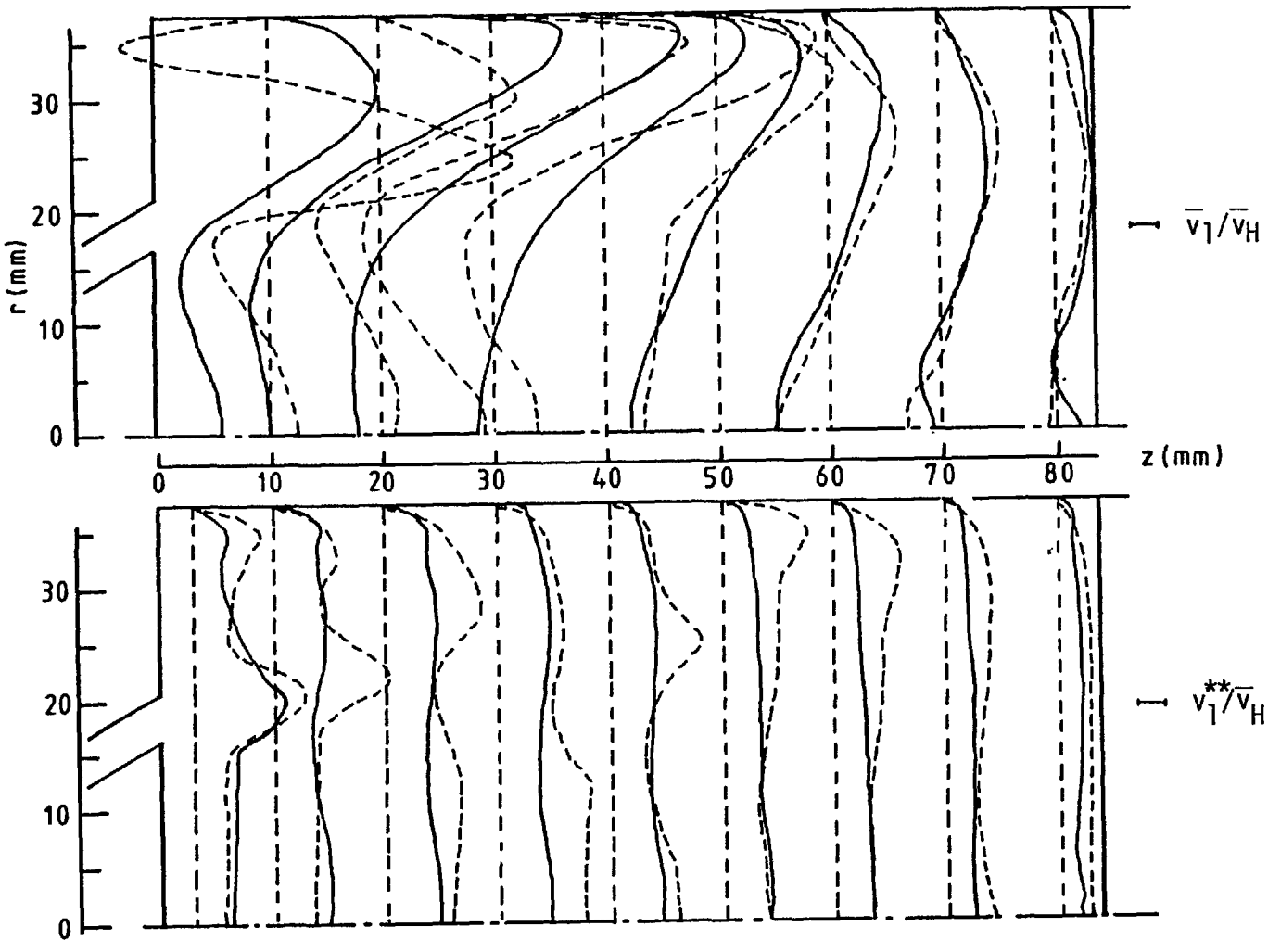

Fig. 5.12 Measured (---) and calculated (—) mean and turbulent axial velocities at 144^{o} for case 2

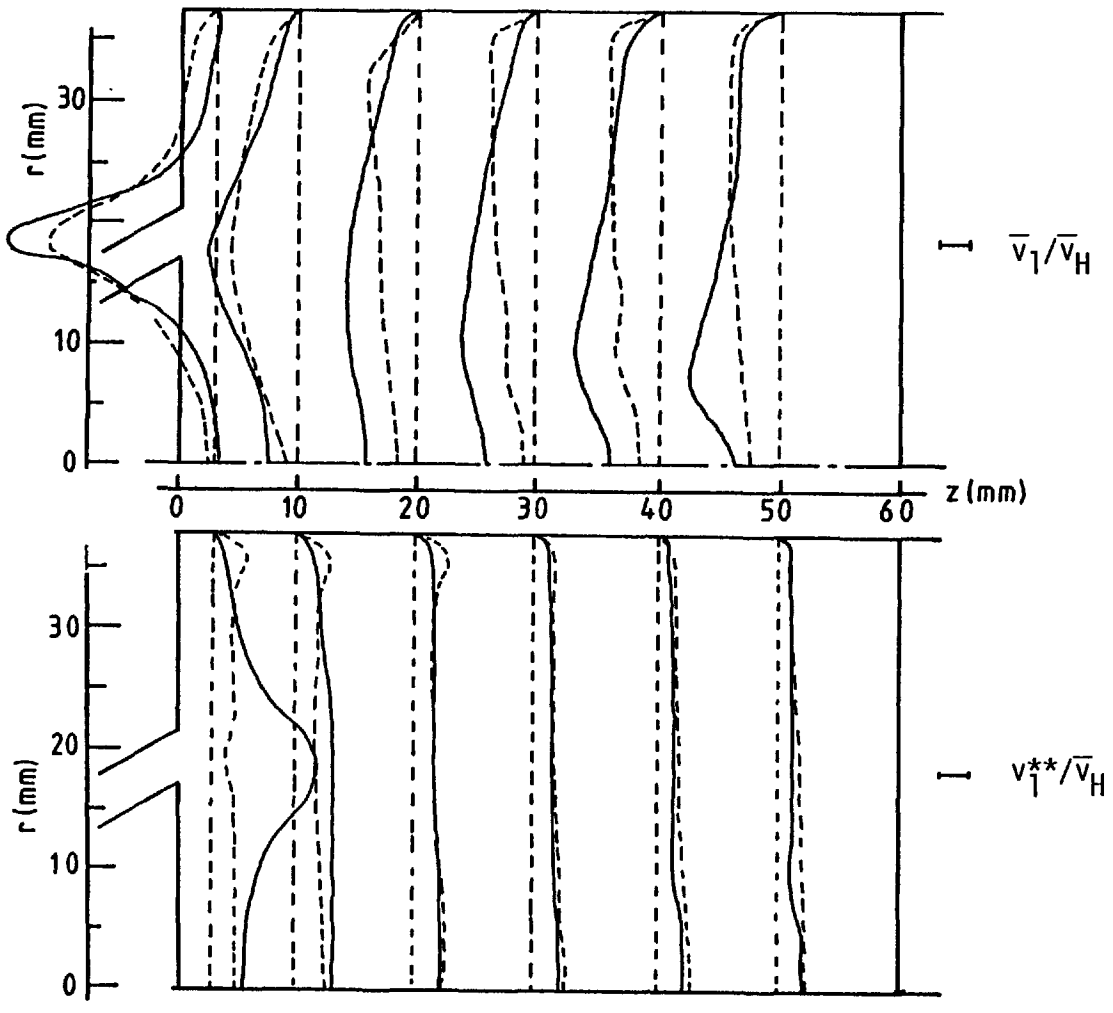

Fig. 5.13 Measured (---) and calculated (—) mean and turbulent axial velocities at 270^{o} for case 2

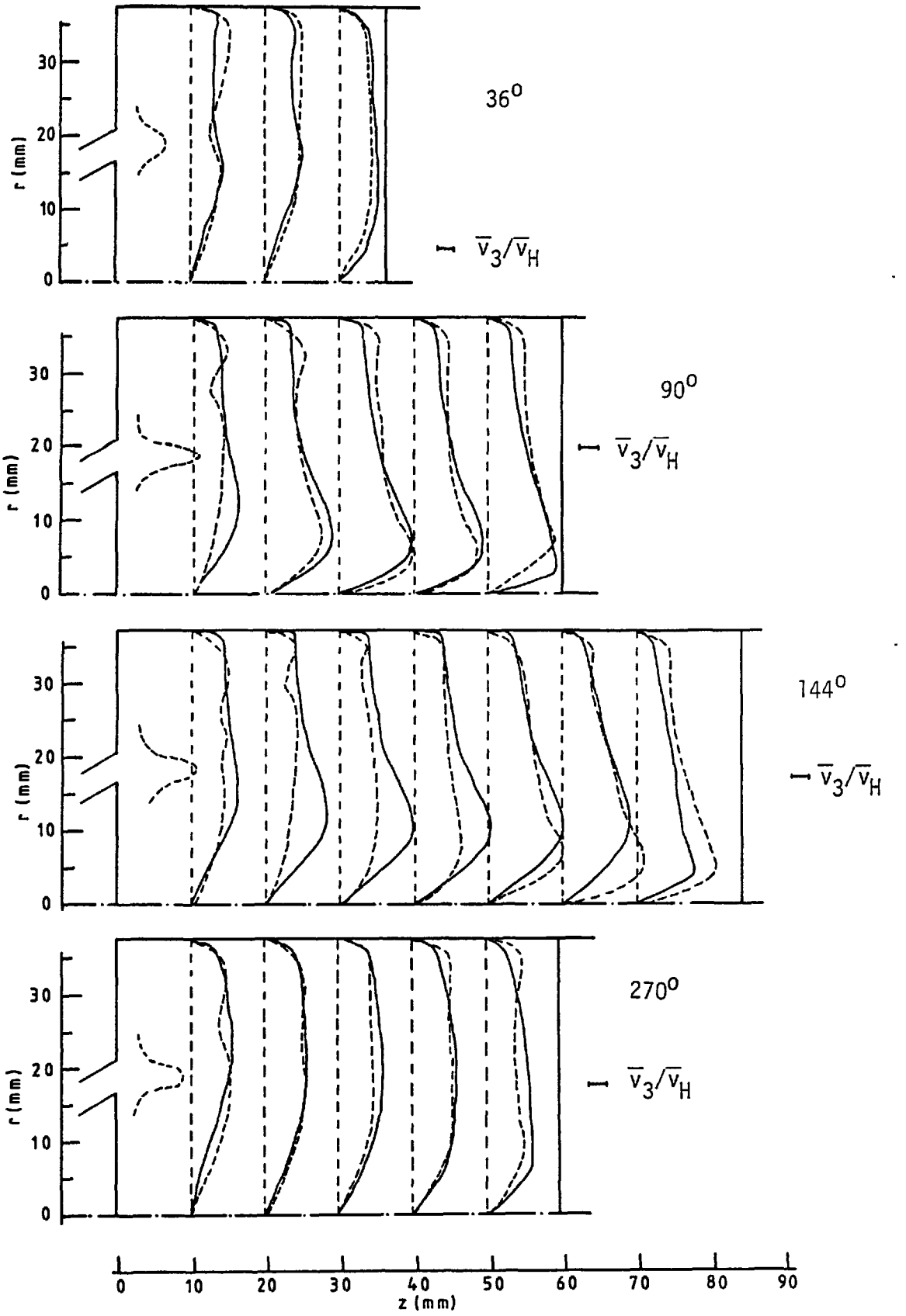

Fig. 5.14 Measured (---) and calculated (—) swirl velocities for case 2

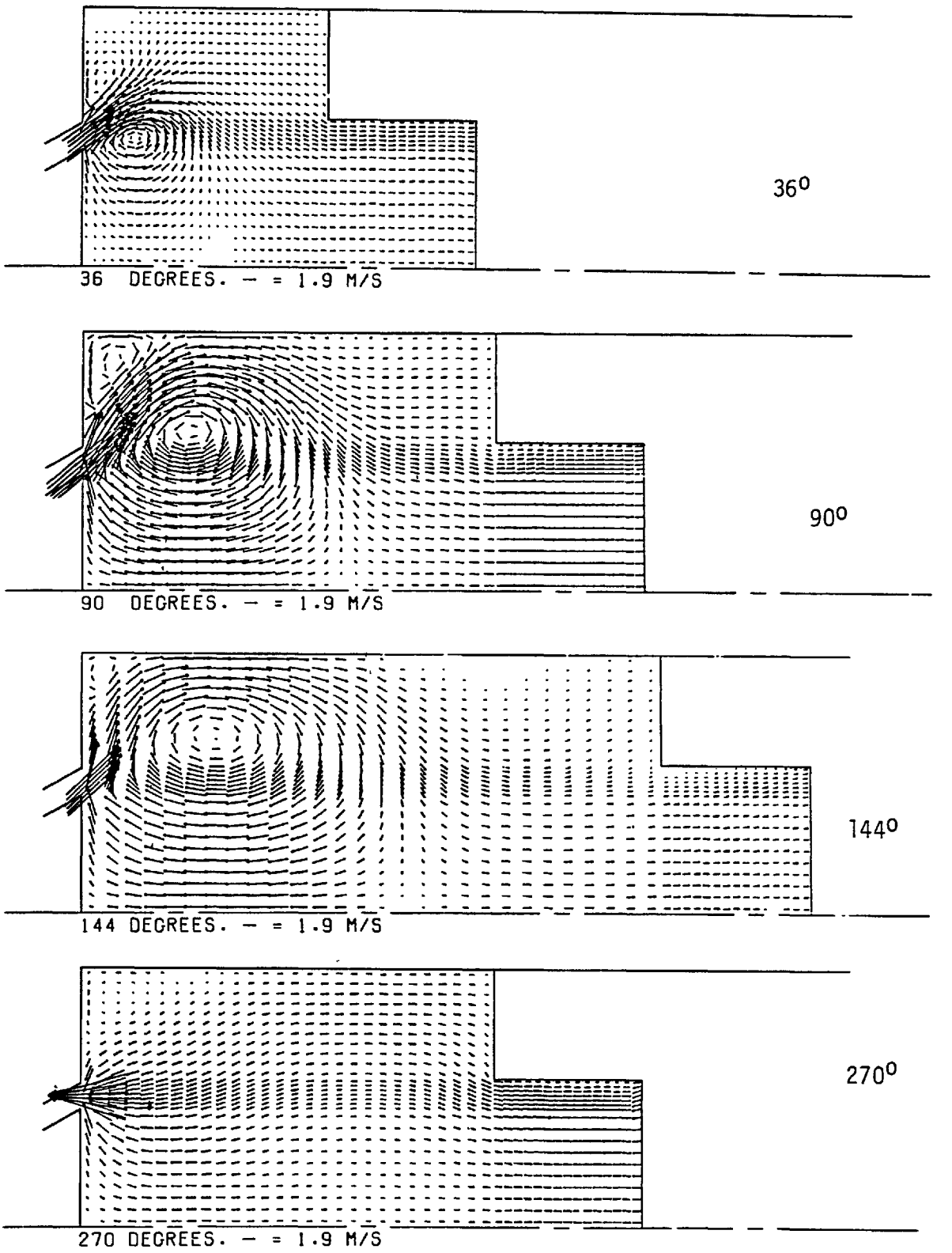

Fig. 5.15 Predicted axial-radial velocity fields for case 3

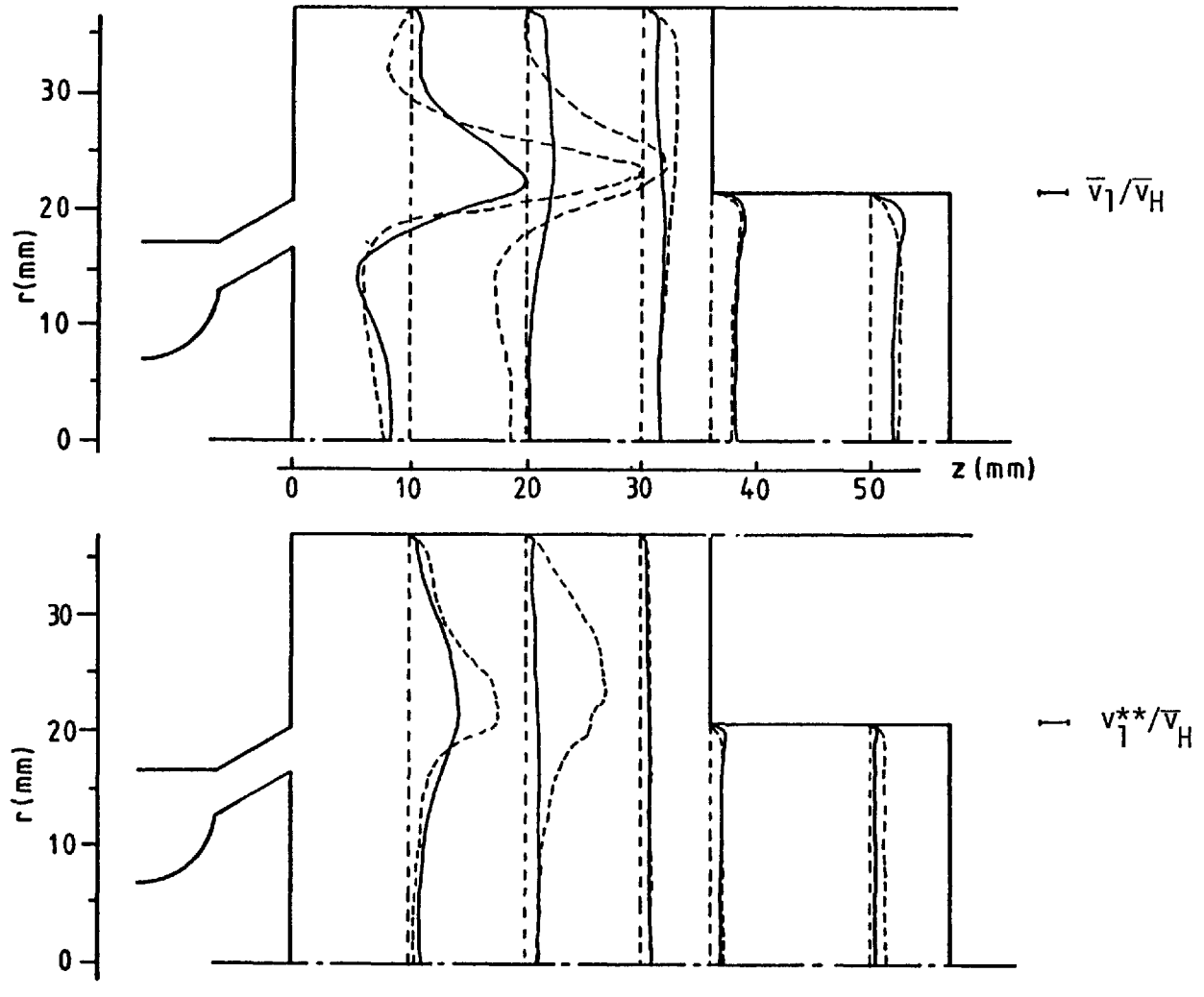

Fig. 5.16 Measured (---) and calculated (—) mean and turbulent axial velocities at 36^o for case 3

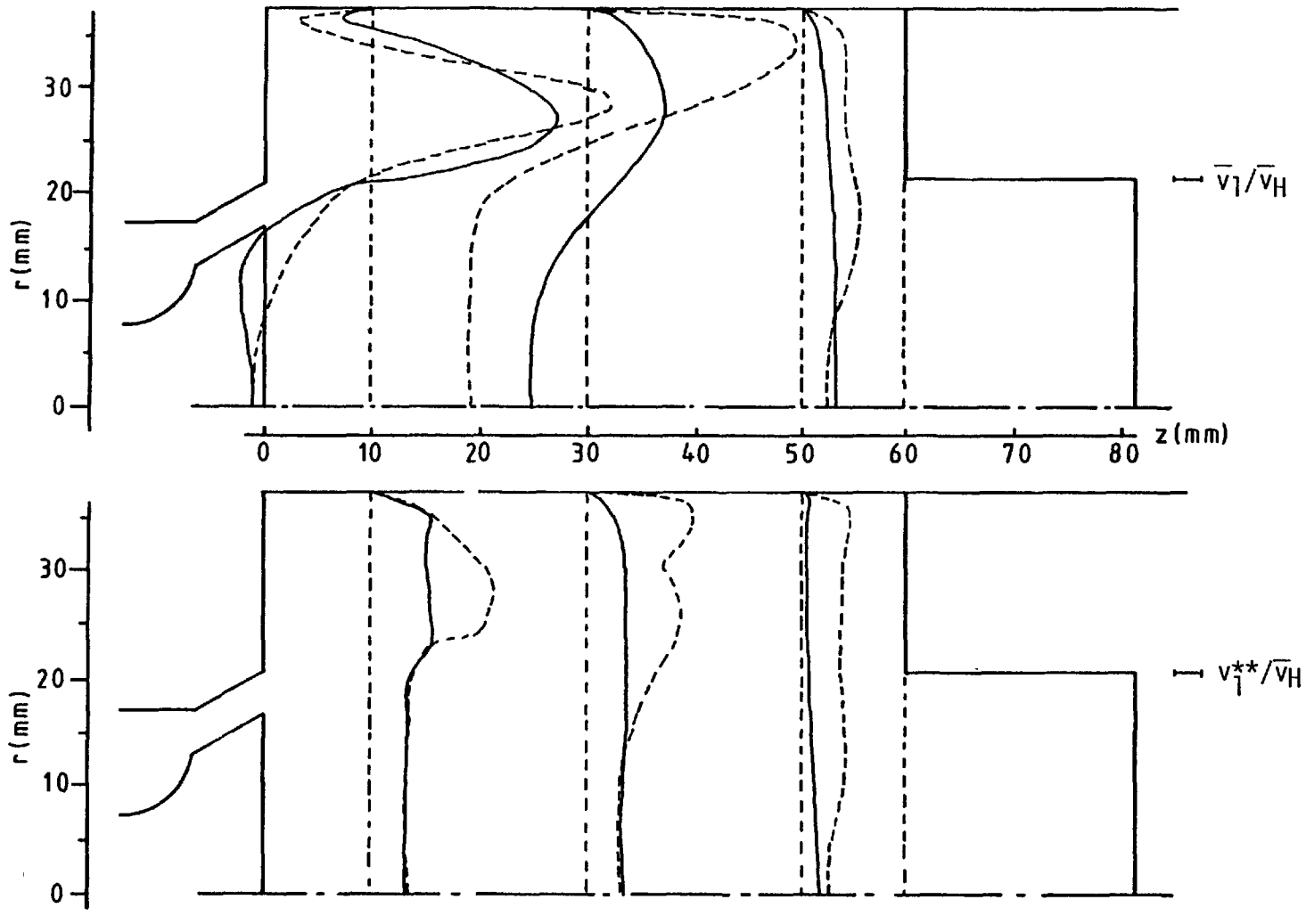

Fig. 5.17 Measured (---) and calculated (—) mean and turbulent axial velocities at 90° for case 3

contd....

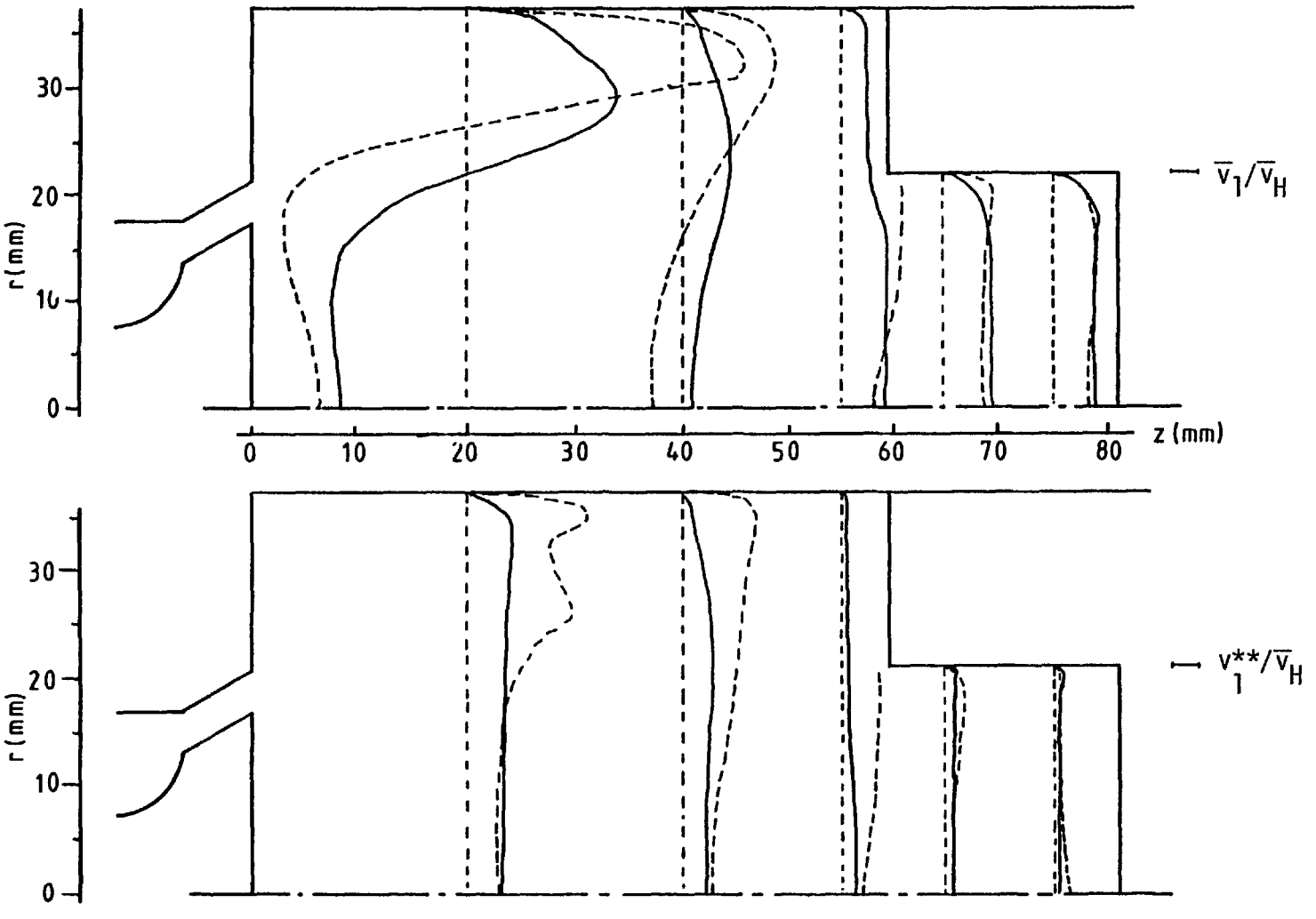

Fig. 5.17 Measured (---) and calculated (—) mean and turbulent axial velocities at 90^0 for case 3

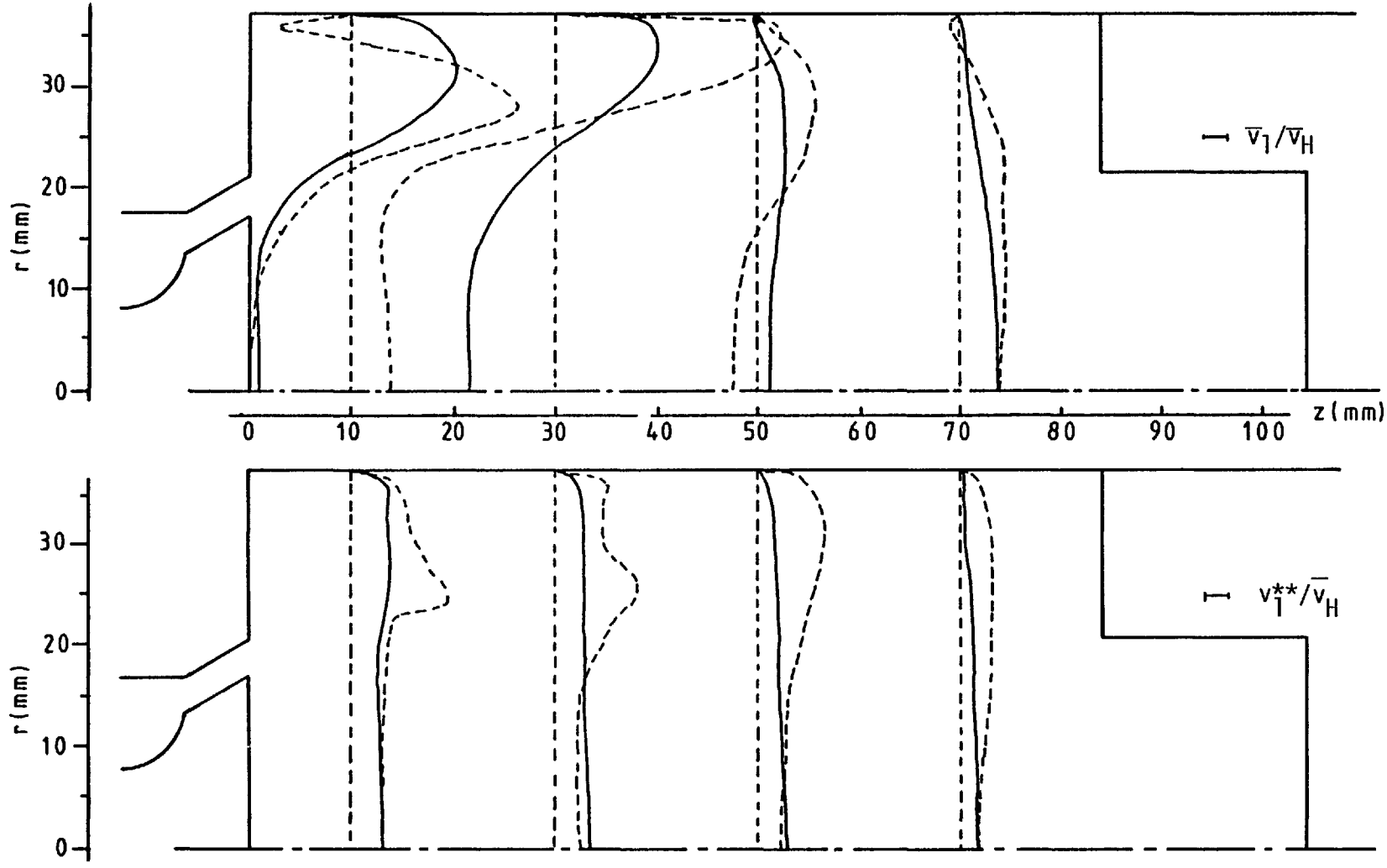

Fig. 5.18 Measured (---) and calculated (—) mean and turbulent axial velocities at 144° for case 3

contd....

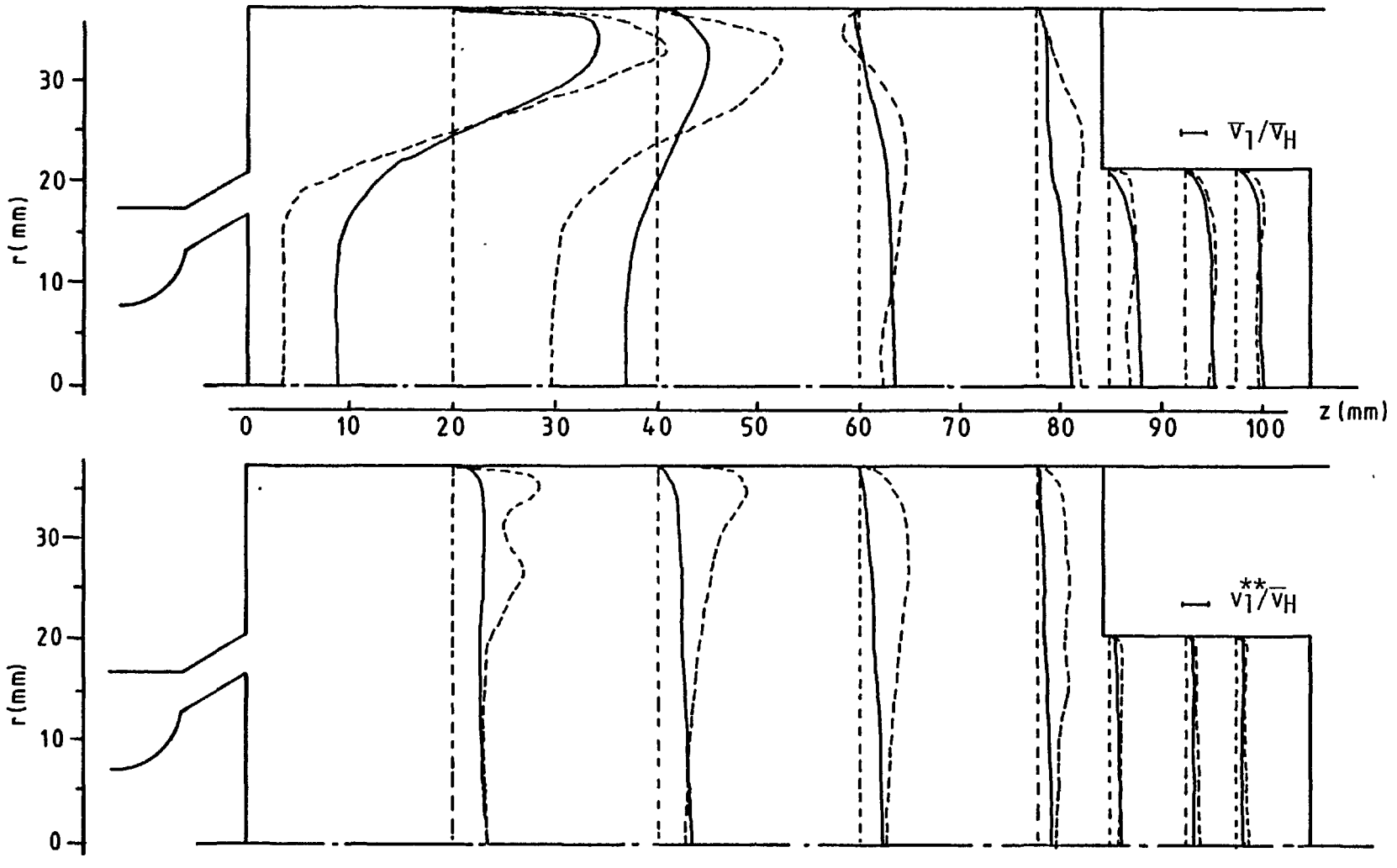

Fig. 5.18 Measured (---) and calculated (—) mean and turbulent axial velocities at 144^o for case 3

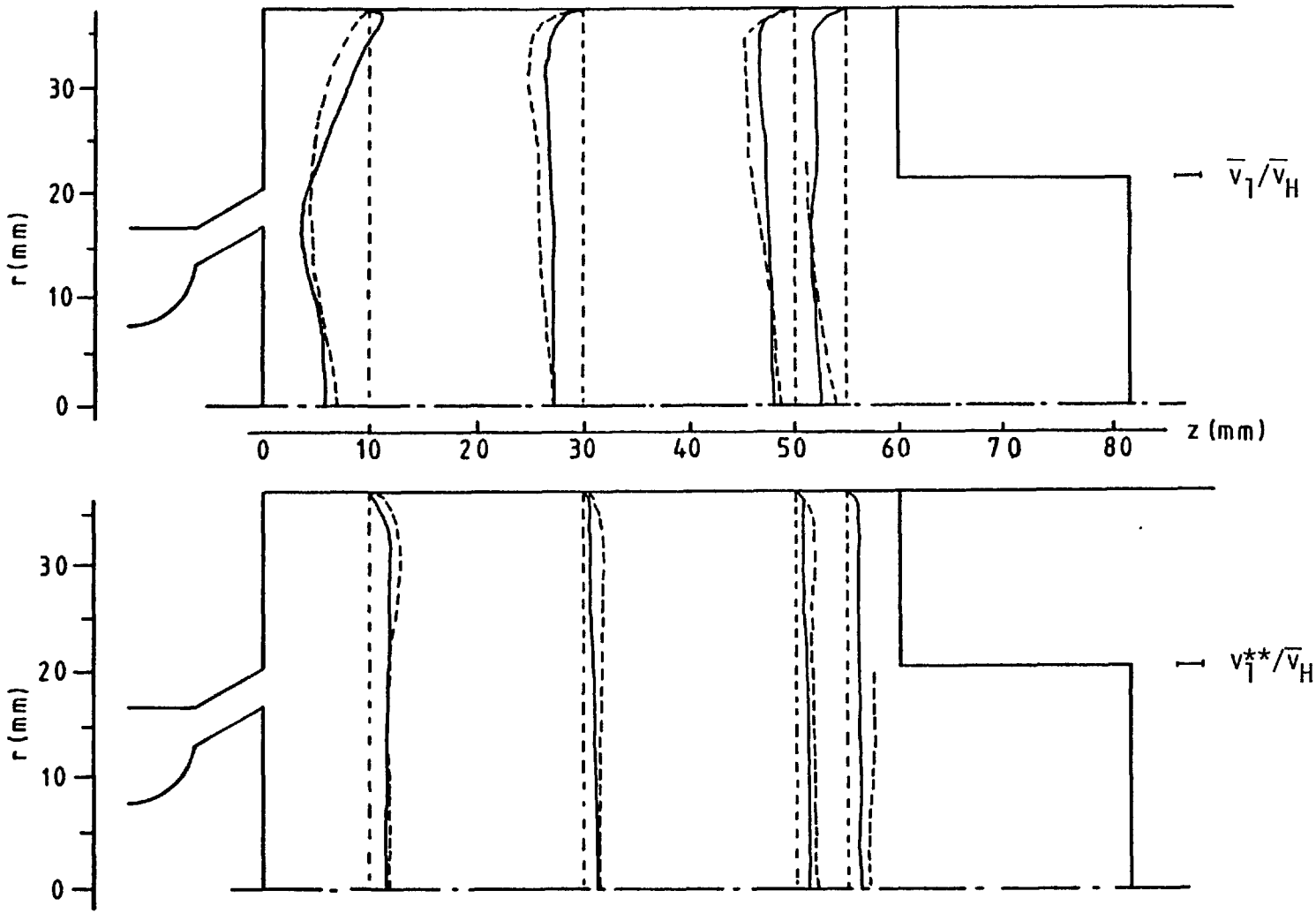

Fig. 5.19 Measured (---) and calculated (—) mean and turbulent axial velocities at 270^{o} for case 3

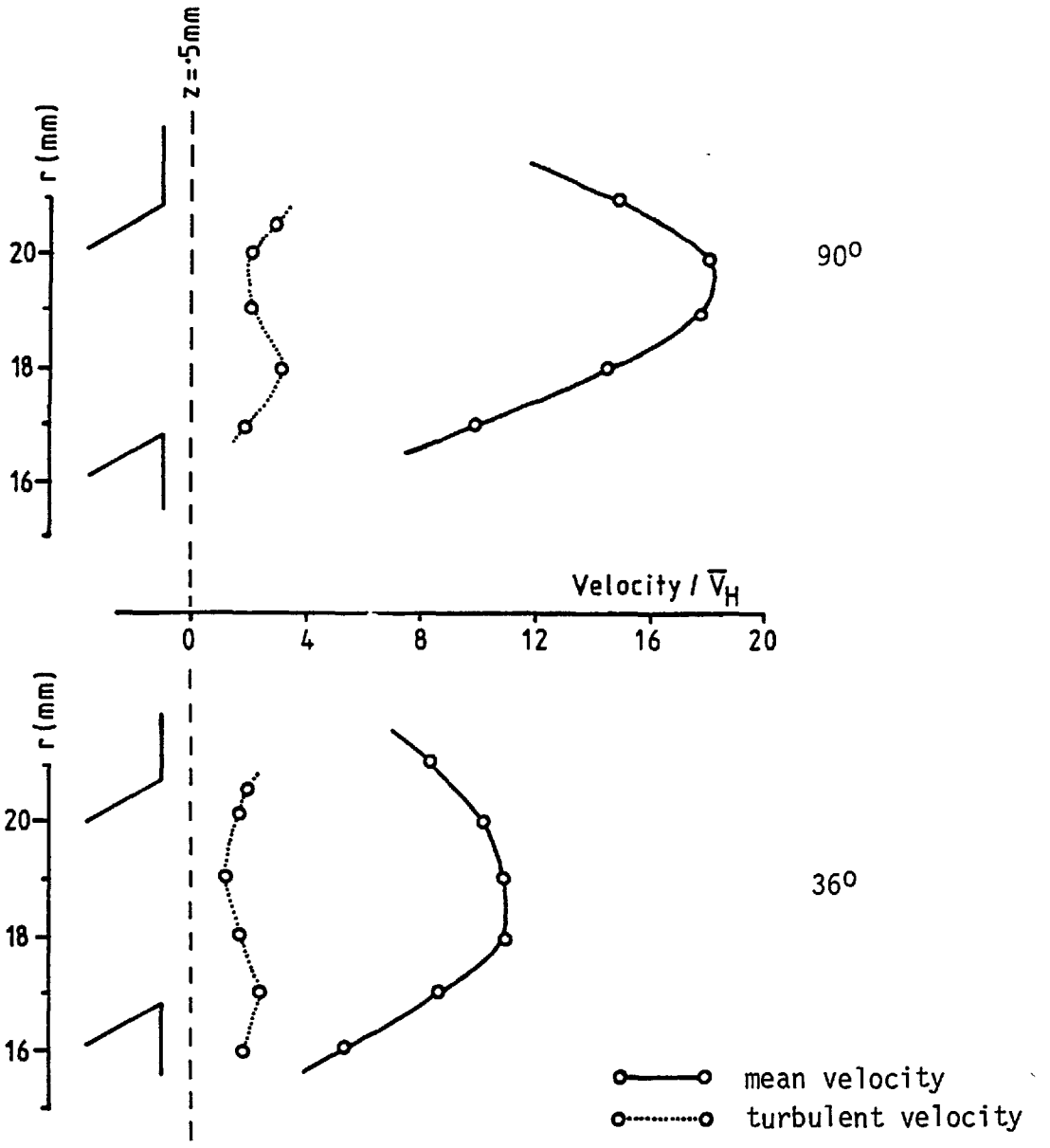

Fig. 5.20 Measured profiles of mean and turbulent axial velocities at the orifice for case 1

contd....

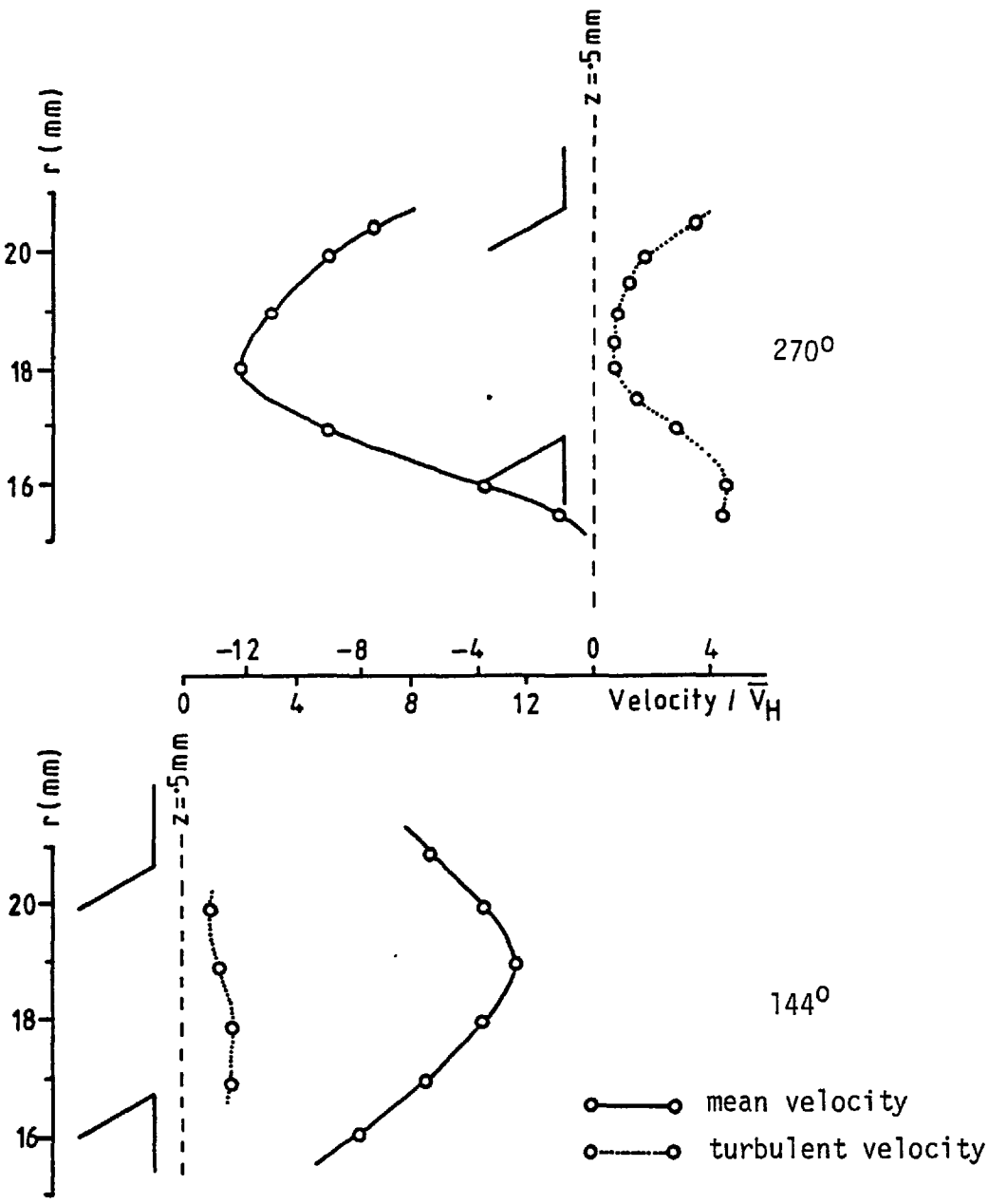

Fig. 5.20 Measured profiles of mean and turbulent axial velocities at the orifice for case 1

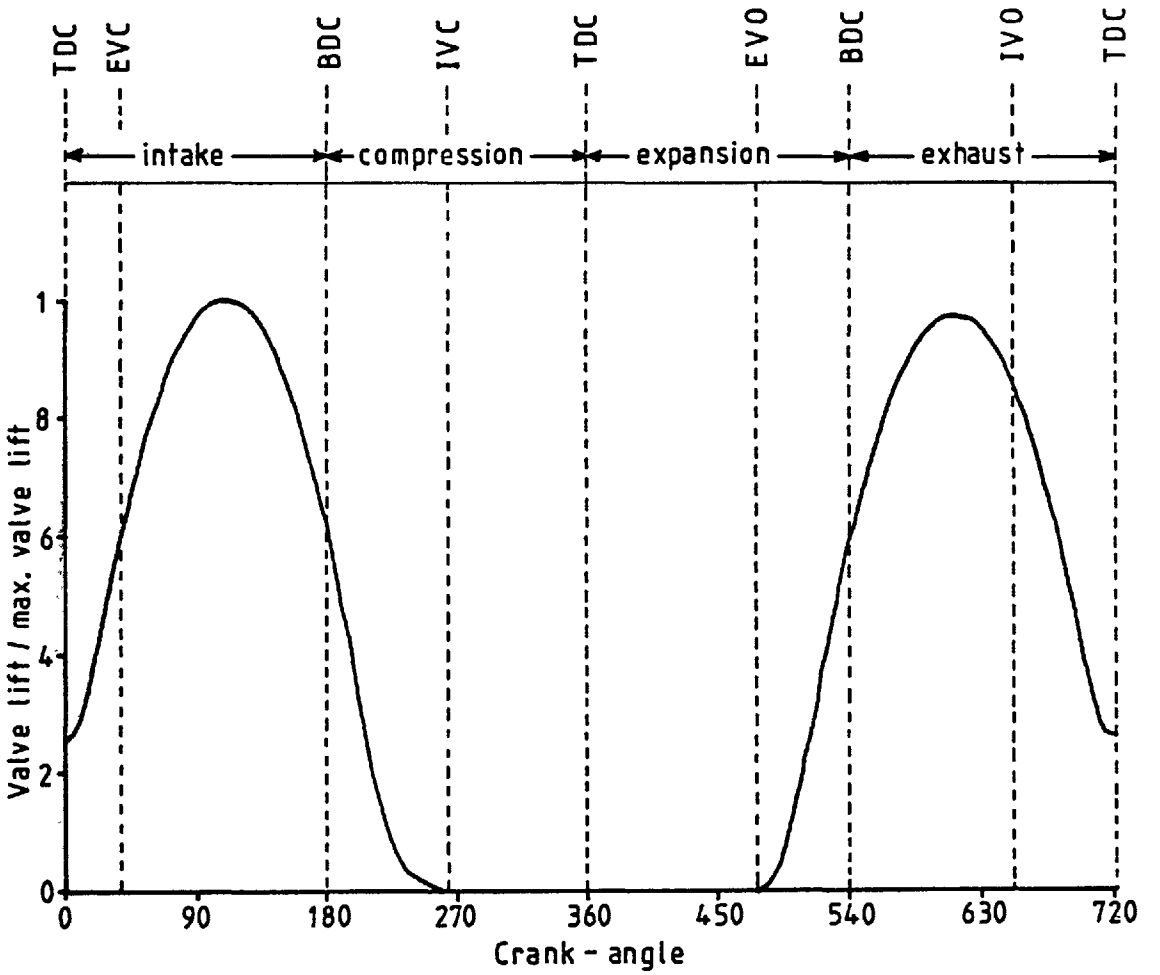

Fig. 5.21 Variation of valve lift with crank-angle for the axisymmetric engine of Witze (1976c)

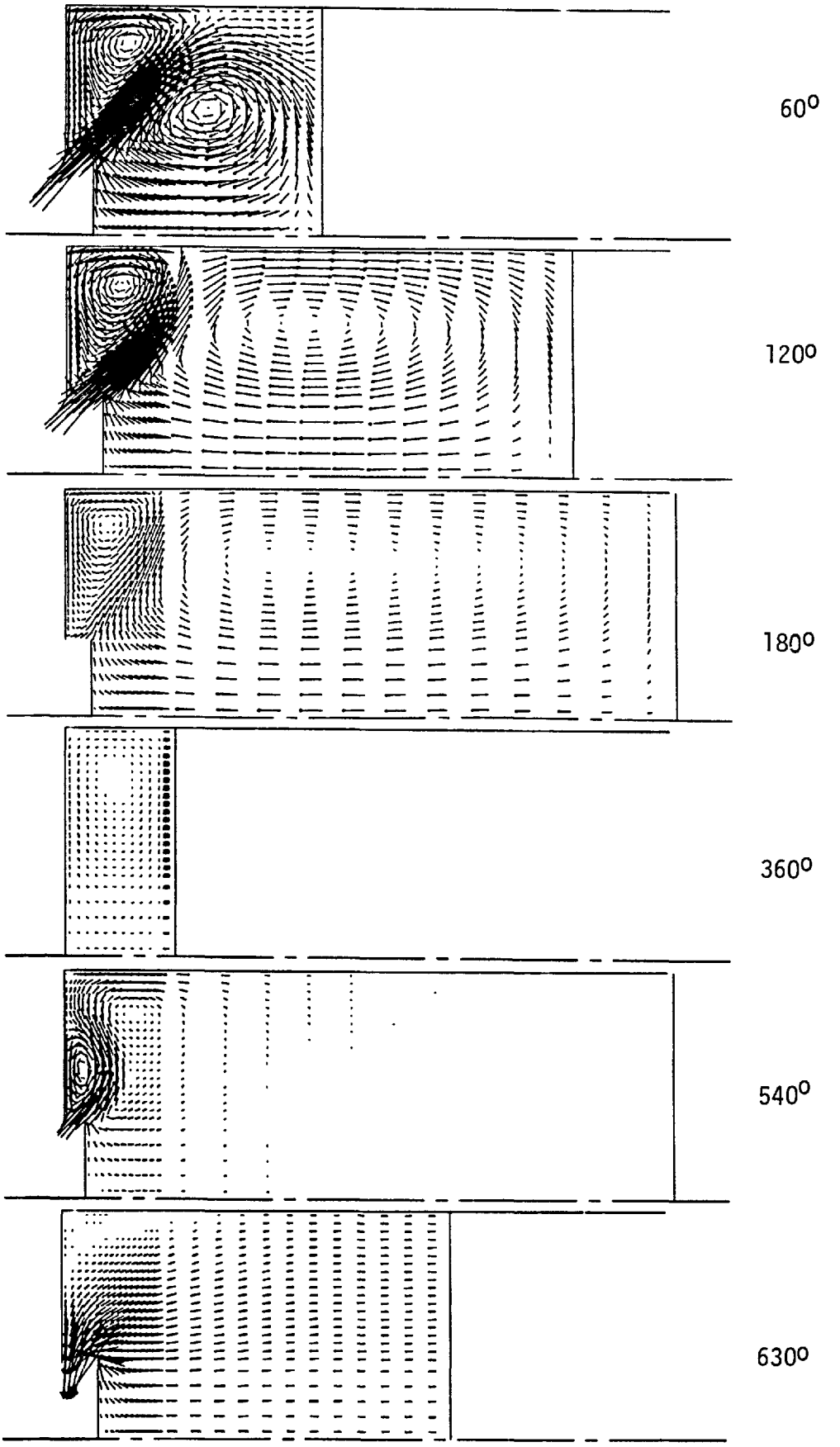

Fig. 5.22 Predicted axial-radial velocity fields for case 4

Contd....

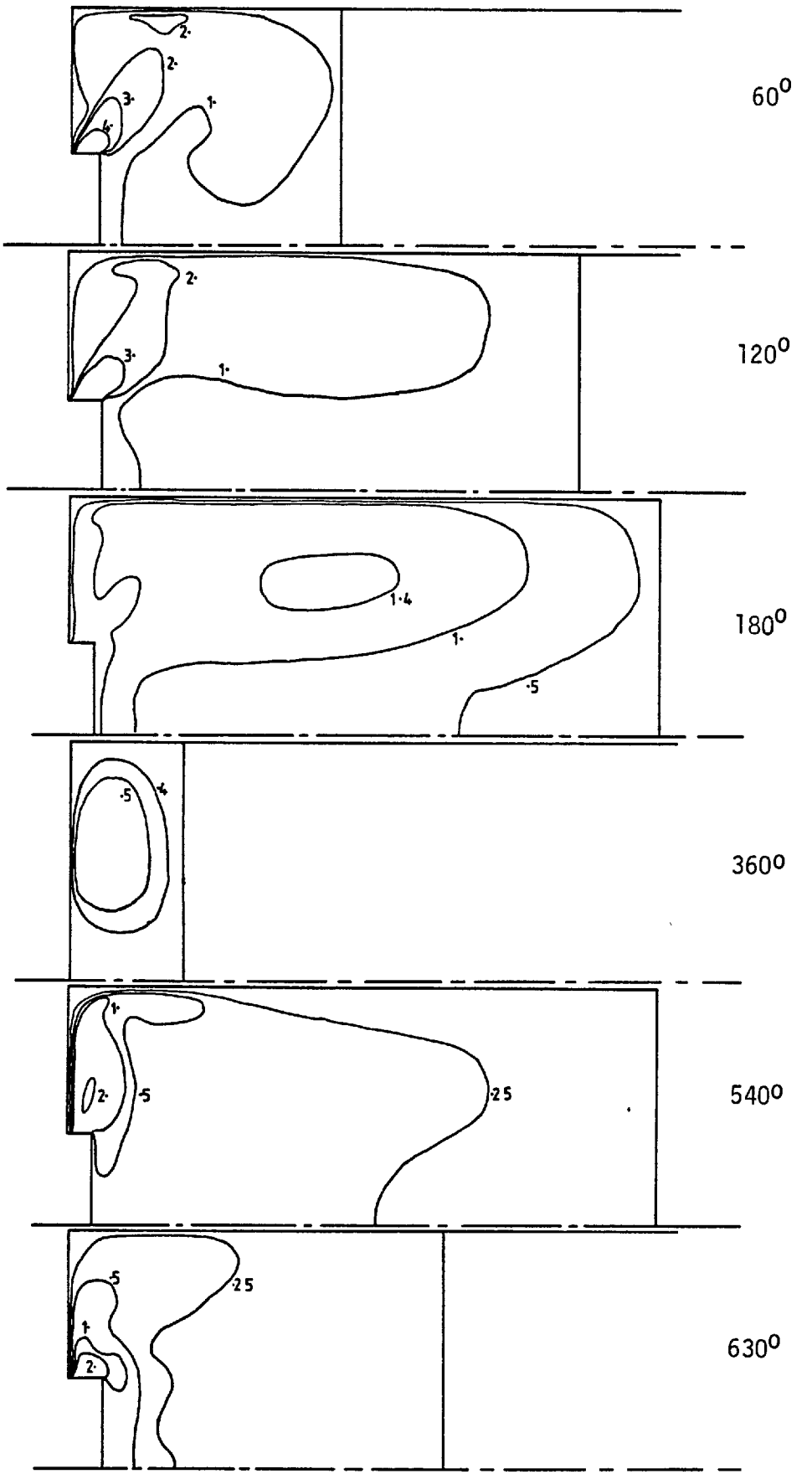

Fig. 5.23 Predicted turbulence intensity fields for case 4

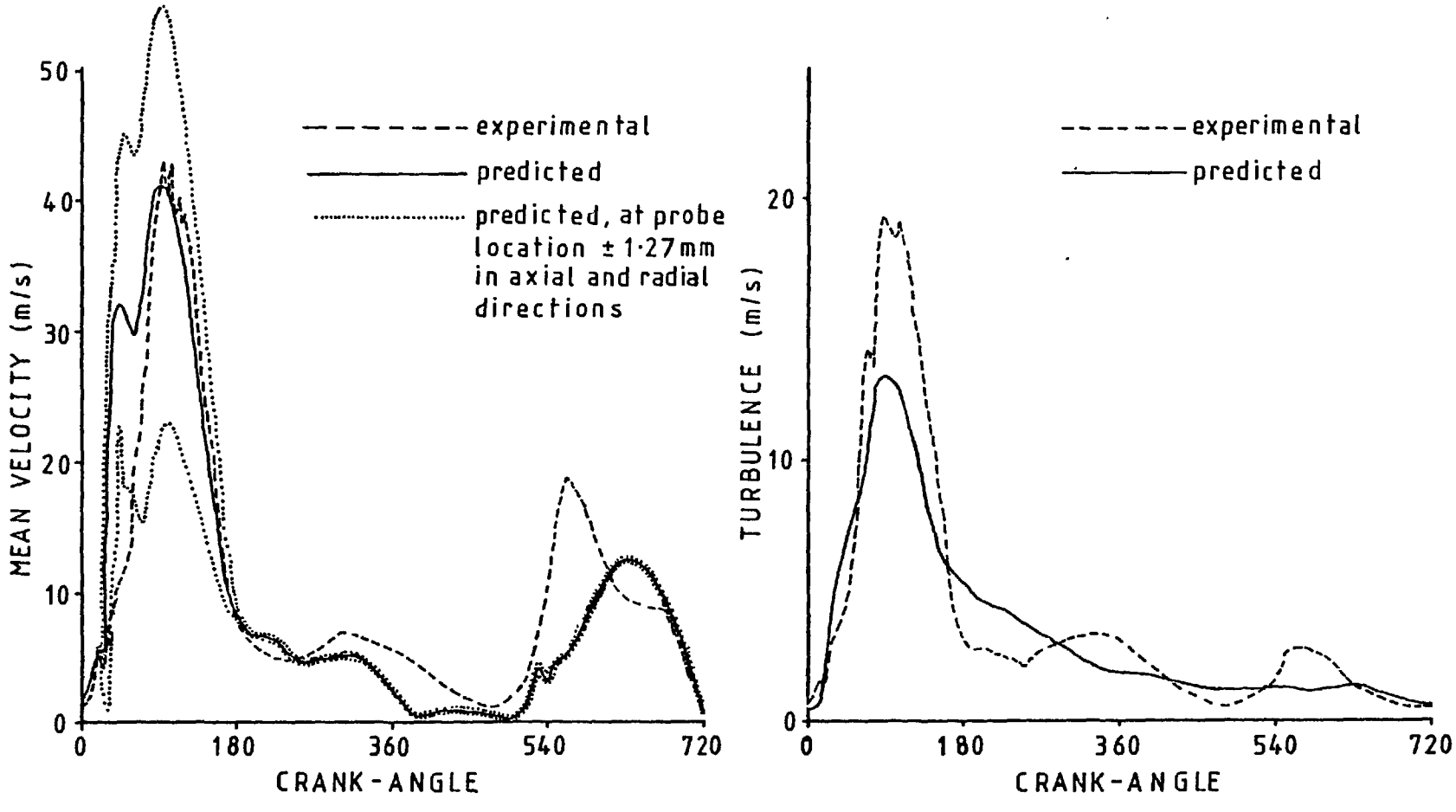

Fig. 5.24 Comparison between measured and calculated mean and turbulent velocities for case 4

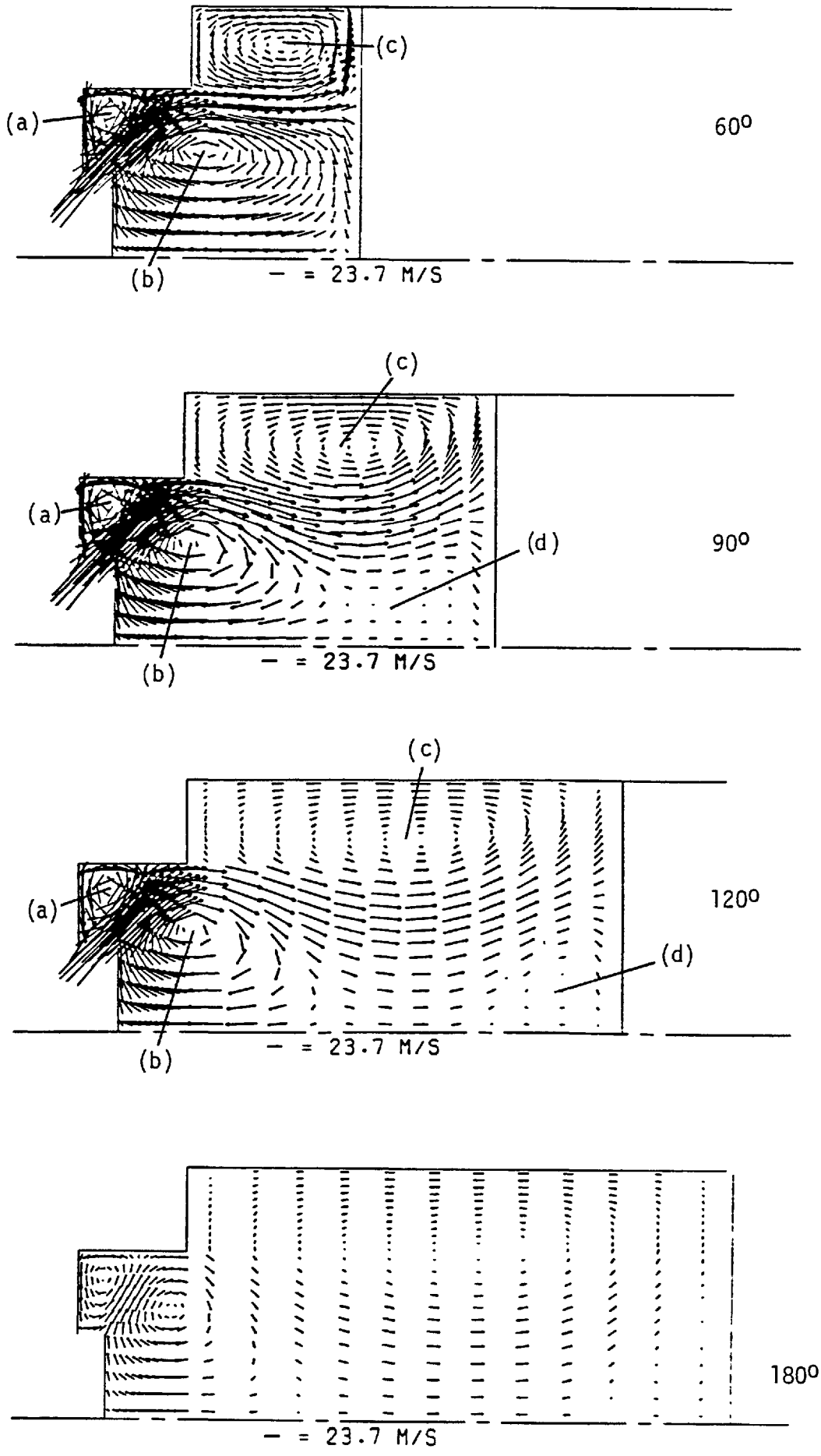

Fig. 5.25 Predicted axial-radial velocity fields for case 5

contd....

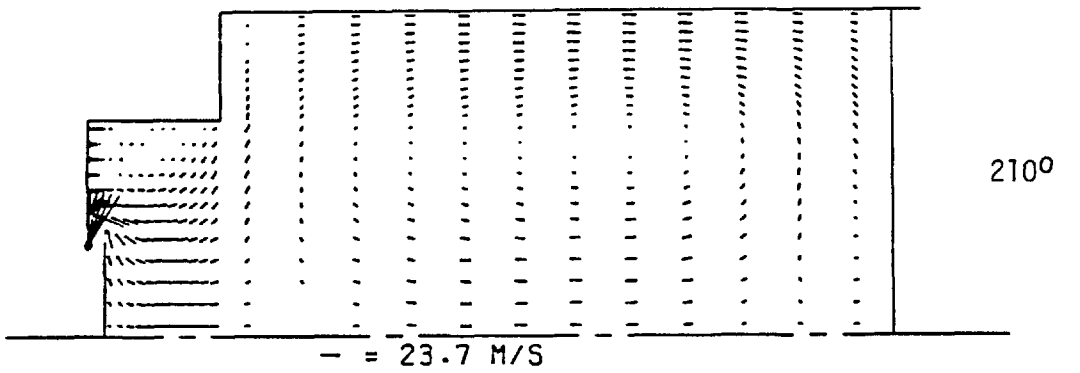

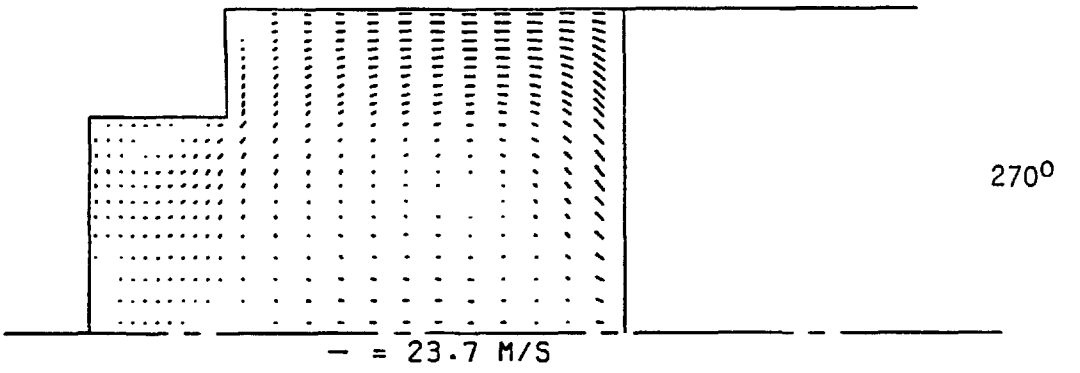

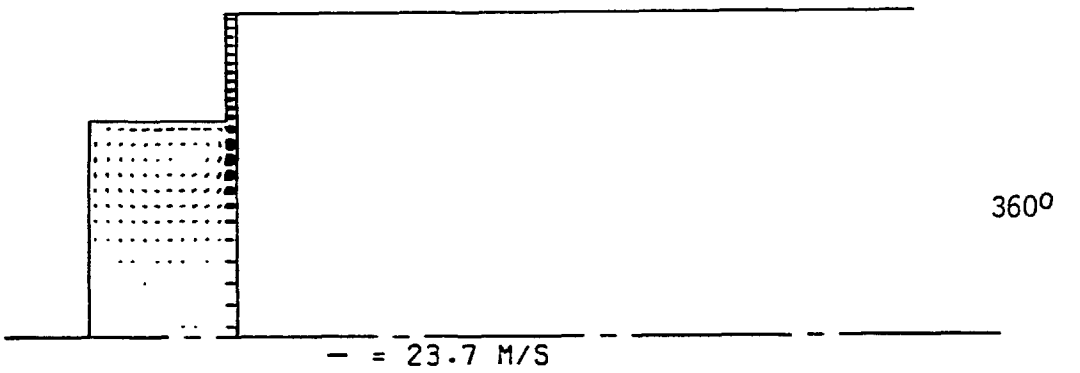

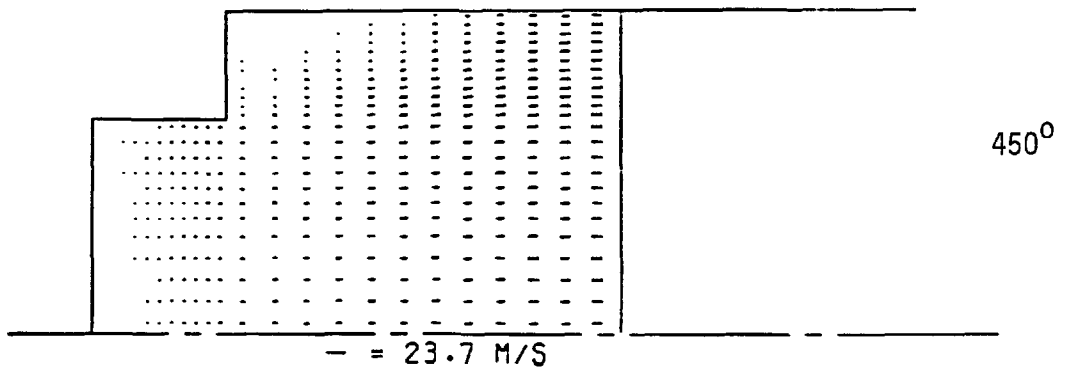

Fig. 5.25 Predicted axial~radial velocity fields for case 5

contd....

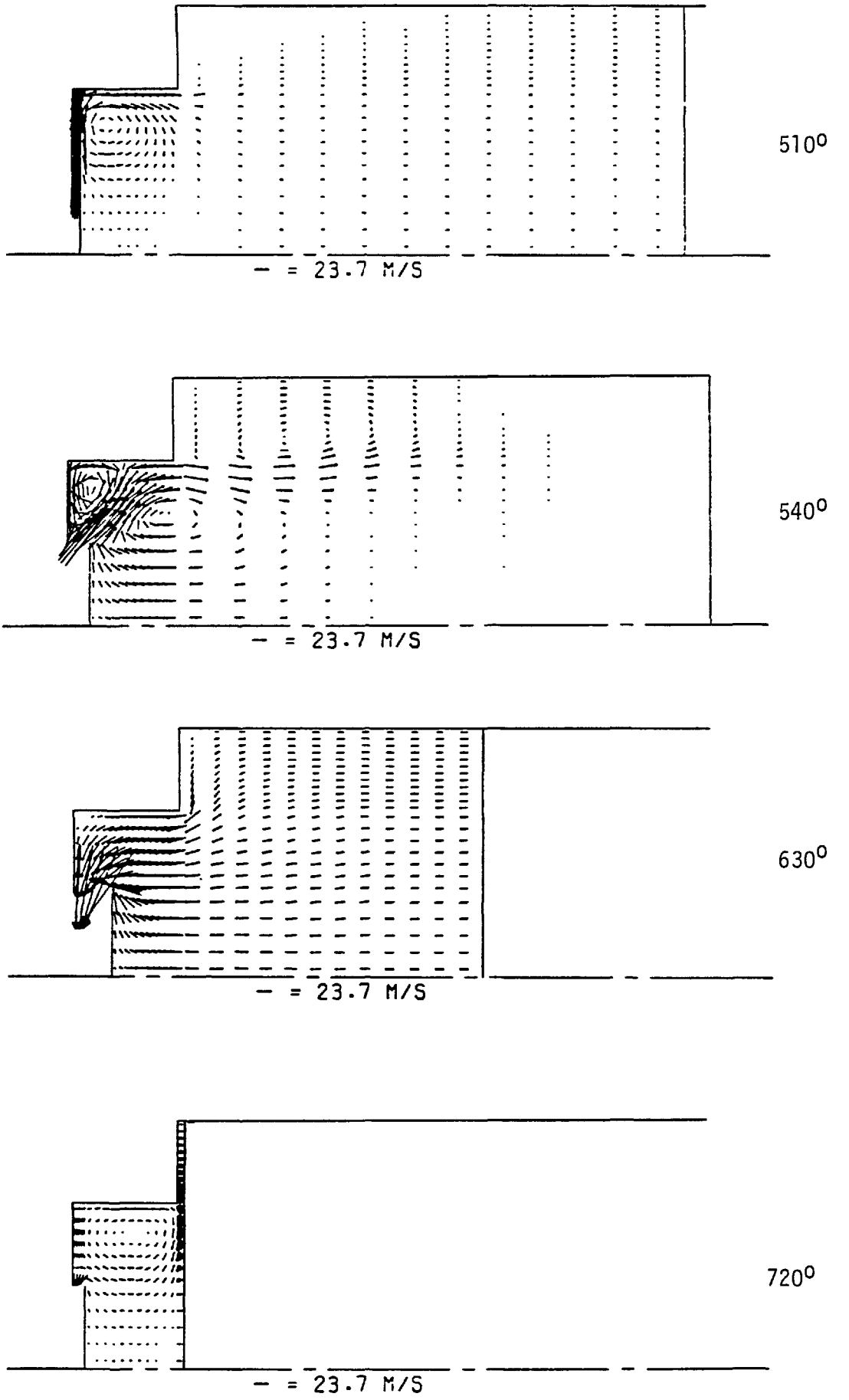

Fig. 5.25 Predicted axial-radial velocity fields for case 5

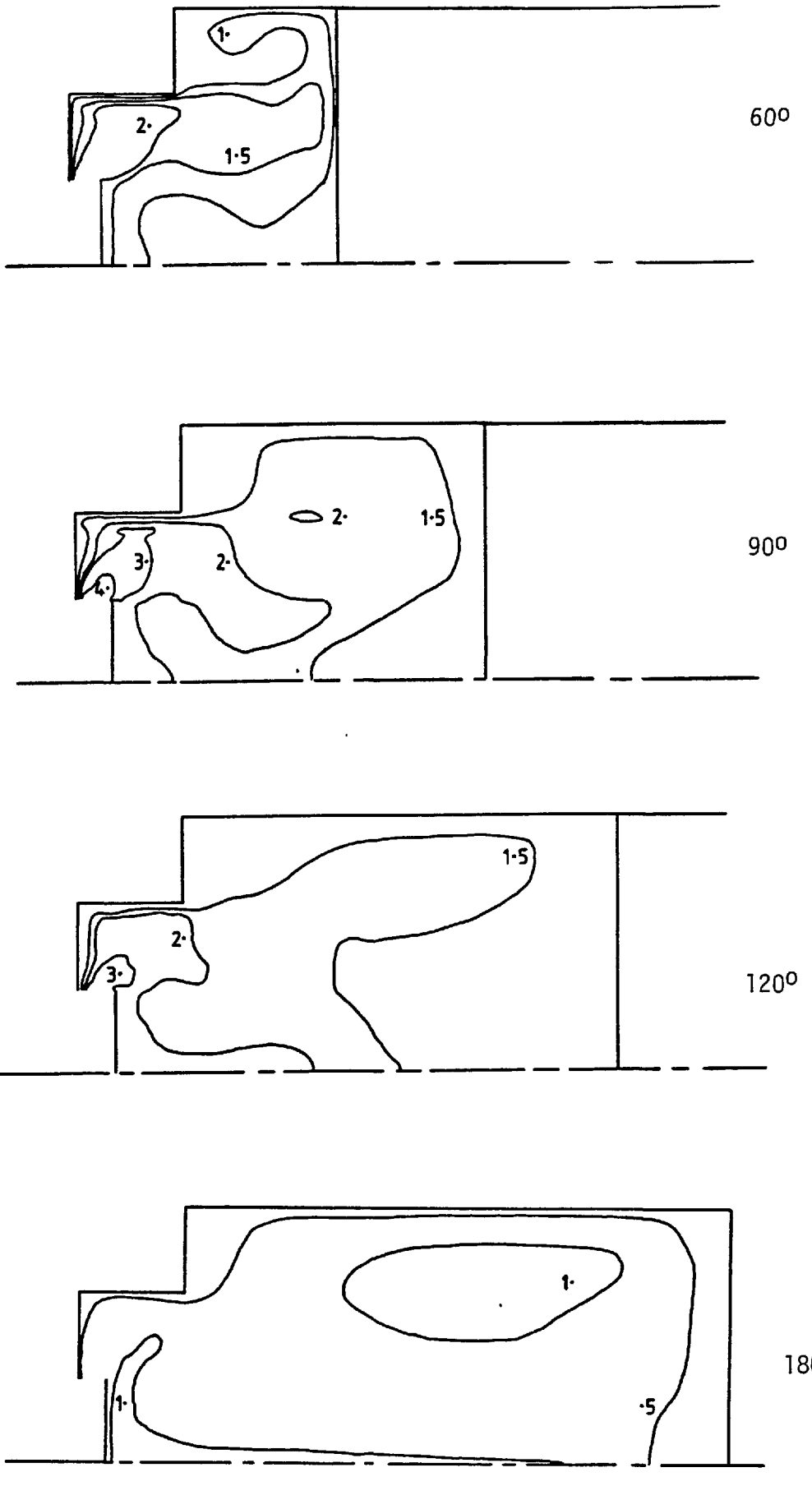

Fig. 5.26 Predicted turbulence intensity fields for case 5

contd....

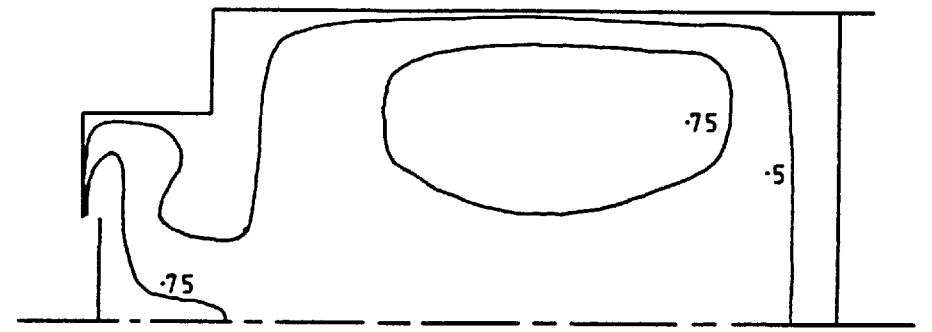

210°

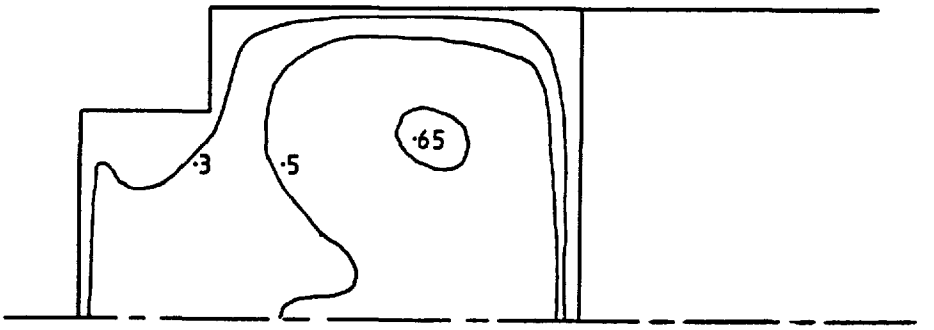

270°

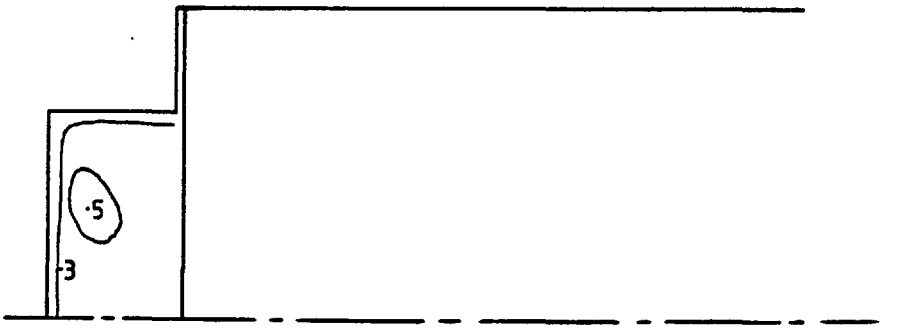

360°

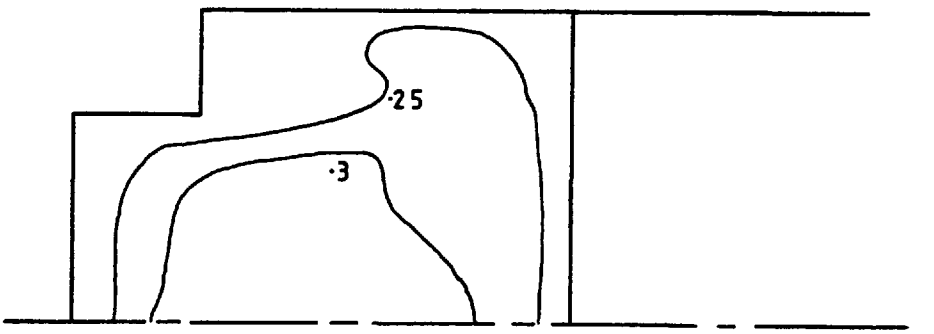

450°

Fig. 5.26 Predicted turbulence intensity fields for case 5

contd....

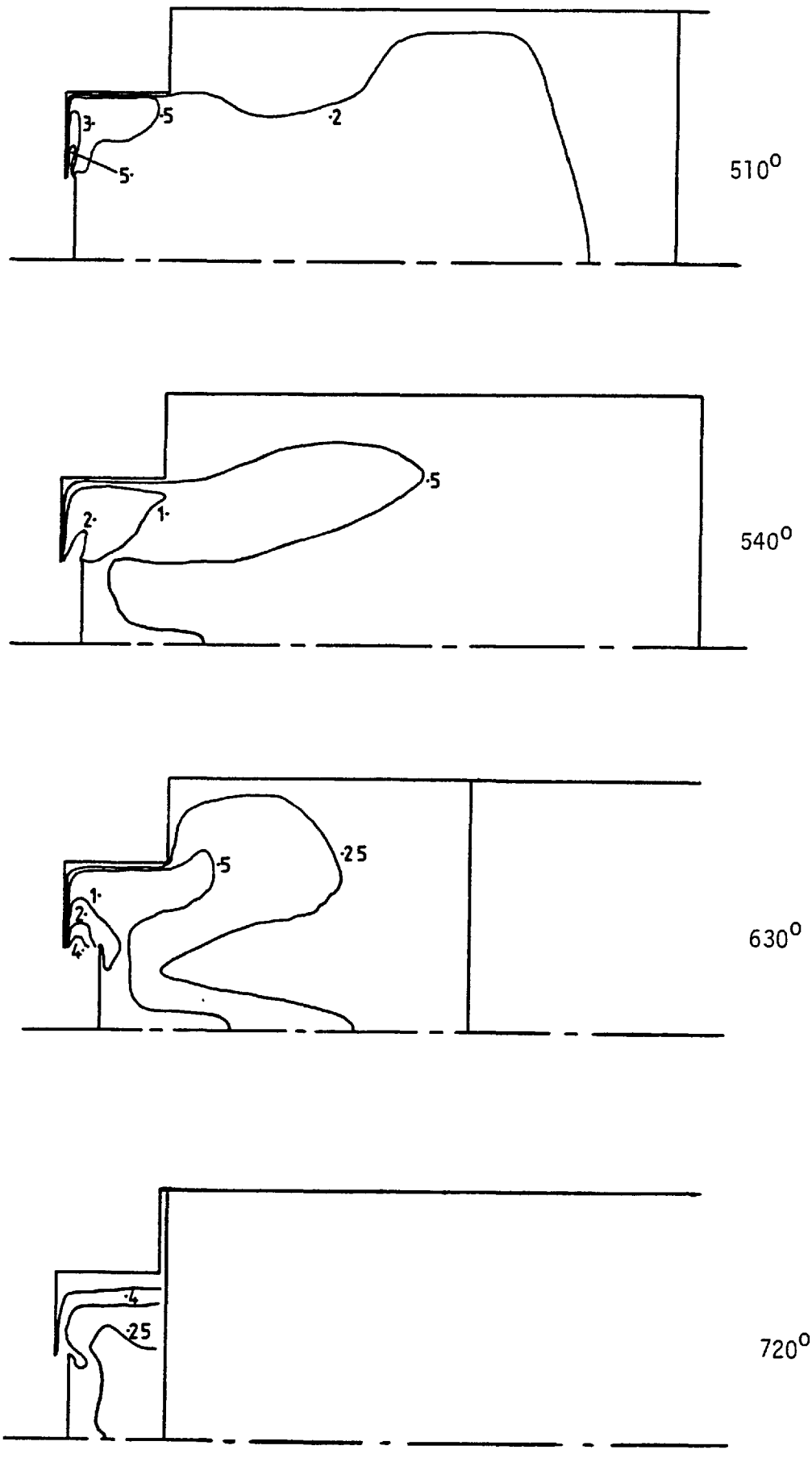

Fig. 5.26 Predicted turbulence intensity fields for case 5

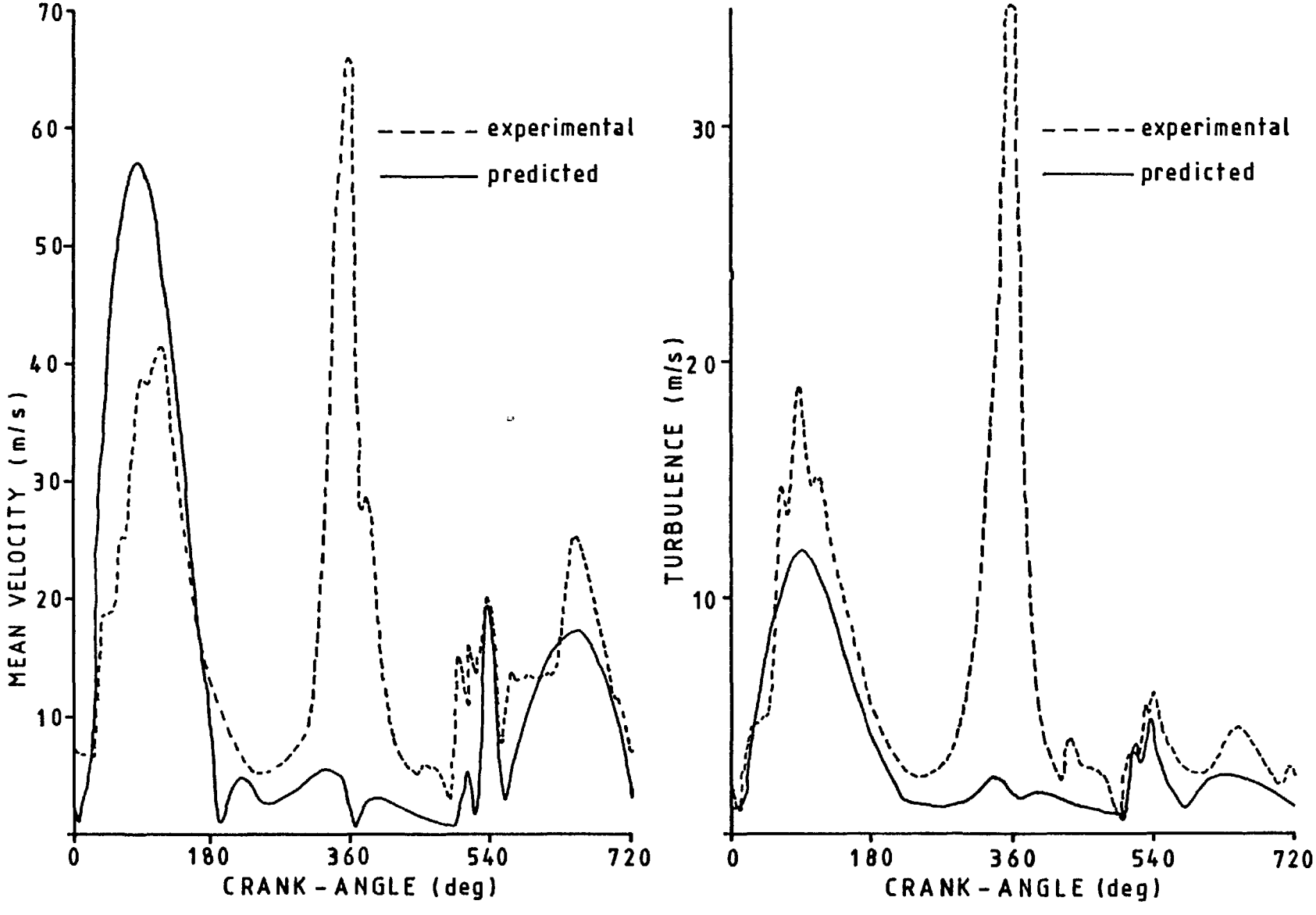

Fig. 5.27 Comparison between measured and calculated mean and turbulent velocities for case 6

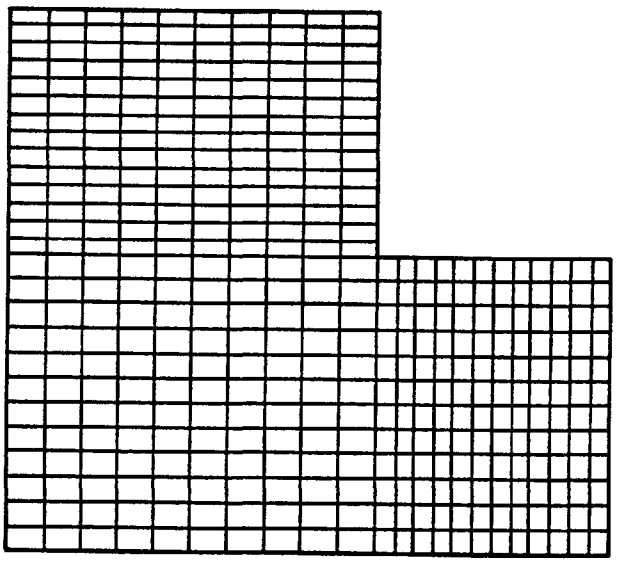

Fig. 5.28 Computational grid used for the simulation of the experiments of Dao et al (1973)

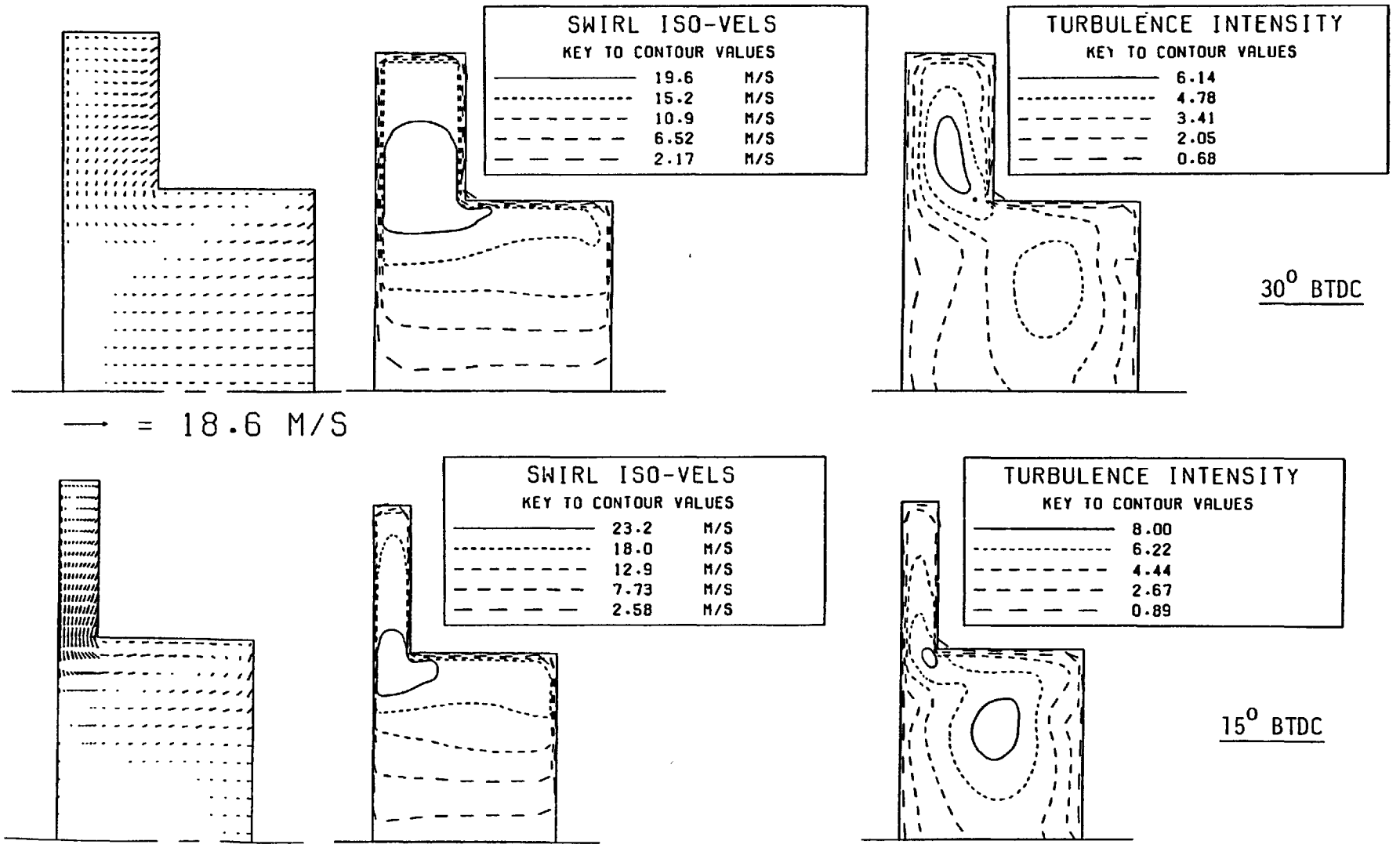

Fig. 5.29 Predicted flow fields for case 6

Contd....

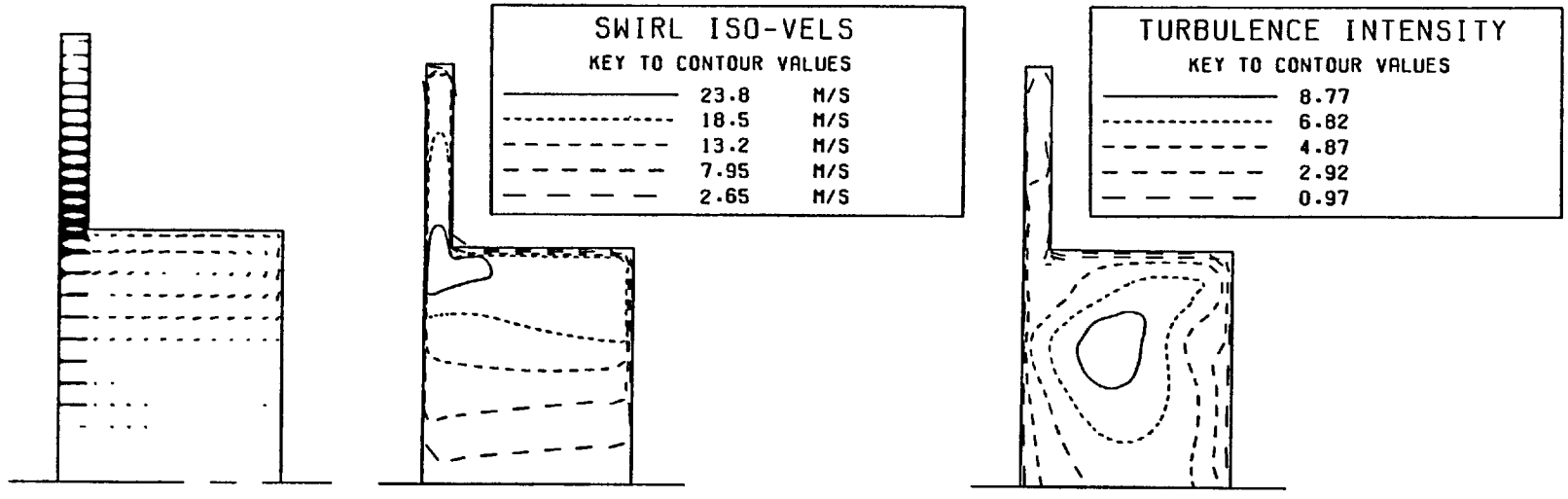

Fig. 5.29 Predicted flow fields for case 6

Contd....

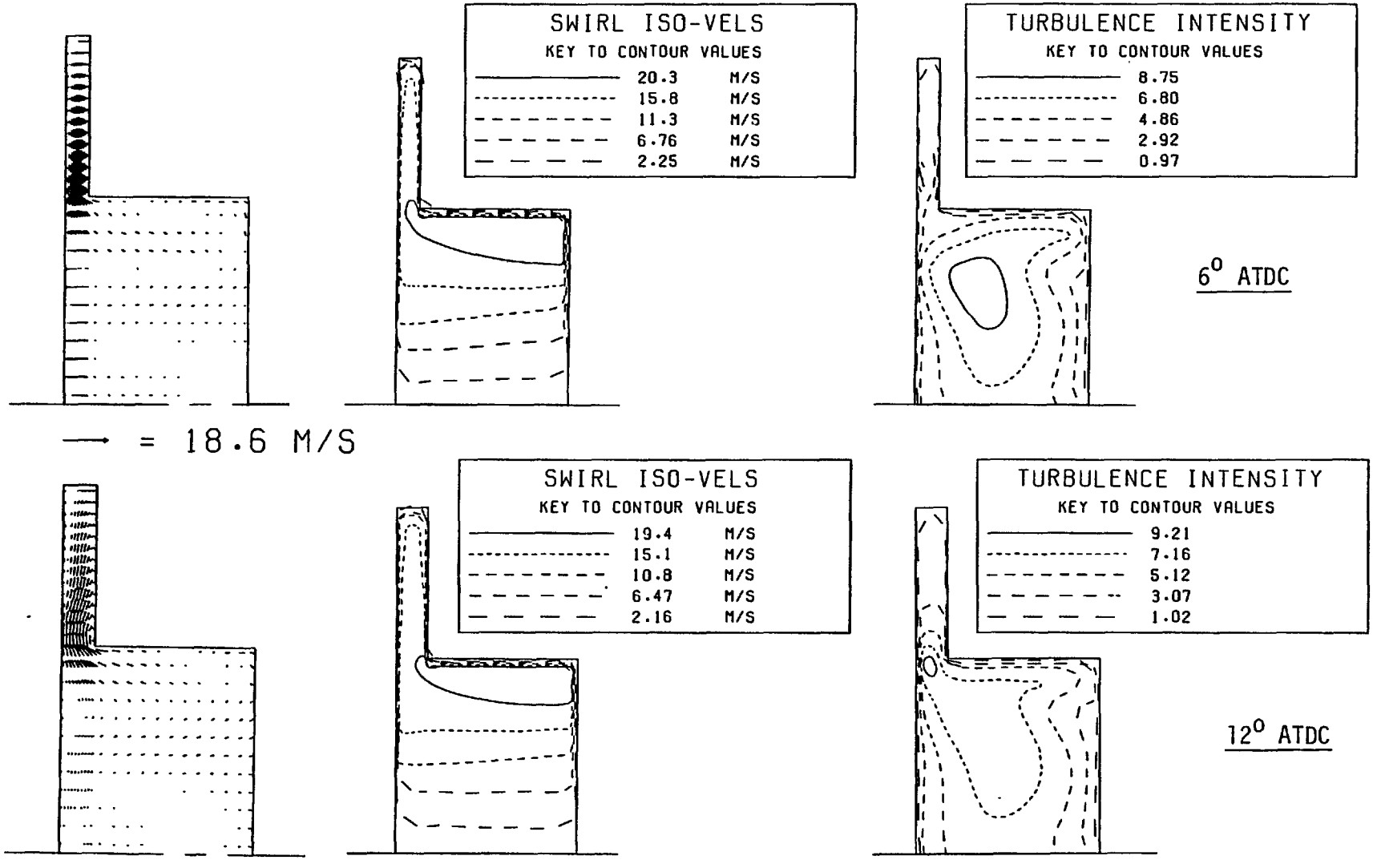

Fig. 5.29 Predicted flow fields for case 6

Contd....

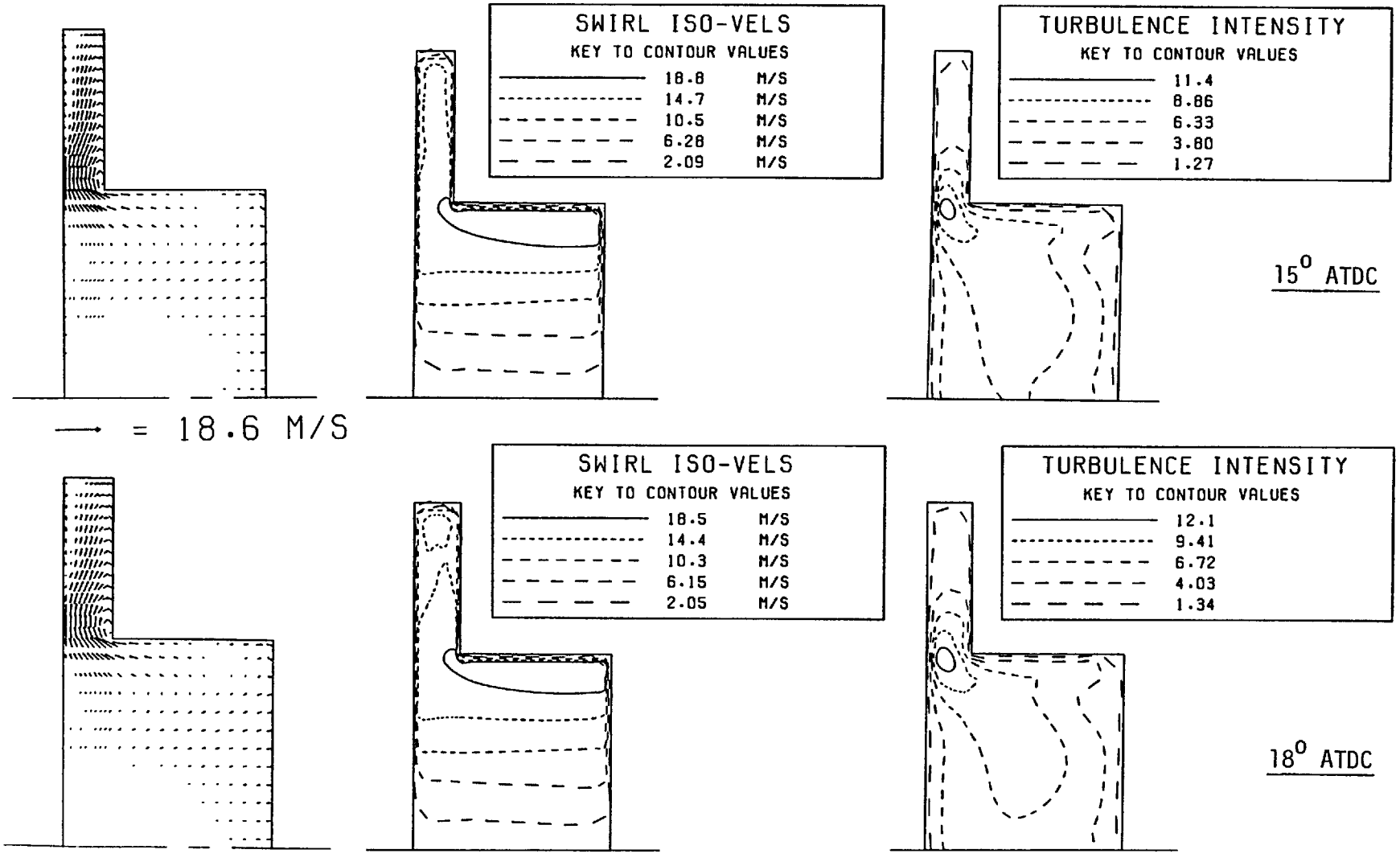

Fig. 5.29 Predicted flow fields for case 6

Contd....

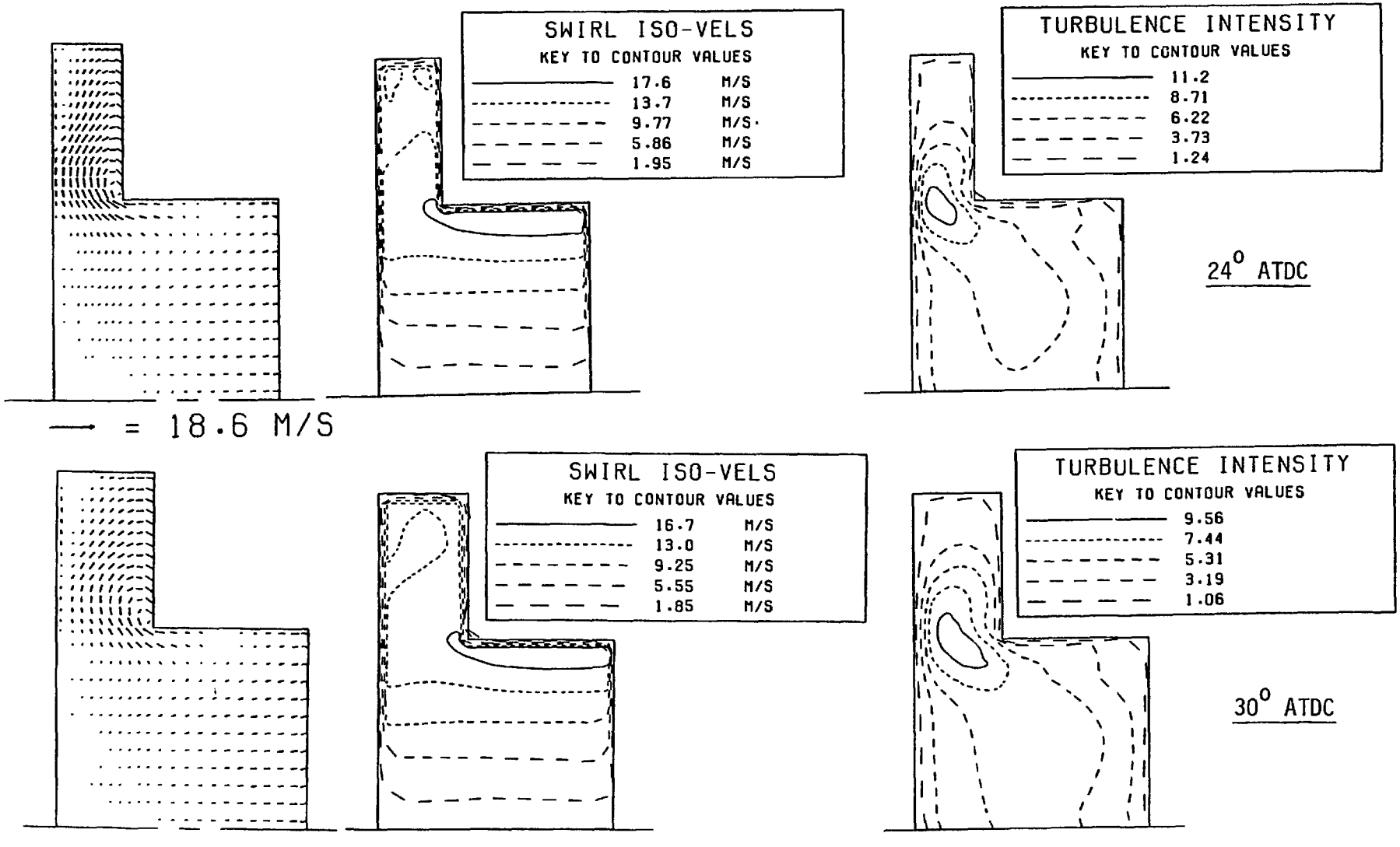

Fig. 5.29 Predicted flow fields for case 6

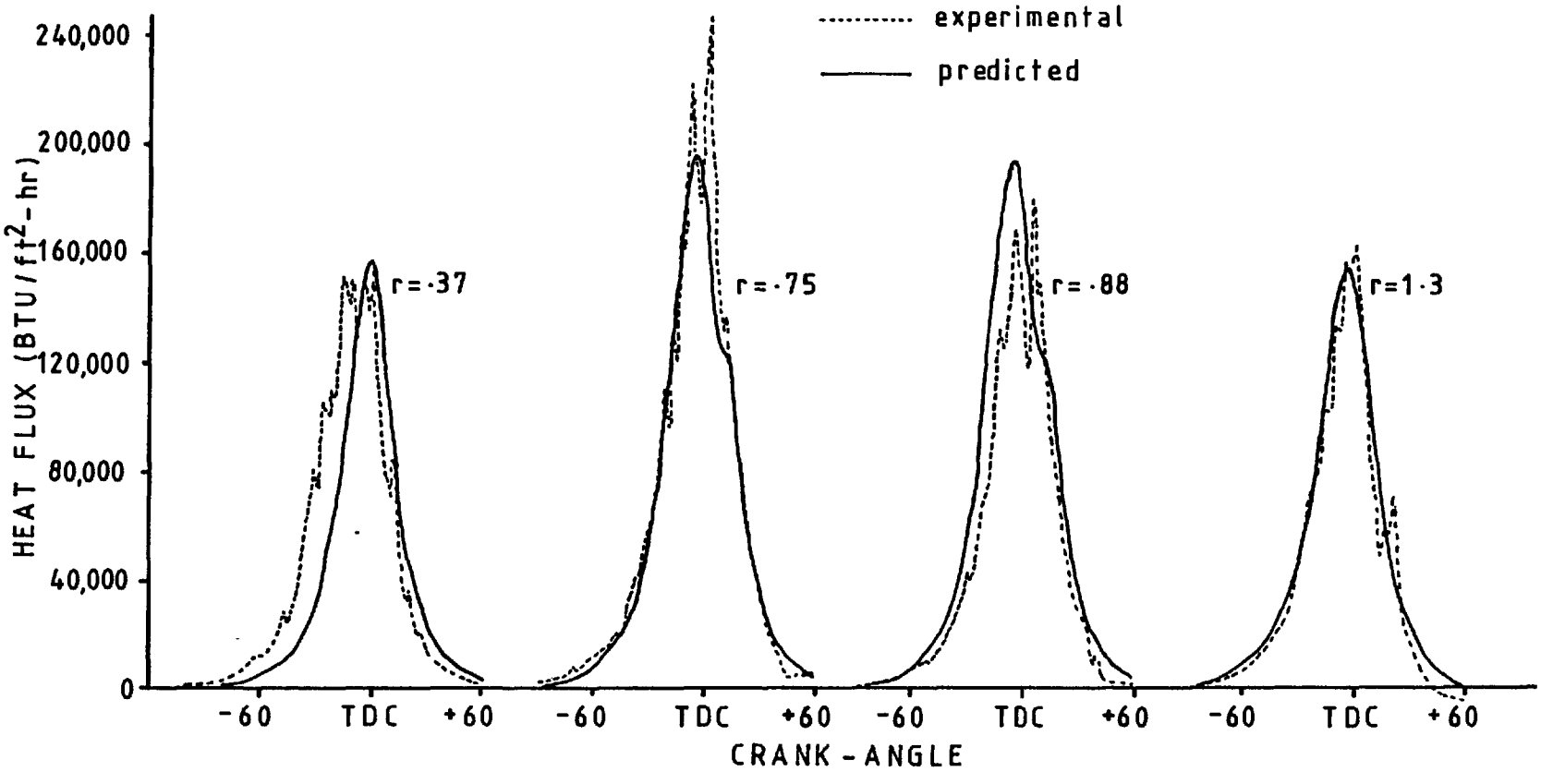

Fig. 5.30 Comparison between measured and predicted instantaneous heat fluxes for case 6

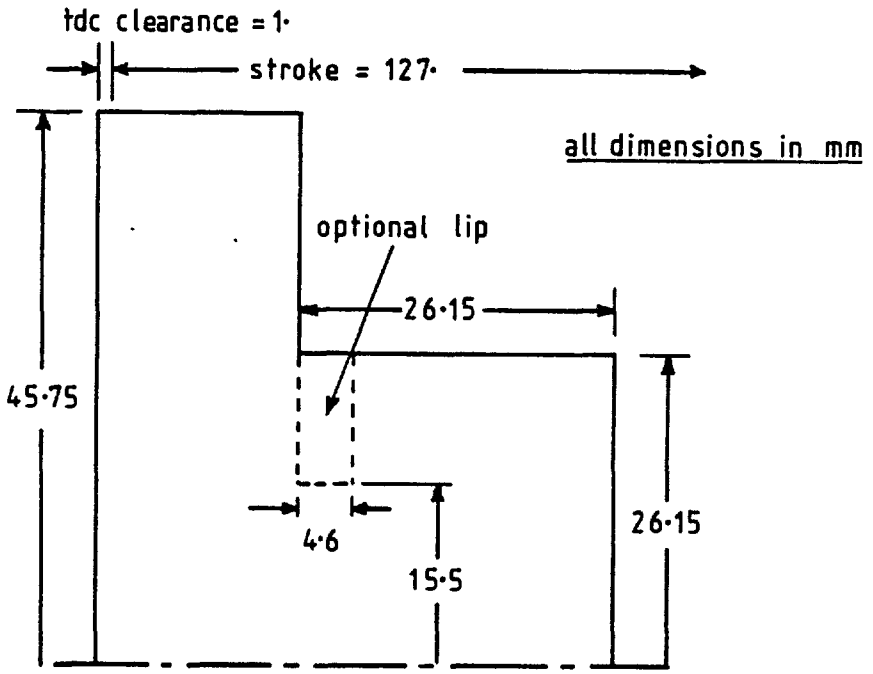

Fig. 6.1 Sketch of the engine geometry used for the swirl studies

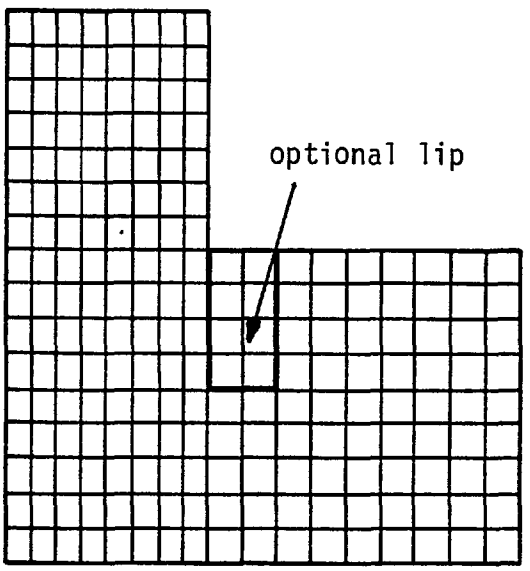

Fig. 6.2 Computational grids used for the geometry of fig. 6.1

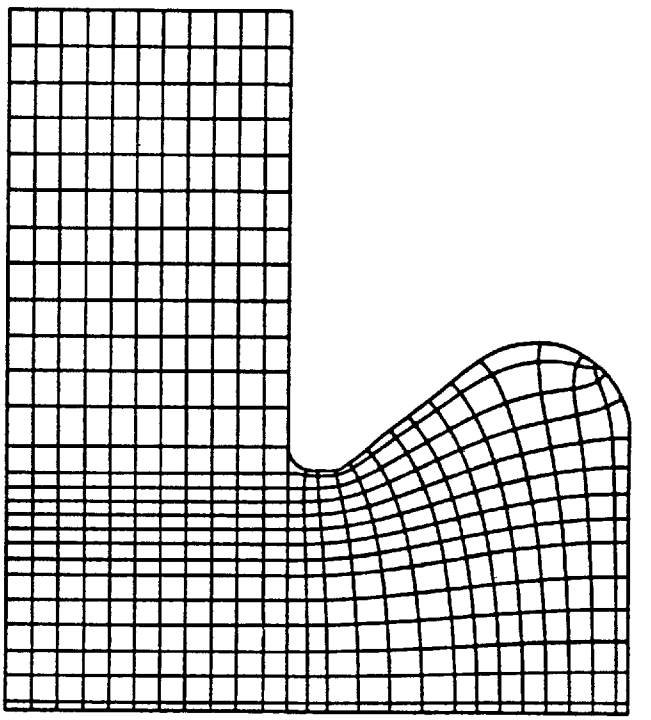

Fig. 6.3 Computational grid used for the 1.11 bowl calculations

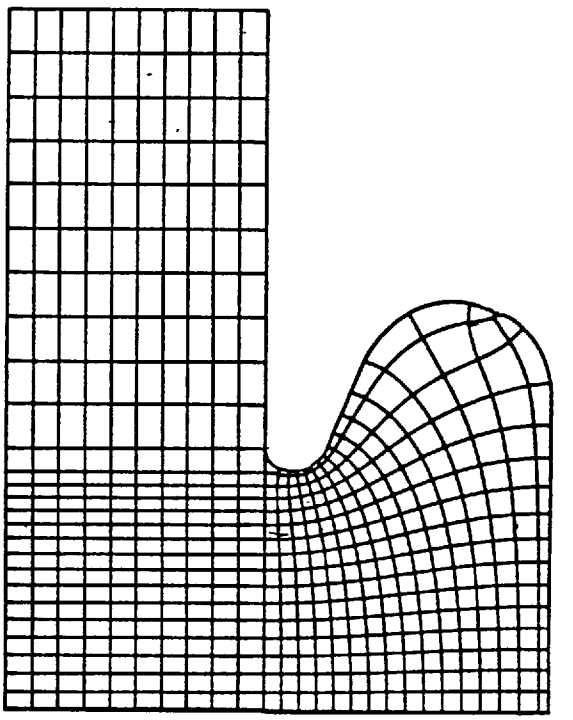

Fig. 6.4 Computational grid used for the 1.2 bowl calculations

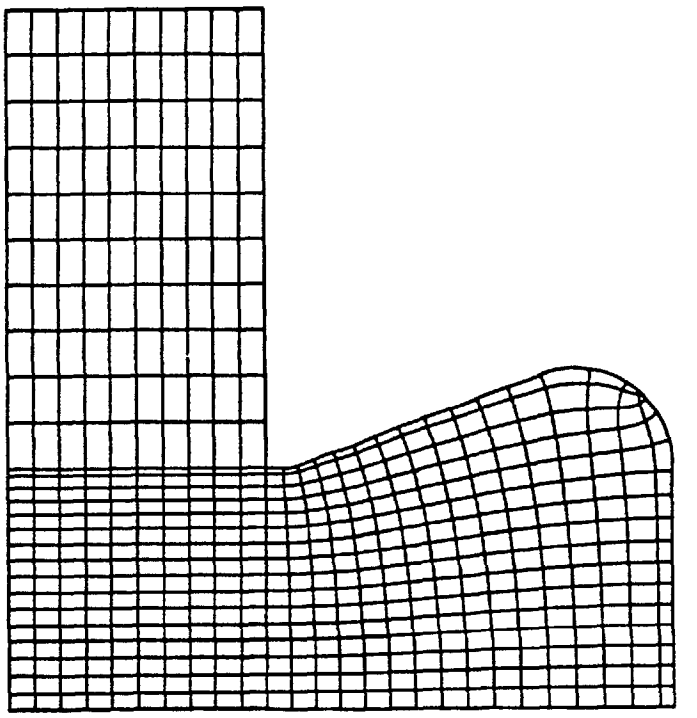

Fig. 6.5 Computational grid used for the 1.12 bowl calculations

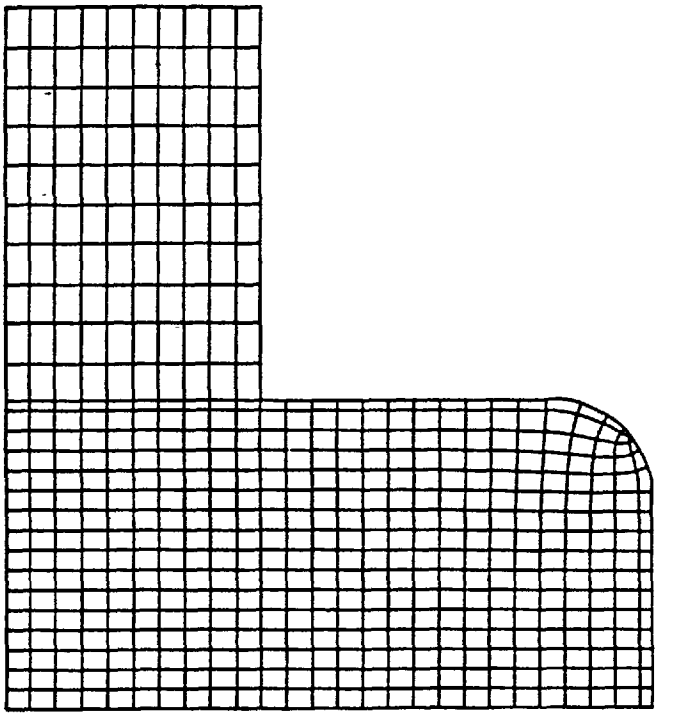

Fig. 6.6 Computational grid used for the 1.3 bowl calculations

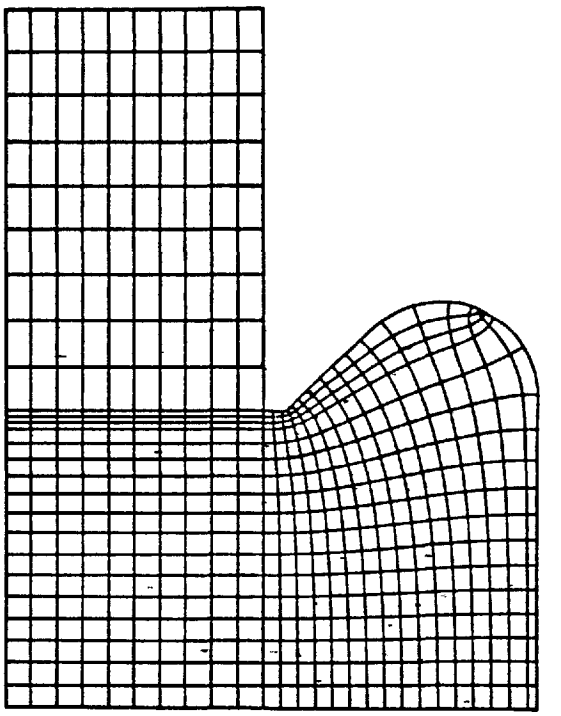

Fig. 6.7 Computational grid used for the 1.15 bowl calculations

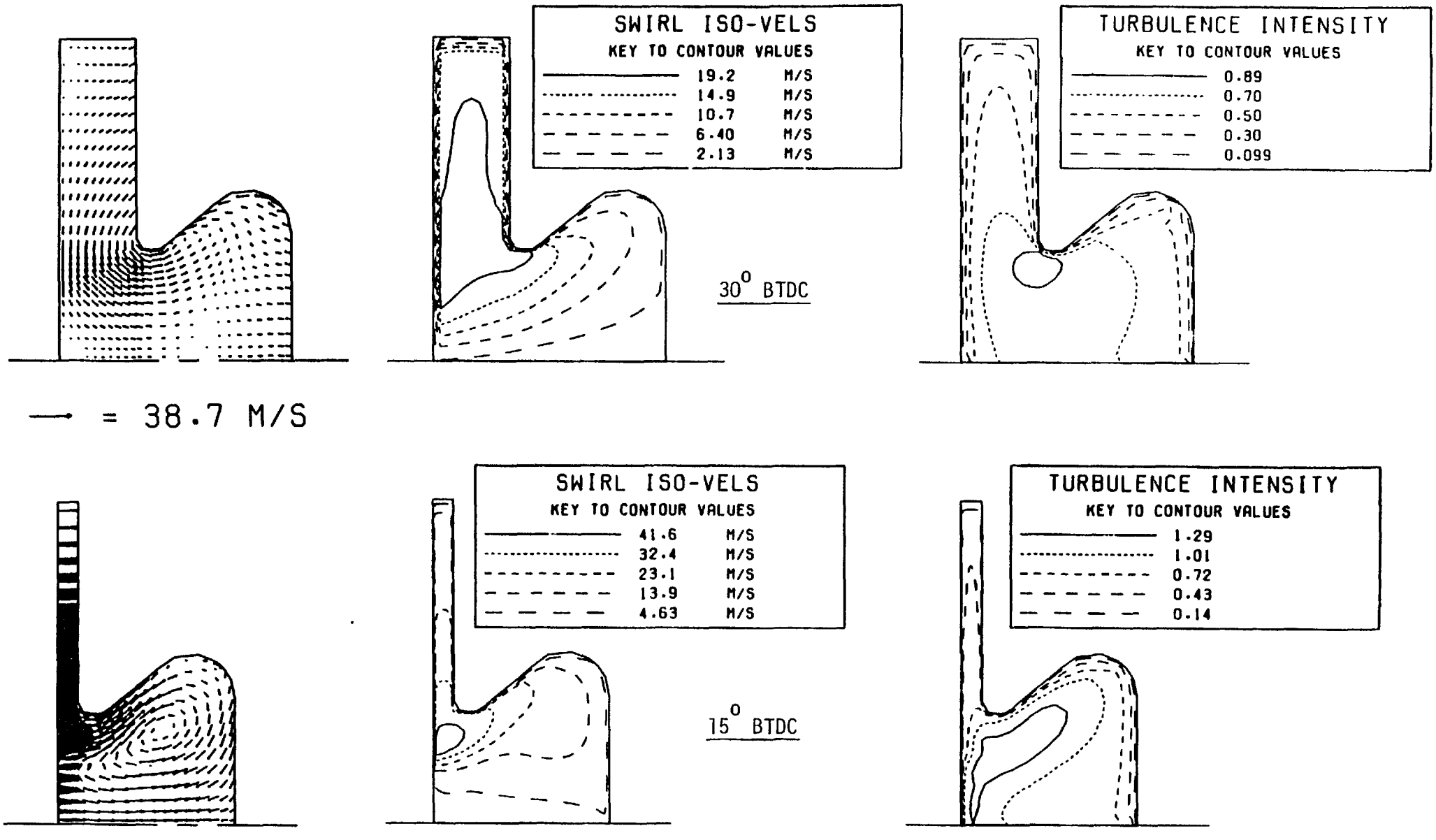

Fig. 6.8(a) Predicted flow fields for the 1.11 bowl configuration

contd....

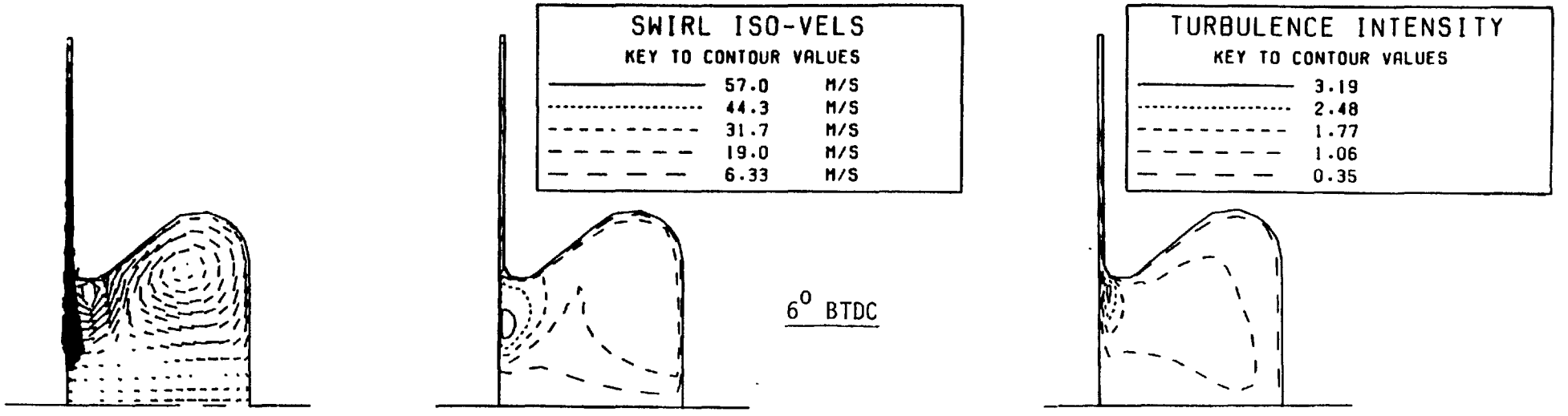

Fig. 6.8(b) Predicted flow fields for the 1.11 bowl configuration

contd....

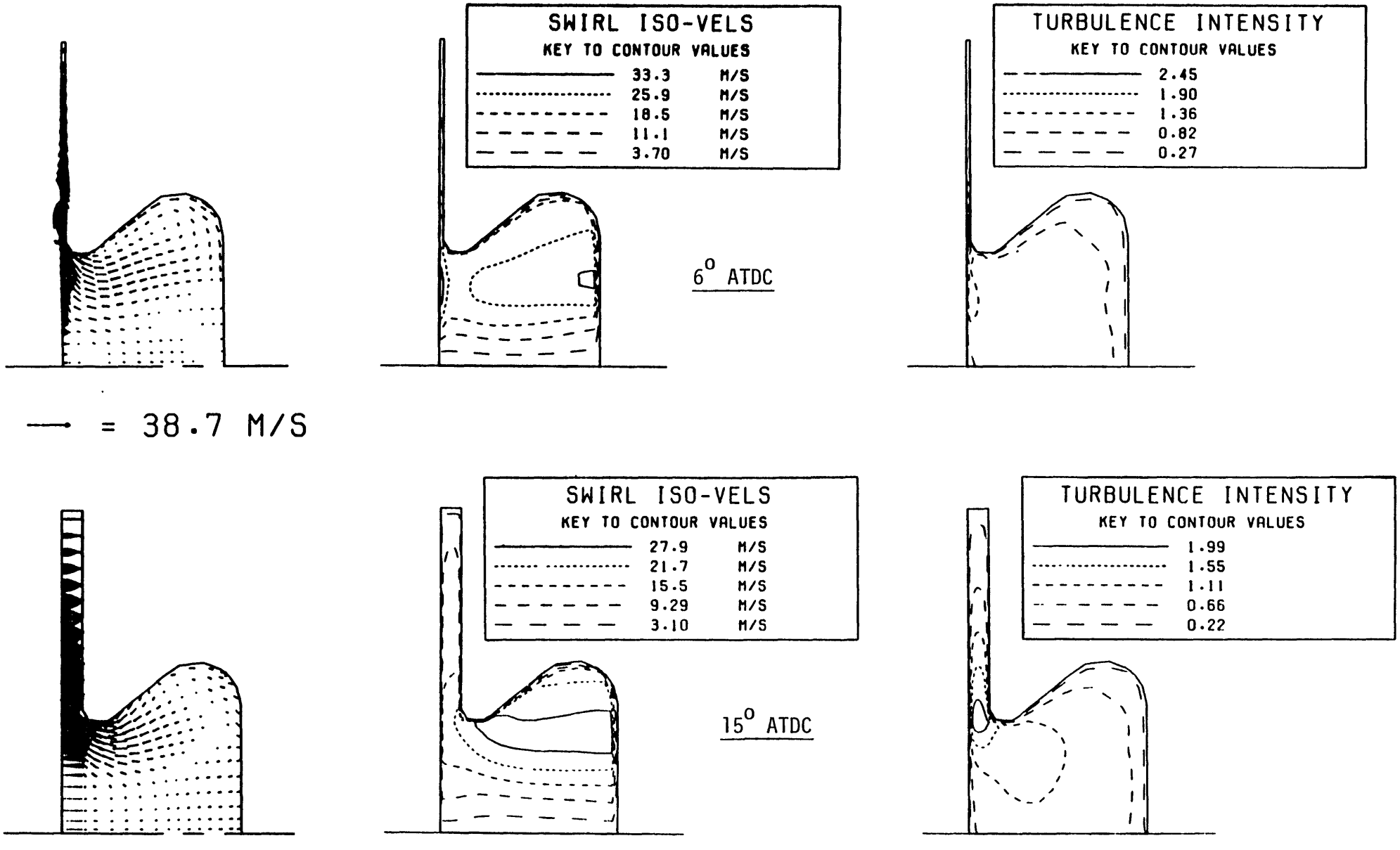

Fig. 6.8(c) Predicted flow fields for the 1.11 bowl configuration

contd....

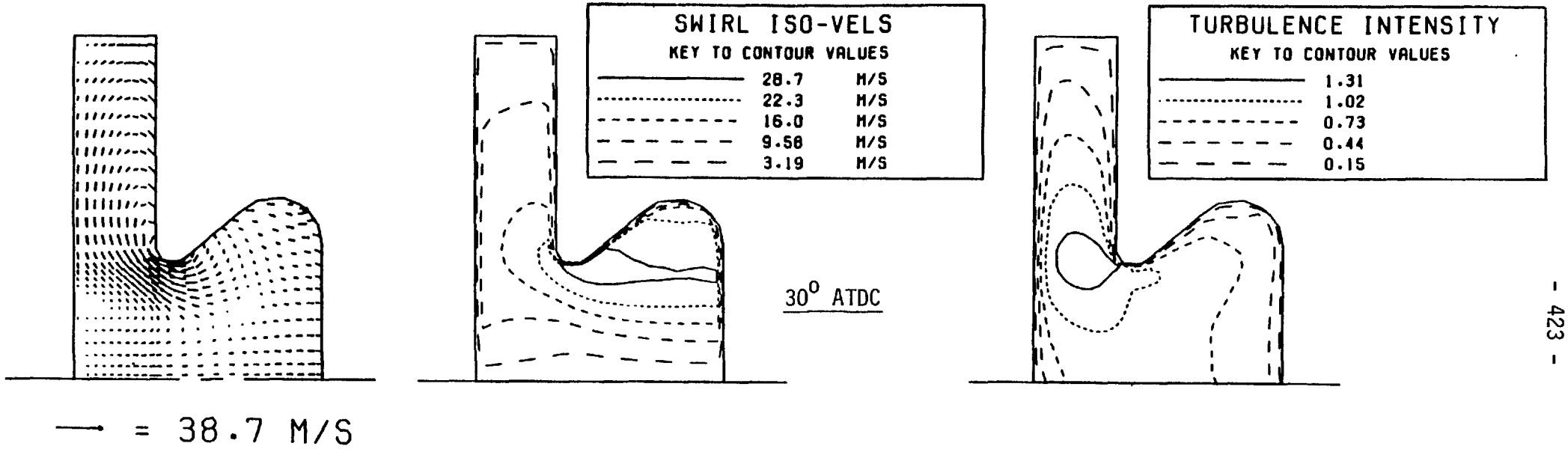

Fig. 6.8(d) Predicted flow fields for the 1.11 bowl configuration

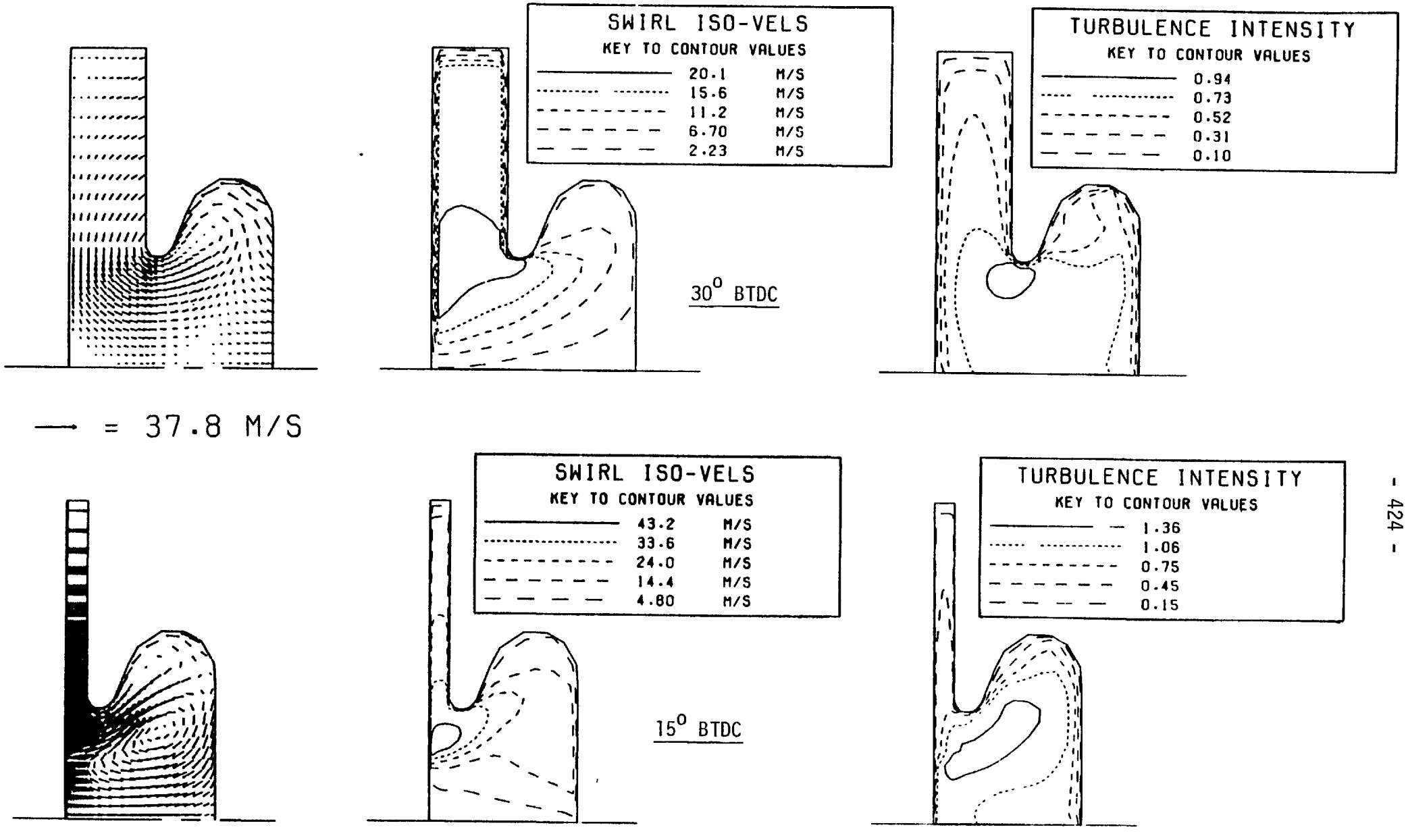

Fig. 6.9(a) Predicted flow fields for the 1.2 bowl configuration

contd....

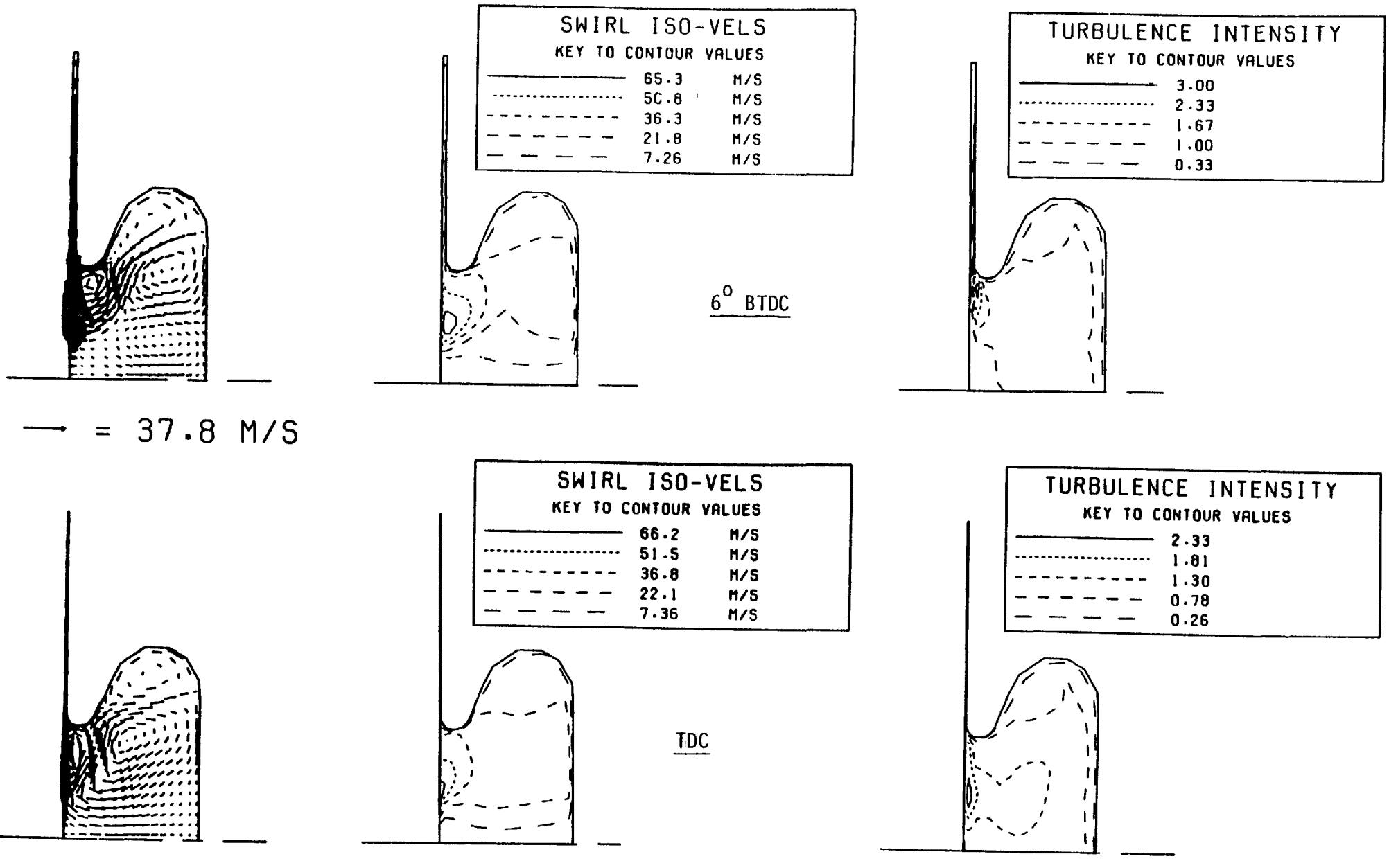

Fig. 6.9(b) Predicted flow fields for the 1.2 bowl configuration

contd....

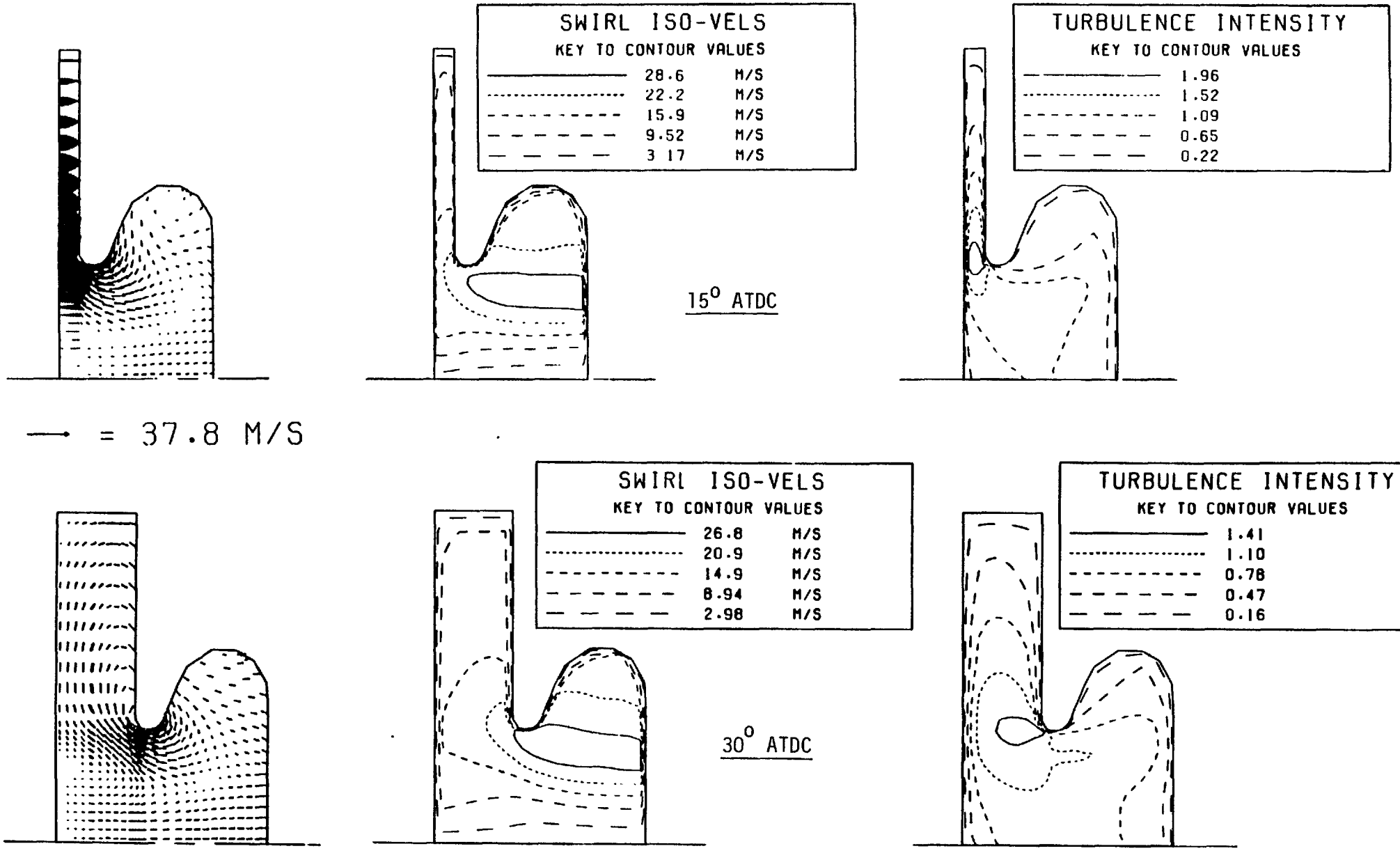

Fig. 6.9(c) Predicted flow fields for the 1.2 bowl configuration

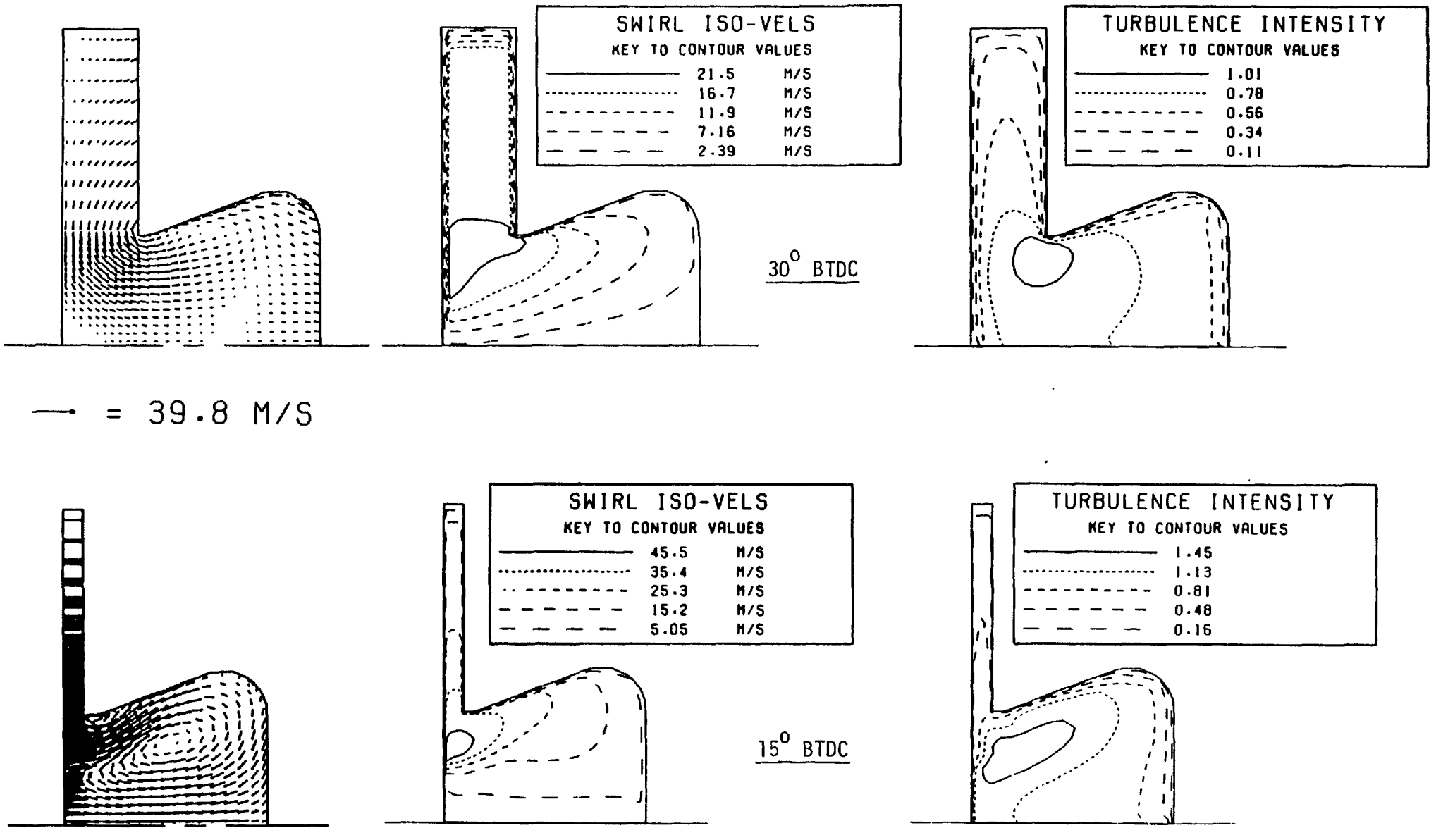

Fig. 6.10(a) Predicted flow fields for the 1.12 bowl configuration

contd....

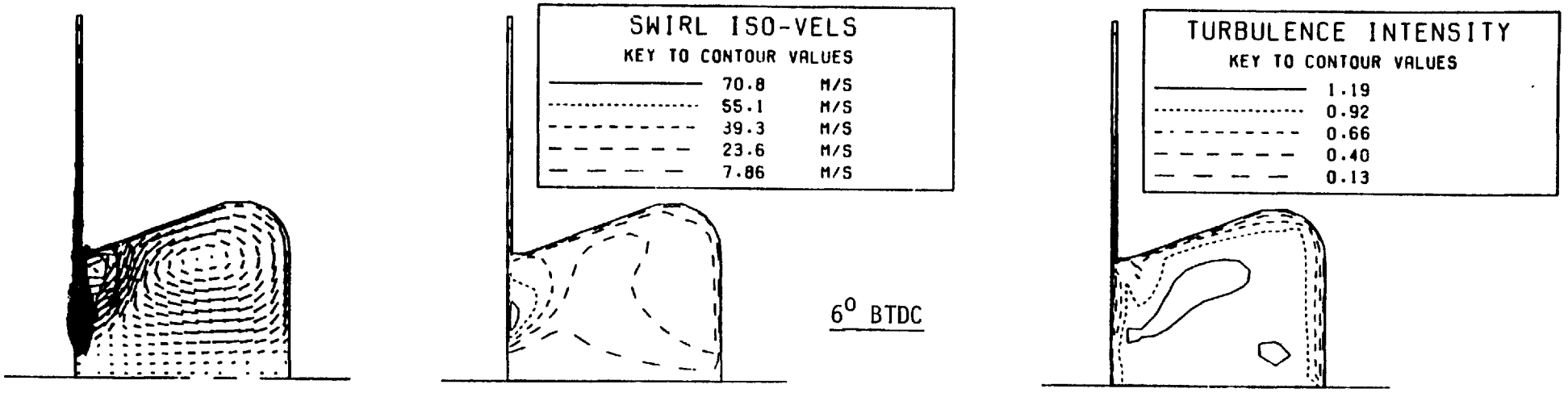

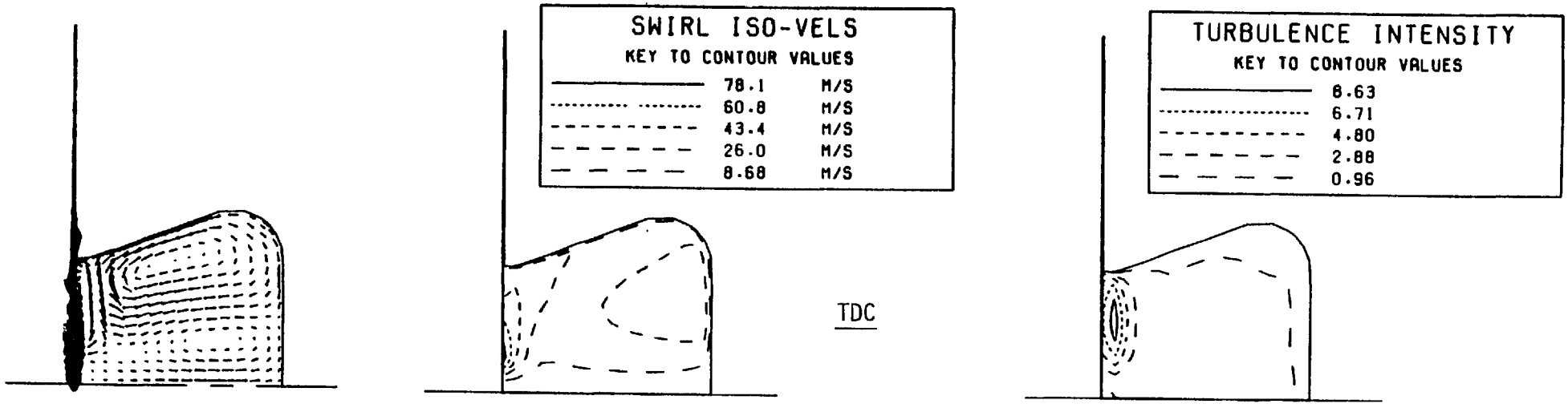

Fig. 6.10(b) Predicted flow fields for the 1.12 bowl configuration

contd....

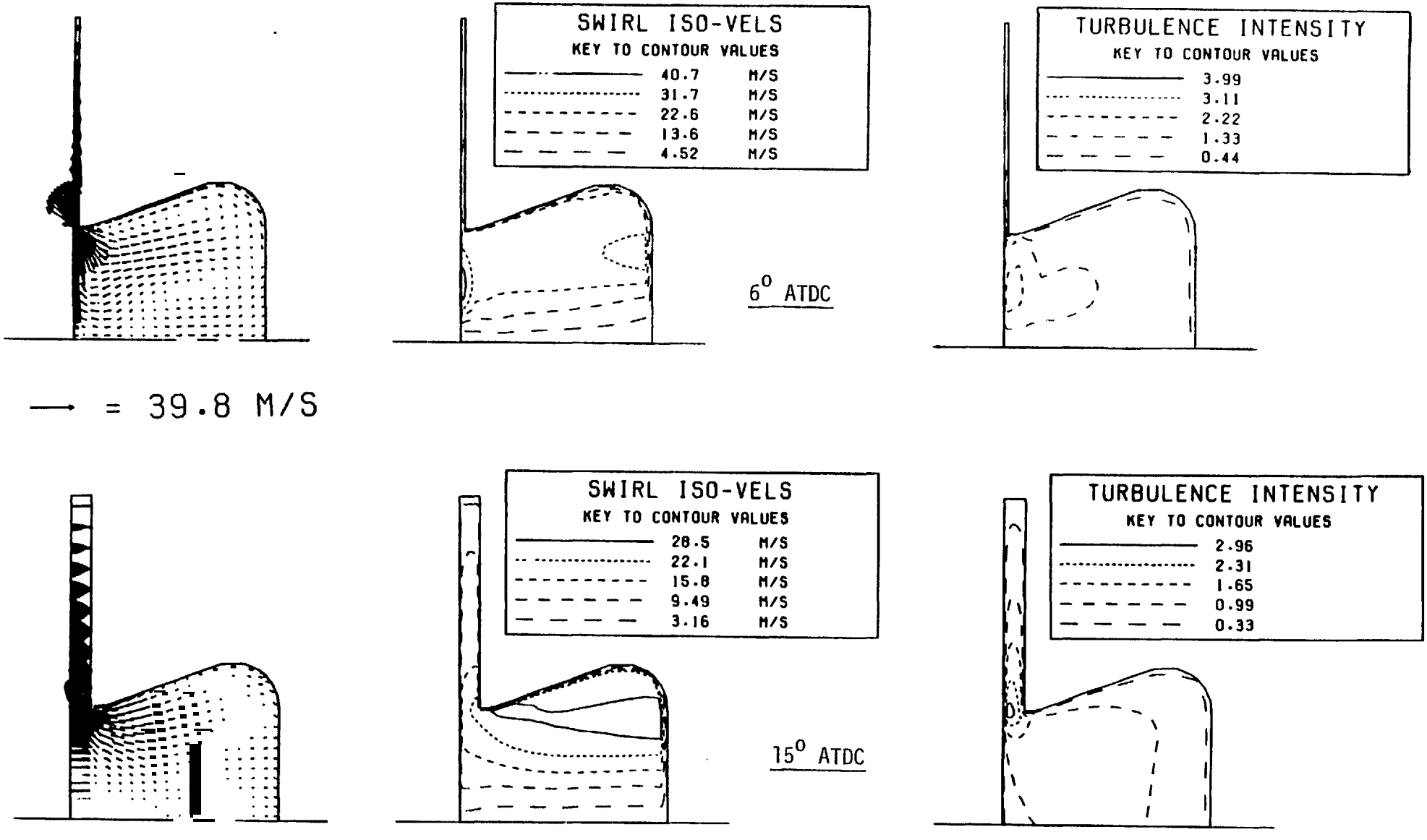

Fig. 6.10(c) Predicted flow fields for the 1.12 bowl configuration

contd....

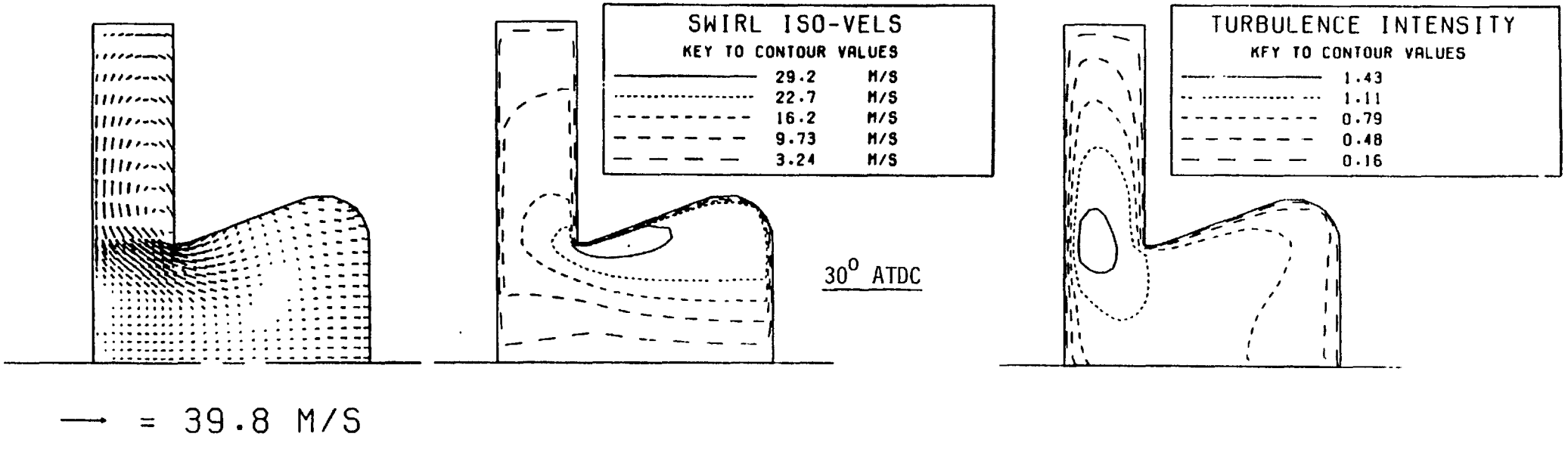

Fig. 6.10(d) Predicted flow fields for the 1.12 bowl configuration

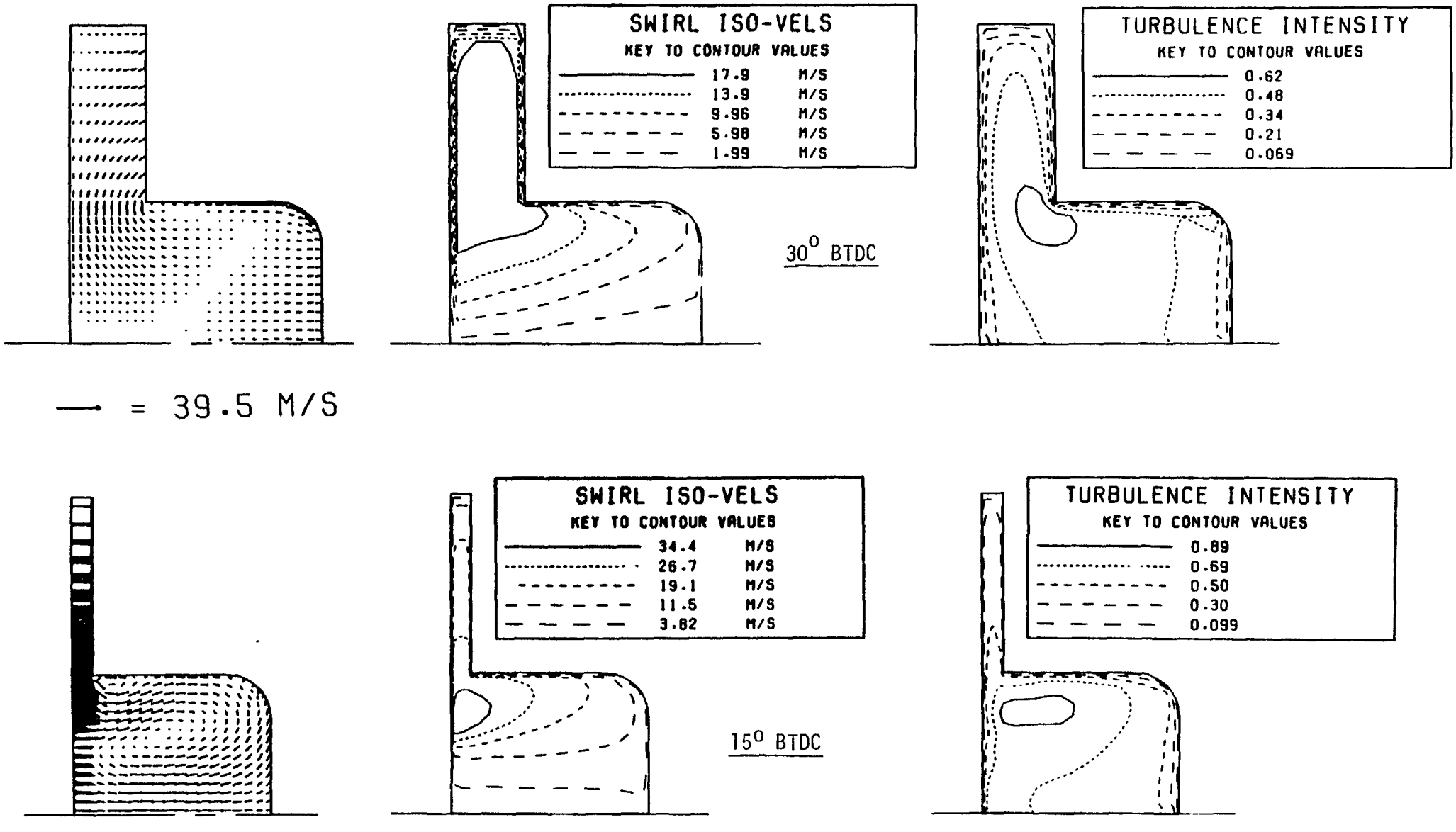

Fig. 6.11(a) Predicted flow fields for the 1.3 bowl configuration

contd....

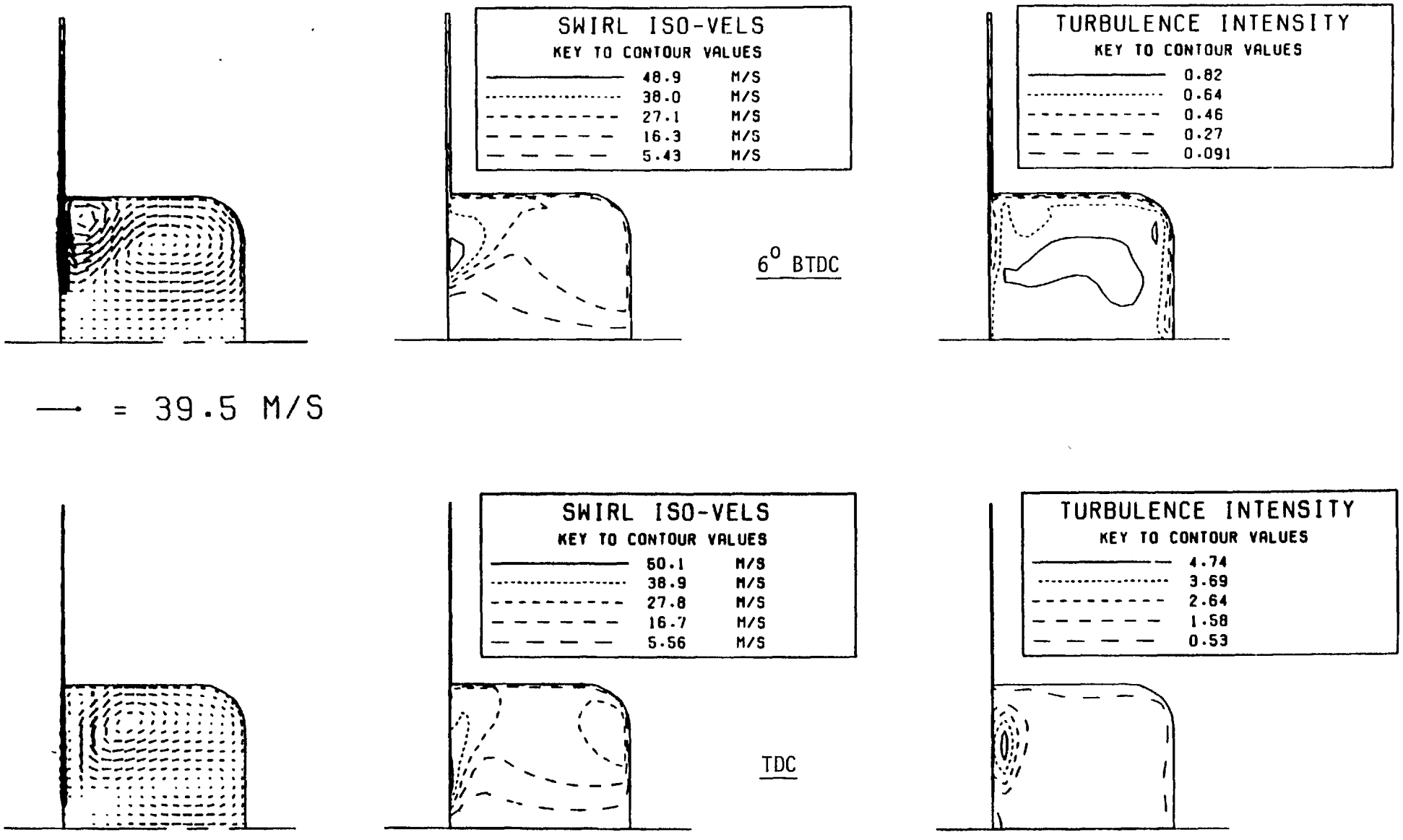

Fig. 6.11(b) Predicted flow fields for the 1.3 bowl configuration

contd....

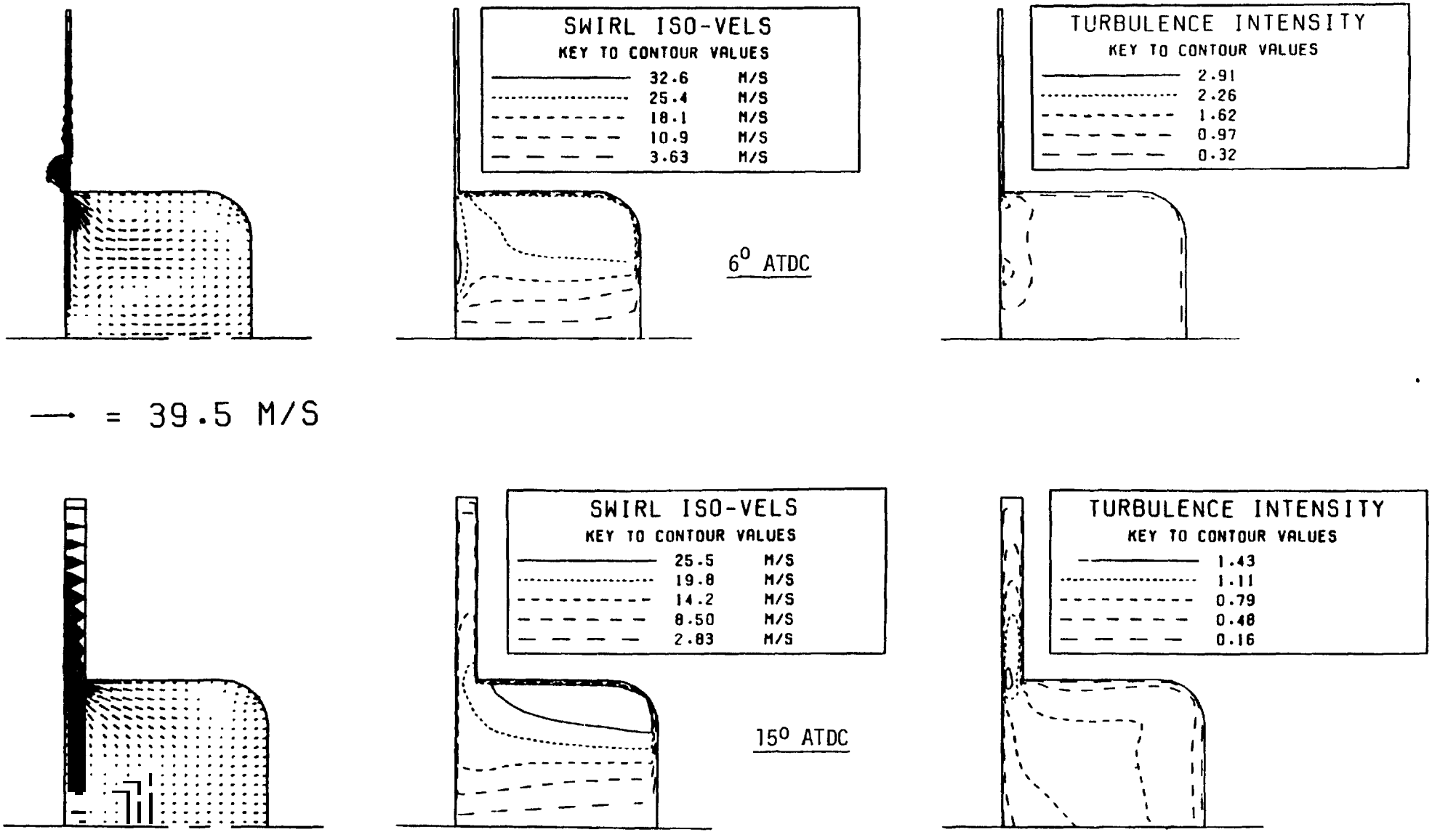

Fig. 6.11(c) Predicted flow fields for the 1.3 bowl configuration

contd....

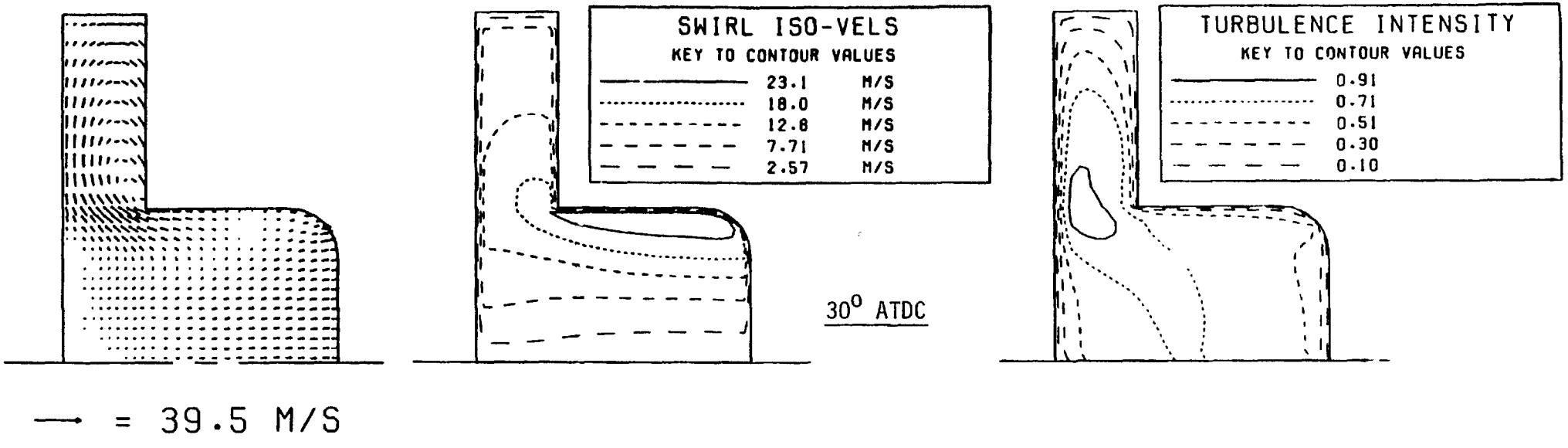

Fig. 6.11(d) Predicted flow fields for the 1.3 bowl configuration

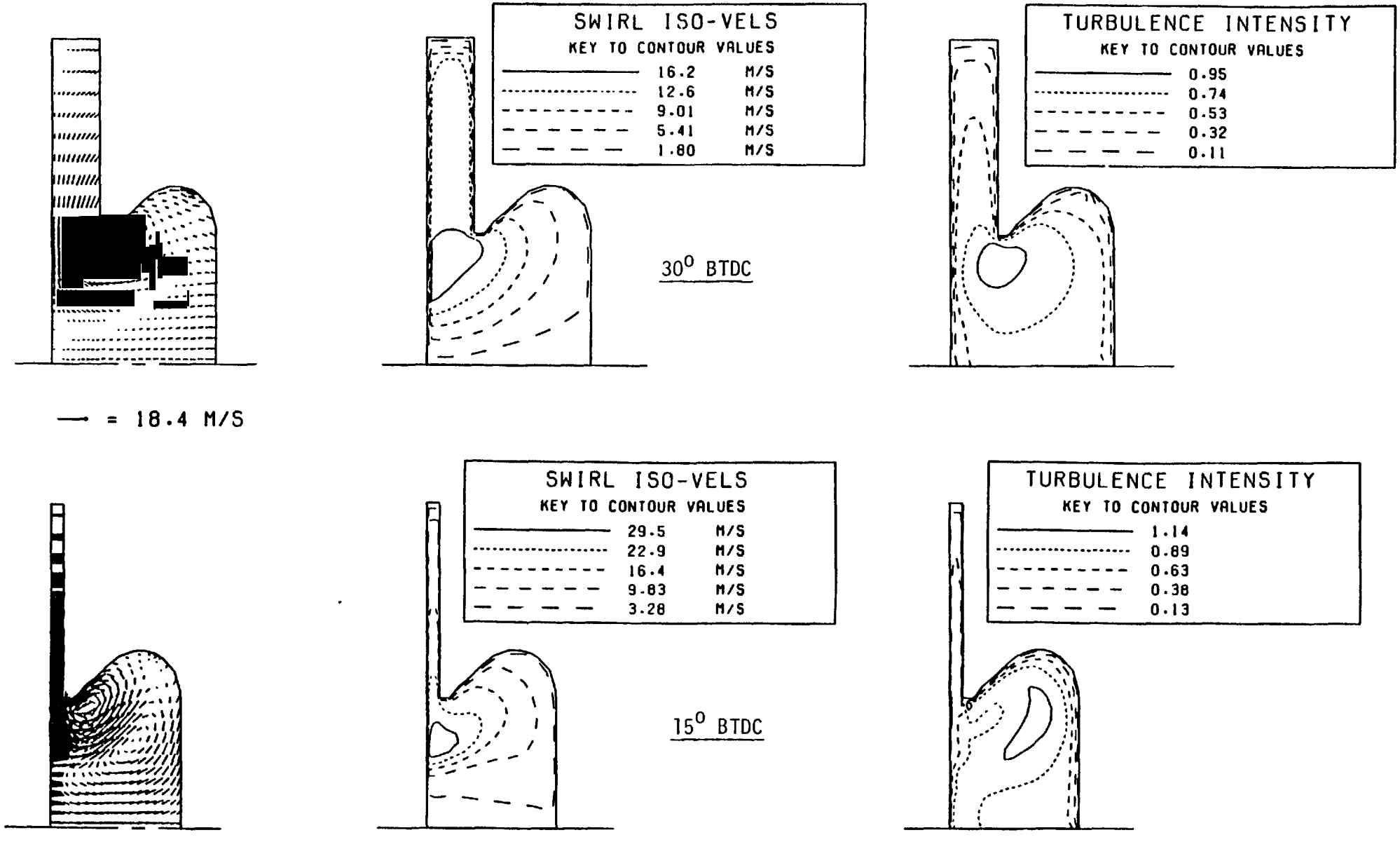

Fig. 6.12(a) Predicted flow fields for the 1.15 bowl configuration

contd....

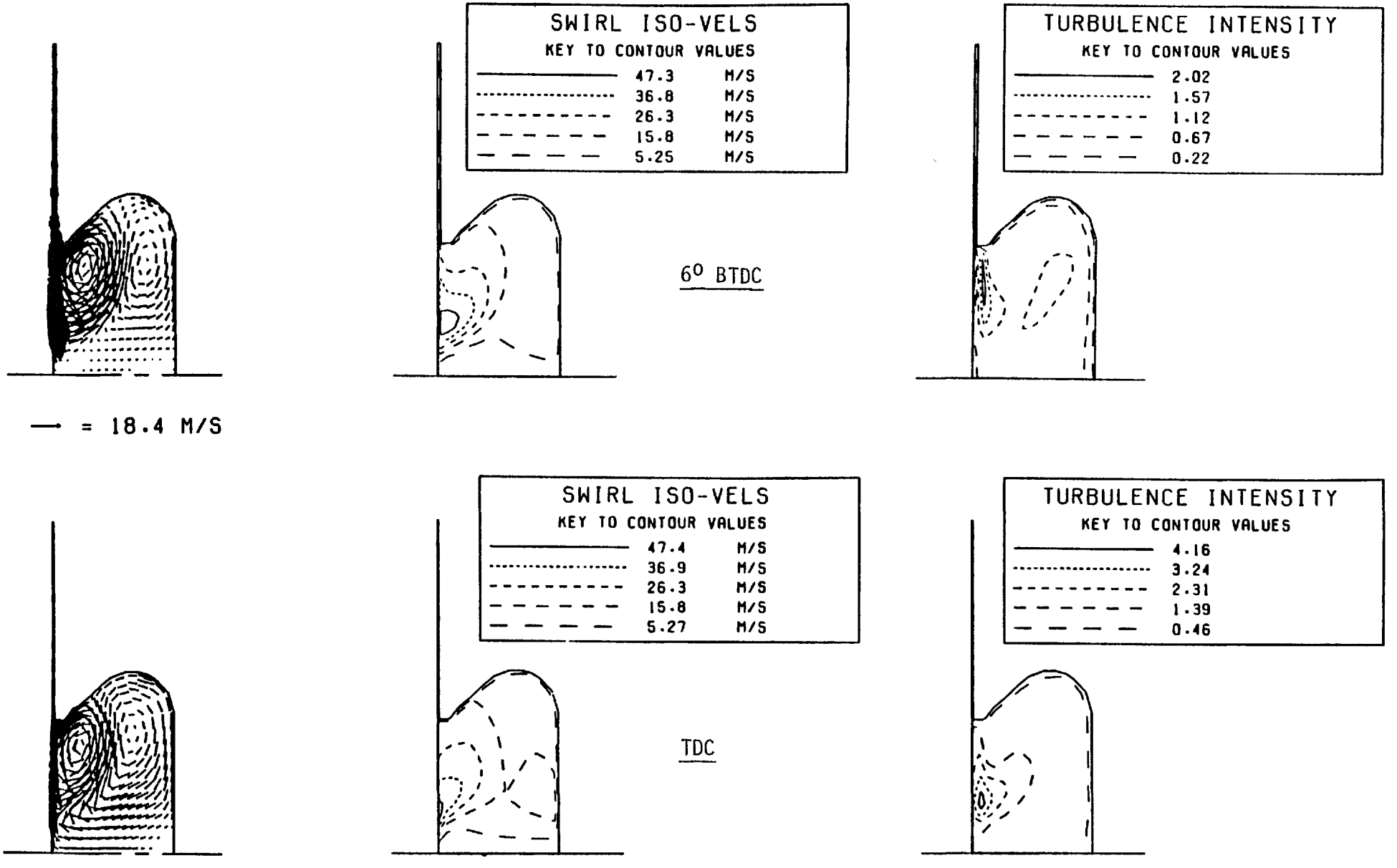

Fig. 6.12(b) Predicted flow fields for the 1.15 bowl configuration

contd....

— = 18.4 M/S

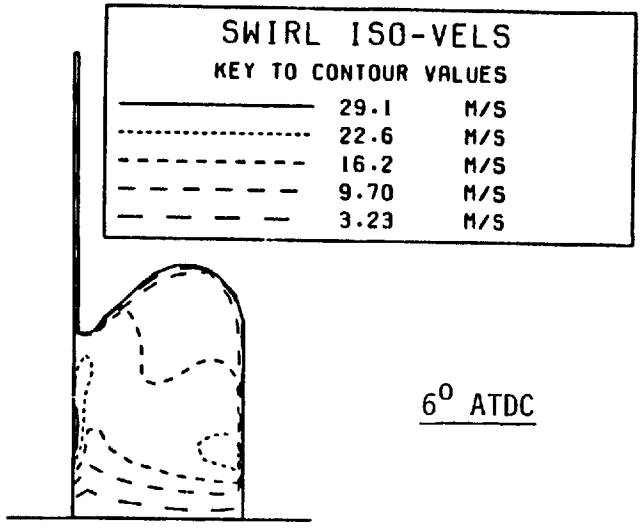

6^{O} ATDC

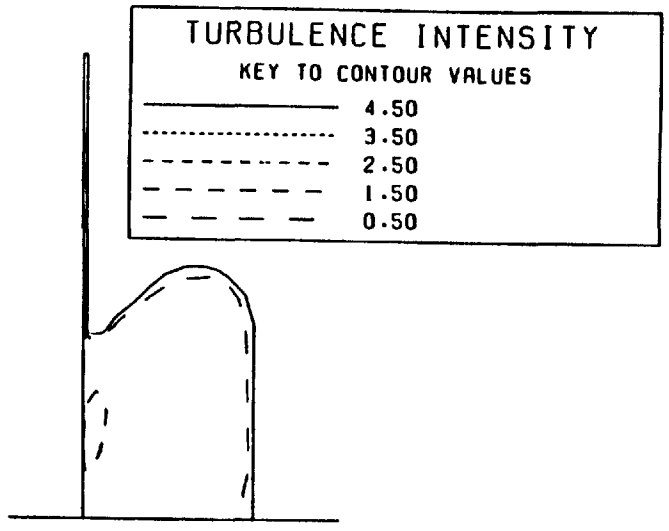

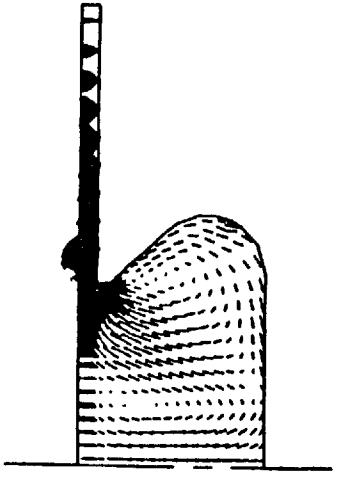

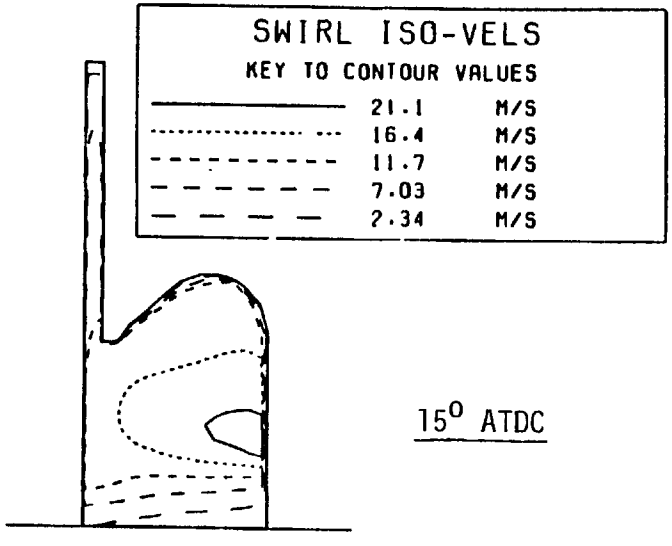

15^{O} ATDC

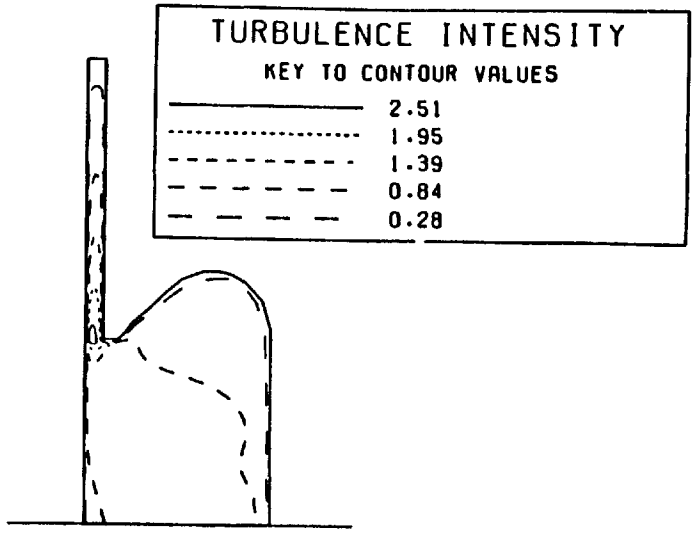

Fig. 6.12(c) Predicted flow fields for the 1.15 bowl configuration

contd....

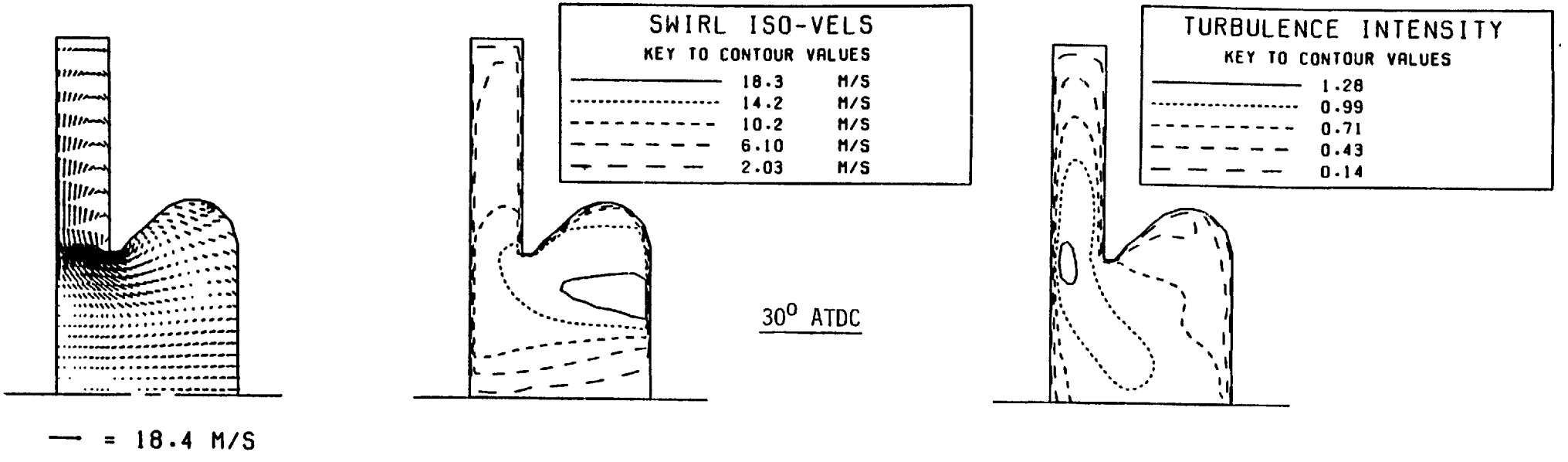

Fig. 6.12(d) Predicted flow fields for the 1.15 bowl configuration

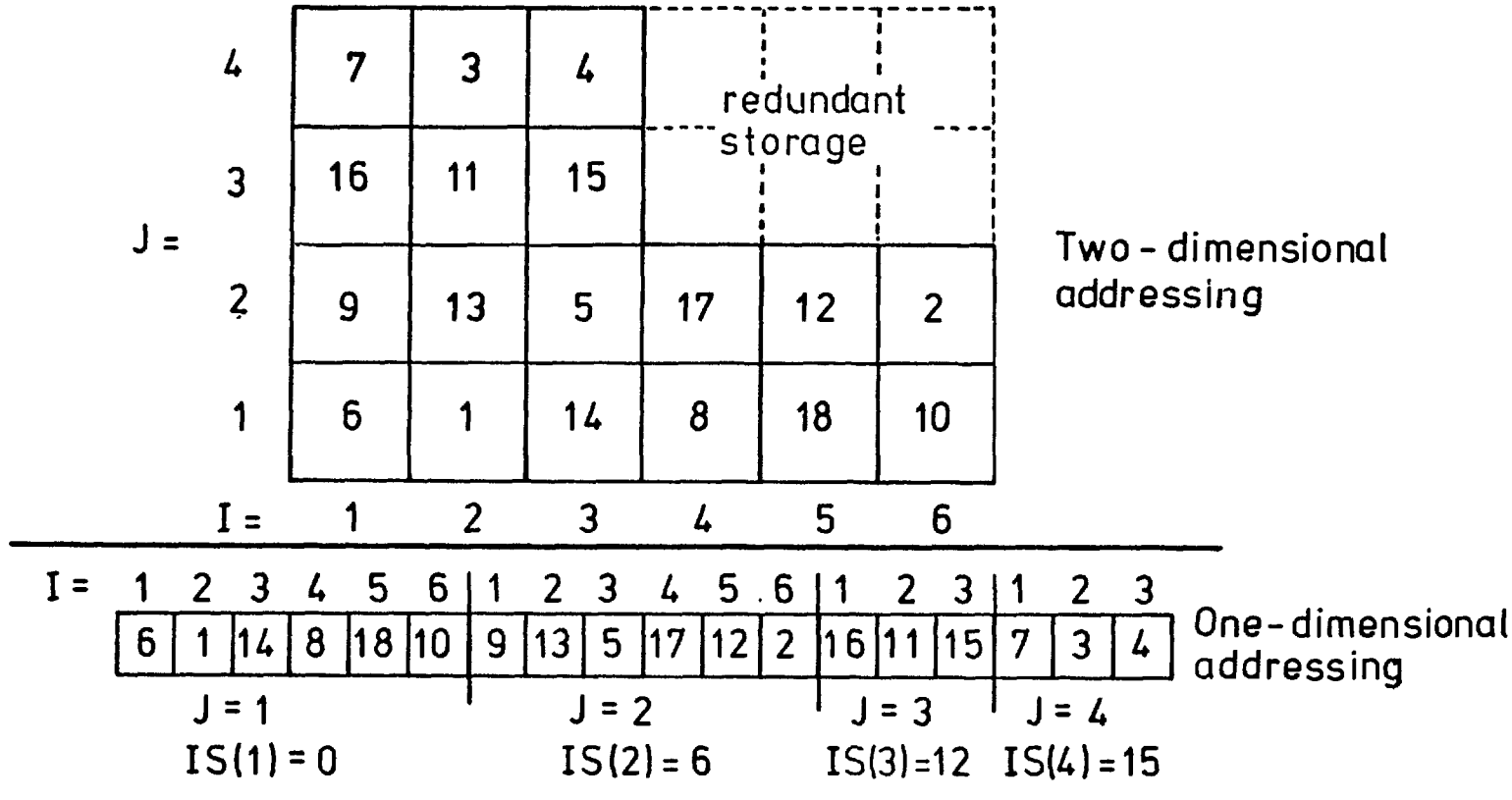

Fig. 7.1 Two-dimensional direct-addressing and one-dimensional indirect-addressing methods

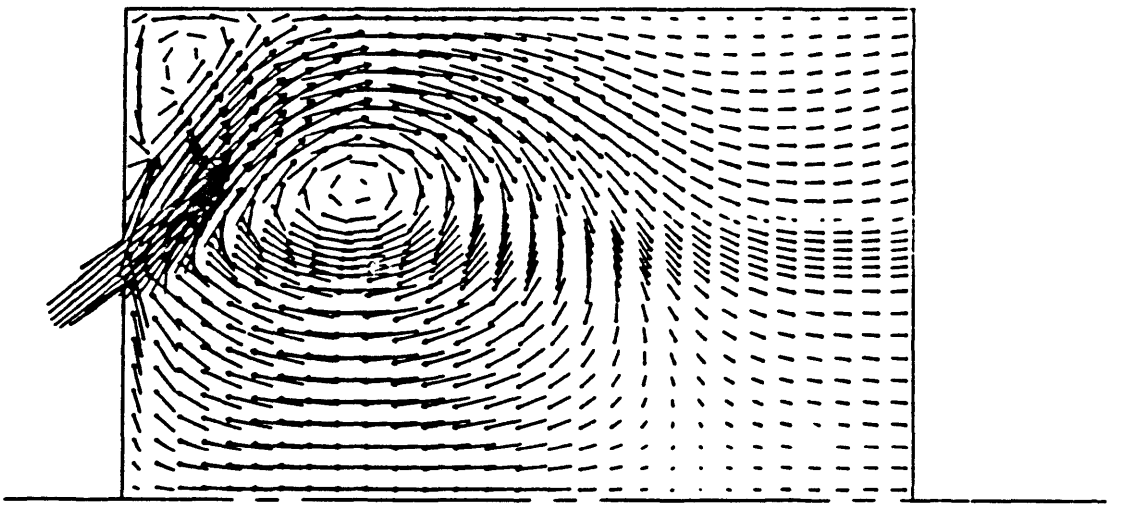

(a) Predicted flow structure at 90^{o} for case 1 of chapter 5

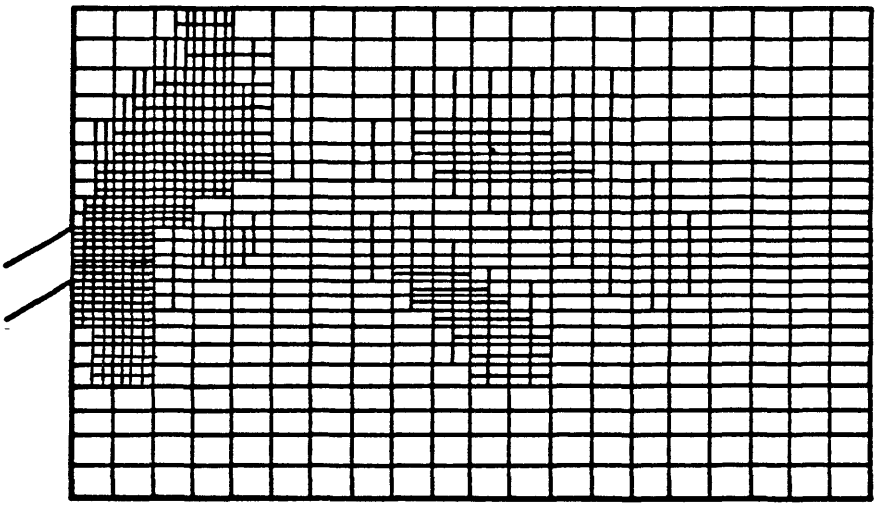

(b) Suggested grid for the flow structure of (a) showing regions of local refinement

Fig. 7.2 Representation of local grid refinement

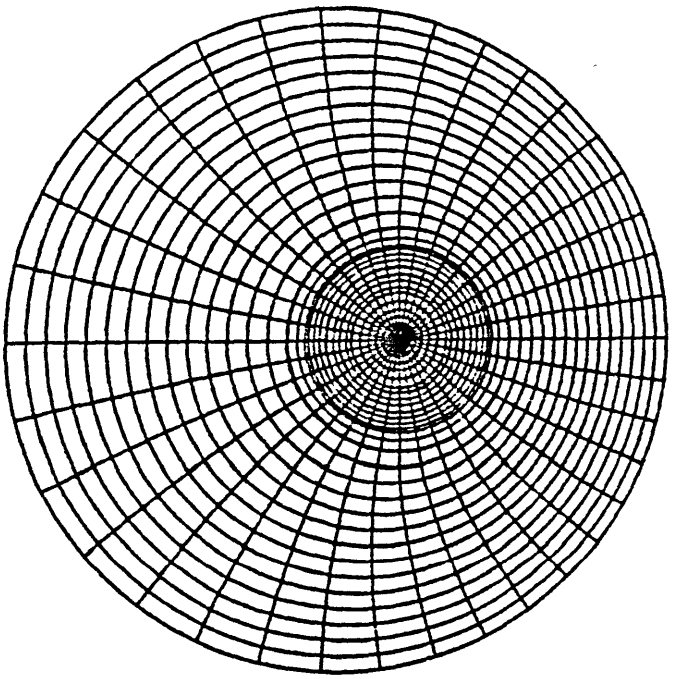

r-θ plane

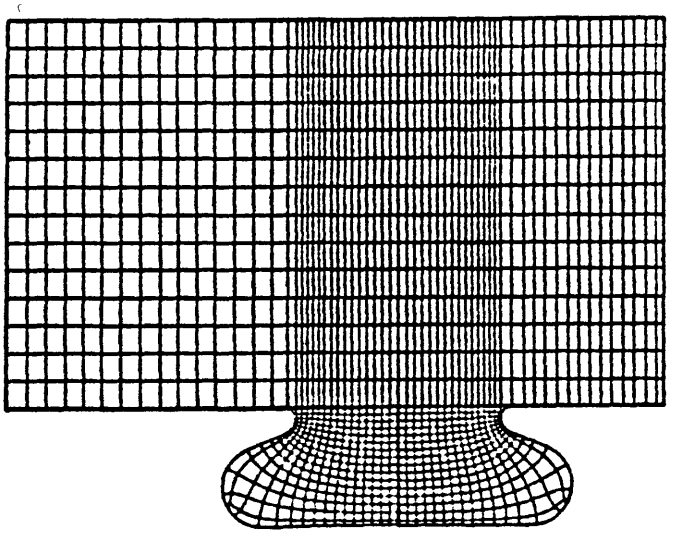

r-z plane

Fig. 7.3 Offset piston-bowl geometry showing computational grid

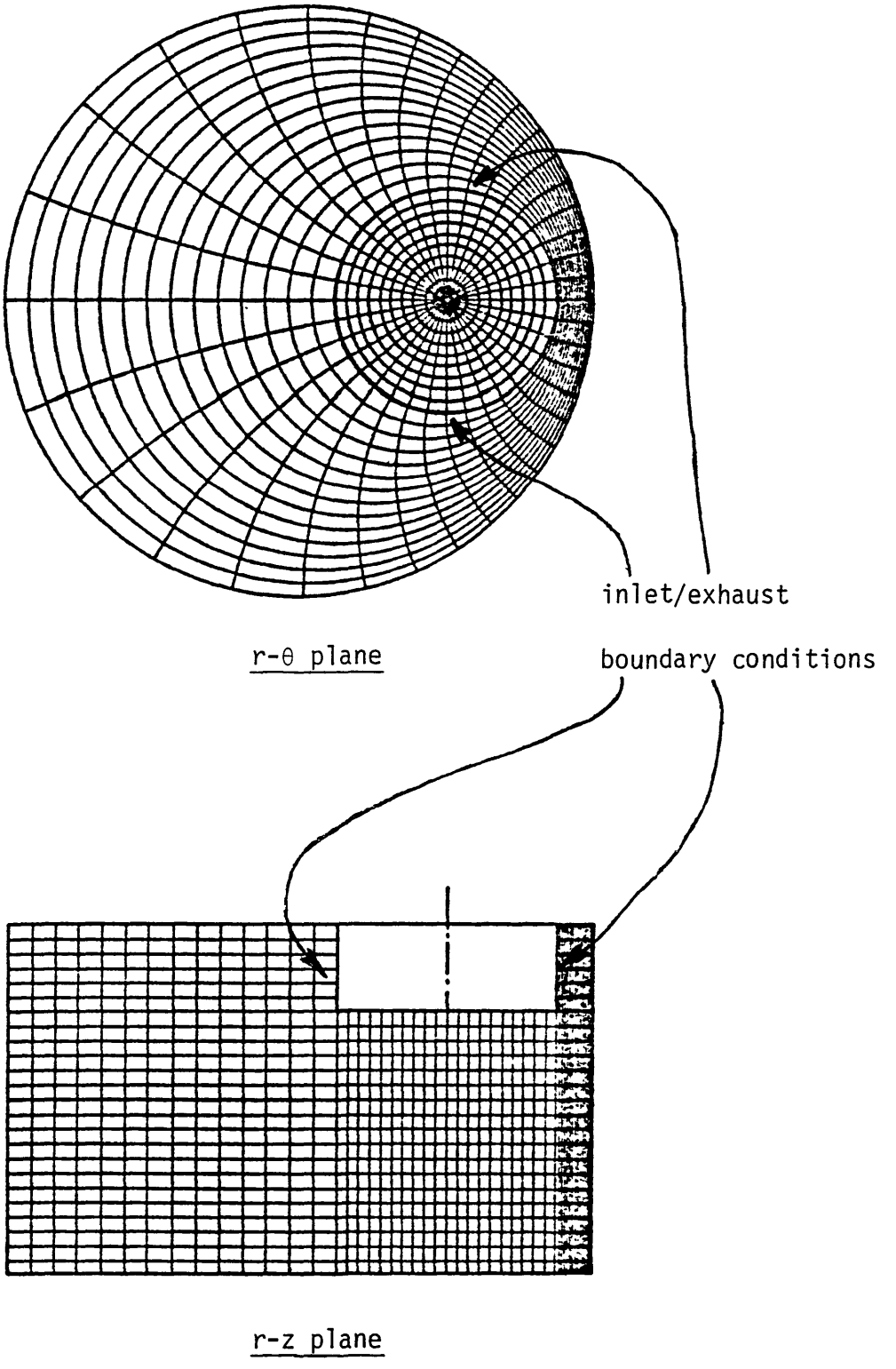

Fig. 7.4 Offset valve geometry showing computational grid

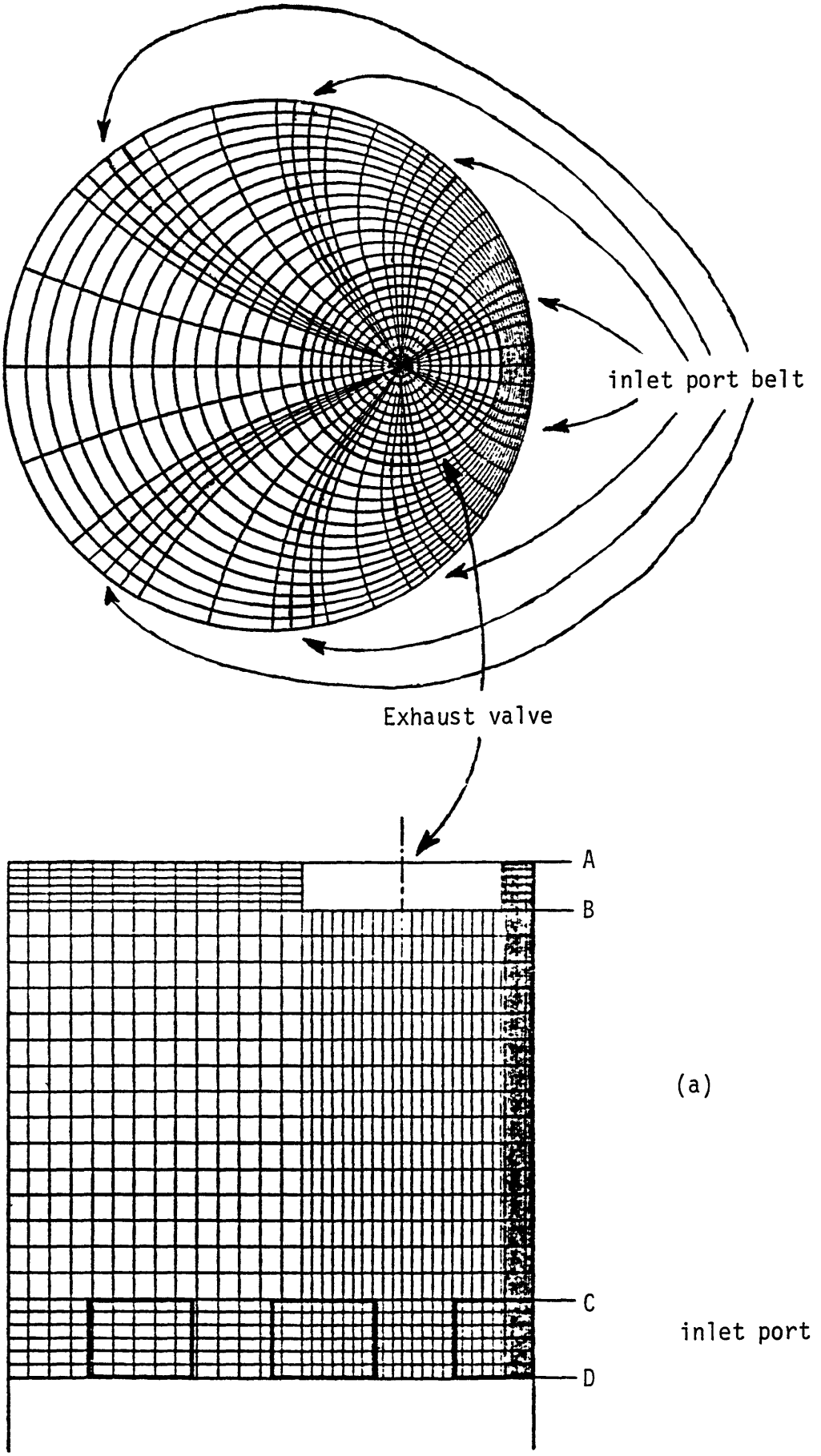

Fig. 7.5 Uniflow-scavenge two-stroke configuration showing proposed grid arrangement

Contd....

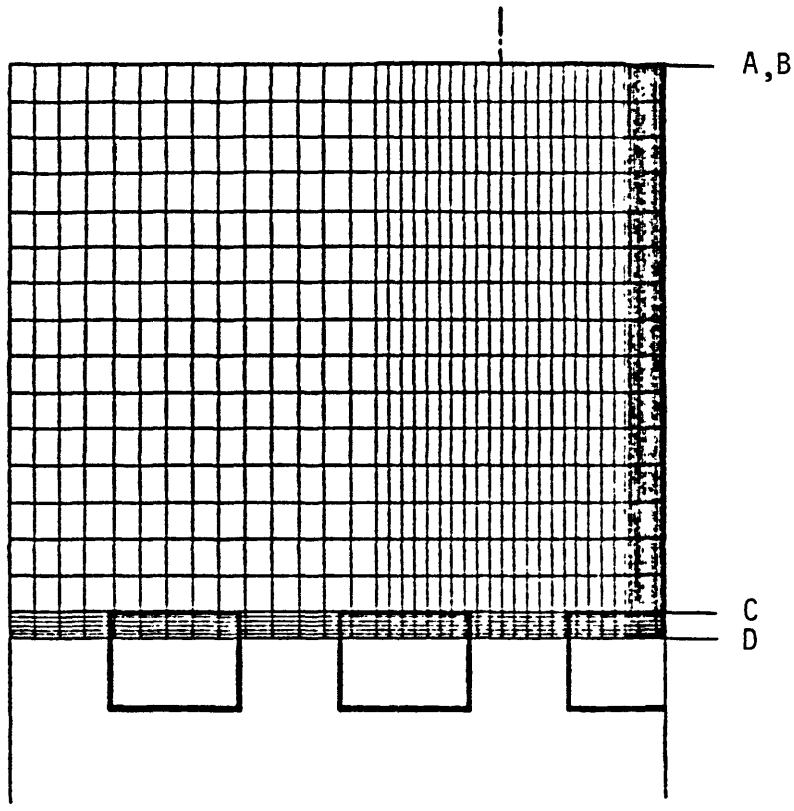

(b)

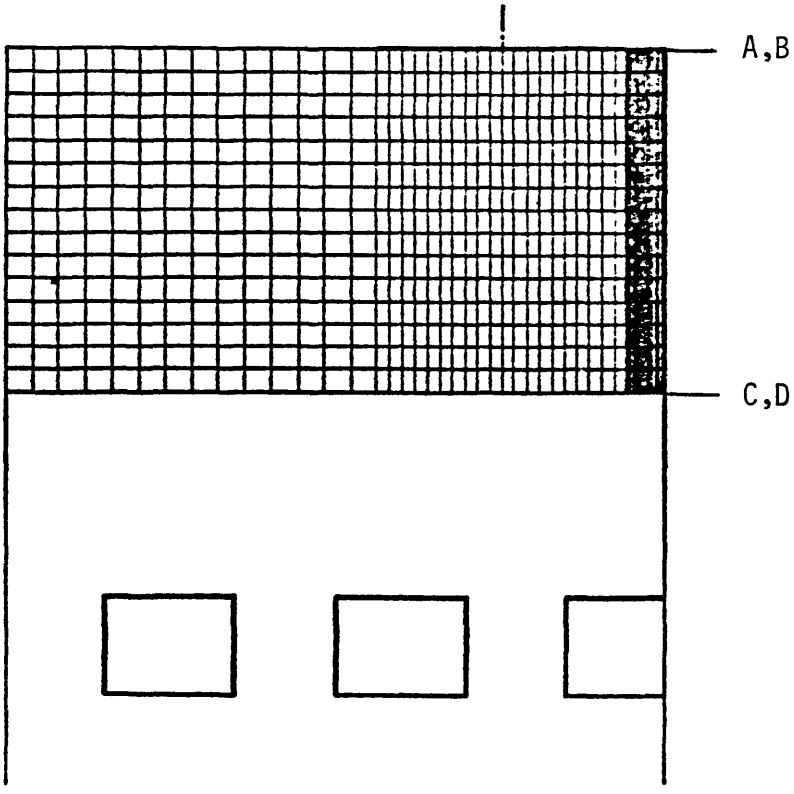

(c)

Fig. 7.5 Uniflow-scavenge two-stroke configuration showing proposed grid arrangement

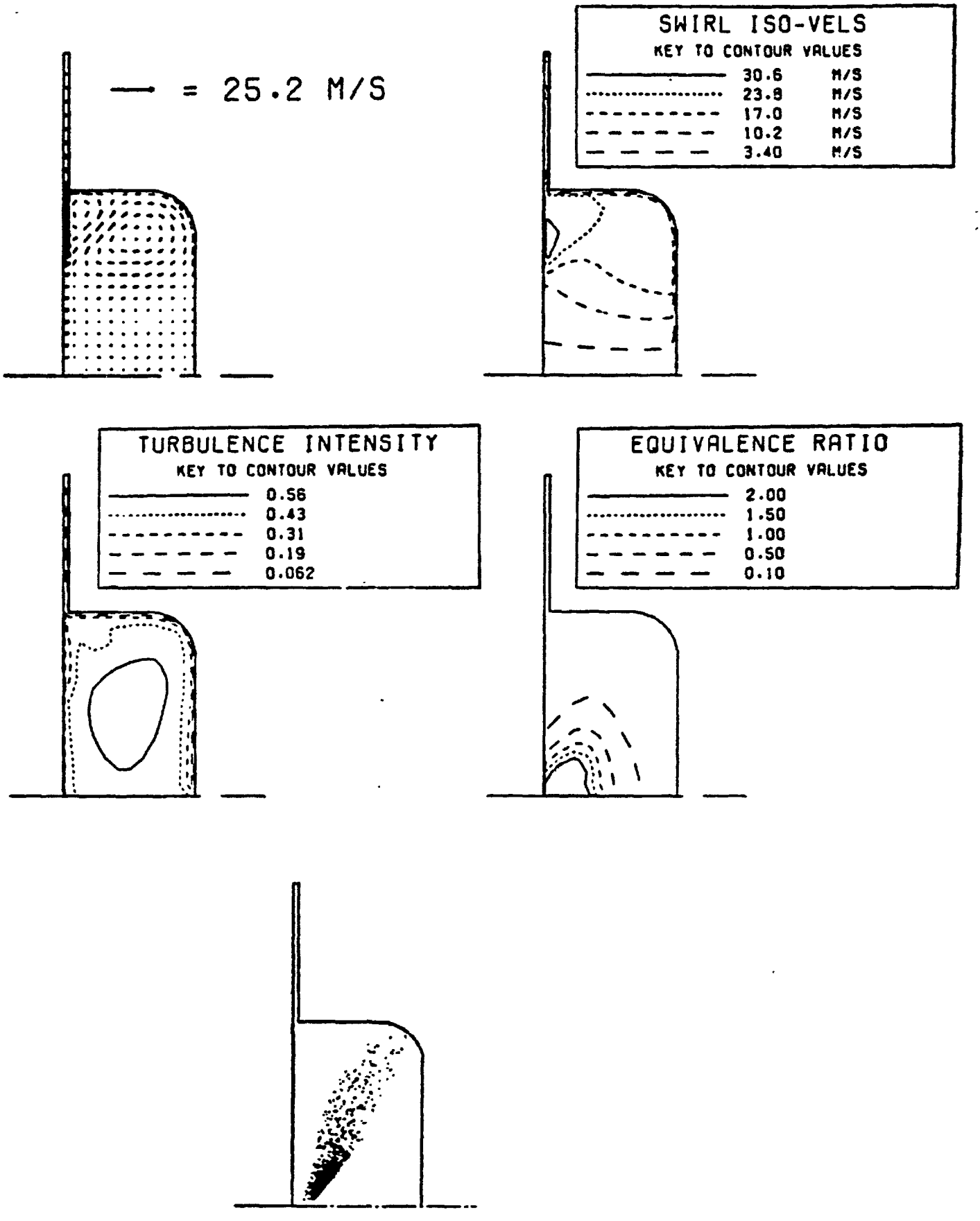

Fig. 7.6 Calculated fuel spray mixing at TDC using partially-coupled solution method (from Gosman and Johns, 1980)

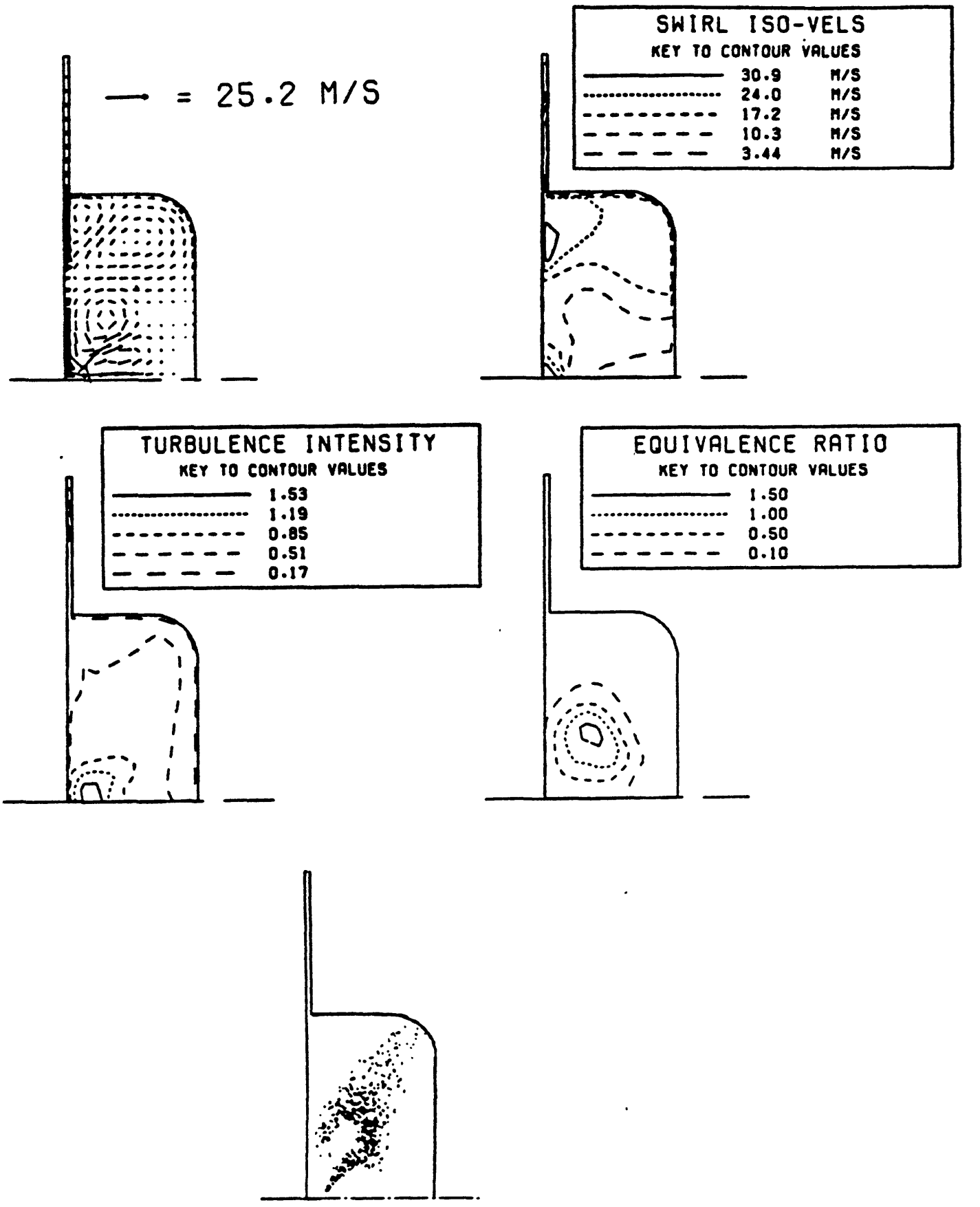

Fig. 7.7 Calculated fuel spray mixing at TDC using fully-coupled solution method (from Gosman and Johns, 1980)